

Analysis and design of plated structures

Related titles:

Inspection and monitoring techniques for bridges and civil structures

(ISBN-13: 978-1-85573-939-0; ISBN-10: 1-85573-939-9)

With the current emphasis on infrastructure rehabilitation and renewal, advanced techniques for bridge monitoring and assessment are of great interest to civil engineers and those researchers involved in the testing, inspection, management, planning, design, construction, maintenance and life extension of civil structures. The integration of these techniques can lead towards more realistic predictions of the time dependant performance of bridges and civil structures. The potential penalties for ineffective inspection can be catastrophic. The overall emphasis now is on a life extension approach which requires the effective use of NDE techniques and reliability monitoring. This comprehensive new book discusses those techniques requiring physical measurement for inspection and/or monitoring of structures.

Corrosion in reinforced concrete structures

(ISBN-13: 978-1-85573-768-6; ISBN-10: 1-85573-768-X)

In this authoritative new book the fundamental aspects of corrosion in concrete are analysed in detail. An overview of current monitoring techniques together with a discussion of practical applications and current numerical methods that simulate the corrosion process provides the civil and structural engineer with an invaluable guide to best practice when it comes to design aimed at minimising the effects of corrosion in concrete. The corrosion protective properties of concrete and modified cements are also discussed. The most frequently used stainless steels are examined together with an analysis of their reinforcement properties. Special attention is given to their handling and their welding requirements and the economics of their use. A comprehensive overview of surface treatments and corrosion inhibitors is presented alongside their practical applications as well as detailed coverage of electrochemical protection and maintenance techniques.

The deformation and processing of structural materials

(ISBN-13: 978-1-85573-738-9; ISBN-10: 1-85573-738-8)

This new study focuses on the latest research in the performance of a wide range of materials used in the construction of structures particularly structural steels. It considers each materials processing and its deformation behaviour in structural applications. This book will help engineers by providing them with a better understanding of the performance of the major structural materials (especially metals) under different conditions in order to select the right type of material for a job and for setting design specifications. It also shows how the microstructural composition of materials is affected by processing and what influence this has on its subsequent *in situ* performance. This book will be the first to give such comprehensive coverage to the deformation and processing of all types of structural materials and will be a valuable resource for researchers in mechanical, civil and structural engineering.

Details of these and other Woodhead Publishing materials books and journals, as well as materials books from Maney Publishing, can be obtained by:

- visiting our web site at www.woodheadpublishing.com
- contacting Customer Services (e-mail: sales@woodhead-publishing.com;
fax: +44 (0) 1223 893694; tel.: +44 (0) 1223 891358 ext. 30; address: Woodhead Publishing Limited, Abington Hall, Abington, Cambridge CB1 6AH, England)

If you would like to receive information on forthcoming titles, please send your address details to: Francis Dodds (address, tel. and fax as above; email: francisdd@woodhead-publishing.com). Please confirm which subject areas you are interested in.

Maney currently publishes 16 peer-reviewed materials science and engineering journals. For further information visit www.maney.co.uk/journals.

Analysis and design of plated structures

Volume 1: Stability

Edited by
N. E. Shanmugam and C. M. Wang

Woodhead Publishing and Maney Publishing
on behalf of
The Institute of Materials, Minerals & Mining

CRC Press
Boca Raton Boston New York Washington, DC

WOODHEAD PUBLISHING LIMITED
Cambridge England

Woodhead Publishing Limited and Maney Publishing Limited on behalf of
The Institute of Materials, Minerals & Mining

Published by Woodhead Publishing Limited, Abington Hall, Abington
Cambridge CB1 6AH, England
www.woodheadpublishing.com

Published in North America by CRC Press LLC, 6000 Broken Sound Parkway, NW,
Suite 300, Boca Raton, FL 33487, USA

First published 2006, Woodhead Publishing Limited and CRC Press LLC
© Woodhead Publishing Limited, 2006
The authors have asserted their moral rights.

This book contains information obtained from authentic and highly regarded sources. Reprinted material is quoted with permission, and sources are indicated. Reasonable efforts have been made to publish reliable data and information, but the authors and the publishers cannot assume responsibility for the validity of all materials. Neither the authors nor the publishers, nor anyone else associated with this publication, shall be liable for any loss, damage or liability directly or indirectly caused or alleged to be caused by this book.

Neither this book nor any part may be reproduced or transmitted in any form or by any means, electronic or mechanical, including photocopying, microfilming and recording, or by any information storage or retrieval system, without permission in writing from the Woodhead Publishing Limited.

The consent of Woodhead Publishing Limited does not extend to copying for general distribution, for promotion, for creating new works, or for resale. Specific permission must be obtained in writing from Woodhead Publishing Limited for such copying.

Trademark notice: Product or corporate names may be trademarks or registered trademarks, and are used only for identification and explanation, without intent to infringe.

British Library Cataloguing in Publication Data

A catalogue record for this book is available from the British Library.

Library of Congress Cataloguing in Publication Data

A catalog record for this book is available from the Library of Congress.

Woodhead Publishing ISBN-13: 978-1-85573-967-3 (book)
Woodhead Publishing ISBN-10: 1-85573-967-4 (book)
Woodhead Publishing ISBN-13: 978-1-84569-096-0 (e-book)
Woodhead Publishing ISBN-10: 1-84569-096-6 (e-book)
CRC Press ISBN-10: 0-8493-9545-3
CRC Press order number: WP9545

The publishers' policy is to use permanent paper from mills that operate a sustainable forestry policy, and which has been manufactured from pulp which is processed using acid-free and elementary chlorine-free practices. Furthermore, the publishers ensure that the text paper and cover board used have met acceptable environmental accreditation standards.

Project managed by Macfarlane Production Services, Dunstable, Bedfordshire
(macfarl@aol.com)

Typeset by Replika Press Pvt Ltd, India

Printed by T J International Limited, Padstow, Cornwall, England

Contributor contact details

(* = main contact)

Editors

Professor N. E. Shanmugam
Department of Civil and Structural
Engineering
Universiti Kebangsaan Malaysia
43600 UKM Bangi
Selangor Darul Ehsan
Malaysia

E-mail: shan@vlsi.eng.ukm.my

Professor C. M. Wang
Department of Civil Engineering
National University of Singapore
Blk E1A #07-03
1 Engineering Drive 2
Singapore 117576

E-mail: cviewcm@nus.edu.sg

Chapter 1

Professor Mark A. Bradford
School of Civil and Environmental
Engineering
The University of New South
Wales
Sydney
NSW 2052
Australia

E-mail: m.bradford@unsw.edu.au

Chapter 2

I. Shufrin and Professor
M. Eisenberger*
Faculty of Civil and Environmental
Engineering
Technion – Israel Institute of
Technology
Technion City
Israel

E-mail:

cvrmosh@techunix.technion.ac.il

Chapter 3

Professor W. Kanok-Nukulchai
School of Civil Engineering
Asian Institute of Technology
PO Box 4
Klong Luang
Pathumthani
12120
Thailand

E-mail: worsak@ait.ac.th

Chapter 4

Professor K. M. Liew*,
S. Kitipornchai and L. X. Peng
Department of Building and
Construction
City University of Hong Kong
Kowloon
Hong Kong
China

Chapter 5

Professor C. M. Wang
Department of Civil Engineering
National University of Singapore
Kent Ridge
Singapore 119260

E-mail: cvwcm@nus.edu.sg

Chapter 6

Professor J. N. Reddy and
R. A. Arciniega
Department of Mechanical
Engineering
Texas A&M University
College Station
TX 77843-3123
USA

E-mail: jnreddy@shakti.tamu.edu
rarciniega@tamu.edu

Chapter 7

Professor Hui-Shen Shen
School of Ocean and Civil
Engineering
Shanghai Jiao Tong University
Shanghai 200030
People's Republic of China

E-mail: hsshens@mail.sjtu.edu.cn

Chapter 8

Professor B. Uy
School of Civil, Mining and
Environmental Engineering
University of Wollongong
Wollongong
NSW 2522
Australia

E-mail: brianuy@uow.edu.au

Chapter 9

Dr Brian G. Falzon
Department of Aeronautics
Imperial College London
South Kensington Campus
London SW7 2AZ
UK

E-mail: b.falzon@imperial.ac.uk

Chapter 10

Professor Tsutomu Usami* and
Dr Hanbin Ge
Department of Civil Engineering
Nagoya University
Nagoya 464-8603
Japan

E-mail: usami@civil.nagoya-u.ac.jp
ge@civil.nagoya-u.ac.jp

Chapter 11

Professor N. E. Shanmugam
Department of Civil and Structural
Engineering
Universiti Kebangsaan Malaysia
43600 UKM Bangi
Selangor Darul Ehsan
Malaysia

E-mail: shan@vlsi.eng.ukm.my

Chapter 12

Professor Eiichi Watanabe*
Chawalit Machimdamrong and
Tomoaki Utsunomiya
Department of Civil Engineering
Kyoto University
Kyoto
Japan

E-mail: watanabe@str.kuciv.kyoto-
u.ac.jp

Masato Kano
Institute of System and Technology
JIP Techno Science Corporation
Kyoto
Japan

E-mail: kanou@jtslab.com

Tsutomu Kadotani
Japan Highway Public Corporation
Tokyo
Japan

Chapter 13

Professor J. S. Davidson
Department of Civil and
Environmental Engineering
The University of Alabama at
Birmingham
Hoehn Building
1075 13th Street South
Birmingham
AL 35294 – 4440
USA

E-mail: jdavidso@uab.edu

Chapter 14

Professor P. Ansourian
Department of Civil Engineering
The University of Sydney
Sydney 2006
Australia

E-mail:
p.ansourian@civil.usyd.edu.au

Chapter 15

Professor Jim Rhodes
Department of Mechanical
Engineering
University of Strathclyde
James Weir Building
75 Montrose Street
Glasgow G11XJ
UK

E-mail: jim.rhodes@strath.ac.uk

Preface

We have great pleasure in writing the preface for this book on *Analysis and Design of Plated Structures: Stability*, the first of the planned set of two volumes on plated structures. The inspiration for these books comes from the recognition of the significant advances that have taken place during the last few decades. As a result of the research findings, our understanding of the behaviour of thin-walled structural (or plate) elements has increased considerably. The improved understanding of the complex stability problems, in turn, has set new trends and caused major changes in the design codes in North America, Europe and Australia. Even the design philosophy has seen a major shift from the permissible stress basis to the concept of limit state; the Specifications concerned with the design of thin-walled structural elements are based on the vast amount of fundamental research findings. Research efforts continue in the field of post-elastic, post-buckling, and ultimate ranges and the benefit to be derived from the research outcomes depends on their effective implementation. It is necessary to remove the misconception amongst the designers and practitioners that solutions for stability problems are fraught with complexities and hence difficult to use in the design office. The objective of this book is to explain the current analytical methods, and to provide the theoretical background to the design specifications for plated structures.

This volume, dedicated to stability of plated structures, contains fifteen chapters, written by well-known experts who have made significant contributions in their relevant fields. Each topic is presented with sufficient introductory material in order to enable an engineering graduate, familiar with basic understanding of structural analysis and structural stability, to follow it without any difficulty. The first chapter addresses the lateral, or flexural-torsional buckling of tapered steel members in bending. Using the technique of ‘design by buckling analysis’, a design proposal is suggested that makes use of the elastic buckling curves, and which interfaces with existing rules for lateral buckling in either the BS5950 or the AS4100 codes. Elastic buckling of thick plates under variable in-plane loads is dealt with in Chapter 2. The effects of transverse shear deformation and the higher order nonlinear terms (curvature terms) on the buckling load are allowed for. Finite

element formulation for plate stability analysis is given in Chapter 3 in which a generic total Lagrangian formulation for nonlinear continuum mechanics is presented to degenerate plate equilibrium equations directly from the 3D field equations. A meshfree Galerkin method is introduced in Chapter 4 for the elastic buckling analysis of stiffened plates and stiffened and un-stiffened corrugated plates. The stiffened plates are modelled as composite structures that combine the plates and stiffeners by imposing displacement compatible conditions between them. Chapter 5 deals with plastic buckling of thick plates under in-plane compressive stresses. Analytical plastic stability criteria are presented for plates with various plan shapes, boundary and inplane loading conditions.

Mechanical and thermal buckling of functionally graded ceramic-metal plates is treated in Chapter 6 whilst Chapter 7 describes a fully nonlinear thermal postbuckling analysis of laminated plates. Local and interaction buckling of plated structures in composite steel-concrete construction are treated in Chapter 8 in which some recommendations on design approaches are also presented. The possibility of designing lightweight postbuckling aircraft structures, without compromising on structural integrity, paves the way for the development of significantly lighter airframes. Experimental and finite element results presented in Chapter 9 explain the behaviour of this form of structure. Strength and ductility research findings related to thin-walled steel members and structures are summarised in Chapter 10. It covers isolated plates, stub-column segments and cantilever-typed columns, subjected to compression, bending, combined compression and bending as well as shear loadings. Both monotonic and cyclic loading conditions have been considered. An analytical method to predict the behaviour of in-filled columns is presented in Chapter 11. Effects of local buckling in the side-walls of the column are accounted for in terms of effective width. In Chapter 12, the analysis for buckling strength in corrugated webs is presented. Materially and geometrically nonlinear analysis is formulated to evaluate elasto-plastic buckling loads. Recent analytical research conducted in the United States on the influence of curvature induced distortion and warping on the strength and stability of curved plate girders used in roadway bridge superstructures is described in Chapter 13. Challenges associated with transporting, lifting, and erecting are described since construction loads are applied when the girder is in minimally braced configurations and therefore is most susceptible to local and global instabilities. Chapter 14 is concerned with the buckling failure of metal structures generally formed of curved plates. These structures are typically used in the liquid and bulk material storage industries, pressure vessels, aerospace vehicles, and in many other contexts. Analysis and design of pressure vessel closures which surprisingly may sustain buckling failure under internal pressure followed by a consideration of buckling under external pressure are the highlights in this chapter. The last chapter examines the

various types of elastic buckling which arise in the behaviour of light gauge steel structural members such as beams and columns. The examination considers only elastic buckling behaviour and its effects on the stiffness and strength of thin plates and members.

We are grateful to all the contributors for their willing participation and for the cooperation they have extended to us in producing this volume. It is hoped that the book will prove stimulating both to the researchers and practising engineers.

N. E. Shanmugam
C. M. Wang

Lateral buckling of tapered steel members

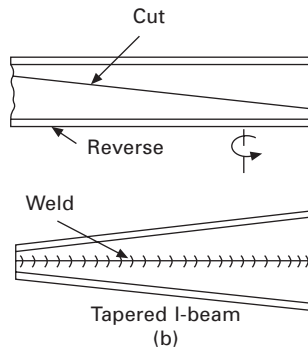
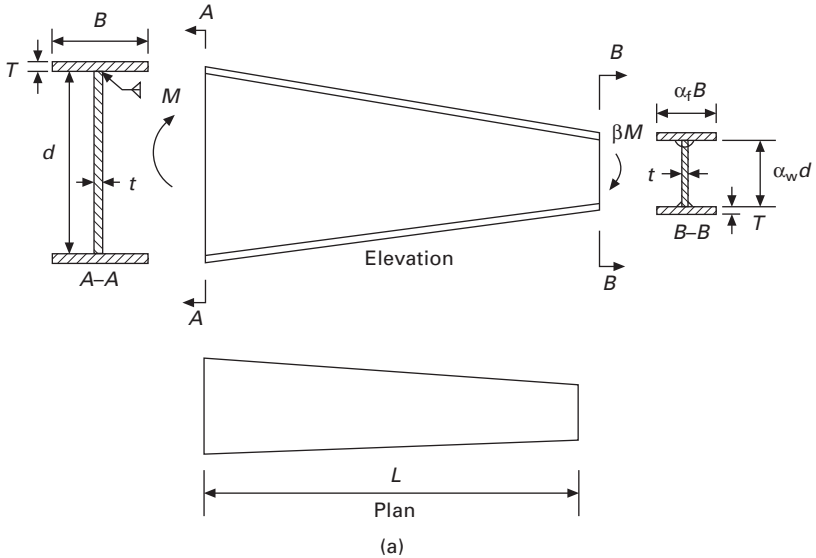
M A B R A D F O R D, The University of New South Wales,
Australia

1.1 Introduction

The modern use of plated structures means that the cross-sectional and lengthwise profiles for a given member may be optimised by welding tapered plates together. Figure 1.1 shows two ways in which a web-tapered member may be manufactured: the first is by welding two flanges to a tapered web plate, while the second shows a diagonal cut through the web of a hot-rolled I-section member, the rotation of the relative portions of the cut member, and its re-welding to produce a tapered profile. The concept of efficient steel design with tapered members is not new (Amirikian 1952), and nowadays web-tapered members of this type find widespread contemporary use in steel portal-frame structures (Woolcock *et al.* 1999), since the deeper flanged portions may be utilised in the high moment regions (at the portal frame eaves) in order to economise the use of steel. However, because members with welded plates are relatively slender, their strength is often governed by lateral (or flexural-torsional) buckling.

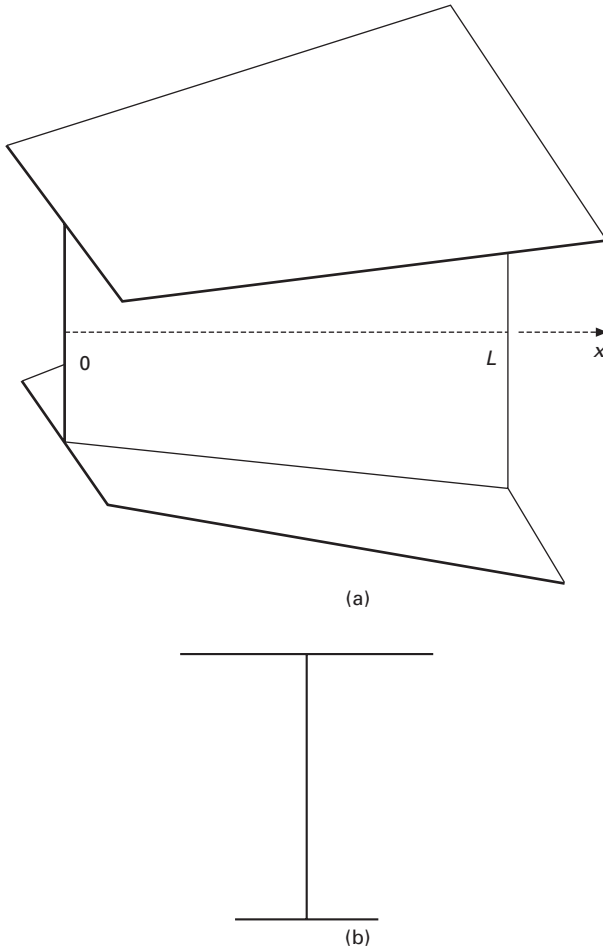
Figure 1.2 shows a generic tapered member, which in a mathematical representation can be thought of as comprising a domain $\Omega \in \mathcal{R}^3$, where $\Omega = \Psi \cup \Lambda$. The subdomain $\Psi \in \mathcal{R}^2$ is the cross-section, which may be monosymmetric as shown in Fig. 1.2, while the subdomain $\Lambda \in \mathcal{R}^1$ represents the member length L , which may be expressed as $\Lambda = [0, L]$, with a cross-section $\Psi(x)$ being defined as that at a position $x \in \Lambda = [0, L]$. A conventional hot-rolled I-section member would be prismatic, in the sense that the cross-section is constant along the member ($d\Psi/dx \equiv 0 \quad \forall x \in \Lambda$). At the other extreme, the cross-section may be monosymmetric, and with both its width and depth changing along the member, so that $d\Psi/dx \neq 0 \quad (x \in \Lambda)$. In principle, with automated fabrication techniques, it is conceivable that a member could be manufactured by tapering its flange widths and web depth in this way to optimise the member of structure with regard to cost, weight, overall depth, or the like.

Research work on the lateral buckling of tapered steel members has been



1.1 Web-tapered beams: (a) welded tapered beam; (b) tapered beam fabricated from a universal beam.

reasonably plentiful, with Kitipornchai and Trahair (1972) presenting a detailed review of research in the area prior to 1971. Most of the treatments of the lateral buckling of tapered members have made recourse to numerical formulations, as closed-form solutions do not in general exist, even if some sweeping simplifying assumptions are made. Some research findings can be found in the work of Lee *et al.* (1972), Nethercot (1973a,b), Morrell and Lee (1974), Taylor *et al.* (1974), Horne and Morris (1977), Horne *et al.* (1979), Brown (1981), Nakane (1984), Wekezer (1985), Bradford and Cuk (1988), Bradford 1988a,b, 1989), Chan (1990), Trahair (1993), Ronagh and Bradford (1994a,b, 1996, 1999) and Ronagh *et al.* (2000a,b). Some of the more recent and rigorous studies have identified some anomalies between solutions for



1.2 Arbitrary tapered monosymmetric structural member: (a) complete tapered monosymmetric member; (b) cross-sectional domain $\Psi(x)$

web-tapered I-section members developed by earlier researchers, and the most profound anomaly was found to be as a result of the omission of an important term in the formulation of the buckling analysis of web-tapered members. This issue has been addressed by Ronagh and Bradford (1994a).

This chapter aims to provide an insight into the lateral buckling of a tapered steel member under transverse loading. Following a discussion of the mechanics of the problem from a mathematical standpoint, a simple finite element beam-type formulation for the problem is then derived, and this simple model has been shown to agree with the more sophisticated nonlinear treatment. The chapter then considers how the concept of ‘design by buckling

analysis' allows for the easy calculation of the design strength of a tapered member, which is consistent with national design codes of practice.

1.2 Nonlinear finite element formulation

In a linear stiffness analysis (that will be shown in Section 1.3 to provide satisfactory solutions for tapered members), the products of displacement derivatives that arise in the derivation are small in comparison with the displacement derivatives themselves, and are ignored. Because of this, the stiffness equations are linearised, resulting in a conventional stiffness analysis in which the stiffness matrix is independent of the buckling displacements.

The 14 degrees of freedom of a finite element are shown in Fig. 1.3. In this nonlinear analysis, it is necessary to determine the secant stiffness matrix $[K_s]$ and the tangent stiffness matrix $[K_t]$. When these are established, the first and second variations of the total potential can be written respectively as:

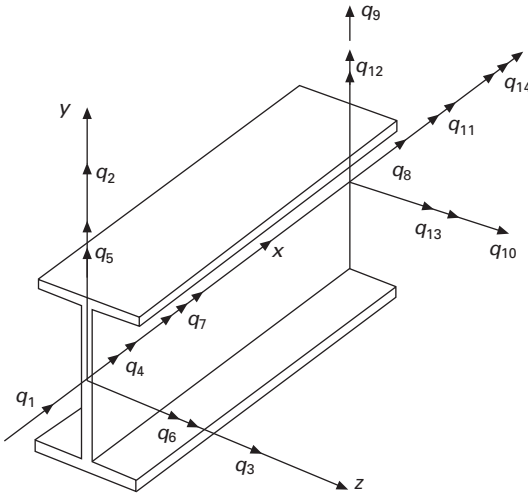
$$\delta\Pi = \{\delta q\}^T([K_s]\{q\} - \{Q\}) \tag{1.1}$$

$$\delta^2\Pi = \frac{1}{2}\{\delta q\}[K_t]\{\delta q\} \tag{1.2}$$

where $\delta(\cdot)$ is the Lagrange operator of simultaneous variations, with total equilibrium being identified as:

$$\{Q\} = [K_s]\{q\} \tag{1.3}$$

$$\{\Delta Q\} = [K_t]\{\Delta q\} \tag{1.4}$$



1.3 Fourteen degrees of freedom nonlinear finite element.

in which $\{Q\}$ is the vector of external loads and $\{\Delta Q\}$ is the increment of this load vector, $\{q\}$ is the displacement vector and $\{\Delta q\}$ is the increment in this vector, with $\{q\} = \langle q_1, q_2, \dots, q_{14} \rangle^T$ in Fig. 1.3. The tangent and secant stiffness matrices can be decomposed (Ronagh and Bradford 1999) into the forms

$$[K_s] = [K_0] + [L_1] + [L_2] + [M_1] + [M_2] \quad 1.5$$

$$\begin{aligned} [K_t] = [K_0] + [L_1] + 2[L_2] + 2([M_1] + [M_1]^T) \\ + 2([M_2] + [M_2]^T) + [N] \end{aligned} \quad 1.6$$

where $[K_0]$ is the conventional linear stiffness matrix, $[L_1]$ is the symmetric first-order initial stress matrix, $[L_2]$ is the symmetric second-order initial stress matrix, $[M_1]$ is the nonsymmetric first-order initial displacement matrix, $[M_2]$ is the non-symmetric second-order initial displacement matrix, and $[N]$ is a symmetric mixed matrix that contains some coupling terms. The terms in $[L_1]$ can be extracted from the derivation of $\delta\Pi$, giving:

$$\begin{aligned} \delta\Pi^{[L_1]} = \int_0^L N \left[\left(v_{0,x} \delta v_{0,x} + w_{0,x} \delta w_{0,x} + \frac{I_p}{A} \phi_{,x} \delta \phi_{,x} \right) \right. \\ \left. + M_{\bar{y}} (\phi \delta v_{0,xx} + v_{0,xx} \delta \phi) + M_{\bar{z}} (\phi \delta w_{0,xx} + w_{0,xx} \delta \phi) \right] dx \\ - M_{y0} [\phi(0) \delta v_{0,x}(0) + v_{0,x}(0) \delta \phi(0)] \\ - M_{yL} [\phi(L) \delta v_{0,x}(L) + v_{0,x}(L) \delta \phi(L)] \\ - M_{z0} [\phi(0) \delta w_{0,x}(0) + w_{0,x}(0) \delta \phi(0)] \\ - M_{zL} [\phi(L) \delta w_{0,x}(L) + w_{0,x}(L) \delta \phi(L)] \\ + (P_{y0} a_{y0} + P_{z0} a_{z0}) \phi(0) \delta \phi(0) \\ + (P_{yL} a_{yL} + P_{zL} a_{zL}) \phi(L) \delta \phi(L) \end{aligned} \quad 1.7$$

where a comma denotes partial differentiation with respect to the corresponding coordinates, and in which u_0 , v_0 , w_0 are the displacements of an arbitrary point $0 \in \Psi$ (recalling the member domain $\Omega = \Psi \cup \Lambda$), and where

$$N = AE \left[u_{0,x} + \frac{1}{2} (v_{0,x})^2 + \frac{1}{2} (w_{0,x})^2 \right] + \frac{1}{2} EI_p (\phi_{,x})^2 \quad 1.8$$

$$M_{\bar{y}} = -EI_y (w_{0,xx} - v_{0,xx} \phi) \quad 1.9$$

$$M_{\bar{z}} = EI_z (v_{0,xx} - w_{0,xx} \phi) \quad 1.10$$

in which $(\cdot)_{,x} \equiv d(\cdot)/dx$ and A , I_p , I_y and I_z are properties of the cross-section Ψ , viz. its area, polar moment of area and principal second moments of area respectively. In a similar fashion, $[L_2]$ can be extracted from $\delta\Pi$, producing

$$\begin{aligned}
\delta\Pi^{[L_2]} = & \int_0^L \left[M_{\bar{y}} \left(w_{0,xx} \phi \delta\phi + \frac{1}{2} \phi^2 \delta w_{0,xx} \right) \right. \\
& \left. - M_{\bar{z}} \left(v_{0,xx} \phi \delta\phi + \frac{1}{2} \delta^2 \delta v_{0,xx} \right) \right] dx \\
& - M_{y0} \left[w_{0,x}(0) \phi(0) \delta\phi(0) + \frac{1}{2} \phi^2(0) \delta w_{0,x}(0) \right] \\
& - M_{yL} \left[w_{0,x}(L) \phi(L) \delta\phi(L) + \frac{1}{2} \phi^2(L) \delta w_{0,x}(L) \right] \\
& + M_{z0} \left[v_{0,x}(0) \phi(0) \delta\phi(0) + \frac{1}{2} \phi^2(0) \delta v_{0,x}(0) \right] \\
& + M_{zL} \left[v_{0,x}(L) \phi(L) \delta\phi(L) + \frac{1}{2} \phi^2(L) \delta v_{0,x}(L) \right] \quad 1.11
\end{aligned}$$

in which

$$M_{\bar{y}} = -EI_y w_{0,xx} \quad M_{\bar{z}} = EI_z v_{0,xx} \quad 1.12$$

and the first and second-order initial displacement matrices can be extracted from $\delta\Pi$, giving

$$\begin{aligned}
\delta\Pi^{[M_1]} = & \int_0^L \left\{ AE \left[\frac{1}{2} (v_{0,x})^2 + \frac{1}{2} (w_{0,x})^2 + \frac{1}{2} \frac{I_p}{A} (\phi_{,x})^2 \right] \delta u_{0,x} \right. \\
& \left. + EI_z (w_{0,xx} \phi) \delta v_{0,xx} - EI_y (v_{0,xx} \phi) \delta w_{0,xx} \right\} dx \quad 1.13
\end{aligned}$$

$$\begin{aligned}
\delta\Pi^{[M_2]} = & \int_0^L \left\{ -\frac{1}{2} EI_z v_{0,xx} \phi^2 \delta v_{0,xx} - \frac{1}{2} EI_y w_{0,xx} \phi^2 \delta w_{0,xx} \right. \\
& \left. + \frac{1}{2} EI_t (\phi_{,x})^3 \delta \phi_{,x} \right\} dx \quad 1.14
\end{aligned}$$

in which

$$I_t = \frac{1}{2} \left\{ \int_A (y^2 + z^2) dA - \frac{(I_p)^2}{A} \right\} \quad 1.15$$

with y and z being measured from the arbitrary point $0 \in \Psi$. Finally, the terms that lead to the matrix $[N]$ can be extracted from the second variation of the potential $\delta^2\Pi$, leading to the formulation

$$\delta^2 \Pi^{[N]} = \frac{1}{2} \int_0^L \left[\begin{aligned} & AE(v_{0,x})^2 (\delta v_{0,x})^2 + AE(w_{0,x})^2 (\delta w_{0,x})^2 \\ & + 2AE(v_{0,x} w_{0,x}) (\delta v_{0,x} \delta w_{0,x}) + EI_c (\phi_{,x})^2 (\delta \phi_{,x})^2 \\ & + 2EI_p (\phi_{,x} v_{0,x}) (\delta \phi_{0,x} \delta v_{0,x}) \\ \times & + 2EI_p (\phi_{,x} w_{0,x}) (\delta \phi_{,x} \delta w_{0,x}) + (EI_y - EI_z) \phi^2 (\delta v_{0,xx})^2 \\ & + (EI_z - EI_y) \phi^2 (\delta w_{0,xx})^2 + \{EI_z (w_{0,xx})^2 \\ & + EI_y (v_{0,xx})^2\} (\delta \phi)^2 + 2EI_y \phi v_{0,xx} (\delta v_{0,xx} \delta \phi) \\ & + 2EI_z \phi w_{0,xx} (\delta w_{0,xx} \delta \phi) \end{aligned} \right] dx \quad 1.16$$

in which

$$I_c = \frac{1}{2} \left\{ \frac{3(I_p)^2}{A} - \int_A (y^2 + z^2)^2 dA \right\} \quad 1.17$$

The expressions given above may be used to assemble the matrices in Eqs. (1.5) and (1.6) for implementation into the nonlinear incremental stiffness relationships, and many standard algorithms have been developed as solution strategies. It is worth noting that Eqs. (1.7) and (1.11) contain boundary terms, whose importance has been discussed by Ronagh and Bradford (1994a). These boundary matrices are applicable only in rare cases, but Ronagh and Bradford (1994a) argued that their omission can lead to erroneous results, particularly in the much-cited early finite element formulation of Barsoum and Gallagher (1970). Trahair (1993) also has made note of the effect of the boundary terms in his text.

Although the nonlinear finite element technique described in this section is applicable to a large number of elastic analyses of thin-walled open section members, its formulation is somewhat difficult and tedious. Because of this, a linearised formulation, based on a more heuristic structural approach in deference to the mathematical one described above, is developed in the following section. Ronagh *et al.* (2000a,b) have shown that the linearised formulation produces good results for the buckling of tapered beams when compared with the nonlinear formulation.

1.3 Linear finite element formulation

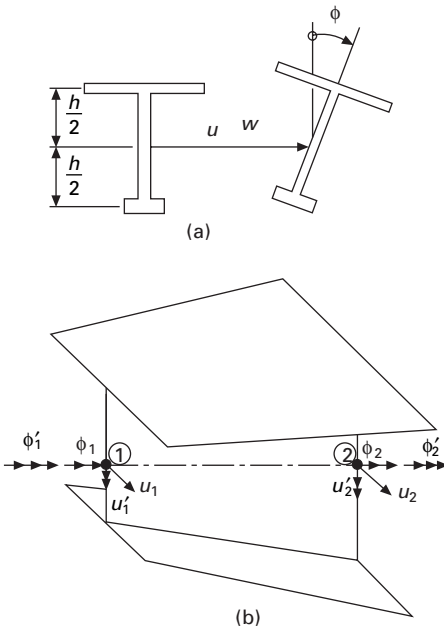
In the present formulation, the assumption is made that the in-plane and out-of-plane (buckling) deformations are uncoupled in Eqs. (1.1) and (1.2). When

this is done, Eq. (1.1) can be written in the linearised form:

$$[K_s]_i \{q\}_i = \{Q\}_i \tag{1.18}$$

where the subscript $(\cdot)_i$ denotes the in-plane value, and this equation may be solved routinely as in the familiar stiffness method of analysis to determine the in-plane actions within the member. The vector of out-of-plane (buckling) displacements $\{w\}$ is shown for a cross-section in Fig. 1.4, and the usual Vlasov assumption is made that the cross-section does not deform during buckling. Hence $\{w\} \in \Lambda$, and has the form:

$$\{w\} = \begin{Bmatrix} w \\ \phi \end{Bmatrix} \tag{1.19}$$



1.4 Deformations of linear element: (a) deformations in the cross-sectional plane; (b) nodal displacements.

which can be written in finite element terminology as

$$\{w\} = [M(x)]\{\alpha\}_b \tag{1.20}$$

where $[M(x)]$ is a cubic interpolation matrix, and $\{\alpha\}_b$ is a vector of kernel buckling (out-of-plane) degrees of freedom. If the vector of structural buckling degrees of freedom is:

$$\{q\}_b = \langle w(0), w(L), w_{,x}(0), w_{,x}(L), \phi(0), \phi(L), \phi_{,x}(0), \phi_{,x}(L) \rangle^T \tag{1.21}$$

then writing

$$[M(x)] = \begin{bmatrix} L & L\xi & L\xi^2 & L\xi^3 & 0 & 0 & 0 & 0 \\ 0 & 0 & 0 & 0 & 1 & \xi & \xi^2 & \xi^3 \end{bmatrix} \quad 1.22$$

in which $\xi = x/L$, leads to Eq. (1.20) becoming

$$\{w\} = [M(x)] \begin{bmatrix} 1/L & 0 & 0 & 0 & 0 & 0 & 0 & 0 \\ 0 & 0 & 1 & 0 & 0 & 0 & 0 & 0 \\ -3/L & 3/L & -2 & -1 & 0 & 0 & 0 & 0 \\ 2/L & -2/L & 1 & 1 & 0 & 0 & 0 & 0 \\ 0 & 0 & 0 & 0 & 1 & 0 & 0 & 0 \\ 0 & 0 & 0 & 0 & 0 & 0 & L & 0 \\ 0 & 0 & 0 & 0 & -3 & 3 & -2L & -L \\ 0 & 0 & 0 & 0 & 2 & -2 & L & L \end{bmatrix} \{q\}_b$$

$$= [M(x)][A]\{q\}_b \quad 1.23$$

The buckling of the cross-section at $x \in \Lambda$ shown in Fig. 1.4 can be thought of as two flanges that undergo membrane and bending deformations during buckling, and a web that undergoes only flexural action during buckling. The resistance to the flange membrane actions is provided by the flange minor axis second moments of area I_{y1} and I_{y2} and to flexural actions by the Saint Venant torsion constants J_1 and J_2 . The resistance of the web to flexural action is provided by its second moment of area about its mid-plane, which is considered negligible and ignored in comparison to I_{y1} and I_{y2} , and by its Saint Venant torsion constant J_w . The increase in strain energy from the prebuckled configuration due to out-of-plane buckling can then be written by modifying the formulation in Trahair (1993) as:

$$U = \frac{1}{2} \int_0^L [EI_{y1}(w_{1,xx})^2 + EI_{y2}(w_{2,xx})^2 + (GJ_1 + GJ_2 + GJ_w)(\phi_{,x})^2] dx \quad 1.24$$

in which

$$1.25$$

where h is the distance between the flange centroids. The substitution of Eq. (1.25) into Eq. (1.24) produces:

$$U = \frac{1}{2} \int_0^L \left[\begin{aligned} &(EI_{y1} + EI_{y2})(w_{,xx})^2 + (h_{,x})^2(EI_{y1} + EI_{y2})(\phi_{,x})^2 \\ &+ \frac{h^2}{4}(EI_{y1} + EI_{y2})(\phi_{,xx})^2 + 2h_{,x}(EI_{y1} - EI_{y2})(w_{,xx}\phi_{,x}) \\ &+ h(EI_{y1} - EI_{y2})(w_{,xx}\phi_{,xx}) + hh_{,x}(EI_{y1} + EI_{y2})(\phi_{,x}\phi_{,xx}) \\ &+ GJ(\phi_{,x})^2 \end{aligned} \right] dx \quad 1.26$$

and when the appropriate substitutions for w , ϕ and its derivatives are made, Eq. (1.26) becomes

$$U = \frac{1}{2} \{q\}_b^T [k]_b \{q\}_b \quad 1.27$$

where $[k]_b$ is a linear buckling stiffness matrix presented explicitly by Bradford and Cuk (1988), and is independent of the buckling deformations.

The kinematics of the buckling displacements may be established using a general theory based on geometric algebra set out by Bradford and Pi (2004) for an arbitrary member curved in space. For a centroidal axis system (with the coordinate $-\bar{y}$ being that of the web mid-height at which the angle of twist is taken), then each fibre F ($F \in \Omega$) of area $\delta A \in \Psi$ and length $\delta x \in \Lambda$ deflects laterally and becomes inclined to its original position. The web mid-height O displaces laterally by w to a new position O^* , and a general point $P \in \Psi$ on the cross-section displaces laterally by w to O^* , and then rotates through an angle ϕ to the position P^* . The coordinates of P are (z, y) and those of P^* are $[z + w - (y + \bar{y})\phi, y + z\phi]$. The displacements in the z and y directions are therefore $[w - (y + \bar{y})\phi, z\phi]$, as shown in Fig. 1.5(a), leading to the rotations of the fibre F through P^* being

$$\theta_y = \frac{d}{dx} [w - (y + \bar{y})\phi] = w_{,x} - (y + \bar{y})\phi_{,x} \quad 1.28$$

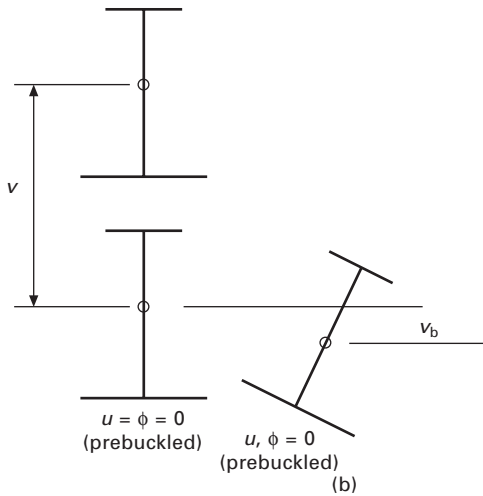
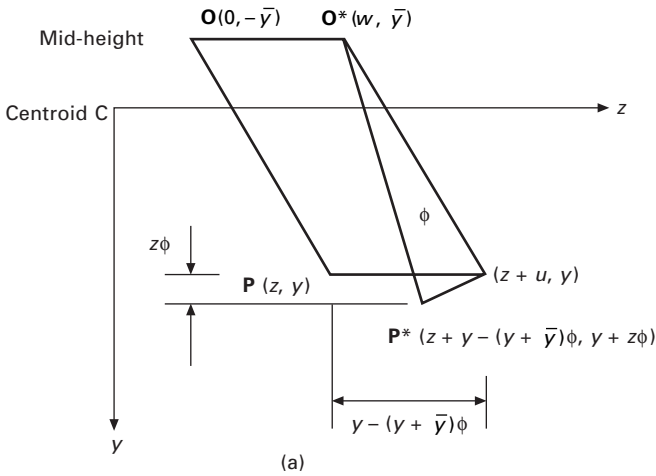
$$\theta_z = \frac{d}{dx} [z\phi] = z\phi_{,x} \quad 1.29$$

When a fibre of length δx rotates through an angle θ , there is an axial shortening $\delta\Delta$ given by

$$\delta\Delta = \delta x - \delta x \cos \theta \quad 1.30$$

so that, to order $0(\theta^3)$ accuracy,

$$\delta\Delta = \frac{1}{2}(\theta)^2 \delta x \quad 1.31$$



1.5 Buckling displacements of linear element: (a) axis system and longitudinal fibre displacement; (b) buckling displacement v_b .

At a buckling load factor of λ , the fibre with an axial force λN shortens owing to the buckling kinematics and so work is done. The axial force on the fibre F is $(\lambda N/A)\delta A$, and so the work done by the axial force over a length dx is:

$$dV^N = \frac{\lambda N}{A} \delta A \left(\frac{1}{2} \theta_y^2 + \frac{1}{2} \theta_z^2 \right) dx \quad 1.32$$

If this expression is now integrated over the whole domain of the element Ω ,

and use is made of the centroidal properties for the cross-sectional domain Ψ that

$$\int_A y dA = 0; \quad \int_A y^2 dA = I_z; \quad \int_A z^2 dA = I_y \quad 1.33$$

then the work done by the axial force λN during buckling can be obtained by integrating Eq. (1.32) to produce

$$V^N = \frac{1}{2} \int_0^L \lambda N [(w_{,x})^2 - 2\bar{y} w_{,x} \phi_{,x} + (r_0^2 + \bar{y}^2)(\phi_{,x})^2] dx \quad 1.34$$

in which r_0 is the polar radius of gyration.

The applied major axis bending moment λM_z causes the monosymmetric section to twist and, when coupled with shears, causes an additional buckling deflection v_b in the plane of symmetry. The moment creates a longitudinal bending stress given by

$$\lambda \sigma_b = \frac{-\lambda M_z y}{I_z} \quad 1.35$$

and the work done by this stress on the fibre F is

$$dV^M = \frac{-\lambda M_z y}{I_z} \delta A \left(\frac{1}{2} \theta_y^2 + \frac{1}{2} \theta_z^2 \right) dx \quad 1.36$$

which when integrated produces

$$V^M = -\frac{1}{2} \int_0^L \lambda M_z \beta_z (\phi_{,x})^2 dx + \int_0^L \lambda M_z w_{,x} \phi_{,x} dx \quad 1.37$$

in which the monosymmetry parameter β_z is given by

$$\begin{aligned} \beta_z &= \frac{1}{I_z} \int_A (yz^2 + y^3) dA + 2\bar{y} \\ &= \frac{1}{I_z} \left\{ (h - \bar{y}) \left[\frac{B_2^3 T_2}{12} + (h - \bar{y})^2 B_2 T_2 + \frac{(h - \bar{y})^3 t}{4} \right] \right. \\ &\quad \left. - \bar{y} \left[\frac{B_1^3 T_1}{12} + B_1 T_1 \bar{y}^2 + \frac{\bar{y}^3 t}{4} \right] \right\} + 2\bar{y} \end{aligned} \quad 1.38$$

The work done by the moments and shears when the line of action of these through 0 displaces by the buckling deformation v_b shown in Fig. 1.5(b) is:

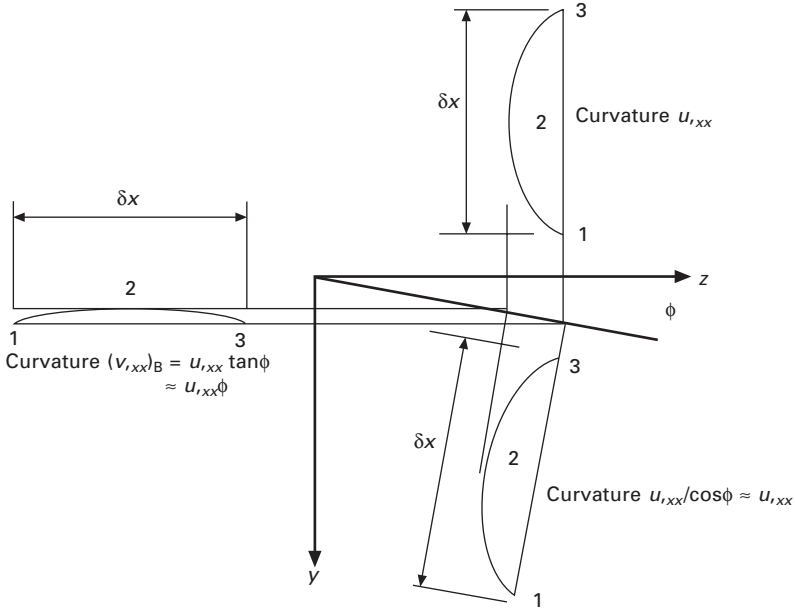
$$\begin{aligned} V^B &= \int_0^L \lambda [V(0)v_b(0) + V(L)v_b(L) \\ &\quad - M(0)v_{b,x}(0) - M(L)v_{b,x}(L)] dx \end{aligned} \quad 1.39$$

Noting from elementary statics that the shear force $V_y = dM_z/dx$, Eq. (1.39) can be integrated by parts to produce:

$$V^B = - \int_0^L \lambda M_z v_{b,xx} dx \quad 1.40$$

By neglecting higher-order terms and considering the fibre curvature diagram in Fig. 1.6, the curvature $v_{b,xx}$ can be written as (Trahair 1993):

$$v_{b,xx} = \phi w_{,xx} \quad 1.41$$



1.6 Fibre curvature diagram.

so that the work done by the moments and shears becomes:

$$V^B = - \int_0^L \lambda M_z \phi w_{,xx} dx \quad 1.42$$

The total work done by the axial forces, shear forces and bending moments can be found by combining Eqs. (1.34), (1.37) and (1.42) to produce:

$$V = \frac{1}{2} \lambda \int_0^L N [(w_{,x})^2 - 2\bar{y} w_{,x} \phi + (r_0^2 + \bar{y}^2) (\phi_{,x})^2] dx - \frac{1}{2} \lambda \int_0^L M_z [\beta_z (\phi_{,x})^2 + 2\phi w_{,xx}] dx \quad 1.43$$

When the appropriate substitutions for w , ϕ and its derivatives are made, Eq. (1.43) becomes

$$V = \frac{1}{2} \{q\}_b^T \lambda [g]_b \{q\}_b \quad 1.44$$

where $[g]_b$ is a buckling stability matrix presented explicitly by Bradford and Cuk (1988) that is independent of the buckling displacements.

Following standard finite element practice, the global stiffness and stability matrices $[K]_b$ and $[S]_b$ may be assembled from the element contributions $[k]_b$ and $[g]_b$. The buckling displacements $\{Q\}_b$ that are assembled from the element buckling displacements are infinitesimal, and because of this the change in potential at the point of buckling is considered in an equilibrium configuration. If Π denotes the total potential, the change in the potential $d\Pi$ due to the infinitesimal buckling displacements $\{Q\}_b$ that defines equilibrium at the point of buckling becomes:

$$\delta\Pi = \frac{1}{2} \{Q\}_b^T ([K]_b - \lambda[G]_b) \{Q\}_b \quad 1.45$$

Invoking the stability criterion in this equation that $\delta^2\Pi = \delta(\delta\Pi) = 0$ for any arbitrary variation $\delta\{Q\}_b$ gives

$$\delta^2\Pi = \delta\{Q\}_b^T ([K]_b - \lambda[G]_b) \{Q\}_b = 0 \quad \forall \delta\{Q\}_b \quad 1.46$$

which leads to the familiar linear buckling eigenproblem stated as

$$([K]_b - \lambda[G]_b) \{Q\}_b = \{0\} \quad 1.47$$

Equation (1.47) may be solved using a standard library package to produce the buckling load factor or eigenvalue λ , and the buckled (eigenvector) shapes $\{Q\}_b$.

1.4 Elastic buckling curves

The linear eigenvalue finite element technique developed in the previous section has been used to calculate the elastic critical loads or moments of tapered doubly symmetric I-beams. These solutions may be used in design, as discussed in the following section. Solutions are given for a beam with flange or web taper with concentrated end-moments, and for a beam with flange or web taper acted upon by a uniformly distributed load.

The differential equations for buckling derived by Kitipornchai and Trahair (1972) are essentially generic in nature and indicate that the beam parameter K is an independent variable, where

$$K = \frac{\pi}{L} \sqrt{\left(\frac{EI_w}{GJ} \right)_0} \quad 1.48$$

in which L is the length of the beam, and where the subscript in $(\cdot)_0$ indicates the value of (\cdot) at the largest section. Because the beam parameter K is an independent variable, only one cross-section with a depth $d = 200$ mm, flange width $B = 50$ mm, flange thickness $T = 3$ mm and web thickness $t = 2$ mm was used to calculate K for the parameter study. Other geometries and beam lengths that produced the same value of K were tried as well, and it was found that these had negligible effect on the buckling solution, indicating the accuracy of the inference of Kitipornchai and Trahair's equations. The value of the beam parameter K may be interpreted as a measure of the slenderness of the beam, with small values of K indicating slender beams, while stocky beams are represented by large values of the beam parameter K . Ten elements were used in the finite element studies.

The lateral buckling of a simply supported beam with end-moments M and βM shown in Fig. 1.1(a) has been studied, and plots of the dimensionless critical moment γ_M given by

$$\gamma_M = \frac{M_{0b}L}{\sqrt{(EI_y GJ)_0}} \quad 1.49$$

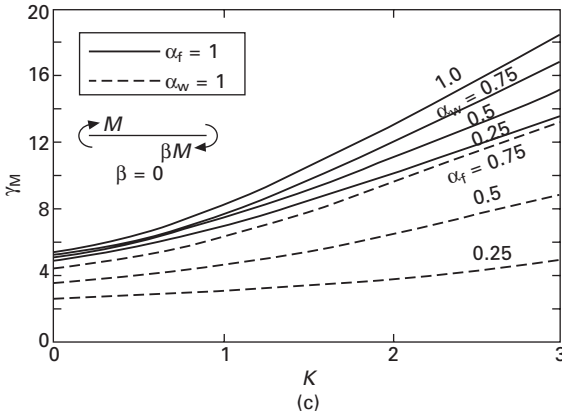
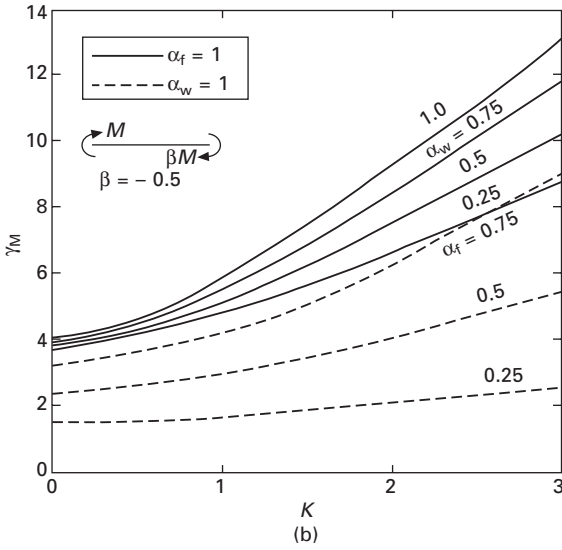
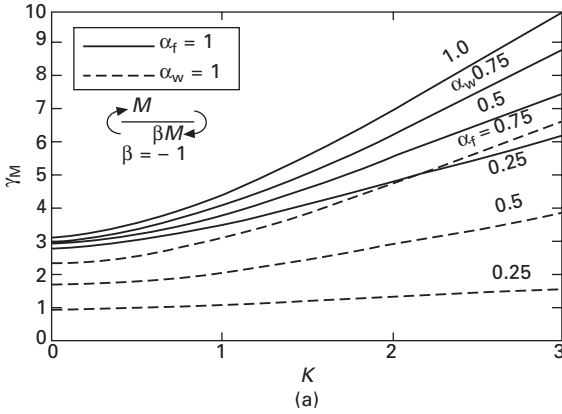
are given in Figs 1.7(a)–(e) for moment gradients $\beta = -1.0, -0.5, 0, 0.5$ and 1.0 . In these figures, the solid lines are for $\alpha_f = 1$ with α_w varying (i.e. web-tapered beams with constant flange width), whilst the dashed lines are for $\alpha_w = 1$ with α_f varying (i.e. flange tapered beams with constant web depth). It can be seen from the figures that while the reductions in g_M due to increasing flange taper are quite large, those due to increasing web taper are much less. Also of interest is the observation that for stocky beams, the elastic critical moment is higher for the $\beta = 0.5$ loading case than for the $\beta = 1.0$ loading case (the latter case has been shown in Trahair and Bradford (1998) to be the safest loading condition for uniform beams), and that this trend increases as the taper parameters a_f and a_w decrease.

The lateral buckling of a tapered beam loaded by a uniformly distributed load w shown in Fig. 1.8 has also been studied using the linear finite element approach. For this beam, the distributed load is assumed to act at a distance \bar{a} below the web mid-height. For an isolated simply supported beam, the end-moment parameter β is zero, and values of the dimensionless elastic critical load

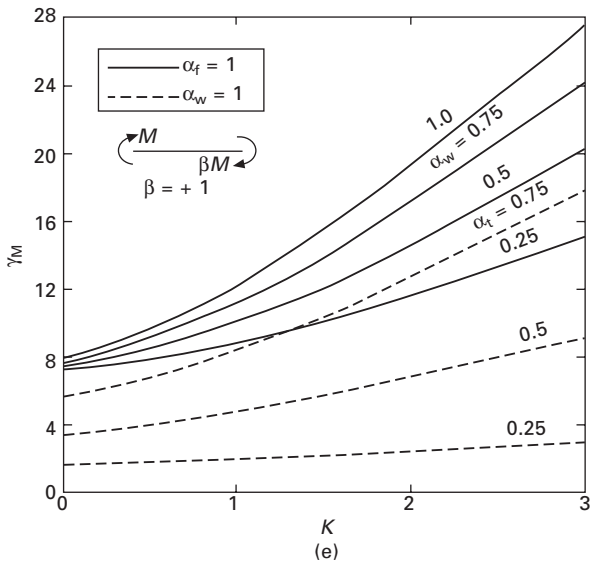
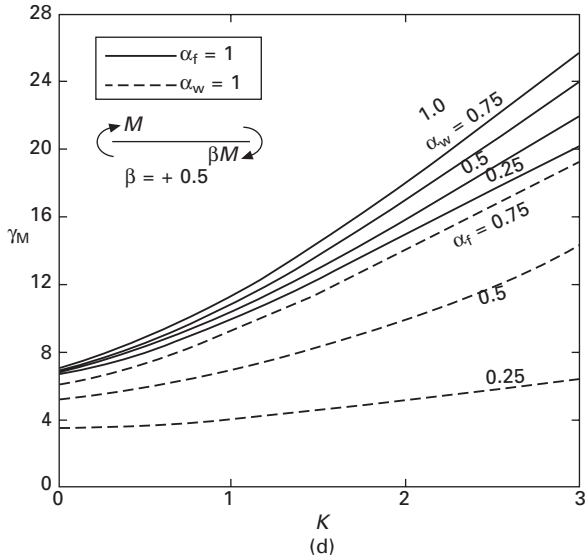
$$\gamma_w = \frac{wL^3}{\sqrt{(EI_y GJ)_0}} \quad 1.50$$

are shown in Figs 1.9(a) to (c) as functions of the beam parameter K and the dimensionless load height parameter ε given by

$$\varepsilon = \frac{\bar{a}}{L} \sqrt{\frac{EI_w}{GJ}} \quad 1.51$$

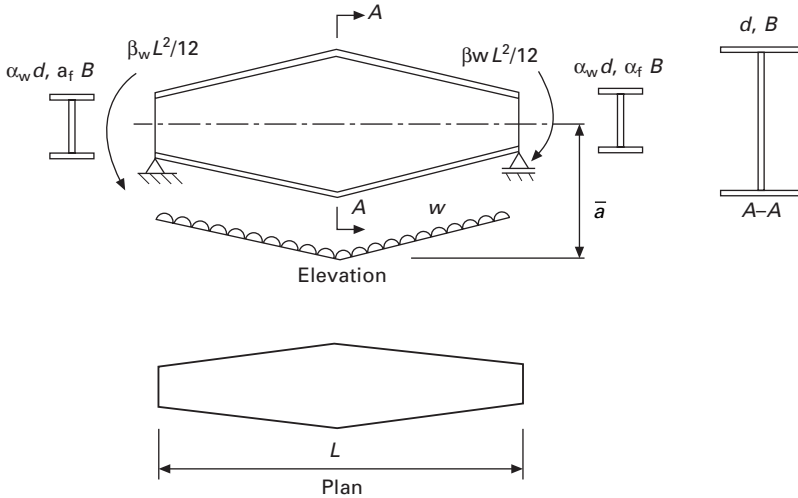


1.7 Tapered beam with end moments (a) $\beta = -1$, (b) $\beta = -0.5$, (c) $\beta = 0$, (d) $\beta = 0.5$, (e) $\beta = 1$.



1.7 Continued.

On the other hand, for ‘continuous’ beams with the end-moment parameter β being taken as unity, the corresponding plots of the dimensionless elastic critical load are also shown in Figs 1.10(a)–(c). In both Figs 1.9 and 1.10, the solid are for $\alpha_f = 1$ with α_w varying, while the dashed lines are for $\alpha_w = 1$ with α_f varying. The dimensionless parametric representations in Eqs. (1.49) to (1.51) appear in the generic equations of Kitipornchai and Trahair (1972).



1.8 Tapered beam with a uniformly distributed load.

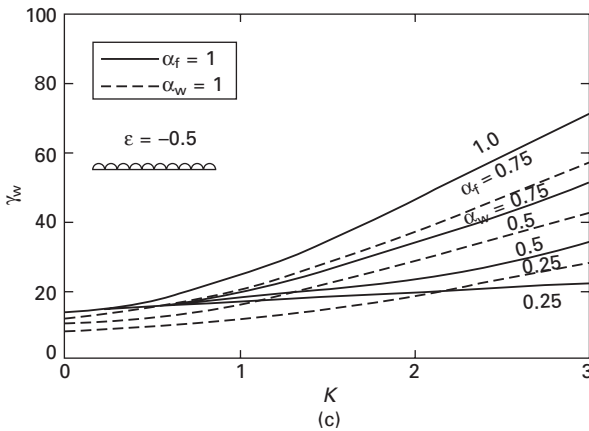
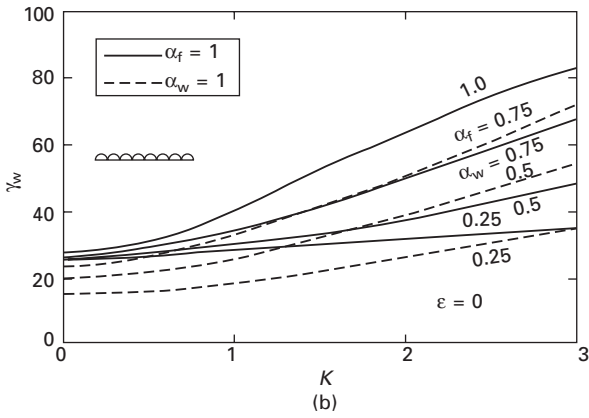
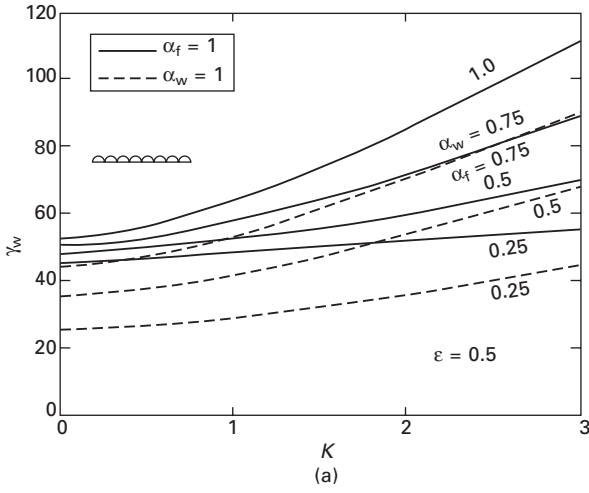
It can be seen from Figs 1.9 and 1.10 that placing the load above the web mid-height ($\epsilon < 0$) results in a significant destabilising effect and reduces the buckling load, while placing the load below the web mid-height ($\epsilon > 0$) tends to stabilise the beam against lateral buckling. The reduction in the dimensionless buckling load γ_w below that for the corresponding uniform beam, expressed as a ratio, is shown in Fig. 1.11 for the beam with $\beta = 0$ loaded at the centroid. The figure demonstrates that increasing the degree of flange taper reduces the ratio of the resistance of the tapered beam to that of the corresponding uniform beam. The reduction in the lateral buckling resistance for web-tapered beams is less dramatic, however, with web tapering having little effect for the more slender beams. In all cases, the reduction in the lateral buckling resistance below that of the corresponding uniform beam increases as the beam parameter K increases and the beam becomes more stocky.

1.5 Design strengths

1.5.1 Codified rules

The limit states British BS5950 (British Standards Institution 2000) and Australian AS4100 (Standards Australia 1998) steel structures standards provide guidance for the calculation of the strength of tapered beams. In BS5950, the equivalent slenderness used is

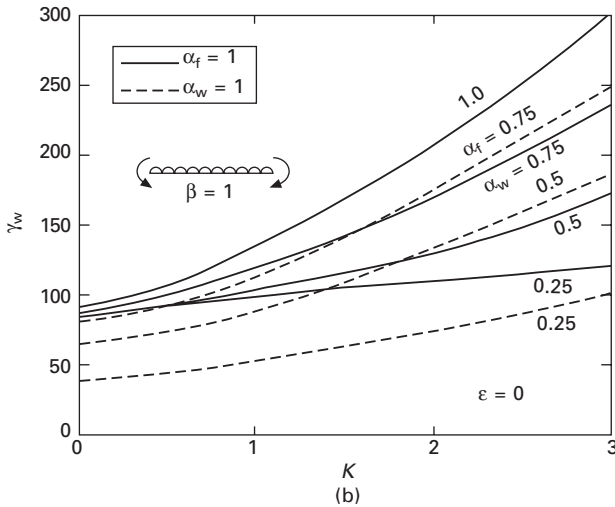
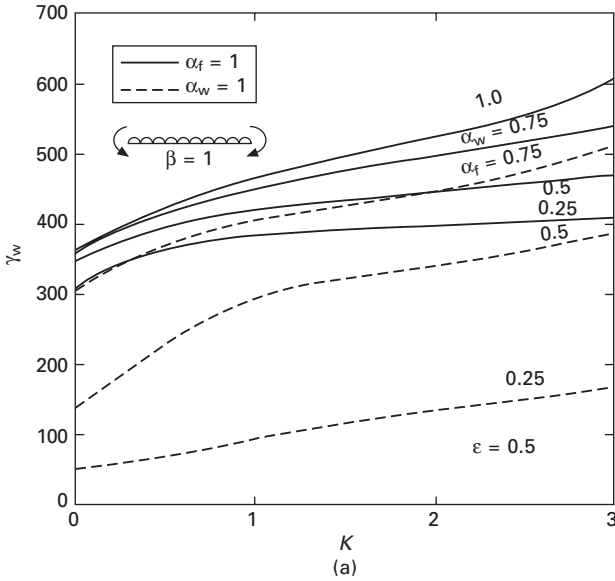
$$\lambda_{LT} = (1.5 - 5R_f)uv\lambda\sqrt{\beta_w} \tag{1.52}$$



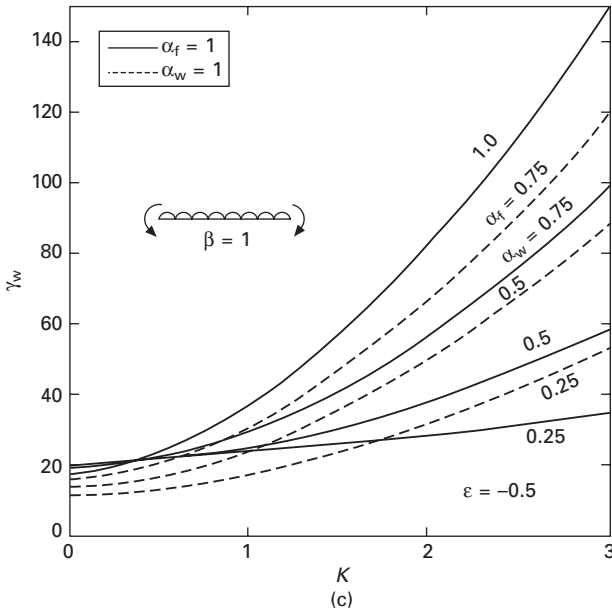
1.9 Buckling curves for a simply supported beam with a uniformly distributed load: (a) load height parameter $\epsilon = -0.5$; (b) $\epsilon = 0$; (c) $\epsilon = 0.5$.

in which R_f is the ratio of the flange areas at the points of minimum and maximum moment, respectively, and where

$$u = \left\{ 4S_x^2 \left(1 - \frac{I_y}{I_x} \right) / (A^2 h_s^2) \right\}^{1/4} \tag{1.53}$$



1.10 Buckling curves for a continuous beam with a uniformly distributed load: (a) load height parameter $\epsilon = -0.5$, (b) $\epsilon = 0$; (c) $\epsilon = -0.5$.



1.10 Continued.

$$v = \left\{ 1 + 0.05 \left(\frac{\lambda}{x} \right)^2 \right\}^{-1/4} \quad 1.54$$

$$\lambda = \frac{L_E}{r_y} \quad 1.55$$

$$x = 0.566 h_s \left(\frac{A}{J} \right)^{1/2} \quad 1.56$$

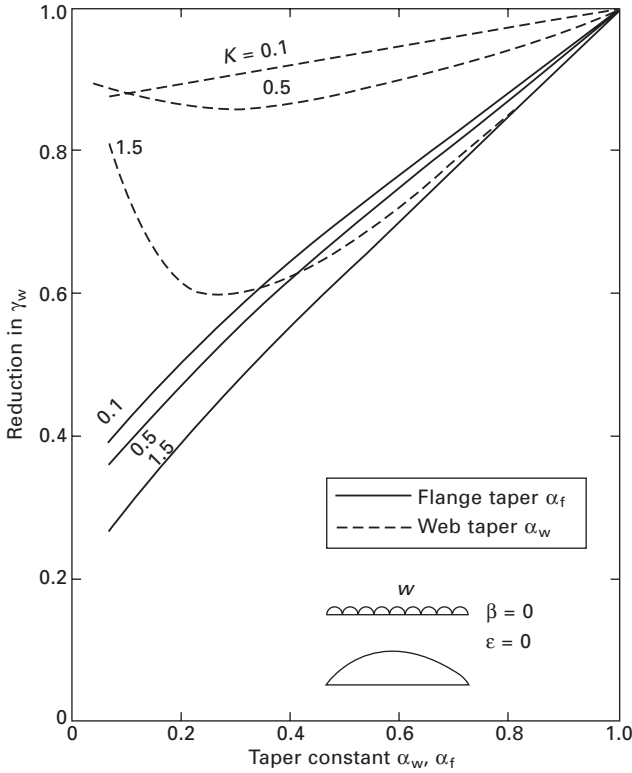
$$\beta_w = \frac{Z_{ex}}{S_x} \quad 1.57$$

in which L_E is the effective length, h_s is the distance between the flange shear centres, Z_{ex} is the effective section modulus and S_x is the plastic section modulus. These equations are based on the elastic critical moment for a tapered beam being expressed as:

$$M_E = \frac{\pi^2 E M_P}{\lambda_{LT}^2 p_y} \quad 1.58$$

in which $M_P (= S_x p_y)$ is the plastic moment and p_y is the yield stress.

In the slightly different method of AS4100, non-uniform beams can be designed using the properties of the most critical cross-section, which is



1.11 Reduction in elastic buckling load due to tapering.

where the ratio of the design bending moment to the section capacity is greatest. The elastic buckling moment is then reduced by multiplying it by the factor:

$$\alpha_{st} = 1.0 - 1.2 \left(\frac{L_r}{L} \right) \left[1 - \left(0.6 + 0.4 \frac{d_m}{d_c} \right) \frac{A_{fm}}{A_{fc}} \right] \tag{1.59}$$

in which A_{fm} and A_{fc} are the flange areas at the minimum and critical cross-sections respectively, d_m and d_c are the section depths at the minimum and critical cross-sections, and where L_r is taken as $0.5L$ for a tapered beam.

1.5.2 Design recommendation

The method of ‘design by buckling analysis’ (Trahair and Bradford, 1998; Trahair *et al.* 2001) makes use of the elastic buckling curves in Section 1.4, which were derived on the basis of an accurate finite element analysis, and allows these to be used to predict accurate design strengths. These curves

can be used to calculate the elastic lateral buckling moment M_{ob} at the critical cross-section, defined again as the cross-section where the ratio of the design bending moment to the section capacity is greatest. The critical moment M_{ob} includes the effects of off-shear centre loading and of nonuniform bending moment distribution. The elastic critical moment M_{obo} is obtained again from the figures for the same beam, but with shear centre loading, and the moment distribution factor α_m is determined from:

$$\alpha_m = \frac{M_{obo}}{M_{oo}} \quad 1.60$$

where the elastic critical moment M_{oo} is that for the same beam under uniform bending. Using the lateral buckling strength design equations of the AS4100, the design strength M_b is then calculated from the elastic buckling moment M_E given by:

$$M_E = \frac{M_{ob}}{\alpha_m} \quad 1.61$$

by using

$$M_b = \alpha_m \alpha_s M_s \quad 1.62$$

where the slenderness reduction factor is:

$$\alpha_s = 0.6 \left\{ \left[\left(\frac{M_s}{M_E} \right)^2 + 3 \right]^{1/2} - \frac{M_s}{M_E} \right\} \quad 1.63$$

in which M_s is the section capacity taken as $Z_{ex} p_y$.

For the design proposal to be applicable to the methodology of the British BS5950, the value of M_E determined from Eq. 1.61 can be used to determine the design strength M_b from:

$$M_b = \frac{\alpha_m M_E M_s}{\phi_B + (\phi_B^2 - M_E M_s)^{1/2}} \quad 1.64$$

in which

$$\phi_B = \frac{M_s + (\eta_{LT} + 1)M_E}{2} \quad 1.65$$

with a suggested Perry coefficient for fabricated sections (whose strengths tend to be lower than those of hot-rolled sections) of

$$\eta_{LT} = 0.0056 \left(\frac{\pi^2 E}{p_y} \right)^{1/2} \left\{ \left(\frac{M_s}{M_E} \right)^{1/2} - 0.4 \right\} \geq 0 \quad 1.66$$

1.6 Concluding remarks

This chapter has addressed the issue of the lateral or flexural-torsional buckling of tapered steel members in bending. General formulations of the solution do not exist in closed form, and hence recourse must be made to numerical solutions. A general nonlinear method of finite element analysis was first described, and this technique is applicable to a wide range of stability problems with flexural members of open cross-section. Because of the complexity of the nonlinear formulation, a linearised finite element was then developed in which the out-of-plane infinitesimal buckling deformations were uncoupled from the prebuckling deformations. This latter formulation leads to a linear eigenproblem, with the eigenvalue representing the buckling load factor. Based on the linear finite element analytical technique, a suite of design curves was presented for the elastic buckling of tapered members of doubly symmetric I-section.

Both the British BS5950 and the Australian AS4100 steel structures standards provide guidance for the design of tapered steel members, based on the limit state of inelastic lateral buckling. However, both design codes account for the elastic lateral buckling using simplistic prescriptive equations. Because of this, this chapter has described a technique, based on the concept of ‘design by buckling analysis’, in which the elastic buckling curves derived from the finite element formulation may be converted into design strengths. This concept uses the equations within both codes that relate the strength of the member to its plastic moment of resistance, and to its elastic buckling load, and the recommendation affords a simple yet accurate alternative to the design of tapered steel members.

1.7 References

- Amirikian, A. (1952), Wedge-beam framing. *Transactions, ASCE*, **117**, 596–652.
- Barsoum, R.S. and Gallagher, R.H. (1970), Finite element analysis of torsional and flexural-torsional stability problems. *International Journal for Numerical Methods in Engineering*, **2**, 335–352.
- Bradford, M.A. (1988a), Stability of tapered I-beams. *Journal of Constructional Steel Research*, **9**, 195–216.
- Bradford, M.A. (1988b), Lateral stability of tapered beam-columns with elastic restraints. *The Structural Engineer*, **66**(22), 376–384.
- Bradford, M.A. (1989), Inelastic buckling of tapered monosymmetric I-beams. *Engineering Structures*, **11**(2), 119–126.
- Bradford, M.A. and Cuk, P.E. (1988), Lateral buckling of tapered monosymmetric I-beams. *Journal of Structural Engineering, ASCE*, **114**(5), 977–996.
- Bradford, M.A. and Pi, Y.-L. (2004), Design of steel arches against in-plane instability. *International Journal of Applied Mechanics and Engineering*, **9**(1), 37–45.
- British Standards Institution (2000), *BS5950: The Structural Use of Steelwork in Building: Part 1: Code of Practice for Design: Rolled and Welded Sections*, BSI, London.

- Brown, T.G. (1981), Lateral torsional buckling of tapered I-beams. *Journal of the Structural Division*, ASCE, **107**(ST4), 689–697.
- Chan, S.L. (1990), Buckling analysis of structures composed of tapered members. *Journal of Structural Engineering*, ASCE, **116**(7), 1893–1906.
- Horne, M.R. and Morris, L.J. (1977), The design against lateral stability of haunched members restrained at intervals along the tension flange. *Proceedings of Second International Colloquium on Stability*, Washington, DC, 618–629.
- Horne, M.R., Shakir-Khalil, H. and Akhtar, S. (1979), Stability of tapered and haunched members. *Proceedings, Institution of Civil Engineers, London*, **67**, Part 2, 677–694.
- Kitipornchai, S. and Trahair, N.S. (1972), Elastic stability of tapered I-beams. *Journal of the Structural Division*, ASCE, **98**(ST3), 713–728.
- Lee, G.C., Morrell, M.L. and Ketter, R.L. (1972), Design of tapered members. *Bulletin No. 173*, Welding Research Council, USA.
- Morrell, M.L. and Lee, G.C. (1974), Allowable stress for web tapered beams. *Bulletin No. 192*, Welding Research Council, USA.
- Nakane, K. (1984), The design for instability of non-uniform beams. *Proceedings, 9th Australasian Conference on the Mechanics of Structures and Materials*, Sydney, 18–22.
- Ronagh, H.R. and Bradford, M.A. (1994a), Some notes on finite element buckling formulations for beams. *Computers and Structures*, **52**(6), 1119–1126.
- Ronagh, H.R. and Bradford, M.A. (1994b), Parameters affecting the distortional buckling of tapered steel members. *Journal of Structural Engineering*, ASCE, **120**(11), 3137–3155.
- Ronagh, H.R. and Bradford, M.A. (1996), A rational model for the distortional buckling of tapered members. *Computer Methods in Applied Mechanics and Engineering*, **130**, 263–277.
- Ronagh, H.R. and Bradford, M.A. (1999), Nonlinear analysis of thin-walled members of open cross-section. *International Journal for Numerical Methods in Engineering*, **46**(3), 535–552.
- Ronagh, H.R., Bradford, M.A. and Attard, M.M. (2000a), Nonlinear analysis of thin-walled members of variable cross-section. 1: Theory. *Computers and Structures*, **77**(3), 285–299.
- Ronagh, H.R., Bradford, M.A. and Attard, M.M. (2000b), Nonlinear analysis of thin-walled members of variable cross section. 2: Application. *Computers and Structures*, **77**(3), 301–313.
- Standards Australia (1998), *AS4100 Steel Structures*. SA, Sydney.
- Taylor, J.C., Dwight, J.B. and Nethercot, D.A. (1974), Buckling of beams and struts: proposals for a new British code. *Proceedings of Conference on Metal Structures and the Practising Engineer*, Melbourne, Australia, 37–41.
- Trahair, N.S. (1993), *Flexural-Torsional Buckling of Structures*. E&FN Spon, London.
- Trahair, N.S. and Bradford, M.A. (1998), *The Behaviour and Design of Steel Structures to AS4100*, 3rd edn (Australian), E&FN Spon, London.
- Trahair, N.S., Bradford, M.A. and Nethercot, D.A. (2001), *The Behaviour and Design of Steel Structures to BS5950*, 3rd edn (British), Spon Press, London.
- Wekezer, J.W. (1985), Instability of thin-walled bars. *Journal of Engineering Mechanics*, ASCE, **111**(7), 923–935.
- Woolcock, S.T., Kitipornchai, S. and Bradford, M.A. (1999), *Design of Portal Frame Buildings*, 3rd edn, AISC, Sydney.

Buckling of plates with variable in-plane forces

I SHUFRIN and M EISENBERGER,
Technion – Israel Institute of Technology, Israel

2.1 Introduction

Plate elements are used in civil, mechanical, aeronautical and marine engineering structures. Consideration of buckling loads for such plates is essential to ensure an efficient and reliable design. The classical Kirchhoff thin plate theory (CPT) is usually used to carry out stability analysis of rectangular plates. CPT assumptions are satisfactory for computation of buckling load for truly thin plates, but they can lead to inaccuracy when the ratio of thickness to the dimensions of the plate is relatively large. This is because that the effect of the transverse shear deformation, which is not considered in the Kirchhoff theory, becomes significant in thick plates. A number of shear deformation plate theories were derived. The simplest one is the First Order shear deformation Plate Theory (FOPT), commonly referred to as Mindlin plate theory. It extends the kinematic assumptions of the CPT by releasing the restriction on the angle of shearing deformations (Reddy 1999, Wang *et al.* 2000).

Many researchers used several analytical and numerical methods to study the stability of rectangular thick plates according to FOPT (Hermann and Armenakas 1960, Dawe and Roufael 1982, Wang *et al.* 1994, Kitipornchai *et al.* 1993, Shufrin and Eisenberger 2005). In shear flexible plate buckling analysis, moment terms due to cross-sectional rotations arise when one considers second order strains in the potential energy formulation of the in-plane loads. These terms were introduced by Sun (1972, 1973) and later on also by Dawe and Craig (1986), Whitney (1987) and Bert and Malik (1997). The same terms are sometimes called curvature terms, and also as rotatory moments resembling the same type of contribution as in the vibration analysis of shear deformable plates where rotary inertia terms arise because of the cross-section rotations. Many of the previous studies dealt with composite plates and found that the inclusion of the curvature terms reduces the buckling load by several per cent, depending on the boundary conditions of the plate. Bert and Malik (1997) considered plates with two opposite edges simply

supported, and the other two with other possible restraint conditions, and concluded that the reduction of the buckling load due to the curvature term effects are small, and do not justify their inclusion at the cost of substantial increase in the computational cost. Bert and Malik (1999) extended the formulation also to Reddy's (1984) higher-order plate theory but did not present numerical results for the effect of the curvature terms on magnitude of the buckling load.

Variable in-plane forces in the buckling analysis of rectangular plates have been recently studied by several authors. All these studies were made on the basis of the classical thin plate theory. Kang and Leissa (2001) presented the results for buckling factors of SS-F-SS-F plate loaded by unidirectional in-plane moment. Later on, Leissa and Kang (2002) extended their solution to SS-C-SS-C plate under the same loading type. For these cases, the stability equation for the thin plate theory assumption can be separated in the two directions as a multiplication of two one-variable functions and the solution was obtained exactly. Kang and Shim (2004) extended the solution for plates with two opposite edges simply supported and any boundary conditions on the other two edges. Romeo and Ferrero (2001) presented results for anisotropic rectangular plates with bidirectional in-plane moment loading. They solved the buckling equation by using the Rayleigh–Ritz method, assuming beam vibration modes in the two directions and minimizing the total energy of the plate. Their results are approximate. Bert and Devarakonda (2003) solved for the buckling factors of rectangular plates with nonlinear in-plane stress distribution. They presented solution for the in-plane prebuckling stress distributions in series form. They solved the thin plate buckling equation only for simply supported plate. Azhari *et al.* (2000) used the spline finite strip method and, by adding bubble functions, were able to improve on the buckling analysis results of plates. They presented approximate solutions for two combinations of boundary conditions only. Grimm and Gerdeen (1975) used the extended Kantorovich method to solve the thin plate buckling equations for unidirectional in-plane moment loading. They used numerical integration for the solution in each step of the procedure and obtained approximate solutions for the cases they solved.

In this chapter, we present highly accurate solutions for the stability problems of plates under linearly varying in-plane loads, in one and two directions, considering the transverse shear effects and the higher-order nonlinear curvature strain terms. The principle of minimum of potential energy is adopted in the derivation of the governing equations and the boundary conditions for Mindlin FOPT. The solution is based on the extended Kantorovich method presented by Kerr (1969) and applied to plate buckling by Eisenberger and Alexandrov (2003) and Shufrin and Eisenberger (2005). According to this approach, the solution is assumed to be separable in the directions of plate edges. Then, the solution in one direction, y for example, is specified *a priori*, and the solution

in the x direction is determined by solving a set of coupled ordinary differential equations with variable coefficients derived from the associated variational process with appropriate boundary conditions. Next, the obtained solution is used as the known function, while the solution in the second direction is determined by another Kantorovich solution process. These iterations are repeated until the acceptable convergence is achieved. For the solution in one direction, the exact element method for stability analysis of variable cross-section members is used as presented by Eisenberger (1991). The stiffness matrix including the effect of in-plane forces is derived. The buckling load is found as a value of the load that leads to singularity of the structure stiffness matrix. Stability of rectangular thick plates is analysed by varying the plate-aspect ratios, and the thickness-to-width ratios. Various combinations of boundary conditions are considered. The results obtained by both neglecting and including the effect of higher-order nonlinear curvature strain terms, are compared with those from the classical thin plate theory and with published results. Many new results are presented.

2.2 Buckling of rectangular plates

2.2.1 Basic equations

According to the Mindlin plate theory the assumptions for the displacement field are:

$$\bar{u}(x, y, z) = z\psi_x(x, y) \tag{2.1a}$$

$$\bar{v}(x, y, z) = z\psi_y(x, y) \tag{2.1b}$$

$$\bar{w}(x, y, z) = w_0(x, y) \tag{2.1c}$$

where $(\bar{u}, \bar{v}, \bar{w})$ are the displacement components along the (x, y, z) coordinate directions, respectively, w_0 is the transverse deflection of a point on the middle plane and ψ_x and ψ_y denote the rotations around the x and y axes. Then, the strain energy of the out-of-plane deflections of the plate is (Reddy 1999):

$$U = \frac{1}{2} \iint_A \left\{ D \left[\left(\frac{\partial \psi_x}{\partial x} \right)^2 + \left(\frac{\partial \psi_y}{\partial y} \right)^2 + 2\nu \frac{\partial \psi_x}{\partial x} \frac{\partial \psi_y}{\partial y} \right] + \frac{1}{2}(1 - \nu) \left(\frac{\partial \psi_x}{\partial y} + \frac{\partial \psi_y}{\partial x} \right)^2 \right\} dx dy \tag{2.2}$$

$$\left[+ kGh \left(\psi_x + \frac{\partial w_0}{\partial x} \right)^2 + kGh \left(\psi_y + \frac{\partial w_0}{\partial y} \right)^2 \right]$$

where $D = Eh^3/[12(1-\nu^2)]$ is the bending rigidity of the plate, $G = E/[2(1 + \nu)]$ is the shear modulus, E denotes Young's modulus of elasticity, and ν is Poisson's ratio. The shear correction factor k is introduced in order to compensate for the discrepancy between the true parabolic distribution of transverse shear stresses and the constant state that result from the kinematic assumptions of this theory. The potential energy of the in-plane loads in the prebuckling state V is:

$$V = \frac{1}{2} \int_A \left[\begin{aligned} & N_x(y) \left(\frac{\partial w_0}{\partial x} \right)^2 + N_x(y) \mu \frac{h^2}{12} \left(\left(\frac{\partial \psi_x}{\partial x} \right)^2 + \left(\frac{\partial \psi_y}{\partial x} \right)^2 \right) \\ & N_y(x) \left(\frac{\partial w_0}{\partial y} \right)^2 + N_y(x) \mu \frac{h^2}{12} \left(\left(\frac{\partial \psi_x}{\partial y} \right)^2 + \left(\frac{\partial \psi_y}{\partial y} \right)^2 \right) \end{aligned} \right] dx dy \quad 2.3$$

where the underlined expressions are the higher-order nonlinear strain terms and μ is scalar indicator. If $\mu = 0$, the higher-order 'curvature' terms are neglected, while if $\mu = 1$, their influence is included.

2.2.2 The Kantorovich procedure

According to the Kantorovich solution procedure (Kerr 1969), the solution is assumed as

$$w_0(x, y) = w(x)W(y) \quad 2.4a$$

$$\psi_x(x, y) = f(x)F(y) \quad 2.4b$$

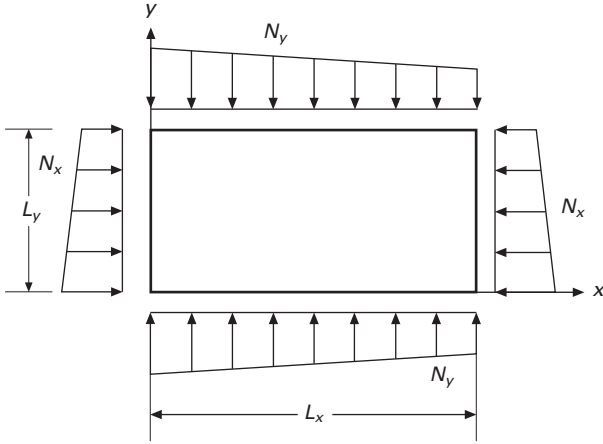
$$\psi_y(x, y) = \phi(x)\Phi(y) \quad 2.4c$$

For the sake of convenience, the following symbols are used in the subsequent derivations: lower case letters indicate the functions of the x -direction only and the upper case letters mean functions in the y -direction. In the extended Kantorovich method, the functions in the y -direction are assumed known. Hence, the substitution of the assumed solution into the energy functional will result in a set of coupled ordinary differential equations after variation as shown below. The in-plane axial forces are taken as (see Fig. 2.1):

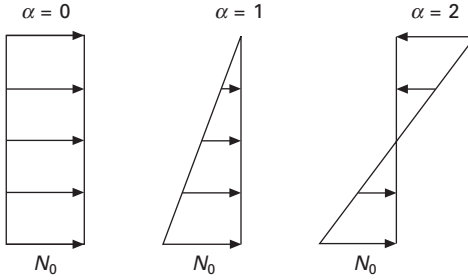
$$N_x(y) = N_{x0}P(y) = N_{x0} \left(1 - \alpha_x \frac{y}{L_y} \right) \quad 2.5a$$

$$N_y(x) = N_{y0}Q(x) = N_{y0} \left(1 - \alpha_y \frac{x}{L_x} \right) \quad 2.5b$$

where α_x and α_y are the factors of load variation (see Fig. 2.2).



2.1 Plate subjected to bidirectional in-plane loading.



2.2 Three types of load variation.

2.2.3 Derivation of buckling equations

The substitution of the assumed displacements and their derivatives and the in-plane load distributions in the energy functional for the plate,

$$\Pi = U - V \quad 2.6$$

and the integration in the y direction yield

$$\Pi = \frac{1}{2} \int_0^{L_x} \left(\begin{aligned} &S_1 f_{,x}^2 + S_2 \phi^2 + 2S_3 f_{,x} \phi + S_4 f^2 + 2S_5 f \phi_{,x} \\ &+ S_6 \phi_{,x}^2 + S_7 f^2 + 2S_8 f w_{,x} + S_9 w_{,x}^2 + S_{10} \phi^2 \\ &+ 2S_{11} \phi w + S_{12} w^2 - N_{x0} S_{13} w_{,x}^2 \\ &- N_{y0} S_{14} q w^2 - \frac{\mu N_{x0}}{2} S_{15} f_{,x}^2 - \frac{\mu N_{x0}}{2} S_{16} \phi_{,x}^2 \\ &- \frac{\mu N_{y0}}{2} S_{17} q f^2 - \frac{\mu N_{y0}}{2} S_{18} q \phi^2 \end{aligned} \right) \quad 2.7$$

where the coefficients S_1 through S_{18} are defined as:

$$\begin{aligned}
 S_1 &= D \int_0^{L_y} F^2 dy & S_2 &= D \int_0^{L_y} \Phi_{,x}^2 dy \\
 S_3 &= \nu D \int_0^{L_y} F \Phi_{,y} dy & S_4 &= \frac{1}{2}(1-\nu) D \int_0^{L_y} F_{,y}^2 dy \\
 S_5 &= \frac{1}{2}(1-\nu) D \int_0^{L_y} F_{,y} \Phi dy & S_6 &= \frac{1}{2}(1-\nu) D \int_0^{L_y} \Phi^2 dy \\
 S_7 &= kGh \int_0^{L_y} F^2 dy & S_8 &= kGh \int_0^{L_y} FW dy \\
 S_9 &= kGh \int_0^{L_y} W^2 dy & S_{10} &= kGh \int_0^{L_y} \Phi^2 dy \\
 S_{11} &= kGh \int_0^{L_y} \Phi W_{,y} dy & S_{12} &= kGh \int_0^{L_y} W_{,y}^2 dy \\
 S_{13} &= \int_0^{L_y} PW^2 dy & S_{14} &= \int_0^{L_y} W_{,y}^2 dy \\
 S_{15} &= h^2 \int_0^{L_y} PF^2 dy & S_{16} &= h^2 \int_0^{L_y} P\Phi^2 dy \\
 S_{17} &= h^2 \int_0^{L_y} F_{,y}^2 dy & S_{18} &= h^2 \int_0^{L_y} \Phi_{,y}^2 dy \quad 2.8
 \end{aligned}$$

According to the principle of minimum energy, the first variation of the functional should be equal to zero. Thus,

$$\delta \Pi = \int_0^{L_x} \left(\begin{aligned}
 &S_1 f_{,x} \delta f_{,x} + S_2 \phi \delta \phi + S_3 f_{,x} \delta \phi + S_3 \phi \delta f_{,x} \\
 &+ S_4 f \delta f + S_5 f \delta \phi_{,x} + S_5 \phi_{,x} \delta f + S_6 \phi_{,x} \delta \phi_{,x} \\
 &+ S_7 f \delta f + S_8 f \delta w_{,x} + S_8 w_{,x} \delta f + S_9 w_{,x} \delta w_{,x} \\
 &+ S_{10} \phi \delta \phi + S_{11} \phi \delta w + S_{11} w \delta \phi + S_{12} w \delta w \\
 &- N_{x0} S_{13} w_{,x} \delta w_{,x} - N_{y0} S_{14} q w \delta w \\
 &- \underline{\mu N_{x0} S_{15} f_{,x} \delta f_{,x}} - \underline{\mu N_{x0} S_{16} \phi_{,x} \delta \phi_{,x}} \\
 &- \underline{\mu N_{y0} S_{17} q f \delta f} - \underline{\mu N_{y0} S_{18} q \phi \delta \phi}
 \end{aligned} \right) dx = 0 \quad 2.9$$

The integration by parts leads to the following system of coupled differential equations:

$$[(S_9 - N_{x0}S_{13})w_{,xx} + S_8f_{,x} - S_{11}\phi - S_{12}w + N_{y0}S_{14}qw]\delta w = 0 \quad 2.10a$$

$$[(S_1 - \underline{\mu N_{x0}S_{15}})f_{,xx} - S_8w_{,x} + (S_3 - S_5)\phi_{,x} - (S_4 - S_7)f + \underline{\mu N_{y0}S_{17}qf}]\delta f = 0 \quad 2.10b$$

$$[(S_6 - \underline{\mu N_{x0}S_{16}})\phi_{,xx} + (S_5 - S_3)f_{,x} - S_{11}w - (S_2 + S_{10})\phi + \underline{\mu N_{y0}S_{18}q\phi}]\delta \phi = 0 \quad 2.10c$$

and the natural boundary conditions are:

$$Q = (S_8f + S_9w_{,x} - N_{x0}S_{13}w_{,x})\delta w|_0^{L_x} \quad 2.11a$$

$$M_b = (S_1f_{,x} + S_3\phi - \underline{\mu N_{x0}S_{15}f_{,x}})\delta f|_0^{L_x} \quad 2.11b$$

$$M_t = (S_5f + S_6\phi_{,x} - \underline{\mu N_{x0}S_{16}\phi_{,x}})\delta \phi|_0^{L_x} \quad 2.11c$$

2.2.4 The solution procedure

For solution, we use the following dimensionless coordinates: $\xi = x/L_x$ and $\eta = y/L_y$. Now we assume the solution of the system Eqs. (2.10a–c) as three infinite power series of the following form:

$$w = \sum_{i=0}^{\infty} w_i \xi^i \quad 2.12a$$

$$f = \sum_{i=0}^{\infty} f_i \xi^i \quad 2.12b$$

$$\phi = \sum_{i=0}^{\infty} \phi_i \xi^i \quad 2.12c$$

Also the load variation is described as polynomials:

$$q = 1 - \alpha_y \xi = \sum_{k=0}^1 q_k \xi^k \quad 2.13$$

where the polynomial coefficients are defined as follows:

$$q_0 = 1; \quad q_1 = -\alpha_y \quad 2.14$$

For solution, we have to find the appropriate coefficients of the polynomials in Eqs. (2.12a–c). By calculating all the derivatives and then substituting them back into Eqs. (2.10a–c), we obtain

$$(S_9 - N_{x0}S_{13}) \sum_{i=0}^{\infty} (i+1)(i+2)w_{i+2}\xi^i + S_8 \sum_{i=0}^{\infty} (i+1)f_{i+1}\xi^i - S_{11} \sum_{i=0}^{\infty} \phi_i \xi^i - S_{12} \sum_{i=0}^{\infty} w_i \xi^i + N_{y0}S_{14} \sum_{i=0}^{\infty} \sum_{k=0}^i q_k w_{i-k} \xi^i = 0 \quad 2.15a$$

$$\begin{aligned}
 & (S_1 - \mu N_{x0} S_{15}) \sum_{i=0}^{\infty} (i+1)(i+2) f_{i+2} \xi^i - S_8 \sum_{i=0}^{\infty} (i+1) w_{i+1} \xi^i \\
 & + (S_3 - S_5) \sum_{i=0}^{\infty} (i+1) \phi_{i+1} \xi^i - (S_4 - S_7) \sum_{i=0}^{\infty} f_i \xi^i \\
 & + \mu N_{y0} S_{17} \sum_{i=0}^{\infty} \sum_{k=0}^i q_k f_{i-k} \xi^i = 0
 \end{aligned} \tag{2.15b}$$

$$\begin{aligned}
 & (S_6 - \mu N_{x0} S_{16}) \sum_{i=0}^{\infty} (i+1)(i+2) \phi_{i+2} \xi^i - (S_5 - S_3) \sum_{i=0}^{\infty} (i+1) f_{i+1} \xi^i \\
 & - S_{11} \sum_{i=0}^{\infty} w_i \xi^i - (S_2 + S_{10}) \sum_{i=0}^{\infty} \phi_i \xi^i + \mu N_{y0} S_{18} \sum_{i=0}^{\infty} \sum_{k=0}^i q_k \phi_{i-k} \xi^i = 0
 \end{aligned} \tag{2.15c}$$

The recurrence formulas for calculating w_{i+2} , f_{i+2} , ϕ_{i+2} in Eqs. (2.15a–c) as a function of the first two terms of each series can be obtained in the following form (Eisenberger 1991, 1995; Eisenberger and Alexandrov 2003):

$$w_{i+2} = \frac{1}{(S_9 - N_{x0} S_{13})(i+1)(i+2)} \left[\begin{array}{l} -S_8 (i+1) f_{i+1} + S_{11} \phi_i \\ + S_{12} w_i - N_{y0} S_{14} \sum_{k=0}^i q_k w_{i-k} \end{array} \right] \tag{2.16a}$$

$$f_{i+2} = \frac{1}{(S_1 - \mu N_{x0} S_{15})(i+1)(i+2)} \left[\begin{array}{l} S_8 (i+1) w_{i+1} \\ + (S_3 - S_5)(i+1) \phi_{i+1} \\ + (S_4 - S_7) f_i \\ - \mu N_{y0} S_{17} \sum_{k=0}^i q_k f_{i-k} \end{array} \right] \tag{2.16b}$$

$$\phi_{i+2} = \frac{1}{(S_6 - \mu N_{x0} S_{16})(i+1)(i+2)} \left[\begin{array}{l} -(S_5 - S_3)(i+1) f_{i+1} \\ + S_{11} w_i + (S_2 + S_{10}) \phi_i \\ - \mu N_{y0} S_{18} \sum_{k=0}^i q_k \phi_{i-k} \end{array} \right] \tag{2.16c}$$

The terms for w_{i+2} , f_{i+2} and ϕ_{i+2} tend to 0 as $i \rightarrow \infty$. Now we have all terms except the first two of each series, which should be found using the boundary conditions (Shufrin and Eisenberger 2005; Eisenberger and Alexandrov 2003). For the FOPT formulation, the degrees of freedom are the lateral displacement and two rotations about the x and y axes at both ends of the strip element. According to Eqs. (2.12a–c) we can easily find the first three terms at the left end ($\xi = 0$):

$$\begin{cases} w_0 = w(0) \\ f_0 = f(0) \\ \phi_0 = \phi(0) \end{cases} \quad 2.17$$

The terms w_1, f_1 and ϕ_1 should be found as follows: all coefficients with index $i > 1$ are linearly dependent on the first two terms of each series, which can be written as

$$\begin{cases} w(1) = C_1^1 w_0 + C_2^1 w_1 + C_3^1 f_0 + C_4^1 f_1 + C_5^1 \phi_0 + C_6^1 \phi_1 = \sum_{i=0}^{\infty} w_i \\ f(1) = C_1^2 w_0 + C_2^2 w_1 + C_3^2 f_0 + C_4^2 f_1 + C_5^2 \phi_0 + C_6^2 \phi_1 = \sum_{i=0}^{\infty} f_i \\ \phi(1) = C_1^3 w_0 + C_2^3 w_1 + C_3^3 f_0 + C_4^3 f_1 + C_5^3 \phi_0 + C_6^3 \phi_1 = \sum_{i=0}^{\infty} \phi_i \end{cases} \quad 2.18$$

The C coefficients are functions of the flexural rigidity and the in-plane forces that can be expressed using the recurrence Eqs. (2.16a–c). For example, when $w_0 = 1, w_1 = f_0 = f_1 = \phi_0 = \phi_1 = 0$, the value of C_1^1 is equal to $w(1)$ and can be calculated using the recurrences. In general we can calculate all the C coefficients as follows:

$$\begin{aligned} C_k^1 &= w(1) = \sum_{i=0}^{\infty} w_i \\ C_k^2 &= f(1) = \sum_{i=0}^{\infty} f_i \\ C_k^3 &= \phi(1) = \sum_{i=0}^{\infty} \phi_i \end{aligned} \quad 2.19$$

when the conditions for the first six terms are:

$$\begin{cases} k = 1, 2 & w_{j=k} = 1, & w_{j \neq k} = f_j = \phi_j = 0, & j = 1, 2 \\ k = 3, 4 & f_{j=k-2} = 1, & w_j = f_{j \neq k-2} = \phi_j = 0, & j = 1, 2 \\ k = 5, 6 & \phi_{j=k-4} = 1, & w_j = f_j = \phi_{j \neq k-4} = 0, & j = 1, 2 \end{cases} \quad 2.20$$

Now, based on the boundary condition at $\xi = 0$ and $\xi = 1$, we can find the yet unknown three terms by solving the following matrix equation:

$$\begin{bmatrix} C_2^1 & C_4^1 & C_6^1 \\ C_2^2 & C_4^2 & C_6^2 \\ C_2^3 & C_4^3 & C_6^3 \end{bmatrix} \begin{bmatrix} w_1 \\ f_1 \\ \phi_1 \end{bmatrix} = \begin{bmatrix} w(1) \\ f(1) \\ \phi(1) \end{bmatrix} - \begin{bmatrix} C_1^1 & C_3^1 & C_5^1 \\ C_1^2 & C_3^2 & C_5^2 \\ C_1^3 & C_3^3 & C_5^3 \end{bmatrix} \begin{bmatrix} w(0) \\ f(0) \\ \phi(0) \end{bmatrix} \quad 2.21$$

Based on above solution technique and using the finite element approach, the six basic shapes can be found with the following boundary conditions:

$$w(0) = 1, w(1) = f(0) = f(1) = \phi(0) = \phi(1) = 0 \quad 2.22a$$

$$w(1) = 1, w(0) = f(0) = f(1) = \phi(0) = \phi(1) = 0 \quad 2.22b$$

$$f(0) = 1, w(0) = f(1) = f(1) = \phi(0) = \phi(1) = 0 \quad 2.22c$$

$$f(1) = 1, w(0) = w(1) = f(0) = \phi(0) = \phi(1) = 0 \quad 2.22d$$

$$\phi(0) = 1, w(0) = w(1) = f(0) = f(1) = \phi(1) = 0 \quad 2.22e$$

$$\phi(1) = 1, w(0) = w(1) = f(0) = f(1) = \phi(0) = 0 \quad 2.22f$$

The calculated shapes are the ‘exact’ solution for the system of differential equations Eqs. (2.10a–c). The word ‘exact’ means ‘as exact as one can get on a digital computer’. This is so since the calculation of the series is stopped according to a preset criterion so that the values of last six terms are less than an arbitrary small tolerance value.

The terms of the stiffness matrix are the holding actions at the ends of the strip element due to a unit displacement in the desired direction when all other degrees of freedom are restrained. Then according to the conditions (2.11a–c), with transformations to the dimensionless coordinates we have for the columns of the axial force dependent transverse stiffness matrix the following expressions:

$$S_M(1, i) = -\left(S_8 f^{(i)} + S_9 w^{(i)} \Big|_{,\xi} \frac{1}{L_x} - N_{x0} S_{13} w^{(i)} \Big|_{,\xi} \frac{1}{L_x} \right) \Big|_{\xi=0} \quad 2.23a$$

$$S_M(2, i) = -\left(S_1 f^{(i)} \Big|_{,\xi} \frac{1}{L_x} + S_3 \phi^{(i)} - \mu N_{x0} S_{15} f^{(i)} \Big|_{,\xi} \frac{1}{L_x} \right) \Big|_{\xi=0} \quad 2.23b$$

$$S_M(3, i) = -\left(S_5 f^{(i)} + S_6 \phi^{(i)} \Big|_{,\xi} \frac{1}{L_x} - \mu N_{x0} S_{16} \phi^{(i)} \Big|_{,\xi} \frac{1}{L_x} \right) \Big|_{\xi=0} \quad 2.23c$$

$$S_M(4, i) = \left(S_8 f^{(i)} + S_9 w^{(i)} \Big|_{,\xi} \frac{1}{L_x} - N_{x0} S_{13} w^{(i)} \Big|_{,\xi} \frac{1}{L_x} \right) \Big|_{\xi=1} \quad 2.23d$$

$$S_M(5, i) = \left(S_1 f^{(i)} \Big|_{,\xi} \frac{1}{L_x} + S_3 \phi^{(i)} - \mu N_{x0} S_{15} f^{(i)} \Big|_{,\xi} \frac{1}{L_x} \right) \Big|_{\xi=1} \quad 2.23e$$

$$S_M(6, i) = \left(S_5 f^{(i)} + S_6 \phi^{(i)} \Big|_{,\xi} \frac{1}{L_x} - \mu N_{x0} S_{16} \phi^{(i)} \Big|_{,\xi} \frac{1}{L_x} \right) \Big|_{\xi=1} \quad 2.23f$$

where $w^{(i)} f^{(i)}$ and $\phi^{(i)}$ the shapes are calculated with the boundary conditions Eqs. (2.22a–f).

The buckling load for the plate is found as the in-plane force that causes the determinant of the corresponding stiffness matrix to become zero. The vector of the nodal displacements is an eigenvector of the matrix, which corresponds to critical value. Hence, the general displacements are determined

by multiplying the basic shape functions by the nodal displacement, which is appropriate to each of them (Shufrin and Eisenberger 2005).

2.3 Numerical examples and discussion

The stability of rectangular thick plates with variable in-plane loading is studied using the proposed method. In all calculations, Poisson's ratio ν is taken as 0.3 and the shear correction factor $k = 5/(6 - \nu)$ is adopted. For convenience of notation, the plates are described by a four-letter symbol defining the boundary conditions at their edges starting from $x = 0$ to $x = L_x$, $y = 0$, $y = L_y$ consequently. For example, SFCC denotes a plate with a simply supported edge at $x = 0$, free at $x = L_x$ and clamped at $y = 0$ and $y = L_y$. The buckling loads are presented by using dimensionless value λ as: $N_{0x} = \lambda \pi^2 D/L_y^2$; $N_{0y} = \beta N_{0x}$, where β is the factor of biaxial compression. The buckling modes are defined by two integers that indicate the number of half-waves in the x and y directions, respectively. Three types of in-plane edge loading variations are considered (see Fig. 2.2): (1) $\alpha = 0$, constant loading, (2) $\alpha = 1$, triangular loading, and (3) $\alpha = 2$, pure in-plane moment loading. The aspect ratio of the plate is defined as $\gamma = L_x/L_y$.

Verifications of the results of the current derivation are made only with results from the classical thin plate theory. In Table 2.1, a comparison is made with published results for thin plates with unidirectional loading with $\alpha_x = 1$ and $\alpha_x = 2$. The results for cases in which two opposite edges are simply supported given by Leissa and Kang (2002) and Kang and Shim (2004) are exact, and the results of the current approach are the same. For the other cases, one can see that the values obtained here are lower than the reference values as these are upper bounds to the exact result.

In Table 2.2 buckling loads for square plates are given for several thickness ratios. Results for four loading combinations are presented. The thickness ratio is varied, and as the thickness is reduced, convergence to the results for thin plates (CPT) can be observed. Five combinations of boundary conditions are presented: in three cases, two opposite edges are simply supported, and for these the results are the exact values, and for the other two the results have very small relative errors. The loading cases considered are unidirectional combination of compressive force and in-plane moment, and bidirectional combination of compressive force and in-plane moment, with $\beta = N_y/N_x$, and the loading direction as shown in Fig. 2.3. All the results given in this Table are for the case where the high-order curvature terms are not considered ($\mu = 0$).

The effect of the higher-order curvature terms on the buckling load is presented in Table 2.3. Results are shown for three different length-to-width ratios, unidirectional and bidirectional in-plane moments, and five combinations of boundary conditions for the plate. Results are given including and neglecting

Table 2.1 Comparison for buckling load parameter $\lambda^*\pi^2$ for rectangular thin plates, ($\beta = 0, \mu = 0, \nu = 0.3$)

α_x	BC	γ	Reference	$\lambda^*\pi^2$
1.0	SSCC	0.5	Present	145.2
			Leissa and Kang (2002)	145.2
		0.7	Present	134.6
			Leissa and Kang (2002)	134.6
		1.4	Present	134.6
			Leissa and Kang (2002)	134.6
CCCC	1.0	Present	193.3791	
		Azhari <i>et al.</i> (2000)	194.4312	
2.0	SSCC	1.0	Present	391.5
			Leissa and Kang (2002)	391.5
		1.2	Present	400.4
			Leissa and Kang (2002)	400.4
	SSSS	1.0	Present	251.9547
			Timoshenko and Gere (1961)	252.6619
	SSCF	1.0	Present	391.43
			Kang and Shim (2004)	391.44
	SSFF	0.5	Present	69.78
			Kang and Shim (2004)	69.78
	SSFS	1.0	Present	25.962
			Kang and Shim (2004)	25.962
	SSSF	2.0	Present	235.44
			Kang and Shim (2004)	235.44

the curvature terms. One can see that the results for the model including the curvature effects are lower for all cases in the table, with up to 8% difference. This is a significant difference and cannot be neglected, as was implied by Bert and Malik (1997) for composite plates.

In Tables 2.4–2.6 results are given for buckling load factors for plates with several combinations of geometric dimensions, seven types of boundary condition combinations and with three types of loading distribution (see Fig. 2.2) in both x and y directions. All these results include the effect of the curvature terms. The values are exact for plates for which two opposite edges at constant x coordinate are simply supported. All other values are very good upper bound approximations for the true load factors.

In Fig. 2.4, the variations of the buckling factors for a unidirectional in-plane moment with respect to the plate aspect ratio for three types of boundary conditions are shown. The behaviour resembles that of plates loaded by constant in-plane forces, but with a more rapid convergence to constant values independent of the aspect ratio.

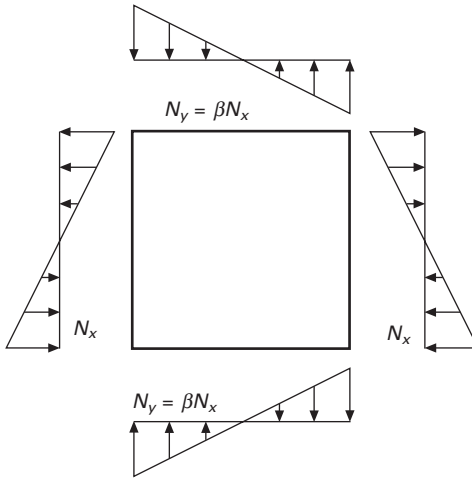
In Figs 2.5–2.9, the influence of the higher-order nonlinear strain terms on the buckling factor as a function of the plate thickness ratio is shown for several types of combined unidirectional and bidirectional in-plane loadings.

Table 2.2 Buckling load parameter λ for square plates, $\gamma = 1$, $\mu = 0$, $\nu = 0.3$

h/Ly	α_x	α_y	λ ($\beta = 0$)	α_x	α_y	λ ($\beta = 0$)	α_x	α_y	λ ($\beta = 1$)	α_x	α_y	λ ($\beta = 1$)
SSSS												
CPT	2	–	25.5283	1	–	7.8120	2	0	3.8068	2	2	13.7636
0.005	2	–	25.5161	1	–	7.8109	2	0	3.8062	2	2	13.7602
0.01	2	–	25.4793	1	–	7.8076	2	0	3.8044	2	2	13.7431
0.05	2	–	24.3571	1	–	7.7045	2	0	3.7481	2	2	13.2661
0.1	2	–	21.4086	1	–	7.3991	2	0	3.5801	2	2	11.9320
0.15	2	–	17.8109	1	–	6.9402	2	0	3.3247	2	2	10.1298
0.2	2	–	14.4145	1	–	6.3852	2	0	3.0114	2	2	8.2266
SSCC												
CPT	2	–	39.6719	1	–	14.7124	2	0	6.6049	2	2	21.4902
0.005	2	–	39.6339	1	–	14.7042	2	0	6.6026	2	2	21.4859
0.01	2	–	39.5131	1	–	14.6798	2	0	6.5960	2	2	21.4337
0.05	2	–	36.2903	1	–	13.9548	2	0	6.3913	2	2	20.1591
0.1	2	–	29.1478	1	–	12.1526	2	0	5.8269	2	2	16.9203
0.15	2	–	20.8065	1	–	10.0708	2	0	5.0743	2	2	13.1309
0.2	2	–	14.1835	1	–	8.1695	2	0	4.2839	2	2	9.6667
SSFF												
CPT	2	–	2.6072	1	–	1.6420	2	0	1.3987	2	2	2.5890
0.005	2	–	2.6033	1	–	1.6409	2	0	1.3947	2	2	2.5855
0.01	2	–	2.5990	1	–	1.6394	2	0	1.3904	2	2	2.5807
0.05	2	–	2.5509	1	–	1.6208	2	0	1.3489	2	2	2.5318
0.1	2	–	2.4606	1	–	1.5791	2	0	1.2818	2	2	2.4396
0.15	2	–	2.3437	1	–	1.5201	2	0	1.2028	2	2	2.3202
0.2	2	–	2.2086	1	–	1.4477	2	0	1.1172	2	2	2.1820

Table 2.2 Continued

h/Ly	α_x	α_y	λ ($\beta = 0$)	α_x	α_y	λ ($\beta = 0$)	α_x	α_y	λ ($\beta = 1$)	α_x	α_y	λ ($\beta = 1$)
CCCC												
CPT	2	–	48.3512	1	–	19.5934	2	0	9.4925	2	2	31.3773
0.005	2	–	48.2922	1	–	19.5830	2	0	9.4874	2	2	31.3574
0.01	2	–	48.1168	1	–	19.5515	2	0	9.4723	2	2	31.2608
0.05	2	–	43.1760	1	–	18.6013	2	0	9.0165	2	2	28.7043
0.1	2	–	32.6262	1	–	16.4712	2	0	7.8420	2	2	22.6695
0.15	2	–	21.8110	1	–	12.7583	2	0	6.4319	2	2	16.2138
0.2	2	–	12.8994	1	–	9.7004	2	0	5.1199	2	2	10.0512
CCFF												
CPT	2	–	7.2877	1	–	5.6945	2	0	3.1018	2	2	7.1597
0.005	2	–	7.2786	1	–	5.6898	2	0	3.0909	2	2	7.1507
0.01	2	–	7.2655	1	–	5.6820	2	0	3.0778	2	2	7.1359
0.05	2	–	7.0239	1	–	5.5134	2	0	2.9082	2	2	6.8823
0.1	2	–	6.4478	1	–	5.0842	2	0	2.5885	2	2	6.2795
0.15	2	–	5.7063	1	–	4.5158	2	0	2.2342	2	2	5.5011
0.2	2	–	4.9334	1	–	3.9131	2	0	1.9037	2	2	4.6844



2.3 Plate subjected to in-plane moments acting in the both directions.

Several combinations of boundary conditions are shown. In all cases, the influence of the curvature terms is increasing as the plate relative thickness is increased. The relative percentage difference is seen to be as high as 8% for $h/L_y = 0.2$.

Figures 2.10 and 2.11 show the buckling modes and buckling factors for plates loaded by unidirectional in-plane moment as a function of the plate-aspect ratio for CCSS and FFSS plates, respectively. For CCSS plate with $\gamma = 0.7$, the buckling mode has two half-waves in both the x and y directions, as the aspect ratio is increased, the buckling factor is reduced and the number of half waves in the y direction changes to one. For the FFSS plate the buckling factor increases as γ increases, and for higher aspect ratios becomes almost constant. The mode changes dramatically as the aspect ratio is raised, from almost rigid body rotation for $\gamma = 0.7$ to the case where most of the deflections take place at the far ends of the plates, where the loads are applied, and the central region of the plate almost does not deform.

Figures 2.12 to 2.15 present the effect of the ratio of the bidirectional in-plane moments on the buckling shape and buckling factor for square plates with eight different combinations of boundary conditions. Buckling factors are given for $\mu = 0$ and $\mu = 1$. The modes are identical for both cases. The two cases in Fig. 2.12, and the first case in Fig. 2.13, are completely symmetric and the reversal of the in-plane moment in the y -direction yields the same buckling factors, and mirror image of the buckling shape. This is not the case for the other five combinations of boundary conditions shown. In these, the reversal of loading direction results in significant changes in the buckling factor as the bidirectionally compressed sub-region of the plate is bounded by different edge restraints for the different cases. The buckling shape changes

Table 2.3 Buckling load parameter λ for rectangular plate: study for higher-order nonlinear strain terms effect

γ	h/L_y	β	α_x	α_y	μ	Boundary conditions						
						SSSS	CCCC	SSCC	SSFF	CCFF		
1	0.1	1	1	0	0	2.51825	6.0189	4.34453	1.14868	2.51689		
						2.4810	5.82457	4.22716	1.13698	2.46446		
		0	2	0	0	0	3.58005	7.84203	5.82695	1.2818	2.58853	
							3.51881	7.55481	5.64308	1.269	2.53705	
		1	1	1	0	0	3.72449	8.92214	6.53345	1.39992	3.71763	
							3.66787	8.62955	6.3645	1.38645	3.62354	
	0.15	1	2	2	0	0	11.932	22.6695	16.9203	2.43965	6.27946	
							11.513	21.4644	16.1643	2.41546	6.09162	
		0	0	0	0	0	0	1.78484	3.95233	2.98475	0.86783	2.04036
								1.73356	3.74182	2.85847	0.85215	1.96429
		1	1	1	1	0	0	3.49215	7.60144	5.71372	1.33704	3.25837
								3.38795	7.18978	5.4584	1.31001	3.11238
1.5	0.1	0	0	0	0	10.1298	16.2138	13.1309	2.32023	5.50112		
						9.52887	15.0861	12.2587	2.27235	5.21371		
	0	0	0	0	0	0	4.03967	7.03177	6.12258	0.41052	1.66077	
							3.96116	6.82377	6.0052	0.40903	1.63875	
	1	1	1	0	0	0	7.76204	13.4502	12.1526	0.75841	2.64939	
							7.60484	13.0453	11.7755	0.75548	2.61111	
1	1	2	0	0	0	21.4793	30.6152	29.1492	1.51473	3.73918		
						20.8502	29.0182	27.3123	1.50792	3.68338		
1	1	0	0	0	0	1.39063	3.67716	3.37153	0.40291	0.96702		
						1.37548	3.5801	3.2895	0.40134	0.95793		
1	1	1	0	0	0	1.64216	4.3237	3.86322	0.54082	1.08776		
						1.62422	4.20459	3.76205	0.53828	1.07915		
1	1	2	0	0	0	1.99809	5.13176	4.49639	0.5922	1.18763		
						1.97596	4.9835	4.36802	0.5899	1.17903		

Table 2.3 Continued

γ	h/L_y	β	α_x	α_y	μ	Boundary conditions				
						SSSS	CCCC	SSCC	SSFF	CCFF
2	0.1	1	2	2	0	8.12658	16.6497	12.8802	1.48054	3.50938
					1	7.93816	15.9436	12.402	1.47334	3.45536
			1	0	0	1.34358	3.90484	3.73483	0.3126	0.54216
					1	1.33076	3.80108	3.63733	0.31176	0.54003
			1	1	0	2.24453	6.06614	5.31704	0.40789	0.93047
					1	2.22124	5.90137	5.17708	0.40688	0.92516
			2	0	0	1.51006	4.32579	4.08306	0.33358	0.58381
					1	1.4956	4.20608	3.97061	0.33291	0.58215
			2	2	0	5.74768	13.0956	10.4383	1.04777	2.25152
					1	5.65872	12.6413	10.0962	1.04461	2.23105

Table 2.4 Buckling load factor λ for rectangular plates subjected to biaxial compression, ($\alpha_x = 0, \mu = 1, \nu = 0.3$)

BC	γ	h/L_y	Buckling load parameter λ			
			$\beta = 0$	$\beta = 1, \alpha_y = 0$	$\beta = 1, \alpha_y = 1$	$\beta = 1, \alpha_y = 2$
SSSS	1.0	0.10	3.7411	1.8706	2.4810	3.5188
		2.0	3.7411	1.1980	1.8419	2.5238
		3.0	3.7411	1.0698	1.6021	2.0829
	1.5	0.15	3.4671	1.7336	2.2968	3.2128
			3.5819	1.2993	1.9227	2.7038
	1.0	0.20	3.1521	1.5760	2.0850	2.8602
			3.1700	1.2076	1.7775	2.4272
SSFF	1.0	0.10	0.9163	0.8915	0.9068	0.9163
	1.0	0.15	0.8787	0.8521	0.8688	0.8787
	1.0	0.20	0.8324	0.8046	0.8224	0.8324
SSCC	1.0	0.10	6.2392	3.3132	4.4607	5.4919
		1.5	6.0052	3.2895	4.1513	4.8155
	1.5	0.15	5.1272	2.8585	3.8161	4.5736
			5.0793	2.8570	3.5510	4.0747
	1.0	0.20	4.1528	2.4168	3.1938	3.7371
CCCC	1.0	0.10	8.1213	4.4495	5.8246	7.5548
		2.0	6.4468	3.4310	4.5546	5.5191
		3.0	6.1236	3.3633	4.1952	4.8818
	1.0	0.15	6.5300	3.7418	4.8605	6.0568
			5.3232	2.9814	3.8958	4.6401
	3.0	0.20	5.1096	2.9146	3.6077	4.1535
CCFF	1.0	0.10	3.4595	2.3032	3.1974	3.4594
		1.5	1.6387	0.9579	1.4730	1.6387
	1.5	0.15	3.0192	1.9643	2.7385	3.0192
			1.5279	0.8687	1.3367	1.5279
	1.0	0.20	2.5781	1.6464	2.3012	2.5781
			1.3992	0.7748	1.3820	1.3992
	CFCF	1.0	0.10	0.9237	0.5604	0.8571
1.0		0.15	0.8692	0.5336	0.8102	1.1150
1.0		0.20	0.8100	0.5049	0.7590	1.0214
SFSF	1.0	0.10	0.3784	0.1960	0.3093	0.6469
	1.0	0.15	0.3665	0.1902	0.2998	0.6229
	1.0	0.20	0.3543	0.1841	0.2901	0.5976

significantly, and in some cases two half-waves arise in the y -direction. Results are shown only for five values of β , in the range -1 to 1 , and for higher values, and intermediate values, one should expect many types of transition in the buckling factors variation tendency, and the shapes of the buckling mode. These are not covered in this chapter.

Table 2.5 Buckling load factor λ for rectangular plates subjected to biaxial compression, ($\alpha_x = 1, \mu = 1, \nu = 0.3$)

BC	γ	h/L_y	Buckling load parameter λ			
			$\beta = 0$	$\beta = 1, \alpha_y = 0$	$\beta = 1, \alpha_y = 1$	$\beta = 1, \alpha_y = 2$
SSSS	1.0	0.10	7.2870	2.4810	3.6679	6.1425
		0.15	7.6048	1.6242	2.6499	4.4951
		0.20	7.2870	1.3308	2.2212	3.5586
	1.5	0.10	6.7342	2.2968	3.3879	5.5199
		0.15	6.8472	1.5341	2.4942	4.1196
		0.20	6.1021	2.0850	3.0667	4.8293
	1.5	0.10	6.0308	1.4255	2.3072	3.6929
0.15		1.5654	1.1370	1.3865	1.5648	
0.20		1.4924	1.0618	1.3100	1.4916	
SSFF	1.0	0.10	1.4048	0.9794	1.2221	1.4039
	1.0	0.15	1.4924	1.0618	1.3100	1.4916
	1.0	0.20	1.4048	0.9794	1.2221	1.4039
SSCC	1.0	0.10	11.7755	4.2272	6.3645	9.0909
		0.15	11.2666	3.6373	5.1771	6.5323
		0.20	9.5634	3.6470	5.4584	7.5418
	2.0	0.10	9.5634	3.1659	4.4738	5.5851
		0.15	7.6562	3.0844	4.5831	6.1172
CCCC	1.0	0.10	15.7082	5.8246	8.6295	13.0190
		0.15	12.3110	3.8011	5.9014	8.2427
		0.20	11.7743	3.6040	5.1482	6.6647
	1.0	0.15	11.9270	4.8605	7.1898	10.2752
		0.20	10.0551	3.3038	5.0834	6.9544
	2.0	0.10	9.6791	3.1421	4.4573	5.7077
		0.15	4.9386	2.4645	3.6235	4.9098
CCFF	1.5	0.10	2.6111	1.0791	1.6994	2.5927
		0.15	4.2863	2.0965	3.1124	4.2515
		0.20	2.4230	0.9790	1.5510	2.4009
	1.0	0.10	3.6443	1.7618	2.6271	3.6032
		0.15	2.2090	0.8738	1.3915	2.1823
	1.5	0.10	3.7233	0.8571	2.7887	5.3638
		0.15	3.4253	0.8102	2.6425	4.7477
0.20		3.0964	0.7590	2.4823	4.1430	
SFSF	1.0	0.10	1.3848	0.3093	0.7539	3.6805
	1.0	0.15	1.3377	0.2998	0.7303	3.4372
	1.0	0.20	1.2876	0.2901	0.7053	3.1646

2.4 Concluding remarks

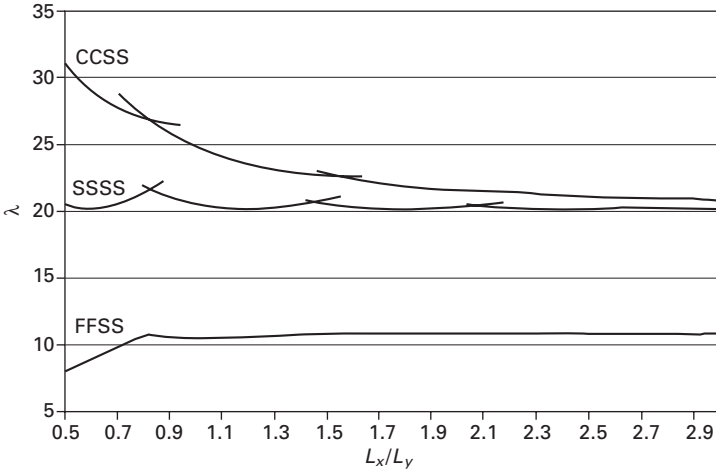
Buckling equations for shear deformable plates, including the effect of the higher-order nonlinear strains on the potential energy of the in-plane loads, were derived. The solution was performed using the extended Kantorovich method which yields an exact solution for several cases of boundary conditions and highly accurate results for other cases. The buckling behaviour of

Table 2.6 Buckling load factor λ for rectangular plates subjected to biaxial compression, ($\alpha_x = 2, \mu = 1, \nu = 0.3$)

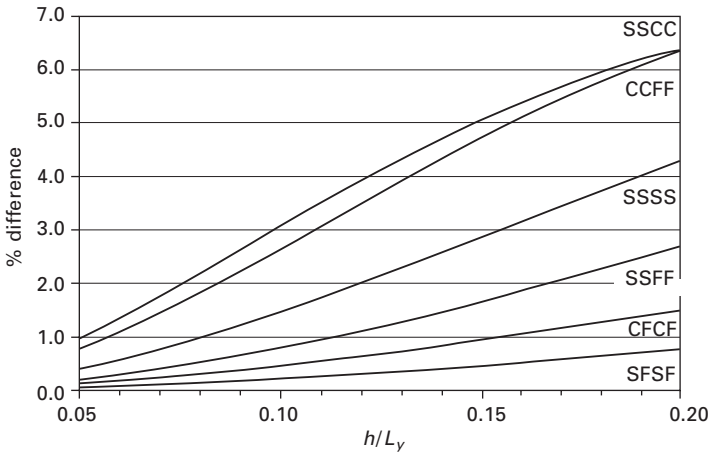
BC	γ	h/L_y	Buckling load parameter λ			
			$\beta = 0$	$\beta = 1, \alpha_y = 0$	$\beta = 1, \alpha_y = 1$	$\beta = 1, \alpha = 2$
SSSS	1.0	0.10	20.5441	3.5188	6.1425	11.5130
		1.5	20.8502	1.9760	3.7131	7.9382
		3.0	20.1788	1.1884	2.0639	3.5411
	1.0	0.15	16.6866	3.2128	5.5199	9.5289
			1.5	16.6866	1.8646	3.4837
	1.0	0.20	13.3230	2.8602	4.8293	7.6207
			1.5	13.3230	1.7304	3.2084
SSFF	1.0	0.10	2.4369	1.2690	1.7243	2.4155
	1.0	0.15	2.2967	1.1782	1.6115	2.2723
	1.0	0.20	2.1376	1.0808	1.4879	2.1097
SSCC	1.0	0.10	27.6905	5.6431	10.0243	16.1643
		1.5	27.3123	4.3680	7.6910	12.4020
	1.0	0.15	19.4654	4.8038	8.3555	12.2587
			1.5	19.6347	3.7822	6.5957
	1.0	0.20	13.2338	3.9927	6.7689	8.9825
CCCC	1.0	0.10	30.9791	7.5548	13.0190	21.4644
		2.0	28.2922	4.2061	7.4079	12.6413
		3.0	27.7529	3.7719	6.0159	9.0099
	1.0	0.15	20.3214	6.0568	10.2752	15.0861
			2.0	19.7485	3.6456	6.3565
	1.0	0.20	19.5897	3.2858	5.2045	7.6348
CCFF	1.0	0.10	6.2573	2.5371	3.8977	6.0916
			1.5	3.6834	1.1790	1.9044
	1.0	0.15	5.4098	2.1566	3.3354	5.2137
			1.5	3.3973	1.0706	1.7387
	1.0	0.20	4.5896	1.8125	2.8103	4.3593
			1.5	3.0820	0.9569	1.5621
CFCF	1.0	0.10	14.6783	1.2028	5.3638	20.3422
	1.0	0.15	10.8640	1.1150	4.7477	14.5932
	1.0	0.20	8.0877	1.0214	4.1430	10.7531
SFSF	1.0	0.10	10.8505	0.6469	3.6805	11.1633
	1.0	0.15	9.0164	0.6229	3.4372	9.4216
	1.0	0.20	7.2739	0.5976	3.1646	7.6123

rectangular plates loaded by unidirectional and bidirectional in-plane linearly varying forces was presented for many combinations of boundary conditions and loading combinations. Several conclusions can be drawn for the extensive number of buckling factors presented here:

- The shear deformations have significant effect on the stability of plates and must be included in the derivation of the buckling equations.

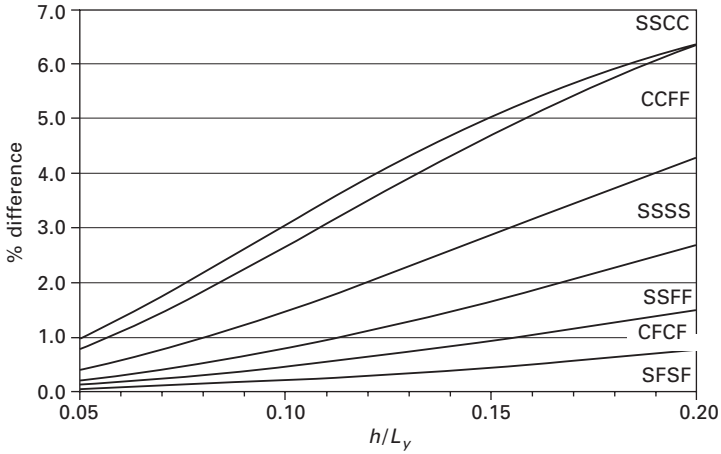


2.4 Buckling load parameters λ for rectangular plates subjected to in-plane moments: study for aspect ratio effect ($h/L_y = 0.1$, $\beta = 0$, $\alpha_x = 2$, $\mu = 1$, $\nu = 0.3$).

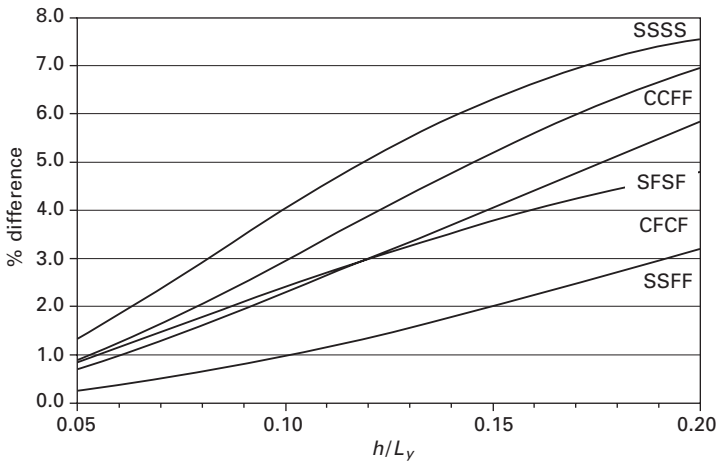


2.5 Influence of higher-order nonlinear strain terms on buckling load parameter for square plates with different boundary conditions: percentage difference $\mu = 0$ to $\mu = 1$. ($\gamma = 1$, $\beta = 0$, $\alpha_x = 0$, $\nu = 0.3$).

- The effect of the nonlinear strain terms on the buckling factor should also be incorporated in all cases, as it results in significant reduction of the buckling factors for many cases. This effect increases as the plate thickness ratio increases.
- The variation of the in-plane forces, and the combination of loading in two directions result in complex mode shapes of buckling, and of the

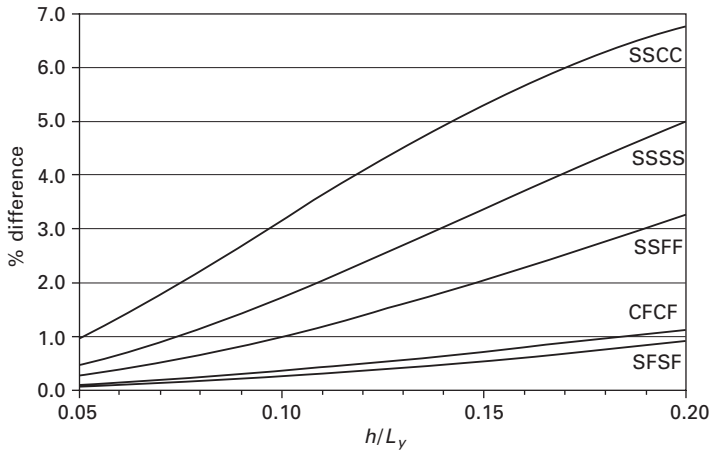


2.6 Influence of higher-order nonlinear strain terms on buckling load parameter for square plates with different boundary conditions: percentage difference $\mu = 0$ to $\mu = 1$ ($\gamma = 1, \beta = 0, \alpha_x = 1, \nu = 0.3$).

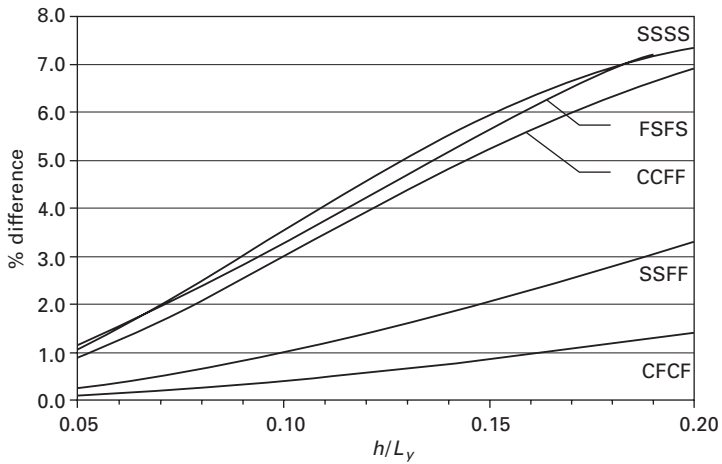


2.7 Influence of higher-order nonlinear strain terms on buckling load parameter for square plates with different boundary conditions: percentage difference $\mu = 0$ to $\mu = 1$ ($\gamma = 1, \beta = 0, \alpha_x = 2, \nu = 0.3$).

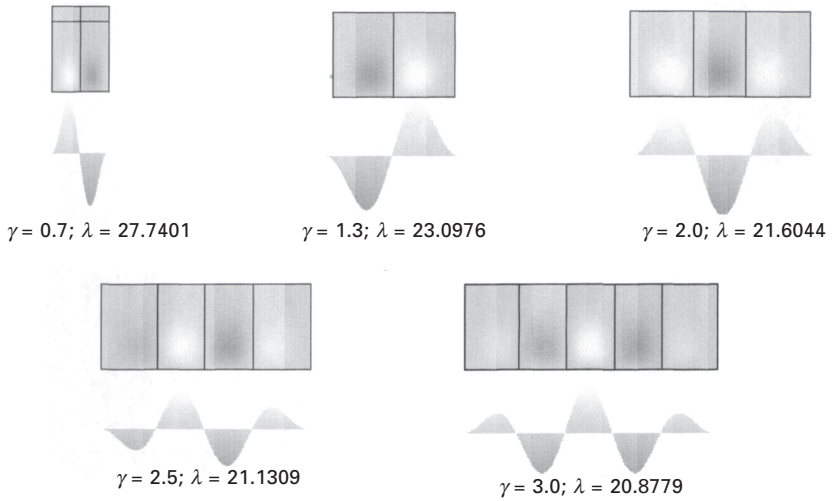
buckling factors which should be further studied and organized in a simple and straightforward fashion so it can be easily used in design. The results presented here may serve as indicators in many cases, and also for comparison by other numerical methods.



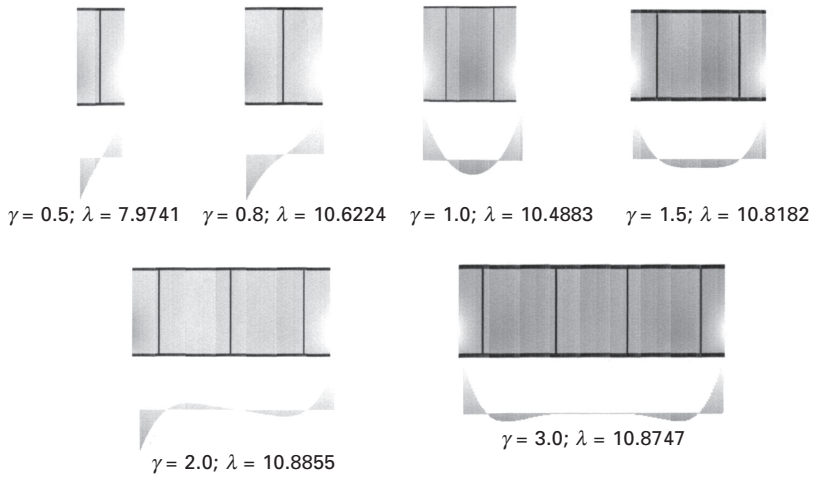
2.8 Influence of higher-order nonlinear strain terms on buckling load parameter for square plates with different boundary conditions: percentage difference $\mu = 0$ to $\mu = 1$ ($\gamma = 1, \beta = 1, \alpha_x = 2, \alpha_y = 0, \nu = 0.3$).



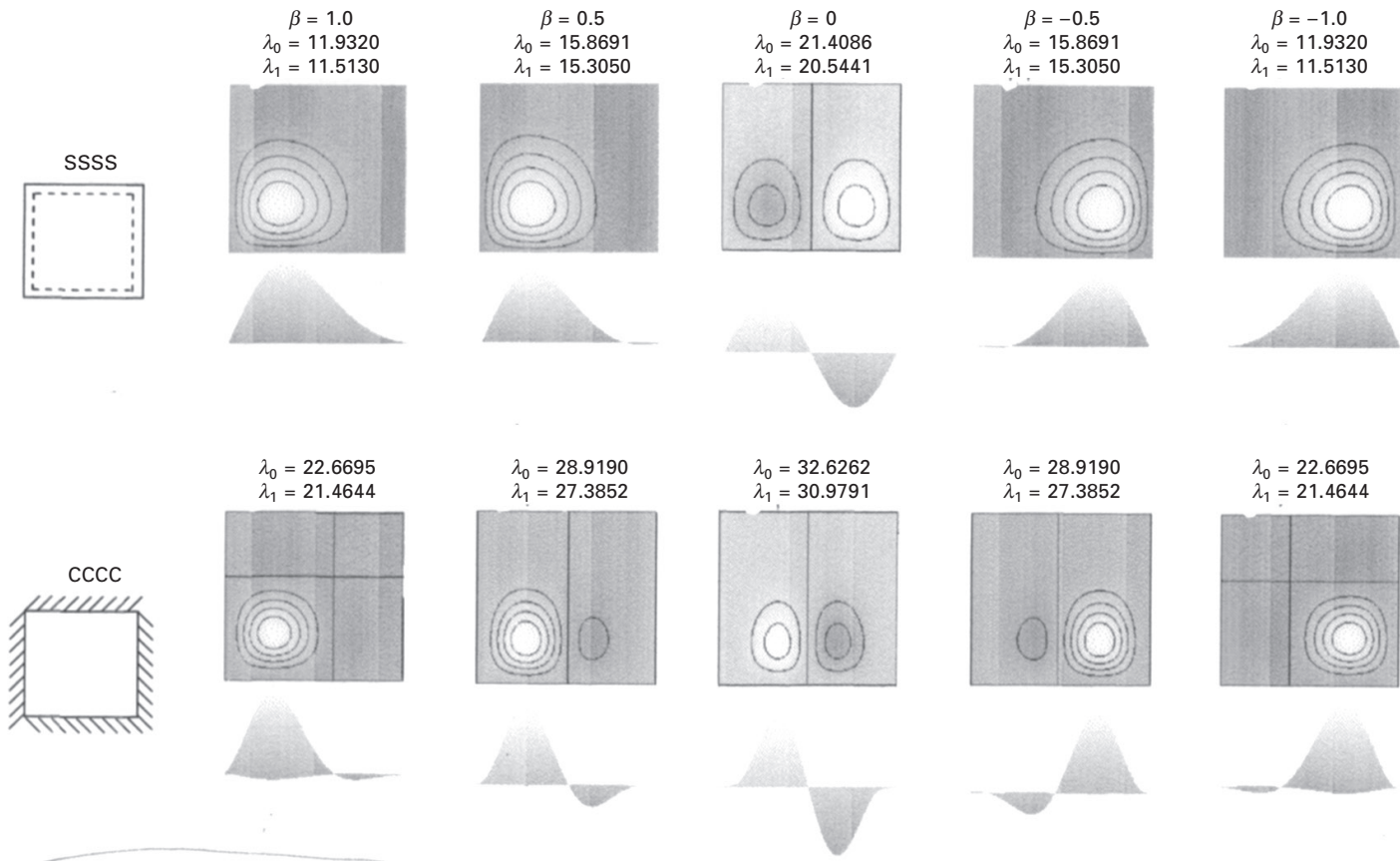
2.9 Influence of higher-order nonlinear strain terms on buckling load parameter for square plates with different boundary conditions: percentage difference $\mu = 0$ to $\mu = 1$ ($\gamma = 1, \beta = 1, \alpha_x = 2, \alpha_y = 2, \nu = 0.3$).



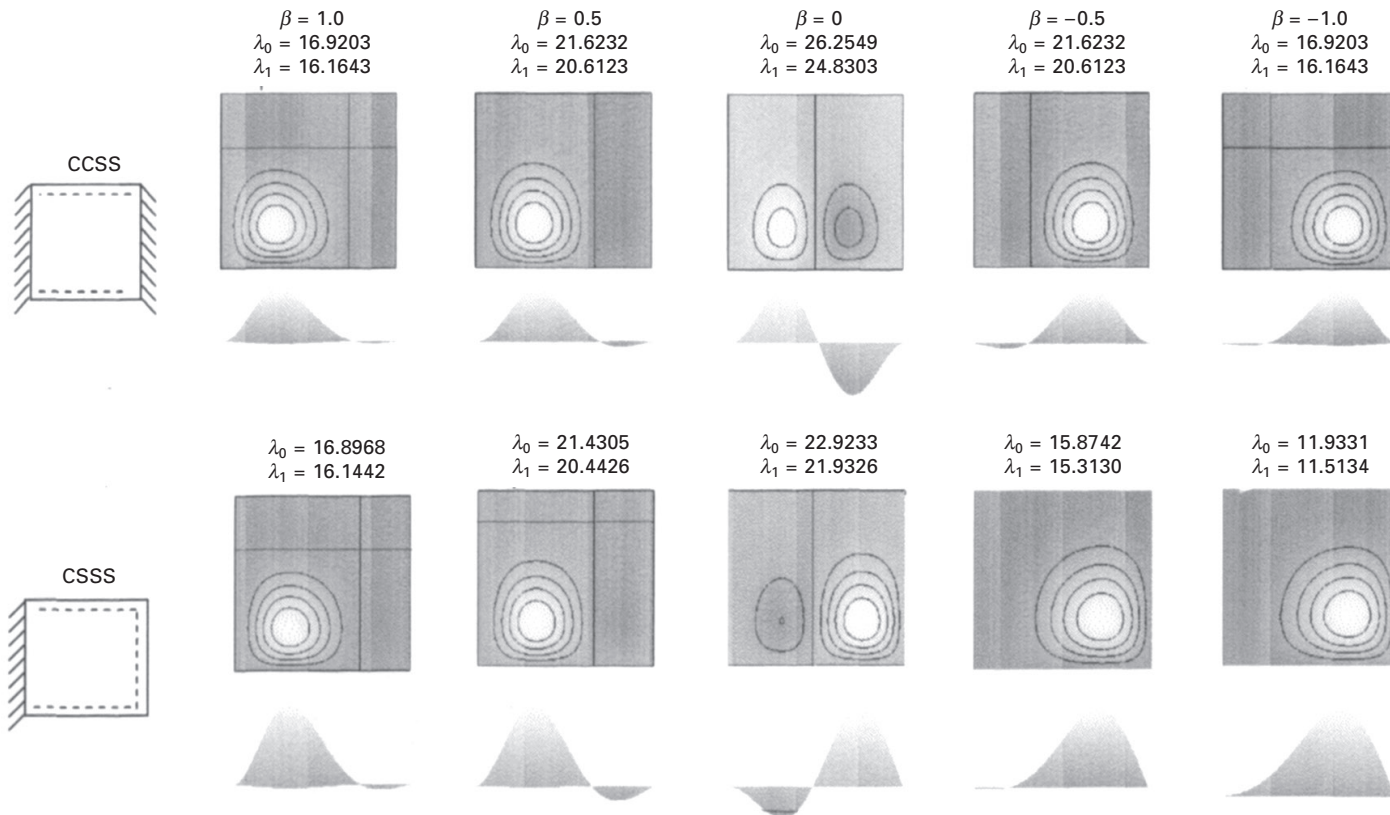
2.10 Buckling shapes for CCSS plate loaded by in-plane moments in x-direction $\alpha_x = 2$, $h/L_y = 0.1$, $\beta = 0$, $\mu = 1$.



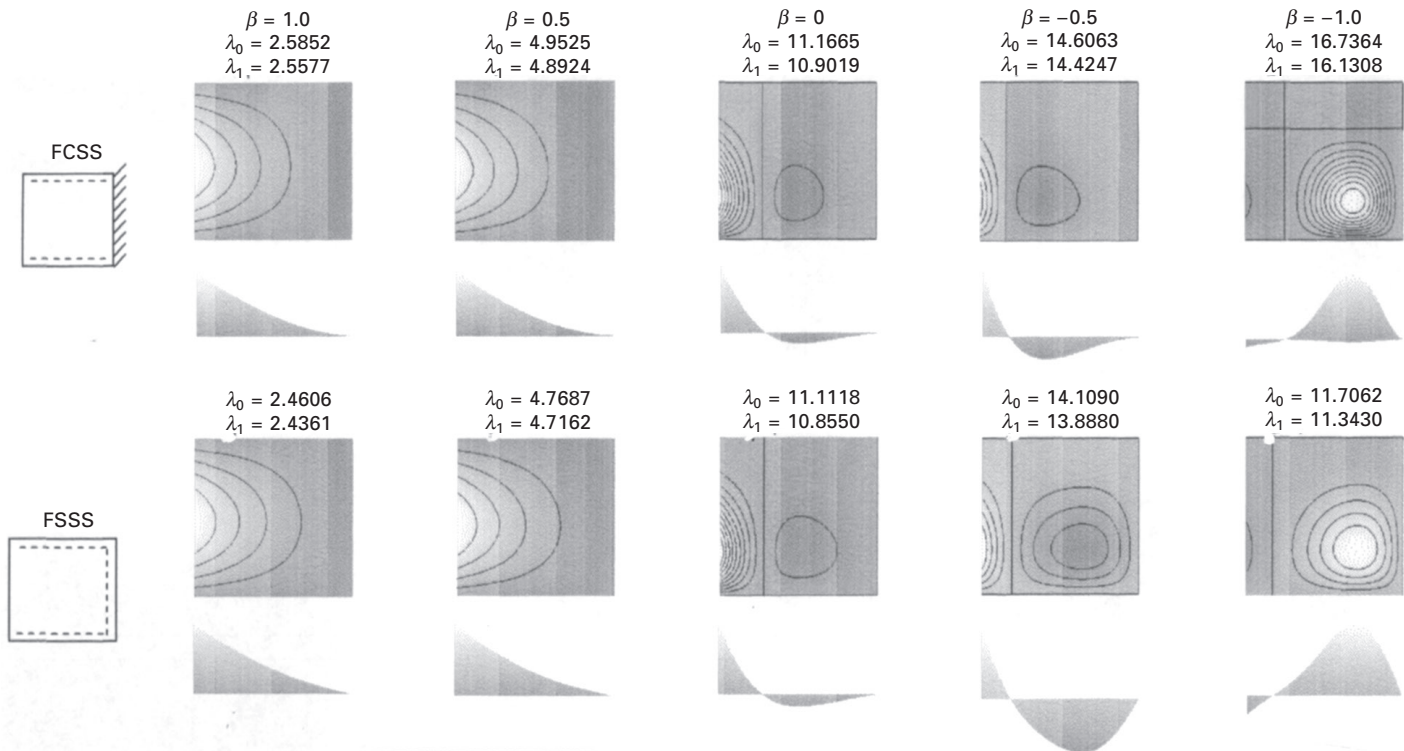
2.11 Buckling shapes for FFSS plate loaded by in-plane moments in x-direction $\alpha_x = 2$, $h/L_y = 0.1$, $\beta = 0$, $\mu = 1$.



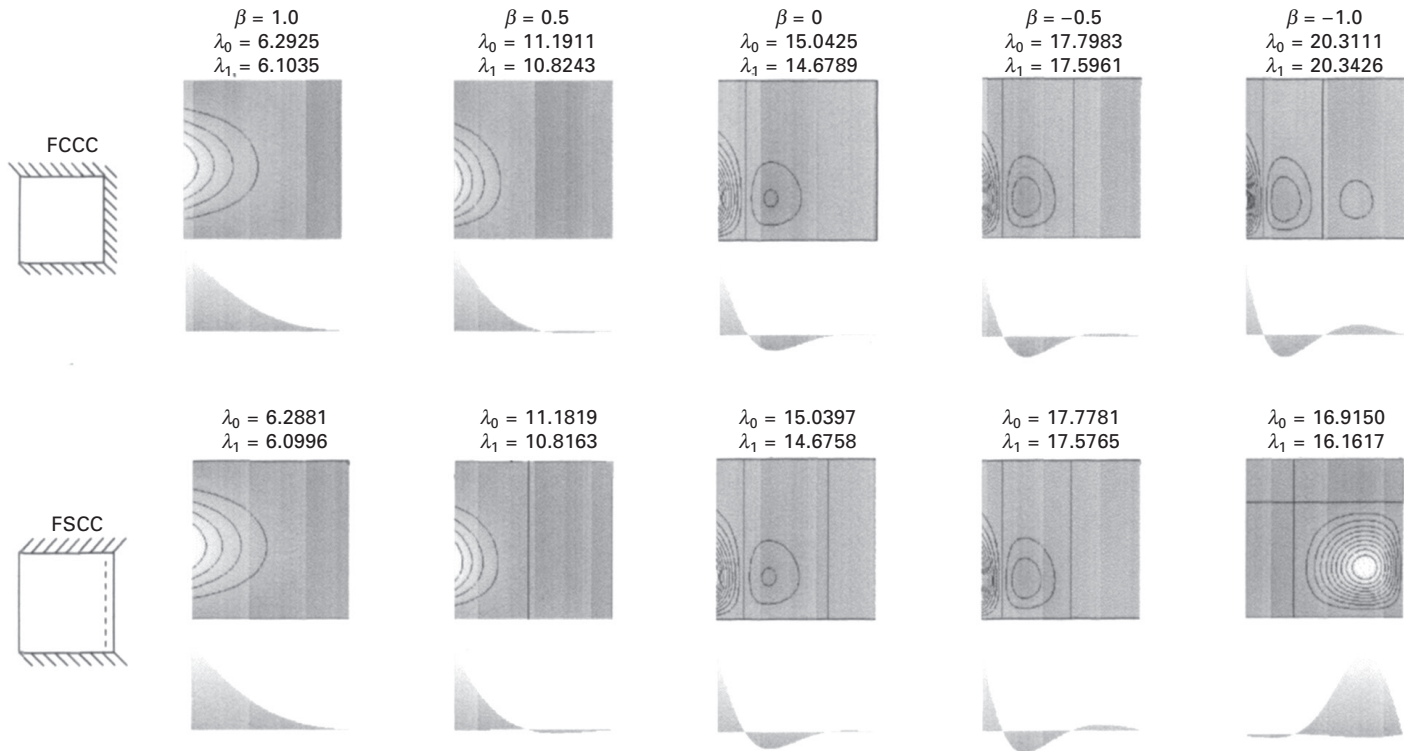
2.12 Buckling load parameters λ and modes for square plates subjected to in-plane moments in both directions, $\alpha_x = 2$, $\alpha_y = 2$, $h/L_y = 0.1$, λ_0 for $\mu = 0$ and λ_1 for $\mu = 1$.



2.13 Buckling load parameters λ and modes for square plates subjected to in-plane moments in both directions, $\alpha_x = 2$, $\alpha_y = 2$, $h/L_y = 0.1$, λ_0 for $\mu = 0$ and λ_1 for $\mu = 1$.



2.14 Buckling load parameters λ and modes for square plates subjected to in-plane moments in both directions, $\alpha_x = 2$, $\alpha_y = 2$, $h/L_y = 0.1$, λ_0 for $\mu = 0$ and λ_1 for $\mu = 1$.



2.15 Buckling load parameters λ and modes for square plates subjected to in-plane moments in both directions, $\alpha_x = 2$, $\alpha_y = 2$, $h/L_y = 0.1$, λ_0 for $\mu = 0$ and λ_1 for $\mu = 1$.

2.5 References

- Azhari, A., Hoshdar, S. and Bradford, M.A. (2000), On the use of bubble functions in the local buckling analysis of plate structures by the spline finite strip method. *International Journal for Numerical Methods in Engineering*, **48**(4), 583–593.
- Bert, C.W. and Devarakonda, K.K. (2003), Buckling of rectangular plates subjected to nonlinearly distributed in-plane loading. *International Journal of Solids and Structures*, **40**(16), 4097–4106.
- Bert, C.W. and Malik, M. (1997), On the buckling characteristics symmetrically laminated cross-ply plates. *Mechanics of Composite Materials and Structures*, **4**(1), 39–67.
- Bert, C.W. and Malik, M. (1999), Buckling analysis of thick laminated plates: higher-order theory with rotatory moments. *Journal of Thermoplastic Composite Materials*, **12**, 336–350.
- Dawe, D.J. and Craig, T.J. (1986), The vibration and stability of symmetrically-laminated composite rectangular plates subjected to in-plane stresses. *Composite Structures*, **5**(2), 281–307.
- Dawe, D.J. and Roufael, O.L. (1982), Buckling of rectangular Mindlin plates. *Computer and Structures*, **15**, 461–471.
- Eisenberger, M. (1991), Buckling loads for variable cross-section members with variable axial forces. *International Journal of Solids and Structures*, **27**(2), 135–143.
- Eisenberger, M. and Alexandrov, A. (2003), Buckling loads of variable thickness thin isotropic plates. *Thin-Walled Structures*, **41**, 871–889.
- Eisenberger, M. (1995), Dynamic stiffness matrix for variable cross-section Timoshenko beams. *Communications in Numerical Methods in Engineering*, **11**(6), 507–513.
- Grimm, T.R. and Gerdeen, J.C. (1975), Instability analysis of thin rectangular plates using the Kantorovich method. *Trans. ASME, Journal of Applied Mechanics*, **42**, 110–114.
- Hermann, G and Armenakas, A.E. (1960), Vibrations and stability of plates under initial stress. *Proc. ASCE, Journal of Engineering Mechanics Division*, **86**, 65–94.
- Kang, J.H. and Leissa, A.W. (2001), Vibration and buckling of SS-F-SS-F rectangular plates loaded by in-plane moments. *International Journal of Structural Stability and Dynamics*, **1**, 527–543.
- Kang, J.H. and Shim, H.J. (2004), Exact solutions for the free vibrations of rectangular plates having in-plane moments acting on two opposite simply supported edges. *Journal of Sound and Vibration*, **273** (4–5), 933–948.
- Kerr, A.D. (1969), An extended Kantorovich method for the solution of eigenvalue problem. *International Journal of Solids and Structures*, **15**, 559–572.
- Kitipornchai, S., Xiang, Y., Wang, C.M. and Liew, K.M. (1993), Buckling of thick skew plates. *International Journal for Numerical Method in Engineering*, **36**, 1299–1310.
- Leissa, A.W. and Kang, J.H. (2002), Exact solutions for vibration and buckling of SS-C-SS-C rectangular plate loaded by linearly varying in-plane stresses. *International Journal of Mechanical Sciences*, **44**, 1925–1945.
- Reddy, J.N. (1984), A simple higher order theory for laminated composite plates. *Trans. ASME, Journal of Applied Mechanics*, **51**(4), 745–752.
- Reddy, J.N. (1999), *Theory and Analysis of Elastic Plates*. Taylor & Francis, Philadelphia, PA.
- Romeo, G. and Ferrero, G. (2001), Analytical/experimental behavior of anisotropic rectangular plates under linearly varying combined loads. *AIAA Journal*, **39**(5), 932–941.

- Shufrin, I. and Eisenberger, M. (2005), Stability and vibration of shear deformable plates – first order and higher order analyses. *International Journal of Solids and Structures*, **42**(3–4), 1225–1251.
- Sun, C.T. (1972), On the equations for a Timoshenko beam under initial stress. *Trans. ASME, Journal of Applied Mechanics*, **39**(1), 282–285.
- Sun, C.T. (1973), Incremental deformations in orthotropic laminated plates under initial stress. *Trans. ASME, Journal of Applied Mechanics*, **40**(1), 193–200.
- Timoshenko, S.P. and Gere, J.M. (1961), *Theory of Elastic Stability*. McGraw-Hill, New York.
- Wang, C.M., Xiang, Y., Kitipornchai, S. and Liew, K.M. (1994), Buckling solutions for Mindlin plates of various shapes. *Engineering Structures*, **16**(2), 119–127.
- Wang, C.M., Reddy, J.N. and Lee, K.H. (2000), *Shear Deformable Beams and Plates; Relationships with Classical Solution*, Elsevier, Amsterdam.
- Whitney, J.M. (1987), Curvature effects in the Buckling of symmetrically-laminated rectangular plates with transverse shear deformation. *Composite Structures*, **8**(2), 85–103.

Finite element formulation for plate stability analysis

W KANOK - NUKULCHAI,
Asian Institute of Technology, Thailand

3.1 Introduction

Structural stability is an important issue in the design of many types of civil, mechanical, and aeronautical structures. This is especially true for structures having one or two dimensions that are small in relation to the rest, such as beam-columns, plates and shells. These structures are susceptible to lateral instability commonly idealized as an elastic buckling. Structural instability, in the form of bifurcation or a snap-through phenomenon, can be rigorously identified by tracing the nonlinear load-displacement paths of the structure. This procedure normally requires extensive amounts of computing time and resources. Practical consideration usually favors a linearized system for determining the critical instability at the bifurcation point. This simply requires solving an eigenvalue problem, considering finite displacement for the components in the transverse direction.

Enormous effort has been directed toward the developments of plate finite elements to serve as the basis for plate instability analysis. In the early days, most developments of plate elements were based on the classical thin plate theory, in which C^1 continuity of the displacement field must be enforced. The earlier C^1 -continuity plate elements were developed by Bell (1969) and Butlin and Ford (1970). However, the need for higher-order derivatives makes these elements cumbersome in imposing the essential boundary conditions. By relaxing this continuity requirement, nonconforming plate elements were proposed by Melosh (1963) and Bazeley *et al.* (1965). In addition, Wemper *et al.* (1968) and Stricklin *et al.* (1969) proposed a 'discrete Kirchhoff hypothesis' approach, by imposing zero shear strains only at selected discrete points.

The first published work on stability analysis of plates using the finite element method was authored by Kapur and Hartz (1966), based on the nonconforming 12 degrees-of-freedom rectangular plate element developed by Melosh (1963). Their nonconforming plate element gives a lower bound to the corresponding analytical solution. Anderson *et al.* (1968) presented a similar application based on nonconforming triangular plate element proposed

earlier by Bazeley *et al.* (1965). Later on, Carson and Newton (1969) solved plate instability problems using a fully conforming 16 degrees-of-freedom rectangular plate element. This conforming plate element provides an upper bound solution that is superior in accuracy to the solution obtained by the nonconforming plate element.

In the 1970s, researchers recognized that more versatile plate elements can be developed in the framework of the Reissner–Mindlin theory of thick plates. By considering the plate transverse shear deformation, the plate rotation field is basically separated from the transverse displacement field, leading to a simple C^0 -continuity requirement for the shape functions representing both the displacement and the rotation fields. However, such thick plate elements can exhibit a so-called *shear locking phenomenon* when the plate becomes relatively thin due to the excessive zero-shear constraint that is similar to the Kirchhoff hypothesis. The first explanation of the shear locking effect was made by Hughes *et al.* (1977), pointing out the over-constraint at the thin plate limit of two incompatible shape functions, representing the rotation and the corresponding slope. In their simple bilinear thick plate element, the shear locking constraint is alleviated by using a *reduced integration* scheme for the shear energy term, as earlier introduced by Zienkiewicz *et al.* (1971). The simplicity of the element lends itself to a concise and efficient computer implementation. It was further shown by Kanok-Nukulchai (1979) and Kanok-Nukulchai *et al.* (1981) that this type of plate element, as well as similar shell elements, can be directly degenerated from the 3D field equations. Since then, the Reissner–Mindlin thick plate theory was widely adopted in plate element formulations by several researchers such as Hughes and Rezdaryan (1981), Crisfield (1984) and Bathe and Dvorkin (1985).

With particular application to plate stability analysis, a nine-noded thick plate element with enhanced shear interpolation was employed by Hinton *et al.* (1988). Smith (1995) introduced a p-version of the finite element method for problems of plate buckling with the inclusion of transverse shear deformation. In theory, a thick plate buckles earlier than a thin plate of the same dimension and boundary conditions. Thus, for the purposes of conservative design, the inclusion of shear deformation may be important.

Numerical analysis of plate stability requires mathematical formulation of elastic and geometric stiffness matrices of the plate element. In the subsequent section, for simplicity, the bilinear degenerated plate/shell element concept proposed by Hughes *et al.* (1977), Kanok-Nukulchai (1979) and Kanok-Nukulchai *et al.* (1981) will be selected to illustrate the formulation of the standard eigenvalue problem to solve for its elastic stability limit. In addition, an axisymmetric annular thick plate element, following the work of Ng (1995), will be used to demonstrate the solution procedure for a tapered circular thick plate with allowance for pre-buckling deformation.

3.2 The formulation

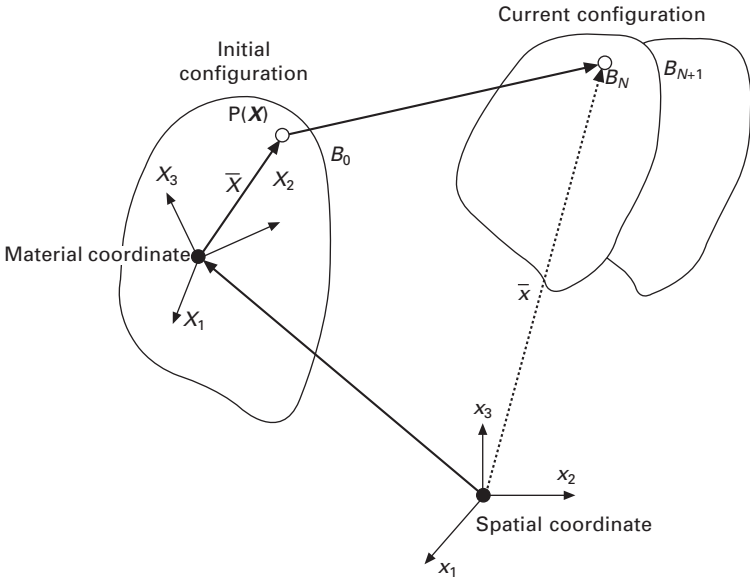
The tangent stiffness at any deformation state in the equilibrium path consists basically of two distinctive terms, namely, the material stiffness and the geometric stiffness. The condition of the tangent stiffness carries some implication on the stability condition of the system. At any specific point in the equilibrium path, if the tangent stiffness matrix is singular, a large magnitude of displacement can emerge even with a small disturbance of load, thus implying the *instability* condition. The section below will derive a standard expression for the tangent stiffness matrix associated with a finite element in the framework of the total Lagrangian formulation (see Kanok-Nukulchai *et al.* (1981)).

As shown in Fig. 3.1, two sets of Cartesian coordinates are used consistently: the spatial coordinate system x and the material coordinate system X . The spatial coordinate system x is used to describe the motion of all continuum particles in space while the material coordinate system X describes the material framework at a reference configuration B_0 .

The motion of a particle P can then be expressed in terms of the displacement vector u from its reference position in configuration B_0 as

$$x_j(\mathbf{X}, t) = \delta_{jJ}X_J + u_j(\mathbf{X}, t) \tag{3.1}$$

in which δ_{jJ} is the Cartesian shifter between x and X systems and d is the position vector of the origin of X . Throughout this formulation, lower case and upper case subscripts are used to differentiate between the components



3.1 Motion of a continuum

associated with \mathbf{x} and \mathbf{X} respectively. The subscript 0 following B refers to the initial undeformed configuration. In what follows, the total Lagrangian mode of description will be used with the initial undeformed configuration B_0 together with its corresponding boundary ∂B_0 being regarded as the reference configuration.

Initially, the total potential energy for finite elasticity can be expressed with respect to the domain of the reference configuration as

$$\pi(\mathbf{E}) = \frac{1}{2} \int_{B_0} S_{KL} E_{KL} dV - \int_{B_0} \rho_0 \mathbf{u}_I \mathbf{b}_I dV - \int_{\delta B_0} \delta \mathbf{u}_I \mathbf{T}_I dS \quad 3.2$$

in which \mathbf{b} and \mathbf{T} are respectively the body force and the traction, \mathbf{u} is the displacement vector, ρ_0 is the mass density, all with respect to the reference configuration, of which B_0 and δB_0 are respectively the domain and the domain boundary. In the same equation, the Green strain tensor \mathbf{E} is defined as

$$\mathbf{E}_{IJ} = \frac{1}{2} (\mathbf{F}_{kI} \mathbf{F}_{kJ} - \delta_{IJ}) \quad 3.3$$

in which \mathbf{F} is the deformation gradient associated with the motion from B_0 to B , and the second Piola-Kirchhoff stress tensor \mathbf{S} , which together with \mathbf{E} defines the material constitution in the form

$$\mathbf{S}_{IJ} = \mathbf{D}_{IJKL} \mathbf{E}_{KL} \quad 3.4$$

where \mathbf{D} is the fourth-order elasticity tensor. By assuming that the motion is sufficiently smooth for differentiation, \mathbf{F} can be obtained by the following equation

$$\mathbf{F}_{jJ} = \frac{\partial x_j}{\partial X_J} = \delta_{jJ} + u_{j,J} \quad 3.5$$

In view of Eqs (3.3)-(3.5), the first variation of Eq. (3.2), $\delta\pi$, can be derived. By forcing $\delta\pi = 0$ and applying integration by parts with Green's Theorem, one can obtain the local balance of linear momentum governing any particle in B_0 in the Lagrangian mode as

$$(\mathbf{S}_{IJ} \mathbf{F}_{jJ})_{,I} + \rho_0 \mathbf{b}_j = 0 \quad 3.6$$

The traction boundary condition associated with boundary surface ∂B_0 is defined as follows

$$n_I \mathbf{S}_{IJ} \mathbf{F}_{jJ} - \hat{\mathbf{T}}_j = 0 \quad 3.7$$

where n is the unit normal vector of ∂B_0 . By using the Galerkin weighted residual method, the equation of linear momentum, Eq. (3.6), and boundary condition, Eq. (3.7), can be combined to construct Galerkin's weak form of the problem as

$$\begin{aligned}
G(\mathbf{u}, \eta) = & - \int_{B_0} (S_{IJ} F_{jI})_{,I} \eta_j dV - \int_{B_0} \rho_0 b_j \eta_j dV \\
& + \int_{\delta B_0} (\eta_I S_{IJ} F_{jI} - \hat{T}_j) \eta_j dA
\end{aligned} \tag{3.8}$$

where η denotes a weight field over B_0 . In the Galerkin method, η belongs to the same function space as the displacement field and satisfies the homogeneous essential boundary conditions.

Applying the Gauss–Green theorem to the first integral of Eq. (3.8) leads to its canonical form. As long as both u and η are continuous over the whole domain, the Galerkin function can be written as an accumulation of individual element contributions, i.e., $G(\mathbf{u}, \eta) = \sum_e G^e(\mathbf{u}, \eta)$ where the canonical form of a typical G^e associated with Eq. (3.8) can be expressed as

$$\begin{aligned}
G^e(\mathbf{u}, \eta) = & \int_{B_0^e} S_{IJ} F_{jI} \eta_{j,I} dV - \int_{B_0^e} \rho_0 b_j \eta_j dV \\
& - \int_{\partial B_0^e} \hat{T}_j \eta_j dA
\end{aligned} \tag{3.9}$$

The displacement field and the weight field of a particle $P(\mathbf{X})$ can be represented as

$$\mathbf{u}(\mathbf{X}) = \sum_{a=1}^n N^a(\mathbf{X}) \mathbf{U}^a \quad \mathbf{X} \in B_0^e \tag{3.10}$$

$$\eta(\mathbf{X}) = \sum_{a=1}^n N^a(\mathbf{X}) \mathbf{H}^a \quad \mathbf{X} \in B_0^e \tag{3.11}$$

where N^a is an interpolation function associated with node a of the element, \mathbf{H}^a denotes the same element nodal values of η , and n is the number of nodes in the element.

The substitution of Eqs. (3.10) and (3.11) into Eq. (3.9) yields

$$G^e(\mathbf{U}, \mathbf{H}) = \mathbf{H}_j^b (\mathbf{K}_j^b - \mathbf{R}_j^b) \tag{3.12}$$

in which the mass matrix, the internal force vector and the generalized force vector are, respectively, expressed by

$$\mathbf{K}_j^b = \int_{B_0^e} S_{IJ} F_{jI} N_{,I}^b dV \tag{3.13}$$

and

$$\mathbf{K}_j^b = \int_{\partial B_0^e} \hat{T}_j N^b dA + \int_{B_0^e} \rho_0 b_j N^b dV \tag{3.14}$$

Observe that the superscripts refer to a node number while the subscripts refer to a spatial basis. By assembling all individual element contributions, one obtains

$$G(\mathbf{U}, \mathbf{H}) = \mathbf{H}^T[\mathbf{K}(\mathbf{U}) - \mathbf{R}] = 0 \quad 3.15$$

Since \mathbf{H} , a term that can be identified with the *virtual displacement* in the virtual work principle, can be arbitrary, Eq. (3.15) reduces to a system of discretized equations of motion in terms of variables \mathbf{U} as

$$\mathbf{K}(\mathbf{U}) - \mathbf{R} = 0 \quad 3.16$$

The solution of this nonlinear system of equations by the Newton–Raphson technique requires the linearization of the nonlinear term, $\mathbf{K}(\mathbf{U})$, with respect to \mathbf{U} . Thus, linearizing Eq. (3.16) with respect to \mathbf{U} leads to

$$\mathbf{DK}(\mathbf{U}_n^m) \Delta \mathbf{U}_n^m = \mathbf{R}_n - \mathbf{K}(\mathbf{U}_n^m) \quad 3.17$$

where $\mathbf{DK}(\mathbf{U}_n^m)$ denotes the tangent stiffness matrix about a trial displacement \mathbf{U}_n^m (assumed at the m th iteration for \mathbf{U}_n , which is the solution corresponding to the n th load step) and $\Delta \mathbf{U}_n^m$ is the iterative increment of the displacement. It is convenient to express the tangent stiffness $\mathbf{DK}(\mathbf{U}_n^m)$ in its componential form as

$$DK_{ji}^{ba}(\mathbf{U}_n^m) = \left. \frac{\partial K_j^b}{\partial U_i^a} \right|_{\mathbf{U}=\mathbf{U}_n^m} \quad 3.18$$

The substitution of Eq. (3.13) into Eq. (3.18) leads to

$$DK_{ji}^{ba}(\mathbf{U}_n^m) = \int_{B_0^e} \left[\frac{\partial S_{IJ}}{\partial U_i^a} F_{jJ} N_{,I}^b + S_{IJ} \frac{\partial F_{jJ}}{\partial U_i^a} N_{,I}^b \right] dV \Bigg|_{\mathbf{U}=\mathbf{U}_n^m} \quad 3.19$$

For an isoparametric element, the same interpolation functions are used to describe the geometry and the displacement field. Thus, the geometry is expressed as

$$\mathbf{x}(\mathbf{X}) = \sum_{a=1}^n N^a(\mathbf{X}) \mathbf{x}^a \quad \mathbf{X} \in B_0^e \quad 3.20$$

From Eqs. (3.1) and (3.20), the deformation gradient \mathbf{F} in the continuum can be evaluated from

$$F_{jJ} = \delta_{jJ} + N_{,J}^b U_j^a \quad 3.21$$

In view of the definition of the Green strain tensor, *i.e.* $E_{IJ} = \frac{1}{2} (F_{kl} F_{kJ} - \delta_{IJ})$, and the chain rule $\frac{\partial S_{IJ}}{\partial U_i^a} = \frac{\partial S_{IJ}}{\partial E_{KL}} \frac{\partial E_{KL}}{\partial U_i^a}$, one can obtain \mathbf{DK} as

$$DK_{ji}^{ba}(\mathbf{U}_n^m) = \left\{ \int_{B_0^e} [F_{jJ}(\mathbf{U})N_{,J}^b] \left[\frac{\partial S_{IJ}}{\partial E_{KL}}(\mathbf{U}) \right] [F_{iL}(\mathbf{U})N_{,K}^a] dV \right. \\ \left. + \int_{B_0^e} \delta_{ij} N_{,I}^b S_{IJ}(\mathbf{U}) N_{,J}^b dV \right\}_{\mathbf{U}=\mathbf{U}_n^m} \quad 3.22$$

Note that the first term on the right-hand side of Eq. (3.22) constitutes an elastic tangent stiffness including the effect of finite displacement, and the other term represents the effect of initial stresses.

So far, the formulation is valid for any material constitution. Focusing on the isotropic, linear elastic materials, the constitutive model for this type of material takes the form

$$D_{IJKL} = \frac{\partial S_{IJ}}{\partial E_{KL}} \quad 3.23$$

in which the fourth order elasticity tensor C_{IJKL} can be expressed in terms of the two Lamé's constants, λ and μ as

$$D_{IJKL} = \lambda \delta_{IJ} \delta_{KL} + \mu (\delta_{IK} \delta_{JL} + \delta_{IL} \delta_{JK}) \quad 3.24$$

Finally, Eqs. (3.13) and (3.22) can be rewritten in a matrix form as

$$\mathbf{K}^b = \int_{B_0^e} \mathbf{F} \mathbf{S} \nabla \mathbf{N}^b dV \quad 3.25$$

and

$$\mathbf{DK}^{ba} = \int_{B_0^e} (\mathbf{B}^b)^T \mathbf{D} \mathbf{B}^a dV + \int_{B_0^e} (\nabla \mathbf{N}^b)^T \mathbf{S} \nabla \mathbf{N}^a dV \cdot \mathbf{I} \quad 3.26$$

where $\nabla \mathbf{N}^b = \{N_{,1}^b \ N_{,2}^b \ N_{,3}^b\}^T$, \mathbf{S} is the matrix of the second Piola–Kirchhoff stress tensor, \mathbf{B}^a relates the vector of Green strains $\mathbf{E} = \{E_{11} \ E_{22} \ E_{33} \ 2E_{12}$

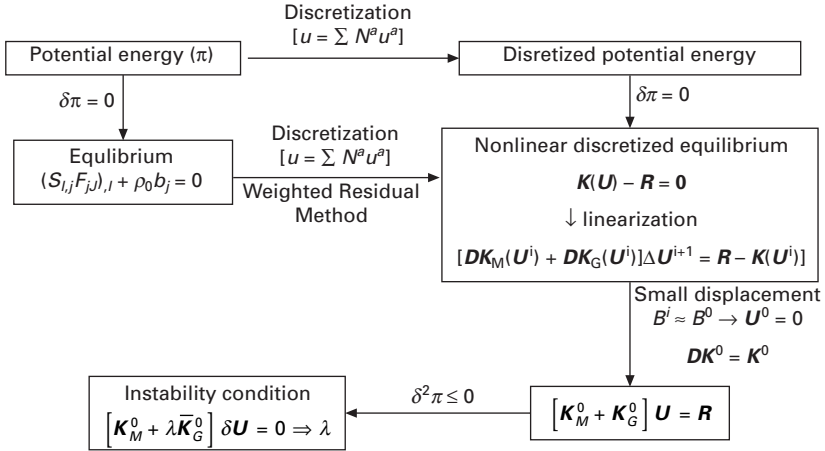
$2E_{23} \ 2E_{31}\}^T$ to the nodal variables \mathbf{U}^a , \mathbf{D} is the matrix form of $\left[\frac{\partial S_{IJ}}{\partial E_{KL}} \right]$

based on the material constitution in Eqs. (3.23) and (3.24), and \mathbf{I} is the identity matrix.

3.3 Elastic stability

Linear elastic buckling is an idealized situation in perfect plate buckling. In terms of the total potential energy, the first variation of the potential energy will result in the same equilibrium equation as in Eq. (3.16). The stability condition requires that the second variation of the potential energy is positive.

Conversely, the instability criterion of the system is given by a negative value of this second variation. A limit on stability exists when the second variation is zero. This is sometimes called neutral equilibrium when the determinant of the tangent stiffness matrix is zero. The diagram showing the derivation paths towards the instability condition is depicted in Fig. 3.2.



3.2 Diagram showing the formulation of instability condition.

For linear elastic buckling of plate neglecting the pre-buckling deformation, the plate structure is assumed to deform within a small displacement range just before the occurrence of the elastic buckling. Hence, the term F_{ij} in Eq. (3.21) can be reduced to δ_{ij} . Also since there is no significant difference between the reference configuration and the deformed configuration, one does not need to differentiate \mathbf{X} and \mathbf{x} . Therefore, the tangent stiffness DK can be reduced to the stiffness matrix evaluated at the initial configuration, K , which can be simplified in a more familiar form as:

$$DK_{ji}^{ba}(U^0) \equiv K_{ji}^{ba} = \int_{B^e} N_{,j}^b d_{jlik} N_{,k}^a dV + \delta_{ij} \int_{B^e} N_{,j}^a \sigma_{lk} N_{,k}^b dV \quad 3.27$$

or

$$\mathbf{K} = \mathbf{K}_M + \mathbf{K}_G(\sigma) \quad 3.28$$

in which the fourth-order elasticity tensor, $d_{ijkl} = \lambda \delta_{ij} \delta_{kl} + \mu(\delta_{ik} \delta_{jl} + \delta_{il} \delta_{jk})$ and σ is referred as the initial stress of the system.

As shown in the diagram in Fig. 3.2, the instability criterion is given by a negative value of the second variation of the potential energy. A limit on stability exists when this second variation is zero. This limit is sometimes referred as neutral equilibrium since the configuration can be changed infinitely

by a small amount of force. One way to ensure stability of the system is the *positive definiteness* of the tangent stiffness matrix in Eq. (3.28). This means that the sign of its determinant must be greater than zero. Numerically, one can obtain the critical magnitude of σ that can cause singularity to \mathbf{K} by solving the associated eigenvalue problem.

Note that in Eq. (3.28) \mathbf{K}_G does not explicitly contain the displacement vector but is proportional to the stress level. Based on the initial stress theory of Trefftz (1933), the following two-step analysis is required to solve elastic buckling problems, as depicted in Table 3.1. In the first step, the reference stress tensor, $\sigma_o = \hat{\sigma}(U_o)$ can be evaluated for each element from its nodal displacements U_o as the result of

$$\mathbf{K}_M U_o = R_o \tag{3.29}$$

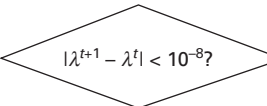
in which R_o is a selected basis for the load vector in the system. In the next step, the geometric stiffness \mathbf{K}_G can be formulated based on this stress level, *i.e.*, $\sigma_o = \hat{\sigma}(U_o)$ as a result of R_o . The load multiplication factor λ can then be determined by solving the following system of eigenvalue system, *i.e.*

$$[\mathbf{K}_M + \lambda \mathbf{K}_G(\sigma_o)] \delta U = 0 \tag{3.30}$$

in which λ and δU represent the eigenvalue and the corresponding eigenvector of the system. Let λ_{cr} be the lowest eigenvalue, then the vector of the critical buckling load can be obtained as $\lambda_{cr} R_o$. Correspondingly, the eigenvector represents the corresponding fundamental buckling mode.

In the above process, the material stiffness was formed based on the initial undeformed configuration. In reality, the structure is undergoing some deformation before the point of instability occurs. Ziegler (1983) found that

Table 3.1 Algorithm for buckling analysis including prebuckling inplane deformation.

Process	Material Stiffness	Geometric stiffness	Force System	Results
Trefftz's Approach (W/o prebuckling deformation)				
1 Unstressed	$[\mathbf{K}_M] = [\mathbf{K}_M(B_0)]$	-	$\{R_0\}$	$[\mathbf{K}_M]\{u\} = \{R_0\} \Rightarrow u \rightarrow S(u)$
2 Initial stress	$[\mathbf{K}_M] = [\mathbf{K}_M(B_0)]$	$[\mathbf{K}_G] = [\mathbf{K}_G(B_0, S)]$	-	$\{\mathbf{K}_M - \lambda \mathbf{K}_G\}\{u\} = 0 \Rightarrow \lambda$
Extended Trefftz's Approach (W prebuckling deformation)				
3 i (initially = 0)	$[\mathbf{K}_M^i] = [\mathbf{K}_u(B_i)]$	-	$\{\lambda^i R_0\}$	$[\mathbf{K}_M^i]\{u^{i+1}\} = \{\lambda^i R_0\} \Rightarrow u^{i+1} \rightarrow B^{i+1}, S^{i+1}$
4 $i = i + 1$	$[\mathbf{K}_M^{i+1}] = [\mathbf{K}_M(B_{i+1})]$	$[\mathbf{K}_G^{i+1}] = [\mathbf{K}_G(B^{i+1}, S^{i+1})]$	-	$[\mathbf{K}_M^{i+1} - \lambda^{i+1} \mathbf{K}_G^{i+1}]\{u\} = 0 \Rightarrow \lambda^{i+1}$
5 Convergent?			NO	Not converged → $i = i + 1$ Go to (3)
			Yes	Converged → $\lambda_{cr} = \lambda^{i+1}$ ⇒ Stop

the effect of this *pre-buckling deformation* may be of the same order of magnitude as that of shear deformation effect especially in thick plates. Based on the algorithm shown in Table 3.1, a more realistic buckling load can be obtained by considering the plate deformation prior to the buckling. The inclusion the pre-buckling deformation can be handled iteratively in Steps (3) and (4) as shown in Table 3.1.

3.4 Element implementation

3.4.1 Degenerated plate element

For a simple illustration, the material and the geometric stiffness matrices of a degenerated plate/shell element based on the works by Hughes *et al.* (1977), Kanok-Nukulchai (1979) and Kanok-Nukulchai *et al.* (1981) will be formulated. This plate/shell element is a direct degeneration from 3D field equations using the thick plate assumptions. For instability analysis of plates, all components of stress tensor are included except the transverse normal stress component that is negligible due to the plane stress effect. Thus, the initial configuration of the plate element is in fact a flat shell element that includes membrane, bending and transverse shear actions.

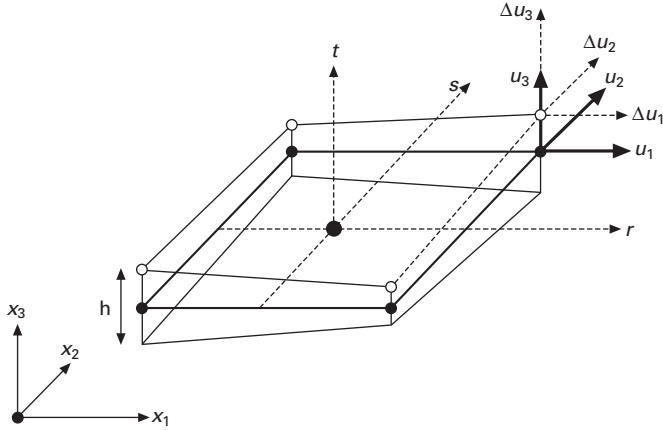
Plate assumptions

The following assumptions are employed in the development of the degenerated plate element: (a) the normals to the mid-surface before deformation remain straight throughout the deformation but do not necessarily remain normal to the deformed mid-surface; (b) the stress component normal to the plate mid-surface is negligible.

The first assumption allows the displacement profile along a plate's director (normal) to be completely described by the displacement on the mid-surface and the rotation of the director. The second assumption avoids the unwanted conditioning that could result from displacement dependency across the plate thickness.

Geometry and displacement field

The present plate element shown in Fig. 3.3 evolves from a 3-D continuum element. Two opposite bilinear faces portray the top and the bottom faces of the plate where as the mean surface between them defines the mid-plane of the plate. The element consists of eight nodes, four mid-plane nodes and four relative nodes on the top plane of the plate element. Nodal variables assigned to each of the mid-plane nodes are three components of displacement while those assigned to each relative node are three components of relative displacement with respect to the corresponding mid-plane node.



3.3 Bilinear plate element.

In Fig. 3.3 the geometry of a typical plate element is described by a set of natural coordinates, $\{r, s, t\}$, such that a bi-unit cube is uniquely mapped into the plate element body. The position of a particle in the element body can be uniquely expressed in terms of the nodal coordinates as

$$\mathbf{x}(r, s, t) = \sum_{I=1}^8 N^I(r, s, t) \mathbf{x}^I \tag{3.31}$$

where \mathbf{x}^I ($I = 1,4$) denotes the coordinates of a mid-plane node, \mathbf{x}^I ($I = 5,8$) denotes the relative position vector of a relative node with respect to the corresponding mid-plane node. The interpolation function N^I consistent with Eq. 3.31 can be expressed as

$$N^I(r, s, t) = \begin{cases} \frac{1}{4} (1 + r^I r)(1 + s^I s) & \text{for } a = 1, 4 \\ \frac{t}{4} (1 + r^I r)(1 + s^I s) & \text{for } a = 5, 8 \end{cases} \tag{3.32}$$

in which r^I and s^I are the natural coordinates of node I .

The displacement vector at any point (r, s, t) in the element body can be expressed in the form

$$\mathbf{u}(r, s, t) = \sum_{I=1}^8 N^I(r, s, t) \mathbf{u}^I \tag{3.33}$$

in which \mathbf{u}^I denotes the absolute displacement vector at node I ($I = 1,4$) on the mid-plane and the relative displacement vector at node I ($I = 5,8$) on the top face.

Stress strain relationship

In the current plate formulation, the elasticity tensor presented by Eq. (3.27) must be modified to include the effect of the plane stress assumption. Accordingly, the modified elasticity tensor can be derived as

$$\bar{d}_{klmn} = d_{klmn} - d_{kl33} \frac{d_{33mn}}{d_{3333}} \quad 3.34$$

By defining the vector of strains as $\mathbf{E} = \{\varepsilon_{11} \ \varepsilon_{22} \ 2\varepsilon_{12} \ 2\varepsilon_{23} \ 2\varepsilon_{31}\}^T$ and the corresponding vector of stresses as $\mathbf{S} = \{\sigma_{11} \ \sigma_{22} \ \sigma_{12} \ \sigma_{23} \ \sigma_{31}\}^T$, the stress strain relationship for a linear isotropic elastic material can be expressed by

$$\mathbf{S} = \mathbf{D}\mathbf{E} \quad 3.35$$

where

$$\mathbf{D} = \begin{bmatrix} \bar{\lambda} + 2\mu & \bar{\lambda} & 0 & 0 & 0 \\ \bar{\lambda} & \bar{\lambda} + 2\mu & 0 & 0 & 0 \\ 0 & 0 & \mu & 0 & 0 \\ 0 & 0 & 0 & \kappa\mu & 0 \\ 0 & 0 & 0 & 0 & \kappa\mu \end{bmatrix} \quad 3.36$$

in which κ is the shear deformation correction factor, i.e. 5/6 for plate problems, μ is the shear modulus, and $\bar{\lambda}$ is the plane-stress reduced Lamé's constant, i.e. $\bar{\lambda} = \nu E / (1 - \nu^2)$, E is the modulus of elasticity and ν is Poisson's ratio.

Implementation

To adopt the reduced integration technique (Hughes *et al.*, 1977), \mathbf{K} and \mathbf{DK} must be partitioned into two parts corresponding to the transverse shear effect and the rest. The stress tensor \mathbf{S} is decomposed into two parts as

$$\mathbf{S} = \mathbf{S}_m + \mathbf{S}_s = \begin{bmatrix} \sigma_{11} & \sigma_{12} & 0 \\ \sigma_{21} & \sigma_{22} & 0 \\ 0 & 0 & 0 \end{bmatrix} + \begin{bmatrix} 0 & 0 & \sigma_{13} \\ 0 & 0 & \sigma_{23} \\ \sigma_{31} & \sigma_{32} & 0 \end{bmatrix} \quad 3.37$$

Since there is no coupling terms in \mathbf{D} between the shear and the in-plane strain, the partition of \mathbf{DK} into the two effects is straightforward. The matrices \mathbf{B} and \mathbf{D} can then be partitioned as

$$\mathbf{B}^a = \begin{bmatrix} \mathbf{B}_m^a \\ \mathbf{B}_s^a \end{bmatrix} = \begin{bmatrix} N_{,1}^a & 0 & 0 \\ 0 & N_{,2}^a & 0 \\ N_{,2}^a & N_{,1}^a & 0 \\ 0 & N_{,3}^a & N_{,2}^a \\ N_{,3}^a & 0 & N_{,2}^a \end{bmatrix} \quad 3.38$$

and

$$\mathbf{D} = \begin{bmatrix} \mathbf{D}_m & \mathbf{0} \\ \mathbf{0} & \mathbf{D}_s \end{bmatrix} = \begin{bmatrix} \bar{\lambda} + 2\mu & \bar{\lambda} & 0 & 0 & 0 \\ \bar{\lambda} & \bar{\lambda} + 2\mu & 0 & 0 & 0 \\ 0 & 0 & \mu & 0 & 0 \\ 0 & 0 & 0 & \kappa\mu & 0 \\ 0 & 0 & 0 & 0 & \kappa\mu \end{bmatrix} \quad 3.39$$

In view of Eqs. (3.38) and (3.39), one can show that

$$\mathbf{K}^{ba} = \mathbf{K}_m^{ba} + \mathbf{K}_s^{ba} \quad 3.40$$

where the membrane-bending effect is given by

$$\mathbf{K}_m^{ba} = \int_{B_0^e} (\mathbf{B}_m^b)^T \mathbf{D}_m \mathbf{B}_m^a dV + \int_{B_0^e} (\nabla \mathbf{N}^b)^T \mathbf{S}_m \nabla \mathbf{N}^a dV \cdot \mathbf{I} \quad 3.41$$

and the transverse shear effect by

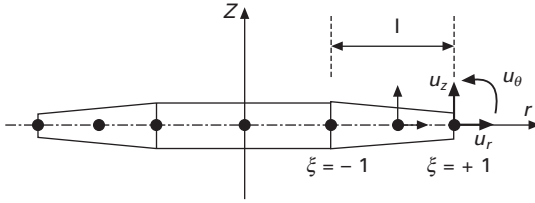
$$\mathbf{K}_s^{ba} = \int_{B_0^e} (\mathbf{B}_s^b)^T \mathbf{D}_s \mathbf{B}_s^a dV + \int_{B_0^e} (\nabla \mathbf{N}^b)^T \mathbf{S}_s \nabla \mathbf{N}^a dV \cdot \mathbf{I} \quad 3.42$$

The full Gaussian quadrature is used to evaluate \mathbf{K}_m while the reduced one-point Gaussian quadrature is used to evaluate \mathbf{K}_s for the bilinear plate element. Full details and the background of reduced integration can be referred to Hughes *et al.* (1977).

3.4.2 Axisymmetric annular plate element

Stability of circular plate under in-plane compressive radial force uniformly distributed around the edge will be considered in this application. Due to axisymmetric nature of this problem, a 3-node axisymmetric annular plate (flat shell) element (Fig. 3.4) will be developed in polar coordinates under the framework of the total potential energy in Eq. (3.2).

In polar coordinates, one should be able derive similar expression of the stiffness matrix as in Eq. (3.27). First the displacement field is defined in



3.4 Three-node axisymmetric annular plate element.

terms of the three degrees of freedom at each of the three nodes along the mid-plane of the plate as

$$\begin{aligned} \begin{Bmatrix} u_r(r, z) \\ u_z(r, z) \end{Bmatrix} &= \begin{bmatrix} 1 & 0 & -z \\ 0 & 1 & 0 \end{bmatrix} \begin{Bmatrix} u_r(r, 0) \\ u_z(r, 0) \\ u_\theta(r, 0) \end{Bmatrix} \\ &= \sum_{l=1}^3 N^l(\xi) \begin{bmatrix} 1 & 0 & -z \\ 0 & 1 & 0 \end{bmatrix} \begin{Bmatrix} u_r^l \\ u_z^l \\ u_\theta^l \end{Bmatrix} \end{aligned} \quad 3.43$$

Where $\langle u_r^l \ u_z^l \ u_\theta^l \rangle$ is nodal vector of radial, transverse and circumferential displacements respectively, $N^l(\xi)$ is the shape functions in terms of a normalized coordinate along the mid-plane of the element in radial direction, where $\xi = [-1, 1]$. Placing 3 nodes at $\xi = (-1, 0, 1)$ respectively, $N^l(\xi)$ is defined as

$$\begin{Bmatrix} N^1(\xi) \\ N^2(\xi) \\ N^3(\xi) \end{Bmatrix} = \begin{Bmatrix} \frac{1}{2}(\xi - 1)\xi \\ \frac{1}{2}(1 + \xi)(1 - \xi) \\ \frac{1}{2}(\xi - 1)\xi \end{Bmatrix} \quad 3.44$$

The relevant strain vector is defined in terms of the nodal displacements as

$$\begin{aligned} \begin{Bmatrix} \bar{\epsilon}_r \\ \bar{\epsilon}_\theta \\ \chi_r \\ \chi_\theta \end{Bmatrix} &= \begin{Bmatrix} \frac{du_r}{dr} \\ -\frac{u_r}{r} \\ \frac{du_\theta}{dr} \\ \frac{u_\theta}{r} \end{Bmatrix} = \sum_{l=1}^3 \begin{bmatrix} N_r^l & 0 & 0 \\ -N^l & 0 & 0 \\ r & 0 & N_{,r}^l \\ 0 & 0 & \frac{N^l}{r} \end{bmatrix} \begin{Bmatrix} u_r^l \\ u_z^l \\ u_\theta^l \end{Bmatrix} \\ &= \sum_{l=1}^3 [B_m^l] \begin{Bmatrix} u_r^l \\ u_z^l \\ u_\theta^l \end{Bmatrix} \end{aligned} \quad 3.45$$

$$\begin{aligned}
\{\gamma_{rz}\} &= \left\{ -u_\theta + \frac{du_z}{dr} \right\} = \sum_{l=1}^3 \left[0 \quad N_{,r}^l \quad -N^l \right] \begin{Bmatrix} u_r^l \\ u_z^l \\ u_\theta^l \end{Bmatrix} \\
&= \sum_{l=1}^3 [B_m^l] \begin{Bmatrix} u_r^l \\ u_z^l \\ u_\theta^l \end{Bmatrix}
\end{aligned} \tag{3.46}$$

In which B_m^l is the membrane-bending and B_s^l the shear part of the B-matrix. Finally, K_M and K_G can be derived from the first variation of the total potential energy in a similar form as in Eqs. (3.41) and (3.43), i.e.

$$K_M^{ba} = \int_{B^e} (\mathbf{B}_m^b)^T \mathbf{D}_m \mathbf{B}_m^a r dr + \int_{B^e} (\mathbf{B}_s^b)^T \mathbf{D}_m \mathbf{B}_s^a r dr \tag{3.47}$$

and

$$K_G^{ba} = \int_{B^e} (\mathbf{B}_z^b)^T \mathbf{S}_z \mathbf{B}_z^a r dr + \int_{B^e} (\mathbf{B}_m^b)^T \mathbf{S}_m \mathbf{B}_m^a r dr \tag{3.48}$$

in which the expressions for \mathbf{B}_m and \mathbf{B}_s are available in Eq. (3.46), \mathbf{B}_z , \mathbf{D}_m , \mathbf{D}_s , \mathbf{S}_m and \mathbf{S}_z are given below:

$$\mathbf{B}_z^b = [0 \quad N_{,r}^b \quad 0] \tag{3.49}$$

$$\mathbf{D}_m = \begin{bmatrix} \frac{Et(r)}{1-\nu^2} & \frac{\nu Et(r)}{1-\nu^2} & 0 & 0 \\ \frac{\nu Et(r)}{1-\nu^2} & \frac{Et(r)}{1-\nu^2} & 0 & 0 \\ 0 & 0 & \frac{Et^3(r)}{12(1-\nu^2)} & 0 \\ 0 & 0 & 0 & \frac{Et^3(r)}{12(1-\nu^2)} \end{bmatrix} \tag{3.50}$$

$$\mathbf{D}_s = \left[\frac{Et(r)}{2(1+\nu)} \right] \tag{3.51}$$

$$\mathbf{S}_m = \begin{bmatrix} \sigma_{rr} t(r) & & & \\ & \sigma_{\vartheta\vartheta} t(r) & & \\ & & \frac{\sigma_{rr} t^3(r)}{12} & \\ & & & \frac{\sigma_{\theta\theta} t^3(r)}{12} \end{bmatrix} \tag{3.52}$$

and

$$S_z = [\sigma_{rr}t(r)] \tag{3.53}$$

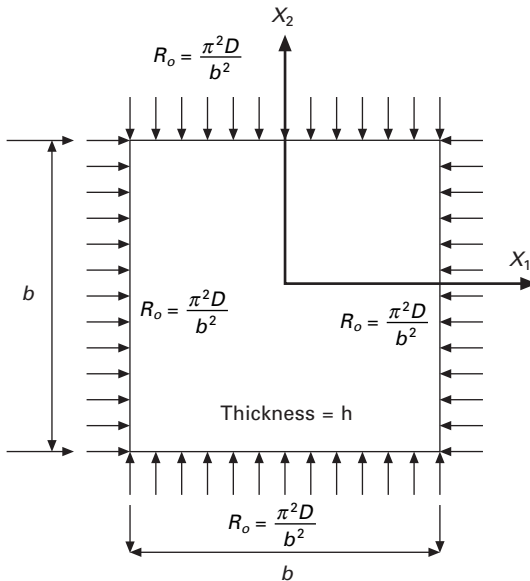
In which E and ν are Young’s modulus and Poisson’s ratio, respectively, $t(r)$ is the thickness variable for the case of tapered plates, σ_{rr} and $\sigma_{\theta\theta}$ are in-plane stresses of the plate in the radial and circumferential directions respectively. The first term of Eq. (3.47) represents membrane-bending part while the second term the shear part of the material tangent stiffness. As usual, a reduced integration must be used for the shear part to treat the shear locking effect. For Eq. (3.48), the first term represents the normal P-delta effect that is the main cause of the plate instability while the second term is due to the effect of the nonlinear terms of the in-plane deformation.

3.5 Numerical examples

In this section, some examples of plate buckling problems are presented to illustrate the validity of the formulation.

3.5.1 Elastic buckling of square plates using degenerated flat shell elements

The first example illustrates the buckling analysis of square thin plates (Fig. 3.5) under in-plane forces. The analytical solutions for both uniaxial and biaxial in-plane compressive forces are available in the following expression (Timoshenko and Gere, 1961)



3.5 A square plate under uniformly applied in-plane compression

$$k = \frac{P_{crit} b^2}{\pi^2 D} \quad 3.54$$

in which k is the buckling load factor, P_{crit} is the critical buckling load, b is the width of plate $D = Eh^3/12(1 - \nu^2)$ is the flexural rigidity of thin plate, h is the thickness of plate, E and ν are the elastic modulus and Poisson's ratio respectively.

This square plate is modeled with a series of meshes, using 4×4 , 6×6 , 8×8 and 10×10 plate elements. The plate is relatively thin with $h/b = 0.01$. It is subjected to different loading and boundary conditions and the results are tabulated in Table 3.2 in comparison with the corresponding analytical results.

Next, the buckling loads of a simply supported square plate under in-plane compression in one direction are tested using a mesh size of 16×16 by varying the plate thickness-to-side aspect ratio. This example will test the applicability of the thick plate element based on the Mindlin plate theory on a range of plate thicknesses.

To give some idea of the performance of the degenerated bilinear plate element, the result will be compared with the case of using 9-node quadrilateral element with enhanced shear strain proposed by Hinton *et al.* (1988). Table 3.3 summarizes the results of the comparison, against the analytical solutions from Iyengar's book (1988). In this situation, it appears that using higher order element is more efficient for buckling analysis, mainly because the representation of the buckling mode shape is sensitive to the fineness of the mesh.

Table 3.2 Coefficient k for simply supported square plate under uniform compression in the x direction

Case	Finite element solution (percentage error)				Analytical solution
	4×4	6×6	8×8	10×10	
Simply supported with uniform compression in one direction	4.368 (9.2%)	4.155 (3.87%)	4.085 (2.12%)	4.053 (1.32%)	4.00
Simply support with uniform compression in both directions	2.184 (9.20%)	2.072 (3.85%)	2.042 (2.10%)	2.026 (1.30%)	2.00
Clamped support with uniform compression in one direction	11.04 (9.63%)	10.57 (4.96%)	10.41 (3.38%)	10.26 (1.89%)	10.07
Clamped support with uniform compression in both directions	5.676 (6.49%)	5.582 (4.73%)	5.487 (2.95%)	5.415 (1.59%)	5.33

Table 3.3 Effect of thickness on the buckling of simply supported square plate under uniform compression in the x direction

References	Plate aspect ratio, $\frac{h}{b}$			
	0.01	0.05	0.10	0.20
Analytical solution	4.000	3.911	3.741	3.150
Hinton, <i>et al.</i> (1988) – 4 × 4 mesh	–	3.932 (0.54%)	(3.734) (–0.19%)	3.128 (–0.70%)
Bilinear plate element (16 × 16 mesh)	4.013 (0.32%)	3.949 (0.97%)	3.795 (1.44%)	3.176 (0.82%)

3.5.2 Elastic buckling of tapered circular plates using annular plate elements

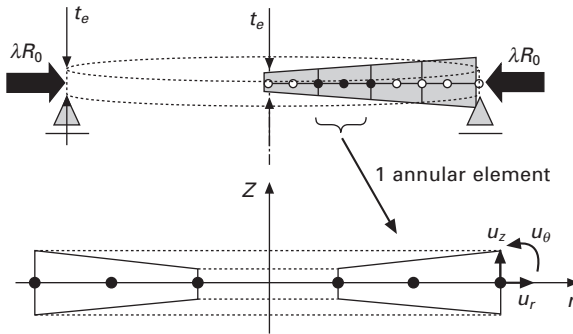
Investigations of stability of a circular plate under uniform radial compression was conducted by many researchers, including Ziegler (1983), Raju and Rao (1986), Wang *et al.* (1993), Xiang (1993), Hong *et al.* (1993), Tan (1994) and Wang *et al.* (1996). However, only Raju and Rao (1986) and Tan (1994) considered tapered Mindlin plates. The former studied the post-buckling plate behavior by using thick plate element in which the displacement field is represented by cubic-order shape functions along the radial direction. On the other hand, Tan (1994) investigated the effects of the pre-buckling deformation on the elastic buckling load of tapered circular plates by applying the Rayleigh–Ritz procedure to the incremental strain energy functional.

Consider a tapered circular plate that can buckle under uniform radial in-plane compressive force. The purpose is to evaluate the critical value of this force and its sensitivity to the variation of plate thickness, the shear deformation and the inclusion of the in-plane deformation before the buckling state. It is assumed that the compressive pressure remains constant despite the pre-buckling in-plane deformation; otherwise the pressure has to be amplified by a factor as a result of the reduction of the loading area. This modification was suggested by Xiang *et al.* (1993) and confirmed by Ng (1995).

In cylindrical co-ordinate system, the thickness of the tapered plates is allowed to vary linearly in the radial direction as

$$t(r) = t_c + (t_e + t_c) \frac{r}{R} \tag{3.55}$$

where t_c and t_e are the values of the plate thickness at the center and at the outer edge respectively. Based on the algorithm shown in Table 3.3, a more realistic buckling load of circular plates can be obtained by considering the in-plane deformation just before the buckling occurs. This can be handled iteratively in Steps (3) and (4) of Table 3.1.



3.6 A three-node annular thick plate element.

To test the convergence characteristic of the annular plate element (Fig. 3.6), a circular plate will be modeled in four cases with 10, 20, 30 and 40 elements for thin and thick plates and with varying taper parameter $t_e/(t_e + t_c)$. The results are presented in Table 3.4 for the cases of simply-supported and clamped plates. The element convergence appears to be confirmed. To control the error under 10^{-4} , 20 elements are sufficient and shall be used for modeling moderate tapered plates, i.e. $0.25 \leq t_e/(t_e + t_c) \leq 0.75$, while 40 elements are used for those outside this range.

Table 3.4 Comparison of critical load $\lambda_{cr} = 12N_{cr}R^2(1 - \nu^2)/Et_c^2$ for linearly tapered circular plate with shear deformation.

Taper parameter, $t_e/(t_e + t_c)$	No. elements	$t_0/R = 0.001$		$t_0/R = 0.25$	
		Clamped	Simply supported	Clamped	Simply supported
0.1	10	9.8400	4.9210	7.4022	4.0486
	20	9.6709	4.9119	7.2630	4.0336
	30	9.6590	4.9100	7.2542	4.0319
	40	9.6569	4.9006	7.2521	4.0315
0.25	10	14.4610	5.7396	11.1347	5.0482
	15	14.4570	5.7391	11.1314	5.0478
	20	14.4564	5.7390	11.1308	5.0477
	25	14.4562	5.7390	11.1306	5.0477
0.5 (uniform)	10	14.6822	4.1978	11.6324	3.9051
	15	14.6800	4.1978	11.6323	3.9051
	20	14.6800	4.1978	11.6323	3.9051
	25	14.6800	4.1978	11.6323	3.9051
0.75	10	10.9101	2.8953	8.9322	2.7627
	15	10.9112	2.8953	8.9330	2.7627
	20	10.9114	2.8953	8.9331	2.7627
	25	10.9115	2.8953	8.9331	2.7627
0.9	10	7.0549	2.4789	5.9061	2.3793
	20	7.0602	2.4789	5.9065	2.3793
	30	7.0615	2.4789	5.9076	2.3793
	40	7.0617	2.4789	5.9078	2.3793

Table 3.5 Comparison of critical load factors, $\lambda_{cr} = 12N_{cr}R^2(1 - \nu^2)/Et_c^2$, for linearly tapered Kirchhoff plates neglecting shear deformation ($t_c/R = 0.001$).

$\frac{t_c - t_e}{t_c}$	Jain (1972)	Turvey (1978)	Raju and Rao Tan (1986)	Tan (1994)	Present FE solution
Simply-supported boundary condition					
0.500	6.2134			5.3272	5.3271
0.333		4.8275		4.8830	4.8830
0.300	5.0586		4.8008	4.8011	4.8011
0.200			4.5748	4.5744	4.5747
0.100	4.4119		4.3737	4.3738	4.3738
0		4.1605	4.1980	4.1978	4.1978
-0.100	4.0292		4.0432	4.0433	4.0433
-0.200			3.9074	3.9070	3.9070
-0.300	3.7865		3.7876	3.7876	3.7876
-0.333		3.7261		3.7509	3.7509
-0.500	3.6218			3.5873	3.5873
Clamped boundary condition					
0.500	17.0404			15.2180	15.2191
0.333		15.1555		15.2675	15.2677
0.300	15.9629		15.2363	15.2354	15.2355
0.200			15.0946	15.0918	15.0918
0.100	15.0756		14.8948	14.9000	14.8998
0		14.3598	14.6800	14.6821	14.6819
-0.100	14.3149		14.4525	14.4507	14.4505
-0.200			14.2131	14.2134	14.2132
-0.300	13.6429		13.9757	13.9774	13.9771
-0.333		13.5469		13.8992	13.8989
-0.500	13.0410			13.5153	13.5149

In comparison with available solutions for the case of thin plates in Table 3.5, the present solution shows good agreement especially with the results obtained by Tan (1994) and Raju and Rao (1986) for both simple-support and clamp boundary conditions.

For elastic buckling of tapered circular plates with allowance of shear deformation, the results of Raju and Rao (1986) and Tan (1994) are compared with the present solution in Table 3.6. It appears that the three set of results are almost identical. The close agreement with Raju and Rao (1986) is not a coincidence. A similar finite element concept was used except that their shape functions are cubic polynomials, while the illustrative element employs quadratic polynomials. For Tan (1994), based on incremental strain energy including shear deformation, the Rayleigh–Ritz procedure was used to solve the elastic buckling load of tapered circular plates, considering the pre-buckling deformation as well. It can be seen from the graphs in Figs 3.7 and 3.8 for simply-supported and clamped plates respectively that both the shear

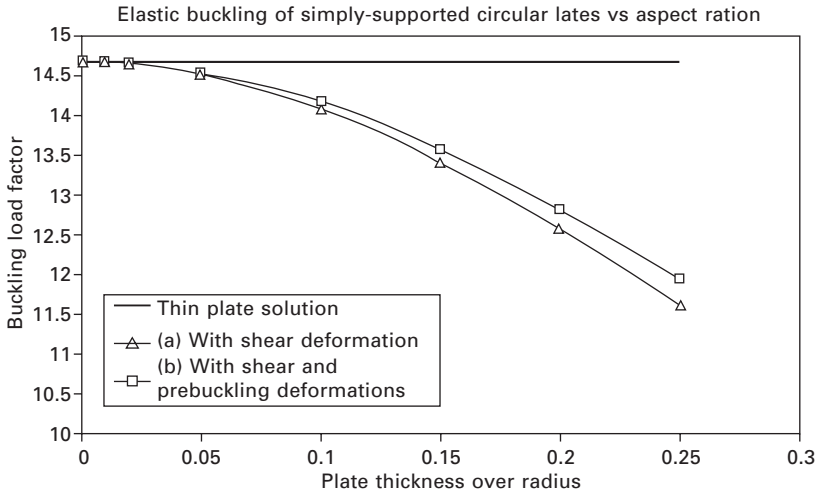
Table 3.6 Comparison of critical load factors, $\lambda_{cr} = 12N_{cr}^2(1 - \nu^2)/Et_c^2$, with shear deformation effect

t_d/R	$\frac{t_c - t_e}{t_c}$	Raju and Rao (1986)	Tan (1994)	Present
Simply-supported boundary condition				
0.001	-0.2	5.688	5.688	5.688
	0	4.198	4.198	4.198
	0.2	2.978	2.978	2.978
0.05	-0.2	5.668	5.668	5.668
	0	4.185	4.185	4.185
	0.2	2.970	2.970	2.970
0.10	-0.2	5.609	5.609	5.609
	0	4.148	4.148	4.148
	0.2	2.948	2.948	2.948
0.15	-0.2	5.514	5.514	5.514
	0	4.087	4.087	4.087
	0.2	2.911	2.911	2.911
0.20	-0.2	5.386	5.386	5.386
	0	4.006	4.006	4.006
	0.2	2.861	2.861	2.861
Clamped boundary condition				
0.001	-0.20	20.69	20.69	20.69
	0.00	14.68	14.68	14.68
	0.20	9.826	9.826	9.824
0.05	-0.20	20.42	20.42	20.42
	0.00	14.53	14.53	14.53
	0.20	9.745	9.745	9.745
0.10	-0.20	19.66	19.66	19.66
	0.00	14.09	14.09	14.09
	0.20	9.515	9.515	9.515
0.15	-0.20	18.51	18.51	18.51
	0.00	13.42	13.42	13.42
	0.20	9.155	9.155	9.155
0.20	-0.20	17.10	17.10	17.10
	0.00	12.57	12.57	12.57
	0.20	8.694	8.694	8.694

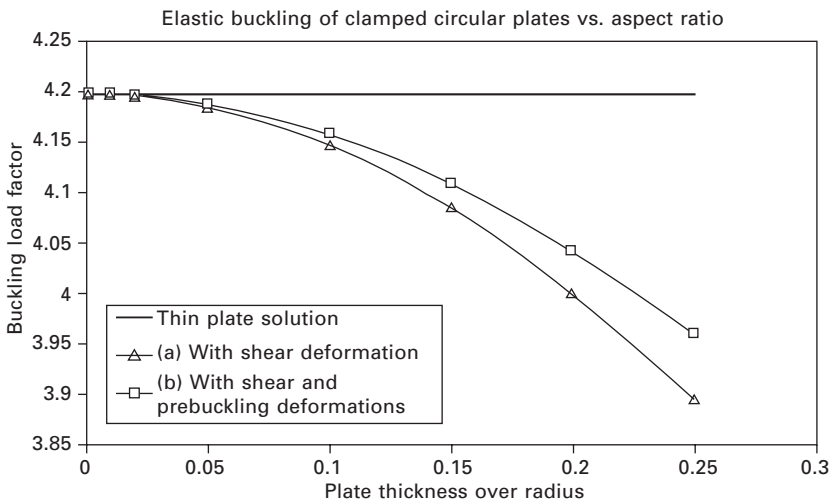
and the pre-buckling deformation effects will be especially pronounced as the thickness of the circular plate increases.

3.6 Concluding remarks

In this chapter, the total Lagrangian formulation is presented to establish typical finite element expressions for the material and the geometric stiffness matrices required to analyze instability of Mindlin plates. Based on the rigorous formulation, the nonlinear deformation of the Mindlin plate prior to



3.7 Elastic buckling load factor of simply-supported circular plates considering effects of the transverse shear deformation and the prebuckling deformations .



3.8 Elastic buckling load factor of clamped circular plates considering effects of the transverse shear deformation and the pre-buckling deformations.

the elastic buckling limit is automatically included in the element stiffness matrices. The advantage of the finite element method is its versatility and power in modeling any shape of thin and thick plates, even plates with non-uniform thickness. Although only two types of elements are illustrated in this chapter, the formulation is fully generic and shall be applicable to any Mindlin plate element.

3.7 References

- Anderson, R.G., Irons, B.M. and Zienkiewicz, O.C. (1968), 'Vibration and stability of plates using finite elements', *Int. J. Solids Structures*, **4**, 1031–1055.
- Bath, K.J. and Dvorkin, E.N. (1985), 'A four-node plate bending element based on Mindlin/Reissner plate theory and a mixed interpolation', *Int. J. Numer. Meth. Engng*, **21**, 367–383.
- Bazeley, G.P., Cheung, Y.K., Irons, B.M. and Zienkiewicz, O.C. (1965), 'Triangular elements in plate bending – conforming and non-conforming solutions', *Proc. Conf. Matrix Meth. Struct. Mech.*, Wright-Patterson Air Force Base, Ohio, 547–576.
- Bell, K. (1969), 'A refined triangular plate bending finite element', *Int. J. Numer. Meth. Engng*, **4**, 95–108.
- Butlin, G. and Ford, R. (1970), 'A compatible triangular plate bending finite element', *Int. J. Solids Structures*, **6**, 323–332.
- Carson, W.G. and Newton, R.E. (1969), 'Plate buckling analysis using a fully compatible finite element', *AIAA Journal*, **7**(3), 527–529.
- Crisfield, M.A. (1984), 'A quadratic Mindlin element using shear constraints', *Computers and Structures*, **18**, 833–852.
- Hinton, E., Vuksanovic, D.J. and Huang, H.C. (1988), 'Finite element free vibration and buckling analysis of initially stressed Mindlin plates', in Hinton E, *Numerical Methods and Software for Dynamic Analysis of Plates and Shells*, Swansea, Pineridge Press, 93–166.
- Hong, G.M., Wong, C.M. and Kanok-Nukulchai, W. (1993), 'Elastic buckling of circular plates allowing for prebuckling deformation', *J. Engng. Mech.*, ASCE, **119**, 905–916.
- Hughes, T.J.R. and Rezaei, T.E. (1981), 'Finite elements based upon Mindlin plate theory with particular reference to the four-node bilinear isoparametric element', *J. Appl. Mech. ASME*, **48**, 587–596.
- Hughes, T.J.R., Taylor, R.L. and Kanok-Nukulchai, W. (1977), 'A simple and efficient finite element for plate bending', *Int. J. Numer. Meth. Engng*, **11**, 1529–1543.
- Iyengar, N.G.R. (1988), *Structural Stability of Columns and Plates*, Chichester, Ellis Horwood Limited.
- Kanok-Nukulchai, W. (1979), 'A simple and efficient finite element for general shell analysis', *Int. J. Numer. Meth. Engng*, **14**, 179–200.
- Kanok-Nukulchai, W., Taylor, R.L. and Hughes, T.J.R. (1981), 'A large deformation formulation for shell analysis by the finite element method', *Computers and Structures*, **13**, 19–27.
- Kapur, K.K. and Hartz, B.J. (1966), 'Stability of plates using the finite element method', *Journal of Engineering Mechanics Division*, Proc. ASCE, **92**, 175–195.
- Melosh, R.J. (1963), 'Basis for derivation of matrices for the direct stiffness method', *AIAA J.*, **1**, 1631–1637.
- Ng, T.K. (1995), 'A numerical investigation of elastic buckling of circular Mindlin plates with allowance for prebuckling inplane deformation', M. Eng. Thesis, Asian Institute of Technology, Bangkok, Thailand.
- Raju, K.K. and Rao, G.V. (1986), 'Post-buckling of linearly tapered moderately thick circular plates by finite element method', *Computers and Structures*, **22**, 307–310.
- Smith, J. P. (1995), 'Buckling of shear deformable plates using the p-version of the finite element method', *Computers and Structures*, **57**, 527–532.
- Stricklin, J.A., Haisler, W.E. and Tisdale, P.R. (1969), 'A rapidly converging triangular plate bending element', *AIAA J.*, **7**, 180–181.

- Tan, T.J. (1994), 'Buckling of plates with allowance for shear and prebuckling inplane deformations', M. Eng. Thesis, National University of Singapore, Singapore.
- Timoshenko, S.P. and Gere, J.M. (1961), *Theory of Elastic Stability*, McGraw-Hill, New York.
- Wang, C.M., Xiang, Y., Kitipornchai, S. and Liew, K.M. (1993), 'Axisymmetric buckling of circular Mindlin plates with ring supports', *J. Struct. Engng*, ASCE, **119**, 1273–79.
- Wang, C.M., Tan, T.J., Hong, G.M. and Alwis W.A.M. (1996), 'Buckling of tapered circular plates: allowances for effects of shear and radial deformations', *Mechanics of Structures and Machines*, **24**(2), 135–153.
- Wemper, G., Oden, J.T. and Kross, D. (1968), 'Finite element analysis of thin shells', *Journal of Engineering Mechanics Division*, Proc. ASCE, **94**, 1273–1294.
- Xiang, Y., Wang C.M., Liew, K.M. and Kitipornchai, S. (1993), 'Mindlin plate buckling with prebuckling in-plane deformation', *J. Engng. Mech.*, ASCE, **119**, 1–17.
- Ziegler, H. (1983), 'The influence of in-plane deformation on the buckling loads of isotropic elastic plates', *Ingenieur-Archiv.*, **53**, 61–72.
- Zienkiewicz, O.C., Taylor, R.L. and Too, J.M. (1971), 'Reduced integration technique in general analysis of plates and shells', *Int. J. Numer. Meth. Engng*, **3**, 575–586.

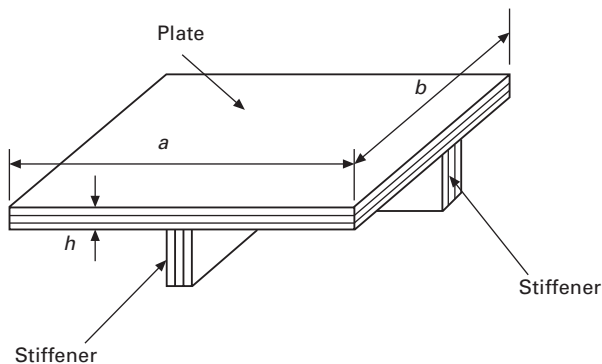
Mesh-free methods for buckling analysis of stiffened and corrugated plates

K M LIEW, S KITIPORNCHAI and
L X PENG, City University of Hong Kong,
China

4.1 Introduction

The stability analysis of plate structures is an important part of engineering practice. Numerous methods (Liew *et al.* 2002a, Teo and Liew 2002) have been introduced to solve the buckling problems of plate structures. In this chapter, a recently developed numerical method, the mesh-free Galerkin method (Belytschko *et al.* 1994, Ren *et al.* 2002, Liew *et al.* 2004a), will be employed to analyze the buckling behavior of popular plate structures in engineering, such as stiffened plates and stiffened and unstiffened corrugated plates.

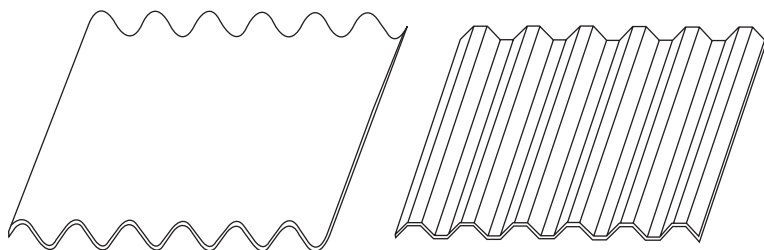
A plate that is stiffened by ribs (Fig. 4.1) can achieve greater strength with relatively less material, which improves its strength to weight ratio and makes the structure cost-efficient. Eccentrically stiffened plates have been widely used in all kinds of circumstances, such as bridges, ship hulls or decks, and aircraft structures. To make full use of the stiffness that is provided by stiffeners, they are often attached to plates along the main load-carrying directions. Many studies have analyzed stiffened plates. Early researchers



4.1 Stiffened plate.

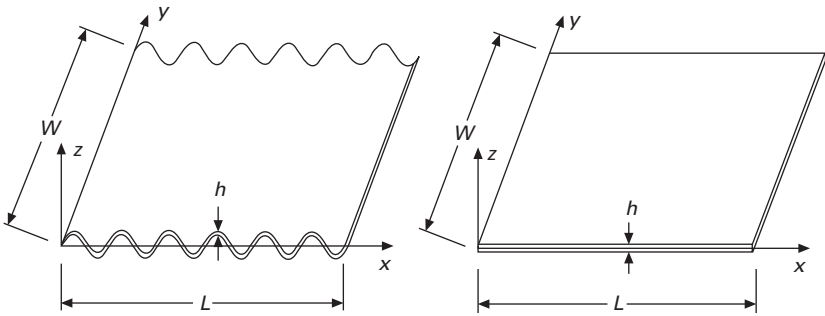
converted the stiffened plate to a single plate of constant thickness, and the stiffeners were modeled as an additional layer that was attached to the original plate. This is the so-called orthotropic model (Schade 1940, Guyon 1946). Another early model is the grillage model (Kendrick 1956). These models were simple in formulation, but did not achieve satisfying results in solving generalized stiffened plate problems. To improve this situation, subsequent researchers considered the stiffened plate as a composite structure that combined the plate and stiffeners through the imposition of displacement compatible conditions. Bryan (1891) first used energy criteria to study the stability of stiffened plates under uniform compression. Timoshenko and Gere (1961) studied rectangular plates that were stiffened by longitudinal and transverse ribs, and gave the numerical tables for buckling loads. Cox (1954) and Martin and Cox (1963) employed the Rayleigh–Ritz method to investigate the initial buckling of simply supported stiffened plates. To keep the stiffened plate from buckling locally, Klitchieff (1973) derived an expression to determine the minimum size of longitudinal stiffeners. Along with the development of computer techniques, numerical methods such as the finite strip method and the finite element method have been introduced into the stability analysis. Turvey (1971) first employed the finite strip method for the stability analysis of stiffened plates. Yoshida and Maegawa (1979) and Cheung and Delcourt (1977) also used the finite strip method to study the elastic stability and vibrations of stiffened plates. Allman (1975), Mukhopadhyay and Mukherjee (1990), Guo and Harik (1992), Rikards *et al.* (2001), Barik and Mukhopadhyay (2002) and Guo *et al.* (2002) all made contributions to the application of the finite element method to the stability analysis of stiffened plates. Other researchers such as Horne and Narayanan (1975, 1977, 1978) and Dowling and colleagues (Chryssanthopoulos *et al.* 1991) also had contributions to buckling analysis of stiffened plates.

Corrugated plates (Fig. 4.2) are another type of plated structure and are widely used in all branches of engineering practice. The corrugations reinforce the plates and improve their strength to weight ratio. Because of these superiorities, corrugated plates are popular in decking, roofing, and sandwich plate core structures. The precise analysis of corrugated plates involves the



4.2 Sinusoidally and trapezoidally corrugated plates.

sheets that lie in different planes for trapezoidally corrugated plates, or shell structures for sinusoidally corrugated plates, both of which require a large amount of computation and are thus time consuming. The procedure is costly and unnecessary, because approximate solutions are generally acceptable in engineering practice. A simple and valid way to obtain an approximate solution for corrugated plates is to analyze them as orthotropic plates (Seydel 1931, Easley and McFarland 1969, Nilson and Ammar 1974, Easley 1975, Davies 1976, Luo and Edlund 1996) of uniform thickness and equivalent rigidity (Fig. 4.3). Compared with a precise analysis, the approximation approach saves a lot of computation time and effort with little loss of precision. The key to the success of the approximate solution is the correct estimation of the equivalent rigidities.



4.3 Corrugated plate and its equivalent plate.

Seydel (1931) was the first to give the estimated equivalent rigidities for corrugated plates. Lau (1981) made improvements to the formula for the developed length l and moment of inertia I of one corrugation. Briassoulis (1986) compared the existing classical expressions (Easley 1975, Davies 1976) for the equivalent rigidities and derived more precise expressions for the extensional rigidity and flexural rigidity of sinusoidally corrugated plates by imposing a constant strain state on the plates. Shimansky and Lele (1995) derived an analytical model for the initial transverse stiffness of sinusoidally corrugated plates. They found that for most corrugated plates, the transverse stiffness is dramatically less than it is for an uncorrugated plate of the same thickness, and that transverse stiffness is not negligible for thick plates with a small degree of corrugation. Samanta and Mukhopadhyay (1999) followed the approach that was adopted by Briassoulis (1986), and derived new expressions for the extensional rigidity of trapezoidally corrugated plates. Employing the new expressions, they carried out nonlinear geometric and free vibration analyses. Semenyuk and Neskhodovskaya (2002) and Machindamrong *et al.* (2004) took into account the transverse shear stresses,

and gave the equivalent expression of the transverse shear modulus for thick corrugated plates. Semenyuk and Neskhodovskaya (2002) also presented the conditions under which a corrugated shell should not be treated as an orthotropic circular shell. Once the equivalent rigidities have been determined, corrugated plates can be analyzed as orthotropic plates by either theoretical or numerical methods. Similarly, stiffened corrugated plates can be considered as stiffened orthotropic plates.

Owing to advances in computing over the past few decades, numerical methods, and especially finite element methods (FEMs), have been extensively applied in industry to solve the problems of stiffened plates and stiffened and unstiffened corrugated plates. FEMs are convenient, and can be used to solve large, complex structures with all kinds of boundary conditions. Nevertheless, FEMs are not perfect. For large deformation and crack propagation problems, FEMs have difficulty in dealing with the discontinuities that do not coincide with the original meshlines. Remeshing is inevitable at each step of the solution procedure, which leads to programming complexity and is time consuming. For stiffened plate problems, most FEMs need the stiffeners to be placed along the meshlines, which limits the possible positions in which the stiffeners can be placed. Once the stiffener position is changed, the plate needs to be remeshed. Because of these disadvantages, researchers have been searching for other powerful numerical tools as alternatives to the FEMs.

In recent years, the meshless (or mesh-free or element-free) methods have gained considerable attention (Lucy 1977, Belytschko *et al.* 1994, Chen *et al.* 1996, Ren *et al.* 2002, Ren and Liew 2002, Wang *et al.* 2002, Liew *et al.* 2002b–h, 2003a–c, 2004a–d, Liew and Huang 2003, Zhao *et al.* 2003, Chen and Liew 2004, Liew and Chen 2004a–c, Zhao *et al.* 2004). Unlike the FEMs, meshless methods construct the approximate solutions for problems entirely in terms of orderly or scattered points that are distributed on the domain of the problem structure that is being studied, and no other element or interrelationship is needed. Meshless methods are thus more applicable than FEMs to moving boundary problems, crack growth with arbitrary and complex paths, and phase transformation problems. Without the meshes, the aforementioned difficulties that are usually encountered by the FEMs disappear.

The objective of this chapter is to propose a mesh-free Galerkin method for elastic buckling analysis of the stiffened plates and stiffened and unstiffened corrugated plates. The convergence and accuracy of the proposed method are demonstrated through the solving of several example problems. Good agreement between the results from the proposed method and those from other researchers or the ANSYS has been observed.

4.2 Mesh-free Galerkin method

By employing a moving least-squares approximation, a function $v(\mathbf{x})$ in a domain Ω can be approximated by $v^h(\mathbf{x})$ in the subdomain Ω_x and

$$v^h(\mathbf{x}) = \sum_{i=1}^m q_i(\mathbf{x})b_i(\mathbf{x}) = \mathbf{q}^T(\mathbf{x})\mathbf{b}(\mathbf{x}) \quad 4.1$$

where $q_i(\mathbf{x})$ are the monomial basis functions, $b_i(\mathbf{x})$ the corresponding coefficients, h a factor that measures the domain of influence of the nodes, and m the number of basis functions. The commonly used bases are the linear basis:

$$\mathbf{q}^T = [1, x], \text{ in 1D, } m = 2; \quad 4.2$$

$$\mathbf{q}^T = [1, x, y], \text{ in 2D, } m = 3 \quad 4.3$$

and the quadratic basis:

$$\mathbf{q}^T = [1, x, x^2], \text{ in 1D, } m = 3 \quad 4.4$$

$$\mathbf{q}^T = [1, x, y, x^2, xy, y^2], \text{ in 2D, } m = 6. \quad 4.5$$

We use here the quadratic basis. The unknown coefficients $b_i(\mathbf{x})$ are obtained by the minimization of a weighted discrete L_2 norm:

$$\Gamma = \sum_{I=1}^n \bar{\omega}(\mathbf{x} - \mathbf{x}_I) [\mathbf{q}(\mathbf{x}_I)^T \mathbf{b}(\mathbf{x}) - v_I]^2, \quad 4.6$$

where $\bar{\omega}(\mathbf{x} - \mathbf{x}_I)$ or $\bar{\omega}_I(\mathbf{x})$ is the weight function that is associated with node I , $\bar{\omega}_I(\mathbf{x}) = 0$ outside Ω_x , n is the number of nodes in Ω_x that make the weight function $\bar{\omega}_I(\mathbf{x}) > 0$, and v_I are the nodal parameters. The minimization of Γ in Eq. (4.6) with respect to $\mathbf{b}(\mathbf{x})$ leads to a set of linear equations:

$$\mathbf{B}(\mathbf{x})\mathbf{b}(\mathbf{x}) = \mathbf{A}(\mathbf{x})\mathbf{v} \quad 4.7$$

where

$$\mathbf{B}(\mathbf{x}) = \sum_{I=1}^n \bar{\omega}(\mathbf{x} - \mathbf{x}_I) \mathbf{q}(\mathbf{x}_I) \mathbf{q}^T(\mathbf{x}_I) \quad 4.8$$

$$\mathbf{A}(\mathbf{x}) = [\bar{\omega}(\mathbf{x} - \mathbf{x}_1) \mathbf{q}(\mathbf{x}_1), \dots, \bar{\omega}(\mathbf{x} - \mathbf{x}_n) \mathbf{q}(\mathbf{x}_n)] \quad 4.9$$

The coefficients $\mathbf{b}(\mathbf{x})$ are then derived from Eq. (4.7)

$$\mathbf{b}(\mathbf{x}) = \mathbf{B}^{-1}(\mathbf{x})\mathbf{A}(\mathbf{x})\mathbf{v} \quad 4.10$$

The substitution of Eq. (4.10) into Eq. (4.1) gives the approximation $v^h(\mathbf{x})$, which may be expressed in a standard form as:

$$v^h(\mathbf{x}) = \sum_{I=1}^n N_I(\mathbf{x})v_I \quad 4.11$$

where the shape function $N_I(\mathbf{x})$ is given by:

$$N_I(\mathbf{x}) = \mathbf{q}^T(\mathbf{x})\mathbf{B}^{-1}(\mathbf{x})\mathbf{A}_I(\mathbf{x}) \tag{4.12}$$

From Eq. (4.9), we obtain:

$$\mathbf{A}_I(\mathbf{x}) = \bar{\omega}(\mathbf{x} - \mathbf{x}_I)\mathbf{q}(\mathbf{x}_I) \tag{4.13}$$

Thus, Eq. (4.12) can be rewritten as

$$N_I(\mathbf{x}) = \mathbf{q}^T(\mathbf{x})\mathbf{B}^{-1}(\mathbf{x})\mathbf{q}(\mathbf{x}_I)\bar{\omega}(\mathbf{x} - \mathbf{x}_I) \tag{4.14}$$

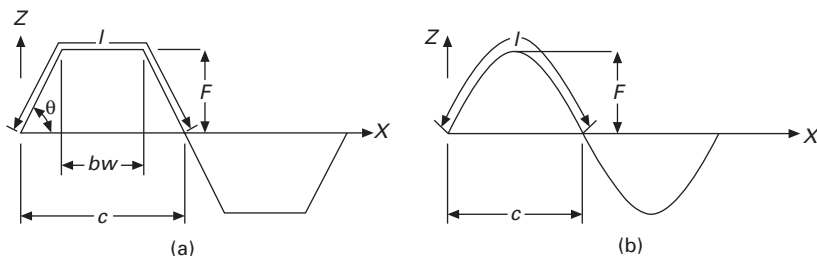
4.3 Estimation of equivalent properties

A corrugated plate demonstrates different flexural characteristics along two perpendicular directions. Therefore, the approximated buckling analysis of a corrugated plate can be conducted by analyzing a correspondingly equivalent orthotropic plate. Assume that Young’s modulus and Poisson’s ratio of a trapezoidally corrugated plate are E and μ , respectively (the dimensions of one corrugation of such a plate are shown in Fig. 4.4a). The stress–strain relations of the corresponding equivalent orthotropic plate are

$$\begin{Bmatrix} \sigma_x \\ \sigma_y \\ \tau_{xy} \end{Bmatrix} = \frac{1}{(1 - \mu_x\mu_y)} \begin{bmatrix} E_x & E_\mu & 0 \\ E_\mu & E_y & 0 \\ 0 & 0 & (1 - \mu_x\mu_y)G_{xy} \end{bmatrix} \begin{Bmatrix} \varepsilon_x \\ \varepsilon_y \\ \gamma_{xy} \end{Bmatrix}$$

and

$$\begin{Bmatrix} \tau_{xz} \\ \tau_{yz} \end{Bmatrix} = \begin{bmatrix} G_{xz} & 0 \\ 0 & G_{xy} \end{bmatrix} \begin{Bmatrix} \gamma_{xz} \\ \gamma_{yz} \end{Bmatrix} \tag{4.15}$$



4.4 One corrugation of the (a) trapezoidally and (b) sinusoidally corrugated plates.

4.3.1 Derivation of the equivalent elastic properties of trapezoidally corrugated plates

A method similar to that introduced by Briassoulis (1986) in deriving the equivalent properties of sinusoidally corrugated plates is adopted to obtain new expressions for the equivalent elastic properties of trapezoidally corrugated plates. By applying a constant curvature $w_{,yy}$ on the cross-section of the trapezoidally corrugated plate (Fig. 4.5), we have

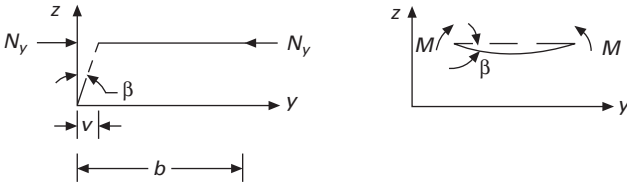
$$v = \int_0^b \frac{N_y}{EA} dy = \frac{N_y b}{EA} \tag{4.16}$$

where N_y is the axial force in the y -direction. This will lead to a non-uniform moment. Since only a linear analysis is considered, we have

$$\beta = \frac{Mb}{EI} = \frac{v}{z} = \frac{N_y b}{EAz} \tag{4.17}$$

where M is the uniform moment that is due to the flexural rigidity of the sheet. Therefore,

$$N_y = M \frac{A}{I} z \tag{4.18}$$



4.5 Cross-section of the trapezoidally corrugated plate.

For an overall average moment M_y over $2c$ (one corrugation):

$$M_y = M + \frac{1}{2c} 2 \int_0^c N_y z dx = M + \frac{MA}{cI} \int_0^c z^2 dx \tag{4.19}$$

where M_y consists of the uniform moment M and the nonuniform moment that is due to the axial force N_y .

Over the interval $x \in [0, c]$,

$$z = \begin{cases} x \tan \theta & 0 \leq x < F/\tan \theta \\ F, & F/\tan \theta \leq x \leq bw + F/\tan \theta \\ 2F - (x - bw)\tan \theta, & bw + F/\tan \theta < x \leq c \end{cases} \tag{4.20}$$

Therefore,

$$\begin{aligned}
 M_y &= M + \frac{MA}{cI} \left[\int_0^{F/\tan\theta} (x \tan\theta)^2 dx + \int_{F/\tan\theta}^{bw+F/\tan\theta} F^2 dx \right. \\
 &\quad \left. + \int_{bw+F/\tan\theta}^c (2F - (x - bw) \tan\theta)^2 dx \right] \\
 &= M + \frac{MA}{cI} \alpha
 \end{aligned} \tag{4.21}$$

where

$$\begin{aligned}
 \alpha &= \frac{F^3}{3 \tan\theta} + F^2 bw + \frac{1}{3} \tan^2\theta [c^3 - (bw + F/\tan\theta)^3] \\
 &\quad - (2F + bw \tan\theta) \tan\theta [c^2 - (bw + F/\tan\theta)^2] \\
 &\quad + (2F + bw \tan\theta)^2 (c - bw - F/\tan\theta)
 \end{aligned}$$

For an equivalent orthotropic plate under constant curvature $w_{,yy}$, the bending moment M_y is uniform. Therefore

$$M_y = B_y w_{,yy} = B_y \frac{\beta}{b} = B_y \frac{Mb/EI}{b} \tag{4.22}$$

where B_y is the flexure rigidity in y direction.

From Eqs (4.21) and (4.22), we have

$$\frac{B_y M}{EI} = M + \frac{MA}{cI} \alpha$$

$$B_y = EI \left(1 + \frac{A}{cI} \right) \alpha$$

or

$$B_y = \frac{Eh^3}{12(1 - \mu^2)} + \frac{Eh}{c} \alpha \tag{4.23}$$

where h is the thickness of the plate.

For the other properties, we adopt the classical expressions (Easley 1975, Davies 1976) or the formulae that are given by Briassoulis (1986):

$$B_x = \frac{Eh^3}{12(1 - \mu^2)} \frac{c}{l}, B_{xy} = \frac{Eh^3}{12(1 + \mu)}, B_\mu = \mu B_x, \mu_y = \mu \tag{4.24}$$

Therefore, we can obtain

$$\frac{\mu_x}{\mu_y} = \frac{E_x}{E_y} = \frac{B_x}{B_y} = \frac{c^2 h^2}{clh^2 + 12\alpha(1 - \mu^2)}$$

or

$$\mu_x = \frac{c^2 h^2}{clh^2 + 12\alpha(1 - \mu^2)} \mu_y = \frac{c^2 h^2 \mu}{clh^2 + 12\alpha(1 - \mu^2)} \quad 4.25$$

As

$$B_x = \frac{E_x h^3}{12(1 - \mu_x \mu_y)}$$

we have

$$E_x = \frac{12(1 - \mu_x \mu_y)}{h^3} B_x = \frac{E(1 - \mu_x \mu_y)c}{(1 - \mu^2)l} \quad 4.26$$

$$E_y = \frac{\mu_y}{\mu_x} E_x \quad 4.27$$

$$E_\mu = \mu E_x \quad 4.28$$

As

$$2B_{xy} = \frac{Eh^3}{6(1 + \mu)} = \frac{G_{xy}h^3}{12}$$

$$\text{then } G_{xy} = \frac{E}{2(1 + \mu)} \quad 4.29$$

In this chapter, the first order shear deformation theory (FSDT) is employed. The equivalent transverse shear properties G_{xz} and G_{yz} are calculated in the same way as in the study of Semenyuk and Neskhodovskaya (2002).

4.3.2 Derivation of the equivalent elastic properties of sinusoidally corrugated plates

For sinusoidally corrugated plates as shown in Fig. 4.4(b) where the corrugation is defined by $z = F \sin \pi x/c$, Briassoulis (1986) has deduced the flexural rigidities as:

$$B_x = \frac{Eh^3}{12(1 - \mu^2)} \frac{c}{l}, B_\mu = \mu B_x, B_y = \frac{Eh^3}{12(1 - \mu^2)} + \frac{EhF^2}{2},$$

$$B_{xy} = \frac{Eh^3}{12(1 + \mu)}, \mu_y = \mu \quad 4.30$$

Therefore, we can obtain:

$$\frac{\mu_x}{\mu_y} = \frac{E_x}{E_y} = \frac{B_x}{B_y} = \frac{c}{l \left[1 + 6(1 - \mu^2) \left(\frac{F}{h} \right)^2 \right]}$$

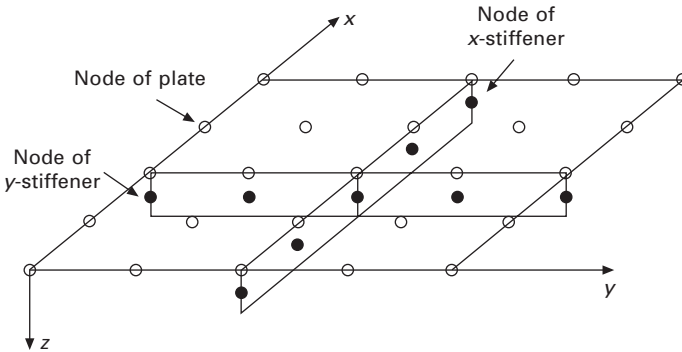
$$\mu_x = \frac{c\mu_y}{l \left[1 + 6(1 - \mu^2) \left(\frac{F}{h} \right)^2 \right]} \tag{4.31}$$

The formulae for other elastic properties are the same as those for the trapezoidally corrugated plate. Thus, we have obtained all of the equivalent elastic properties for the trapezoidally and sinusoidally corrugated plates.

4.4 Formulation for stiffened and corrugated plates

Stiffened corrugated plates can be approximated by stiffened orthotropic plates after the equivalent elastic properties have been derived by the method described in Section 4.3. Stiffened isotropic plates are special cases of stiffened orthotropic plates. Therefore, we need only study the buckling behavior of stiffened orthotropic plates.

The mesh-free model of a stiffened orthotropic plate, shown in Fig. 4.6, is composed of an orthotropic plate and two stiffeners that are regarded as beams. The plate and the beams are prescribed with a set of nodes, and the degrees of freedom (DOF) of every node of the plate are $(w_p, \varphi_{px}, \varphi_{py})$. The DOF of every node of the x -stiffener are (w_{sx}, φ_{sx}) and of every node of the y -stiffener are (w_{sy}, φ_{sy}) . Here, we have neglected the in-plane bending of the stiffeners that have negligible torsional stiffness. The stiffeners are assumed to be made from the same material as the original corrugated plate or the isotropic plates.



4.6 Meshless model of a stiffened orthotropic plate.

4.4.1 Displacements approximation

According to the mesh-free Galerkin method, the displacements of the plate can be approximated by:

$$u_p(x, y, z) = -z\varphi_{px} = -z \sum_{I=1}^n N_I(x, y)\varphi_{pxI} \quad 4.32$$

$$v_p(x, y, z) = -z\varphi_{py} = -z \sum_{I=1}^n N_I(x, y)\varphi_{pyI} \quad 4.33$$

$$w_p(x, y) = \sum_{I=1}^n N_I(x, y)w_{pI} \quad 4.34$$

where φ_{pxI} , φ_{pyI} , and w_{pI} are the nodal parameters of the plate and n is the number of nodes of the plate. φ_{pxI} , φ_{pyI} are independent of w_{pI} . The displacement field of the x -stiffener is:

$$u_{sx}(x, z) = -z\varphi_{sx} = -z \sum_{I=1}^N \Phi_{xI}(x)\varphi_{sxI} \quad 4.35$$

$$w_{sx}(x) = \sum_{I=1}^N \Phi_{xI}(x)w_{sxI} \quad 4.36$$

where φ_{sxI} and w_{sxI} are the x -stiffener's nodal parameters and N is the number of nodes of the stiffener. The displacement field of the y -stiffener is:

$$v_{sy}(y, z) = -z\varphi_{sy} = -z \sum_{I=1}^N \Phi_{yI}(y)\varphi_{syI} \quad 4.37$$

$$w_{sy}(y) = \sum_{I=1}^N \Phi_{yI}(y)w_{syI} \quad 4.38$$

where φ_{syI} and w_{syI} are the y -stiffener's nodal parameters. The shape functions $N_I(x, y)$, $\Phi_{xI}(x)$ and $\Phi_{yI}(y)$ are obtained from Eq. (4.14). A cubic spline function

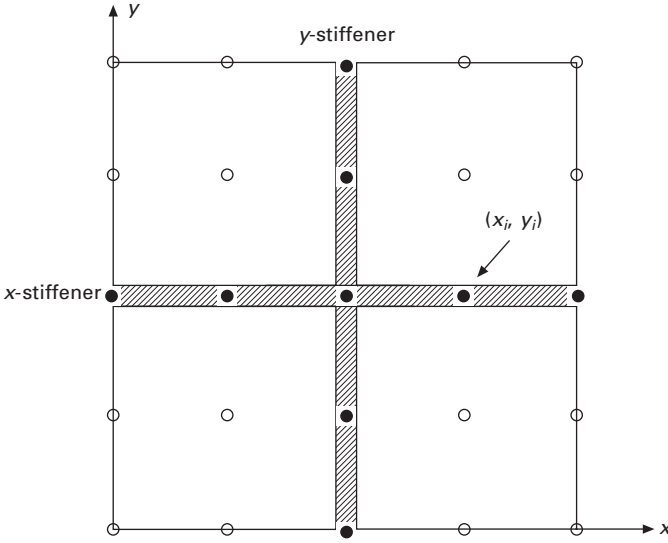
$$\bar{w}(s) = \begin{cases} \frac{2}{3} - 4s^2 + 4s^3, & s \leq \frac{1}{2} \\ \frac{4}{3} - 4s + 4s^2 - \frac{4}{3}s^3, & \frac{1}{2} < s \leq 1 \\ 0, & s > 1 \end{cases} \quad 4.39$$

is used as the weight function. The quadratic basis \mathbf{p}^T is employed to compute the shape functions.

4.4.2 Transformation equations

As shown in Fig. 4.7, at every point along the connection line between the plate and the x -stiffener, we have

$$[\varphi_{px}]_{z=-h_p/2} = [\varphi_{sx}]_{z=h_s/2} \quad 4.40$$



4.7 Plan of the stiffened plate.

$$[w_p]_{z=-h_p/2} = [w_{sx}]_{z=h_s/2} \tag{4.41}$$

where h_p is the thickness of the plate and h_s is the depth of the *x*-stiffener.

In view of Eqs (4.40) and (4.41), it can be deduced that

$$[\varphi_{px}]_i = [\varphi_{sx}]_i \tag{4.42}$$

$$[w_p]_i = [w_{sx}]_i \quad (i = 1, \dots, N) \tag{4.43}$$

or

$$\varphi_{px}(x_i, y_i) = \varphi_{sx}(x_i, y_i) \tag{4.44}$$

$$w_p(x_i, y_i) = w_{sx}(x_i, y_i), \quad (i = 1, \dots, N) \tag{4.45}$$

where N is the number of nodes of the *x*-stiffener. According to the mesh-free Galerkin method, Eqs (4.44) and (4.45) can be rewritten as

$$\sum_{I=1}^n N_I(x_i, y_i) \varphi_{pxI} = \sum_{J=1}^N \Phi_{xJ}(x_i) \varphi_{sxJ} \tag{4.46}$$

$$\sum_{I=1}^n N_I(x_i, y_i) w_{pI} = \sum_{J=1}^N \Phi_{xJ}(x_i) w_{sxJ} \tag{4.47}$$

$$(i = 1, \dots, N)$$

or in matrix form

$$\mathbf{T}_{px\varphi} \boldsymbol{\delta}_{px\varphi} = \mathbf{T}_{sx\varphi} \boldsymbol{\delta}_{sx\varphi} \tag{4.48}$$

where

$$\begin{aligned}
 \mathbf{T}_{px\varphi} &= \begin{bmatrix} N_1(x_1, y_1) & N_2(x_1, y_1) & \dots & N_n(x_1, y_1) \\ \vdots & \vdots & \ddots & \vdots \\ N_1(x_N, y_N) & N_2(x_N, y_N) & \dots & N_n(x_N, y_N) \end{bmatrix}, \\
 \boldsymbol{\delta}_{px\varphi} &= \begin{bmatrix} \varphi_{px1} \\ \vdots \\ \varphi_{pxn} \end{bmatrix} \\
 \mathbf{T}_{sx\varphi} &= \begin{bmatrix} \Phi_{x1}(x_1) & \Phi_{x2}(x_1) & \dots & \Phi_{xN}(x_1) \\ \vdots & \vdots & \ddots & \vdots \\ \Phi_{x1}(x_N) & \Phi_{x2}(x_N) & \dots & \Phi_{xN}(x_N) \end{bmatrix}, \boldsymbol{\delta}_{sx\varphi} = \begin{bmatrix} \varphi_{sx1} \\ \vdots \\ \varphi_{sxN} \end{bmatrix} \\
 \mathbf{T}_{pw} \boldsymbol{\delta}_{pw} &= \mathbf{T}_{sxw} \boldsymbol{\delta}_{sxw} \tag{4.49}
 \end{aligned}$$

where

$$\begin{aligned}
 \mathbf{T}_{pw} &= \begin{bmatrix} N_1(x_1, y_1) & N_2(x_1, y_1) & \dots & N_n(x_1, y_1) \\ \vdots & \vdots & \ddots & \vdots \\ N_1(x_N, y_N) & N_2(x_N, y_N) & \dots & N_n(x_N, y_N) \end{bmatrix}, \\
 \boldsymbol{\delta}_{pw} &= \begin{bmatrix} w_{p1} \\ \vdots \\ w_{pn} \end{bmatrix} \\
 \mathbf{T}_{sxw} &= \begin{bmatrix} \Phi_{x1}(x_1) & \Phi_{x2}(x_1) & \dots & \Phi_{xN}(x_1) \\ \vdots & \vdots & \ddots & \vdots \\ \Phi_{x1}(x_N) & \Phi_{x2}(x_N) & \dots & \Phi_{xN}(x_N) \end{bmatrix}, \\
 \boldsymbol{\delta}_{sxw} &= \begin{bmatrix} w_{sx1} \\ \vdots \\ w_{sxN} \end{bmatrix}
 \end{aligned}$$

From Eqs (4.48) and (4.49), we obtain:

$$\boldsymbol{\delta}_{sx\varphi} = \mathbf{T}_{spx\varphi} \boldsymbol{\delta}_{px\varphi} \tag{4.50}$$

where

$$\begin{aligned} \mathbf{T}_{spx\varphi} &= \mathbf{T}_{sx\varphi}^{-1} \mathbf{T}_{px\varphi} \\ \boldsymbol{\delta}_{sxw} &= \mathbf{T}_{spxw} \boldsymbol{\delta}_{pw} \end{aligned} \quad 4.51$$

where

$$\mathbf{T}_{spxw} = \mathbf{T}_{sxw}^{-1} \mathbf{T}_{pw}$$

From Eqs (4.50) and (4.51), we can form the transformation equation:

$$\boldsymbol{\delta}_{sx} = \mathbf{T}_{spx} \boldsymbol{\delta}_p \quad 4.52$$

where

$$\boldsymbol{\delta}_{sx} = \begin{bmatrix} w_{sx1} \\ \varphi_{sx1} \\ 0 \\ w_{sx2} \\ \varphi_{sx2} \\ 0 \\ \vdots \\ w_{sxN} \\ \varphi_{sxN} \\ 0 \end{bmatrix}, \boldsymbol{\delta}_p = \begin{bmatrix} w_{p1} \\ \varphi_{px1} \\ \varphi_{py1} \\ w_{p2} \\ \varphi_{px2} \\ \varphi_{py2} \\ \vdots \\ w_{pn} \\ \varphi_{pxn} \\ \varphi_{pyn} \end{bmatrix}$$

and \mathbf{T}_{spx} is the $3N \times 3n$ matrix that transforms the nodal parameters of the x -stiffener into the nodal parameters of the plate.

Similarly, we can obtain the transformation equation:

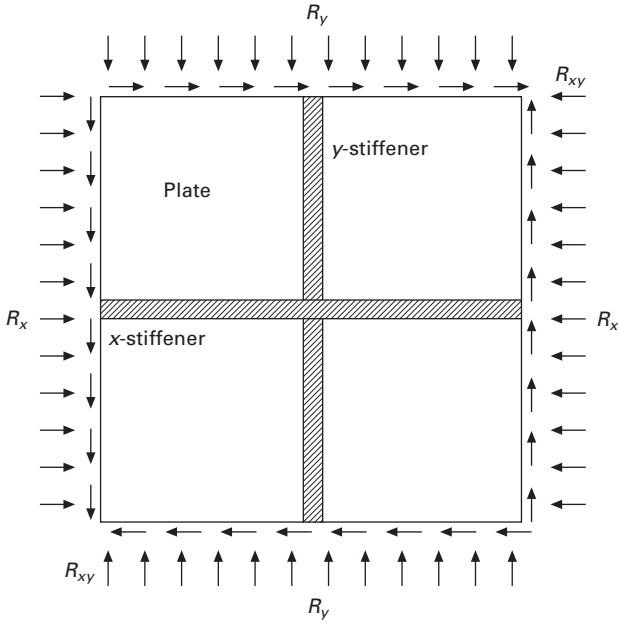
$$\boldsymbol{\delta}_{sy} = \mathbf{T}_{syy} \boldsymbol{\delta}_p \quad 4.53$$

for the y -stiffener.

4.4.3 Stability analysis of stiffened plates

By applying the in-plane forces that are shown in Fig. 4.8 to the stiffened plate, the potential energy of the plate can be expressed as

$$\begin{aligned} \Pi_p &= \frac{1}{2} \iint_{\Omega} \boldsymbol{\varepsilon}_p^T \mathbf{D} \boldsymbol{\varepsilon}_p \, dx \, dy - \frac{1}{2} \iint_{\Omega} \boldsymbol{\beta}^T \mathbf{R} \boldsymbol{\beta} \, dx \, dy \\ &+ \iint_{\Omega} \frac{G_{xz} h_p}{2k} \left(\frac{\partial w_p}{\partial x} - \varphi_{px} \right)^2 \, dx \, dy \\ &+ \iint_{\Omega} \frac{G_{yz} h_p}{2k} \left(\frac{\partial w_p}{\partial y} - \varphi_{py} \right)^2 \, dx \, dy \end{aligned} \quad 4.54$$



4.8 Stiffened plate under in-plane compression.

where

$$\varepsilon_p = \begin{bmatrix} -\frac{\partial\varphi_{px}}{\partial x} \\ -\frac{\partial\varphi_{py}}{\partial y} \\ -\left(\frac{\partial\varphi_{px}}{\partial y} + \frac{\partial\varphi_{py}}{\partial x}\right) \end{bmatrix}, \quad D = \frac{h_p^3}{12(1 - \mu_x\mu_y)}$$

$$\times \begin{bmatrix} E_x & E_\mu & 0 \\ E_\mu & E_y & 0 \\ 0 & 0 & (1 - \mu_x\mu_y)G_{xy} \end{bmatrix} \beta = \begin{bmatrix} \frac{\partial w_p}{\partial x} \\ \frac{\partial w_p}{\partial y} \end{bmatrix} \quad 4.55$$

and the in-plane load

$$\mathbf{R} = \begin{bmatrix} R_x & R_{xy} \\ R_{xy} & R_y \end{bmatrix} \quad 4.56$$

$k = 5/6$ is the shear correction factor. $E_x, E_\mu, E_y, \mu_x, \mu_y, G_{xy}, G_{xz}$, and G_{yz} are the equivalent elastic properties of the orthotropic plate that are derived in Section 4.3. For the stiffened isotropic plate, we simply take

$$\begin{aligned} E_x &= E_y = E, E_\mu = \mu E, \mu_x = \mu_y = \mu, \\ G_{xy} &= G_{xz} = G_{yz} = G = E/2(1 + \mu) \end{aligned}$$

The potential energy of the x -stiffener is:

$$\begin{aligned} \Pi_{sx} &= \int_l \frac{1}{2} EI_{sx} \left(-\frac{d\varphi_{sx}}{dx} \right)^2 dx - \frac{1}{2} \int_l \frac{R_x A_{sx}}{h_p} \left(\frac{dw_{sx}}{dx} \right)^2 dx \\ &\quad + \int_l \frac{1}{2} \frac{GA_{sx}}{k} \left(\frac{dw_{sx}}{dx} - \varphi_{sx} \right)^2 dx \end{aligned} \quad 4.57$$

where I_{sx} is the moment of inertia of the x -stiffener, A_{sx} the area of the cross-section of the x -stiffener, and h_{sx} the depth.

The potential energy of the y -stiffener is

$$\begin{aligned} \Pi_{sy} &= \int_l \frac{1}{2} EI_{sy} \left(-\frac{d\varphi_{sy}}{dy} \right)^2 dy - \frac{1}{2} \int_l \frac{R_y A_{sy}}{h_p} \left(\frac{dw_{sy}}{dy} \right)^2 dy \\ &\quad + \int_l \frac{1}{2} \frac{GA_{sy}}{k} \left(\frac{dw_{sy}}{dy} - \varphi_{sy} \right)^2 dy \end{aligned} \quad 4.58$$

where I_{sy} is the moment of inertia of the y -stiffener, A_{sy} is the area of the cross-section of the y -stiffener, and h_{sy} is the depth.

Therefore, the potential energy of the stiffened plate is

$$\Pi = \Pi_p + \Pi_{sx} + \Pi_{sy} \quad 4.59$$

By substitution of Eqs (4.32) to (4.38) into Eq. (4.59), we obtain:

$$\begin{aligned} \Pi &= \frac{1}{2} \delta_p^T \mathbf{K}_p \delta_p - \frac{1}{2} \delta_p^T \mathbf{G}_p \delta_p + \frac{1}{2} \delta_{sx}^T \mathbf{K}_{sx} \delta_{sx} - \frac{1}{2} \delta_{sx}^T \mathbf{G}_{sx} \delta_{sx} \\ &\quad + \frac{1}{2} \delta_{sy}^T \mathbf{K}_{sy} \delta_{sy} - \frac{1}{2} \delta_{sy}^T \mathbf{G}_{sy} \delta_{sy} \end{aligned} \quad 4.60$$

where

$$\begin{aligned} [\mathbf{K}_p]_{ij} &= \iint_{\Omega} (\mathbf{B}_{bi}^T \mathbf{D} \mathbf{B}_{bj} + \alpha_{xz} \mathbf{B}_{xi}^T \mathbf{B}_{xj} + \alpha_{yz} \mathbf{B}_{yi}^T \mathbf{B}_{yj}) dx dy \\ [\mathbf{K}_{sx}]_{ij} &= \int_l (\mathbf{B}_{sxi}^T EI_{sx} \mathbf{B}_{sxj} + c_{sx} \mathbf{B}_{sksi}^T \mathbf{B}_{sxsj}) dx \\ [\mathbf{K}_{sy}]_{ij} &= \int_l (\mathbf{B}_{syi}^T EI_{sy} \mathbf{B}_{syj} + c_{sy} \mathbf{B}_{sysi}^T \mathbf{B}_{sysj}) dy \end{aligned}$$

and

$$\mathbf{B}_{bi} = \begin{bmatrix} 0 & -N_{i,x} & 0 \\ 0 & 0 & -N_{i,y} \\ 0 & -N_{i,y} & -N_{i,x} \end{bmatrix}, \mathbf{B}_{si} = \begin{bmatrix} N_{i,x} & -N_i & 0 \\ N_{i,y} & 0 & -N_i \end{bmatrix}$$

$$\mathbf{B}_{sxi} = [0 \quad -\Phi_{xi,x} \quad 0], \mathbf{B}_{sysi} = [\Phi_{xi,x} \quad -\Phi_{xi} \quad 0]$$

$$\mathbf{B}_{syi} = [0 \quad 0 \quad -\Phi_{yi,y}] \quad , \mathbf{B}_{sysi} = [\Phi_{yi,y} \quad 0 \quad -\Phi_{yi}]$$

$$\alpha_{xz} = G_{xz}h_p/k, \alpha_{yz} = G_{yz}h_p/k, c_{sx} = GA_{sx}/k, c_{sy} = GA_{sy}/k$$

$$[\mathbf{G}_p]_{ij} = \iint_{\Omega} \begin{bmatrix} R & 0 & 0 \\ 0 & 0 & 0 \\ 0 & 0 & 0 \end{bmatrix} dx dy \quad 4.61$$

$$R = R_x N_{i,x} N_{j,x} + R_y N_{i,y} N_{j,y} + R_{xy} (N_{i,x} N_{j,y} + N_{i,y} N_{j,x})$$

$$[\mathbf{G}_{sx}]_{ij} = \frac{R_x A_{sx}}{h_p} \int_l \begin{bmatrix} \Phi_{xi,x} \Phi_{xj,x} & 0 \\ 0 & 0 \end{bmatrix} dx \quad 4.62$$

$$[\mathbf{G}_{sy}]_{ij} = \frac{R_y A_{sy}}{h_p} \int_l \begin{bmatrix} \Phi_{yi,y} \Phi_{yj,y} & 0 \\ 0 & 0 \end{bmatrix} dy \quad 4.63$$

By substituting Eqs (4.52) and (4.53) into Eq. (4.60), we have

$$\begin{aligned} \Pi &= \frac{1}{2} \delta_p^T \mathbf{K}_p \delta_p + \frac{1}{2} \delta_p^T \mathbf{T}_{spx}^T \mathbf{K}_{sx} \mathbf{T}_{spx} \delta_p + \frac{1}{2} \delta_p^T \mathbf{T}_{spy}^T \mathbf{K}_{sy} \mathbf{T}_{spy} \delta_p \\ &\quad - \frac{1}{2} \delta_p^T \mathbf{G}_p \delta_p - \frac{1}{2} \delta_p^T \mathbf{T}_{spx}^T \mathbf{G}_{sx} \mathbf{T}_{spx} \delta_p - \frac{1}{2} \delta_p^T \mathbf{T}_{spy}^T \mathbf{G}_{sy} \mathbf{T}_{spy} \delta_p \end{aligned} \quad 4.64$$

or

$$\Pi = \frac{1}{2} \delta_p^T \mathbf{K} \delta_p - \frac{1}{2} \delta_p^T \mathbf{G} \delta_p \quad 4.65$$

where

$$\mathbf{K} = \mathbf{K}_p + \mathbf{T}_{spx}^T \mathbf{K}_{sx} \mathbf{T}_{spx} + \mathbf{T}_{spy}^T \mathbf{K}_{sy} \mathbf{T}_{spy}$$

$$\mathbf{G} = \mathbf{G}_p + \mathbf{T}_{spx}^T \mathbf{G}_{sx} \mathbf{T}_{spx} + \mathbf{T}_{spy}^T \mathbf{G}_{sy} \mathbf{T}_{spy}$$

Invoking $\delta \Pi = 0$ results in the following equation:

$$(\mathbf{K} - \mathbf{G}) \delta_p = 0 \quad 4.66$$

Assume that $R_x = a_1 R_y$ and $R_x = a_2 R_{xy}$, where a_1 and a_2 are constants. Then by extracting R_x from \mathbf{G} , we obtain:

$$(\mathbf{K} - R_x \mathbf{G}') \hat{\delta}_p = 0 \quad 4.67$$

The solution of this eigenvalue problem is the buckling load R_{cr} . The critical value of the compressive stress is therefore given by

$$\sigma_{cr} = \frac{R_{cr}}{h_p} \quad 4.68$$

where h_p is the thickness of the plate.

4.4.4 Enforcement of essential boundary conditions

Owing to lack of Kronecker delta properties in the meshless shape functions, the imposition of the essential boundary conditions is usually difficult in meshless methods. Here, we use the following full transformation method that was introduced by Chen *et al.* (1996) to enforce the essential boundary conditions.

The full transformation method

The meshless approximation of $u(\mathbf{x})$ is

$$u_i^h(\mathbf{x}) = \sum_{I=1}^N N_I(\mathbf{x}) u_{iI} \quad 4.69$$

where the subscript i denotes the i th coordinate direction. $N_I(\mathbf{x})$ is the shape function of node I , and N is the total number of nodes in the domain. Let $\tilde{u}_{iJ} \equiv u_i^h(\mathbf{x}_J)$, and we have

$$\tilde{u}_{iJ} \equiv \sum_{I=1}^N N_I(\mathbf{x}_J) u_{iI} = \sum_{I=1}^N \mathbf{A}_{IJ} u_{iI} \quad 4.70$$

Equation (4.70) can thus be rewritten as

$$u_{iI} = \sum_{K=1}^N \mathbf{A}_{KI}^{-1} \tilde{u}_{iK} \quad 4.71$$

in which

$$\mathbf{A}_{IJ} = N_I(\mathbf{x}_J) \quad 4.72$$

The substitution of Eq. (4.71) into Eq. (4.69) leads to

$$\begin{aligned} u_i^h(\mathbf{x}) &= \sum_{I=1}^N N_I(\mathbf{x}) u_{iI} \\ &= \sum_{I=1}^N N_I(\mathbf{x}) \sum_{K=1}^N \mathbf{A}_{KI}^{-1} \tilde{u}_{iK} \end{aligned}$$

$$\begin{aligned}
 &= \sum_{K=1}^N \sum_{I=1}^N N_I(\mathbf{x}) \mathbf{A}_{KI}^{-1} \tilde{u}_{iK} \\
 &= \sum_{K=1}^N \tilde{N}_K(\mathbf{x}) \tilde{u}_{iK}
 \end{aligned} \tag{4.73}$$

where

$$\tilde{N}_K(\mathbf{x}) = \sum_{I=1}^N \mathbf{A}_{KI}^{-1} N_I(\mathbf{x}) \tag{4.74}$$

Note that $\tilde{N}_I(\mathbf{x}_J) = \sum_{K=1}^N \mathbf{A}_{IK}^{-1} N_K(\mathbf{x}_J) = \sum_{K=1}^N \mathbf{A}_{IK}^{-1} \mathbf{A}_{KJ} = \delta_{IJ}$, and $\tilde{u}_{iI} \equiv u_i^h(\mathbf{x}_I)$ is the nodal value of u_i^h at node \mathbf{x}_I .

Meanwhile, u^h and δu^h satisfy the following boundary conditions:

$$u_i^h(\mathbf{x}_I) = \sum_{J=1}^N \tilde{N}_J(\mathbf{x}_I) \tilde{u}_{iJ} = g_i(\mathbf{x}_I), \quad \forall I \in \eta_{gi} \tag{4.75}$$

$$\delta u_i^h(\mathbf{x}_I) = \sum_{J=1}^N \tilde{N}_J(\mathbf{x}_I) \delta \tilde{u}_{iJ} = 0, \quad \forall I \in \eta_{gi} \tag{4.76}$$

where η_{gi} denotes a set of node numbers in which the associated nodes are located on the boundary Γ_{gi} , and as $\tilde{N}_I(\mathbf{x}_J) = \delta_{IJ}$, the unknown coefficients can be directly obtained from:

$$\tilde{u}_{iI} = g_i(\mathbf{x}_I), \quad \forall I \in \eta_{gi}$$

$$\delta \tilde{u}_{iI} = 0, \quad \forall J \in \eta_{gi} \tag{4.77}$$

The introduction of the transformed shape function into the weak form of the equilibrium equations furnishes the following discretized meshless formulation:

$$\tilde{\mathbf{K}} \tilde{\mathbf{U}} = \tilde{\mathbf{F}} \tag{4.78}$$

where the transformed matrices are defined as

$$\tilde{\mathbf{K}} = \mathbf{\Lambda}^{-1} \mathbf{K} \mathbf{\Lambda}^{-T} \tag{4.79}$$

$$\tilde{\mathbf{F}} = \mathbf{\Lambda}^{-1} \mathbf{F} \tag{4.80}$$

$$\tilde{\mathbf{U}} = \mathbf{\Lambda}^T \mathbf{U} \tag{4.81}$$

where \mathbf{K} is the stiffness matrix that is obtained by the mesh-free Galerkin method, and the transformation matrix is

$$\Lambda_{ij} = A_{ij} \mathbf{I} \tag{4.82}$$

with \mathbf{I} being the identity matrix.

4.5 Validation studies

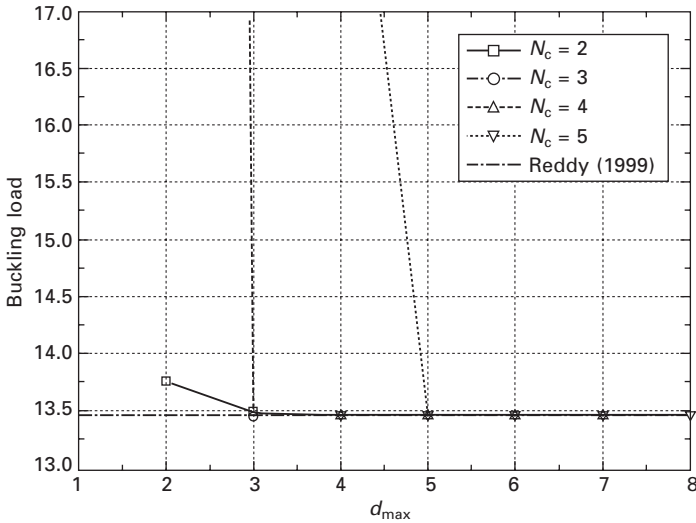
An example is employed to show the convergence of the proposed method, and the effects that the domain of influence of the nodes and the order basis functions have on this convergence.

A simply supported orthotropic square plate under uniaxial in-plane compression is considered. The elastic moduli of the plate are $E_x = 10E_y$, $G_{xy} = G_{xz} = 0.5E_y$, $G_{yz} = 0.2E_y$, and $\mu_x = 0.25$. The side-to-thickness ratio of the plate is $L/h = 0.01$. The nondimensionalized buckling load that is obtained by the proposed method under a different scaling factor d_{max} and a different completeness order basis function N_c , as shown in Fig. 4.9, is compared with the result that is given by Reddy (1999). The nondimensionalized buckling load is defined as:

$$\bar{R} = R_{cr}L^2 / (\pi^2 D_{22}) \tag{4.83}$$

where

$$D_{22} = E_y h_p^3 / 12 (1 - \mu_x \mu_y)$$



4.9 Nondimensionalized buckling load of the orthotropic plate under different d_{max} and N_c .

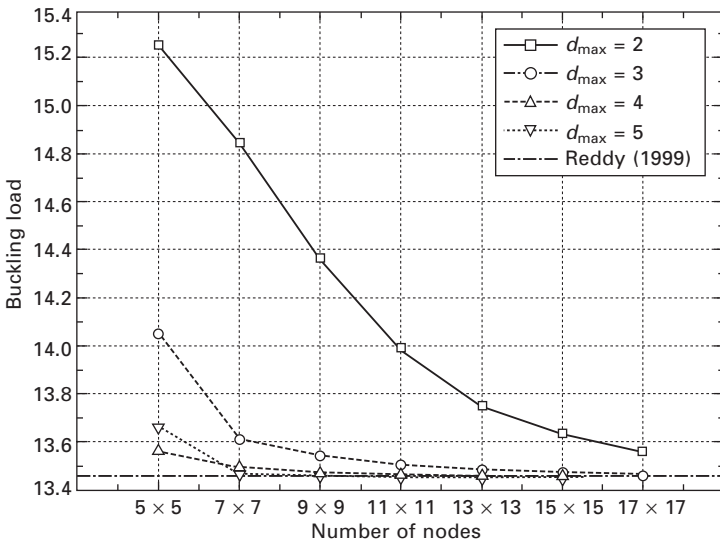
The meshless scheme for the plate is chosen to be 13×13 nodes.

Here, a rectangular support is employed, and thus the scaling factors d_{max}^x and d_{max}^y are defined as

$$d_{max}^x = \frac{l_x}{h_{mx}} \text{ and } d_{max}^y = \frac{l_y}{h_{my}} \tag{4.84}$$

where l_x, l_y are the lengths of the rectangular support in x and y directions, respectively, and h_{mx} and h_{my} are the distances between two neighboring nodes in the x and y directions, respectively. For convenience, we choose $d_{max}^x = d_{max}^y = d_{max}$. Figure 4.9 shows that for a certain N_c , a larger support size, denoted by d_{max} , gives relatively more accurate results. A larger support size is needed for a higher completeness order (N_c) basis function to achieve better results.

The study of convergence is implemented by increasing the nodes for the plate and the scaling factor d_{max} under certain N_c . Figures 4.10 to 4.13 show the variations in the nondimensionalized buckling load with a different number of nodes and d_{max} under different N_c . The solution by Reddy (1999) is also included in the figures for comparison. For a certain d_{max} , the solution converges when the number of nodes increases. A higher completeness order basis function needs a larger support size to make the solution converge. Moreover, a higher completeness order basis function can achieve better convergence characteristics than a lower completeness order basis function.

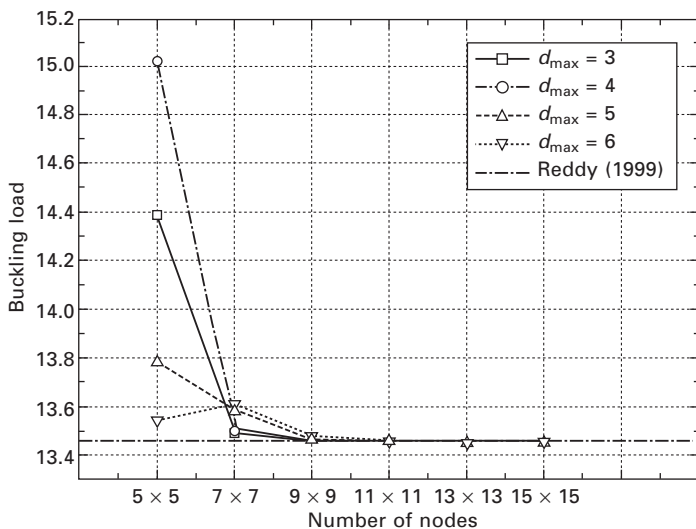


4.10 Variation of the nondimensionalized buckling load of the orthotropic plate, $N_c = 2$.

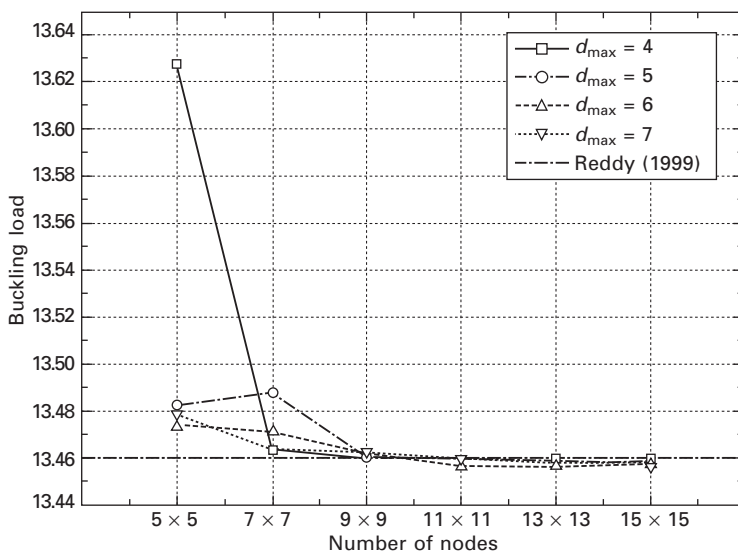
4.6 Some numerical examples

4.6.1 Simply supported stiffened isotropic plate under in-plane compression

The buckling behavior of a simply supported stiffened rectangular isotropic plate under uniaxial in-plane compression (Fig. 4.14) has been studied. A

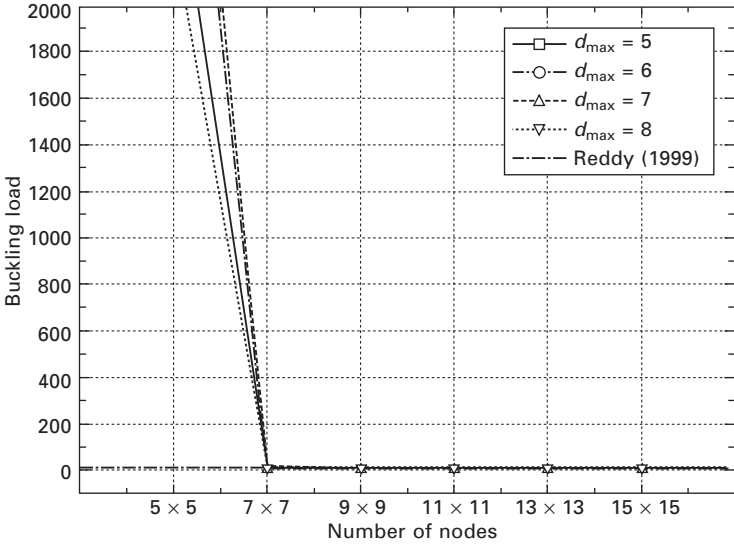


4.11 Variation of the nondimensionalized buckling load of the orthotropic plate, $N_c = 3$.

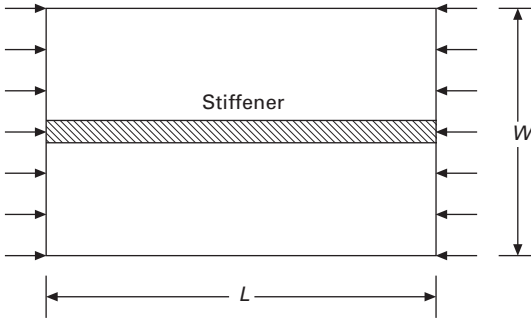


4.12 Variation of the nondimensionalized buckling load of the orthotropic plate, $N_c = 4$.

stiffener is placed along the centerline of the plate. The plate and the stiffener are made of the same material, with a Poisson’s ratio of $\mu = 0.3$. The ratio of the plate thickness to the length is assumed to be 0.01. The buckling coefficient



4.13 Variation of the nondimensionalized buckling load of the orthotropic plate, $N_c = 5$.



4.14 Simply supported stiffened plate under in-plane compression.

$$k = \sigma_{cr} W^2 h_p / (\pi^2 D) \tag{4.85}$$

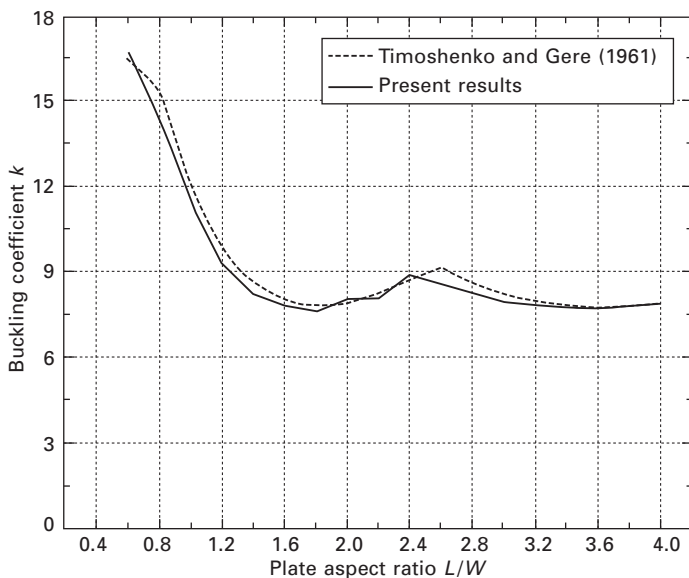
is computed for different plate aspect ratios L/W , where σ_{cr} is the critical stress and

$$D = E h_p^3 / 12 (1 - \mu^2)$$

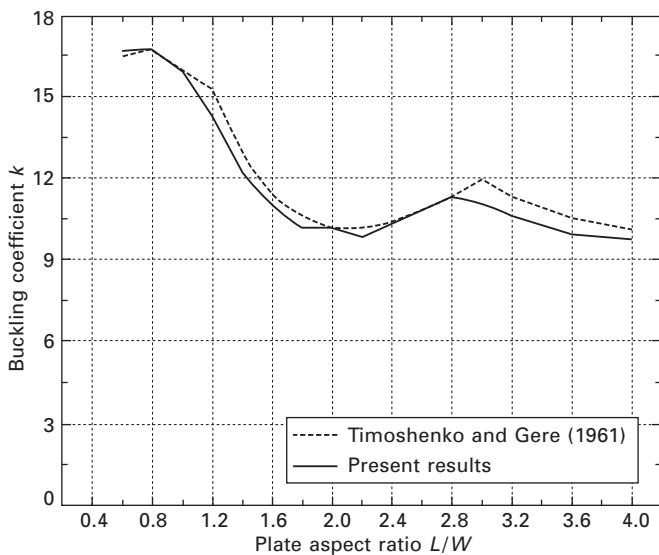
Figures 4.15 to 4.19 compare the buckling coefficients that are obtained by the authors and those of Timoshenko and Gere (1961), where

$$\gamma = EI_{sx} / (WD) \text{ and } \delta = W_{sx} h_{sx} / (W h_p) \tag{4.86}$$

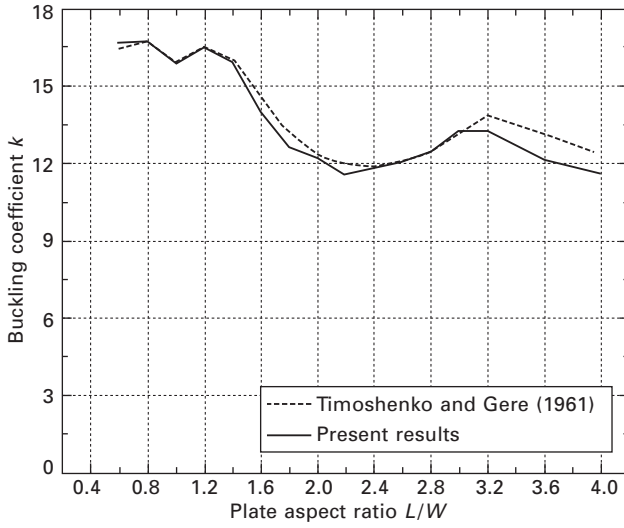
Most results are very close to those that are given by Timoshenko and



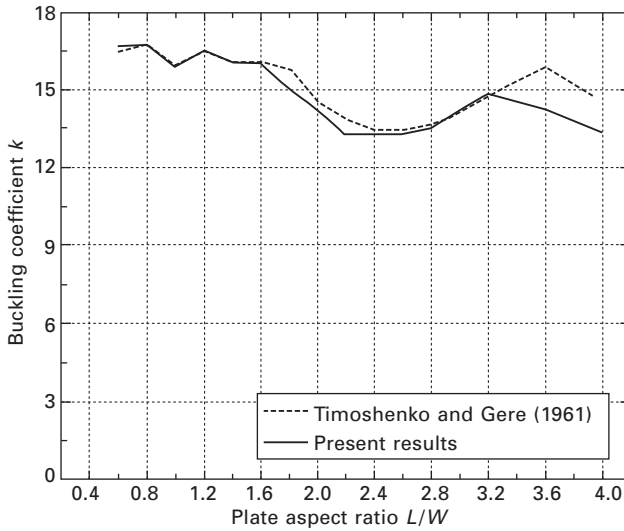
4.15 Buckling coefficient of stiffened plates of different aspect ratios ($\gamma = 5, \delta = 0.05$).



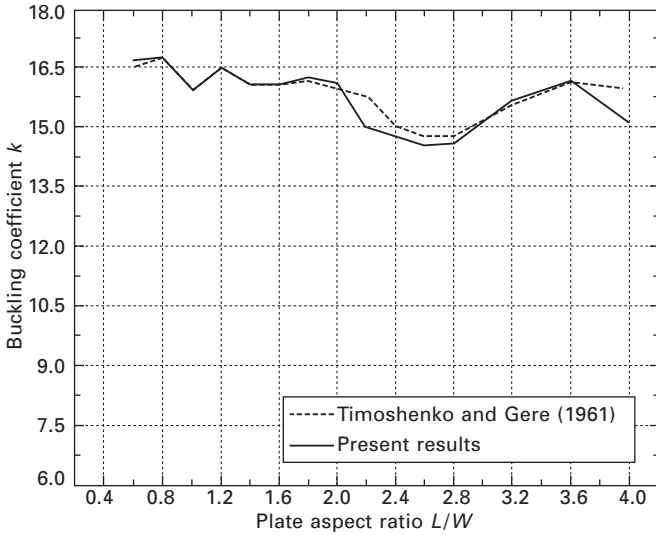
4.16 Buckling coefficient of stiffened plates of different aspect ratios ($\gamma = 10, \delta = 0.05$).



4.17 Buckling coefficient of stiffened plates of different aspect ratios ($\gamma = 15, \delta = 0.05$).



4.18 Buckling coefficient of stiffened plates of different aspect ratios ($\gamma = 20, \delta = 0.05$).

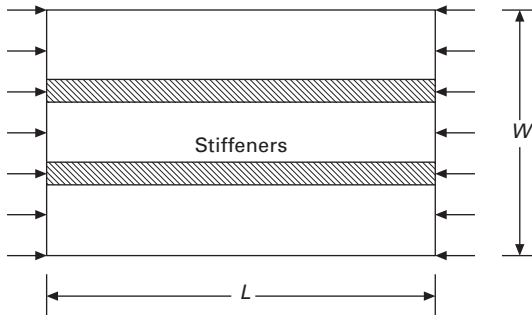


4.19 Buckling coefficient of stiffened plates of different aspect ratios ($\gamma = 25, \delta = 0.05$).

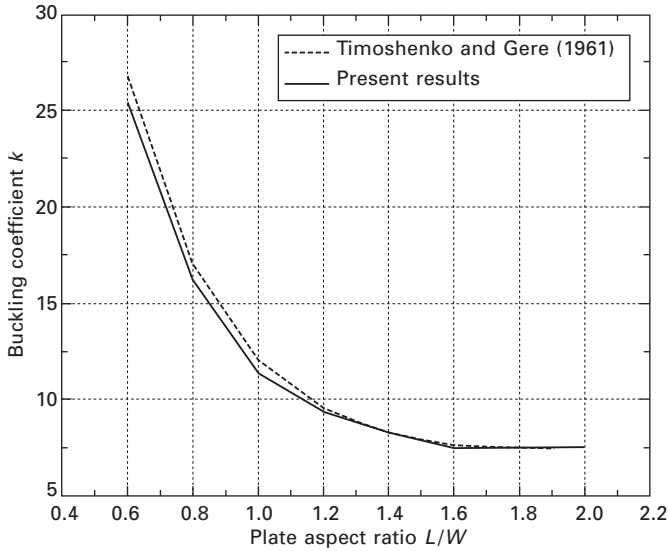
Gere, except when the plate aspect ratio is larger than 2.8 or 3.2, when there is a slight difference.

4.6.2 Simply supported stiffened isotropic plate with two stiffeners under in-plane compression

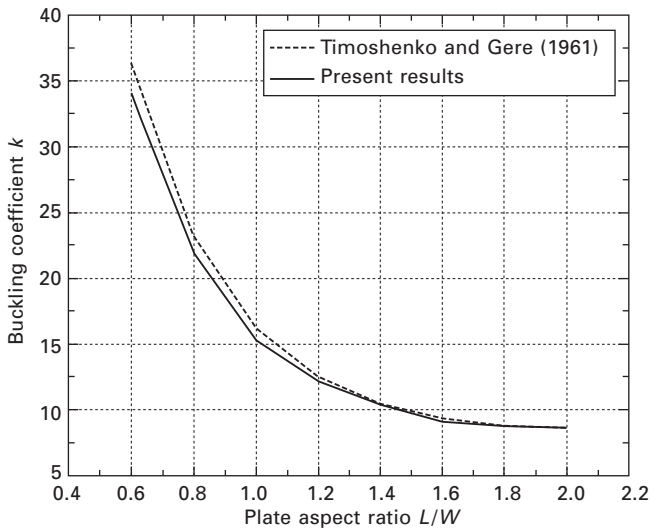
This example is the same as in 4.6.1, except that the plate is stiffened by two stiffeners that divide the width of the plate into three equal parts (Fig. 4.20). Figures 4.21 to 4.24 compare the buckling coefficient obtained by the authors with those by Timoshenko and Gere (1961). The agreement between the two results is very good.



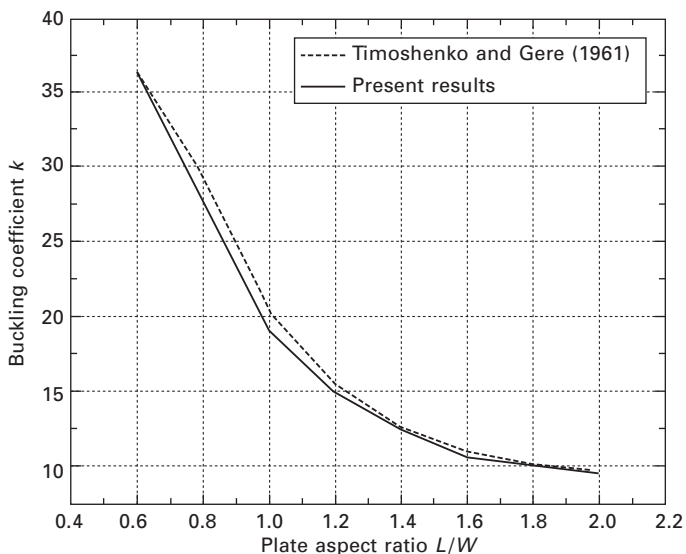
4.20 Simply supported stiffened plate with two stiffeners under in-plane compression.



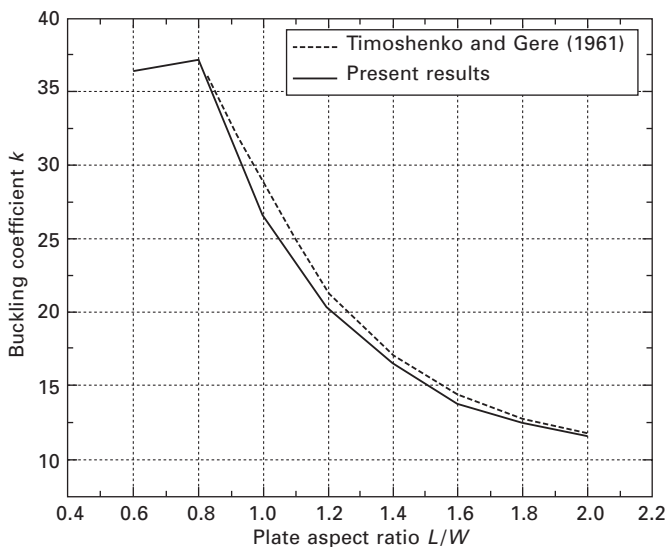
4.21 Buckling coefficient of different aspect ratio plates stiffened by two stiffeners ($\gamma = 10/3$, $\delta = 0.05$).



4.22 Buckling coefficient of different aspect ratio plates stiffened by two stiffeners ($\gamma = 5$, $\delta = 0.05$).



4.23 Buckling coefficient of different aspect ratio plates stiffened by two stiffeners ($\gamma = 20/3$, $\delta = 0.05$).



4.24 Buckling coefficient of different aspect ratio plates stiffened by two stiffeners ($\gamma = 10$, $\delta = 0.05$).

4.6.3 Clamped stiffened square isotropic plate with one stiffener under in-plane compression

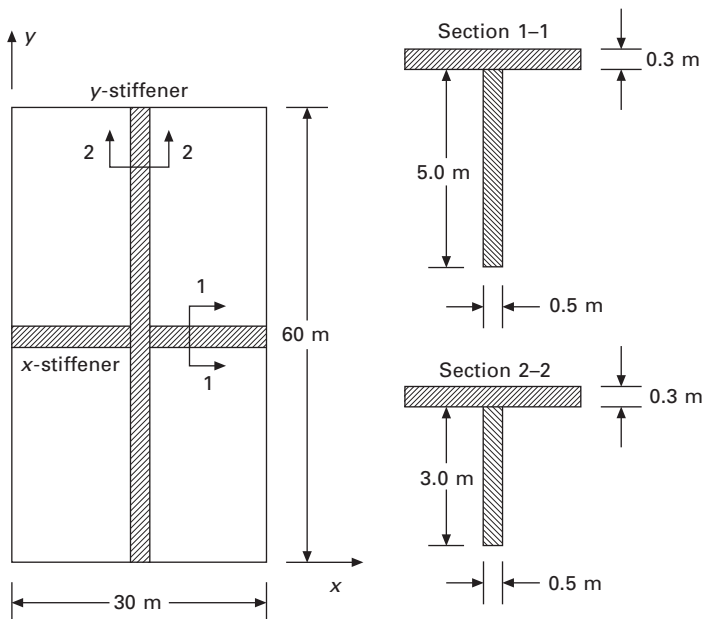
This example is the same as that in Section 4.6.1, except that the plate is clamped and has the following parameters: $L/W = 1$, $\gamma = 0.2$, $\delta = 20$, $h_s = 10.483h_p$, $h_s/W_s = 2.75$, and $L/h_p = 200$. Table 4.1 lists the buckling coefficients k that are obtained by the authors, Rikards *et al.* (2001), and Mukhopadhyay (1989).

Table 4.1 Buckling coefficient of the clamped stiffened plate with single stiffener

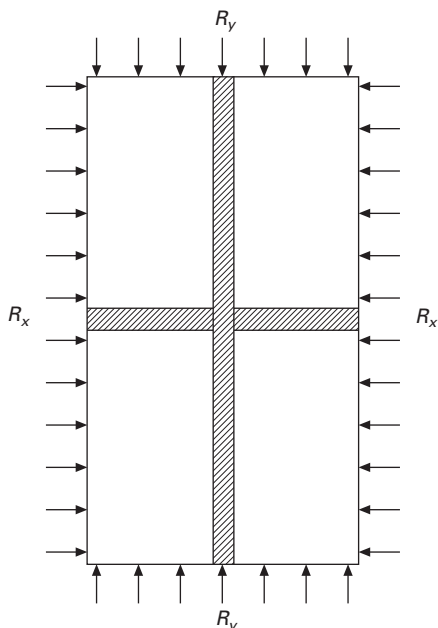
Buckling coefficient	Rikards <i>et al.</i> (2001)	Rikards <i>et al.</i> (2001) (ANSYS)	Mukhopadhyay (1989)	Present result
k	24.85	23.44	25.46	25.33

4.6.4 Simply supported rectangular stiffened isotropic plate with two stiffeners under in-plane compressions

A rectangular isotropic plate (Fig. 4.25) under two direction in-plane compressions R_x, R_y , is considered (Fig. 4.26). R_x is equal to R_y . The critical



4.25 Stiffened rectangular plate with two stiffeners.



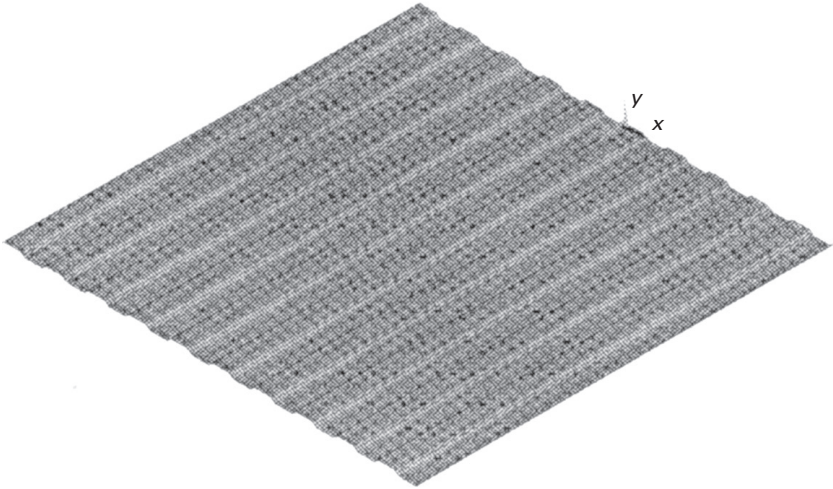
4.26 Rectangular stiffened plate under two direction in-plane compression.

stress that is obtained by the authors is 13.71 kPa. For comparison, the problem is also calculated using ANSYS. The result that is given by ANSYS is 13.43 kPa. When the plate thickness is increased to 1.5 m, the critical stress that is obtained by the authors is 193.11 kPa. The result that is given by ANSYS is 196.59 kPa. When the thickness of the plate is increased to 3.0 m, the critical stress that is obtained by the authors is 427.8 kPa. The result that is given by ANSYS is 456.7 kPa.

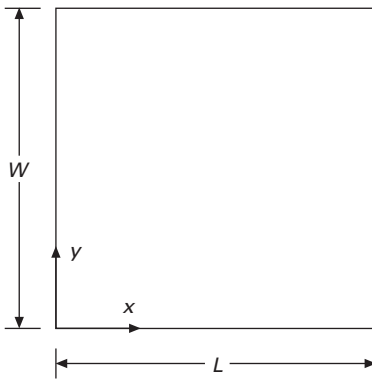
4.6.5 Trapezoidally corrugated plate under uniaxial in-plane compression

A trapezoidally corrugated plate (Figs 4.27 and 4.28) is studied under the action of uniaxial in-plane compression applied along the y -direction (The definition of positive y -direction is given in Figs 4.3 and 4.28). The dimensions of the plate are $L = 2$ m, $W = 2$ m, $F = 0.008$ m, $h = 0.02$ m, $c = 0.1$ m, and $\theta = 45^\circ$, and the plate has 10 corrugations (h is the thickness, and the definitions of F , c , θ are given in Fig. 4.4a). The elastic properties are $E = 30$ GPa and $\mu = 0.3$.

The buckling loads under different boundary conditions are presented in Table 4.2. In the table, ‘S’ means simply supported, ‘C’ means clamped



4.27 Trapezoidally corrugated plate.



4.28 Plan of the trapezoidally corrugated plate.

Table 4.2 Buckling loads of the trapezoidally corrugated plate under uniaxial in-plane compression

Boundaries	Present results (N)	ANSYS (N)
SSSS	296228	283447
SSCS	386110	369277
SSCC	533991	509149

edge. The boundary condition of the sides of the plate where the in-plane compression is applied is always simply supported. We also perform a three-dimensional study for this plate using the FEM software ANSYS. In ANSYS, the SHELL63 element is employed, and the discretization scheme is shown in Fig. 4.27 where 24612 nodes are used.

4.6.6 Stiffened trapezoidally corrugated plate under uniaxial in-plane compression

The trapezoidally corrugated plate in Section 4.6.5 is attached with a 2 m long stiffener along the centerline ($x = 1$). The stiffener is made from the same material as the plate. The cross-section of the stiffener is rectangular (width = 0.1 m, height = 0.2 m). The buckling loads obtained by the proposed method and those from ANSYS analysis under different boundary conditions are listed in Table 4.3.

Table 4.3 Buckling loads of the stiffened trapezoidally corrugated plate under uniaxial in-plane compression

Boundaries	Present results (N)	ANSYS (N)
SSSS	1 185 890	1 149 639
SSCS	1 277 690	1 238 150
SSCC	1 543 100	1 495 596

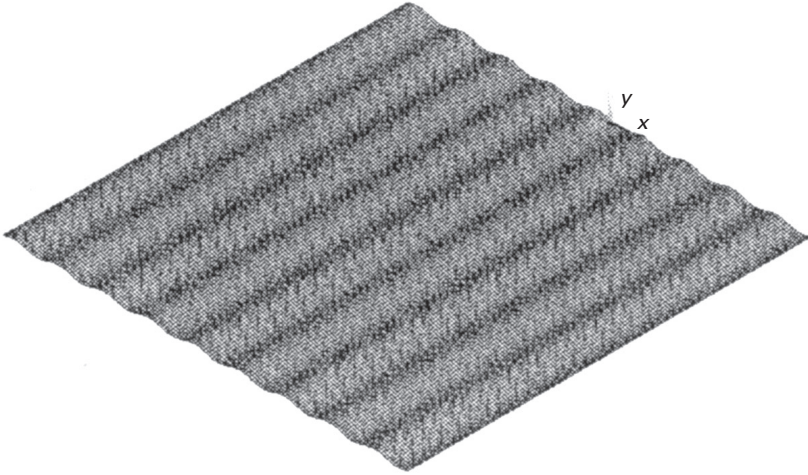
4.6.7 Sinusoidally corrugated plate under uniaxial in-plane compression

A sinusoidally corrugated plate (Fig. 4.29) under uniaxial in-plane compression applied along the y-direction is considered. The boundary condition of the sides of the plate where the in-plane compression is applied is always simply supported. The dimensions of the plate are $L = 1.8$ m, $W = 1.8$ m, $F = 0.01$ m, $h = 0.018$ m, $c = 0.1$ m, and the plate has nine corrugations. The elastic properties are $E = 30$ GPa and $\mu = 0.3$.

We analyze this problem using both the proposed method and ANSYS. The buckling loads of the plate obtained by both methods are listed in Table 4.4. As in Section 4.6.5, the SHELL63 element is used to carry out the analysis in ANSYS. The discretization scheme is shown in Fig. 4.29 where 6723 nodes are adopted.

Table 4.4 Buckling loads of the sinusoidally corrugated plate under uniaxial in-plane compression

Boundaries	Present results (N)	ANSYS (N)
SSSS	275578	266268
SSCS	358934	348116
SSCC	496084	482091



4.29 Sinusoidally corrugated plate.

4.6.8 Stiffened sinusoidally corrugated plate under uniaxial in-plane compression

The sinusoidally corrugated plate in Section 4.6.7 is fitted with a 1.8 m long stiffener along the centerline ($x = 0.9$). The stiffener is made from the same material as the plate, and the cross-section of the stiffener is rectangular (width = 0.05 m, height = 0.1 m).

The buckling loads of the stiffened corrugated plate calculated using the proposed method and a comparison with the results from the ANSYS analysis are shown in Table 4.5.

4.7 Concluding remarks

In this chapter, a mesh-free Galerkin method for the buckling analysis of stiffened plates and stiffened and unstiffened corrugated plates has been proposed. The corrugated plates were approximated as orthotropic plates, and the equivalent elastic properties of trapezoidally corrugated plates were

Table 4.5 Buckling loads of the stiffened sinusoidally corrugated plate under uniaxial in-plane compression

Boundaries	Present results (N)	ANSYS (N)
SSSS	1 102 020	1 085 304
SSCS	1 181 460	1 164 859
SSCC	1 431 120	1 417 154

derived. The stiffened corrugated plate was analyzed as a stiffened orthotropic plate, which is a composite structure of an orthotropic plate and stiffeners. The stiffened isotropic plate can be analyzed as a special case of stiffened orthotropic plates. The stiffness matrix of the structure was derived by the superimposition of the strain energy of the orthotropic plate and the stiffeners after the displacement field of the stiffeners was expressed in terms of the displacements of the plate. Because the proposed method is mesh-free, it avoids the difficulties that the mesh-based FEMs encounter. The proposed method has been verified by applying to several examples, and the results show good agreement with those obtained using the ANSYS software and those reported by other researchers.

4.8 Acknowledgements

The work that is described in this chapter has been supported by a grant awarded by the Research Grants Council of the Hong Kong Special Administrative Region, China (Project No. CityU 1140/03E).

4.9 References

- Allman, D.J. (1975), 'Calculation of the elastic buckling loads of thin flat plates using triangular finite element', *International Journal for Numerical Methods in Engineering*, **9**, 415–432.
- Barik, M. and Mukhopadhyay, M. (2002), 'A new stiffened plate element for the analysis of arbitrary plates', *Thin-Walled Structures*, **40**, 625–639.
- Belytschko, T., Lu, Y.Y. and Gu, L. (1994), 'Element-free Galerkin methods', *International Journal for Numerical Methods in Engineering*, **37**, 229–256.
- Briassoulis, D. (1986), 'Equivalent orthotropic properties of corrugated sheets', *Computers and Structures*, **23**, 129–138.
- Bryan, G.H. (1891), 'On the stability of a plane plate under thrust in its own plane, with applications to the 'buckling' of the sides of a ship', *Proceedings of the London Mathematical Society*, **22**, 54–67.
- Chen, J.S., Pan, C., Wu, C.T. and Liu, W.K. (1996), 'Reproducing kernel particle methods for large deformation analysis of nonlinear structures', *Computer Methods in Applied Mechanics and Engineering*, **139**, 195–227.
- Chen, X.L. and Liew, K.M. (2004), 'Buckling of rectangular functionally graded material

- plates subjected to nonlinearly distributed in-plane edge loads', *Smart Materials and Structures*, **13**, 1–8.
- Cheung, Y.K. and Delcourt, C. (1977), 'Buckling and vibration of thin flat-walled structures continuous over several spans', *Proceedings of the Institution of Civil Engineers*, Part II, 93–103.
- Chryssanthopoulos, M.K., Baker, M.J. and Dowling P.J. (1991), 'Imperfection modeling for buckling analysis of stiffened cylinders', *Journal of Structural Engineering – ASCE*, **117**, 1998–2017.
- Cox, H.L. (1954), 'Computation of initial buckling stress of sheet stiffener combinations', *Journal of the Royal Aeronautical Society*, **58**, 634–638.
- Davies, J.M. (1976), 'Calculation of steel diaphragm behavior', *Journal of the Structural Division*, **102**, 1411–1430.
- Easley, J.T. (1975), 'Buckling formulas for corrugated metal shear diaphragms', *Journal of the Structural Division – ASCE*, **101**, 1403–1417.
- Easley, J.T. and McFarland, D.E. (1969), 'Buckling of light-gage corrugated metal shear diaphragms', *Journal of the Structural Division, ASCE* **95**, 1497–1516.
- Guo, M. and Harik, I.E. (1992), 'Stability of eccentrically stiffened plates', *Thin-Walled Structures*, **14**, 1–20.
- Guo, M.W., Harik I.E. and Ren, W.X. (2002), 'Buckling behavior of stiffened laminated plates', *International Journal of Solids and Structures*, **39**, 3039–3055.
- Guyon, Y. (1946), 'Calcul des ponts larges à poutres multiples solidarisees par des entretoises', *Annales des Pont et Chaussées de France*, **10**, 553–612.
- Horne, M.R. and Narayanan, R. (1975), 'Approximate method for design of stiffened steel compression panels', *Proceedings of the Institution of Civil Engineers Part 2 – Research and Theory*, **59**, 501–514.
- Horne, M.R. and Narayanan, R. (1977), 'Design of axially loaded stiffened plates', *Journal of the Structural Division – ASCE*, **103**, 2243–2257.
- Horne, M.R. and Narayanan, R. (1978), 'Stiffened steel compression panels – theoretical failure analysis', *Structural Engineer Part A*, **56**, 191–197.
- Kendrick, S. (1956), 'The analysis of a flat plated grillage', *European Shipbuilding*, **5**, 4–10.
- Klitchieff, J.M. (1973), 'On the stability of plates reinforced by longitudinal ribs', *Journal of Applied Mechanics, Transactions of the ASME*, **73**, 364–366.
- Lau, J.H. (1981), 'Stiffness of corrugated plate', *Journal of the Engineering Mechanics Division – ASCE*, **107**, 271–275.
- Liew, K.M. and Huang, Y.Q. (2003), 'Bending and buckling of thick symmetric rectangular laminates using the moving least-squares differential quadrature method', *International Journal of Mechanical Sciences*, **45**, 95–114.
- Liew, K.M. and Chen, X.L. (2004a), 'Mesh-free radial basis function method for buckling analysis of non-uniformly loaded arbitrarily shaped shear deformable plates', *Computer Methods in Applied Mechanics and Engineering*, **193**, 205–224.
- Liew, K.M. and Chen, X.L. (2004b), 'Buckling of rectangular Mindlin plates subjected to partial in-plane edge loads using the radial point interpolation method', *International Journal of Solids and Structures*, **41**, 1677–1695.
- Liew, K.M. and Chen, X.L. (2004c), 'Mesh-free radial point interpolation method for the buckling analysis of Mindlin plates subjected to in-plane point loads', *International Journal for Numerical Methods in Engineering*, **60**, 1861–1877.
- Liew, K.M., Ng, T.Y. and Zhang, J.Z. (2002a), 'Differential quadrature-layerwise modeling technique for three-dimensional analysis of cross-ply laminated plates of various

- edge-supports', *Computer Methods in Applied Mechanics and Engineering*, **191**, 3811–3832.
- Liew, K.M., Lim, H.K., Tan, M.J. and He, X.Q. (2002b), 'Analysis of laminated composite beams and plates with piezoelectric patches using the element-free Galerkin method', *Computational Mechanics*, **29**, 486–497.
- Liew, K.M., Huang, Y.Q. and Reddy, J.N. (2002c), 'A hybrid moving least squares and differential quadrature (MLSDQ) meshfree method', *International Journal of Computational Engineering Science*, **3**, 1–12.
- Liew, K.M., Ng, T.Y. and Wu, Y.C. (2002d), 'Meshfree method for large deformation analysis – a reproducing kernel particle approach', *Engineering Structures*, **24**, 543–551.
- Liew, K.M., Ng, T.Y., Zhao, X. and Reddy, J.N. (2002e), 'Harmonic reproducing kernel particle method for free vibration analysis of rotating cylindrical shells', *Computer Methods in Applied Mechanics and Engineering*, **191**, 4141–4157.
- Liew, K.M., Wu, H.Y. and Ng, T.Y. (2002f), 'Meshless method for modeling of human proximal femur: treatment of nonconvex boundaries and stress analysis', *Computational Mechanics*, **28**, 390–400.
- Liew, K.M., Wu, Y.C., Zou, G.P. and Ng, T.Y. (2002g), 'Elasto-plasticity revisited: numerical analysis via reproducing kernel particle method and parametric quadratic programming', *International Journal for Numerical Methods in Engineering*, **55**, 669–683.
- Liew, K.M., Zhao, X. and Ng, T.Y. (2002h), 'The element-free kp-Ritz method for vibration of laminated rotating cylindrical panels', *International Journal of Structural Stability and Dynamics*, **2**, 523–558.
- Liew, K.M., Huang, Y.Q. and Reddy, J.N. (2003a), 'Moving least square differential quadrature method and its application to the analysis of shear deformable plates', *International Journal for Numerical Methods in Engineering*, **56**, 2331–2351.
- Liew, K.M., Huang, Y.Q. and Reddy, J.N. (2003b), 'Vibration analysis of symmetrically laminated plates based on FSDT using the moving least squares differential quadrature method', *Computer Methods in Applied Mechanics and Engineering*, **192**, 2203–2222.
- Liew, K.M., Zou, G.P. and Rajendran, S. (2003c), 'A spline strip kernel particle method and its application to two-dimensional elasticity problems', *International Journal for Numerical Methods in Engineering*, **57**, 599–616.
- Liew, K.M., Ren, J. and Kitipornchai, S. (2004a), 'Analysis of the pseudoelastic behavior of a SMA beam by the element-free Galerkin method', *Engineering Analysis with Boundary Elements*, **28**, 497–507.
- Liew, K.M., Huang, Y.Q. and Reddy, J.N. (2004b), 'Analysis of general shaped thin plates by the moving least square differential quadrature method', *Finite Elements in Analysis and Design*, **40**, 1453–1474.
- Liew, K.M., Wang, J., Ng, T.Y. and Tan, M.J. (2004c), 'Free vibration and buckling analyses of shear deformable plates based on FSDT meshfree method', *Journal of Sound and Vibration*, **276**, 997–1017.
- Liew, K.M., Wang, J., Tan, M.J. and Rajendran, S. (2004d), 'Nonlinear analysis of laminated composite plates using the mesh-free kp-Ritz method based on FSDT', *Computer Methods in Applied Mechanics and Engineering*, **193**, 4763–4779.
- Lucy, L.B. (1977), 'A numerical approach to the testing of the fission hypothesis', *Astronomical Journal*, **82**, 1013–1024.
- Luo, R. and Edlund, B. (1996), 'Shear capacity of plate girders with trapezoidally corrugated webs', *Thin-Walled Structures*, **26**, 19–44.

- Machimdamrong, C., Watanabe, E. and Utsunomiya, T. (2004), 'Shear buckling of corrugated plates with edges elastically restrained against rotation', *International Journal of Structural Stability and Dynamics*, **4**, 89–104.
- Martin, D.W. and Cox, H.L. (1963), 'The buckling modes of longitudinally stiffened flat panel', *Aeronautical Quarterly*, **14**, 346–398.
- Mukhopadhyay, M. (1989), 'Vibration and stability analysis of stiffened plates by semi-analytical finite difference method. Part I: consideration of bending displacements only', *Journal of Sound and Vibration*, **130**, 27–39.
- Mukhopadhyay, M. and Mukherjee, A. (1990), 'Finite element buckling analysis of stiffened plates', *Computers and Structures*, **34**, 795–803.
- Nilson, A.H. and Ammar, A.R. (1974), 'Finite element analysis of metal deck shear diaphragms', *Journal of the Structural Division – ASCE*, **100** (NST4), 711–726.
- Reddy, J.N. (1999), *Theory and Analysis of Elastic Plates*, Taylor & Francis, London.
- Ren, J. and Liew, K.M. (2002), 'Mesh-free method revisited: two new approaches for the treatment of essential boundary conditions', *International Journal of Computational Engineering Science*, **3**, 219–233.
- Ren, J., Liew, K.M. and Meguid, S.A. (2002), 'Modelling and simulation of the superelastic behaviour of shape memory alloys using the element-free Galerkin method', *International Journal of Mechanical Sciences*, **44**, 2393–2413.
- Rikards, R., Chate, A. and Ozolinsh, O. (2001), 'Analysis for buckling and vibrations of composite stiffened shells and plates', *Composite Structures*, **51**, 361–370.
- Samanta, A. and Mukhopadhyay, M. (1999), 'Finite element static and dynamic analyses of folded plates', *Engineering Structures*, **21**, 277–287.
- Schade, H.A. (1940), 'The orthogonally stiffened plate under uniform lateral load', *Journal of Applied Mechanics ASME*, **62**, 143–146.
- Semenyuk, N.P. and Neskhodovskaya, N.A. (2002), 'On design models in stability problems for corrugated cylindrical shells', *International Applied Mechanics*, **38**, 1245–1252.
- Seydel, E.B. (1931), *Schubknickversuche mit Wellblechtafeln*, Jahrbuch d. Deutsch. Versuchsanstalt für Luftfahrt, Munich, Berlin, 233–235.
- Shimansky, R.A. and Lele, M.M. (1995), 'Transverse stiffness of a sinusoidally corrugated plate', *Mechanics of Structures and Machines*, **23**, 439–451.
- Teo, T.M. and Liew, K.M. (2002), 'Differential cubature method for analysis of shear deformable rectangular plates on Pasternak foundations', *International Journal of Mechanical Sciences*, **44**, 1179–1194.
- Timoshenko, S.P. and Gere, J.M. (1961), *Theory of Elastic Stability*, McGraw-Hill, New York.
- Turvey G. (1971), *A contribution to the elastic stability of thin walled structures fabricated from isotropic and orthotropic materials*, PhD Dissertation, University of Birmingham.
- Wang, J., Liew, K.M., Tan, M.J. and Rajendran, S. (2002), 'Analysis of rectangular laminated composite plates via FSDT meshless method', *International Journal of Mechanical Sciences*, **44**, 1275–1293.
- Yoshida, H. and Maegawa, K. (1979), 'Buckling strength of orthogonally stiffened plates', *Journal of Structural Mechanics*, **7**, 161–191.
- Zhao, X., Liew, K.M. and Ng, T.Y. (2003), 'Vibration analysis of laminated composite cylindrical panels via a meshfree approach', *International Journal of Solids and Structures*, **40**, 161–180.
- Zhao, X., Ng, T.Y. and Liew, K.M. (2004), 'Free vibration of two-side simply-supported laminated cylindrical panels via the mesh-free kp-Ritz method', *International Journal of Mechanical Sciences*, **46**, 123–142.

5.1 Introduction

Elastic bifurcation buckling behaviour of thin plates has been extensively studied and well documented in standard texts such as Timoshenko and Gere (1961), Bulson (1970) and Bazant and Cedolin (1991). When the plate thickness to length ratio is greater than $1/20$, it is necessary to use thick plate theories, such as the Mindlin (1951) plate theory, in order to predict the buckling load accurately. Otherwise the buckling load will be overestimated because the effect of transverse shear deformation becomes significant in these thick plates. Elastic buckling of Mindlin plates has been investigated by many researchers (for example, Herrmann and Armenakas 1960, Brunelle 1971, Kanaka Raju and Venkateswara 1983, Chen and Doong 1984, Dumir 1985, Hong *et al.* 1993, Wang *et al.* 1993, 1994, 1996, Wang 1995).

Although elastic buckling loads are useful as upper bound solutions and as basic reference parameters for design formulae in codes, they do not reflect the true buckling load values owing to the presence of inelastic effect, except when the structures are very slender. To account for the inelastic effect, various plastic theories have been proposed. These theories may be categorized under (a) the incremental or flow theory of plasticity (see Handelman and Prager 1948, Pearson 1950), (b) the deformation theory of plasticity (see Kaufmann 1936, Illyushin 1947, Stowell 1948, Bijlaard 1949, El-Ghazaly and Sherbourne 1986), and (c) the slip theory (see Bartdorf 1949, Inoue and Kato 1993). The crucial difference between the first two commonly used plasticity theories is that the strain in the former theory depends on the manner in which the state of stress is built up, whereas in the latter theory the strain that corresponds to a certain state of stress is entirely independent of the manner in which this state of stress has been reached. The success of these theories is varied. For example, the deformation theory gives a better prediction of buckling loads for long, simply supported plates (e.g. Pride and Heimerl 1949, Dietrich *et al.* 1978) while the incremental theory gives better results for cylinders under compression and torsion.

Accordingly, some researchers (e.g. Shrivastava 1979, Ore and Durban 1989, Tugcu 1991, Durban and Zuckerman 1999) presented the plastic buckling loads of plates based on both plasticity theories. There are, however, other simplified theories such as the one proposed by Bleich (1952). Bleich assumed a two-moduli plate where the modulus in the direction of stress that is likely to exceed the proportional limit be taken as the tangent modulus E_T while in the direction where there is little stress, the elastic modulus E be taken. Furthermore, the factor for the twisting moment curvature relation is arbitrarily chosen as $\sqrt{E_T/E}$. Bleich's simplified theory seems to give results in close agreement with large-scale test results obtained by Kollbrunner (1946).

Most studies on plastic buckling analysis of plates, however, adopted the classical thin plate theory. Durban and Zuckerman (1999) carried out a detailed parametric study on the elasto-plastic buckling of rectangular plates under biaxial compression. Apart from confirming that DT furnishes lower buckling stresses than those computed using IT, they reported the existence of an optimal loading part for DT model. Betten and Shin (2000) investigated the influences of aspect ratios, load ratios and hardening factors on the buckling stresses of rectangular plates subjected to biaxial loads. Moen *et al.* (1998) investigated the effect of plastic anisotropy on the elasto-plastic buckling behaviour of anisotropic aluminium plate elements. Soh *et al.* (2000) studied the plastic buckling of a simply supported, rectangular, composite plate subjected to edge compression. The fibre composite plates considered include carbon epoxy, glass epoxy and boron aluminium. Their theoretical results obtained are deemed comparable to experimental test results. Chakrabarty (2002) demonstrated the influence of plastic anisotropy on the buckling stress for the plastic buckling of rectangular plates under unidirectional compression. The buckling stress is shown to be significantly lowered by the presence of plastic anisotropy when compared with the corresponding isotropic material. Wang *et al.* (2004) solved the plastic buckling problem of rectangular plates subjected to intermediate and end in-plane loads.

The subject of plastic buckling of thick plates is, however, relatively less studied by researchers. One of the early papers on plastic buckling of thick plates was written by Shrivastava (1979). He derived closed-form expressions for the buckling loads of (a) infinitely long, simply supported plates, (b) simply supported square, plates and (c) infinitely long plates that are simply supported on three sides and free on one unloaded edge. Wang *et al.* (2001) derived analytically the elastic/plastic stability criteria for (a) uniaxially and equibiaxially loaded rectangular plates with two opposite edges simply supported while the other two edges may take on any combination of free, simply supported or clamped boundary condition and (b) uniformly in-plane loaded circular plates with either simply supported edge or clamped edge. Wang (2004) treated the plastic buckling of uniformly in-plane loaded, simply supported, polygonal, thick plates and gave an analytical relationship between

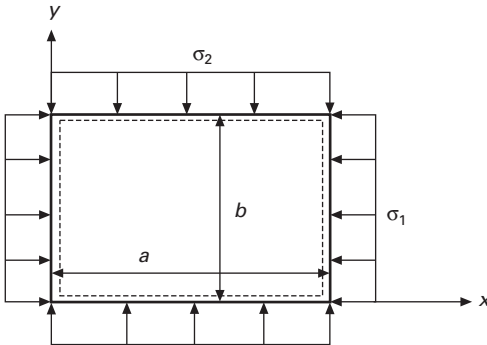
the plastic buckling load and its corresponding elastic thin plate buckling load.

In this chapter, the author’s studies on plastic buckling of thick plates are collated. Considering the two plasticity theories (i.e. the incremental theory of plasticity with the Prandtl–Reuss constitutive equations and the deformation theory of plasticity with the Hencky stress–strain relation), the governing equations for plastic buckling of thick (Mindlin) plates are presented. As shown herein, these equations can be solved analytically for the plastic buckling solutions of (a) uniaxially and equibiaxially loaded rectangular plates with two opposite edges simply supported while the other two edges may take on any combination of free, simply supported, or clamped boundary condition, (b) uniformly inplane loaded circular plates with either simply supported edge or clamped edge, (c) uniformly loaded annular plates with various edge conditions, and (d) uniformly loaded polygonal plates with simply supported edges.

5.2 Buckling of rectangular plates

5.2.1 Basic equations

Consider a flat, rectangular plate whose sides are of lengths a and b and of uniform thickness h as shown in Fig. 5.1. The plate is subjected to in-plane compressive stresses of magnitudes σ_1 and σ_2 in the x - and y -directions, respectively.



5.1 Rectangular plate under biaxial loads.

According to the Mindlin plate theory and the plasticity theories, the governing differential equations are given by (Chakrabarty 2000, Wang *et al.* 2001):

$$\kappa^2 Gh \left(\frac{\partial \phi_x}{\partial x} + \frac{\partial \phi_y}{\partial y} + \frac{\partial^2 w}{\partial x^2} + \frac{\partial^2 w}{\partial y^2} \right) = \sigma_1 h \frac{\partial^2 w}{\partial x^2} + \sigma_2 h \frac{\partial^2 w}{\partial y^2} \quad 5.1a$$

$$\frac{\partial}{\partial x} \left(\frac{\alpha E h^3}{12} \frac{\partial \phi_x}{\partial x} + \frac{\beta E h^3}{12} \frac{\partial \phi_y}{\partial y} \right) + \frac{\partial}{\partial y} \left[\frac{G h^3}{12} \left(\frac{\partial \phi_x}{\partial y} + \frac{\partial \phi_y}{\partial x} \right) \right] - \kappa^2 G h \left(\phi_x + \frac{\partial w}{\partial x} \right) = 0 \quad 5.1b$$

$$\frac{\partial}{\partial y} \left(\frac{\gamma E h^3}{12} \frac{\partial \phi_y}{\partial y} + \frac{\beta E h^3}{12} \frac{\partial \phi_x}{\partial x} \right) + \frac{\partial}{\partial x} \left[\frac{G h^3}{12} \left(\frac{\partial \phi_x}{\partial y} + \frac{\partial \phi_y}{\partial x} \right) \right] - \kappa^2 G h \left(\phi_y + \frac{\partial w}{\partial y} \right) = 0 \quad 5.1c$$

where ϕ_x , ϕ_y are the rotation rates about the y and x axes, respectively, w is the transverse velocity, E is Young's modulus, κ^2 is the shear correction factor, and the parameters α , β , γ are given by the following:

In the case of the incremental theory (IT):

$$\alpha = \frac{1}{\rho} \left[4 - 3 \left(1 - \frac{E_T}{E} \right) \frac{\sigma_1^2}{\bar{\sigma}^2} \right] \quad 5.2a$$

$$\beta = \frac{1}{\rho} \left[2 - 2(1 - 2\nu) \frac{E_T}{E} - 3 \left(1 - \frac{E_T}{E} \right) \frac{\sigma_1 \sigma_2}{\bar{\sigma}^2} \right] \quad 5.2b$$

$$\gamma = \frac{1}{\rho} \left[4 - 3 \left(1 - \frac{E_T}{E} \right) \frac{\sigma_2^2}{\bar{\sigma}^2} \right] \quad 5.2c$$

$$\rho = (5 - 4\nu) + (1 - 2\nu)^2 \frac{E_T}{E} - 3(1 - 2\nu) \left(1 - \frac{E_T}{E} \right) \frac{\sigma_1 \sigma_2}{\bar{\sigma}^2} \quad 5.2d$$

$$\frac{E}{G} = 2(1 + \nu) \quad 5.2e$$

In the case of the deformation theory (DT):

$$\alpha = \frac{1}{\rho} \left[4 - 3 \left(1 - \frac{E_T}{E_S} \right) \frac{\sigma_1^2}{\bar{\sigma}^2} \right] \quad 5.3a$$

$$\beta = \frac{1}{\rho} \left[2 - 2(1 - 2\nu) \frac{E_T}{E_S} - 3 \left(1 - \frac{E_T}{E_S} \right) \frac{\sigma_1 \sigma_2}{\bar{\sigma}^2} \right] \quad 5.3b$$

$$\gamma = \frac{1}{\rho} \left[4 - 3 \left(1 - \frac{E_T}{E_S} \right) \frac{\sigma_1^2}{\bar{\sigma}^2} \right] \quad 5.3c$$

$$\rho = 3 \frac{E}{E_S} + (1 - 2\nu) \left[2 - (1 - 2\nu) \frac{E_T}{E} - 3 \left(1 - \frac{E_T}{E_S} \right) \frac{\sigma_1 \sigma_2}{\bar{\sigma}^2} \right] \quad 5.3d$$

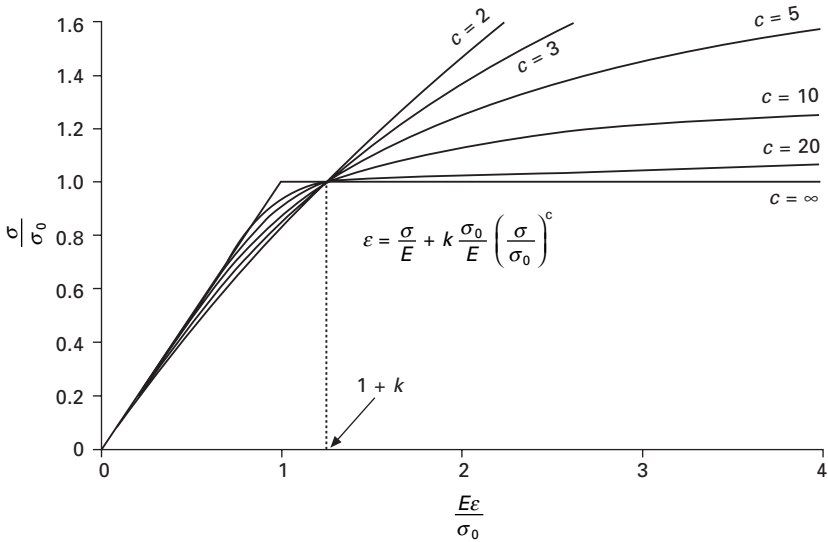
$$\frac{E}{G} = 2 + 2\nu + 3 \left(\frac{E}{E_S} - 1 \right) \quad 5.3e$$

where the ratios of the elastic modulus E to the tangent modulus E_T , and the secant modulus E_S at the onset of buckling are expressed by the Ramberg–Osgood elastoplastic characteristic in the forms of:

$$\frac{E}{E_T} = 1 + ck \left(\frac{\bar{\sigma}}{\sigma_0} \right)^{c-1} ; \quad c > 1 \quad 5.4$$

$$\frac{E}{E_S} = 1 + k \left(\frac{\bar{\sigma}}{\sigma_0} \right)^{c-1} ; \quad c > 1 \quad 5.5$$

where σ_0 is a nominal yield stress, c the hardening index that describes the shape of the stress–strain relationship with $c = \infty$ for an elastic–perfectly plastic response, and k the horizontal distance between the knee of $c = \infty$ curve and the intersection of the c curve with the $\sigma/\sigma_0 = 1$ line as shown in Fig. 5.2.



5.2 Ramberg–Osgood stress–strain relation.

The equivalent stress $\bar{\sigma}$, defined on the basis of von Mises yield criterion, is given by:

$$\bar{\sigma}^2 = \sigma_1^2 - \sigma_1\sigma_2 + \sigma_2^2 \quad 5.6$$

If the tangent modulus and the secant modulus at the point of bifurcation are made the same as the elastic modulus, i.e. $E_T = E_S = E$, then

$$\alpha = \gamma = \frac{1}{1 - \nu^2}, \quad \beta = \frac{\nu}{1 - \nu^2} \quad 5.7a,b$$

In view of Eqs. (5.7a,b), the governing equations reduce to those equations for the elastic buckling of Mindlin plates (Brunelle 1971, Wang 1995).

5.2.2 Buckling solutions for simply supported rectangular plates

For a rectangular plate with simply supported edges as shown in Fig. 5.1, the boundary conditions are:

$$w(0, y) = M_{xx}(0, y) = \phi_y(0, y) = 0 \quad 5.8a$$

$$w(x, 0) = M_{yy}(x, 0) = \phi_x(x, 0) = 0 \quad 5.8b$$

$$w(a, y) = M_{xx}(a, y) = \phi_y(a, y) = 0 \quad 5.8c$$

$$w(x, b) = M_{yy}(x, b) = \phi_x(x, b) = 0 \quad 5.8d$$

where the bending moment rates are:

$$M_{xx} = \frac{Eh^3}{12} \left(\alpha \frac{\partial \phi_x}{\partial x} + \beta \frac{\partial \phi_y}{\partial y} \right), \quad M_{yy} = \frac{Eh^3}{12} \left(\beta \frac{\partial \phi_x}{\partial x} + \gamma \frac{\partial \phi_y}{\partial y} \right) \quad 5.9a,b$$

The rates of displacement and rotations that satisfy the foregoing boundary conditions are given by:

$$w = C_{mn}^w \sin\left(\frac{m\pi x}{a}\right) \sin\left(\frac{n\pi y}{b}\right) \quad 5.10a$$

$$\phi_x = C_{mn}^{\phi_x} \cos\left(\frac{m\pi x}{a}\right) \sin\left(\frac{n\pi y}{b}\right) \quad 5.10b$$

$$\phi_y = C_{mn}^{\phi_y} \sin\left(\frac{m\pi x}{a}\right) \cos\left(\frac{n\pi y}{b}\right) \quad 5.10c$$

where C_{mn}^w , $C_{mn}^{\phi_x}$, $C_{mn}^{\phi_y}$ are constants and $m, n = 1, 2, 3, \dots$

The substitution of Eqs (5.10a–c) into Eqs (5.1a–c) results in the following three equations which may be expressed as:

$$\begin{bmatrix} K_{11} & K_{12} & K_{13} \\ & K_{22} & K_{23} \\ \text{sym} & & K_{33} \end{bmatrix} \begin{Bmatrix} C_{mn}^w \\ C_{mn}^{\phi_x} \\ C_{mn}^{\phi_y} \end{Bmatrix} = \begin{Bmatrix} 0 \\ 0 \\ 0 \end{Bmatrix} \quad 5.11$$

where

$$K_{11} = \kappa^2 Gh \left(\frac{m^2 \pi^2}{a^2} + \frac{n^2 \pi^2}{b^2} \right) - \sigma_1 h \left(\frac{m^2 \pi^2}{a^2} \right) - \alpha_2 h \left(\frac{n^2 \pi^2}{b^2} \right) \quad 5.12a$$

$$K_{12} = \kappa^2 Gh \left(\frac{m\pi}{a} \right), \quad K_{13} = \kappa^2 Gh \left(\frac{n\pi}{b} \right) \quad 5.12b,c$$

$$K_{22} = \frac{\alpha Eh^3}{12} \left(\frac{m^2 \pi^2}{a^2} \right) + \frac{Gh^3}{12} \left(\frac{n^2 \pi^2}{b^2} \right) + \kappa^2 Gh \quad 5.12d$$

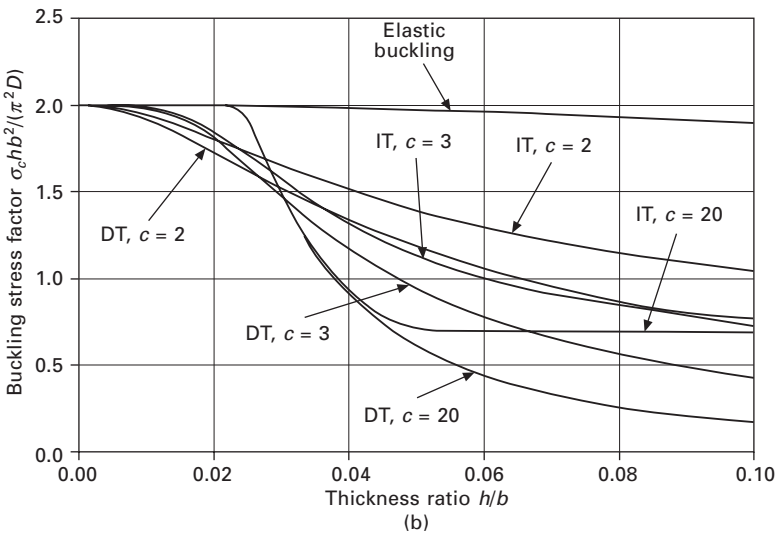
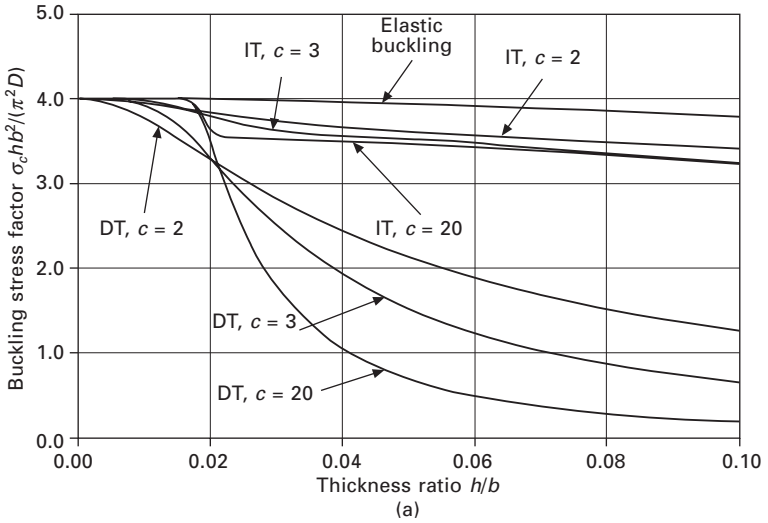
$$K_{23} = \left(\frac{\beta Eh^3}{12} + \frac{Gh^3}{12} \right) \left(\frac{mn\pi^2}{ab} \right) \quad 5.12e$$

$$K_{33} = \frac{\gamma Eh^3}{12} \left(\frac{n^2 \pi^2}{b^2} \right) + \frac{Gh^3}{12} \left(\frac{m^2 \pi^2}{a^2} \right) + \kappa^2 Gh \quad 5.12f$$

The critical plastic buckling stress can be determined by setting the determinant of the matrix [K] to zero and then solving the characteristic equation for the lowest positive root.

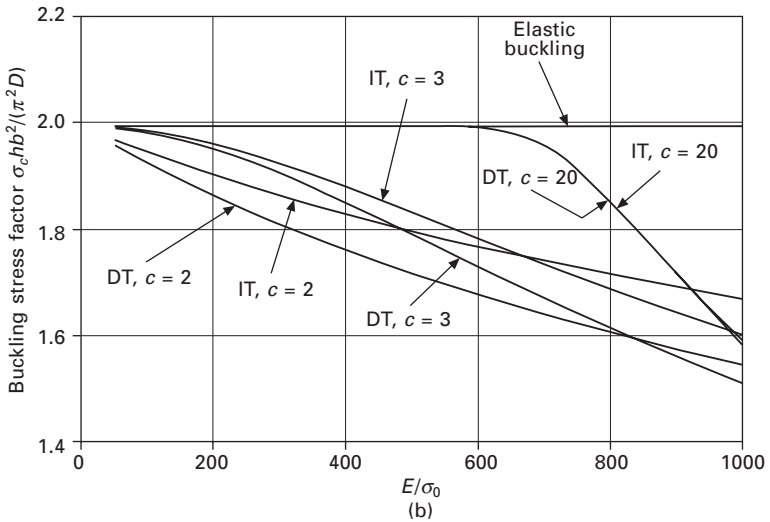
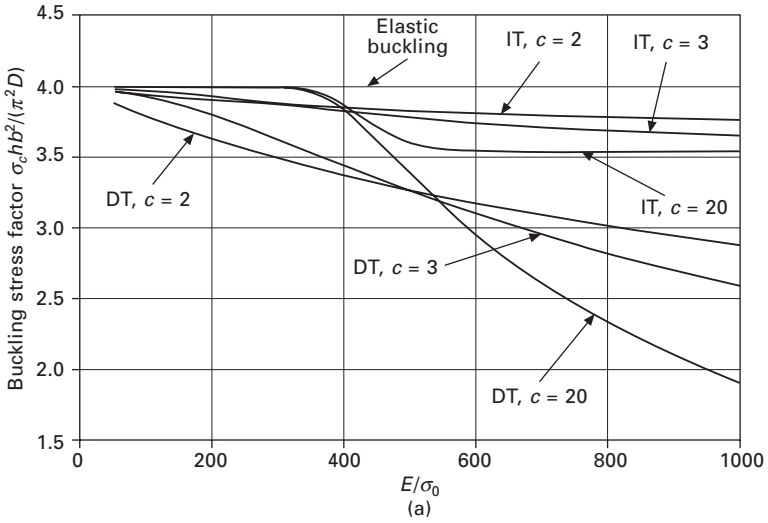
Figures 5.3 and 5.4 present critical buckling stress factors $\sigma_c hb^2/(\pi^2 D)$ for simply supported, square plates with different thickness to width ratios h/b , and various values of c and E/σ_0 . Note that $D = Eh^3/[12(1 - \nu^2)]$ is the flexural rigidity of the plate. The Poisson ratio $\nu = 0.3$, the shear correction factor $\kappa^2 = 5/6$ and the Ramberg–Osgood parameter $k = 0.25$ have been assumed for the calculations. The plate is subjected to either a uniaxial in-plane load or an equibiaxial in-plane load. It can be observed that the buckling stress factors obtained by the deformation theory are consistently lower than those obtained by the incremental theory. Generally, the differences of results of these two theories increase with (a) increasing plate thickness (i.e. h/b values) as evident from Figs 5.3(a) and 5.3(b), and (b) increasing E/σ_0 values as can be seen from Figs 5.4(a) and 5.4(b). The hardening index c and the loading configuration (i.e. uniaxial load or equibiaxial loads) also affect the divergence of results from the two theories. Both theories give somewhat similar results when the plate is thin, equibiaxially loaded and c value is large (say 20). Apart from the aforementioned situations, there is a marked difference in buckling stress factors from the two theories, which could be tapped when designing experimental tests on plates to establish which one of the theories gives better estimates of the buckling results for thick plates.

Figure 5.5(a) presents the variations of the buckling stress factors, from the two theories, with respect to the aspect ratio a/b of uniaxially loaded, simply supported rectangular plates (having $h/b = 0.025$) for various c values. It is worth noting that the kinks, where the number of half-waves switches, are displaced as a result of transverse shear deformation as well as the



5.3 Buckling stress factor $\sigma_c h b^2 / (\pi^2 D)$ versus thickness ratio h/b for simply supported, square plates subjected to (a) uniaxial load ($E/\sigma_0 = 750$, $\nu = 0.3$, $\kappa^2 = 5/6$, $k = 0.25$); (b) equibiaxial load ($E/\sigma_0 = 750$, $\nu = 0.3$, $\kappa^2 = 5/6$, $k = 0.25$).

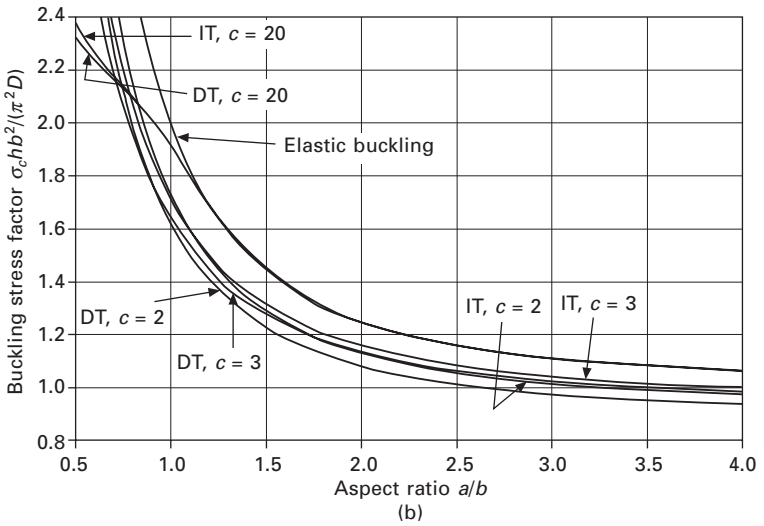
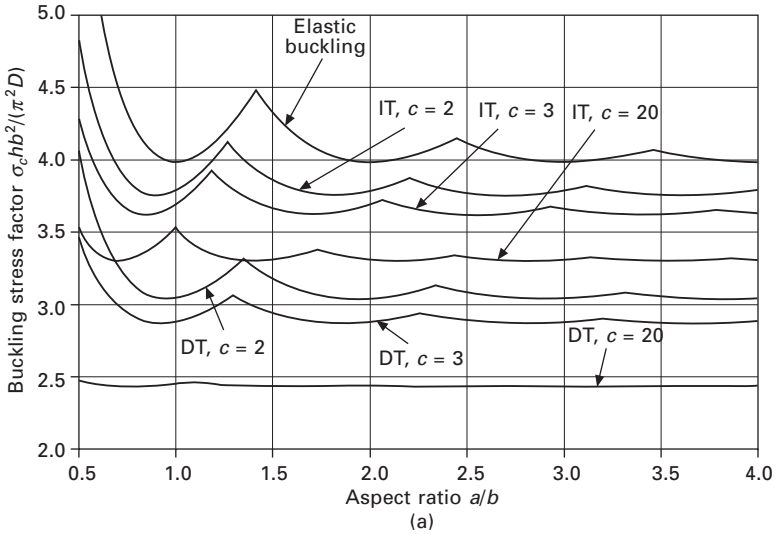
inelastic characteristics. Figure 5.5(b) shows the buckling stress factor variations for equibiaxially loaded rectangular plates. In contrast to the uniaxial loaded plate case, there are no kinks in the variations of the buckling stress factors with respect to the aspect ratio, indicating that there is no mode switching.



5.4 Buckling stress factor $\sigma_c hb^2 / (\pi^2 D)$ versus E/σ_0 for simply supported, square plates subjected to (a) uniaxial load ($h/b = 0.025$, $\nu = 0.3$, $\kappa^2 = 5/6$, $k = 0.25$); (b) equibiaxial load ($h/b = 0.025$, $\nu = 0.3$, $\kappa^2 = 5/6$, $k = 0.25$).

5.2.3 Buckling solutions for rectangular plates with two opposite sides simply supported

Next, we consider rectangular plates with two opposite edges simply supported (edges $y = 0$ and $y = b$), while the other edges (edge $x = 0$ and edge $x = a$) may take on any combination of free, simply supported and clamped edges.



5.5 Buckling stress factor $\sigma_c hb^2 / (\pi^2 D)$ versus aspect ratio a/b for simply supported, rectangular plates subjected to uniaxial load ($E/\sigma_0 = 750$, $h/b = 0.025$, $\nu = 0.3$, $\kappa^2 = 5/6$, $k = 0.25$); (b) equibiaxial load ($E/\sigma_0 = 750$, $h/b = 0.025$, $\nu = 0.3$, $\kappa^2 = 5/6$, $k = 0.25$).

The boundary conditions for the two simply supported parallel edges ($y = 0$ and $y = b$) are:

$$w(x, 0) = M_{yy}(x, 0) = \phi_x(x, 0) = 0 \tag{5.13a}$$

$$w(x, b) = M_{yy}(x, b) = \phi_x(x, b) = 0 \tag{5.13b}$$

and the boundary conditions for the other two edges ($x = 0$ and $x = a$) are given by (Xiang *et al.* 1996):

$$M_{xx} = M_{yx} = 0, \quad Q_x - \sigma_1 h \frac{\partial w}{\partial x} = 0 \quad \text{if the edge is free} \quad 5.14a$$

$$w = M_{xx} = \phi_y = 0 \quad \text{if the edge is simply supported} \quad 5.15$$

$$w = \phi_x = \phi_y = 0 \quad \text{if the edge is clamped} \quad 5.16$$

in which

$$Q_x = \kappa^2 Gh \left(\phi_x + \frac{\partial w}{\partial x} \right), \quad M_{xx} = \frac{Eh^3}{12} \left(\alpha \frac{\partial \phi_x}{\partial x} + \beta \frac{\partial \phi_y}{\partial y} \right) \quad 5.17a,b$$

$$M_{yy} = \frac{Eh^3}{12} \left(\beta \frac{\partial \phi_x}{\partial x} + \gamma \frac{\partial \phi_y}{\partial y} \right), \quad M_{xy} = \frac{Gh^3}{12} \left(\frac{\partial \phi_x}{\partial y} + \frac{\partial \phi_y}{\partial x} \right) \quad 5.17c,d$$

For such rectangular plates with two opposite sides simply supported, the Levy-type solution procedure may be used to solve the governing differential equations (5.1a–c). The velocity fields of the plate may be expressed as (Xiang *et al.* 1996):

$$\begin{cases} w(x, y) \\ \phi_x(x, y) \\ \phi_y(x, y) \end{cases} = \begin{cases} f_w(x) \sin \frac{m\pi y}{b} \\ f_x(x) \sin \frac{m\pi y}{b} \\ f_y(x) \cos \frac{m\pi y}{b} \end{cases} \quad 5.18$$

in which $f_w(x)$, $f_x(x)$ and $f_y(x)$ are unknown functions to be determined, and $m = 1, 2, \dots, \infty$ is the number of half-waves of the buckling mode shape in the y direction. Equation (5.18) satisfies the simply supported boundary conditions on edges $y = 0$ and $y = b$.

By substituting Eq. (5.18) into Eqs (5.1a–c), the following differential equation system can be derived:

$$\{\Psi'\} = [H]\{\Psi\} \quad 5.19$$

where $\Psi = [f_w f_w' f_x f_x' f_y f_y']^T$ and Ψ' is the first derivative of Ψ with respect to x , the prime (') represents the derivative with respect to x , and $[H]$ is a (6×6) matrix with the following non-zero elements:

$$H_{12} = H_{34} = H_{56} = 1 \quad 5.20a$$

$$H_{21} = \frac{(\kappa^2 Gh - \sigma_2 h)(m\pi/b)^2}{\kappa^2 Gh - \sigma_1 h} \quad 5.20b$$

$$H_{24} = \frac{-\kappa^2 Gh}{\kappa^2 Gh - \sigma_1 h} \quad 5.20c$$

$$H_{25} = \frac{\kappa^2 Gh(m\pi/b)}{\kappa^2 Gh - \sigma_1 h} \quad 5.20d$$

$$H_{42} = \frac{\kappa^2 Gh}{(\alpha Eh^3/12)} \quad 5.20e$$

$$H_{43} = \frac{\kappa^2 Gh + (Gh^3/12)(m\pi/b)^2}{(\alpha Eh^3/12)} \quad 5.20f$$

$$H_{46} = \frac{[(\beta Eh^3/12) + (Gh^3/12)](m\pi/b)}{(\alpha Eh^3/12)} \quad 5.20g$$

$$H_{61} = \frac{\kappa^2 Gh(m\pi/b)}{(Gh^3/12)} \quad 5.20h$$

$$H_{64} = \frac{-[(\beta Eh^3/12) + (Gh^3/12)](m\pi/b)}{(Gh^3/12)} \quad 5.20i$$

$$H_{65} = \frac{[\kappa^2 Gh + (\gamma Eh^3/12)(m\pi/b)^2]}{(Gh^3/12)} \quad 5.20j$$

The solution for the system of differential equation (5.19) may be expressed as

$$\Psi = e^{Hx} \mathbf{c} \quad 5.21$$

where \mathbf{c} is constant column vector that can be determined from the boundary conditions of the plate and e^{Hx} is the general matrix solution.

By applying the boundary conditions for the edges parallel to the y axis, a homogeneous system of equations is obtained:

$$[\mathbf{K}]\{\mathbf{c}\} = \{\mathbf{0}\} \quad 5.22$$

The buckling stresses σ_1 and σ_2 are determined by setting the determinant of $[\mathbf{K}]$ to zero. As the buckling stresses are embedded in matrix $[\mathbf{H}]$, it cannot be obtained directly from Eq. (5.22). A numerical iteration procedure was used for the calculations (see Xiang *et al.* 1996 for details).

Tables 5.1 to 5.3 present the buckling stress factors of square plates under uniaxial and equibiaxial loads. In the calculations, $\kappa^2 = 5/6$ and $\nu = 0.3$ were assumed. For brevity's sake, we shall use the letters F for free edge, S for simply supported edge and C for clamped edge and a four-letter designation to represent the boundary conditions of the plate. So, for example, a $CSFS$ plate will have a clamped edge along $x = 0$, a simply supported edge along

Table 5.1 Buckling stress factors $\sigma_c h b^2 / (\pi^2 D)$ for FSFS square plates under (a) uniaxial load in x direction; (b) equibiaxial load

c	E/σ_0	$h/b = 0.025$		$h/b = 0.050$		$h/b = 0.075$	
		IT	DT	IT	DT	IT	DT
(a)							
<i>Elastic</i>	–	1.999	1.999	1.946	1.946	1.888	1.888
2	200	1.967	1.872	1.835	1.582	1.683	1.315
	300	1.952	1.819	1.794	1.473	1.624	1.188
	500	1.925	1.729	1.729	1.316	1.542	1.024
5	200	1.998	1.996	1.805	1.694	1.381	1.115
	300	1.994	1.988	1.624	1.424	1.240	0.8580
	500	1.965	1.926	1.392	1.060	1.133	0.5995
20	200	1.999	1.999	1.881	1.869	1.136	0.9993
	300	1.999	1.999	1.467	1.418	1.104	0.8187
	500	1.999	1.999	1.198	0.9164	1.104	0.4725
(b)							
<i>Elastic</i>	–	0.9280	0.9280	0.9207	0.9207	0.9106	0.9106
2	200	0.9147	0.8992	0.8735	0.8241	0.8195	0.7372
	300	0.9083	0.8860	0.8531	0.7882	0.7852	0.6856
	500	0.8961	0.8618	0.8173	0.7308	0.7306	0.6119
5	200	0.9279	0.9279	0.9118	0.9074	0.7964	0.7659
	300	0.9278	0.9277	0.8821	0.8670	0.6709	0.6314
	500	0.9265	0.9257	0.7701	0.7367	0.5072	0.4618
20	200	0.9280	0.9280	0.9207	0.9207	0.8461	0.8428
	300	0.9280	0.9280	0.9206	0.9207	0.6217	0.6174
	500	0.9280	0.9280	0.7914	0.7877	0.4000	0.3930

$y = 0$, a free edge along $x = a$ and a simply supported edge along $y = b$. It can be observed that for very thick plates ($h/b = 0.075$) and high values of c , the buckling load factors of the incremental theory do not vary much with respect to the E/σ_0 ratios. In contrast, the corresponding buckling results from the deformation theory decrease significantly with increasing E/σ_0 values for very thick plates. The buckling factors are much lower when compared with their thin plate counterparts due to the effect of transverse shear deformation.

5.3 Axisymmetric buckling of circular plates

5.3.1 Basic equations

Consider a circular plate with radius a and uniform thickness h . The plate is subjected to a uniform in-plane compressive stress of magnitude σ . For axisymmetric buckling, the governing equations are given by:

$$\kappa^2 Gh \left(\phi + \frac{dw}{dr} \right) = \sigma h \frac{dw}{dr} \Rightarrow \frac{dw}{dr} = - \frac{\phi}{1 - \frac{\sigma}{\kappa^2 G}} \tag{5.23}$$

Table 5.2 Buckling stress factors $\sigma_c h b^2 / (\pi^2 D)$ for SSFS square plates under (a) uniaxial load in x direction; (b) equibiaxial load

c	E/σ_0	$h/b = 0.025$		$h/b = 0.050$		$h/b = 0.075$	
		IT	DT	IT	DT	IT	DT
(a)							
Elastic	–	2.312	2.312	2.245	2.245	2.169	2.169
2	200	2.232	2.132	2.013	1.758	1.797	1.436
	300	2.199	2.061	1.943	1.624	1.714	1.288
	500	2.143	1.942	1.844	1.437	1.606	1.101
5	200	2.307	2.305	1.926	1.809	1.402	1.143
	300	2.292	2.282	1.678	1.482	1.240	0.8736
	500	2.199	2.149	1.408	1.085	1.151	0.6074
20	200	2.311	2.311	1.973	1.959	1.150	1.002
	300	2.311	2.311	1.479	1.430	1.129	0.6965
	500	2.310	2.310	1.215	0.9185	1.129	0.4350
(b)							
Elastic	–	1.046	1.046	1.032	1.032	1.015	1.015
2	200	1.034	1.010	0.9911	0.9162	0.9364	0.8112
	300	1.028	0.9942	0.9726	0.8738	0.9045	0.7521
	500	1.017	0.9649	0.9393	0.8070	0.8523	0.6686
5	200	1.046	1.046	1.022	1.013	0.8859	0.8305
	300	1.045	1.045	0.9865	0.9569	0.7484	0.6772
	500	1.044	1.042	0.8577	0.7976	0.5791	0.4915
20	200	1.046	1.046	1.032	1.032	0.8919	0.8847
	300	1.046	1.046	1.031	1.032	0.6465	0.6362
	500	1.046	1.046	0.8266	0.8190	0.4306	0.4041

and

$$\frac{\alpha E h^3}{12} r \frac{d^2 \phi}{dr^2} + \frac{\alpha E h^3}{12} \frac{d \phi}{dr} - \frac{\alpha E h^3}{12} \frac{\phi}{r} - r \kappa^2 G h \left(\phi + \frac{dw}{dr} \right) = 0 \quad 5.24$$

5.3.2 Buckling solutions

The elimination of the derivative of w in Eq. (5.24) by using Eq. (5.23) yields:

$$r^2 \frac{d^2 \phi}{dr^2} + r \frac{d \phi}{dr} + (\lambda^2 r^2 - 1) \phi = 0 \quad 5.25$$

where

$$\lambda^2 = \frac{\sigma h}{\frac{\alpha E h^3}{12} \left(1 - \frac{\sigma h}{\kappa^2 G h} \right)} \quad 5.26$$

Table 5.3 Buckling stress factors $\sigma_c hb^2/(\pi^2 D)$ for CSFS square plates under (a) uniaxial load in x direction; (b) equibiaxial load

c	E/σ_0	$h/b = 0.025$		$h/b = 0.050$		$h/b = 0.075$	
		IT	DT	IT	DT	IT	DT
(a)							
<i>Elastic</i>	–	2.336	2.336	2.268	2.268	2.189	2.189
2	200	2.251	2.150	2.022	1.767	1.801	1.441
	300	2.217	2.077	1.950	1.631	1.716	1.292
	500	2.157	1.955	1.848	1.442	1.607	1.103
5	200	2.332	2.329	1.931	1.815	1.402	1.144
	300	2.315	2.304	1.679	1.483	1.241	0.8737
	500	2.215	2.163	1.408	1.085	1.153	0.6074
20	200	2.336	2.336	1.976	1.962	1.151	1.002
	300	2.336	2.336	1.479	1.431	1.131	0.6965
	500	2.335	2.335	1.216	0.9185	1.131	0.4351
(b)							
<i>Elastic</i>	–	1.130	1.130	1.112	1.112	1.090	1.090
2	200	1.119	1.089	1.075	0.9807	1.020	0.8622
	300	1.114	1.071	1.059	0.9335	0.9913	0.7976
	500	1.104	1.038	1.028	0.8597	0.9431	0.7070
5	200	1.130	1.130	1.100	1.086	0.9530	0.8729
	300	1.130	1.129	1.062	1.018	0.8101	0.7073
	500	1.128	1.125	0.9253	0.8380	0.6381	0.5110
20	200	1.130	1.130	1.112	1.112	0.9207	0.9090
	300	1.130	1.130	1.109	1.112	0.6674	0.6489
	500	1.130	1.130	0.8514	0.8386	0.4771	0.4109

Equation (5.25) is a Bessel’s differential equation with the general solution:

$$\phi = AJ_1(\lambda r) + BY_1(\lambda r) \tag{5.27}$$

where A and B are constants, $J_1(\bullet)$ and $Y_1(\bullet)$ are first order Bessel functions of the first kind and second kind, respectively. Since from the axisymmetric condition $\phi = 0$ at the plate centre (i.e. at $r = 0$), the constant B must vanish in Eq. (5.27). Thus, Eq. (5.27) reduces to

$$\phi = AJ_1(\lambda r) \tag{5.28}$$

Clamped circular plate

For a clamped circular plate, the rotation at the edge must vanish at the edge, i.e. $\phi = 0$ at $r = a$. Thus in view of this boundary condition and Eq. (5.28), the bifurcation criterion is given by:

$$J_1(\lambda a) = 0 \tag{5.29}$$

Since λ involves σ/E for any given stress–strain curve, the solution must be found by an iterative method, such as the false position method.

Simply supported circular plate

For a simply supported circular plate, the bending moment in the radial direction must vanish at the edge, i.e. $d\phi/dr + (\beta\phi)/(\alpha r) = 0$ at $r = a$. Thus, in view of Eq. (5.28) and noting the fact that $J_1'(\lambda r) = J_0(\lambda r) - J_1(\lambda r)/(\lambda r)$, one obtains the bifurcation criterion as:

$$\frac{\lambda a J_0(\lambda a)}{J_1(\lambda a)} = 1 - \frac{\beta}{\alpha} \tag{5.30}$$

Since the left-hand side of this equation depends on the value of σ/E , the critical stress has to be computed iteratively.

Tables 5.4 and 5.5 present the buckling stress factors for simply supported and clamped circular plates, respectively, for various c values and thickness to radius ratios h/a . In the calculations, $\kappa^2 = 5/6$ and $\nu = 0.3$ were assumed. The elastic buckling stress factors, obtained by setting $E_T = E_S = E$, are also given for comparison purposes and these elastic results check out with those obtained by Kanaka Raju and Venkateswara Rao (1983) and Hong *et al.* (1993).

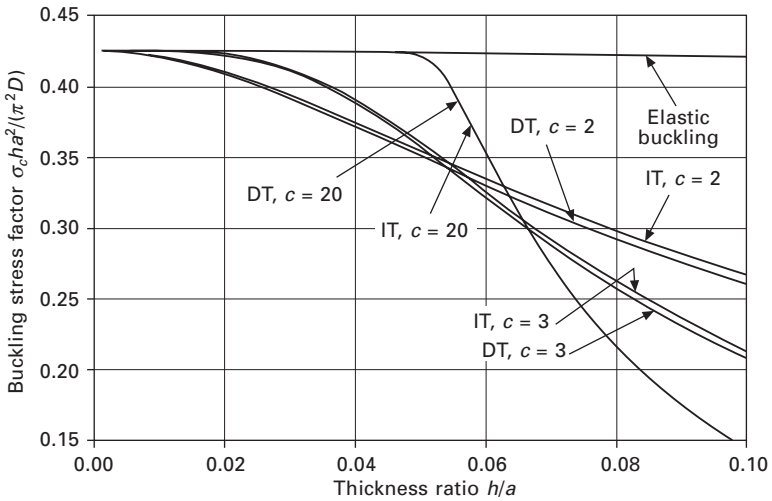
Table 5.4 Buckling stress factors $\sigma_c h a^2 / (\pi^2 D)$ for simply supported circular plates

c	E/σ_0	$h/a = 0.025$		$h/a = 0.050$		$h/a = 0.075$	
		IT	DT	IT	DT	IT	DT
<i>Elastic</i>	–	0.4250	0.4250	0.4241	0.4241	0.4225	0.4225
2	200	0.4185	0.4181	0.4002	0.3988	0.3756	0.3728
	300	0.4153	0.4147	0.3902	0.3881	0.3586	0.3549
	500	0.4094	0.4084	0.3726	0.3697	0.3317	0.3270
5	200	0.4250	0.4250	0.4236	0.4236	0.4121	0.4118
	300	0.4250	0.4250	0.4217	0.4217	0.3850	0.3843
	500	0.4249	0.4249	0.4087	0.4084	0.3160	0.3146
20	200	0.4250	0.4250	0.4241	0.4241	0.4225	0.4225
	300	0.4250	0.4250	0.4241	0.4241	0.4222	0.4221
	500	0.4250	0.4250	0.4241	0.4241	0.3425	0.3424

Figure 5.6 shows the difference between the buckling results of the two theories for $E/\sigma_0 = 750$ for simply supported circular plates. It can be seen that for simply supported plates, the buckling stress factors decrease with increasing plate thickness h/a , but may increase or decrease depending on the values of E/σ_0 and c . Both theories of plasticity give more or less similar buckling stress factors with the incremental theory furnishing slightly higher results. Figure 5.7 shows the difference between the buckling results of the two theories for $E/\sigma_0 = 750$ for clamped circular plates. For clamped plates, the buckling stress factors decrease with increasing plate thickness h/a , but

Table 5.5 Buckling stress factors $\sigma_c ha^2/(\pi^2 D)$ for clamped circular plates

c	E/σ_0	$h/a = 0.025$		$h/a = 0.050$		$h/a = 0.075$	
		IT	DT	IT	DT	IT	DT
Elastic	–	1.484	1.484	1.472	1.472	1.453	1.453
	200	1.431	1.409	1.307	1.241	1.176	1.069
	300	1.408	1.377	1.252	1.166	1.105	0.9742
	500	1.367	1.320	1.168	1.055	1.009	0.8483
5	200	1.483	1.483	1.364	1.348	0.9997	0.9467
	300	1.480	1.480	1.203	1.171	0.8168	0.7388
	500	1.460	1.456	0.9534	0.8941	0.6443	0.5223
20	200	1.484	1.484	1.471	1.471	0.9316	0.9243
	300	1.484	1.484	1.283	1.279	0.6689	0.6500
	500	1.484	1.484	0.8550	0.8456	0.5178	0.4112

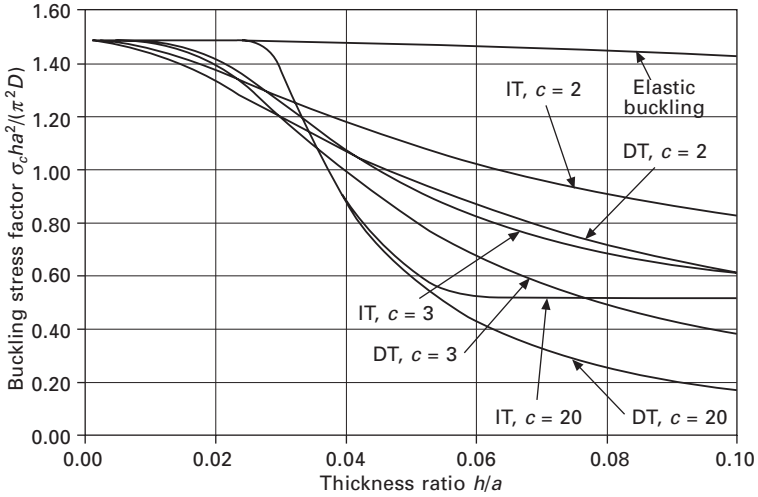


5.6 Buckling stress factor $\sigma_c ha^2/(\pi^2 D)$ versus thickness ratio h/a for simply supported circular plates subjected to uniform in-plane stress ($E/\sigma_0 = 750$, $\nu = 0.3$, $\kappa^2 = 5/6$, $k = 0.25$).

may increase or decrease depending on the values of E/σ_0 and c . In contrast to the simply supported plate case, we see that buckling stress factors of clamped plates differ significantly using the incremental theory and the deformation theory.

5.4 Buckling of annular plates

Consider an annular plate with outer radius a , inner radius b and uniform thickness h . The plate is subjected to a uniform in-plane compressive stress



5.7 Buckling stress factor $\sigma_c h a^2 / (\pi^2 D)$ versus thickness ratio h/a for clamped circular plates subjected to uniform in-plane stress ($E/\sigma_0 = 750$, $\nu = 0.3$, $\kappa^2 = 5/6$, $k = 0.25$).

of magnitude σ . The governing equations are given by

$$\begin{aligned} & \frac{\alpha E h^3}{12} \left\{ \frac{\phi_r}{r^2} + \frac{1}{r^2} \left(\frac{\partial \phi_\theta}{\partial \theta} \right) - \frac{1}{r} \left(\frac{\partial \phi_r}{\partial r} \right) - \frac{\partial^2 \phi_r}{\partial r^2} \right\} \\ & - \frac{\beta E h^3}{12} \left\{ \frac{1}{r} \left(\frac{\partial^2 \phi_\theta}{\partial r \partial \theta} \right) \right\} + \kappa^2 G h \left\{ \phi_r + \frac{\partial w}{\partial r} \right\} \\ & - \frac{G h^3}{12} \left\{ \frac{1}{r^2} \left(\frac{\partial^2 \phi_r}{\partial \theta^2} \right) + \frac{1}{r} \left(\frac{\partial^2 \phi_\theta}{\partial r \partial \theta} \right) - \frac{1}{r^2} \left(\frac{\partial \phi_\theta}{\partial \theta} \right) \right\} = 0 \end{aligned} \quad 5.31a$$

$$\begin{aligned} & \frac{\alpha E h^3}{12} \left\{ \frac{1}{r^2} \left(\frac{\partial^2 \phi_\theta}{\partial \theta^2} \right) + \frac{1}{r^2} \left(\frac{\partial \phi_r}{\partial \theta} \right) \right\} + \frac{\beta E h^3}{12} \left\{ \frac{1}{r} \left(\frac{\partial^2 \phi_r}{\partial r \partial \theta} \right) \right\} \\ & - \kappa^2 G h \left\{ \phi_\theta + \frac{1}{r} \frac{\partial w}{\partial \theta} \right\} + \frac{G h^3}{12} \\ & \times \left\{ \frac{1}{r} \left(\frac{\partial^2 \phi_r}{\partial r \partial \theta} \right) + \frac{1}{r^2} \left(\frac{\partial \phi_r}{\partial \theta} \right) + \frac{\partial^2 \phi_\theta}{\partial r^2} + \frac{1}{r} \left(\frac{\partial \phi_\theta}{\partial r} \right) - \frac{\phi_\theta}{r^2} \right\} = 0 \end{aligned} \quad 5.31b$$

$$(\kappa^2 G h - \sigma h) \nabla^2 w + \kappa^2 G h \left[\frac{\partial \phi_r}{\partial r} + \frac{\phi_r}{r} + \frac{1}{r} \left(\frac{\partial \phi_\theta}{\partial \theta} \right) \right] = 0 \quad 5.31c$$

where $\nabla^2(\bullet) = \partial^2(\bullet)/\partial r^2 + (1/r)\partial(\bullet)/\partial r + (1/r^2)\partial^2(\bullet)/\partial \theta^2$.

Following the work of Mindlin and Deresiewicz (1954), the transverse deflection w and the rotations (ϕ_r, ϕ_θ) may be expressed in terms of three potential functions $\Theta_1, \Theta_2, \Theta_3$ as follows:

$$w = \Theta_1 + \Theta_2 \quad 5.32a$$

$$\phi_r = -\frac{\partial\Theta_1}{\partial r} + \left(\frac{\sigma}{\kappa^2 G} - 1\right)\frac{\partial\Theta_2}{\partial r} + \frac{1}{r}\frac{\partial\Theta_3}{\partial\theta} \quad 5.32b$$

$$\phi_\theta = -\frac{1}{r}\frac{\partial\Theta_1}{\partial\theta} + \left(\frac{\sigma}{\kappa^2 G} - 1\right)\frac{1}{r}\frac{\partial\Theta_2}{\partial\theta} - \frac{\partial\Theta_3}{\partial r} \quad 5.32c$$

In view of Eqs (5.32a–c), Eqs (5.31a–c) may be compactly written as:

$$\nabla^2\Theta_1 = 0, (\nabla^2 + \lambda^2)\Theta_2 = 0, (\nabla^2 + \delta^2)\Theta_3 = 0 \quad 5.33a-c$$

where

$$\lambda^2 = \frac{\sigma h}{\frac{\alpha E h^3}{12} \left(1 - \frac{\sigma h}{\kappa^2 G h}\right)}, \quad \delta^2 = -\frac{12\kappa^2}{h^2} \quad 5.34a,b$$

The general solutions to Eqs (5.33a–c) are given by

$$\Theta_1 = A_1 r^n \cos(n\theta) + B_1 \left[\frac{\log r}{r^{-n}} \right] \cos(n\theta) \quad 5.35a$$

$$\Theta_2 = A_2 J_n(\lambda r) \cos(n\theta) + B_2 Y_n(\lambda r) \cos(n\theta) \quad 5.35b$$

$$\Theta_3 = A_3 I_n(\delta r) \sin(n\theta) + B_3 K_n(\delta r) \sin(n\theta) \quad 5.35c$$

where the top form of Eq. (5.35a) is used for $n = 0$ (axisymmetric buckling) and the bottom form for $n \neq 0$ (asymmetric buckling), n is the number of nodal diameters, A_1, A_2, A_3 , and B_1, B_2, B_3 are unknown constants, $J_n(\bullet)$ and $I_n(\bullet)$ are Bessel functions of the first kind and the modified first kind of order n , respectively, and $Y_n(\bullet)$ and $K_n(\bullet)$ are Bessel functions of the second kind and the modified second kind of order n , respectively.

The boundary conditions are given by

$$w = 0, M_{rr} = 0, \phi_\theta = 0 \quad \text{for simply supported edge} \quad 5.36a-c$$

$$w = 0, \phi_r = 0, \phi_\theta = 0 \quad \text{for clamped edge} \quad 5.37a-c$$

$$M_{rr} = 0, M_{r\theta} = 0, Q_r - \sigma h \frac{\partial w}{\partial r} = 0 \quad \text{for free edge} \quad 5.38a-c$$

where the stress resultants for bending moment M_{rr} , twisting moment $M_{r\theta}$ and shear force Q_r are given by

$$M_{rr} = \frac{Eh^3}{12} \left[\alpha \frac{\partial \phi_r}{\partial r} + \frac{\beta}{r} \left(\phi_r + \frac{\partial \phi_\theta}{\partial \theta} \right) \right] \tag{5.39a}$$

$$M_{r\theta} = \frac{Gh^3}{12} \left[\frac{1}{r} \left(\frac{\partial \phi_r}{\partial \theta} - \phi_\theta \right) + \frac{\partial \phi_\theta}{\partial r} \right] \tag{5.39b}$$

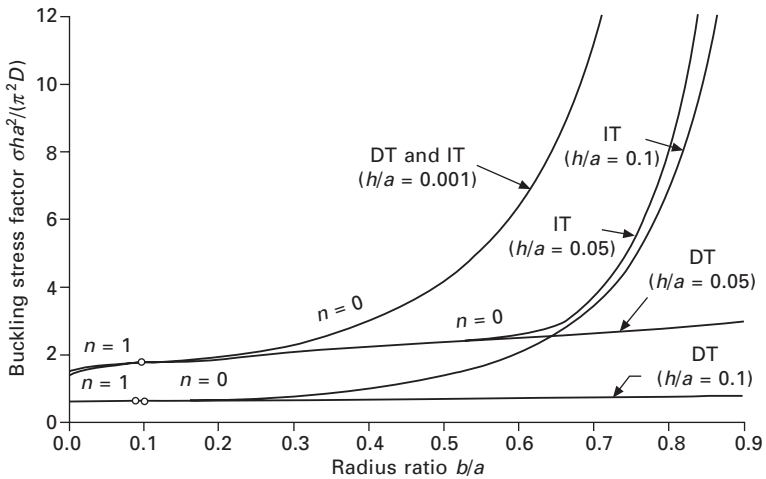
$$Q_r = \kappa^2 Gh \left(\frac{\partial w}{\partial r} + \phi_r \right) \tag{5.39c}$$

In view of Eqs (5.32a–c), (5.35a–c) and (5.39a–c), a set of homogeneous equations can be derived by implementing the boundary conditions [Eqs (5.36a–c) to (5.38a–c)] of the annular plate. These equations can be expressed in the following matrix form:

$$[K]_{6 \times 6} \{\Phi\}_{6 \times 1} = \{0\} \tag{5.40}$$

where $\{\Phi\}_{6 \times 1} = [A_1 \ A_2 \ A_3 \ B_1 \ B_2 \ B_3]^T$. The buckling stress factor $\sigma ha^2/(\pi^2 D)$ is evaluated by setting the determinant of $[K]_{6 \times 6}$ in Eq. (5.40) to zero and then solving the characteristic equation for the lowest positive root.

The annular plates with various boundary conditions are denoted by a two-letter symbol, e.g. CF denotes an annular plate with a clamped C outer edge and a free F inner edge. The critical buckling stress factors are presented here for only two types of boundary conditions, SS and CF, because of space limitations. Figure 5.8 and Table 5.6 present the critical buckling stress factors $\sigma ha^2/(\pi^2 D)$ for various radii ratios b/a of SS annular plates while



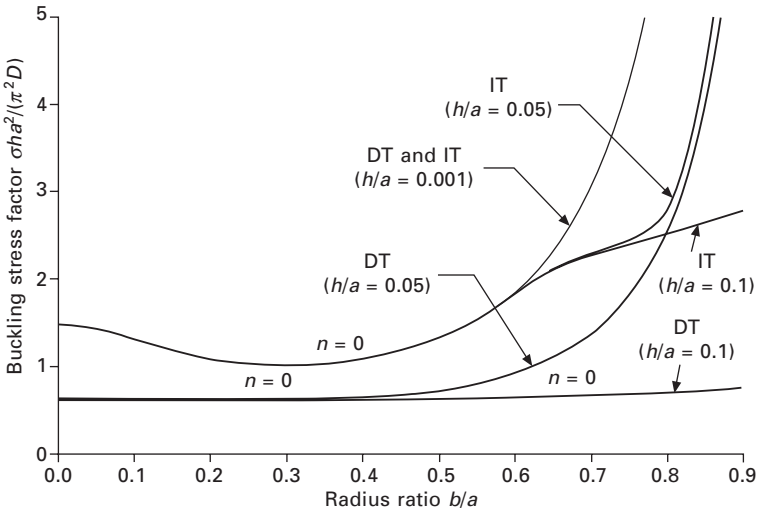
5.8 Buckling stress factor $\sigma ha^2/(\pi^2 D)$ versus radius ratio b/a for simply supported annular plates subjected to uniform in-plane stress.

Table 5.6 Buckling stress factors $\sigma ha^2/(\pi^2 D)$ for annular plates with both edges simply supported

$\frac{h}{a}$	Theories of plasticity	Radius ratio b/a						
		0.1	0.2	0.3	0.4	0.5	0.6	0.7
0.001	DT	1.789	1.904	2.281	2.961	4.148	6.374	11.217
	IT	1.789	1.904	2.281	2.961	4.148	6.374	11.217
0.05	DT	1.751	1.854	2.069	2.224	2.346	2.470	2.606
	IT	1.752	1.855	2.073	2.233	2.370	2.570	3.697
0.1	DT	0.621*	0.628	0.640	0.654	0.671	0.690	0.712
	IT	0.641	0.664	0.735	0.949	1.331	2.016	3.410

*The buckled mode is asymmetric with the number of nodal diameter $n = 1$.

Fig. 5.9 and Table 5.7 present the buckling stress factors for CF plates. For the calculations, we have adopted $\sigma_0 = 61.4$ ksi, $E = 10700$ ksi, $\nu = 0.32$, $c = 20$ and $k = 0.3485$, properties that are associated with a 14S-T6 aluminium alloy (Shrivastava 1979).



5.9 Buckling stress factor $\sigma ha^2/(\pi^2 D)$ versus radius ratio b/a for CF annular plates subjected to uniform in-plane stress.

As before, the deformation theory gives results that are consistently lower than those from the incremental theory. The differences become significant when the plate thickness or radius ratio increases. The buckling stress factors of deformation theory do not much vary with respect to radii ratio b/a when the plate thickness increases. For SS plates, the plates buckle with one nodal diameter ($n = 1$) for small values of b/a (i.e. $b/a < 0.1$) and in an axisymmetric

Table 5.7 Buckling stress factors $\sigma h a^2 / (\pi^2 D)$ for annular plate with outer edge clamped and inner edge free

$\frac{h}{a}$	Theories of plasticity	Radius ratio b/a						
		0.1	0.2	0.3	0.4	0.5	0.6	0.7
0.001	DT	1.325	1.092	1.015	1.089	1.332	1.862	3.073
	IT	1.325	1.092	1.015	1.089	1.332	1.862	3.073
0.05	DT	1.313	1.083	1.008	1.080	1.319	1.826	2.263
	IT	1.313	1.083	1.008	1.080	1.319	1.827	2.282
0.1	DT	0.610	0.606	0.604	0.611	0.625	0.644	0.668
	IT	0.630	0.626	0.629	0.648	0.711	0.911	1.363

form ($n = 0$) for b/a greater than about 0.1. For the case of CF plates, the buckling mode is always axisymmetric.

5.5 Buckling of polygonal plates

5.5.1 Basic equations

Consider a polygonal plate of uniform thickness h and simply supported on all the straight edges. The plate is subjected to a uniform compressive stress σ (i.e. the applied inplane load is constant all round the plate edges). According to the Mindlin plate theory, the governing equations for the plastic buckling of such loaded plates may be expressed as (Wang 2004):

$$\nabla^2(\nabla^2 + \lambda)w = 0 \tag{5.41}$$

where the plastic buckling stress factor λ is given by:

$$\lambda = \frac{\sigma h}{\frac{\alpha E h^3}{12} \left(1 - \frac{\sigma h}{\kappa^2 G h} \right)} \tag{5.42}$$

For a straight, simply supported edge, the boundary conditions along the edge are:

$$w = 0, M_{nn} = \frac{E h^3}{12} \left(\alpha \frac{\partial \phi_n}{\partial n} + \beta \frac{\partial \phi_s}{\partial s} \right) = 0, \phi_s = 0 \tag{5.43a-c}$$

where n and s are, respectively, the normal and tangential directions to the edge.

5.5.2 Exact relationship between plastic buckling stress and elastic buckling stress

In view of Eq. (5.1a) and the boundary conditions given by Eqs (5.43a–c), one can deduce that along a straight, simply supported edge:

$$w = 0 \quad \text{and} \quad \nabla^2 w = 0 \quad 5.44$$

The governing plastic buckling Eq. (5.41) and the boundary conditions given by Eq. (5.44) are of the same mathematical form as those of their corresponding elastic buckling problem of simply supported, Kirchhoff (or classical thin) plates of polygonal shape (Irschik 1985, Wang 1995). For the latter problem, the elastic buckling stress factor λ_e is given by:

$$\lambda_e = \frac{\sigma_e h}{D} \quad 5.45$$

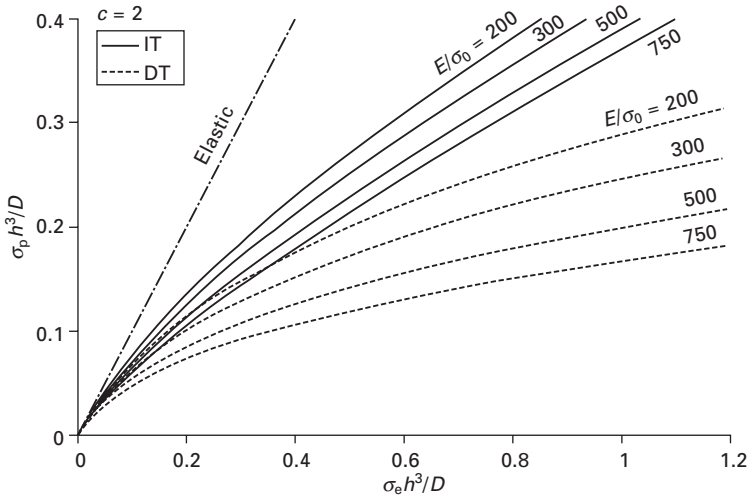
in which σ_e is the critical elastic buckling stress and $D = Eh^3/[12(1 - \nu^2)]$ the flexural rigidity of the plate.

Thus, for the same polygonal plate dimensions, the plastic buckling stress based on the Mindlin plate theory may be related to its elastic buckling stress based on the Kirchhoff (or classical thin) plate theory by

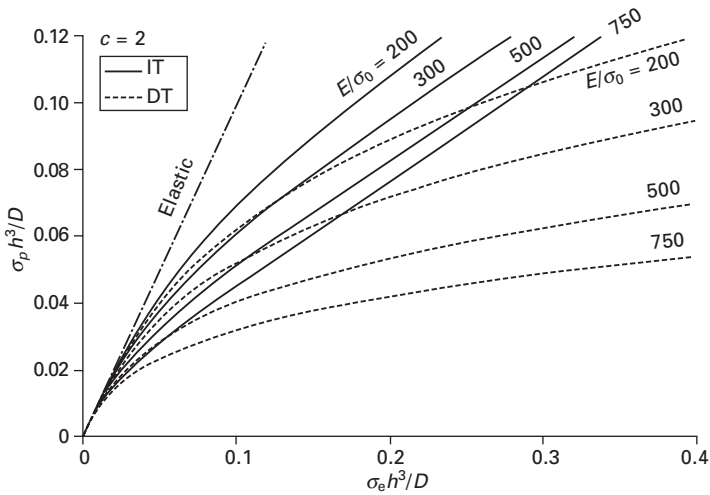
$$\lambda = \lambda_e \Rightarrow \frac{\sigma}{\alpha(1 - \nu^2) \left(1 - \frac{\sigma}{\kappa^2 G}\right)} = \sigma_e \quad 5.46$$

where α and G are given by Eqs (5.2a) and (5.2e) when the incremental theory of plasticity is adopted and they are given by Eqs (5.3a) and (5.3e) for the deformation theory of plasticity. The buckling stress relationship given in Eq. (5.46) is a valuable key relationship for unlocking the critical plastic buckling stresses of simply supported, polygonal Mindlin plates under a uniform in-plane compressive stress. To obtain the plastic buckling stresses, one needs simply to provide the elastic buckling stresses of simply supported, polygonal Kirchhoff plates. Owing to existing analogies between the buckling and vibration problems of simply supported, polygonal plates (see Conway 1960), vibration frequencies may be used if there are no buckling solutions available in the literature. These elastic buckling stresses/vibration frequencies may be readily obtained from (a) standard textbooks on plate buckling and vibration such as Bulson (1970) and Leissa (1969), (b) handbooks such as the *Handbook of Structural Stability* (1970) produced by the Column Research Committee of Japan and (c) papers such as Wang *et al.* (1994) and Wang and Liew (1994).

Graphical representations of the buckling stress relationship given by Eq. (5.46) are shown in Figs 5.10 to 5.12 for hardening indices $c = 2, 3, 10$, respectively. In generating these curves, various values of $E/\sigma_0 = 200, 300, 500, 750$, and $\nu = 0.3$ and $\kappa^2 = 5/6$ have been assumed. By nondimensionalizing the buckling stresses using h and D , the curves shown in Figs 5.10 to 5.12 are valid for any polygonal plate shape with simply supported edges! It can be seen that the plastic buckling stresses computed using the deformation theory (DT) are lower than the corresponding buckling stresses obtained using the incremental theory (IT). It is evident that as the plate thickness increases or

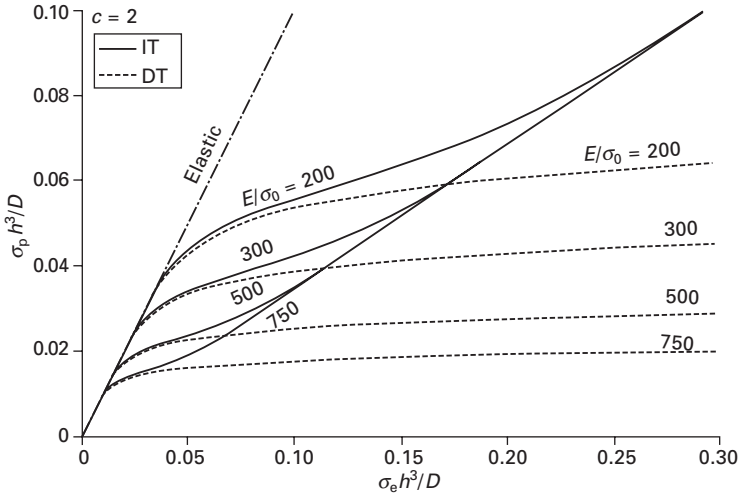


5.10 Relationship between plastic buckling stress of simply supported, polygonal Mindlin plates and elastic buckling stress of corresponding Kirchhoff plates ($k = 0.25$ and $c = 2$).



5.11 Relationship between plastic buckling stress of simply supported, polygonal Mindlin plates and elastic buckling stress of corresponding Kirchhoff plates ($k = 0.25$ and $c = 3$).

the buckling stress increases (due to the plate shape), the deviation between the DT and IT results increases and both these plastic buckling results increasingly diverge from the elastic buckling stress counterpart.



5.12 Relationship between plastic buckling stress of simply supported, polygonal Mindlin plates and elastic buckling stress of corresponding Kirchhoff plates ($k = 0.25$ and $c = 10$).

5.5.3 Plastic buckling stress factors for plates of various polygonal shapes

Tables 5.8 and 5.9 present some plastic buckling stress factors of simply supported Mindlin plates of equilateral triangular shape and square shape, respectively. These results have been calculated from Eq. (5.46) and existing elastic buckling stress factors of classical thin plates. The critical plastic buckling stress factors are determined for plates with different thickness to width ratios h/b , and various values of c and E/σ_0 . The Poisson ratio $\nu = 0.3$ and the shear correction factor $\kappa^2 = 5/6$ were used in all calculations.

It can be seen that the buckling stress factors are significantly lower as the plate thickness increases due to the combined effect of transverse shear deformation and the inelastic characteristics. Thus, it is crucial that a shear deformable plate theory is used when dealing with thick plates, otherwise the buckling load will be grossly overestimated. Moreover, it can be observed that the buckling stress factors obtained by the deformation theory are consistently lower than those obtained by the incremental theory.

5.6 Concluding remarks

The elastic/plastic buckling equations for thick plates have been presented. The Mindlin plate theory was adopted to admit the effect of transverse shear deformation which becomes significant in thick plates. To capture the more practical elastic/plastic behaviour, two competing plasticity theories have

Table 5.8 Buckling stress factors $\sigma_c hb^2/(\pi^2 D)$ for simply supported, equilateral triangular plates (of side length b) under a uniform in-plane compressive stress

Elastic buckling factor based on Kirchhoff plate theory	E/σ_0	$h/b = 0.025$		$h/b = 0.050$		$h/b = 0.075$		$h/b = 0.10$	
		IT	DT	IT	DT	IT	DT	IT	DT
$\frac{\sigma_e hb^2}{\pi^2 D} = 5.333$									
Elastic buckling stress factor based on Mindlin plate theory		5.283		5.140		4.917		4.636	
$c = 2$	200	4.736	4.517	3.887	3.407	3.272	2.622	2.841	2.082
	300	4.548	4.261	3.619	3.053	3.024	2.291	2.632	1.794
	500	4.259	3.876	3.281	2.607	2.737	1.902	2.403	1.468
$c = 10$	200	5.231	5.226	2.453	2.291	1.820	1.160	1.773	0.702
	300	4.672	4.642	1.974	1.642	1.813	0.817	1.773	0.492
	500	3.398	3.319	1.845	1.063	1.813	0.522	1.773	0.313

Table 5.9 Buckling stress factors $\sigma_c hb^2/(\pi^2 D)$ for simply supported square plates under a uniform inplane compressive stress

Elastic buckling factor based on Kirchhoff plate theory	E/σ_0	$h/b = 0.025$		$h/b = 0.050$		$h/b = 0.075$		$h/b = 0.10$	
		IT	DT	IT	DT	IT	DT	IT	DT
$\frac{\sigma_c hb^2}{\pi^2 D} = 2$									
Elastic buckling stress factor based on Mindlin plate theory		1.993		1.972		1.939		1.893	
$c = 2$	200	1.901	1.863	1.700	1.592	1.504	1.337	1.343	1.131
	300	1.862	1.809	1.616	1.480	1.405	1.206	1.244	1.000
	500	1.795	1.716	1.495	1.320	1.276	1.037	1.125	0.8412
$c = 10$	200	1.993	1.993	1.749	1.737	1.031	0.985	0.7371	0.6146
	300	1.993	1.993	1.368	1.343	0.8004	0.7094	0.6890	0.4359
	500	1.981	1.980	0.9632	0.9076	0.6965	0.4615	0.6865	0.2800

been considered: the incremental theory of plasticity with the Prandtl–Reuss constitutive equations and the deformation theory of plasticity with the Hencky constitutive equations. The stability criteria were derived for uniaxially and equibiaxially loaded rectangular plates, uniformly radially loaded circular and annular plates and uniformly loaded polygonal plates. Extensive closed-form buckling stresses were generated for these plates obeying the Ramberg–Osgood elastoplastic characteristic. These exact results should be useful as benchmark analytical results for researchers who are developing plate buckling software and for checking numerical results.

Generally, plastic buckling stress factors are much reduced from their elastic counterparts, especially when the plate is thick, E/σ_0 and the hardening index c have large values. The buckling stress factors obtained using the deformation theory are consistently lower than the corresponding factors of the incremental theory. The divergence of these two results increases with increasing plate thickness, E/σ_0 and c values. This marked difference in buckling stress factors observed for thick plates could be exploited when designing experimental tests on plates to establish which of the two considered theories of plasticity give better buckling results for thick plates.

5.7 Acknowledgements

The author wishes to thank Prof. J. Chakrabarty and Prof. Xiang Yang for their contributions in solving the plastic buckling problems of thick rectangular plates. The author is also grateful to Mr Tun Myint Aung for generating the plastic buckling solutions of thick annular plates under uniform compressive stress.

5.8 References

- Bartdorf, S.B. (1949), Theories of plastic buckling. *Journal of the Aeronautical Sciences*, **16**, 405–408.
- Bazant, Z.P. and Cedolin, L. (1991), *Stability of Structures*. Oxford University Press, New York.
- Betten, J. and Shin, C.H. (2000), Elastic-plastic buckling analysis of rectangular plates subjected to biaxial loads. *Forschung Im Ingenieurwesen – Engineering Research*, **65**(9), 273–278.
- Bijlaard, P.P. (1949), Theory and tests on the plastic stability of plates and shells. *Journal of the Aeronautical Sciences*, **16**, 529–541.
- Bleich, F. (1952), *Buckling Strength of Metal Structures*. McGraw-Hill, New York.
- Brunelle, E.J. (1971), Buckling of transversely isotropic Mindlin plates. *AIAA Journal*, **9**(6), 1018–1022.
- Bulson, P.S. (1970), *The Stability of Flat Plates*. Chatto and Windus, London.
- Chakrabarty, J. (2000), *Applied Plasticity*. Springer-Verlag, New York.
- Chakrabarty, J. (2002), Influence of anisotropy on the plastic buckling of rectangular plates. *Proceedings of 2nd International Conference on Structural Stability and Dynamics*,

- edited by C.M. Wang, G.R. Liu and K.K. Ang, pp. 448–452. World Scientific, Singapore, December 16–18.
- Chen, L.W. and Doong, J.L. (1984), Postbuckling behaviour of a thick circular plate. *AIAA Journal*, **22**, 564–566.
- Column Research Committee of Japan (1970), *Handbook of Structural Stability*. Corona, Tokyo, Japan.
- Conway, H.D. (1960), Analogies between the buckling and vibration of polygonal plates and membranes. *Canadian Aeronautical Journal*, **6**, 263.
- Dietrich, L., Kawahara, W. and Phillips, A. (1978), An experimental study of plastic buckling of a simply supported plate under edge thrusts, *ACTA Mechanica*, **29**, 257–269.
- Dumir, P.C. (1985), Axisymmetric postbuckling of orthotropic tapered thick annular plates. *Trans. ASME, Journal of Applied Mechanics*, **52**, 725–727.
- Durban, D. and Zuckerman, Z. (1999), Elastoplastic buckling of rectangular plates in biaxial compression/tension. *International Journal of Mechanical Science*, **41**, 751–765.
- El-Ghazaly, H.A. and Sherbourne, A.N. (1986), Deformation theory for elastic-plastic buckling analysis of plates under non-proportional planar loading. *Computers and Structures*, **22**(2), 131–149.
- Handelman, G.H. and Prager, W. (1948), Plastic buckling of rectangular plates under edge thrusts. *NACA Tech. Note No. 1530*, Washington, DC, USA.
- Herrmann, G. and Armenakas, A.E. (1960), Vibrations and stability of plates under initial stress. *Proc. ASCE, Journal of Engineering Mechanics Division*, **86**, 65–94.
- Hong, G.M., Wang, C.M. and Tan, T.J. (1993), Analytical buckling solutions for circular Mindlin plates: inclusion of inplane prebuckling deformation. *Archive of Applied Mechanics*, **63**, 534–542.
- Ilyushin, A.A. (1947), The elastic plastic stability of plates. *NACA Tech. Memorandum 1188*, Washington, DC, USA.
- Inoue, T. and Kato, B. (1993), Analysis of plastic buckling of steel plates. *International Journal of Solids and Structures*, **30**(6), 835–856.
- Irschik, H. (1985), Membrane-type eigenmotions of Mindlin plates. *Acta Mechanica*, **55**, 1–20.
- Kanaka Raju, K. and Venkateswara Rao, G. (1983), Postbuckling analysis of moderately thick elastic circular plates. *Trans. ASME, Journal of Applied Mechanics*, **50**, 468–470.
- Kaufmann, W. (1936), Uber unelastisches Knicken rechtiger Platten. *Ing. Archiv.*, **7**, (6), 156.
- Kollbrunner, C.F. (1946), Das Ausbeulen der auf einseitigen, gleichmassig verteilten Druck beanspruchten Platten im elastischen und plastischen Bereich. *Mitteilungen*, **17**, *Institut fur Baustatic, Eidgenossische Technische Hochschule*, Zurich.
- Leissa, A.W. (1969), *Vibration of Plates*. US Government Printing Office, NASA SP-160, reprinted by the Acoustical Society of America (1993).
- Mindlin, R.D. (1951), Influence of rotatory inertia and shear on flexural motions of isotropic, elastic plates. *Trans. ASME, Journal of Applied Mechanics*, **18**, 31–38.
- Mindlin, R.D. and Deresiewicz, H. (1954), Thickness-shear and flexural vibrations of a circular disk. *Journal of Applied Physics*, **25**(10), 1329–1332.
- Moen, L.A., Langseth, M. and Hopperstad, O.S. (1998), Elastoplastic buckling of anisotropic aluminium plate elements. *Journal of Structural Engineering*, **124**(6), 712–719.

- Ore, E. and Durban, D. (1989), Elastoplastic buckling of annular plates in pure shear. *Trans. ASME, Journal of Applied Mechanics*, **56**, 644–651.
- Pearson, C.E. (1950), Bifurcation criteria and plastic buckling of plates and columns. *Journal of the Aeronautical Sciences*, **7**, 417–424.
- Pride, R.A. and Heimerl, G.J. (1949), Plastic buckling of simply supported compressed plates. *NACA Technical Note 1817*, Washington, DC.
- Shrivastava, S.C. (1979), Inelastic buckling of plates including shear effects. *International Journal of Solids and Structures*, **15**, 567–575.
- Soh, A.K., Bian, L.C. and Chakrabarty, J. (2000), Elastic/plastic buckling of a composite flat plate subjected to uniform edge compression. *Thin-Walled Structures*, **38**(3), 247–265.
- Stowell, E.Z. (1948), A unified theory of plastic buckling of columns and plates. *NACA Technical Note 1556*, Washington, DC.
- Timoshenko, S.P. and Gere, J.M. (1961), *Theory of Elastic Stability*. McGraw-Hill, New York.
- Tugcu, P. (1991), Plate buckling in the plastic range. *International Journal of Mechanical Science*, **33**(1), 1–11.
- Xiang, Y., Liew, K.M. and Kitipornchai, S. (1996), Exact buckling solutions for composite laminates: proper free edge conditions under in-plane loadings. *Acta Mechanica*, **117**(3–4), 115–128.
- Wang, C.M. (1995), Allowance for prebuckling deformations in buckling load relationship between Mindlin and Kirchhoff simply supported plates of general polygonal shape. *Engineering Structures*, **17**(6), 413–418.
- Wang, C.M. (2004), Plastic buckling of simply supported, polygonal Mindlin plates. *Journal of Engineering Mechanics*, **130**(1), 117–122.
- Wang, C.M. and Liew, K.M. (1994), Buckling of triangular plates under uniform compression. *Engineering Structures*, **16**(1), 43–50.
- Wang, C.M., Xiang, Y. and Kitipornchai, S. (1993), Axisymmetric buckling of circular Mindlin plates with ring supports. *Journal of Structural Engineering, ASCE*, **119**(3), 782–793.
- Wang, C.M., Xiang, Y., Kitipornchai, S. and Liew, K.M. (1994), Buckling solutions for Mindlin plates of various shapes. *Engineering Structures*, **16**(2), 119–127.
- Wang, C.M., Tan, T.J., Hong, G.M. and Alwis, W.A.M. (1996), Buckling of tapered circular plates: allowances for effects of shear and radial deformation. *Mechanics of Structures and Machines*, **24**(2), 135–153.
- Wang, C.M., Xiang, Y. and Chakrabarty, J. (2001), Elastic/plastic buckling of thick plates. *International Journal of Solids and Structures*, **38**(48–49), 8617–8640.
- Wang, C.M., Chen, Y. and Xiang, Y. (2004), Plastic buckling of rectangular plates subjected to intermediate and end inplane loads. *International Journal of Solids and Structures*, **41**, 4279–4297.

Mechanical and thermal buckling of ceramic–metal plates

J N REDDY and R A ARCINIEGA,
Texas A&M University USA

6.1 Introduction

Functionally graded materials (FGMs) are a special kind of composite in which the material properties vary smoothly and continuously from one surface to the other. These materials are microscopically inhomogeneous and are typically made from isotropic components. One of the main advantages of FGMs is that they mitigate severe stress concentrations and singularities at intersections between interfaces usually presented in composite laminates because of their abrupt transitions in material compositions and properties. Applications of FGMs are extensive, especially in high-temperature environments such as nuclear reactors, chemical plants and high-speed spacecrafts.

The term ‘functionally graded materials’ was originated in the mid-1980s by a group of scientists in Sendai, Japan [1, 2]. Since then, an effort to develop high-resistant materials using FGMs had been continued. Usually, FGMs are made from a mixture of ceramic and metal or combinations of different metals. It is known that these materials withstand high-temperature gradient environments while maintaining their structural integrity. The ceramic constituent of the material provides the high-temperature resistance due to its low thermal conductivity. On the other hand, the ductility of the metal constituent prevents fracture caused by stresses due to high-temperature gradient in a very short period of time. Additionally, ceramic–metal FGMs with continuously varying volume fraction can be easily manufactured.

A review of the technical literature in the last decade shows that most of research studies in FGMs had more focused on thermal stress analysis and fracture mechanics (see [3–5]). Limited work has been done to study the buckling and vibration response of FGM structures. In the following, we introduce some research works related to the present study. We cite the paper of Praveen and Reddy [6] who examined the nonlinear thermoelastic response of functionally graded ceramic–metal plates using a finite element model based on the first order shear deformation theory (FSDT) with von Kármán

nonlinearity. Further, Reddy and Chin [7] analyzed the dynamic thermoelastic response of functionally graded cylinders and plates.

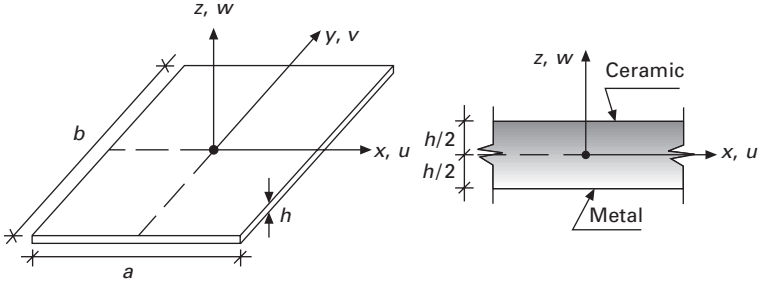
Important studies on the subject of thermal stability of composite structures are available in the literature. Among them we can mention the articles of Tauchert [8], Huang and Tauchert [9], Meyers and Hyer [10], and Shiau and Kuo [11]. Mechanical buckling of functionally graded plates was studied by Feldman and Aboudi [12]. In this work, a method based on a combination of micromechanical and structural approaches was employed. Javaheri and Eslami [13] derived the equilibrium and stability equations of FGM plates under thermal loads, based on the Kirchhoff theory. Closed-form solutions for thermal buckling were obtained for four types of thermal loads. In a similar approach, Lanhe [14] obtained analytical solutions using the first-order plate theory. Shen [15] carried out a postbuckling analysis for FGM panels and plates subjected to axial compression in thermal environments. Finally, Na and Kim [16] presented a 3D finite element solution for thermal buckling of functionally graded plates. In this formulation, material properties were assumed to be temperature dependent and they vary continuously through the thickness according to a simple power law.

An assessment of previous research works for FGMs plates indicates that studies in thermal buckling are scarce and only a few very recent articles deal with this problem. Our aim in this paper is to present a study of the buckling of functionally graded ceramic–metal plates under mechanical and thermal loading. The analysis is performed using the third order and the first order shear theories. A displacement finite element model to study the problem is developed using C^0 -continuity elements. To avoid shear locking, high-order Lagrange polynomials are employed. Numerical results include comparisons with previous formulations and solutions for critical temperature under three different temperature distributions. Finally, the effects of the volume fraction exponent and relative thickness on the critical buckling load and critical temperature changes of FGM plates are examined.

6.2 Theoretical formulation

6.2.1 Kinematics and equilibrium equations

The plate is modeled using the equivalent single layer theory [17]. As we know, this theory predicts the global behavior accurately. The geometry of the plate is depicted in Fig. 6.1, where the coordinates x and y are taken in the mid-plane of the plate. The equilibrium equations and kinematics of the plate are based on the third order plate theory together with the von Kármán nonlinear strains. Thus, the displacement components are assumed to be of the following form (see Reddy [18, 19]):



6.1 Geometry of the plate.

$$\begin{cases} u_1(x, y, z) = u + z\varphi_1 + z^3k(w_{,x} + \varphi_1) \\ u_2(x, y, z) = v + z\varphi_2 + z^3k(w_{,y} + \varphi_2) \\ u_3(x, y, z) = w \end{cases} \quad 6.1$$

where u, v, w denote displacements of the point $(x, y, 0)$ on the mid-plane; φ_1, φ_2 are rotations with respect to the y and x axes respectively and k is a constant defined as $-4/3h^2$.

Displacement finite element models based on Eq. 6.1 require C^1 -continuity because of the presence of first derivatives of the transverse displacement in the displacement field (or second order derivatives in the total potential energy). To relax the continuity in the finite element formulation, we introduce the following auxiliary variables:

$$\begin{cases} \psi_1 = w_{,x} + \varphi_1 \\ \psi_2 = w_{,y} + \varphi_2 \end{cases} \quad 6.2$$

Substituting Eq. 6.2 into Eq. 6.1, we obtain:

$$\begin{cases} u_1(x, y, z) = u + z\varphi_1 + z^3k\psi_1 \\ u_2(x, y, z) = v + z\varphi_2 + z^3k\psi_2 \\ u_3(x, y, z) = w \end{cases} \quad 6.3$$

Now it is clear that only C^0 -continuity of all variables is required.

The strains of the plate associated with the displacement field given in Eq. 6.3 are:

$$\begin{aligned} \varepsilon_i &= \varepsilon_i^0 + k_i^1 z + k_i^3 z^3 \quad (i = 1, 2, 6) \\ \varepsilon_m &= \varepsilon_m^0 + k_m^2 z^2 \quad (m = 4, 5) \end{aligned} \quad 6.4$$

where

$$\begin{aligned} \varepsilon_1^0 &= u_{,x} + \frac{1}{2} w_{,x}^2, & \varepsilon_2^0 &= v_{,y} + \frac{1}{2} w_{,y}^2, & \varepsilon_6^0 &= u_{,y} + v_{,x} + w_{,x} w_{,y}, \\ \varepsilon_4^0 &= w_{,y} + \varphi_2, & \varepsilon_5^0 &= w_{,x} + \varphi_1, & & \end{aligned} \quad 6.5$$

are the deformations of the mid-plane (i.e. membrane strains) and

$$\begin{aligned}
 k_1^1 &= \varphi_{1,x}, & k_2^1 &= \varphi_{2,y}, & k_6^1 &= \varphi_{1,y} + \varphi_{2,x}, \\
 k_1^3 &= k\psi_{1,x}, & k_2^3 &= k\psi_{2,y}, & k_6^3 &= k(\psi_{1,y} + \psi_{2,x}), \\
 k_4^2 &= 3k\psi_{2,y}, & k_5^2 &= 3k\psi_{1,x}
 \end{aligned} \tag{6.6}$$

are the curvatures (i.e. bending strains). Note that the formulation contains seven variables and still satisfies the shear boundary conditions on the bottom and top of the plate.

The static governing equations of the plate are derived from the principle of virtual work. In the absence of body moments and thermal loading, the equations are given by (see Reddy [17], Putcha and Reddy [20] and Nayak *et al.* [21]):

$$\begin{aligned}
 \delta u: \quad & \frac{\partial N_1}{\partial x} + \frac{\partial N_6}{\partial y} = 0 \\
 \delta v: \quad & \frac{\partial N_6}{\partial x} + \frac{\partial N_2}{\partial y} = 0 \\
 \delta w: \quad & \frac{\partial Q_1}{\partial x} + \frac{\partial Q_2}{\partial y} + q + \bar{N} = 0 \\
 \delta \varphi_1: \quad & \frac{\partial M_1}{\partial x} + \frac{\partial M_6}{\partial y} - Q_1 = 0 \\
 \delta \varphi_2: \quad & \frac{\partial M_6}{\partial x} + \frac{\partial M_2}{\partial y} - Q_2 = 0 \\
 \delta \psi_1: \quad & \left(\frac{\partial P_1}{\partial x} + \frac{\partial P_6}{\partial y} \right) - 3R_1 = 0 \\
 \delta \psi_2: \quad & \left(\frac{\partial P_6}{\partial x} + \frac{\partial P_2}{\partial y} \right) - 3R_2 = 0
 \end{aligned} \tag{6.7}$$

where the stress resultants N_i , M_i , P_i , Q_i and R_i are defined by

$$\begin{aligned}
 (N_i, M_i, P_i) &= \int_{-h/2}^{h/2} \sigma_i(1, z, z^3) dz \quad (i = 1, 2, 6), \\
 (Q_1, R_1) &= \int_{-h/2}^{h/2} \sigma_5(1, z^2) dz, \quad (Q_2, R_2) = \int_{-h/2}^{h/2} \sigma_4(1, z^2) dz
 \end{aligned} \tag{6.8}$$

The variable \bar{N} is a nonlinear force resultant that depends on the stress resultant N_j . It is expressed as

$$\bar{N} = \frac{\partial}{\partial x} \left(N_1 \frac{\partial w}{\partial x} + N_6 \frac{\partial w}{\partial y} \right) + \frac{\partial}{\partial y} \left(N_6 \frac{\partial w}{\partial x} + N_2 \frac{\partial w}{\partial y} \right) \quad 6.9$$

Note that the nonlinearity is only observed in the third expression of Eq. 6.7.

6.2.2 Functionally graded plates

The FGMs considered here are made from a mixture of ceramics and metals. The ceramic constituent provides heat and corrosion resistance; meanwhile the metal constituent provides the strength, toughness and ductility necessary to prevent fractures due to high-temperature gradient in a short period of time. In this two-phase functionally graded material, the properties are assumed to vary through the thickness of the plate. However, material properties are considered to be temperature independent. The material in the bottom and top surfaces is metal and ceramic respectively (see Fig. 6.1). We also assume a rule of mixtures based on the Voigt model [22]. Therefore, the composite modulus is given by the weighted average of the moduli of the constituents, namely

$$E(z) = E_c f_c + E_m f_m \quad 6.10$$

where the subscripts m and c refer to the metal and ceramic constituencies and f is the volume fraction of the phase. The volume fractions of the ceramic f_c and metal f_m corresponding to the power law are expressed as (see Praveen and Reddy [6]):

$$f_c = \left(\frac{z}{h} + \frac{1}{2} \right)^n, f_m = 1 - f_c \quad 6.11$$

where n is the volume fraction exponent which takes values greater than or equal to zero. The value of n equal to zero represents a fully ceramic plate. Conversely, we have a fully metal plate as n tends to infinity.

Likewise, the coefficient of thermal expansion α is assumed to be of the form:

$$\alpha(z) = \alpha_c f_c + \alpha_m f_m = \alpha_{cm} f_c + \alpha_m \quad 6.12$$

while Poisson's ratio is taken to be constant, $\nu(z) = \nu_0$. Here $\alpha_{cm} = \alpha_c - \alpha_m$. Next, we write the constitutive equations of the plate:

$$\begin{cases} \sigma_1 \\ \sigma_2 \\ \sigma_6 \end{cases} = \begin{bmatrix} Q_{11}(z) & Q_{12}(z) & 0 \\ Q_{12}(z) & Q_{22}(z) & 0 \\ 0 & 0 & Q_{66}(z) \end{bmatrix} \begin{cases} \varepsilon_1 \\ \varepsilon_2 \\ \varepsilon_6 \end{cases}$$

$$\begin{cases} \sigma_4 \\ \sigma_5 \end{cases} = \begin{bmatrix} Q_{44}(z) & 0 \\ 0 & Q_{55}(z) \end{bmatrix} \begin{cases} \varepsilon_4 \\ \varepsilon_5 \end{cases} \quad 6.13$$

where Q_{ij} are the material constants of the plate and are expressed as

$$\begin{aligned} Q_{11}(z) = Q_{22}(z) &= \frac{E(z)}{1 - \nu^2}, & Q_{12}(z) &= \frac{\nu E(z)}{1 - \nu^2} \\ Q_{66}(z) = Q_{44}(z) = Q_{55}(z) &= \frac{E(z)}{2(1 + \nu)} \end{aligned} \quad 6.14$$

The substitution of Eq. 6.13 into Eq. 6.8 gives:

$$\begin{aligned} N_i &= A_{ij}\varepsilon_j^0 + B_{ij}k_j^1 + E_{ij}k_j^3 \\ M_i &= B_{ij}\varepsilon_j^0 + D_{ij}k_j^1 + F_{ij}k_j^3 \quad (i, j = 1, 2, 6) \\ P_i &= E_{ij}\varepsilon_j^0 + F_{ij}k_j^1 + H_{ij}k_j^3 \end{aligned} \quad 6.15$$

and

$$\begin{aligned} Q_1 &= \bar{A}_{5j}\varepsilon_j^0 + \bar{D}_{5j}k_j^2, & Q_2 &= \bar{A}_{4j}\varepsilon_j^0 + \bar{D}_{4j}k_j^2 \\ R_1 &= \bar{D}_{5j}\varepsilon_j^0 + \bar{F}_{5j}k_j^2, & R_2 &= \bar{D}_{4j}\varepsilon_j^0 + \bar{F}_{4j}k_j^2 \end{aligned} \quad (i, j = 4, 5) \quad 6.16$$

where the material stiffness coefficients are given by:

$$\begin{aligned} (A_{ij}, B_{ij}, D_{ij}, E_{ij}, F_{ij}, H_{ij}) &= \int_{-h/2}^{h/2} (Q_{ij}^{cm} f_c + Q_{ij}^m)(1, z, z^2, z^3, z^4, z^6) dz \\ (\bar{A}_{ij}, \bar{D}_{ij}, \bar{F}_{ij}, \bar{H}_{ij}) &= \int_{-h/2}^{h/2} (Q_{ij}^{cm} f_c + Q_{ij}^m)(1, z^2, z^4) dz \end{aligned} \quad 6.17$$

for $(i, j = 1, 2, 6)$ and $(i, j = 4, 5)$ respectively, and $Q_{ij}^{cm} = Q_{ij}^c - Q_{ij}^m$.

The thermal stresses are easily incorporated in the formulation. They can be expressed as:

$$\begin{cases} \sigma_1 \\ \sigma_2 \\ \sigma_6 \end{cases}^T = - \begin{bmatrix} Q_{11}(z) & Q_{12}(z) & 0 \\ Q_{12}(z) & Q_{22}(z) & 0 \\ 0 & 0 & Q_{66}(z) \end{bmatrix} \begin{cases} \alpha(z) \\ \alpha(z) \\ 0 \end{cases} T(x, y, z) \quad 6.18$$

where $T(x, y, z)$ is the temperature increment from a reference state, which is a known function. Finally, we define the thermal stress resultants as:

$$\begin{aligned}
 (N^T, M^T, P^T) &= - \frac{1}{(1 - \nu)} \\
 &\times \int_{-h/2}^{h/2} (E_{cm}f_c + E_m)(\alpha_{cm}f_c + \alpha_m)T(x, y, z)(1, z, z^2)dz \quad 6.19
 \end{aligned}$$

Note that because of the isotropy on each plane of the plate, the thermal resultants corresponding to the x direction are the same as those of y , and also the twisting thermal resultants become zero.

6.2.3 Stability analysis

The stability problem of the plate is based on the variational formulation. This asserts that a static conservative system is in equilibrium if its total potential energy is a minimum [23]. For the stability analysis, the generalized displacement field is assumed to be in the incremental form as

$$U \rightarrow U^F + U^I \quad 6.20$$

where U^F denotes a fundamental prebuckling solution and U^I denotes the incremental displacements (arbitrary perturbation of the equilibrium). Such an increment is called a variation of U . The potential energy increment may be written in the form:

$$\Delta\Pi = \Pi(U^F + U^I) - \Pi(U^F) = \sum_{n=1}^4 \frac{1}{n!} \delta^n \Pi \quad 6.21$$

by using Taylor's expansion.

The necessary condition for Π to be a relative minimum is that its first variation $\delta\Pi$ vanishes ([24]. Consequently the sign of $\Delta\Pi$ is governed by the sign of the second variation. Then, the critical load is defined as the smallest load for which the second variation is no longer positive definite. The limit of positive-definiteness for a continuous system can be expressed as:

$$\delta[\delta^2\Pi] = 0 \quad 6.22$$

which is known as the Trefftz criterion.

In this approach the fundamental solution (prebuckling state) is considered as a pure membrane state where bending and rotations are neglected. Consequently the total solution can be written as:

$$U \rightarrow \begin{cases} u = u^0 + u^1, & v = v^0 + v^1, & w = w^1 \\ \varphi_1 = \varphi_1^1, & \varphi_2 = \varphi_2^1 \\ \psi_1 = \psi_1^1, & \psi_2 = \psi_2^1 \end{cases} \quad 6.23$$

where the superscripts '0' and '1' refer to the prebuckling and incremental states, respectively. By substituting Eq. 6.23 into Eqs 6.5 and 6.6 and then

computing the second variation of the incremental potential energy in Eq. 6.22, we can distinguish two different parts: one with only incremental terms and the other with couple terms (incremental and fundamental). Thus

$$\delta(\delta^2\Pi_I) + \delta(\delta^2\Pi_{FI}) = 0 \quad 6.24$$

The second term of Eq. 6.24 can be expressed in terms of the prebuckling stress resultants as:

$$\delta^2\Pi_{FI} = \frac{1}{2} \int_{\Omega} \{N_1^0 (w_{,x}^1)^2 + 2N_6^0 w_{,x}^1 w_{,y}^1 + N_2^0 (w_{,y}^1)^2\} dx dy \quad 6.25$$

and taking the variation of this equation we arrive at the following expression

$$\begin{aligned} & \delta(\delta^2\Pi_{FI}) \\ &= \int_{\Omega} \{N_1^0 w_{,x}^1 \delta w_{,x}^1 + N_6^0 (w_{,x}^1 \delta w_{,y}^1 + w_{,y}^1 \delta w_{,x}^1) + N_2^0 w_{,y}^1 \delta w_{,y}^1\} dx dy \end{aligned} \quad 6.26$$

in which N_i^0 denote the stress resultants in the prebuckling state.

Note that Eq. 6.26 comes from the von Kármán nonlinearity included in the formulation and shown in Eq. 6.5. The resultant stability equations are similar to those given in Eq. 6.7 in which the stress resultants are referred to the incremental state $(N_i^1, M_i^1, P_i^1, Q_i^1, R_i^1)$, and \bar{N}^0 is given by:

$$\bar{N}^0 = \frac{\partial}{\partial x} \left(N_1^0 \frac{\partial w}{\partial x} + N_6^0 \frac{\partial w}{\partial y} \right) + \frac{\partial}{\partial y} \left(N_6^0 \frac{\partial w}{\partial x} + N_2^0 \frac{\partial w}{\partial y} \right) \quad 6.27$$

6.2.4 Mechanical and thermal buckling

In this chapter, the buckling analysis is limited to cases in which the stress resultants in the prebuckling state are constant.

Mechanical load

We assume that the only applied loads are the following in-plane forces:

$$N_1^0 = -\alpha_1 N_{cr}, \quad N_2^0 = -\alpha_2 N_{cr}, \quad N_6^0 = -\alpha_3 N_{cr} \quad 6.28$$

Here, we contemplate three possible cases of mechanical buckling: uniaxial compression ($\alpha_1 = 1, \alpha_2 = \alpha_3 = 0$), biaxial compression ($\alpha_1 = 1, \alpha_2 = 1, \alpha_3 = 0$) and the general case with shear loading ($\alpha_1 = 1, \alpha_2 = 1, \alpha_3 = 1$).

Thermal load

For this case we should first find the prebuckling stresses. It can be shown

that for simply supported and fixed boundary conditions the fundamental solution of the plate is trivial (see Meyers and Hyer [10] and Tauchert [8]). Nevertheless, it experiences nonzero thermal stresses, namely:

$$N_1^0 = N_{cr}^T, \quad N_2^0 = N_{cr}^T, \quad N_6^0 = 0 \quad 6.29$$

where

$$N_{cr}^T = -\frac{1}{(1-\nu)} \int_{-h/2}^{h/2} (E_{cm}f_c + E_m)(\alpha_{cm}f_c + \alpha_m)T(x, y, z) dz \quad 6.30$$

The following three cases are considered for thermal buckling: uniform temperature rise, linear temperature change across the thickness and nonlinear temperature change across the thickness. For the first case the initial temperature of the plate is assumed to be T_i . Next, the temperature is raised to the final value T_f such that the plate buckles. Then, the temperature distribution can be written as:

$$T(z) = T_f - T_i = T_{cr} \quad 6.31$$

For the second case the temperature distribution is expressed as:

$$T(z) = T_{cr} \left(\frac{z}{h} + \frac{1}{2} \right) - T_m \quad 6.32$$

where $T_{cr} = T_c - T_m$. Finally for nonlinear temperature change across the thickness, the temperature distribution is obtained by solving a simple steady state heat transfer equation through the thickness of the plate. That is:

$$\begin{cases} -\frac{d}{dz} \left(K(z) \frac{dT(z)}{dz} \right) = 0, \\ T(-h/2) = T_m, \quad T(h/2) = T_c \end{cases} \quad 6.33$$

where $K(z)$ is the thermal conductivity of the plate, which is expressed as:

$$\begin{aligned} K(z) &= K_{cm}f_c + K_m \\ K_{cm} &= K_c - K_m \end{aligned} \quad 6.34$$

The subscripts m and c refer to the metal and ceramic respectively. The solution of Eq. 6.33 can be obtained by polynomial series. Taking the first seven terms of the series [13, 14], the thermal distribution of the plate is given by:

$$T(z) = T_m + \frac{T_{cr}}{D} \sum_{j=0}^5 \frac{1}{(jn+1)} \left(-\frac{K_{cm}}{K_m} \right)^j \left(\frac{z}{h} + \frac{1}{2} \right)^{(jn+1)} \quad 6.35$$

where $T_{cr} = T_c - T_m$ and

$$D = \sum_{j=0}^5 \frac{1}{(jn+1)} \left(-\frac{K_{cm}}{K_m} \right)^j \quad 6.36$$

Thermal distributions given in Eqs 6.31, 6.32 and 6.35 are then substituted in Eqs 6.30 and 6.29. The problem is reduced to find the smaller eigenvalue (N_{cr} or T_{cr}) that satisfies Eq. 6.24.

6.2.5 Finite element implementation

This section is devoted to the development of a displacement finite element model based on the principle of virtual work. As we know, the displacement field requires only C^0 -continuity in all its variables. The number of variables to be interpolated in the finite element model is seven for the third order shear deformation theory (TSDT) and five for the FSDT. The finite element equations are obtained by discretizing the incremental displacements and rotations. Consequently:

$$\begin{aligned} u &= \sum_{j=1}^m u_j N_j(x, y), \quad v = \sum_{j=1}^m v_j N_j(x, y), \quad w = \sum_{j=1}^m w_j N_j(x, y) \\ \varphi_1 &= \sum_{j=1}^m \varphi_j^1 N_j(x, y), \quad \varphi_2 = \sum_{j=1}^m \varphi_j^2 N_j(x, y) \\ \psi_1 &= \sum_{j=1}^m \psi_j^1 N_j(x, y), \quad \psi_2 = \sum_{j=1}^m \psi_j^2 N_j(x, y) \end{aligned} \quad 6.37$$

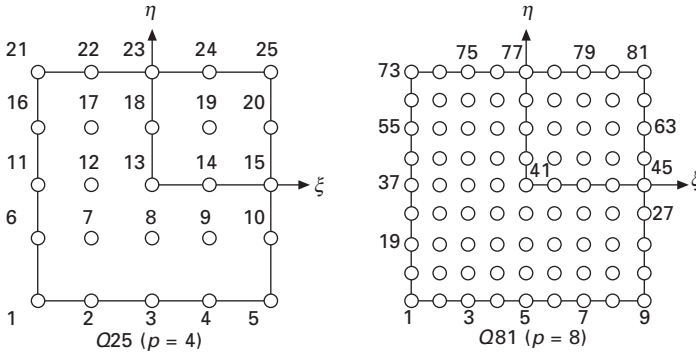
where m is the number of nodes of the element, $N_j(x, y)$ is the Lagrange interpolation function at the node j and $(u_j, v_j, w_j, \varphi_j^1, \varphi_j^2, \psi_j^1, \psi_j^2)$ denote the nodal values of the displacements. The Lagrange polynomials are given by:

$$\begin{aligned} L_i^1(\xi) &= \prod_{\substack{k=1 \\ k \neq i}}^{p+1} \frac{(\xi - \xi_k)}{(\xi_i - \xi_k)}, \\ L_i^2(\eta) &= \prod_{\substack{k=1 \\ k \neq i}}^{p+1} \frac{(\eta - \eta_k)}{(\eta_i - \eta_k)}, \quad i = 1, \dots, p+1 \end{aligned} \quad 6.38$$

where p is the polynomial degree. Finally, the shape functions are of the form:

$$N_k = L_i^1(\xi) L_j^2(\eta), \quad k = (j-1)(p+1) + i \quad 6.39$$

In this paper, a family of high-order Lagrange interpolations is developed. This kind of element is seen to be free of locking. Basically we use elements labeled $Q25$ and $Q81$ (see Fig. 6.2). Table 6.1 shows the family of high-order Lagrange elements and the corresponding number of degrees of freedom for the FSDT and TSDT.



6.2 Basic p -elements used in the present formulation.

Table 6.1 Number of degrees of freedom per element for different p levels

Element	p level	FSDT (DOF)	TSDT (DOF)
Q4	1	20	28
Q9	2	45	63
Q25	4	125	175
Q81	8	405	567

Substituting the interpolants 6.37 into Eq. 6.24 we obtain the following matrix equation:

$$[K]\{\Delta\} = \lambda[K_g]\{\Delta\} \tag{6.40}$$

where $[K]$ is the stiffness matrix, λ is the eigenvalue (N_{cr} or T_{cr}), and $[K_g]$ is the geometric stiffness matrix obtained from the variational equation 6.26. Since we are analyzing the critical mechanical or thermal buckling (i.e. the smallest eigenvalue), Eq. 6.40 can be solved by the inverse iteration method which is suitable for positive definite stiffness matrices.

6.3 Numerical results

In this section, some numerical examples obtained with the displacement finite element formulation for stability problems are presented. The mechanical and thermal buckling together with the FSDT and TSDT formulations are evaluated by solving several problems for isotropic, composite and functionally graded plates.

6.3.1 Comparisons with other formulations

In the present study, $Q25$ and $Q81$ elements with five and seven degrees of freedom per node (for the FSDT and TSDT, respectively) were utilized. The

flexibility of these elements (using polynomials of fourth and eighth degree) mitigates any possible shear locking in the numerical computation. Therefore, no reduced integration is used in the evaluation of the stiffness coefficients (i.e. full Gauss integration rule is employed in all examples). Also, regular meshes of 4×4 Q25 and 2×2 Q81 elements were chosen after convergence studies in a full plate.

First, Table 6.2 contains the dimensionless critical loads for uniaxial, biaxial and biaxial with shear loading for symmetric cross-ply rectangular plates ($0^\circ/90^\circ/0^\circ$) with two plate aspect ratios, $a/b = 1$ and 2 and for side-to-thickness ratio $b/h = 10$. Our results are compared with 3D layer-wise FEM results of Setoodeh and Karami [25] and the analytical solutions based on FSDT by Xiang *et al.* [26] (also see Reddy [17]). The following lamina properties are used in the numerical examples:

$$E_1/E_2 = 40, \quad G_{13} = G_{12} = 0.6E_2, \quad G_{23} = 0.5E_2, \quad \nu_{12} = 0.25$$

Table 6.2 Comparison of the dimensionless critical load for symmetric three cross-ply laminated plates under uniaxial and biaxial compression, and shear loading (4×4 Q25 full integration)

a/b	Theory	$\bar{N}_{cr} = N_{cr}b^2/E_2h^3$		
		Uniaxial	Biaxial	Shear
1	LW3D	22.2347	9.9424	8.8184
	FSDT	22.3151	10.2024	–
	Present TSDT	22.1164	9.9330	8.7369
	Present FSDT	22.3151	10.2024	8.9672
2	LW3D	16.4247	3.2694	3.1317
	FSDT	16.4340	3.2868	–
	Present TSDT	16.2986	3.2597	3.1285
	Present FSDT	16.4340	3.2868	3.1579

The simply-supported boundary conditions used are

$$\text{At } x = \pm a/2 \quad v = w = \varphi_2 = \psi_2 = 0$$

$$\text{At } y = \pm b/2 \quad u = w = \varphi_1 = \psi_1 = 0$$

The results obtained with the present formulation are in close agreement with those found in the literature.

Numerical results for the critical loads of antisymmetric cross-ply laminated square plates ($0^\circ/90^\circ$) are presented in Tables 6.3 and 6.4. In Table 6.3 we show results of the uniaxial buckling load in the y direction under different types of boundary conditions. Again, comparisons are made with the 3D layer-wise results of Setoodeh and Karamy [25] and the Lévy-type solutions of Reddy and Khdeir [27]. The material properties are the same as the last example and the following boundary conditions are used in the analysis

Table 6.3 Comparison of the uniaxial critical load for antisymmetric two cross-ply laminated square plates for various boundary conditions (2×2 Q81 full integration)

h/a	Theory	$\bar{N}_{cr} = N_{cr}b^2/E_2h^3$		
		SSSS	SCSC	SFSF
0.1	LW3D	11.2560	19.5762	4.7662
	TSDT	11.562	21.464	4.940
	FSDT	11.353	20.067	4.851
	Present TSDT	11.5193	21.0224	4.9185
	Present FSDT	11.3526	20.0669	4.8507
0.2	LW3D	8.0732	8.9584	3.4867
	TSDT	8.769	11.490	3.905
	FSDT	8.277	9.757	3.682
	Present TSDT	8.6514	10.7516	3.8449
	Present FSDT	8.2773	9.7566	3.6817

Table 6.4 Comparison of the uniaxial critical load for antisymmetric two cross-ply laminated square plates for various ratios E_1/E_2 (2×2 Q81 full integration)

Theory	$\bar{N}_{cr} = N_{cr}b^2/E_2h^3$		
	$E_1/E_2 = 40$	$E_1/E_2 = 30$	$E_1/E_2 = 20$
Noor	10.817	9.3746	7.8196
LW3D	11.2382	9.6995	8.0455
TSDT	11.563	9.8695	8.1151
FSDT	11.353	9.7347	8.0423
Present TSDT	11.5193	9.8454	8.1049
Present FSDT	11.3526	9.7347	8.0423

At $x = \pm a/2$ $v = w = \varphi_2 = \psi_2 = 0$ (SS)

At $x = \pm a/2$ $u = v = w = \varphi_1 = \varphi_2 = \psi_1 = \psi_2 = 0$ (CC)

At $x = \pm a/2$ *Free* (FF)

At $y = \pm b/2$ $u = w = \varphi_1 = \psi_1 = 0$ (SS)

A comparison of the present results for critical loads with other formulations is presented in Table 6.4. A uniaxial compressive load in the x direction was applied to laminated square plates (ratio $a/h = 10$) with different degrees of the orthotropy (material properties given above) and simply supported boundary conditions. As it was pointed out by Setoodeh, the lower bound of the critical load corresponds to the 3D solutions of Noor [28]. In both cases a mesh of 2×2 Q81 elements was used in the analysis. The present results are in satisfactory agreement with the corresponding 3D analytical solutions of

Noor [28], the 3D layer-wise FEM results [25] and the analytical Lévy solutions [27].

The next two examples deal with thermal buckling of isotropic and functionally graded plates. The critical temperatures of simply supported and clamped isotropic plates under uniform temperature rise are shown in Table 6.5. They are verified against the 3D finite element formulation of Na and Kim [16] and the finite element results of Thangaratnam *et al.* [29]. The coefficient of thermal expansion and Poisson's ratio used here are given by

$$\alpha = 2 \times 10^6 (1/K), \quad \nu = 0.3$$

Table 6.5 Comparison of the critical temperature for isotropic square plates subjected to uniform temperature rise (4×4 Q25 full integration)

Theory	$T_{cr}(K)$	
	Simply supported	Clamped
Na and Kim [16]	–	167.73
Thangaratnam <i>et al.</i> [29]	63.33	167.70
Present TSDT	63.231	167.503
Present FSDT	63.231	167.502

with a ratio $S = a/h = 100$. The results show to be in good agreement with the other numerical solutions. Finally, Table 6.6 contains the critical change of temperatures for thin and thick FGM plates under nonlinear temperature rise across the thickness. The results are given for various aspect ratios a/b and values of volume fraction exponent n . Young's modulus, the thermal conductivity, the coefficient of thermal expansion and Poisson's ratio for alumina powder (ceramic material) and aluminum are:

$$E_c = 380 \text{ GPa}, K_c = 10.4 \text{ W/mK}, \alpha_c = 7.4 \times 10^{-6} (1/^\circ\text{C}), \nu_c = 0.3$$

$$E_m = 70 \text{ GPa}, K_m = 204 \text{ W/mK}, \alpha_m = 23 \times 10^{-6} (1/^\circ\text{C}), \nu_m = 0.3$$

respectively. We consider a temperature rise of $T_m = 5^\circ\text{C}$ in the metal-rich surface of the plate. The present results are compared with analytical results of Lanhe [14] using the FSDT and Javaheri and Eslami [13] using the classical plate theory. It is observed that the critical temperature increases as the plate aspect ratio increases. For thin plates the present results are in good agreement with those found in the literature. However, for thick plates ($a/h = 10$) the differences are significant with the Javaheri and Eslami [13] formulation. This is due to the fact that the Javaheri and Eslami formulation does not account for the transverse shear deformation and the shear deformation cannot be neglected in thick composite plates. We also note a small difference between the results of the present FSDT and TSDT formulations. The difference increases with the aspect ratio a/b and for the volume fraction index n that

Table 6.6 Comparison of the critical temperature of FGM plates under nonlinear temperature rise (4×4 Q25 full integration)

n	Theory	$a/b = 1$	$a/b = 2$	$a/b = 3$	$a/b = 4$	$a/b = 5$
$T_{cr}(a/h = 100, T_m = 5^\circ)$						
0.0	Lanhe [14]	24.1622	75.3952	160.5901	279.5281	431.8769
	Javaheri and Eslami [13]	24.1982	75.4955	160.9910	280.6848	434.5767
	Present TSDT	24.1790	75.3752	160.5104	279.2983	431.3415
	Present FSDT	24.1790	75.3752	160.5104	279.2981	431.3412
1.0	Lanhe [14]	7.6554	38.6328	90.1801	162.1757	254.4500
	Javaheri and Eslami [13]	7.6636	38.6838	90.3843	162.7649	255.8247
	Present TSDT	7.6538	38.6226	90.1395	162.0586	254.1769
	Present FSDT	7.6538	38.6226	90.1395	162.0585	254.1768
5.0	Lanhe [14]	4.8699	28.2918	67.2531	121.6415	191.3010
	Javaheri and Eslami [13]	4.8774	28.3389	67.4414	122.1849	192.5693
	Present TSDT	4.8665	28.2705	67.1683	121.3975	190.7334
	Present FSDT	4.8684	28.2824	67.2155	121.5334	191.0494
$T_{cr}(a/h = 10, T_m = 5^\circ)$						
0.0	Lanhe [14]	3256.310	7640.640	13853.53	20760.85	27586.74
	Javaheri and Eslami [13]	3409.821	8539.554	17089.10	29058.47	44447.67
	Present TSDT	3227.363	7484.611	13337.61	19674.28	25731.38
	Present FSDT	3227.248	7483.072	13327.95	19639.08	25641.06
1.0	Lanhe [14]	1976.297	4691.69	8619.42	13141.43	17740.25
	Javaheri and Eslami [13]	2055.00	5157.03	10327.07	17565.13	26871.21
	Present TSDT	1961.329	4609.313	8348.69	12530.97	16663.80
	Present FSDT	1961.269	4608.498	8343.41	12511.06	16611.01
5.0	Lanhe [14]	1481.30	3478.32	6288.94	9415.58	12481.59
	Javaheri and Eslami [13]	1553.34	3899.48	7809.73	13284.08	20322.53
	Present TSDT	1450.99	3317.92	5789.28	8352.37	10707.20
	Present FSDT	1467.68	3404.76	6053.10	8897.18	11587.11

is not zero or infinity. This difference is attributed to the fact that the TSDT includes higher-order stiffness terms that seem to have an effect on the solution when $n \neq 0$ and $n \neq \infty$.

6.3.2 Additional parametric studies

Mechanical buckling

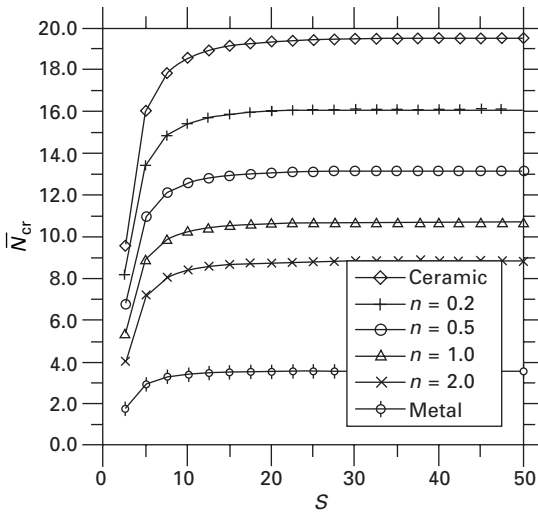
The next few examples deal with simply supported FGM plates using the TSDT. A mesh of 4×4 Q25 (full integration) in a full computational domain is utilized in all subsequent results. We present solutions for buckling of

FGM plates under mechanical loads. Two combinations of materials (metal–ceramic) are used here: aluminum–alumina (with properties given earlier) and aluminum–zirconia. The material properties of the zirconia are

$$E_c = 151 \text{ GPa}, \quad K_c = 2.09 \text{ W/mK}, \quad \alpha_c = 10 \times 10^{-6} (1/^\circ\text{C}), \quad \nu_c = 0.3$$

Figure 6.3 and 6.4 show the dimensionless critical loads of functionally graded ceramic–metal square plates under uniaxial compression versus the side-to-thickness ratio S . Curves are plotted for different volume fraction exponents n . The following dimensionless critical load parameter is employed:

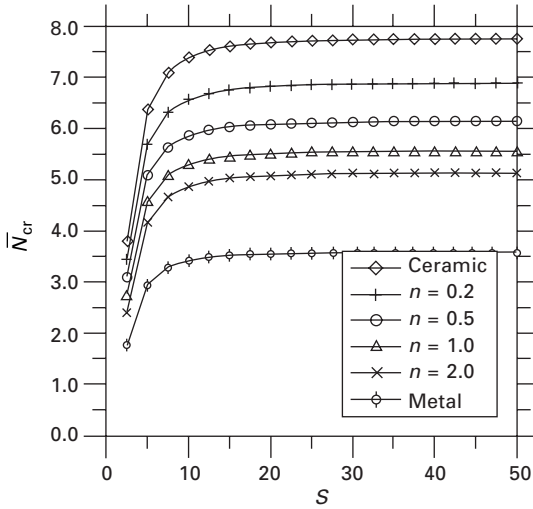
$$\bar{N}_{cr} = \frac{N_{cr} b^2}{E_m h^3}, \quad S = \frac{a}{h}$$



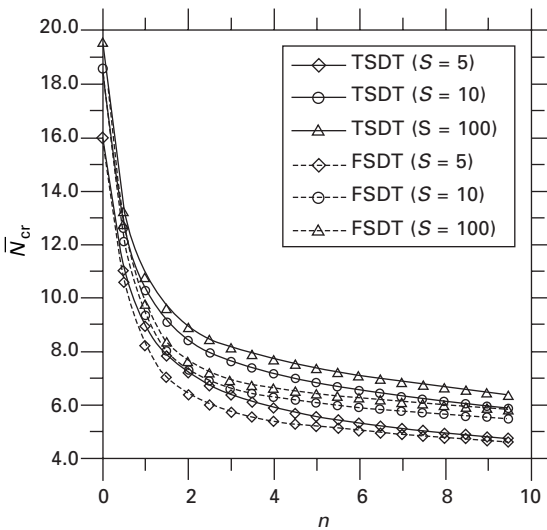
6.3 Effect of the ratio a/h on the critical buckling load of FGM square plates under uniaxial compression (aluminum–alumina).

As expected, the critical load increases when the volume fraction exponent decreases since ceramic has a higher Young’s modulus than metal. It is also noticed that the critical load tends to asymptotically reach some value when the ratio S increases. For S equal to 20 we can expect constant dimensionless critical load.

The effect of the volume fraction exponent on the critical buckling loads of FGM square plates under uniaxial compression is illustrated in Fig. 6.5 and 6.6 for two different ceramic–metal materials. The present FSDT and TSDT are compared for ratios $S = 5, 10, 100$. In all results the FSDT gives smaller critical loads than the TSDT. The difference between both formulations increases for FGM plates. However, for fully ceramic or fully metal plates the difference is negligible.



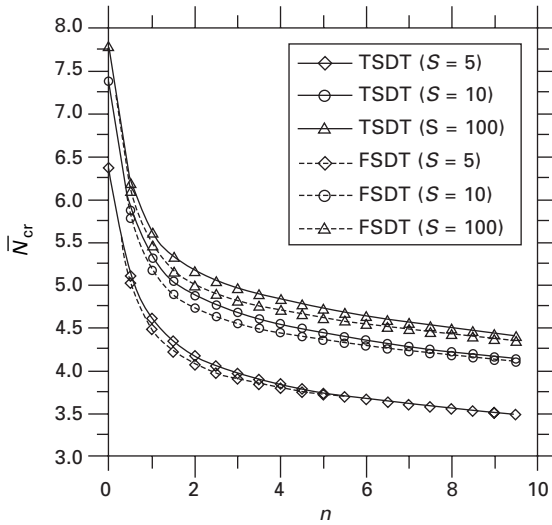
6.4 Effect of the ratio a/h on the critical buckling load of FGM square plates under uniaxial compression (aluminum–zirconia).



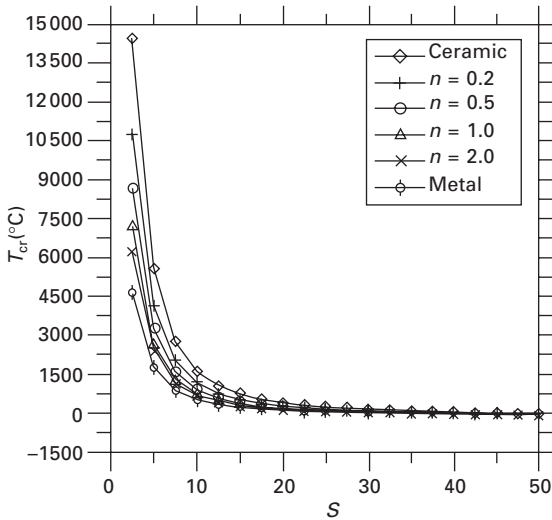
6.5 Effect of the volume fraction exponent on the critical buckling load of FGM square plates under uniaxial compression (aluminum–alumina).

Thermal buckling

In the following examples we present results for the critical buckling temperature of FGM square plates with simply-supported boundary conditions and aluminum–alumina material. Figure 6.7 contains the buckling temperature

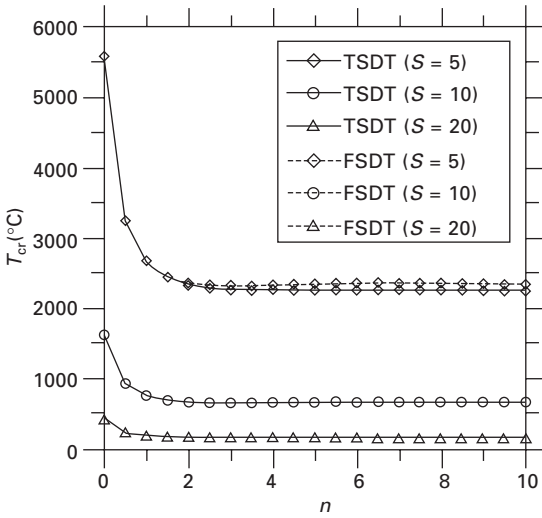


6.6 Effect of the volume fraction exponent on the critical buckling load of FGM square plates under uniaxial compression (aluminum–zirconia).



6.7 Effect of the ratio a/h on the critical buckling temperature of FGM square plates under uniform temperature rise (aluminum–alumina).

under uniform temperature rise versus the ratio S for different values of the volume fraction exponent n . It is seen that the critical temperature decreases gradually when the ratio S increases. For values of S greater than 50 we can expect the same constant response for the critical temperature. Figure 6.8



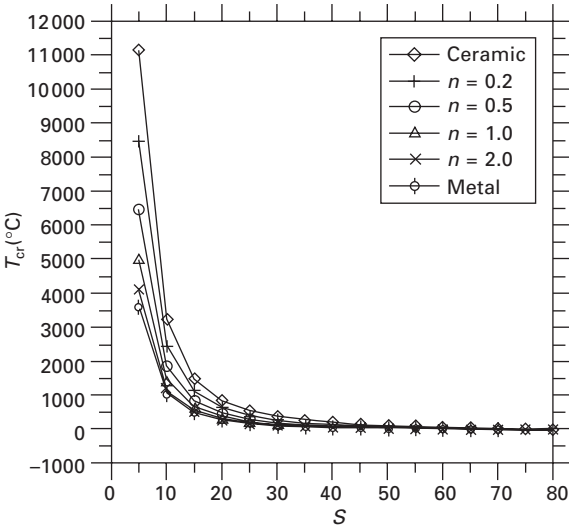
6.8 Effect of the volume fraction exponent on the critical buckling temperature of FGM square plates under uniform temperature rise (aluminum–alumina).

illustrates the effect of the volume fraction exponent on the critical buckling temperature of FGM plates under uniform temperature rise. Small changes in the critical temperature are observed for volume fraction exponent n greater than 2. Again, for thick FGM plates we note slight differences in the results for the FSDT and TSDT.

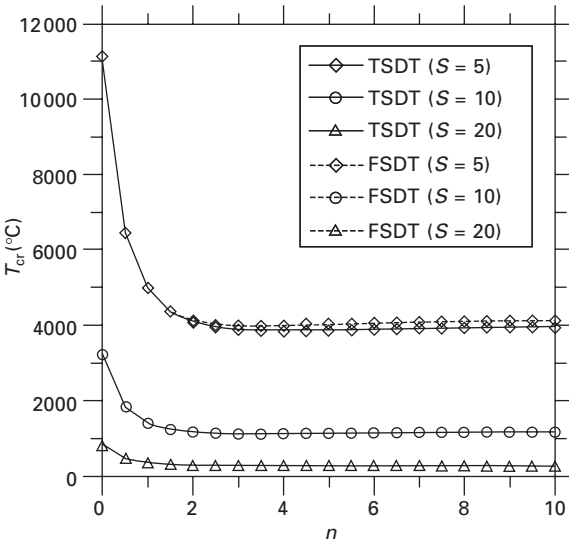
Figures 6.9 and 6.10 show the critical buckling temperature of FGM plates under linear temperature change across the thickness, while Figs 6.11 and 6.12 present the critical temperature under nonlinear temperature change across the thickness. The temperature rises 5 °C in the metal-rich surface of the plate. Similarly to the case of the uniform temperature raise, the critical temperature for values of S greater than 50 decreases very slowly (Figs 6.9 and 6.11). Finally, we note again that thick, homogeneous plates show smaller differences in the results of the FSDT and TSDT (Figs 6.10 and 6.12) than for FGM plates.

6.4 Concluding remarks

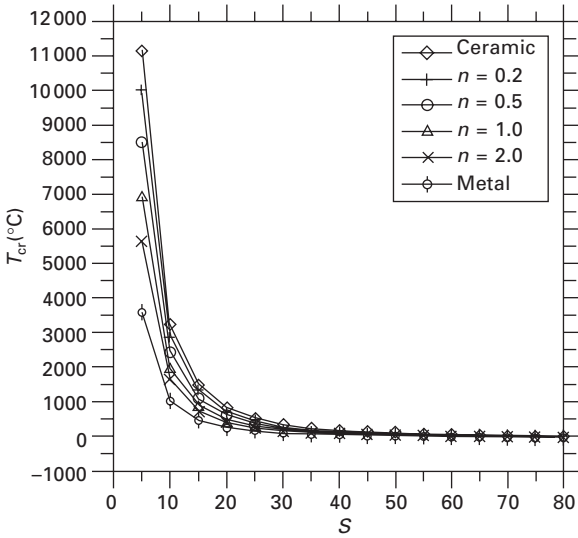
In the present study, the mechanical and thermal buckling of functionally graded plates has been examined, using the third-order deformation theory. The formulation consists of seven independent variables. Results of the first-order theory also have been included here. The gradation of properties through the thickness was assumed to be of the power law type, yet, material properties are considered temperature-independent. Analytical expressions for material



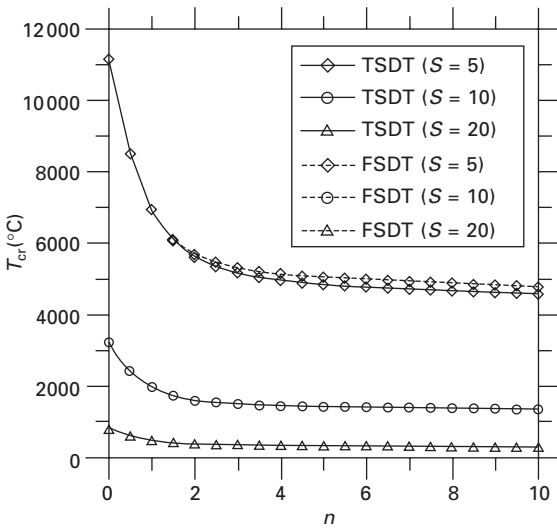
6.9 Effect of the ratio a/h on the critical buckling temperature of FGM square plates under linear temperature change across the thickness (aluminum–alumina).



6.10 Effect of the volume fraction exponent on the critical buckling temperature of FGM square plates under linear temperature change across the thickness (aluminum–alumina).



6.11 Effect of the ratio a/h on the critical buckling temperature of FGM square plates under nonlinear temperature change across the thickness (aluminum–alumina).



6.12 Effect of the volume fraction exponent on the critical buckling temperature of FGM square plates under nonlinear temperature change across the thickness (aluminum–alumina).

stiffness coefficients of the functionally graded plate were employed. A displacement finite element model for stability problems was derived with C° -continuity elements and high-order interpolation degrees. It is known that these types of element mitigate shear locking observed in shear deformable theories. Comparison of our results with others found in the literature validates the present formulation. As expected, it is found that the critical load or critical temperature of FGM plates lies between that of the fully ceramic and fully metal plates. It is noticed that the critical temperature change decreases when the volume fraction exponent n increases. The same response is seen when the ratio a/h increases. The effect of the shear deformation is significant (see Table 6.6), especially for thick plates, hence it cannot be neglected. Finally, differences in the results of the TSDT and FSDT are minor but more significant for FGM plates than those of homogeneous plates (i.e. fully ceramic or fully metal plates).

6.5 Acknowledgement

The first author gratefully acknowledges the support by the Oscar S. Wyatt Endowed professorship.

6.6 References

1. Koizumi, M., 'FGM activities in Japan,' *Compos. Part B: Engng.* **28B**, pp. 1–4, 1997.
2. Yamanouchi, M., Koizumi, M., Hirai, T. and Shiota, I., (eds.), *Proc. First Int. Sympos. Functionally Graded Materials*, Japan 1990.
3. Tanigawa, Y., Matsumoto M. and Akai, T., 'Optimization of material composition to minimize thermal stresses in nonhomogeneous plate subjected to unsteady heat supply,' *Japan Society of Mechanical Engineers International Series A* **40**(1), pp. 84–93, 1997.
4. Takezono, S., Tao, K., Inamura E. and Inoue, M., 'Thermal stress and deformation in functionally graded material shells of revolution under thermal loading due to fluid,' *Japan Society of Mechanical Engineers International Series A* **62**(594), pp. 474–481, 1996.
5. Paulino, G.H., Fannjiang, A.C. and Chan, J.S., 'Gradient elasticity theory for mode III fracture in functionally graded materials – Part A: Crack perpendicular to the material gradation,' *ASME Journal of Applied Mechanics* **70**, pp. 531–542, 2003.
6. Praveen, G.N. and Reddy, J.N., 'Nonlinear transient thermoelastic analysis of functionally graded ceramic-metal plates,' *International Journal of Solids and Structures* **35**, pp. 4457–4476, 1998.
7. Reddy, J.N. and Chin, C.D., 'Thermomechanical analysis of functional cylinders and plates,' *Journal of Thermal Stresses* **21**, pp. 593–626, 1998.
8. Tauchert, T.R., 'Thermal buckling of thick antisymmetric angle-ply laminates,' *Journal of Thermal Stresses* **10**, pp. 113–124, 1987.
9. Huang, N.N. and Tauchert, T.R., 'Postbuckling response of antisymmetric angle-ply laminates to uniform temperature loading,' *Acta Mechanical* **72**, pp. 173–183, 1989.

10. Meyers, C.A. and Hyer, M.W., 'Thermal buckling and postbuckling of symmetrically laminated composite plates,' *Journal of Thermal Stresses* **14**, pp. 519–540, 1991.
11. Shiau, L.C. and Kuo, S.Y., 'Thermal buckling of composite sandwich plates,' *Mechanics Based Design of Structures and Machinery* **32**, pp. 57–72, 2004.
12. Feldman, E. and Aboudi, J., 'Buckling analysis of functionally graded plates subjected to uniaxial loading,' *Composite Structures* **38**, pp. 29–36, 1997.
13. Javaheri, R. and Eslami, M.R., 'Thermal buckling of functionally graded plates,' *AIAA Journal* **40**, pp. 162–169, 2002.
14. Lanhe, W., 'Thermal buckling of a simply supported moderately thick rectangular FGM plate,' *Composite Structures* **64**, pp. 211–218, 2004.
15. Shen, H.S., 'Postbuckling analysis of axially loaded functionally graded cylindrical panels in thermal environments,' *International Journal of Solids and Structures*, **39**, pp. 5991–6010, 2002.
16. Na, K.S. and Kim, J.H., 'Three-dimensional thermal buckling analysis of functionally graded materials,' *Composites Part B: Engineering* **35**, pp. 429–437, 2004.
17. Reddy, J.N., *Mechanics of Laminated Composite Plates and Shells: Theory and Analysis*, CRC Press, 2nd edition, Boca Raton, Florida 2004.
18. Reddy, J.N., 'A simple higher-order theory for laminated composite plates,' *ASME Journal of Applied Mechanics* **51**, pp. 745–752, 1984.
19. Reddy, J.N. and Arciniega, R.A. 'Shear deformation plate and shell theories from Stavsky to present,' *Mechanics of Advanced Materials and Structures*, **11**(6), 535–582, 2004.
20. Putcha, N.S. and Reddy, J.N., 'Stability and natural vibration analysis of laminated plates by using a mixed element based on a refined plate theory,' *Journal of Sound and Vibration* **104**, pp. 285–300, 1986.
21. Nayak, A.K., Moy, S.J. and Sheno, R.A., 'Free vibration analysis of composite sandwich plates based on Reddy's higher-order theory,' *Composites Part B: Engineering* **33**, pp. 505–519, 2002.
22. Suresh, S. and Mortensen, A., *Fundamentals of Functionally Graded Materials*, IOM Commun. Ltd, Cambridge, UK 1998.
23. Brush, D.O. and Bo Almroth, O., *Buckling of Bars, Plates, and Shells*, McGraw-Hill, New York, 1975.
24. Reddy, J.N., *Energy Principles and Variational Methods in Applied Mechanics*, John Wiley & Sons, Inc., New York 2002.
25. Setoodeh, A.R. and Karami, G., 'Static, free vibration and buckling analysis of anisotropic thick laminated composite plates on distributed and point elastic supports using a 3-D layer-wise FEM,' *Engineering Structures* **26**, pp. 211–220, 2004.
26. Xiang, Y., Kitipornchai, S. and Liew, K.M., 'Buckling and vibration of thick laminates on Pasternak foundations,' *ASCE Journal of Engineering Mechanics* **122**(1), pp. 54–63, 1996.
27. Reddy, J.N. and Khdeir, A.A., 'Buckling and vibration of laminated composite plates using various plate theories,' *AIAA Journal* **27**, pp. 1808–1817, 1989.
28. Noor, A.K., 'Stability of multilayered composite plates,' *Fibre Science and Technology* **8**, pp. 181–189, 1975.
29. Thangaratnam, K.R., Palaninathan, R. and Ramachandran, J., 'Thermal buckling of composite laminated plates,' *Computers & Structures* **32**, pp. 1117–1124, 1989.

Thermal buckling and postbuckling of laminated plates

H-S S H E N, Shanghai Jiao Tong University,
People's Republic of China

7.1 Introduction

Designs of airframes for high-speed flight and spacecraft structures have to consider carefully the effect of the thermal environment on structural and material behavior. The plate structures are often subjected to severe thermal environments during launch and re-entry and may have significant and unavoidable initial geometric imperfections. It is essential to understand the problems associated with the determination of the buckling and postbuckling of laminated plates under such environmental conditions for a better understanding and exploitation of a plate's load-carrying capacity.

Thornton has presented his works on thermal buckling of plates and shells (Thornton 1993) and Noor and Burton (1992) described computational models for high-temperature, multilayered composite plates and shells. When the thermal load exceeds the plate's critical buckling temperature, nonlinear strain-displacement relations have to be employed. As a result, a set of nonlinear equations will appear no matter what kind of analysis method is used. Huang and Tauchert (1988) and Meyers and Hyer (1991) investigated the thermal buckling and postbuckling response of antisymmetric angle-ply and symmetric laminated plates, respectively, subjected to uniform temperature rise using the Rayleigh–Ritz method. They found that as the temperature increases, the out-of-plane displacements increase even for small deflections. Singh and Rao (1993) also studied thermal postbuckling response of antisymmetric cross-ply laminated plates subjected to uniform temperature rise using the Rayleigh–Ritz method. Chen and Chen (1989) calculated the thermal postbuckling response of laminated plates subjected to tent-like temperature field by the finite element method (FEM). Shi *et al.* (1999) employed finite elements in modal coordinates to investigate the thermal postbuckling behavior of laminated plates subjected to uniform temperature rise. They confirmed that the postbuckling deflection was not given by any one of the linear buckling modes but by a combination of them. These

studies assumed only perfectly flat initial configurations, and initial geometric imperfection of the plate was usually not accounted for. Shen and Lin (1995) provided the thermal postbuckling analysis for antisymmetric angle-ply and symmetric cross-ply laminated plates subjected to uniform and one-way parabolic temperature field. An analytical approach using a mixed Galerkin-perturbation method was employed. Initial imperfections of the plate were considered in order to study their influence on the thermal postbuckling response of the plate subjected to thermal loading. This work was then extended to the case of laminated plates resting on Pasternak-type and softening nonlinear elastic foundations by Shen and Williams (1997a,b).

All the above results are for thin plates based on the classical laminated plate theory, that is, the theory based on the Kirchhoff–Love hypothesis. It is well known that this is adequate for plates when the thickness to side ratio is very small. Owing to low transverse shear moduli relative to the in-plane Young's moduli, transverse shear deformations are even more pronounced in composite laminates. Moreover, the lay-up of loaded laminates may play a much more important role for thick plates than for thin ones. As a result, the analysis of moderately thick laminated plates requires the use of shear deformation plate theory. Among those, Bhimaraddi and Chandrashekhara (1993) investigated the nonlinear response, including postbuckling response, of antisymmetric angle-ply laminated plates subjected to uniform temperature rise based on a parabolic shear deformation plate theory. In their analysis, since the out-of-plane deflection was assumed to have the form as the linear buckling mode, the solutions cannot produce more accurate results. Shen (1997a,1999) provided the thermal postbuckling analysis for antisymmetric angle-ply and symmetric cross-ply laminated plates with or without elastic foundations subjected to uniform and non-uniform tent-like or two-way parabolic temperature field based on a higher-order shear deformation plate theory. Effects of foundation stiffness, thermal load ratio, transverse shear deformation, plate aspect ratio, total number of plies, fiber orientation, and initial geometric imperfections were studied parametrically.

In the above studies the boundary conditions are considered to be simply supported (SSSS) and/or clamped (CCCC). The thermal postbuckling analysis for antisymmetric angle-ply laminated plates with combined simply supported and clamped boundary conditions, e.g. CCCS, CSCS, and CSSS, was presented by Nath and Shukla (2001) using Chebyshev polynomials. Lee and Lee (1997) gave the numerical analysis of thermal postbuckling and nature vibration of thermally postbuckled symmetric angle-ply laminated plates subjected to uniform temperature rise. Ganapathi and Touratier (1997) calculated thermal postbuckling response of symmetric and antisymmetric, cross-ply and angle-ply laminated plates subjected to tent-like temperature field. In these last two analyses, nonlinear finite element equations based on first order shear

deformation plate theory were formulated. Singh *et al.* (1994) and Thankam *et al.* (2003) observed the existence of secondary instability while investigating the thermal postbuckling characteristics of unsymmetric laminated plates using the finite element method based on a parabolic shear deformation plate theory. However, Leissa (1986) and Qatu and Leissa (1993) have proved that buckling may always occur for symmetric laminated plates with arbitrary in-plane loading and boundary conditions. It was also proved that for unsymmetric cross-ply laminated plates with all four edges simply supported, the bifurcation buckling did not exist due to the stretching/bending coupling effect. Since the solutions of Singh and Rao (1993), Ganapathi and Touratier (1997), Singh *et al.* (1994), and Thankam *et al.* (2003) do not satisfy equilibrium equations, the results given by them for perfect SSSS unsymmetric cross-ply laminated plates are still questionable.

The postbuckling response of laminated thin plates subjected to combined mechanical and thermal loading has been reported by Birman and Bert (1993), Shen and Williams (1996), and Shen *et al.* (1996). Noor and Peters (1992) and Noor *et al.* (1993) calculated buckling loads and postbuckling load-deflection curves for perfect, symmetrically laminated plates subjected to combined axial load and a uniform temperature rise. The analysis used a mixed finite element method and it was based on the first order shear deformation plate theory. Librescu and Souza (1993) and Librescu *et al.* (1995) studied the postbuckling response of imperfect plates, symmetrically laminated of transversely isotropic material layers, exposed to a stationary temperature field and in-plane compressive edge loads. An analytical approach using the Galerkin method and based on the first order or higher-order shear deformation plate theory was employed. This work is then extended to the case of laminated plates resting on softening nonlinear elastic foundations by Lin and Librescu (1998). Argyris and Tenek (1995) calculated the postbuckling response of imperfect, symmetric laminated plates under the combined action of both mechanical load and temperature. In the analytical approach the natural mode method was employed. The postbuckling of thermally stressed symmetric laminated plates was then examined by Tenek (2001). It is found that the $(0/90)_{2S}$ symmetric cross-ply laminated plate is very sensitive to the amount of initial thermal stressing, whereas the $(\pm 45/0/90)_S$ quasi-isotropic laminated plate exhibits less sensitivity to initial thermal stressing. Shen (1998, 2000a) provided the thermomechanical postbuckling analysis for antisymmetric angle-ply and symmetric cross-ply laminated plates with or without elastic foundations subjected to combined action of in-plane compressive loads and a uniform temperature rise. The two cases of thermal postbuckling of initially compressed plates and of compressive postbuckling of initially heated plates were considered and the formulations based on a higher-order shear deformation plate theory. Then thermal postbuckling analysis for antisymmetric angle-ply and symmetric cross-ply laminated plates with

or without elastic foundations subjected to a uniform lateral pressure and non-uniform tent-like or two-way parabolic temperature field was presented by Shen (2000b). It is found that in the case of initially pressurized plates, the thermal deflections deviate greatly from those of a plate without any lateral pressure, and at higher postbuckling loads the net deflection for preloaded plates is smaller than that for a plate without any lateral pressure. The postbuckling analysis for angle-ply and cross-ply laminated plates subjected to in-plane edge compressive loads and a linear temperature change across the plate thickness under various boundary conditions was presented by Shukla and Nath (2001, 2002) using Chebyshev polynomials. The finite element equation was formulated based on the first order shear deformation plate theory.

One of the recent advances in material and structural engineering is in the field of smart structures which incorporates adaptive materials. Oh *et al.* (2000, 2001) studied the nonlinear vibration and thermal postbuckling of piezolaminated plates with fully covered or partially distributed actuators subjected to thermal and electrical loads. In their analysis, nonlinear finite element equations based on layerwise displacement theory were formulated. Shen (2001a,b) presented the postbuckling and thermal postbuckling response of laminated plates with surface-bonded or embedded piezoelectric layers subjected to the combined action of mechanical, electric, and thermal loads. It was concluded that the minus control voltages increase the buckling temperature and decrease the postbuckled deflection at the same temperature rise, whereas the plus control voltages decrease the buckling temperature and induce larger postbuckled deflections. Functionally graded materials (FGMs) are microscopically inhomogeneous composites usually made from a mixture of metals and ceramics. Recently, Liew *et al.* (2003) studied compressive postbuckling and thermal postbuckling behavior of FGM plates with two opposite edges clamped and with surface-bonded piezoelectric actuators subjected to thermo-electro-mechanical loads. They confirmed that the FGM plates with simply supported edges, even for the FGM hybrid plate which are not fully clamped, have no bifurcation buckling loads.

In the references cited above, the material properties of the composites were assumed to be independent of temperature. Chen and Chen (1991) calculated the thermal postbuckling load-deflection curves for antisymmetric angle-ply laminated plates having linear variation of mechanical and thermal properties with temperature. In their analysis, the finite element method was used based on the classical laminated plate theory. Singh *et al.* (2001) presented thermal postbuckling response of symmetric angle-ply laminated plates subjected to uniform and linearly varying temperature rise through the thickness by using shear deformable finite element. In Chen and Chen (1991) and Singh *et al.* (2001) the results were only for perfect plates. Shen (2001c) provided thermal postbuckling analysis for perfect and imperfect shear

deformable laminated plates resting on elastic foundations. Temperature-dependent thermoelastic properties of the plates were considered and their effects on the deflection were discussed. The results reveal that the buckling temperature and thermal postbuckling load-deflection curves are always decreased by temperature dependency. The effects of hygrothermal condition on the postbuckling of shear deformable laminated plates were determined by Shen (2001d). In the analysis the material properties are considered to be dependent on temperature and moisture, which are given explicitly in terms of the fiber and matrix properties and the fiber volume ratio.

This chapter describes the thermal buckling and postbuckling of laminated plates subjected to uniform and/or non-uniform temperature rise or combined loadings. The material properties are assumed to be temperature dependent. The governing equations of the plate are based on Reddy's higher-order shear deformation plate theory that includes thermal effects. All four edges of the plate are assumed to be simply supported with no in-plane displacement. A two-step perturbation technique is employed to determine buckling temperature and postbuckling equilibrium paths. The initial geometric imperfection of the plate is taken into account but, for simplicity, its form is assumed to be the same as the initial buckling mode of the plate.

7.2 Governing equations

Consider a rectangular plate of length a , width b and constant thickness t , consisting of N plies. Each ply may be made of different materials. The plate is assumed to be geometrically imperfect, and is subjected to the combined action of mechanical, thermal, and electrical loads. As usual, the coordinate system has its origin at the corner of the plate on the mid-plane. Let \bar{U} , \bar{V} and \bar{W} be the plate displacements parallel to a right-hand set of axes (X, Y, Z) , where X is longitudinal and Z is perpendicular to the plate. $\bar{\Psi}_x$ and $\bar{\Psi}_y$ are the mid-plane rotations of the normal about the Y and X axes, respectively. Denoting the initial geometric imperfection by $\bar{W}^*(X, Y)$, let $\bar{W}(X, Y)$ be the additional deflection and $\bar{F}(X, Y)$ be the stress function for the stress resultants defined by $\bar{N}_x = \bar{F}_{,yy}$, $\bar{N}_y = \bar{F}_{,xx}$ and $\bar{N}_{xy} = -\bar{F}_{,xy}$, where a comma denotes partial differentiation with respect to the corresponding coordinates.

Reddy (1984a) developed a simple higher-order shear deformation plate theory, in which the transverse shear strains are assumed to be parabolically distributed across the plate thickness. The theory is simple in the sense that it contains the same dependent unknowns as in the first order shear deformation theory, and no shear correction factors are required. Based on Reddy's higher-order shear deformation theory with a von Kármán-type of kinematic nonlinearity (Reddy 1984b) and including thermal effects, Shen (1997b) derived a set of general von Kármán-type equations which can be expressed in terms of a stress function \bar{F} , two rotations $\bar{\Psi}_x$ and $\bar{\Psi}_y$, and a transverse

displacement \bar{W} , along with the initial geometric imperfection \bar{W}^* . They are

$$\begin{aligned} & \tilde{L}_{11}(\bar{W}) - \tilde{L}_{12}(\bar{\Psi}_x) - \tilde{L}_{13}(\bar{\Psi}_y) + \tilde{L}_{14}(\bar{F}) \\ & - \tilde{L}_{15}(\bar{N}^T) - \tilde{L}_{16}(\bar{M}^T) = \tilde{L}(\bar{W} + \bar{W}^*, \bar{F}) \end{aligned} \quad 7.1$$

$$\begin{aligned} & \tilde{L}_{21}(\bar{F}) + \tilde{L}_{22}(\bar{\Psi}_x) + \tilde{L}_{23}(\bar{\Psi}_y) - \tilde{L}_{24}(\bar{W}) - \tilde{L}_{25}(\bar{N}^T) \\ & = -\frac{1}{2}\tilde{L}(\bar{W} + 2\bar{W}^*, \bar{W}) \end{aligned} \quad 7.2$$

$$\begin{aligned} & \tilde{L}_{31}(\bar{W}) + \tilde{L}_{32}(\bar{\Psi}_x) + \tilde{L}_{33}(\bar{\Psi}_y) \\ & + \tilde{L}_{34}(\bar{F}) - \tilde{L}_{35}(\bar{N}^T) - \tilde{L}_{36}(\bar{S}^T) = 0 \end{aligned} \quad 7.3$$

$$\begin{aligned} & \tilde{L}_{41}(\bar{W}) + \tilde{L}_{42}(\bar{\Psi}_x) + \tilde{L}_{43}(\bar{\Psi}_y) + \tilde{L}_{44}(\bar{F}) \\ & - \tilde{L}_{45}(\bar{N}^T) - \tilde{L}_{46}(\bar{S}^T) = 0 \end{aligned} \quad 7.4$$

in which all linear operators $\tilde{L}_{ij}(\cdot)$ and the nonlinear operator $\tilde{L}(\cdot)$ are defined as in Shen (1997b,1999), and given in detail in Appendix A.

Three cases of thermal loading are considered, i.e.

Case 1, uniform temperature field, defined by:

$$T(X, Y, Z) = T_0 \text{ (constant)} \quad 7.5a$$

Case 2, non-uniform tent-like temperature field, defined by:

$$T(X, Y, Z) = \begin{cases} T_0 + 2T_1 \frac{Y}{b} & 0 \leq Y \leq \frac{b}{2} \\ T_0 + 2T_1 \left(1 - \frac{Y}{b}\right) & \frac{b}{2} \leq Y \leq b \end{cases} \quad 7.5b$$

Case 3, non-uniform parabolic temperature field, defined by:

$$T(X, Y, Z) = T_0 + T_1 \left[1 - \left(\frac{2X-a}{a}\right)^2\right] \left[1 - \left(\frac{2Y-b}{b}\right)^2\right] \quad 7.5c$$

in which T_0 and T_1 denote the temperature amplitude and gradient, respectively.

The forces and moments caused by elevated temperature are defined by:

$$\begin{bmatrix} \bar{N}_x^T & \bar{M}_x^T & \bar{P}_x^T \\ \bar{N}_y^T & \bar{M}_y^T & \bar{P}_y^T \\ \bar{N}_{xy}^T & \bar{M}_{xy}^T & \bar{P}_{xy}^T \end{bmatrix} = \sum_{k=1}^n \int_{t_{k-1}}^{t_k} \begin{bmatrix} A_x \\ A_y \\ A_{xy} \end{bmatrix}_k (1, Z, Z^3) T(X, Y, Z) dZ \tag{7.6a}$$

$$\begin{bmatrix} \bar{S}_x^T \\ \bar{S}_y^T \\ \bar{S}_{xy}^T \end{bmatrix} = \begin{bmatrix} \bar{M}_x^T \\ \bar{M}_y^T \\ \bar{M}_{xy}^T \end{bmatrix} - \frac{4}{3t^2} \begin{bmatrix} \bar{P}_x^T \\ \bar{P}_y^T \\ \bar{P}_{xy}^T \end{bmatrix} \tag{7.6b}$$

in which

$$\begin{bmatrix} A_x \\ A_y \\ A_{xy} \end{bmatrix} = - \begin{bmatrix} \bar{Q}_{11} & \bar{Q}_{12} & \bar{Q}_{16} \\ \bar{Q}_{12} & \bar{Q}_{22} & \bar{Q}_{26} \\ Q_{16} & \bar{Q}_{26} & \bar{Q}_{66} \end{bmatrix} \begin{bmatrix} c^2 & s^2 \\ s^2 & c^2 \\ 2cs & -2cs \end{bmatrix} \begin{bmatrix} \alpha_{11} \\ \alpha_{22} \end{bmatrix} \tag{7.7}$$

where α_{11} and α_{22} are the thermal expansion coefficients measured in the longitudinal and transverse directions, respectively, and \bar{Q}_{ij} are the transformed elastic constants, defined by:

$$\begin{bmatrix} \bar{Q}_{11} \\ \bar{Q}_{12} \\ \bar{Q}_{22} \\ \bar{Q}_{16} \\ \bar{Q}_{26} \\ \bar{Q}_{66} \end{bmatrix} = \begin{bmatrix} c^4 & 2c^2s^2 & s^4 & 4c^2s^2 \\ c^2s^2 & c^4 + s^4 & c^2s^2 & -4c^2s^2 \\ s^4 & 2c^2s^2 & c^4 & 4c^2s^2 \\ c^3s & cs^3 - c^3s & -cs^3 & -2cs(c^2 - s^2) \\ cs^3 & c^3s - cs^3 & -c^3s & 2cs(c^2 - s^2) \\ c^2s^2 & -2c^2s^2 & c^2s^2 & (c^2 - s^2)^2 \end{bmatrix} \begin{bmatrix} Q_{11} \\ Q_{12} \\ Q_{22} \\ Q_{66} \end{bmatrix} \tag{7.8a}$$

$$\begin{bmatrix} \bar{Q}_{44} \\ \bar{Q}_{45} \\ \bar{Q}_{55} \end{bmatrix} = \begin{bmatrix} c^2 & s^2 \\ -cs & cs \\ s^2 & c^2 \end{bmatrix} \begin{bmatrix} Q_{44} \\ Q_{55} \end{bmatrix} \tag{7.8b}$$

where

$$Q_{11} = \frac{E_{11}}{(1 - \nu_{12}\nu_{21})}, Q_{22} = \frac{E_{22}}{(1 - \nu_{12}\nu_{21})}, Q_{12} = \frac{\nu_{21}E_{11}}{(1 - \nu_{12}\nu_{21})}, \tag{7.8c}$$

$$Q_{44} = G_{23}, Q_{55} = G_{13}, Q_{66} = G_{12}$$

$E_{11}, E_{22}, G_{12}, G_{13}, G_{23}, \nu_{12}$ and ν_{21} have their usual meanings, and $c = \cos \theta, s = \sin \theta$ 7.8d

where θ is the lamination angle with respect to the plate X -axis.

All four edges of the plate are assumed to be simply supported with no in-plane displacements. The boundary conditions are:

$X = 0, a$:

$$\bar{W} = \bar{\Psi}_y = 0 \tag{7.9a}$$

$$\bar{U} = 0 \tag{7.9b}$$

$$\bar{N}_{xy} = 0, \bar{M}_x = \bar{P}_x = 0 \tag{7.9c}$$

$Y = 0, b$:

$$\bar{W} = \bar{\Psi}_x = 0 \tag{7.9d}$$

$$\bar{V} = 0 \tag{7.9e}$$

$$\bar{N}_{xy} = 0, \bar{M}_y = \bar{P}_y = 0 \tag{7.9f}$$

where \bar{M}_x and \bar{M}_y are the bending moments and \bar{P}_x and \bar{P}_y are the higher-order moments as defined in Reddy (1984a, b).

The condition expressing the immovability condition, $\bar{U} = 0$ (on $X = 0, a$) and $\bar{V} = 0$ (on $Y = 0, b$), is fulfilled on the average sense as

$$\int_0^b \int_0^a \frac{\partial \bar{U}}{\partial X} dX dY = 0 \tag{7.10a}$$

or

$$\begin{aligned} & \int_0^b \int_0^a \left\{ \left[\left(A_{11}^* \frac{\partial^2 \bar{F}}{\partial Y^2} + A_{12}^* \frac{\partial^2 \bar{F}}{\partial X^2} - A_{16}^* \frac{\partial^2 \bar{F}}{\partial X \partial Y} \right) \right. \right. \\ & + \left(B_{11}^* - \frac{4}{3t^2} E_{11}^* \right) \frac{\partial \bar{\Psi}_x}{\partial X} + \left(B_{12}^* - \frac{4}{3t^2} E_{12}^* \right) \frac{\partial \bar{\Psi}_y}{\partial Y} \\ & + \left(B_{16}^* - \frac{4}{3t^2} E_{16}^* \right) \left(\frac{\partial \bar{\Psi}_x}{\partial X} + \frac{\partial \bar{\Psi}_y}{\partial Y} \right) \\ & - \left. \frac{4}{3t^2} \left(E_{11}^* \frac{\partial^2 \bar{W}}{\partial X^2} + E_{12}^* \frac{\partial^2 \bar{W}}{\partial Y^2} + 2E_{16}^* \frac{\partial^2 \bar{W}}{\partial X \partial Y} \right) \right] - \frac{1}{2} \left(\frac{\partial \bar{W}}{\partial X} \right)^2 \\ & - \left. \frac{\partial \bar{W}}{\partial X} \frac{\partial \bar{W}^*}{\partial X} - (A_{11}^* \bar{N}_x^T + A_{12}^* \bar{N}_y^T + A_{16}^* \bar{N}_{xy}^T) \right\} dX dY = 0 \tag{7.10b} \end{aligned}$$

and

$$\int_0^a \int_0^b \frac{\partial \bar{V}}{\partial Y} dY dX = 0 \tag{7.10c}$$

or

$$\int_0^a \int_0^b \left\{ \left[\left(A_{22}^* \frac{\partial^2 \bar{F}}{\partial X^2} + A_{12}^* \frac{\partial^2 \bar{F}}{\partial Y^2} - A_{26}^* \frac{\partial^2 \bar{F}}{\partial X \partial Y} \right) + \left(B_{21}^* - \frac{4}{3t^2} E_{21}^* \right) \frac{\partial \bar{\Psi}_x}{\partial X} + \left(B_{22}^* - \frac{4}{3t^2} E_{22}^* \right) \frac{\partial \bar{\Psi}_y}{\partial Y} \right] + \left(B_{26}^* - \frac{4}{3t^2} E_{26}^* \right) \left(\frac{\partial \bar{\Psi}_x}{\partial Y} + \frac{\partial \bar{\Psi}_y}{\partial X} \right) - \frac{4}{3t^2} \left(E_{21}^* \frac{\partial^2 \bar{W}}{\partial X^2} + E_{22}^* \frac{\partial^2 \bar{W}}{\partial Y^2} + 2E_{26}^* \frac{\partial^2 \bar{W}}{\partial X \partial Y} \right) \right] - \frac{1}{2} \left(\frac{\partial \bar{W}}{\partial Y} \right)^2 - \frac{\partial \bar{W}}{\partial Y} \frac{\partial \bar{W}^*}{\partial Y} - (A_{12}^* \bar{N}_x^T + A_{22}^* \bar{N}_y^T + A_{26}^* N_{xy}^T) \right\} dY dX = 0 \quad 7.10d$$

In the above equations and what follows, the reduced stiffness matrices $[A_{ij}^*]$, $[B_{ij}^*]$, $[D_{ij}^*]$, $[E_{ij}^*]$, $[F_{ij}^*]$ and $[H_{ij}^*]$ ($i, j = 1, 2, 6$) are functions of temperature, determined through relationships (Shen 1997b, 1999)

$$A^* = A^{-1}, B^* = -A^{-1}B, D^* = D - BA^{-1}B, E^* = -A^{-1}E, \\ F^* = F - EA^{-1}B, H^* = H - EA^{-1}E \quad 7.11$$

where A_{ij} , B_{ij} etc., are the plate stiffnesses, defined in the standard way, i.e.

$$(A_{ij}, B_{ij}, D_{ij}, E_{ij}, F_{ij}, H_{ij}) \\ = \sum_{k=1}^{t_k} \int_{t_{k-1}}^{t_k} (\bar{Q}_{ij})_k (1, Z, Z^2, Z^3, Z^4, Z^6) dZ \quad (i, j = 1, 2, 6) \quad 7.12a$$

$$(A_{ij}, D_{ij}, F_{ij}) = \sum_{k=1}^{t_k} \int_{t_{k-1}}^{t_k} (\bar{Q}_{ij})_k (1, Z^2, Z^4) dZ \quad (i, j = 4, 5) \quad 7.12b$$

7.3 Analytical method and asymptotic solutions

Perturbation technique is a powerful tool for solving nonlinear problems, e.g. nonlinear bending, postbuckling, and nonlinear vibration of shear deformable laminated plates (Shen 1997a, 1998, 1999, 2000a,b,c, 2002, 2004, Huang and Shen 2004, Huang *et al.* 2004). Before proceeding, it is convenient first to define the following dimensionless quantities:

$$x = \pi X/a, y = \pi Y/b, \beta = a/b, \\ (W, W^*) = (\bar{W}, \bar{W}^*)/[D_{11}^* D_{22}^* A_{11}^* A_{22}^*]^{1/4}$$

$$\begin{aligned}
 F &= \bar{F} / [D_{11}^* D_{22}^*]^{1/2}, (\Psi_x, \Psi_y) = (\bar{\Psi}_x, \bar{\Psi}_y) a / \pi [D_{11}^* D_{22}^* A_{11}^* A_{22}^*]^{1/4} \\
 \gamma_{14} &= [D_{22}^* / D_{11}^*]^{1/2}, \gamma_{24} = [A_{11}^* / A_{22}^*]^{1/2}, \gamma_5 = -A_{12}^* / A_{22}^* \\
 (M_x, M_y, P_x, P_y) \\
 &= (\bar{M}_x, \bar{M}_y, 4\bar{P}_x / 3t^2, 4\bar{P}_y / 3t^2) a^2 / \pi^2 D_{11}^* [D_{11}^* D_{22}^* A_{11}^* A_{22}^*]^{1/4} \\
 (\gamma_{T1}, \gamma_{T2}) &= (A_x^T, A_y^T) a^2 / \alpha_0 \pi^2 [D_{11}^* D_{22}^*]^{1/2} \\
 \gamma_{T3} &= (B_{xy}^T - 4E_{xy}^T / 3t^2) a^2 / \alpha_0 \pi^2 [D_{11}^* D_{22}^* A_{11}^* A_{22}^*]^{1/4} \quad 7.13
 \end{aligned}$$

Let $\lambda_T = \alpha_0 T_i$, where $i = 0$ for uniform temperature distribution and $i = 1$ otherwise, and let

$$\alpha_{11} = a_{11} \alpha_0, \alpha_{22} = a_{22} \alpha_0 \quad 7.14$$

where α_0 is an arbitrary reference value.

In Eq. (7.13), A_x^T, A_y^T, B_{xy}^T and E_{xy}^T are defined by:

$$(A_x^T, A_y^T) = - \sum_{k=1}^{t_k} \int_{t_{k-1}}^{t_k} (A_x, A_y)_k dZ \quad 7.15a$$

$$(B_{xy}^T, E_{xy}^T) = - \sum_{k=1}^{t_k} \int_{t_{k-1}}^{t_k} (Z, Z^3) (A_{xy})_k dZ \quad 7.15b$$

The nonlinear Eqs. (7.1)–(7.4) may then be written in dimensionless form as:

$$\begin{aligned}
 L_{11}(W) - L_{12}(\Psi_x) - L_{13}(\Psi_y) + \gamma_{14} L_{14}(F) \\
 = \gamma_{14} \beta^2 L(W + W^*, F) \quad 7.16
 \end{aligned}$$

$$\begin{aligned}
 L_{21}(F) + \gamma_{24} L_{22}(\Psi_x) + \gamma_{24} L_{23}(\Psi_y) - \gamma_{24} L_{24}(W) \\
 + C_1 = -\frac{1}{2} \gamma_{24} \beta^2 L(W + 2W^*, W) \quad 7.17
 \end{aligned}$$

$$L_{31}(W) + L_{32}(\Psi_x) + L_{33}(\Psi_y) + \gamma_{14} L_{34}(F) + C_2 = 0 \quad 7.18$$

$$L_{41}(W) + L_{42}(\Psi_x) + L_{43}(\Psi_y) + \gamma_{14} L_{44}(F) = 0 \quad 7.19$$

where the nondimensional linear operators $L_{ij}(\cdot)$ and the nonlinear operator $L(\cdot)$ are defined as in Appendix B.

The boundary conditions expressed by Eq. (7.9) become:

$x = 0, \pi$:

$$W = \Psi_y = 0 \quad 7.20a$$

$$\delta_x = 0 \quad 7.20b$$

$$F_{,xy} = M_x = P_x = 0 \quad 7.20c$$

$y = 0, \pi$:

$$W = \Psi_x = 0 \quad 7.20d$$

$$\delta_y = 0 \quad 7.20e$$

$$F_{,xy} = M_y = P_y = 0 \quad 7.20f$$

in which:

$$\begin{aligned} \delta_x = & -\frac{1}{4\pi^2\beta^2\gamma_{24}} \int_0^\pi \int_0^\pi \left\{ \left[\gamma_{24}^2\beta^2 \frac{\partial^2 F}{\partial y^2} - \gamma_5 \frac{\partial^2 F}{\partial x^2} \right. \right. \\ & + \gamma_{24} \left(\gamma_{511} \frac{\partial \Psi_x}{\partial x} + \gamma_{233} \beta \frac{\partial \Psi_y}{\partial y} \right) \\ & + \gamma_{24}\gamma_{223} \left(\beta \frac{\partial \Psi_x}{\partial y} + \frac{\partial \Psi_y}{\partial x} \right) \\ & \left. - \gamma_{24} \left(\gamma_{611} \frac{\partial^2 W}{\partial x^2} + \gamma_{244}\beta^2 \frac{\partial^2 W}{\partial y^2} + 2\gamma_{516}\beta \frac{\partial^2 W}{\partial x \partial y} \right) \right] \\ & - \frac{1}{2}\gamma_{24} \left(\frac{\partial W}{\partial x} \right)^2 - \gamma_{24} \frac{\partial W}{\partial x} \frac{\partial W^*}{\partial x} \\ & \left. + (\gamma_{24}^2\gamma_{T1} - \gamma_5\gamma_{T2})\lambda_T C_3 \right\} dx dy \quad 7.21a \end{aligned}$$

$$\begin{aligned} \delta_y = & -\frac{1}{4\pi^2\beta^2\gamma_{24}} \int_0^\pi \int_0^\pi \left\{ \left[\frac{\partial^2 F}{\partial x^2} - \gamma_5\beta^2 \frac{\partial^2 F}{\partial y^2} \right. \right. \\ & + \gamma_{24} \left(\gamma_{220} \frac{\partial \Psi_x}{\partial x} + \gamma_{522}\beta \frac{\partial \Psi_y}{\partial y} \right) \\ & + \gamma_{24}\gamma_{230} \left(\beta \frac{\partial \Psi_x}{\partial y} + \frac{\partial \Psi_y}{\partial x} \right) \\ & \left. - \gamma_{24} \left(\gamma_{240} \frac{\partial^2 W}{\partial x^2} + \gamma_{622}\beta^2 \frac{\partial^2 W}{\partial y^2} + 2\gamma_{526}\beta \frac{\partial^2 W}{\partial x \partial y} \right) \right] \\ & - \frac{1}{2}\gamma_{24}\beta^2 \left(\frac{\partial W}{\partial y} \right)^2 - \gamma_{24}\beta^2 \frac{\partial W}{\partial y} \frac{\partial W^*}{\partial y} \\ & \left. + (\gamma_{T2} - \gamma_5\gamma_{T1})\lambda_T C_3 \right\} dy dx \quad 7.21b \end{aligned}$$

In Eq. (7.21) and what follows, γ_{ijk} are defined as in Appendix B.

Now we are in a position to solve Eqs. (7.16)–(7.19) with boundary conditions (7.20). A two-step perturbation technique is developed, for which the small perturbation parameter has no physical meaning at the first step, and is then replaced by a dimensionless deflection at the second step. The essence of this procedure, in the present case, is to assume that:

$$W(x, y, \varepsilon) = \sum_{j=1} \varepsilon^j w_j(x, y), F(x, y, \varepsilon) = \sum_{j=0} \varepsilon^j f_j(x, y)$$

$$\Psi_x(x, y, \varepsilon) = \sum_{j=1} \varepsilon^j \psi_{xj}(x, y), \Psi_y(x, y, \varepsilon) = \sum_{j=1} \varepsilon^j \psi_{yj}(x, y) \quad 7.22$$

where ε is a small perturbation parameter and the first term of $w_j(x, y)$ is assumed to have the form:

$$w_1(x, y) = A_{11}^{(1)} \sin mx \sin ny \quad 7.23$$

and the initial geometric imperfection is assumed to have a similar form:

$$W^*(x, y, \varepsilon) = \varepsilon a_{11}^* \sin mx \sin ny = \varepsilon \mu A_{11}^{(1)} \sin mx \sin ny \quad 7.24$$

where $\mu = a_{11}^*/A_{11}^{(1)}$ is the imperfection parameter.

Substituting Eq. (7.22) into Eqs. (7.16)–(7.19) and collecting the terms of the same order of ε , we derive a set of perturbation equations which can be written, for example, as:

$$O(\varepsilon^0): L_{14}(f_0) = 0 \quad 7.25a$$

$$L_{21}(f_0) + C_1 = 0 \quad 7.25b$$

$$L_{34}(f_0) + C_2 = 0 \quad 7.25c$$

$$L_{44}(f_0) = 0 \quad 7.25d$$

$$O(\varepsilon^1): L_{11}(w_1) - L_{12}(\psi_{x1}) - L_{13}(\psi_{y1}) + \gamma_{14}L_{14}(f_1)$$

$$= \gamma_{14}\beta^2 L(w_1 + W^*, f_0) \quad 7.26a$$

$$L_{21}(f_1) + \gamma_{24}L_{22}(\psi_{x1}) + \gamma_{24}L_{23}(\psi_{y1}) - \gamma_{24}L_{24}(w_1) = 0 \quad 7.26b$$

$$L_{31}(w_1) + L_{32}(\psi_{x1}) - L_{33}(\psi_{y1}) + \gamma_{14}L_{34}(f_1) = 0 \quad 7.26c$$

$$L_{41}(w_1) - L_{42}(\psi_{x1}) + L_{43}(\psi_{y1}) + \gamma_{14}L_{44}(f_1) = 0 \quad 7.26d$$

$$O(\varepsilon^2): L_{11}(w_2) - L_{12}(\psi_{x2}) - L_{13}(\psi_{y2}) + \gamma_{14}L_{14}(f_2)$$

$$= \gamma_{14}\beta^2 [L(w_2, f_0) + L(w_1 + W^*, f_1)] \quad 7.27a$$

$$L_{21}(f_2) + \gamma_{24}L_{22}(\psi_{x2}) + \gamma_{24}L_{23}(\psi_{y2}) - \gamma_{24}L_{24}(w_2)$$

$$= -\frac{1}{2}\gamma_{24}\beta^2 L(w_1 + 2W^*, w_1) \quad 7.27b$$

$$L_{31}(w_2) + L_{32}(\psi_{x2}) - L_{33}(\psi_{y2}) + \gamma_{14}L_{34}(f_2) = 0 \quad 7.27c$$

$$L_{41}(w_2) - L_{42}(\psi_{x2}) + L_{43}(\psi_{y2}) + \gamma_{14}L_{44}(f_2) = 0 \quad 7.27d$$

By using Eqs. (7.23) and (7.24) to solve these perturbation equations of each order, the amplitudes of the terms $w_j(x, y)$, $f_j(x, y)$, $\psi_{xj}(x, y)$ and $\psi_{yj}(x, y)$ are determined step by step. As a result, up to fourth-order asymptotic solutions can be obtained:

$$\begin{aligned} W = & \varepsilon[A_{11}^{(1)} \sin mx \sin ny] + \varepsilon^3[A_{13}^{(3)} \sin mx \sin 3ny + A_{31}^{(3)} \sin 3mx \sin ny \\ & + \varepsilon^4[A_{22}^{(4)} \sin 2mx \sin 2ny + A_{24}^{(4)} \sin 2mx \sin 4ny] \\ & + A_{42}^{(4)} \sin 4mx \sin 2ny] + O(\varepsilon^5) \end{aligned} \quad 7.28$$

$$\begin{aligned} F = & -B_{00}^{(0)} \left(\frac{y^2}{2} - C_4 \frac{y^3}{6} - C_5 \frac{y^5}{120} + C_5 \frac{y^6}{360\pi} \right) \\ & - b_{00}^{(0)} \left(\frac{x^2}{2} - C_6 \frac{x^5}{120} + C_6 \frac{x^6}{360\pi} \right) + \varepsilon[B_{11}^{(1)} \cos mx \cos ny] \\ & + \varepsilon^2 \left[-B_{00}^{(2)} \left(\frac{y^2}{2} - C_4 \frac{y^3}{6} - C_5 \frac{y^5}{120} + C_5 \frac{y^6}{360\pi} \right) \right. \\ & \left. - b_{00}^{(2)} \left(\frac{x^2}{2} - C_6 \frac{x^5}{120} + C_6 \frac{x^6}{360\pi} \right) + B_{20}^{(2)} \cos 2mx \right. \\ & \left. + B_{02}^{(2)} \cos 2ny \right] + \varepsilon^3[B_{13}^{(3)} \cos mx \cos 3ny \\ & + B_{31}^{(3)} \cos 3mx \cos ny] \\ & + \varepsilon^4 \left[-B_{00}^{(4)} \left(\frac{y^2}{2} - C_4 \frac{y^3}{6} - C_5 \frac{y^5}{120} + C_5 \frac{y^6}{360\pi} \right) \right. \\ & \left. - b_{00}^{(4)} \left(\frac{x^2}{2} - C_6 \frac{x^5}{120} + C_6 \frac{x^6}{360\pi} \right) \right. \\ & \left. + B_{20}^{(4)} \cos 2mx + B_{02}^{(4)} \cos 2ny + B_{22}^{(4)} \cos 2mx \cos 2ny \right. \\ & \left. + B_{40}^{(4)} \cos 4mx + B_{04}^{(4)} \cos 4ny + B_{24}^{(4)} \cos 2mx \cos 4ny \right. \\ & \left. + B_{42}^{(4)} \cos 4mx \cos 2ny \right] + O(\varepsilon^5) \end{aligned} \quad 7.29$$

$$\begin{aligned}
 \Psi_x = & \varepsilon [C_{11}^{(1)} \cos mx \sin ny] + \varepsilon^2 [C_{02}^{(2)} \sin 2ny] \\
 & + \varepsilon^3 [C_{13}^{(3)} \cos mx \sin 3ny + C_{31}^{(3)} \cos 3mx \sin ny] \\
 & + \varepsilon^4 [C_{02}^{(4)} \sin 2ny + C_{04}^{(4)} \sin 4ny + C_{22}^{(4)} \cos 2mx \sin 2ny \\
 & + C_{24}^{(4)} \cos 2mx \sin 4ny + C_{42}^{(4)} \cos 4mx \sin 2ny] + O(\varepsilon^5)
 \end{aligned} \tag{7.30}$$

$$\begin{aligned}
 \Psi_y = & \varepsilon [D_{11}^{(1)} \sin mx \cos ny] + \varepsilon^2 [D_{20}^{(2)} \sin 2mx] \\
 & + \varepsilon^3 [D_{13}^{(3)} \sin mx \cos 3ny + D_{31}^{(3)} \sin 3mx \cos ny] \\
 & + \varepsilon^4 [D_{20}^{(4)} \sin 2mx + D_{40}^{(4)} \sin 4mx + D_{22}^{(4)} \sin 2mx \cos 2ny \\
 & + D_{24}^{(4)} \sin 2mx \cos 4ny + D_{42}^{(4)} \sin 4mx \cos 2ny] + O(\varepsilon^5)
 \end{aligned} \tag{7.31}$$

It is mentioned that all coefficients in Eqs. (7.28)–(7.31) are related and can be expressed in terms of $A_{11}^{(1)}$ but, for the sake of brevity, the detailed expressions are not shown.

Next, upon substitution of Eqs. (7.28)–(7.31) into the boundary conditions $\delta_x = 0$ and $\delta_y = 0$, one has:

$$\begin{aligned}
 \beta^2 B_{00}^{(0)} + \varepsilon^2 \beta^2 B_{00}^{(2)} + \varepsilon^4 \beta^2 B_{00}^{(4)} + \dots = \lambda_T C_7 \\
 - \frac{1}{8} \frac{m^2 + \gamma_5 n^2 \beta^2}{\gamma_{24}^2 - \gamma_5^2} (1 + 2\mu) (A_{11}^{(1)} \varepsilon)^2
 \end{aligned} \tag{7.32a}$$

$$\begin{aligned}
 b_{00}^{(0)} + \varepsilon^2 b_{00}^{(2)} + \varepsilon^4 b_{00}^{(4)} + \dots = \lambda_T C_8 \\
 - \frac{1}{8} \frac{\gamma_5 m^2 + \gamma_{24}^2 n^2 \beta^2}{\gamma_{24}^2 - \gamma_5^2} (1 + 2\mu) (A_{11}^{(1)} \varepsilon)^2
 \end{aligned} \tag{7.32b}$$

By adding $B_{00}^{(j)}$ and $b_{00}^{(j)}$ ($i = 0, 2, 4, \dots$), one has:

$$\begin{aligned}
 \gamma_{14} [(\beta^2 B_{00}^{(0)} + \varepsilon^2 \beta^2 B_{00}^{(2)} + \varepsilon^4 \beta^2 B_{00}^{(4)} + \dots) m^2 C_9 \\
 + (b_{00}^{(0)} + \varepsilon^2 b_{00}^{(2)} + \varepsilon^4 b_{00}^{(4)} + \dots) n^2 \beta^2 C_{10}] = \frac{S_{11}}{(1 + \mu)} \\
 + \frac{1}{16(1 + \mu)} \Theta_{22} (A_{11}^{(1)} \varepsilon)^2 - \frac{1}{256} C_{11} C_{44} (A_{11}^{(1)} \varepsilon)^4 \dots
 \end{aligned} \tag{7.33}$$

From Eqs. (7.32) and (7.33), the thermal postbuckling equilibrium path can be written as

$$\lambda_T = \lambda_T^{(0)} + \lambda_T^{(2)}(A_{11}^{(1)}\varepsilon)^2 + \lambda_T^{(4)}(A_{11}^{(1)}\varepsilon)^4 + \dots \quad 7.34$$

In Eq. (7.34), $(A_{11}^{(1)}\varepsilon)$ is taken as the second perturbation parameter relating to the dimensionless maximum deflection of the plate. If the maximum deflection is assumed to be at the point $(x, y) = (\pi/2m, \pi/2n)$, from Eq. (7.28) one has:

$$A_{11}^{(1)}\varepsilon = W_m + \Theta_3 W_m^3 + \dots \quad 7.35$$

Finally, one has:

$$\lambda_T = \lambda_T^{(0)} + \lambda_T^{(2)}W_m^2 + \lambda_T^{(4)}W_m^4 + \dots \quad 7.36$$

in which $\lambda_T^{(0)}$, $\lambda_T^{(2)}$ and $\lambda_T^{(4)}$ are all temperature-dependent and given in detail in Appendix C.

To obtain numerical results, it is necessary to solve Eq. (7.36) by an iterative numerical procedure with the following steps:

1. Begin with $\bar{W}/t = 0$.
2. Assume that elastic constants and the thermal expansion coefficients are constant. The thermal buckling load for the plates of temperature-independent material is obtained.
3. Use the temperature determined in the previous step, the temperature-dependent material properties may be decided and the thermal buckling load is obtained again.
4. Repeat step (3) until the thermal buckling temperature converges.
5. Specify the new value of \bar{W}/t , and repeat steps (2)–(4) until the thermal postbuckling temperature converges.

7.4 Thermal postbuckling of antisymmetric angle-ply laminated plates

Firstly, we consider the thermal postbuckling of simply supported antisymmetric angle-ply shear deformable laminated plates subjected to non-uniform, tent-like temperature loading as defined in Eq. (7.5b). For such a plate the following plate stiffnesses are identically zero, i.e.:

$$\begin{aligned} A_{16} = A_{26} = D_{16} = D_{26} = F_{16} = F_{26} = H_{16} = H_{26} = 0, \\ A_{45} = D_{45} = F_{45} = 0 \\ B_{11} = B_{22} = B_{12} = B_{66} = 0, E_{11} = E_{22} = E_{12} = E_{66} = 0 \end{aligned} \quad 7.37$$

and in Eqs. (7.17), (7.18), (7.21) and (7.29), $C_1 = C_5 = C_6 = 0$, $C_2 = \pm 2\lambda_T\beta [\gamma_{14}(\gamma_{223}\gamma_{T_1} + \gamma_{230}\gamma_{T_2}) + \gamma_{T_3}]/\pi$ and $C_3 = T_0/T_1 + 1/2$.

The elastic constants and thermal expansion coefficients of each ply are assumed to be linear functions of temperature change ΔT , but Poisson's ratio depends weakly on temperature change and is assumed to be constant:

$$\begin{aligned}
 E_{11}(T) &= E_{110}(1 + E_{111}\Delta T), \quad E_{22}(T) = E_{220}(1 + E_{221}\Delta T) \\
 G_{12}(T) &= G_{120}(1 + G_{121}\Delta T), \quad G_{13}(T) = G_{130}(1 + G_{131}\Delta T), \\
 G_{23}(T) &= G_{230}(1 + G_{231}\Delta T) \quad \alpha_{11}(T) = \alpha_{110}(1 + \alpha_{111}\Delta T), \\
 \alpha_{22}(T) &= \alpha_{220}(1 + \alpha_{221}\Delta T)
 \end{aligned}
 \tag{7.38}$$

where $E_{110}, E_{220}, G_{120}, G_{130}, G_{230}, \alpha_{110}, \alpha_{220}, E_{111}, E_{221}, G_{121}, G_{131}, G_{231}, \alpha_{111}, \alpha_{221}$ are constants.

Tables 7.1–7.3 show the comparisons of the thermal postbuckling for antisymmetric angle-ply laminated plates subjected to uniform temperature

Table 7.1 Comparisons of thermal postbuckling response for thin $(\pm 45)_{2T}$ laminated rectangular plates subjected to a uniform temperature rise ($b/t = 100, E_{11}/E_{22} = 25, G_{12}/E_{22} = G_{13}/E_{22} = 0.5, G_{23}/E_{22} = 0.2, \nu_{12} = 0.25$ and $\alpha_{22}/\alpha_{11} = 10$)

\bar{W}/t	$\lambda_T/(\lambda_T)_{cr}$					
	$\beta = 0.75$		$\beta = 1.0$		$\beta = 1.5$	
	Thankam et al. (2003)	Present	Thankam et al. (2003)	Present	Thankam et al. (2003)	Present
0.0	1.0	1.0	1.0	1.0	1.0	1.0
0.2	1.042	1.0412	1.039	1.0392	1.043	1.0427
0.4	1.167	1.1649	1.158	1.1570	1.174	1.1713
0.6	1.376	1.3720	1.356	1.3539	1.393	1.3868
0.8	1.670	1.6640	1.635	1.6309	1.702	1.6911
1.0	2.053	2.0426	1.995	1.9892	2.101	2.0866
$\lambda_T = \alpha_{22}T_{cr}(b/t)^2$	12.709	12.649	9.493	9.4584	6.410	6.3939

Table 7.2 Comparisons of postbuckling temperature $T(^{\circ}\text{C})$ for moderately thick $(\pm 45)_{2T}$ laminated square plates subjected to a uniform temperature rise ($b/t = 20, E_{11}/E_{22} = 15, G_{12}/E_{22} = G_{13}/E_{22} = 0.5, G_{23}/E_{22} = 0.2, \nu_{12} = 0.25, \alpha_{22}/\alpha_{11} = 10$)

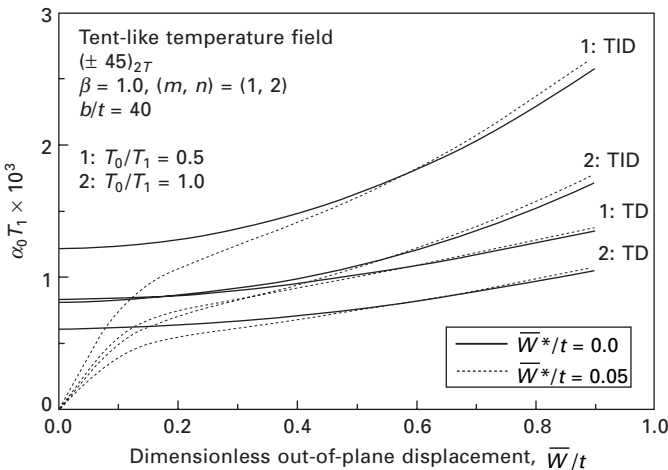
\bar{W}/t	Present	Ganapathi and Touratier (1997)
0.0	2050.0	2063.25
0.1	2073.1	2086.22
0.2	2142.7	2155.20
0.3	2258.8	2270.33
0.4	2421.7	2431.85
0.5	2631.7	2638.96
0.6	2889.3	2893.03
0.7	3195.0	3196.05

Table 7.3 Comparisons of thermal postbuckling response for thin (± 45)_{6T} laminated square plates subjected to a uniform temperature rise ($b/t = 100$, $E_{110}/E_{220} = 40$, $G_{120}/E_{220} = G_{130}/E_{220} = G_{230}/E_{220} = 0.5$, $\nu_{12} = 0.25$, $\alpha_{110} = \alpha_{220} = 1.0 \times 10^{-6}/^\circ\text{C}$, $E_{221} = G_{121} = G_{131} = G_{231} = \alpha_{111} = \alpha_{222} = 0$)

\bar{W}/t	$\alpha_0 T_0 \times 10^6$							
	$E_{111} = 0$		$E_{111} = -0.0005$		$E_{111} = -0.001$		$E_{111} = -0.002$	
	Present	Chen and Chen (1991)	Present	Chen and Chen (1991)	Present	Chen and Chen (1991)	Present	Chen and Chen (1991)
0.0	158.1825	159.64	158.1459	159.50	158.0851	159.34	157.8599	158.92
0.1	159.4729	160.91	159.4396	160.78	159.3823	160.62	159.1644	160.21
0.2	163.3450	164.72	163.3159	164.60	163.2624	164.46	163.0492	164.07
0.3	169.8015	171.09	169.7696	170.98	169.7112	170.86	169.4775	170.52
0.4	178.8468	180.00	178.7982	179.92	178.7181	179.84	178.4177	179.58

rise. The thermal postbuckling responses for $(\pm 45)_{2T}$ laminated rectangular thin plates ($b/t = 100$) subjected to a uniform temperature rise are calculated and compared in Table 7.1 with the FEM results of Thankam *et al.* (2003). The material properties adopted are: $E_{11}/E_{22} = 25$, $G_{12}/E_{22} = G_{13}/E_{22} = 0.5$, $G_{23}/E_{22} = 0.2$, $\nu_{12} = 0.25$, and $\alpha_{22}/\alpha_{11} = 10$. Then the thermal postbuckling responses for a moderately thick ($b/t = 20$) $(\pm 45)_{2T}$ laminated square plate subjected to a uniform temperature rise are calculated and compared in Table 7.2 with the FEM results of Ganapathi and Touratier (1997). The material properties adopted are: $E_{11}/E_{22} = 15$, $G_{12}/E_{22} = G_{13}/E_{22} = 0.5$, $G_{23}/E_{22} = 0.2$, $\nu_{12} = 0.25$ and $\alpha_{22}/\alpha_{11} = 10$. In addition, the thermal postbuckling responses for $(\pm 45)_{6T}$ laminated square thin plates ($b/t = 100$) with temperature-dependent thermoelastic properties and subjected to a uniform temperature rise are calculated and compared in Table 7.3 with the FEM results of Chen and Chen (1991). The material properties are: $E_{110}/E_{220} = 40$, $G_{120}/E_{220} = G_{130}/E_{220} = G_{230}/E_{220} = 0.5$, $\nu_{12} = 0.25$, $\alpha_{110} = \alpha_{220} = 1.0 \times 10^{-6}/^\circ\text{C}$, $E_{221} = G_{121} = G_{131} = G_{231} = \alpha_{111} = \alpha_{221} = 0$. Only E_{11} is assumed to be a function of temperature and $E_{111} = 0, -0.0005, -0.001$ and -0.002 , respectively. These comparisons show that the results from the present method are in good agreement with the existing results, thus verifying the reliability and accuracy of the present method.

Figure 7.1 shows the thermal postbuckling load-deflection curves for a $(\pm 45)_{2T}$ shear deformable laminated square plate ($b/t = 40$) subjected to nonuniform tent-like temperature loading under two cases of thermoelastic properties. TD represents both elastic constants and thermal expansion



7.1 Effect of material properties on the thermal postbuckling of a $(\pm 45)_{2T}$ laminated square plate subjected to tent-like temperature loading.

coefficients are temperature-dependent, i.e. $E_{110}/E_{220} = 40$, $G_{120}/E_{220} = G_{130}/E_{220} = 0.5$, $G_{230}/E_{220} = 0.2$, $\nu_{12} = 0.25$, $\alpha_{110}/\alpha_0 = 1$, $\alpha_{220}/\alpha_0 = 10$, $\alpha_0 = 1.0 \times 10^{-6}/^\circ\text{C}$ and $E_{111} = -0.0005$, $E_{221} = G_{121} = G_{131} = G_{231} = -0.0002$, $\alpha_{111} = \alpha_{221} = 0.0005$. TID represents both elastic constants and thermal expansion coefficients are temperature-independent. For the TID case, the constants E_{111} , E_{221} , G_{121} , G_{131} , G_{231} , α_{111} and α_{221} are set equal to zero. It can be seen that the thermal postbuckling equilibrium path becomes significantly lower when the temperature-dependent properties are taken into account. It can also be found that the postbuckling strength is decreased by increasing T_0/T_1 .

It is appreciated that in Fig. 7.1 and what follows, $\bar{W}^*/t = 0.05$ denotes the dimensionless maximum initial geometric imperfection of the plate.

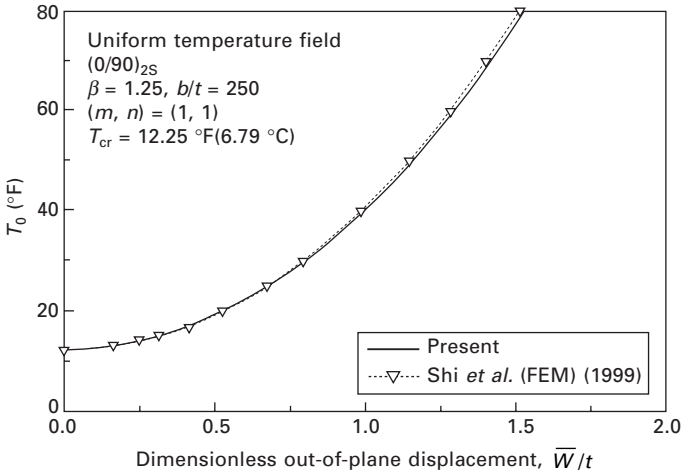
7.5 Thermal postbuckling of symmetric cross-ply laminated plates

Next we consider the thermal postbuckling of simply supported symmetric cross-ply shear deformable laminated plates subjected to non-uniform parabolic temperature loading as defined in Eq. (7.5c). For such a plate the following plate stiffnesses are identical to zero, i.e.

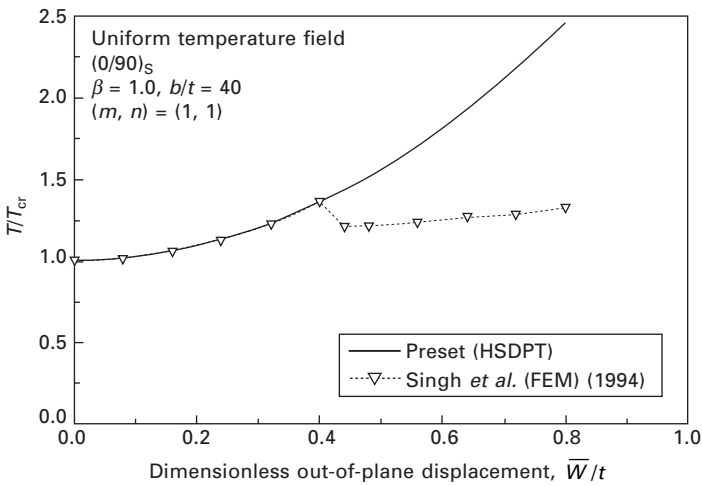
$$\begin{aligned} B_{ij} = E_{ij} = 0, A_{16} = A_{26} = D_{16} = D_{26} = F_{16} = F_{26} = H_{16} = H_{26} = 0, \\ A_{45} = D_{45} = F_{45} = 0 \end{aligned} \quad 7.39$$

and in Eqs. (7.17), (7.18), (7.21) and (7.29), $C_1 = -(32/\pi^2\beta^2)\lambda_T[(\gamma_{24}^2\gamma_{T_1} - \gamma_5\gamma_{T_2})(x/\pi - x^2/\pi^2) + (\gamma_{T_2} - \gamma_5\gamma_{T_1})(y/\pi - y^2/\pi^2)]$, $C_2 = C_4 = 0$, $C_3 = T_0/T_1 + 16(x/\pi - x^2/\pi^2)(y/\pi - y^2/\pi^2)$. The materials properties are still taken as linear functions of temperature expressed by Eq. (7.38).

Figures 7.2 and 7.3 show the comparisons of the thermal postbuckling for symmetric cross-ply laminated plates with temperature-independent properties and subjected to uniform temperature rise. The thermal postbuckling responses for a $(0/90)_{2S}$ laminated rectangular thin plate ($\beta = 1.25$, $b/t = 250$) subjected to a uniform temperature rise are compared in Fig. 7.2 with the FEM results of Shi *et al.* (1999). The material properties adopted are: $E_{11} = 155$ GPa, $E_{22} = 8.07$ GPa, $G_{12} = 4.55$ GPa, $\nu_{12} = 0.22$, $\alpha_{11} = -0.04 \times 10^{-6}/^\circ\text{F}$ and $\alpha_{22} = 16.7 \times 10^{-6}/^\circ\text{F}$. Then the thermal postbuckling responses for a moderately thick $(0/90)_S$ laminated square plate ($b/t = 40$) subjected to a uniform temperature rise are compared in Fig. 7.3 with the FEM results of Singh *et al.* (1994). The material properties adopted are: $E_{11}/E_{22} = 25$, $G_{12}/E_{22} = G_{13}/E_{22} = 0.5$, $G_{23}/E_{22} = 0.2$, $\nu_{12} = 0.25$ and $\alpha_{22}/\alpha_{11} = 10$. In addition, the thermal postbuckling responses for an isotropic shear deformable plate ($b/t = 40$) subjected to nonuniform parabolic temperature loading with $T_0/T_1 = 1.0$ are compared in Fig. 7.4 with the finite difference method solutions of Kamiya and Fukui (1982). Again, good agreement is achieved in each of them.

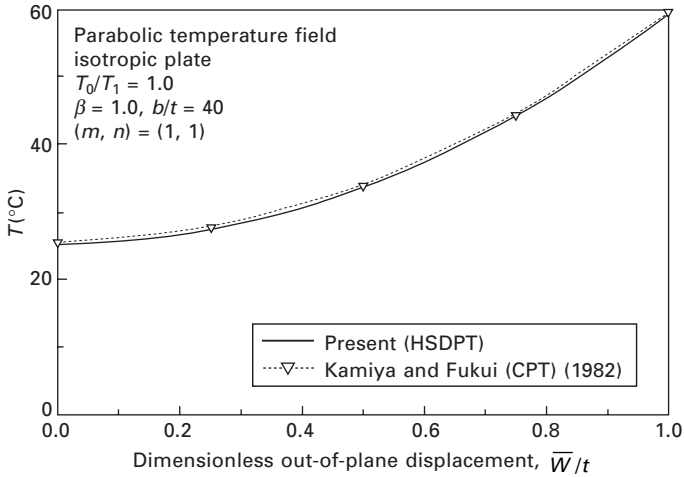


7.2 Comparisons of thermal postbuckling response for a $(0/90)_{2S}$ laminated thin plate subjected to uniform temperature rise.

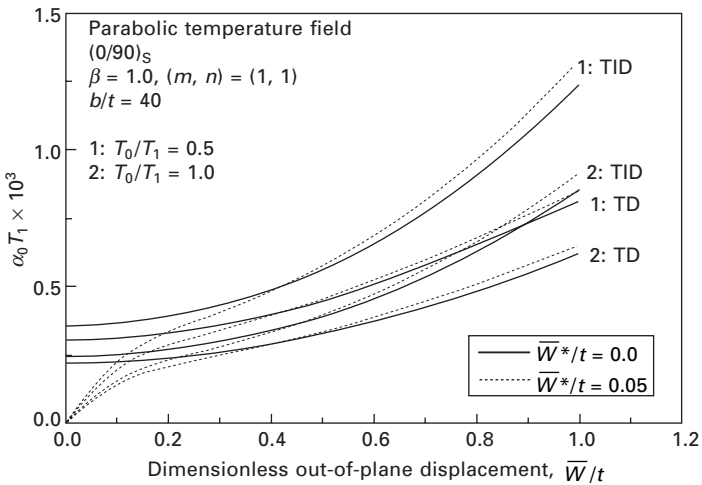


7.3 Comparisons of thermal postbuckling response for a $(0/90)_S$ shear deformable laminated plate subjected to uniform temperature rise.

Figure 7.5 shows the thermal postbuckling load-deflection curves for a $(0/90)_S$ shear deformable laminated square plate ($b/t = 40$) subjected to nonuniform parabolic temperature loading under two cases of thermoelastic properties as used in Fig. 7.1, and leads to broadly the same conclusions as Fig. 7.1 does. It can also be found that the $(0/90)_S$ plate has a lower buckling



7.4 Comparisons of thermal postbuckling response for an isotropic shear deformable plate subjected to non-uniform parabolic temperature loading.



7.5 Effect of material properties on the thermal postbuckling of $(0/90)_S$ laminated square of plates subjected to parabolic temperature loading.

temperature than $(\pm 45)_{2T}$ plate does, but its thermal postbuckling response is stiffer than that of the $(\pm 45)_{2T}$ plate.

7.6 Thermal postbuckling of a symmetric cross-ply laminated plate with piezoelectric layers

We now turn our attention to the thermal postbuckling of shear deformable laminated plates with piezoelectric actuators subjected to a uniform or nonuniform parabolic temperature rise combined with electric loads. The plate is also assumed to have special material symmetries. In such a case, Eq. (7.39) is still valid, but we need to replace \bar{N}^T , \bar{M}^T and \bar{S}^T in Eqs. (7.1)–(7.4) and (7.10) with equivalent thermo-piezoelectric loads \bar{N}^P , \bar{M}^P and \bar{S}^P , which are defined by

$$\begin{bmatrix} \bar{N}^P \\ \bar{M}^P \\ \bar{S}^P \end{bmatrix} = \begin{bmatrix} \bar{N}^T \\ \bar{M}^T \\ \bar{S}^T \end{bmatrix} + \begin{bmatrix} \bar{N}^E \\ \bar{M}^E \\ \bar{S}^E \end{bmatrix} \quad 7.40$$

where \bar{N}^T , \bar{M}^T , \bar{P}^T and \bar{N}^E , \bar{M}^E , \bar{P}^E are the forces, moments, and higher-order moments caused by the elevated temperature and electric field, respectively.

For the plate-type piezoelectric material, only the transverse direction electric field component E_z is dominant, and E_z is defined as $E_z = -\Phi_{,z}$, where Φ is the potential field. If the voltage applied to the actuator is in the thickness only, then

$$E_z = \frac{V_k}{t_p} \quad 7.41$$

where V_k is the applied voltage across the k th ply and t_p is the thickness of the piezoelectric ply.

The forces, moments and higher-order moments caused by electric field are defined by

$$\begin{bmatrix} \bar{N}_x^E & \bar{M}_x^E & \bar{P}_x^E \\ \bar{N}_y^E & \bar{M}_y^E & \bar{P}_y^E \\ \bar{N}_{xy}^E & \bar{M}_{xy}^E & \bar{P}_{xy}^E \end{bmatrix} = \sum_{k=1} \int_{t_{k-1}}^{t_k} \begin{bmatrix} B_x \\ B_y \\ B_{xy} \end{bmatrix}_k (1, Z, Z^3) \frac{V_k}{t_p} dZ \quad 7.42a$$

$$\begin{bmatrix} \bar{S}_x^E \\ \bar{S}_y^E \\ \bar{S}_{xy}^E \end{bmatrix} = \begin{bmatrix} \bar{M}_x^E \\ \bar{M}_y^E \\ \bar{M}_{xy}^E \end{bmatrix} - \frac{4}{3t^2} \begin{bmatrix} \bar{P}_x^E \\ \bar{P}_y^E \\ \bar{P}_{xy}^E \end{bmatrix} \quad 7.42b$$

in which

$$\begin{bmatrix} B_x \\ B_y \\ B_{xy} \end{bmatrix} = - \begin{bmatrix} \bar{Q}_{11} & \bar{Q}_{12} & \bar{Q}_{16} \\ \bar{Q}_{12} & \bar{Q}_{22} & \bar{Q}_{26} \\ \bar{Q}_{16} & \bar{Q}_{26} & \bar{Q}_{66} \end{bmatrix} \begin{bmatrix} c^2 & s^2 \\ s^2 & c^2 \\ 2cs & -2cs \end{bmatrix} \begin{bmatrix} d_{31} \\ d_{32} \end{bmatrix} \quad 7.43$$

where d_{31} and d_{32} are the piezoelectric strain constants of a single ply, and \bar{Q}_{ij} are the transformed elastic constants defined as in Eq. (7.8). It is noted that from Eqs. (7.6) and (7.42), in the present case, the thermal and electric forces \bar{N}_{xy}^T and \bar{N}_{xy}^E , the thermal and electric moments and the higher-order moments are all zero.

In this section graphite/epoxy composite material and PZT-5A are selected for the substrate orthotropic layers and piezoelectric layers, respectively. The material properties, as linear functions of temperature, for graphite/epoxy orthotropic layers of the substrate are: $E_{110} = 150.0$ GPa, $E_{220} = 9.0$ GPa, $G_{120} = G_{130} = 7.1$ GPa, $G_{230} = 2.5$ GPa, $\nu_{12} = 0.3$, $\alpha_{110} = 1.1 \times 10^{-6} / ^\circ\text{C}$, $\alpha_{220} = 25.2 \times 10^{-6} / ^\circ\text{C}$, and for PZT-5A piezoelectric layers $E_{110} = E_{220} = 63.0$ GPa, $G_{120} = G_{130} = G_{230} = 24.2$ GPa, $\nu_{12} = 0.3$, $\alpha_{110} = \alpha_{220} = 0.9 \times 10^{-6} / ^\circ\text{C}$ and $d_{310} = d_{320} = 2.54 \times 10^{-10}$ m/V; and $E_{111} = -0.0005$, $E_{221} = G_{121} = G_{131} = G_{231} = -0.0002$, $\alpha_{111} = \alpha_{221} = 0.0005$ for both graphite/epoxy orthotropic layers and piezoelectric layers. Two types of hybrid laminated plates, Type A and Type B, are configured. For Type A, two piezoelectric layers are bonded to the upper and bottom surfaces of the $(0/90)_2$ S plate, referred to as $(P/(0/90)_2)_S$. For Type B, two piezoelectric layers are embedded in the $(0/90)_2$ S plate, referred to as $(0/P/90/0/90)_S$. The total thickness of the plate $t = 1.2$ mm, whereas the thickness of the piezoelectric layer $t_p = 0.1$ mm, and all other orthotropic layers are of equal thickness.

Table 7.4 shows the thermal buckling temperature T_{cr} (in $^\circ\text{C}$) for perfect, moderately thick, $(P/(0/90)_2)_S$ and $(0/P/90/0/90)_S$ hybrid laminated plates ($b/t = 40$) subjected to uniform and nonuniform temperature rises. The control voltages with the same sign are also applied to the upper and lower piezoelectric layers, and are referred to as V_U and V_L . Three electrical loading cases, $V_U = V_L = -100, 0, +100$ V, are considered. Here $V_U = V_L = 0$ V implies that the buckling occurs under a grounding condition. It can be seen that the buckling temperature of $(P/(0/90)_2)_S$ and $(0/P/90/0/90)_S$ hybrid laminated plates with temperature-dependent material properties (referred to as TD) is lower than that of the same plate with temperature-independent material properties (referred to as TID) under the same loading conditions. It can also be seen that the control voltage has a significant effect on the thermal buckling loads for these two hybrid laminated plates.

Figure 7.6 shows the thermal postbuckling load-deflection curves for perfect and imperfect, $(P/(0/90)_2)_S$ and $(0/P/90/0/90)_S$ hybrid laminated square plates ($b/t = 40$) subjected to nonuniform parabolic temperature rise and three sets of electrical loads under two cases of thermoelastic properties TID and TD.

Table 7.4 Comparisons of buckling temperature $T(^{\circ}\text{C})$ for $(0/90)_{2S}$ plates with surface-bonded or embedded piezoelectric actuators under uniform and nonuniform parabolic temperature rise and three sets of electrical loading conditions ($b/t = 40, a/b = 1.0$)

$V_U = V_L$	Uniform temperature rise	Nonuniform parabolic temperature rise		
		$T_0/T_1 = 0.0$	$T_0/T_1 = 0.5$	$T_0/T_1 = 1.0$
		$(P/0/90)_{2S}, \text{TID}$		
-100 V	297.8174	490.0772	268.8608	185.2442
0 V	279.4457	459.8408	252.2754	173.8169
+ 100 V	261.0740	429.6093	235.6899	162.3896
		$(P/(0/90)_{2S}), \text{TD}$		
-100 V	261.0516	403.1087	238.4538	169.8347
0 V	246.4487	381.3779	225.0090	160.0406
+ 100 V	231.6839	359.3391	211.4259	150.1681
		$(0/P/90/0/90)_{S}, \text{TID}$		
-100 V	281.3445	462.9654	253.9896	174.9980
0 V	262.9728	432.7339	237.4042	163.5707
+ 100 V	244.6012	402.5025	220.8188	152.1434
		$(0/P/90/0/90)_{S}, \text{TD}$		
-100 V	246.3166	379.6782	225.0283	160.3572
0 V	231.6571	357.8734	211.5345	150.5326
+ 100 V	216.8325	335.7512	197.8997	140.6284

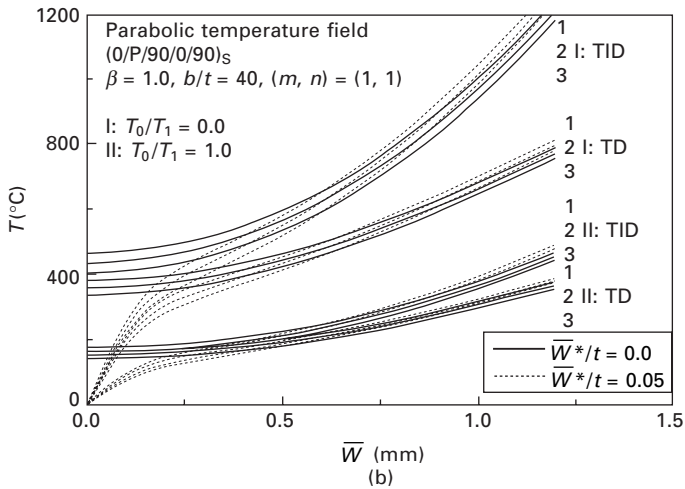
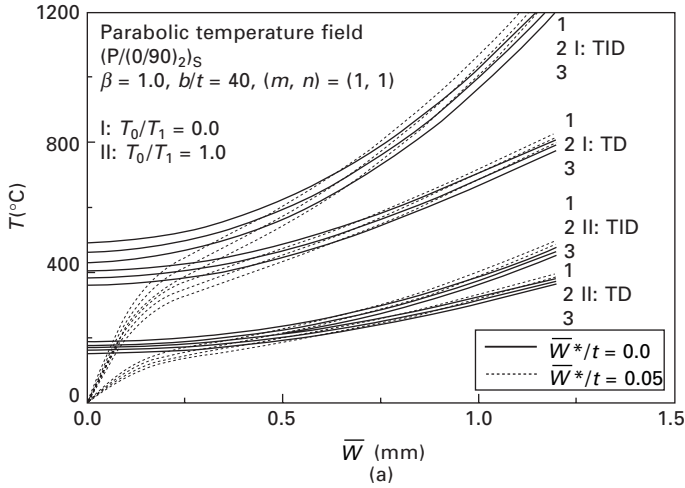
The results show that the minus control voltages increase the buckling temperature and decrease the postbuckled deflection at the same temperature rise, whereas the plus control voltages decrease the buckling temperature and induce more large postbuckled deflections. They also confirm that the temperature-dependent thermoelastic property has a significant effect on both buckling temperature and postbuckling thermal strength of the hybrid laminated plate.

7.7 Thermal postbuckling of FGM hybrid laminated plates

Finally, we consider the thermal postbuckling of FGM hybrid laminated plates subjected to a uniform temperature rise combined with electric loads. The substrate FGM layer is made from a mixture of ceramics and metals, the mixing ratio of which is varied continuously and smoothly in the Z direction, so that the effective material properties P_f (Young’s modulus E_f or thermal expansion coefficient α_f) can be expressed as:

$$P_f = P_c V_c + P_m V_m \tag{7.44}$$

where P_c and P_m denote the temperature-dependent properties of the ceramic



7.6 Effect of material properties on the thermal postbuckling of $(0/90)_2S$ laminated square plates with piezoelectric actuators subjected to parabolic temperature loading: (a) $(P/(0/90)_2)_S$ plate; (b) $(0/P/90/0/90)_S$ plate (1: $V_U = V_L = -100$ V; 2: $V_U = V_L = 0$ V; 3: $V_U = V_L = +100$ V).

and metal, respectively, and V_c and V_m are the ceramic and metal volume fractions and are related by:

$$V_c + V_m = 1 \tag{7.45}$$

The volume fraction V_m follows a simple power law:

$$V_m = \left(\frac{Z - t_1}{t_2 - t_1} \right)^N \tag{7.46}$$

where the volume fraction index N dictates the material variation profile through the FGM layer thickness.

It is assumed that the effective Young's modulus E_f and thermal expansion coefficient α_f of the FGM layer are temperature-dependent, whereas Poisson's ratio ν_f depends weakly on temperature change and is assumed to be a constant. From Eqs. (7.44)–(7.46), one has:

$$E_f(Z, T) = [E_m(T) - E_c(T)] \left(\frac{Z - t_1}{t_2 - t_1} \right)^N + E_c(T) \tag{7.47a}$$

$$\alpha_f(Z, T) = [\alpha_m(T) - \alpha_c(T)] \left(\frac{Z - t_1}{t_2 - t_1} \right)^N + \alpha_c(T) \tag{7.47b}$$

It is evident that when $Z = t_1$, $E_f = E_c$ and $\alpha_f = \alpha_c$, and when $Z = t_2$, $E_f = E_m$ and $\alpha_f = \alpha_m$. Furthermore, E_f and α_f are both temperature and position dependent. Note that for an FGM layer, $\alpha_{11} = \alpha_{22} = \alpha_f$ is given in detail in Eq. (7.47b), and $\bar{Q}_{ij} = Q_{ij}$ in which

$$Q_{11} = Q_{22} = \frac{E_f(Z, T)}{1 - \nu_f^2}, Q_{12} = \frac{\nu_f E_f(Z, T)}{1 - \nu_f^2},$$

$$Q_{16} = Q_{26} = 0, Q_{44} = Q_{55} = Q_{66} = \frac{E_f(Z, T)}{2(1 + \nu_f)} \tag{7.48}$$

where E_f is also given in detail in Eq. (7.47a), and varies in the thickness direction.

It has been pointed out by Shen (2002) that the governing differential equations for an FGM plate are identical in form to those of unsymmetric cross-ply laminated plates. In such a case, the following plate stiffnesses are identical to zero, i.e.:

$$A_{16} = A_{26} = D_{16} = D_{26} = F_{16} = F_{26} = H_{16} = H_{26} = 0,$$

$$A_{45} = D_{45} = F_{45} = 0, B_{16} = B_{26} = E_{16} = E_{26} = 0 \tag{7.49}$$

It is evident that the governing equations involve the stretching/bending coupling, as predicted by B_{ij} and E_{ij} . As argued previously, even for an FGM plate with all four edges simply supported, no bifurcation buckling could occur. For this reason, we consider here two types of hybrid laminated plate, referred to as (P/FGM)_S and (FGM/P)_S, which consist of four plies and are mid-plane symmetric. In such a case, the stretching/bending coupling is zero-valued, i.e. $B_{ij} = E_{ij} = 0$. As a result, $\tilde{L}_{14} = \tilde{L}_{15} = \tilde{L}_{22} = \tilde{L}_{23} = \tilde{L}_{24} = \tilde{L}_{34} = \tilde{L}_{35} = \tilde{L}_{44} = \tilde{L}_{45} = 0$, and all reduced stiffness matrices are functions of temperature and position.

In this section, two sets of material mixture for FGMs are considered. One is silicon nitride and stainless steel, referred to as Si₃N₄/SUS304, and the

other is zirconium oxide and titanium alloy, referred to as ZrO₂/Ti-6Al-4V. The material properties P_f , such as Young’s modulus E_f and thermal expansion coefficient α_f , can be expressed as a nonlinear function of temperature as (Touloukian 1967):

$$P_f = P_0(P_{-1}T^{-1} + 1 + P_1T + P_2T^2 + P_3T^3) \tag{7.50}$$

in which $T = T_0 + \Delta T$, and $T_0 = 300$ K. P_0, P_{-1}, P_1, P_2 and P_3 are the coefficients of temperature T (K) and are unique to the constituent materials. Typical values for Young’s modulus E_f (in Pa) and thermal expansion coefficient α_f (in /K) of these materials are listed in Table 7.5 (Reddy and Chin 1998). Poisson’s ratio ν_f is assumed to be a constant, and $\nu_f = 0.28$. PZT-5A is selected for the piezoelectric layers. The material properties of which, as linear functions of temperature, are: $E_{110} = E_{220} = 63$ GPa, $G_{120} = G_{130} = G_{230} = 24.2$ GPa, $\nu_{12} = 0.3$, $\alpha_{110} = \alpha_{220} = 0.9 \times 10^{-6}$ /K and $d_{310} = d_{320} = 2.54 \times 10^{-10}$ m/V, and $E_{111} = -0.0005$, $E_{221} = G_{121} = G_{131} = G_{231} = -0.0002$, $\alpha_{111} = \alpha_{221} = 0.0005$. The thickness of the FGM layer $t_f = 1$ mm whereas the thickness of the piezoelectric layer $t_p = 0.1$ mm, so that the total thickness of the plate $t = 2.2$ mm.

Table 7.5 Temperature-dependent coefficients for ceramics and metals, from Reddy and Chin (1998)

Materials		P_0	P_{-1}	P_1	P_2	P_3
Zirconia	E_f	244.27×10^9	0	-1.371×10^{-3}	1.214×10^{-6}	-3.681×10^{-10}
	α_f	12.766×10^{-6}	0	-1.491×10^{-3}	1.006×10^{-5}	-6.778×10^{-11}
Silicon nitride	E_f	348.43×10^9	0	-3.070×10^{-4}	2.160×10^{-7}	-8.946×10^{-11}
	α_f	5.8723×10^{-6}	0	9.095×10^{-4}	0	0
Ti-6Al-4V	E_f	122.56×10^9	0	-4.586×10^{-4}	0	0
	α_f	7.5788×10^{-6}	0	6.638×10^{-4}	-3.147×10^{-6}	0
Stainless steel	E_f	201.04×10^9	0	3.079×10^{-4}	-6.534×10^{-7}	0
	α_f	12.330×10^{-6}	0	8.086×10^{-4}	0	0

Tables 7.6 and 7.7 present the thermal buckling loads ΔT_{cr} (in K) for perfect, moderately thick, (P/FGM)_S and (FGM/P)_S hybrid laminated plates ($b/t = 40$) with different values of the volume fraction index N ($= 0.0, 0.2, 0.5, 1.0, 2.0,$ and 5.0) subjected to a uniform temperature rise under three cases of thermoelastic properties. Here, TD represents material properties in which both substrate FGM layer and piezoelectric layers are temperature dependent. TD-F represents material properties in which substrate FGM layer are temperature dependent but material properties of piezoelectric layers are temperature independent. TID represents material properties in which

Table 7.6 Comparisons of buckling temperature $\Delta T(K)$ for $Si_3N_4/SUS304$ plates with piezoelectric actuators under uniform temperature rise and three sets of electrical loading conditions ($b/t = 40$, $a/b = 1.0$, $T_0 = 300$ K)

$V_U(=V_L)$ or V_M	$N = 0.0$	$N = 0.2$	$N = 0.5$	$N = 1.0$	$N = 2.0$	$N = 5.0$
			(P/FGM) _S , TID			
-200 V	48.5298	55.7882	63.5644	71.6558	79.8093	87.7327
0 V	47.4976	54.7489	62.4959	70.5406	78.6306	86.4724
+ 200 V	46.4655	53.7095	61.4275	69.4254	77.4519	85.2120
			(P/FGM) _S , TD-F			
-200 V	47.1170	53.8840	61.0684	68.4743	75.8671	82.9841
0 V	46.1381	52.9051	60.0696	67.4399	74.7823	81.8335
+ 200 V	45.1582	51.9254	59.0699	66.4046	73.6966	80.6818
			(P/FGM) _S , TD			
-200 V	47.0534	53.8113	60.9842	68.3766	75.7535	82.8524
0 V	46.0886	52.8484	60.0037	67.3633	74.6932	81.7300
+ 200 V	45.1223	51.8841	59.0219	66.3486	73.6313	80.6059
			(FGM/P) _S , TID			
- 200 V	58.3405	67.5093	77.3737	87.7226	98.2747	108.6605
0 V	57.3084	66.4699	76.3052	86.6073	97.0960	107.4002
+ 200 V	56.2762	65.4306	75.2367	85.4921	95.9173	106.1398
			(FGM/P) _S , TD-F			
-200 V	56.2913	64.7211	73.6895	82.9885	92.3550	101.4237
0 V	55.3225	63.7538	72.7041	81.9697	91.2888	100.2963
+ 200 V	54.3527	62.7857	71.7179	80.9501	90.2217	99.1678
			(FGM/P) _S , TD			
-200 V	56.2744	64.7015	73.6665	82.9616	92.3234	101.3862
0 V	55.3211	63.7520	72.7017	81.9667	91.2850	100.2915
+ 200 V	54.3664	62.8012	71.7356	80.9705	90.2451	99.1951

both substrate FGM layer and piezoelectric layers are temperature independent. The control voltages with the same sign are also applied to the upper, lower or middle piezoelectric layers, and are referred to as V_U , V_L , and V_M . Three electrical loading cases $V_U = V_L = -200, 0, + 200$ V, are considered.

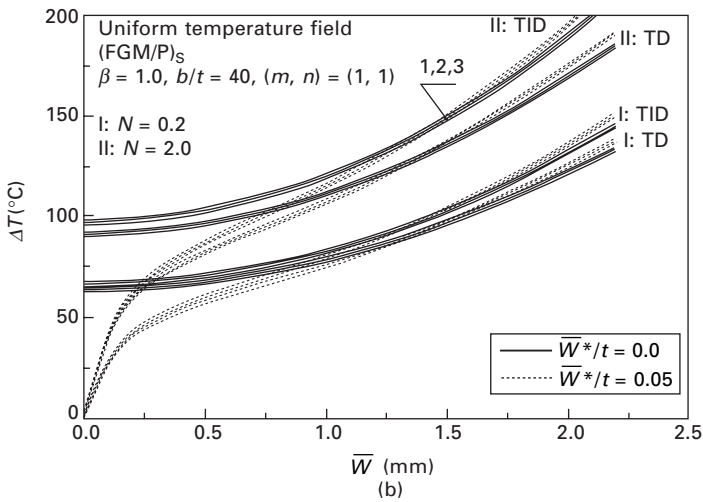
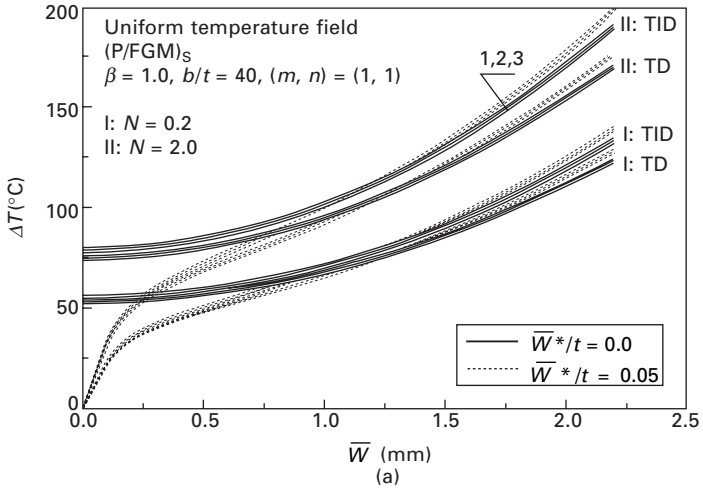
Two kinds of substrate FGM layers, i.e. $Si_3N_4/SUS304$ and $ZrO_2/Ti-6Al-4V$ are considered. It can be seen that, for the hybrid plates with $Si_3N_4/SUS304$ substrate, a fully metallic plate ($N = 0$) has lowest buckling temperature and that the buckling temperature increases as the volume fraction index N increases. It is found that the increase is about +77% for the (P/FGM)_S plate, and about +81% for the (FGM/P)_S one, from $N = 0$ to $N = 5$, under TD-F and TD cases. It can also be seen that the buckling temperature of an FGM hybrid laminated plate with temperature-dependent material properties is lower than that of the FGM hybrid laminated plate with temperature-independent material properties, but the thermal buckling loads under TD-F and TD cases are very close. As a result, the material properties of piezoelectric layers may be assumed to be independent of the temperature, and the solutions

Table 7.7 Comparisons of buckling temperature $\Delta T(K)$ for $ZrO_2/Ti-6Al-4V$ plates with piezoelectric actuators under uniform temperature rise and three sets of electrical loading conditions ($b/t = 40$, $a/b = 1.0$, $T_0 = 300 K$)

$V_U (= V_L)$ or V_M	$N = 0.0$	$N = 0.2$	$N = 0.5$	$N = 1.0$	$N = 2.0$	$N = 5.0$
			(P/FGM) _S , TID			
-200 V	92.3981	80.2041	69.7123	61.0008	53.5606	46.9526
0 V	88.9100	77.5408	67.6177	59.3005	52.1421	45.7423
+ 200 V	85.4219	74.8775	65.5230	57.6002	50.7235	44.5320
			(P/FGM) _S , TD-F			
-200 V	90.2062	73.1978	61.9584	53.7603	47.2333	41.6491
0 V	86.7401	70.8758	60.2205	52.3728	46.0767	40.6543
+ 200 V	83.2799	68.5461	58.4752	50.9792	44.9152	39.6556
			(P/FGM) _S , TD			
-200 V	89.7716	72.9613	61.8082	53.6562	47.1572	41.5915
0 V	86.4080	70.6931	60.1041	52.2920	46.0175	40.6095
+ 200 V	83.0432	68.4146	58.3911	50.9208	44.8724	39.6232
			(FGM/P) _S , TID			
-200 V	102.0487	90.1491	79.4161	70.2522	62.2506	54.9843
0 V	98.5606	87.4859	77.3214	68.5519	60.8321	53.7741
+ 200 V	95.0725	84.8226	75.2268	66.8515	59.4136	52.5638
			(FGM/P) _S , TD-F			
-200 V	98.5558	80.7987	69.0785	60.4969	53.6130	47.6470
0 V	95.1197	78.5290	67.3911	59.1540	52.4951	46.6856
+ 200 V	91.6894	76.2520	65.6965	57.8054	51.3727	45.7204
			(FGM/P) _S , TD			
- 200 V	98.4460	80.7397	69.0412	60.4711	53.5941	47.6327
0 V	95.1069	78.5229	67.3875	59.1518	52.4936	46.6845
+ 200 V	91.7668	76.2961	65.7254	57.8259	51.3879	45.7322

are acceptable. In contrast, it is seen that the buckling temperature of hybrid plates with $ZrO_2/Ti-6Al-4V$ substrate is decreased as the volume fraction index N increases. It can also be seen that the control voltage has a small effect on the thermal buckling loads for these two FGM hybrid laminated plates.

Figure 7.7 shows the thermal postbuckling load-deflection curves for perfect and imperfect, (P/FGM)_S and (FGM/P)_S hybrid laminated square plates ($b/t = 40$) with $Si_3N_4/SUS304$ substrate subjected to uniform temperature rise and three sets of electrical loads under two cases of thermoelastic properties TID and TD. It can be seen that the increase of the volume fraction index N yields an increase of the buckling temperature and thermal postbuckling strength. The results also confirm that the thermal postbuckling equilibrium path becomes lower when the temperature-dependent properties are taken into account. In contrast, the control voltage has a small effect on the buckling temperature and thermal postbuckling response of FGM hybrid laminated plates.



7.7 Effects of volume fraction index N and material properties on the thermal postbuckling behavior of $\text{Si}_3\text{N}_4/\text{SUS304}$ hybrid laminated plates subjected to uniform temperature loading: (a) (P/FGM)_S plate (1: $V_U = V_L = -200$ V; 2: $V_U = V_L = 0$ V; 3: $V_U = V_L = +200$ V); (b) (FGM/P)_S plate (1: $V_M = -200$ V; 2: $V_M = 0$ V; 3: $V_M = +200$ V).

7.8 Concluding remarks

In order to assess the effects of temperature dependency on the thermal postbuckling behavior of laminated plates, a fully nonlinear thermal postbuckling analysis has been described. The governing equations are based on a higher-order shear deformation plate theory that includes thermopiezoelectric effects. A two-step perturbation technique is employed to

determine buckling temperature and postbuckling equilibrium paths. Numerical calculations have been made for (1) fiber-reinforced composite antisymmetric angle-ply and symmetric cross-ply laminated plates; (2) symmetric cross-ply laminated plates with surface-bonded or embedded piezoelectric actuators; and (3) mid-plane symmetric FGM plates with fully covered or embedded piezoelectric actuators. The results show that in all these cases the plate has lower buckling temperature and postbuckling load-deflection curves when the temperature-dependent properties are taken into account. The control voltage has a significant effect on the thermal buckling and postbuckling loads for $(0/90)_{2S}$ laminated plates with piezoelectric actuators, but it has a small effect on the thermal buckling and postbuckling loads for FGM hybrid laminated plates.

It is hoped that the results reported herein will contribute to a better understanding of the thermal postbuckling behavior for hybrid laminated plates with temperature-dependent properties.

7.9 Acknowledgement

The support for this work, provided by the National Natural Science Foundation of China under Grant 59975058 and 50375091, is gratefully acknowledged.

7.10 References

- Argyris, J. and Tenek, L. (1995), 'Postbuckling of composite laminates under compressive load and temperature', *Computer Methods in Applied Mechanics and Engineering*, **128**, 49–80.
- Bhimaraddi, A. and Chandashekhara, K. (1993), 'Nonlinear vibrations of heated antisymmetric angle-ply laminated plates', *International Journal of Solids and Structures*, **30**, 1255–1268.
- Birman, V. and Bert, C.W. (1993), 'Buckling and post-buckling of composite plates and shells subjected to elevated temperature', *Journal of Applied Mechanics ASME*, **60**, 514–519.
- Chen, L-W. and Chen, L-Y. (1989), 'Thermal postbuckling analysis of laminated composite plates by the finite element method', *Composite Structures*, **12**, 257–270.
- Chen, L-W. and Chen, L-Y. (1991), 'Thermal postbuckling behaviors of laminated composite plates with temperature-dependent properties', *Composite Structures*, **15**, 267–283.
- Ganapathi, M. and Touratier, M. (1997), 'A study on thermal postbuckling behaviour of laminated composite plates using a shear-flexible element', *Finite Elements in Analysis and Design*, **28**, 115–135.
- Huang, N.N. and Tauchert, T.R. (1988), 'Postbuckling response of antisymmetric angle-ply laminates to uniform temperature loading', *Acta Mechanica*, **72**, 173–183.
- Huang, X-L. and Shen, H-S. (2004), 'Nonlinear vibration and dynamic response of functionally graded plates in thermal environments', *International Journal of Solids and Structures*, **41**, 2403–2427.
- Huang, X-L., Shen, H-S. and Zheng, J-J. (2004), 'Nonlinear vibration and dynamic

- response of shear deformable laminated plates in hygrothermal environments', *Composites Science and Technology*, **64**, 1419–1435.
- Kamiya, N. and Fukui, A. (1982), 'Finite deflection and postbuckling behavior of heated rectangular plates with temperature-dependent properties', *Nuclear Engineering and Design*, **72**, 415–420.
- Lee, D-M. and Lee, I. (1997), 'Vibration behaviors of thermally postbuckled anisotropic plates using first-order shear deformable plate theory', *Computers and Structures*, **63**, 371–378.
- Leissa, A.W. (1986), 'Conditions for laminated plates to remain flat under inplane loading', *Composite Structures*, **6**, 261–270.
- Librescu, L. and Souza, M.A. (1993), 'Post-buckling of geometrically imperfect shear-deformable flat panels under combined thermal and compressive edge loadings', *Journal of Applied Mechanics ASME*, **60**, 526–533.
- Librescu, L., Lin, W., Nemeth, M.P. and Starnes, J.H. (1995), 'Thermomechanical postbuckling of geometrically imperfect flat and curved panels taking into account tangential edge constraints', *Journal of Thermal Stresses*, **18**, 465–482.
- Liew, K.M., Yang, J. and Kitipornchai, S. (2003), 'Postbuckling of piezoelectric FGM plates subject to thermo-electro-mechanical loading', *International Journal of Solids and Structures*, **40**, 3869–3892.
- Lin, W. and Librescu, L. (1998), 'Thermomechanical postbuckling of geometrically imperfect shear-deformable flat and curved panels on a nonlinear elastic foundation', *International Journal of Engineering Science*, **36**, 189–206.
- Meyers, C.A. and Hyer, M.W. (1991), 'Thermal buckling and postbuckling of symmetrically laminated composite plates', *Journal of Thermal Stresses*, **14**, 519–540.
- Nath, Y. and Shukla, K.K. (2001), 'Postbuckling of angle-ply laminated plates under thermal loading', *Communications in Nonlinear Science & Numerical Simulation*, **6**, 1–16.
- Noor, A.K. and Burton, W.S. (1992), 'Computational models for high-temperature multilayered composite plates and shells', *Applied Mechanics Review*, **45**, 419–446.
- Noor, A.K. and Peters, J.M. (1992), 'Postbuckling of multilayered composite plates subjected to combined axial and thermal loads', *Finite Elements in Analysis and Design*, **11**, 91–104.
- Noor, A.K., Starnes, J.H. and Peters, J.M. (1993), 'Thermomechanical buckling and postbuckling of multilayered composite panels', *Composite Structures*, **23**, 233–251.
- Oh, I.K., Han, J.H. and Lee, I. (2000), 'Postbuckling and vibration characteristics of piezolaminated composite plate subjected to thermo-piezoelectric loads', *Journal of Sound and Vibration*, **233**, 19–40.
- Oh, I.K., Han, J.H. and Lee, I. (2001), 'Thermopiezoelastic snapping of piezolaminated plates using layerwise nonlinear finite elements', *AIAA Journal*, **39**, 1188–1197.
- Qatu, M.S. and Leissa, A.W. (1993), 'Buckling or transverse deflections of unsymmetrically laminated plates subjected to in-plane loads', *AIAA Journal*, **31**, 189–194.
- Reddy, J.N. (1984a), 'A simple higher-order theory for laminated composite plates', *Journal of Applied Mechanics ASME*, **51**, 745–752.
- Reddy, J.N. (1984b), 'A refined nonlinear theory of plates with transverse shear deformation', *International Journal of Solids and Structures*, **20**, 881–896.
- Reddy, J.N. and Chin, C.D. (1998), 'Thermoelastical analysis of functionally graded cylinders and plates', *Journal of Thermal Stresses*, **21**, 593–626.
- Shen, H-S. (1997a), 'Thermal postbuckling analysis of imperfect laminated plates using a higher-order shear deformation theory', *International Journal of Non-Linear Mechanics*, **32**, 1035–1050.

- Shen, H-S. (1997b), 'Kármán-type equations for a higher-order shear deformation plate theory and its use in the thermal postbuckling analysis', *Applied Mathematics and Mechanics*, **18**, 1137–1152.
- Shen, H-S. (1998), 'Thermomechanical post-buckling analysis of imperfect laminated plates using a higher-order shear-deformation theory', *Computers and Structures*, **66**, 395–409.
- Shen, H-S. (1999), 'Thermal postbuckling of imperfect shear deformable laminated plates on two-parameter elastic foundations', *Mechanics of Composite Materials and Structures*, **6**, 207–228.
- Shen, H-S. (2000a), 'Thermomechanical postbuckling of imperfect shear deformable laminated plates on elastic foundations', *Computer Methods in Applied Mechanics and Engineering*, **189**, 761–784.
- Shen, H-S. (2000b), 'Thermal postbuckling of preloaded shear deformable laminated plates', *Journal of Engineering Mechanics ASCE*, **126**, 488–496.
- Shen, H-S. (2000c), 'Non-linear bending of shear deformable laminated plates under lateral pressure and thermal loading and resting on elastic foundations', *Journal of Strain Analysis for Engineering Design*, **35**, 93–108.
- Shen, H-S. (2001a), 'Thermal postbuckling of shear deformable laminated plates with piezoelectric actuators', *Composites Science and Technology*, **61**, 1931–1943.
- Shen, H-S. (2001b), 'Postbuckling of shear deformable laminated plates with piezoelectric actuators under complex loading conditions', *International Journal of Solids and Structures*, **38**, 7703–7721.
- Shen, H-S. (2001c), 'Thermal postbuckling behavior of imperfect shear deformable laminated plates with temperature-dependent properties', *Computer Methods in Applied Mechanics and Engineering*, **190**, 5377–5390.
- Shen, H-S. (2001d), 'Hygrothermal effects on the postbuckling of shear deformable laminated plates', *International Journal of Mechanical Sciences*, **43**, 1259–1281.
- Shen, H-S. (2002), 'Nonlinear bending response of functionally graded plates subjected to transverse loads and in thermal environments', *International Journal of Mechanical Sciences*, **44**, 561–584.
- Shen, H-S. (2004), 'Nonlinear bending analysis of unsymmetric cross-ply laminated plates with piezoelectric actuators in thermal environments', *Composite Structures*, **63**, 167–177.
- Shen, H-S. and Lin, Z-Q. (1995), 'Thermal postbuckling analysis of imperfect laminated plates', *Computers and Structures*, **57**, 533–540.
- Shen, H-S. and Williams, F.W. (1996), 'Post-buckling analysis of imperfect laminated plates under combined axial and thermal loads', *Computational Mechanics*, **17**, 226–233.
- Shen, H-S. and Williams, F.W. (1997a), 'Thermal postbuckling analysis of imperfect laminated plates on two-parameter elastic foundations', *Journal of Applied Mechanics ASME*, **64**, 700–704.
- Shen, H-S. and Williams, F.W. (1997b), 'Thermal postbuckling analysis of imperfect laminated plates on softening nonlinear elastic foundations', *Composites Science and Technology*, **57**, 719–728.
- Shen, H-S., Sun, G. and Williams, F.W. (1996), 'Thermomechanical postbuckling analysis of imperfect laminated plates on two-parameter elastic foundations', *Composite Structures*, **34**, 325–338.
- Shi, Y., Lee, R.Y.Y. and Mei, C. (1999), 'Thermal postbuckling of composite plates using the finite element modal coordinate method', *Journal of Thermal Stresses*, **22**, 595–614.

- Shukla, K.K. and Nath, Y. (2001), 'Analytical solution for buckling and post-buckling of angle-ply laminated plates under thermomechanical loading', *International Journal of Non-Linear Mechanics* **36**, 1097–1108.
- Shukla, K.K. and Nath, Y. (2002), 'Thermomechanical postbuckling of cross-ply laminated rectangular plates', *Journal of Engineering Mechanics ASCE*, **128**, 93–101.
- Singh, G. and Rao, G.V. (1993), 'Thermal postbuckling behavior of rectangular antisymmetric cross-ply composite plates', *Acta Mechanica*, **98**, 39–50.
- Singh, G., Rao, G.V. and Iyengar, N.G.R. (1994), 'Thermal postbuckling behavior of laminated composite plates', *AIAA Journal*, **32**, 1336–1338.
- Singh, M.K., Ramachandra, L.S. and Bandyopadhyay, J.N. (2001), 'Thermal postbuckling analysis of laminated composite plates', *Composite Structures*, **54**, 453–458.
- Tenek, L. (2001), 'Postbuckling of thermally stressed composite plates', *AIAA Journal*, **39**, 546–548.
- Thankam, V.S., Singh, G., Rao, G.V. and Rath, A.K. (2003), 'Thermal post-buckling behaviour of laminated plates using a shear-flexible element based on coupled-displacement field', *Composite Structures*, **59**, 351–359.
- Thornton, E.A. (1993), 'Thermal buckling of plates and shells', *Applied Mechanics Review*, **46**, 485–506.
- Touloukian, Y.S. (1967), *Thermophysical properties of high temperature solid materials*, McMillan, New York.

7.11 Appendix A

In Eqs. (7.1)–(7.4) all linear operators $\tilde{L}_{ij}(\cdot)$ and the nonlinear operator $\tilde{L}(\cdot)$ are defined by:

$$\begin{aligned} \tilde{L}_{11}(\cdot) = & \frac{4}{3t^2} \left[F_{11}^* \frac{\partial^4}{\partial X^4} + 2(F_{16}^* + F_{61}^*) \frac{\partial^4}{\partial X^3 \partial Y} \right. \\ & + (F_{12}^* + F_{21}^* + 4F_{66}^*) \frac{\partial^4}{\partial X^2 \partial Y^2} \\ & \left. + 2(F_{26}^* + F_{62}^*) \frac{\partial^4}{\partial X \partial Y^3} + F_{22}^* \frac{\partial^4}{\partial Y^4} \right] \end{aligned}$$

$$\tilde{L}_{12}(\cdot)$$

$$\begin{aligned} = & \left[D_{11}^* - \frac{4}{3t^2} F_{11}^* \right] \frac{\partial^3}{\partial X^3} + \left[3D_{16}^* - \frac{4}{3t^2} (F_{61}^* + 2F_{16}^*) \right] \frac{\partial^3}{\partial X^2 \partial Y} \\ & + \left[(D_{12}^* + 2D_{66}^*) - \frac{4}{3t^2} (F_{12}^* + 2F_{66}^*) \right] \frac{\partial^3}{\partial X \partial Y^2} \\ & + \left[D_{26}^* - \frac{4}{3t^2} F_{26}^* \right] \frac{\partial^3}{\partial Y^3} \end{aligned}$$

$$\begin{aligned}
\tilde{L}_{13}(\cdot) &= \left[D_{16}^* - \frac{4}{3t^2} F_{16}^* \right] \frac{\partial^3}{\partial X^3} \\
&+ \left[(D_{12}^* + 2D_{66}^*) - \frac{4}{3t^2} (F_{21}^* + 2F_{66}^*) \right] \frac{\partial^3}{\partial X^2 \partial Y} \\
&+ \left[3D_{26}^* - \frac{4}{3t^2} (F_{62}^* + 2F_{26}^*) \right] \frac{\partial^3}{\partial X \partial Y^2} \\
&+ \left[D_{22}^* - \frac{4}{3t^2} F_{22}^* \right] \frac{\partial^3}{\partial Y^3} \\
\tilde{L}_{14}(\cdot) &= B_{21}^* \frac{\partial^4}{\partial X^4} + (2B_{26}^* - B_{61}^*) \frac{\partial^4}{\partial X^3 \partial Y} \\
&+ (B_{11}^* + B_{22}^* - 2B_{66}^*) \frac{\partial^4}{\partial X^2 \partial Y^2} \\
&+ (2B_{16}^* - B_{62}^*) \frac{\partial^4}{\partial X \partial Y^3} + B_{12}^* \frac{\partial^4}{\partial Y^4} \\
\tilde{L}_{15}(\bar{N}^T) &= \frac{\partial^2}{\partial X^2} (B_{11}^* \bar{N}_x^T + B_{21}^* \bar{N}_y^T + B_{61}^* \bar{N}_{xy}^T) \\
&+ 2 \frac{\partial^2}{\partial X \partial Y} (B_{16}^* \bar{N}_x^T + B_{26}^* \bar{N}_y^T + B_{66}^* \bar{N}_{xy}^T) \\
&+ \frac{\partial^2}{\partial Y^2} (B_{12}^* \bar{N}_x^T + B_{22}^* \bar{N}_y^T + B_{62}^* \bar{N}_{xy}^T) \\
\tilde{L}_{16}(\bar{M}^T) &= \frac{\partial^2}{\partial X^2} (\bar{M}_x^T) + 2 \frac{\partial^2}{\partial X \partial Y} (\bar{M}_{xy}^T) + \frac{\partial^2}{\partial Y^2} (\bar{M}_y^T) \\
\tilde{L}_{21}(\cdot) &= A_{22}^* \frac{\partial^4}{\partial X^4} - 2A_{26}^* \frac{\partial^4}{\partial X^3 \partial Y} + (2A_{12}^* + A_{66}^*) \frac{\partial^4}{\partial X^2 \partial Y^2} \\
&- 2A_{16}^* \frac{\partial^4}{\partial X \partial Y^3} + A_{11}^* \frac{\partial^4}{\partial Y^4} \\
\tilde{L}_{22}(\cdot) &= \left[B_{21}^* - \frac{4}{3t^2} E_{21}^* \right] \frac{\partial^3}{\partial X^3} \\
&+ \left[(B_{26}^* - B_{61}^*) - \frac{4}{3t^2} (E_{26}^* - E_{61}^*) \right] \frac{\partial^3}{\partial X^2 \partial Y}
\end{aligned}$$

$$\begin{aligned}
 & + \left[(B_{11}^* - B_{66}^*) - \frac{4}{3t^2} (E_{11}^* - E_{66}^*) \right] \frac{\partial^3}{\partial X \partial Y^2} \\
 & + \left[B_{16}^* - \frac{4}{3t^2} E_{16}^* \right] \frac{\partial^3}{\partial Y^3} \\
 \tilde{L}_{23}(\cdot) = & \left[B_{26}^* - \frac{4}{3t^2} E_{26}^* \right] \frac{\partial^3}{\partial X^3} \\
 & + \left[(B_{22}^* - B_{66}^*) - \frac{4}{3t^2} (E_{22}^* - E_{66}^*) \right] \frac{\partial^3}{\partial X^2 \partial Y} \\
 & + \left[(B_{16}^* - B_{62}^*) - \frac{4}{3t^2} (E_{16}^* - E_{62}^*) \right] \frac{\partial^3}{\partial X \partial Y^2} \\
 & + \left[B_{12}^* - \frac{4}{3t^2} E_{12}^* \right] \frac{\partial^3}{\partial Y^3} \\
 \tilde{L}_{24}(\cdot) = & \frac{4}{3t^2} \left[E_{21}^* \frac{\partial^4}{\partial X^4} + (2E_{26}^* - E_{61}^*) \frac{\partial^4}{\partial X^3 \partial Y} \right. \\
 & + (E_{11}^* + E_{22}^* - 2E_{66}^*) \frac{\partial^4}{\partial X^2 \partial Y^2} \\
 & \left. + (2E_{16}^* - E_{62}^*) \frac{\partial^4}{\partial X \partial Y^3} + E_{12}^* \frac{\partial^4}{\partial Y^4} \right] \\
 \tilde{L}_{25}(\bar{N}^T) = & \frac{\partial^2}{\partial X^2} (A_{12}^* \bar{N}_x^T + A_{22}^* \bar{N}_y^T + A_{26}^* \bar{N}_{xy}^T) \\
 & - \frac{\partial^2}{\partial X \partial Y} (A_{16}^* \bar{N}_x^T + A_{26}^* \bar{N}_y^T + A_{66}^* \bar{N}_{xy}^T) \\
 & + \frac{\partial^2}{\partial Y^2} (A_{11}^* \bar{N}_x^T + A_{12}^* \bar{N}_y^T + A_{16}^* \bar{N}_{xy}^T) \\
 \tilde{L}_{31}(\cdot) = & \left[A_{55} - \frac{8}{t^2} D_{55} + \frac{16}{t^4} F_{55} \right] \frac{\partial}{\partial X} \\
 & + \left[A_{45} - \frac{8}{t^2} D_{45} + \frac{16}{t^4} F_{45} \right] \frac{\partial}{\partial Y} \\
 & + \frac{4}{3t^2} \left[\left(F_{11}^* - \frac{4}{3t^2} H_{11}^* \right) \frac{\partial^3}{\partial X^3} \right.
 \end{aligned}$$

$$\begin{aligned}
& + \left((F_{16}^* + 2F_{61}^*) - \frac{4}{t^2} H_{16}^* \right) \frac{\partial^3}{\partial X^2 \partial Y} \\
& + \left((F_{21}^* + 2F_{66}^*) - \frac{4}{3t^2} (H_{12}^* + 2H_{66}^*) \right) \frac{\partial^3}{\partial X \partial Y^2} \\
& + \left(F_{26}^* - \frac{4}{3t^2} H_{26}^* \right) \frac{\partial^3}{\partial Y^3} \Big] \\
\tilde{L}_{32}(\cdot) = & \left[A_{55} - \frac{8}{t^2} D_{55} + \frac{16}{t^4} F_{55} \right] \\
& - \left[D_{11}^* - \frac{8}{3t^2} F_{11}^* + \frac{16}{9t^4} H_{11}^* \right] \frac{\partial^2}{\partial X^2} \\
& - 2 \left[D_{16}^* - \frac{4}{3t^2} (F_{16}^* + F_{61}^*) + \frac{16}{9t^4} H_{16}^* \right] \frac{\partial^2}{\partial X \partial Y} \\
& - \left[D_{66}^* - \frac{4}{3t^2} F_{66}^* + \frac{16}{9t^4} H_{66}^* \right] \frac{\partial^2}{\partial Y^2} \\
\tilde{L}_{33}(\cdot) = & \left[A_{45} - \frac{8}{t^2} D_{45} + \frac{16}{t^4} F_{45} \right] \\
& - \left[D_{16}^* - \frac{4}{3t^2} (F_{16}^* + F_{61}^*) + \frac{16}{9t^4} H_{16}^* \right] \frac{\partial^2}{\partial X^2} \\
& - \left[(D_{12}^* + D_{66}^*) - \frac{4}{3t^2} (F_{12}^* + F_{21}^* + 2F_{66}^*) \right. \\
& \left. + \frac{16}{9t^4} (H_{12}^* + H_{66}^*) \right] \frac{\partial^2}{\partial X \partial Y} \\
& - \left[D_{26}^* - \frac{4}{3t^2} (F_{26}^* + F_{62}^*) + \frac{16}{9t^4} H_{26}^* \right] \frac{\partial^2}{\partial Y^2} \\
\tilde{L}_{34}(\cdot) = & \tilde{L}_{22}(\cdot) \\
\tilde{L}_{35}(\bar{N}^T) = & \frac{\partial}{\partial X} \left[\left(B_{11}^* - \frac{4}{3t^2} E_{11}^* \right) \bar{N}_x^T \right. \\
& \left. + \left(B_{21}^* - \frac{4}{3t^2} E_{21}^* \right) \bar{N}_y^T + \left(B_{61}^* - \frac{4}{3t^2} E_{61}^* \right) \bar{N}_{xy}^T \right]
\end{aligned}$$

$$\begin{aligned}
 & + \frac{\partial}{\partial Y} \left[\left(B_{16}^* - \frac{4}{3t^2} E_{16}^* \right) \bar{N}_x^T + \left(B_{26}^* - \frac{4}{3t^2} E_{26}^* \right) \bar{N}_y^T \right. \\
 & \left. + \left(B_{66}^* - \frac{4}{3t^2} E_{66}^* \right) \bar{N}_{xy}^T \right]
 \end{aligned}$$

$$\tilde{L}_{36}(\bar{S}^T) = \frac{\partial}{\partial X}(\bar{S}_x^T) + \frac{\partial}{\partial Y}(\bar{S}_{xy}^T)$$

$$\begin{aligned}
 \tilde{L}_{41}(\cdot) &= \left[A_{45} - \frac{8}{t^2} D_{45} + \frac{16}{t^4} F_{45} \right] \frac{\partial}{\partial X} \\
 &+ \left[A_{44} - \frac{8}{t^2} D_{44} + \frac{16}{t^4} F_{44} \right] \frac{\partial}{\partial Y} \\
 &+ \frac{4}{3t^2} \left[\left(F_{16}^* - \frac{4}{3t^2} H_{16}^* \right) \frac{\partial^3}{\partial X^3} \right. \\
 &+ \left. \left((F_{12}^* + 2F_{66}^*) - \frac{4}{3t^2} (H_{12}^* - 2H_{66}^*) \right) \frac{\partial^3}{\partial X \partial Y^2} \right. \\
 &+ \left. \left. \left((F_{26}^* + 2F_{62}^*) - \frac{4}{t^2} H_{26}^* \right) \frac{\partial^3}{\partial X \partial Y^2} + \left(F_{22}^* - \frac{4}{3t^2} H_{22}^* \right) \frac{\partial^3}{\partial Y^3} \right]
 \end{aligned}$$

$$\tilde{L}_{42}(\cdot) = \tilde{L}_{33}(\cdot)$$

$$\begin{aligned}
 \tilde{L}_{43}(\cdot) &= \left[A_{44} - \frac{8}{t^2} D_{44} + \frac{16}{t^4} F_{44} \right] \\
 &- \left[D_{66}^* - \frac{8}{3t^2} F_{66} + \frac{16}{9t^4} H_{66}^* \right] \frac{\partial^2}{\partial X^2} \\
 &- 2 \left[D_{26}^* - \frac{4}{3t^2} (F_{26}^* + H_{62}^*) + \frac{16}{9t^4} H_{26}^* \right] \frac{\partial^2}{\partial X \partial Y} \\
 &- \left[D_{22}^* - \frac{8}{3t^2} F_{22}^* + \frac{16}{9t^4} H_{22}^* \right] \frac{\partial^2}{\partial Y^2}
 \end{aligned}$$

$$\tilde{L}_{44}(\cdot) = \tilde{L}_{23}(\cdot)$$

$$\begin{aligned}
 \tilde{L}_{45}(\bar{N}^T) &= \frac{\partial}{\partial X} \left[\left(B_{16}^* - \frac{4}{3t^2} E_{16}^* \right) \bar{N}_x^T + \left(B_{26}^* - \frac{4}{3t^2} E_{26}^* \right) \bar{N}_y^T \right. \\
 &+ \left. \left(B_{66}^* - \frac{4}{3t^2} E_{66}^* \right) \bar{N}_{xy}^T \right] + \frac{\partial}{\partial Y} \left[\left(B_{12}^* - \frac{4}{3t^2} E_{12}^* \right) \bar{N}_x^T \right.
 \end{aligned}$$

$$\left. + \left(B_{22}^* - \frac{4}{3t^2} E_{22}^* \right) \bar{N}_y^T + \left(B_{62}^* - \frac{4}{3t^2} E_{62}^* \right) \bar{N}_{xy}^T \right]$$

$$\tilde{L}_{46}(\bar{S}^T) = \frac{\partial}{\partial X}(\bar{S}_{xy}^T) + \frac{\partial}{\partial Y}(\bar{S}_y^T)$$

$$\tilde{L}(\cdot) = \frac{\partial^2}{\partial X^2} \frac{\partial^2}{\partial Y^2} - 2 \frac{\partial^2}{\partial X \partial Y} \frac{\partial^2}{\partial X \partial Y} + \frac{\partial^2}{\partial Y^2} \frac{\partial^2}{\partial X^2}$$

7.12 Appendix B

In Eqs. (7.16)–(7.19) the nondimensional linear operators $L_{ij}(\cdot)$ and the nonlinear operator $L(\cdot)$ are defined by:

$$L_{11}(\cdot) = \gamma_{110} \frac{\partial^4}{\partial x^4} + \gamma_{111} \beta \frac{\partial^4}{\partial x^3 \partial y}$$

$$+ 2\gamma_{112} \beta^2 \frac{\partial^4}{\partial x^2 \partial y^2} + \gamma_{113} \beta^3 \frac{\partial^4}{\partial x \partial y^3} + \gamma_{114} \beta^4 \frac{\partial^4}{\partial y^4}$$

$$L_{12}(\cdot) = \gamma_{120} \frac{\partial^3}{\partial x^3} + \gamma_{121} \beta \frac{\partial^3}{\partial x^2 \partial y} + \gamma_{122} \beta^2 \frac{\partial^3}{\partial x \partial y^2} + \gamma_{123} \beta^3 \frac{\partial^3}{\partial y^3}$$

$$L_{13}(\cdot) = \gamma_{130} \frac{\partial^3}{\partial x^3} + \gamma_{131} \beta \frac{\partial^3}{\partial x^2 \partial y} + \gamma_{132} \beta^2 \frac{\partial^3}{\partial x \partial y^2} + \gamma_{133} \beta^3 \frac{\partial^3}{\partial y^3}$$

$$L_{14}(\cdot) = \gamma_{140} \frac{\partial^4}{\partial x^4} + \gamma_{141} \beta \frac{\partial^4}{\partial x^3 \partial y} + \gamma_{142} \beta^2 \frac{\partial^4}{\partial x^2 \partial y^2}$$

$$+ \gamma_{143} \beta^3 \frac{\partial^4}{\partial x \partial y^3} + \gamma_{144} \beta^4 \frac{\partial^4}{\partial y^4}$$

$$L_{21}(\cdot) = \frac{\partial^4}{\partial x^4} + \gamma_{211} \beta \frac{\partial^4}{\partial x^3 \partial y} + 2\gamma_{212} \beta^2 \frac{\partial^4}{\partial x^2 \partial y^2}$$

$$+ \gamma_{213} \beta^3 \frac{\partial^4}{\partial x \partial y^3} + \gamma_{214} \beta^4 \frac{\partial^4}{\partial y^4}$$

$$L_{22}(\cdot) = L_{34}(\cdot) = \gamma_{220} \frac{\partial^3}{\partial x^3} + \gamma_{221} \beta \frac{\partial^3}{\partial x^2 \partial y}$$

$$+ \gamma_{222} \beta^2 \frac{\partial^3}{\partial x \partial y^2} + \gamma_{223} \beta^3 \frac{\partial^3}{\partial y^3}$$

$$L_{23}(\cdot) = L_{44}(\cdot) = \gamma_{230} \frac{\partial^3}{\partial x^3} + \gamma_{231} \beta \frac{\partial^3}{\partial x^2 \partial y}$$

$$+ \gamma_{232} \beta^2 \frac{\partial^3}{\partial x \partial y^2} + \gamma_{233} \beta^3 \frac{\partial^3}{\partial y^3}$$

$$\begin{aligned}
 L_{24}(\cdot) &= \gamma_{240} \frac{\partial^4}{\partial x^4} + \gamma_{241} \beta \frac{\partial^4}{\partial x^3 \partial y} + \gamma_{242} \beta^2 \frac{\partial^4}{\partial x^2 \partial y^2} \\
 &\quad + \gamma_{243} \beta^3 \frac{\partial^4}{\partial x \partial y^3} + \gamma_{244} \beta^4 \frac{\partial^4}{\partial y^4} \\
 L_{31}(\cdot) &= \gamma_{31} \frac{\partial}{\partial x} + \gamma_{32} \beta \frac{\partial}{\partial y} + \gamma_{310} \frac{\partial^3}{\partial x^3} + \gamma_{311} \beta \frac{\partial^3}{\partial x^2 \partial y} \\
 &\quad + \gamma_{312} \beta^2 \frac{\partial^3}{\partial x \partial y^2} + \gamma_{313} \beta^3 \frac{\partial^3}{\partial y^3} \\
 L_{32}(\cdot) &= \gamma_{31} - \gamma_{320} \frac{\partial^2}{\partial x^2} - \gamma_{321} \beta \frac{\partial^2}{\partial x \partial y} - \gamma_{322} \beta^2 \frac{\partial^2}{\partial y^2} \\
 L_{33}(\cdot) &= \gamma_{32} - \gamma_{330} \frac{\partial^2}{\partial x^2} - \gamma_{331} \beta \frac{\partial^2}{\partial x \partial y} - \gamma_{332} \beta^2 \frac{\partial^2}{\partial y^2} \\
 L_{34}(\cdot) &= L_{22}(\cdot) \\
 L_{41}(\cdot) &= \gamma_{41} \frac{\partial}{\partial x} + \gamma_{42} \beta \frac{\partial}{\partial y} + \gamma_{410} \frac{\partial^3}{\partial x^3} + \gamma_{411} \beta \frac{\partial^3}{\partial x^2 \partial y} \\
 &\quad + \gamma_{412} \beta^2 \frac{\partial^3}{\partial x \partial y^2} + \gamma_{413} \beta^3 \frac{\partial^3}{\partial y^3} \\
 L_{42}(\cdot) &= L_{33}(\cdot) \\
 L_{43}(\cdot) &= \gamma_{41} - \gamma_{430} \frac{\partial^2}{\partial x^2} - \gamma_{431} \beta \frac{\partial^2}{\partial x \partial y} - \gamma_{432} \beta^2 \frac{\partial^2}{\partial y^2} \\
 L_{44}(\cdot) &= L_{23}(\cdot) \\
 L(\cdot) &= \frac{\partial^2}{\partial x^2} \frac{\partial^2}{\partial y^2} - 2 \frac{\partial^2}{\partial x \partial y} \frac{\partial^2}{\partial x \partial y} + \frac{\partial^2}{\partial y^2} \frac{\partial^2}{\partial x^2}
 \end{aligned}$$

in the above equations

$$\begin{aligned}
 (\gamma_{110}, \gamma_{112}, \gamma_{114}) &= (4/3t^2)[F_{11}^*, (F_{12}^* + F_{21}^* + 4F_{66}^*)/2, F_{22}^*]/D_{11}^* \\
 (\gamma_{111}, \gamma_{113}) &= (4/3t^2)[2(F_{16}^* + F_{61}^*), 2(F_{26}^* + F_{62}^*)]/D_{11}^* \\
 (\gamma_{120}, \gamma_{122}) &= [D_{11}^* - 4F_{11}^*/3t^2, (D_{12}^* + 2D_{66}^*) - 4(F_{12}^* + 2F_{66}^*)/3t^3]/D_{11}^* \\
 (\gamma_{121}, \gamma_{123}) &= [3D_{16}^* - 4(F_{61}^* + 2F_{16}^*)/3t^2, D_{26}^* - 4F_{26}^*/3t^2]/D_{11}^* \\
 (\gamma_{130}, \gamma_{132}) &= [D_{16}^* - 4F_{16}^*/3t^2, 3D_{26}^* - 4(F_{62}^* + 2F_{26}^*)/3t^2]/D_{11}^* \\
 (\gamma_{131}, \gamma_{133}) &= [(D_{12}^* + 2D_{66}^*) - 4(F_{21}^* + 2F_{66}^*)/3t^2, \\
 &\quad D_{22}^* - 4F_{22}^*/3t^2]/D_{11}^*
 \end{aligned}$$

$$(\gamma_{140}, \gamma_{142}, \gamma_{144}) = [B_{21}^*, (B_{11}^* + B_{22}^* - 2B_{66}^*), \\ B_{12}^*]/[D_{11}^* D_{22}^* A_{11}^* A_{22}^*]^{1/4}$$

$$(\gamma_{141}, \gamma_{143}) = (2B_{26}^* - B_{61}^*, 2B_{16}^* - B_{62}^*)/[D_{11}^* D_{22}^* A_{11}^* A_{22}^*]^{1/4}$$

$$(\gamma_{211}, \gamma_{213}) = -2(A_{26}^*, A_{16}^*)/A_{22}^*$$

$$(\gamma_{212}, \gamma_{214}) = (A_{12}^* + A_{66}^*/2, A_{11}^*)/A_{22}^*$$

$$(\gamma_{220}, \gamma_{222}) = [B_{21}^* - 4E_{21}^*/3t^2, (B_{11}^* - B_{66}^*) - 4(E_{11}^* - E_{66}^*)/3t^2] \\ / [D_{11}^* D_{22}^* A_{11}^* A_{22}^*]^{1/4}$$

$$(\gamma_{221}, \gamma_{223}) = [(B_{26}^* - B_{61}^*) - 4(E_{26}^* - E_{61}^*)/3t^2, B_{16}^* - 4E_{16}^*/3t^2] \\ / [D_{11}^* D_{22}^* A_{11}^* A_{22}^*]^{1/4}$$

$$(\gamma_{230}, \gamma_{232}) = [B_{26}^* - 4E_{26}^*/3t^2, (B_{16}^* - B_{62}^*) - 4(E_{16}^* - E_{62}^*)/3t^2] \\ / [D_{11}^* D_{22}^* A_{11}^* A_{22}^*]^{1/4}$$

$$(\gamma_{231}, \gamma_{233}) = [(B_{22}^* - B_{66}^*) - 4(E_{22}^* - E_{66}^*)/3t^2, B_{12}^* - 4E_{12}^*/3t^2] \\ / [D_{11}^* D_{22}^* A_{11}^* A_{22}^*]^{1/4}$$

$$(\gamma_{240}, \gamma_{242}, \gamma_{244}) = (4/3t^2)[E_{21}^*, (E_{11}^* + E_{22}^* - 2E_{66}^*), E_{12}^*] \\ / [D_{11}^* D_{22}^* A_{11}^* A_{22}^*]^{1/4}$$

$$(\gamma_{241}, \gamma_{243}) = (4/3t^2)(2E_{26}^* - E_{61}^*, 2E_{16}^* - E_{62}^*) \\ / [D_{11}^* D_{22}^* A_{11}^* A_{22}^*]^{1/4}$$

$$(\gamma_{310}, \gamma_{312}) = (4/3t^2)[F_{11}^* - 4H_{11}^*/3t^2, (F_{21}^* + 2F_{66}^*) \\ - 4(H_{12}^* + 2H_{66}^*)/3t^2]/D_{11}^*$$

$$(\gamma_{311}, \gamma_{313}) \\ = (4/3t^2)[(F_{16}^* + 2F_{61}^*) - 4H_{16}^*/t^2, F_{26}^* - 4H_{26}^*/3t^2]/D_{11}^*$$

$$(\gamma_{320}, \gamma_{322}) = (D_{11}^* - 8F_{11}^*/3t^2 + 16H_{11}^*/9t^4, D_{66}^* \\ - 8F_{66}^*/3t^2 + 16H_{66}^*/9t^4)/D_{11}^*$$

$$\gamma_{321} = 2[D_{16}^* - 4(F_{16}^* + F_{61}^*)/3t^2 + 16H_{16}^*/9t^4]/D_{11}^*$$

$$(\gamma_{31}, \gamma_{42}) = (a^2/\pi^2)[A_{55} - 8D_{55}/t^2 + 16F_{55}/t^4, \\ A_{44} - 8D_{44}/t^2 + 16F_{44}/t^4]/D_{11}^*$$

$$\begin{aligned}
 \gamma_{32} = \gamma_{41} &= (a^2/\pi^2)[A_{45} - 8D_{45}/t^2 + 16F_{45}/t^4]/D_{11}^*, \\
 (\gamma_{330}, \gamma_{332}) &= [D_{16}^* - 4(F_{16}^* + F_{61}^*)/3t^2 + 16H_{16}^*/9t^4, \\
 &\quad D_{26}^* - 4(F_{26}^* + F_{62}^*)/3t^2 + 16H_{26}^*/9t^4]/D_{11}^* \\
 \gamma_{331} &= [(D_{12}^* + D_{66}^*) - 4(F_{12}^* + F_{21}^* + 2F_{66}^*)/3t^2 \\
 &\quad + 16(H_{12}^* + H_{66}^*)/9t^4]/D_{11}^* \\
 (\gamma_{410}, \gamma_{412}) &= (4/3t^2)[F_{16}^* - 4H_{16}^*/3t^2, (F_{26}^* + 2F_{62}^*) - 4H_{26}^*/t^2]/D_{11}^* \\
 (\gamma_{411}, \gamma_{413}) &= (4/3t^2)[(F_{12}^* + 2F_{66}^*) - 4(H_{12}^* + 2H_{66}^*)/3t^2, \\
 &\quad F_{22}^* - 4H_{22}^*/3t^2]/D_{11}^* \\
 (\gamma_{430}, \gamma_{432}) &= (D_{66}^* - 8F_{66}^*/3t^2 + 16H_{66}^*/9t^4, \\
 &\quad D_{22}^* - 8F_{22}^*/3t^2 + 16H_{22}^*/9t^4)/D_{11}^* \\
 \gamma_{431} &= 2[D_{26}^* - 4(F_{26}^* + F_{62}^*)/3t^2 + 16H_{26}^*/9t^4]/D_{11}^* \\
 (\gamma_{511}, \gamma_{522}) &= (B_{11}^* - 4E_{11}^*/3t^2, B_{22}^* - 4E_{22}^*/3t^2)/[D_{11}^*D_{22}^*A_{11}^*A_{22}^*]^{1/4} \\
 (\gamma_{516}, \gamma_{526}) &= (4/3t^2)(E_{16}^*, E_{26}^*)/[D_{11}^*D_{22}^*A_{11}^*A_{22}^*]^{1/4} \\
 (\gamma_{611}, \gamma_{622}) &= (4/3t^2)(E_{11}^*, E_{22}^*)/[D_{11}^*D_{22}^*A_{11}^*A_{22}^*]^{1/4}
 \end{aligned}$$

7.13 Appendix C

In Eq. (7.36)

$$(\lambda_T^{(0)}, \lambda_T^{(2)}, \lambda_T^{(4)}) = \frac{1}{\gamma_{14}C_{11}}(S_0, S_2, S_4)$$

in which (with g_{ij} and g_{ijk} are defined as in Shen 1997b, 1999)

$$S_0 = \frac{\Theta_{11}}{(1 + \mu)} - S_0^P, S_2 = \frac{1}{16} \frac{\gamma_{14}}{\gamma_{24}} \Theta_2 (1 + 2\mu),$$

$$S_4 = \frac{1}{256} \frac{\gamma_{14}^2}{\gamma_{24}^2} C_{11} (C_{24} - C_{44})$$

$$S_0^P = \gamma_{14} n^2 \beta^2 (\gamma_{P2} - \gamma_5 \gamma_{P1}) \Delta V,$$

$$\Theta_{11} = g_{08} + \gamma_{14} \gamma_{24} m^2 n^2 \beta^2 \frac{g_{05} g_{07}}{g_{06}}$$

$$\Theta_2 = \frac{(3\gamma_{24}^2 - \gamma_5^2)(m^4 + \gamma_{24}^2 n^4 \beta^4) + 4\gamma_5 \gamma_{24}^2 m^2 n^2 \beta^2}{\gamma_{24}^2 - \gamma_5^2}$$

$$\Theta_{13} = g_{138} + \gamma_{14} \gamma_{24} 9m^2 n^2 \beta^2 \frac{g_{135} g_{317}}{g_{136}},$$

$$\Theta_{31} = g_{318} + \gamma_{14} \gamma_{24} 9m^2 n^2 \beta^2 \frac{g_{315} g_{317}}{g_{316}}$$

$$C_{24} = 2(1 + \mu)^2 (1 + 2\mu)^2 \Theta_2 \left(\frac{m^4}{J_{13}} + \frac{\gamma_{24}^4 n^4 \beta^4}{J_{31}} \right)$$

$$C_{44} = (1 + \mu)(1 + 2\mu)[2(1 + \mu)^2 + (1 + 2\mu)] \left(\frac{m^8}{J_{13}} + \frac{\gamma_{24}^4 n^8 \beta^8}{J_{31}} \right)$$

$$J_{13} = \Theta_{13} C_{11}(1 + \mu) - \Theta_{11} C_{13} - \gamma_{14}(1 + \mu)[C_{11} S_{13} - C_{13} S_{11}] \Delta V$$

$$J_{31} = \Theta_{31} C_{11}(1 + \mu) - \Theta_{11} C_{31} - \gamma_{14}(1 + \mu)[C_{11} S_{31} - C_{31} S_{11}] \Delta V$$

$$S_{11} = (\gamma_{P_1} m^2 + \gamma_{P_2} n^2 \beta^2), S_{13} = (\gamma_{P_1} m^2 + 9\gamma_{P_2} n^2 \beta^2),$$

$$S_{31} = (9\gamma_{P_1} m^2 + \gamma_{P_2} n^2 \beta^2)$$

in the above equations, for uniform temperature loading:

$$C_{11} = (\gamma_{T_1} m^2 + \gamma_{T_2} n^2 \beta^2), C_{13} = (\gamma_{T_1} m^2 + 9\gamma_{T_2} n^2 \beta^2),$$

$$C_{31} = (9\gamma_{T_1} m^2 + \gamma_{T_2} n^2 \beta^2)$$

$$C_7 = \gamma_{T_1}, C_8 = \gamma_{T_2}, C_9 = C_{10} = 1.0$$

and for nonuniform tent-like temperature loading:

$$C_{11} = (\gamma_{T_1} m^2 + \gamma_{T_2} n^2 \beta^2) \left(\frac{T_0}{T_1} + \frac{1}{2} \right) + 2\gamma_9 \frac{m^2}{\pi^2 n^2}$$

$$C_{13} = (\gamma_{T_1} m^2 + 9\gamma_{T_2} n^2 \beta^2) \left(\frac{T_0}{T_1} + \frac{1}{2} \right) + \frac{2}{9} \gamma_9 \frac{m^2}{\pi^2 n^2}$$

$$C_{31} = (9\gamma_{T_1} m^2 + \gamma_{T_2} n^2 \beta^2) \left(\frac{T_0}{T_1} + \frac{1}{2} \right) + 18\gamma_9 \frac{m^2}{\pi^2 n^2}$$

$$C_7 = \gamma_{T_1} \left(\frac{T_0}{T_1} + \frac{1}{2} \right) + \frac{1}{2} \gamma_9, C_8 = \gamma_{T_2} \left(\frac{T_0}{T_1} + \frac{1}{2} \right),$$

$$C_9 = 1 - \frac{\pi}{4} \left(1 - \frac{4}{\pi^2 n^2} \right) C_4, C_{10} = 1.0$$

and for nonuniform parabolic temperature loading

$$\begin{aligned}
C_{11} &= (\gamma_{T_1} m^2 + \gamma_{T_2} n^2 \beta^2) \left(\frac{T_0}{T_1} + \frac{4}{9} \right) \\
&\quad + \frac{m^2 \gamma_{T_2} - \gamma_5 \gamma_{T_1}}{\beta^2 \gamma_{24}^2} \left(\frac{4}{3\pi^2 n^2} + \frac{4}{\pi^4 n^4} \right) \\
&\quad + n^2 \beta^2 (\gamma_{24}^2 \gamma_{T_1} - \gamma_5 \gamma_{T_2}) \left(\frac{4}{3\pi^2 m^2} + \frac{4}{\pi^4 m^4} \right) \\
C_{13} &= (\gamma_{T_1} m^2 + 9\gamma_{T_2} n^2 \beta^2) \left(\frac{T_0}{T_1} + \frac{4}{9} \right) \\
&\quad + \frac{m^2 \gamma_{T_2} - \gamma_5 \gamma_{T_1}}{\beta^2 \gamma_{24}^2} \left(\frac{4}{27\pi^2 n^2} + \frac{4}{81\pi^4 n^4} \right) \\
&\quad + 9n^2 \beta^2 (\gamma_{24}^2 \gamma_{T_1} - \gamma_5 \gamma_{T_2}) \left(\frac{4}{3\pi^2 m^2} + \frac{4}{\pi^4 m^4} \right) \\
C_{31} &= (9\gamma_{T_1} m^2 + \gamma_{T_2} n^2 \beta^2) \left(\frac{T_0}{T_1} + \frac{4}{9} \right) \\
&\quad + \frac{9m^2 \gamma_{T_2} - \gamma_5 \gamma_{T_1}}{\beta^2 \gamma_{24}^2} \left(\frac{4}{3\pi^2 n^2} + \frac{4}{\pi^4 n^4} \right) \\
&\quad + n^2 \beta^2 (\gamma_{24}^2 \gamma_{T_1} - \gamma_5 \gamma_{T_2}) \left(\frac{4}{27\pi^2 m^2} + \frac{4}{81\pi^4 m^4} \right) \\
C_7 &= \gamma_{T_1} \left(\frac{T_0}{T_1} + \frac{4}{9} \right) + \frac{4}{5} \frac{\gamma_{T_2} - \gamma_5 \gamma_{T_1}}{\beta^2 \gamma_{24}^2}, \\
C_8 &= \gamma_{T_2} \left(\frac{T_0}{T_1} + \frac{4}{9} \right) + \frac{4}{5} \beta^2 (\gamma_{24}^2 \gamma_{T_1} - \gamma_5 \gamma_{T_2}) \\
C_9 &= 1 - \frac{C_5}{24\pi} \left(\frac{3}{5} \pi^4 - \frac{\pi^2}{n^2} - \frac{3}{n^4} \right), \\
C_{10} &= 1 - \frac{C_6}{24\pi} \left(\frac{3}{5} \pi^4 - \frac{\pi^2}{m^2} - \frac{3}{m^4} \right)
\end{aligned}$$

Local and interaction buckling of composite construction members

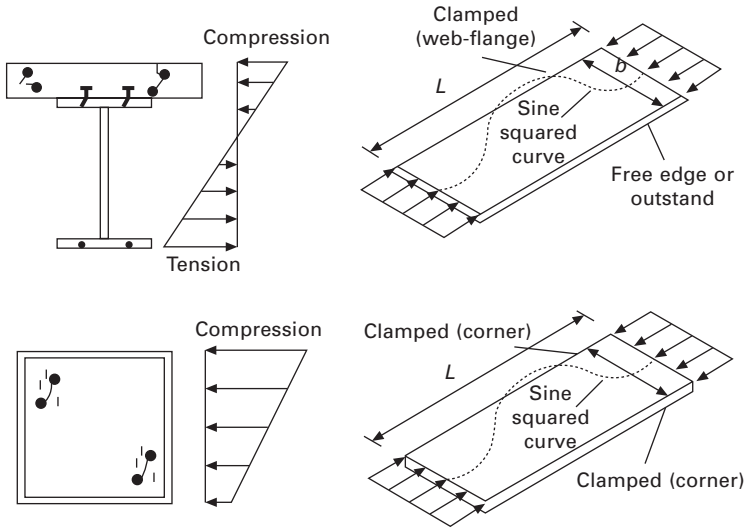
B U Y, University of Wollongong, Australia

8.1 Introduction

This chapter is concerned with the behaviour and design of the local and interaction buckling of plated structures in composite steel–concrete construction forms with particular reference to composite steel–concrete beams and columns. The juxtaposition of steel and concrete in structural members provides an increased resistance of the steel component to local and interaction buckling, and it is the premise of this chapter to give proper treatment to this issue. The chapter will confine itself to the consideration of conventional composite steel–concrete beam construction and square concrete-filled steel sections with some discussion on thin-walled encased sections. Localised and interaction buckling can occur in thin-walled plated structures due to high compressive loads. These compressive loads may be induced by the actions of axial compression and/or bending moments. Compressive stresses give rise to instability when the elements and/or members are slender and unrestrained to cross-section distortion or member out-of-plane movements. When slender or thin-walled plated structures are used, cross-section instability may occur. The most common and well-studied form of cross-section instability is associated with localised buckling. Local buckling, although not being an overall failure mode, can give rise to a reduced stiffness and strength of an overall structure. Figure 8.1 illustrates some typical local buckling modes for composite steel–concrete forms.

Global buckling is associated with an overall member. This form of buckling involves the member becoming unstable and moving out of plane and is usually termed flexural buckling. Figure 8.2 illustrates conceptually the behaviour of a column when it becomes unstable. The member is subjected to an axial force N and an associated out-of-plane displacement, δ occurs when instability arises and the column displaces to the position suggested by the dashed line.

Interaction buckling of a member results when localised buckling occurs prior to overall instability and a coupled local and global buckling mode



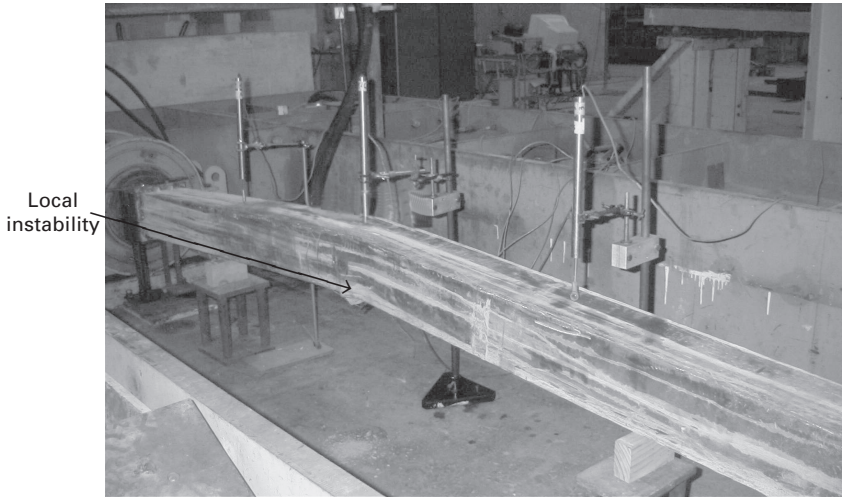
8.1 Local buckling modes of a variety of composite steel–concrete cross-sections.



8.2 Global buckling of a member.

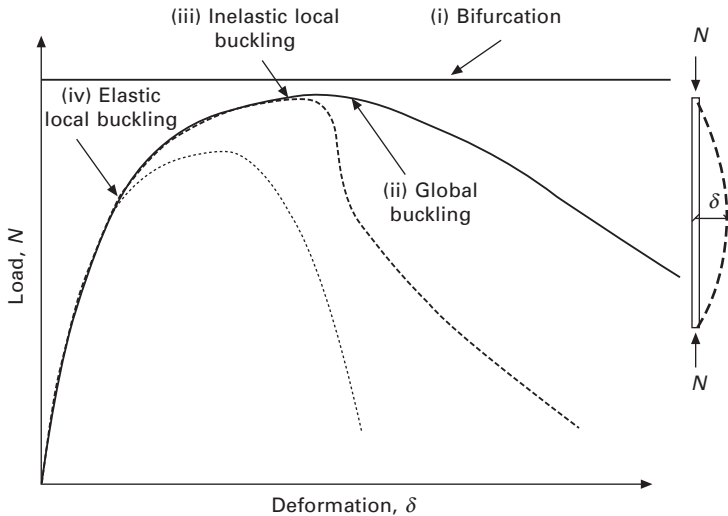
develops. This is thus considered to be a coupled instability and is best illustrated for a composite column in Fig. 8.3. Here the column has a localised buckle at the mid-height, together with a flexural buckle which has formed along the length of the member.

The global buckling load is reduced by the presence of local buckling, which can be either elastic or inelastic. Generally if local buckling occurs in the elastic range, a reduced buckling load will ensue. When buckling occurs in the inelastic range, the stiffness can be reduced and it is generally the



8.3 Interaction buckling of a composite steel-concrete member.

postbuckling response that is affected, rather than the ultimate load. Figure 8.4 illustrates the various responses for a structural column member: (i) the load-lateral deformation response of a member which bifurcates (perfect member); (ii) a member that undergoes non-linear global buckling with a compact cross-section; (iii) a member that suffers from inelastic local buckling coupled with global buckling; and (iv) load-lateral deformation behaviour of a column undergoing elastic local buckling coupled with global buckling.



8.4 Generalised structural response of a column member subjected to compressive loads.

8.2 Forms of composite steel–concrete members

The two forms of composite steel–concrete composite members that will be considered are (i) conventional steel–concrete composite beams, composed of a steel joist supporting either a solid concrete or profiled composite slab; and (ii) square composite columns, either concrete-filled or encased steel sections.

8.2.1 Composite steel–concrete beams

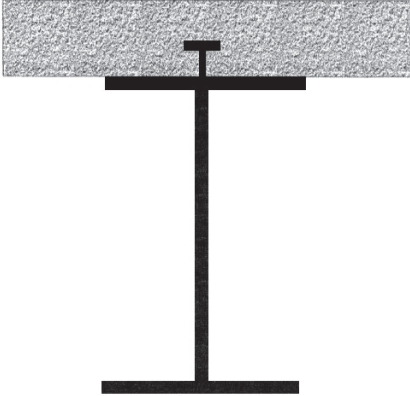
Conventional steel–concrete beams, employing the use of either hot-rolled or welded steel sections and made composite with a solid or profiled composite slab, are generally the structural system of choice for most modern steel-framed buildings throughout the world. A typical floor system is shown in Fig. 8.5 for a steel-framed building recently constructed in London. A typical composite steel–concrete beam cross-section is illustrated in Fig. 8.6 and it is the local instability of the top flange of these types of cross-sections that will be considered herein.



8.5 Composite steel–concrete beams, More London, UK.

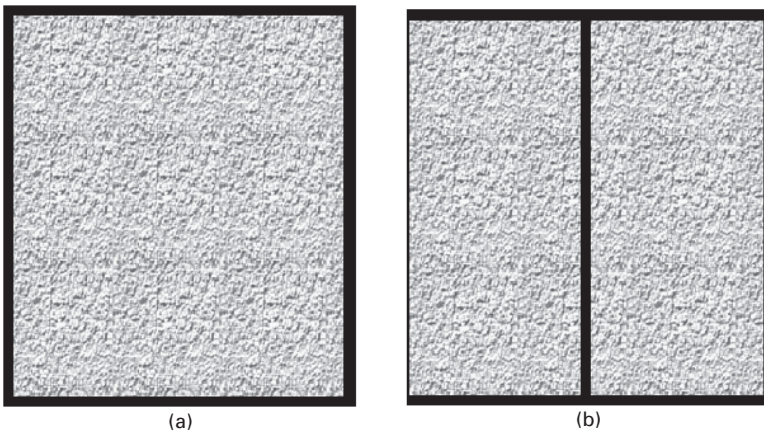
8.2.2 Composite steel–concrete columns

Composite columns have been used for over 100 years, with steel-encased sections being incorporated in buildings in the USA during the late nineteenth century (Uy 1998a). The initial application of composite columns was for fire rating requirements of the steel section. Later developments saw composite



8.6 Typical composite steel-concrete beam section.

action fully utilised for strength and stability. Composite action in columns utilises the favourable tensile and compressive characteristics of the steel and concrete respectively. One major benefit of this system has been the ability to achieve higher steel percentages than conventional reinforced concrete structures and the steel erection column allows rapid construction of steel floor systems in steel-framed buildings. Uy (1998a) has presented the practical applications and design procedures for concrete-filled box sections highlighted in Fig. 8.7(a), and this chapter will present local buckling studies that are associated with this form of construction. Furthermore, Tremblay *et al.* (2000) considered the effects of noncompact steel sections filled with concrete as illustrated in Fig. 8.7(b). Once again, local buckling studies are presented in this chapter to illustrate the benefits of the concrete infill for these applications.



8.7 Concrete-filled rectangular columns: (a) concrete-filled box sections; (b) concrete-filled wide flange sections.

8.3 Background to buckling

This section provides a background to buckling. An in-depth treatment of the classical methods will not be provided, as there have been many such published articles and monographs on the theoretical background to local and global stability. Instead, an exposé of the results of local, global and interaction buckling studies of composite steel–concrete members, which will highlight the beneficial effects of the presence of concrete in close proximity of thin-walled steel sections.

8.3.1 Local buckling

There are many comprehensive treatments to the background of local buckling, including Timoshenko and Gere (1963) and Bazant and Cedolin (1991). For the foundations of stability, readers are referred to these monographs. We will actually consider the results of local buckling studies conducted on composite steel–concrete structures. The local plate buckling results σ_{ol} , will be presented in the form of that of Bulson (1970) as detailed in Equation 8.1. The local buckling stress σ_{ol} is determined as:

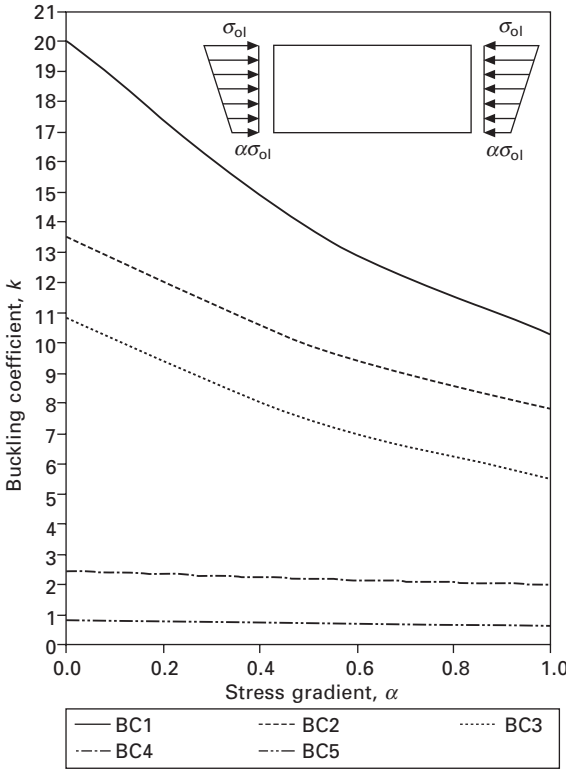
$$\sigma_{ol} = \frac{k\pi^2 E}{12(1 - \nu^2)\left(\frac{b}{t}\right)^2} \quad 8.1$$

where k is the elastic local buckling coefficient, E the elastic modulus, ν Poisson's ratio and b and t are the plate width and thickness, respectively. Composite construction members can result in a reduced load-carrying capacity when localised buckling occurs in the component plates in the member.

Uy and Bradford (1996) developed a finite strip method to investigate the effects of boundary conditions germane to composite construction. The five boundary conditions (BC) considered are given below:

- BC1 – four edges clamped
- BC2 – one unloaded edge clamped and one simply supported
- BC3 – both unloaded edges simply supported
- BC4 – one unloaded edge free and one clamped
- BC5 – one unloaded edge free and one simply supported

In particular this chapter is mainly concerned with boundary conditions BC1 and BC4. Boundary condition BC1 is the boundary condition with four edges clamped which can be used to simulate the behaviour of the component plates of a square or rectangular concrete-filled steel section. Boundary condition BC4 is the boundary condition with three edges clamped which can be used to simulate the flange outstand that is in contact with the concrete slab in a steel–concrete composite beam. Figure 8.8 provides a summary of



8.8 Buckling coefficients versus stress gradient, α for steel juxtaposed with concrete (Uy and Bradford, 1996).

the local buckling coefficients for various boundary conditions and stress gradients, where α represents the ratio of the minimum stress ($\alpha\sigma_{0l}$) to the maximum stress in the plate (σ_{0l}).

If one were to idealise the component plates of a square hollow section and a square concrete filled steel section and undertake a plate buckling analysis on the plates, minimum local buckling coefficients of $k = 4.0$ and 10.3 would be obtained respectively. Similarly the elastic local buckling coefficient for a flange outstand increases from 0.425 to 2.0 when the presence of concrete is included in the stability analysis.

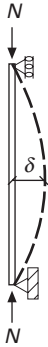
Conceptually, the elastic local buckling stress, σ_{0l} can be used to determine an axial load N_{0l} at which this occurs, where

$$N_{0l} = \sigma_{0l}A_g \tag{8.2}$$

where A_g is the gross cross-sectional area. However, this is not the maximum load, merely the load at which local buckling is initiated. The post-local buckling reserve of strength of the component plates will ensure that a higher axial load than that suggested in equation 8.2 occurs.

8.3.2 Global buckling

Once again a full treatment will not be given here regarding the theoretical background to global buckling, as this has been given in other monographs, such as those presented by Timoshenko and Gere (1963) and Bazant and Cedolin (1991). Euler in 1744 (Timoshenko and Gere, 1963) developed a closed-form solution for the buckling load of a simply supported column as illustrated in Fig. 8.9.



8.9 Global buckling of a member.

The critical load N_{cr} is calculated using the expression in equation 8.3:

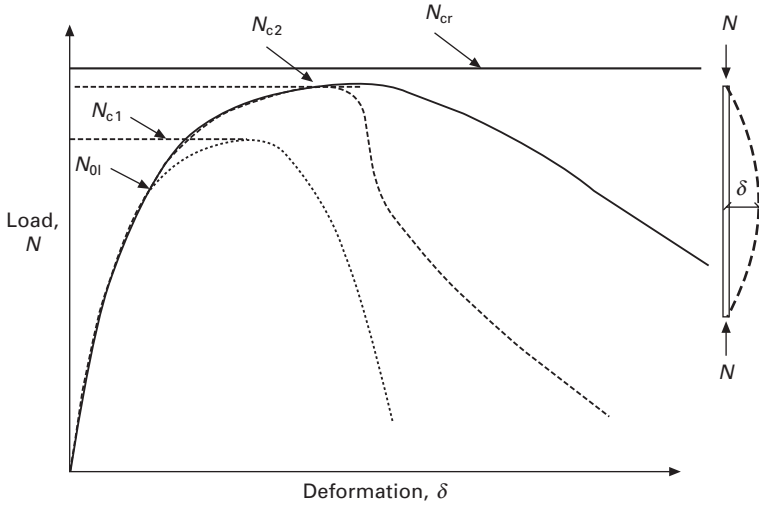
$$N_{cr} = \frac{\pi^2 EI}{L^2} \quad 8.3$$

where E is the elastic modulus, I is the second moment of area and L is the effective length of the column. This critical load does not consider the effects of residual stresses and geometric imperfections and applies only for perfect columns. Furthermore, one also needs to consider the strength (squash load) of the column and any effects due to local buckling which compromise the strength in equation 8.3 from being reached.

8.3.3 Interaction buckling

The interaction of local and global buckling in steel and steel–concrete composite structures occurs when either elastic or inelastic local buckling takes place. The load associated with each of these cases is more specifically presented in Fig. 8.10 for a column. A generalised expression could be written so that:

$$N_C = \alpha_C N_S \quad 8.4$$



8.10 Interaction buckling of a member.

where α_c is a factor to account for slenderness, residual stresses and geometric imperfections and the squash load, N_s , is calculated as:

$$N_s = A_e \sigma_y \tag{8.5}$$

where A_e is the effective area (a function of the sum of the effective widths, b_e , of the component plates) which accounts for local buckling and σ_y is the nominal yield stress of the steel material.

Figure 8.10 illustrates the two different buckling loads, N_{c1} and N_{c2} . N_{c1} is the buckling load associated with a column which suffers from elastic local buckling, whereas, N_{c2} is the buckling load of a column which suffers from inelastic local buckling or is compact in cross-section.

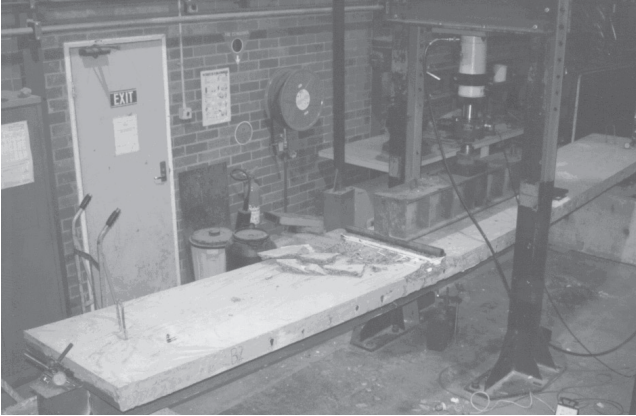
8.4 Local buckling of composite steel–concrete members

This section will consider the local and post-local buckling behaviour of composite steel–concrete members, and in particular summarise the results of extensive experimental and analytical studies to determine the slenderness limits for thin-walled steel sections when the steel is juxtaposed with concrete.

8.4.1 Composite steel–concrete beams

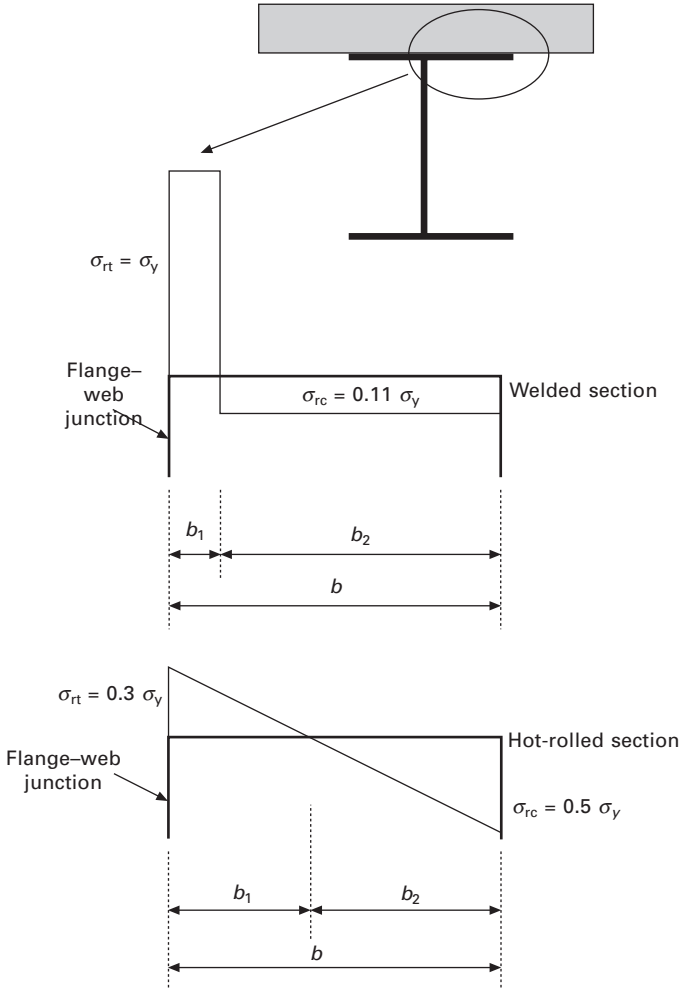
Composite steel–concrete beams subjected to sagging bending can suffer from local buckling when the plastic neutral axis lies either within the steel section, or when partial shear connection is used and compressive strains are

therefore developed in the top flange. Figure 8.11 shows a simply supported composite steel–concrete beam which at failure has formed a local buckle in the top flange.



8.11 Local buckling of a composite steel–concrete beam (Uy and Sloane, 1998).

Bradford and Uy (1995) developed an inelastic finite strip method incorporating the residual stress patterns illustrated in Fig. 8.12 for welded and hot-rolled sections. The results of this study showed that the current existing guidelines for slenderness limits of these flanges as suggested by Eurocode 4 (European Committee for Standardisation, 1992) were conservative. Bradford and Uy (1995) proposed new slenderness limits based on hot-rolled and welded sections which are provided in Table 8.1.



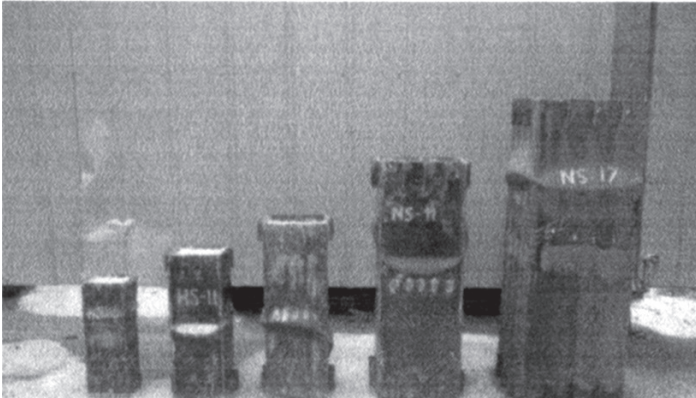
8.12 Residual stresses of a flange in a composite steel–concrete beam (Bradford and Uy, 1995).

Table 8.1 Table of slenderness limits for compression flanges in composite steel–concrete composite beams (Bradford and Uy, 1995)

	$\frac{b}{t} \sqrt{\frac{\sigma_y}{235}}$	
	Eurocode 4	Bradford and Uy
Hot-rolled or stress-relieved	20	31
Welded	18	26

8.4.2 Composite steel–concrete columns

This section will consider the local and post-local buckling of composite steel–concrete columns. Figure 8.13 shows the local buckling modes experienced in (a) concrete-filled box sections, and (b) concrete-filled wide flange (I) sections. The behaviour of concrete-filled steel sections from a



(a)



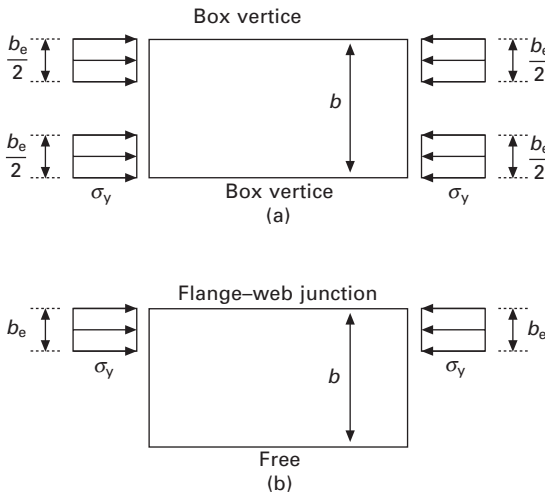
(b)

8.13 Local buckling of a variety of square composite steel–concrete cross-sections (Uy, 1998b, Uy 2001): (a) concrete-filled box sections; (b) concrete-filled wide flange (I) section.

stability perspective is heavily dependent on the local and post-local buckling of the component plates. Post-local buckling is often predicted using the effective width concept as for both box sections and outstand sections illustrated in Fig. 8.14. Effective width models for hot-rolled and fabricated sections have been modified to incorporate residual stresses and initial imperfections by Bradford (1985) and Bradford *et al.* (1987) which was adopted in the Australian Standard AS 4100-1998 (Standards Australia 1998). This model which is also present in steel codes in the USA and Europe is of the form shown in equation 8.6:

$$\frac{b_e}{b} = \beta \sqrt{\frac{\sigma_{ol}}{\sigma_y}} \tag{8.6}$$

where β is a parameter used to account for residual stresses and initial geometric imperfections. This parameter also varies depending on the type of section and its method of fabrication. Furthermore, the type of boundary condition also affects the determination of β . Values for this parameter including all these factors are summarised in Table 8.2. These parameters were thus used in calibrating the model with the post-local buckling test results of Uy (2001).

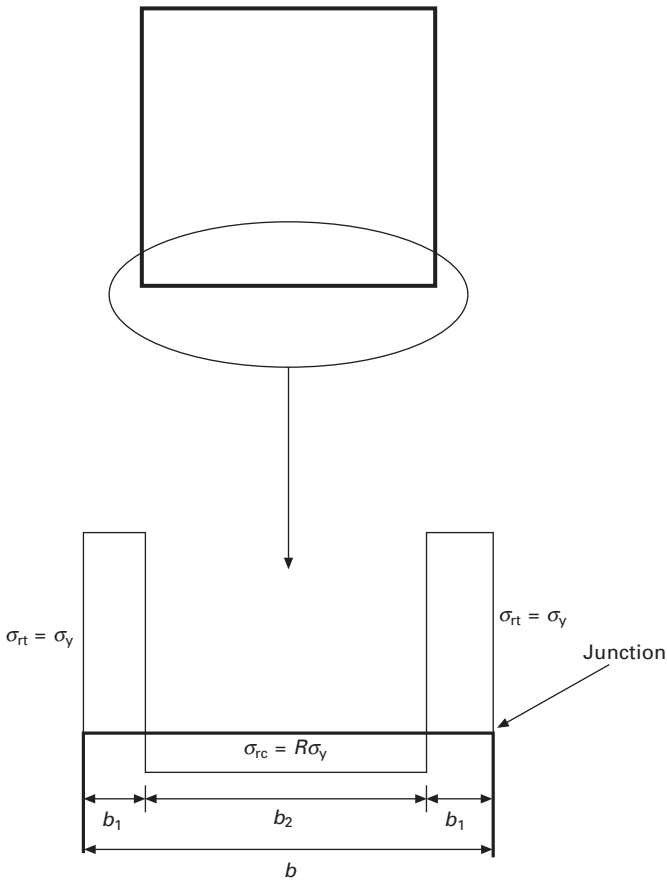


8.14 Effective width concept for various assemblies: (a) box sections; (b) flange outstands.

The tendon force concept was used for both cases of boundary conditions to simulate residual stresses as illustrated in Figs 8.15 and 8.16. Results for various cases of effective widths, b_e are illustrated in Figs 8.17 and 8.18 respectively, where R represents the level of residual compressive stress as a function of the yield stress. The benefits of the inclusion of the concrete in

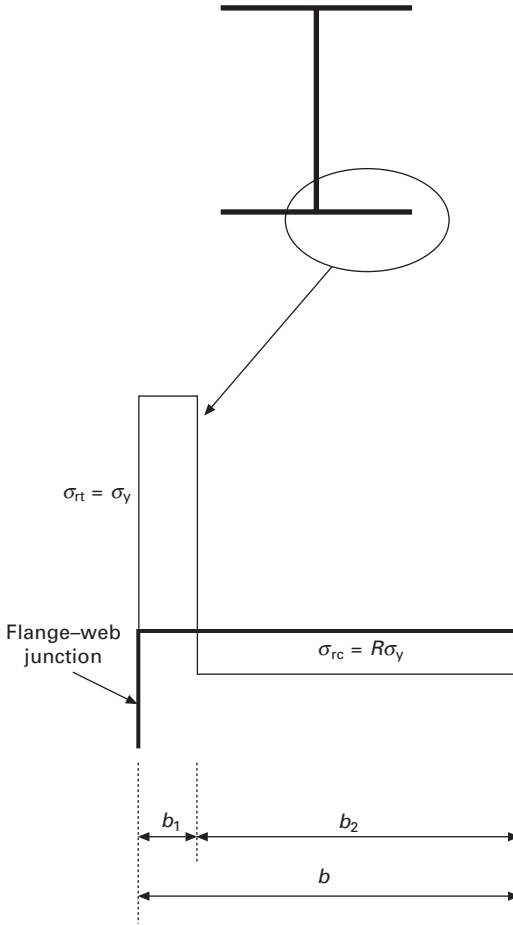
Table 8.2 Table of β values

Boundary condition	Method of manufacture	β
Supported on two longitudinal edges	Stress relieved	0.84
Supported on two longitudinal edges	Hot-rolled	0.84
Supported on two longitudinal edges	Lightly welded (LW)	0.74
Supported on two longitudinal edges	Heavily welded (HW)	0.65
Supported on one longitudinal edge	Stress relieved	0.91
Supported on one longitudinal edge	Hot-rolled	0.91
Supported on one longitudinal edge	Lightly welded (LW)	0.86
Supported on one longitudinal edge	Heavily welded (HW)	0.80



8.15 Residual stress distributions for box sections (Uy, 2001).

the assessment of the local stability of steel sections is best evidenced by the suggested slenderness limits which are summarised in Table 8.3. These limits have been determined from the results given in Figs 8.17 and 8.18.



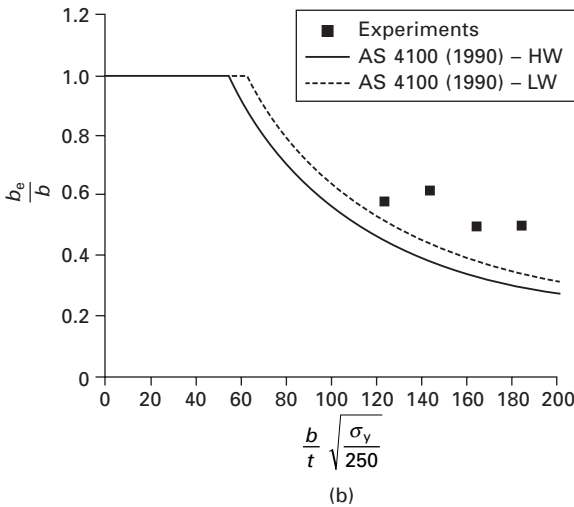
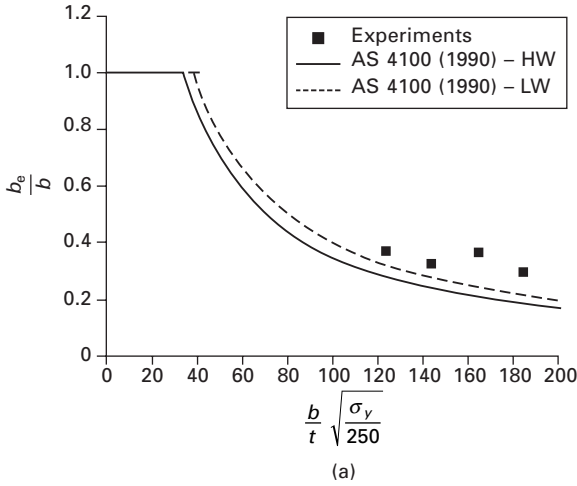
8.16 Residual stress distributions for I sections (Uy, 2001).

8.5 Interaction buckling of composite steel-concrete members

Thus far this chapter has considered the local and post-local buckling behaviour of composite steel-concrete cross-sections. This section will consider the effects of the coupling of local and global buckling, often termed interaction buckling.

8.5.1 Composite steel-concrete beams

Composite steel-concrete beams generally are constructed with a steel section, which is either hot-rolled or welded. In conventional composite steel-concrete composite beams, headed shear studs as illustrated in Fig. 8.19 are provided

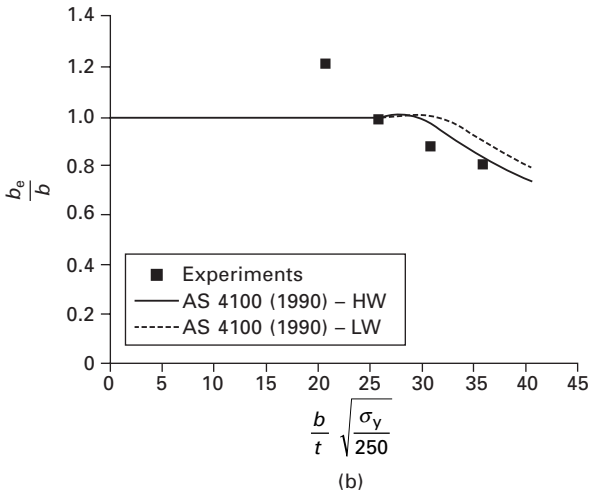
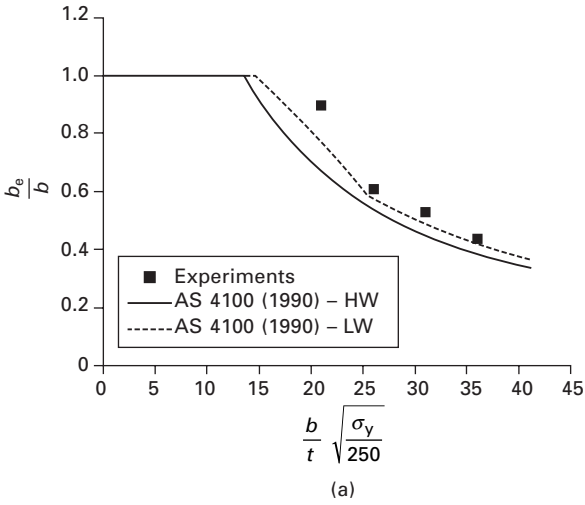


8.17 Post-local buckling comparisons for box sections (Uy, 2001); (a) hollow box sections; (b) concrete-filled box sections.

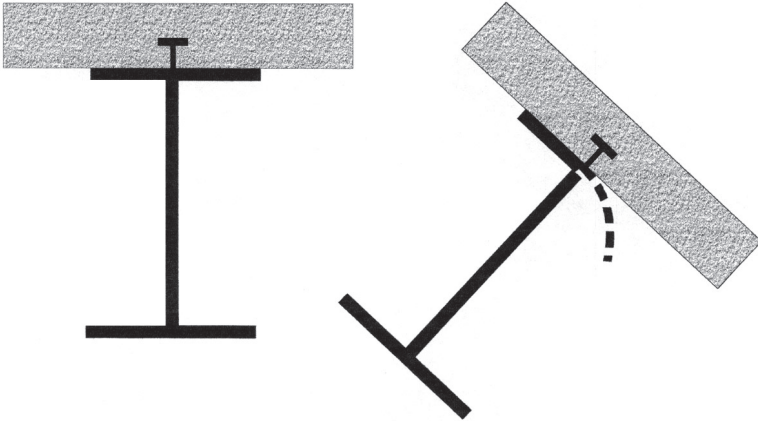
at fairly close spacing to provide longitudinal shear transfer between the concrete slab and steel beam. The presence of the headed shear studs generally at a maximum spacing of 600 mm according to Australian Standard AS2327.1 (Standards Australia, 2003) precludes global buckling from occurring in this structural form. This is because the presence of the headed shear studs, generally provides full lateral restraint along the entire length of the beam. Owing to the unlikelihood of global flexural-torsional buckling from occurring,

Table 8.3 Table of slenderness limits for composite steel-concrete columns, (Uy, 2001)

	$\frac{b}{t} \sqrt{\frac{\sigma_y}{250}}$	
	AS4100	Uy
Welded box sections	40	60
Welded I sections	12.5	25



8.18 Post-local buckling comparisons for I sections (Uy, 2001): (a) hollow I sections; (b) concrete-filled I sections.



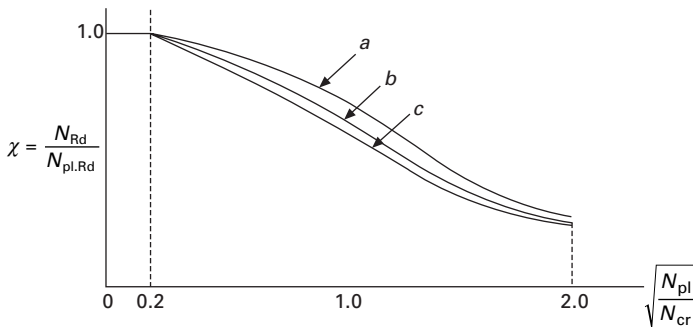
8.19 Interaction buckling of a composite beam.

one does not need to consider interaction buckling in composite steel–concrete beams.

There may be some special cases when global buckling in the form of flexural-torsional buckling may occur, which is illustrated in Fig. 8.19. For composite steel–concrete edge beams which may experience compatibility torsion, cracking of the concrete slab may occur and thus lateral-torsional instability may be likely. Lindner (1998) has considered this form of global instability of composite steel–concrete beams.

8.5.2 Composite steel–concrete columns

From a design context, composite columns can be designed using the EC4 or AS4100-1998 (European Committee for Standardisation, 1992, Standards Australia, 1998) method of column curve approach when compact sections are used (Uy and Liew, 2002), which is illustrated in Fig. 8.20. However, this



8.20 Column curves for slender composite columns (Uy and Liew, 2002).

model has also been shown to be valid by Mursi and Uy (2003) when slender cross-sections are used. The study showed that curve *a* is the most suitable approach to be used for composite columns. Furthermore, the presence of concrete infill ensured that the growth of imperfections was minimised. A generalised expression for the capacity of the slender column, N_c can be given as:

$$N_c = \chi N_s \tag{8.7}$$

where χ is a function of slenderness, residual stresses and geometric imperfections, where $N_s = A_e \sigma_y$.

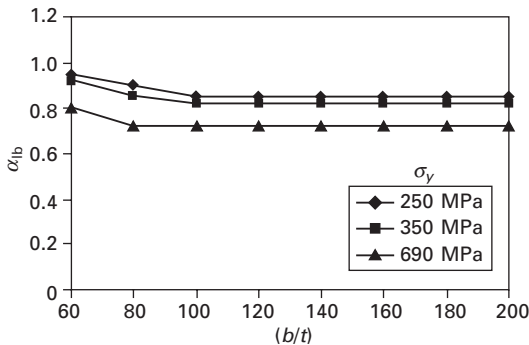
As an alternative, Vrcelj and Uy (2002) conducted an extensive parametric study based on a coupled buckling analysis, which resulted in a design method being proposed for the strength calculation of a slender concrete-filled steel box column loaded in compression. To predict the local buckling strength of the slender concrete-filled steel box column, the following relationship was proposed on the basis of the parametric analyses undertaken. The slender column buckling load, N_{clb} , which incorporates local buckling, can be represented in the form of equation (8.8) in terms of N_c , which is the column-buckling load, which ignores the effects of local buckling:

$$N_{clb} = \alpha_{lb} N_c \tag{8.8}$$

where α_{lb} is the interaction coefficient to account for local buckling and is in the range:

$$0 \leq \alpha_{lb} \leq 1.0 \tag{8.9}$$

This is illustrated in Fig. 8.21 for various yield stresses.



8.21 Parameter α_{lb} versus plate slenderness (Vrcelj and Uy, 2002).

8.6 Concluding remarks

This chapter has presented a comprehensive overview of local and interaction buckling in composite steel–concrete beams and concrete-filled steel composite

columns. Methods have been presented to illustrate how these particular failure modes can be addressed from a design perspective. Firstly, local and post-local buckling of cross-sections has been considered. Furthermore, the effects of member slenderness have been considered and approaches for addressing interaction buckling have been presented. Finally, suggestions for design in accordance with European and Australian practice have been provided. The results and procedures here will become increasingly more pertinent as structures are being designed and constructed with cross-sections of a very thin-walled nature. Further research is required to try to implement the effects of local and interaction buckling in both advanced analysis and commercial software codes, as this will provide structural engineers with considerable power to fully optimise building designs. Other approaches based on a stiffness method of analysis have been developed by Shanmugam *et al.* (2002), which could be used in future for inclusion in advanced analysis methods as outlined by Liew and Uy (2001).

8.7 References

- Bazant, Z.P. and Cedolin, L. (1991), *Stability of Structures*, Dover, New York.
- Bradford, M.A. (1985), Local and post-local buckling of fabricated box members, *Civil Engineering Transactions, Institution of Engineers, Australia*, **27**(4), 391–396.
- Bradford, M.A. and Uy, B. (1995), Spacing of shear connectors to prevent local buckling of composite beams. *Proceedings of the Third International Conference on Steel and Aluminum Structures, Istanbul, Turkey, Elsevier*, Oxford, pp. 483–490.
- Bradford, M.A., Bridge, R.Q., Hancock, G.J., Rotter, J.M. and Trahair, N.S. (1987), Australian limit state design rules for the stability of steel structures, *Proceedings, First Structural Engineering Conference, Institution of Engineers, Australia, Melbourne*, 209–216.
- Bulson, P.S. (1970), *The Stability of Flat Plates*, Chatto and Windus, London.
- European Committee for Standardisation (1992) CEN. PrENV 1994-1-1 Eurocode 4. *Design of Composite Steel and Concrete Structures, Part 1.1 General Rules and Rules for Buildings*, Brussels.
- Liew, J.Y.R. and Uy, B. (2001), Advanced analysis of composite frames, *Progress in Structural Engineering and Materials*, **3**(2), 159–169.
- Lindner, J. (1998), Lateral torsional buckling of composite beams, *Journal of Constructional Steel Research*, **46**(1–3), 222.
- Mursi, M. and Uy, B. (2003), Strength of concrete filled steel box columns incorporating interaction buckling, *Journal of Structural Engineering, ASCE*, **29**(5), 626–639.
- Shanmugam, N.E., Lakshmi, B. and Uy, B. (2002), An analytical model for thin-walled steel box columns with concrete in-fill, *Engineering Structures, An International Journal*, **24**(6), 825–838.
- Standards Australia (1998), AS4100-1998, *Australian Standard – Steel Structures*, Sydney.
- Standards Australia (2003), AS2327.1-2003, *Composite Structures: Simply Supported Beams*, Sydney.
- Timoshenko, S.P. and Gere, J.M. (1963), *Theory of Elastic Stability*, Second edition, McGraw-Hill, New York.

- Tremblay, R., Chicoine, T. and Masicotte, B. (2000), Design equation for the axial capacity of partially encased non-compact columns, *Proceedings of an Engineering Foundation Conference, ASCE, Banff*.
- Uy, B. (1998a), Concrete filled fabricated steel box columns for multistorey buildings: behaviour and design, *Progress in Structural Engineering and Materials, Construction Research Communications*, **1**(2), 150–158.
- Uy, B. (1998b), Local and post-local buckling of concrete filled steel welded box columns, *Journal of Constructional Steel Research, An International Journal*, **47**(1–2), 47–72.
- Uy, B. (2001), Local and post-local buckling of fabricated thin-walled steel and steel-concrete composite sections, *Journal of Structural Engineering, ASCE*, **127**(6), 666–677.
- Uy, B. and Bradford, M.A. (1996), Elastic local buckling of steel plates in composite steel–concrete members, *Engineering Structures, An International Journal*, **18**(3), 193–200.
- Uy, B. and Liew, J.Y.R. (2002), Composite steel–concrete structures, Chapter 51 *Civil Engineering Handbook*, CRC Press, Boca Raton, FL (edited by W.F. Chen and J.Y. Richard Liew).
- Uy, B. and Sloane, R.J. (1998), Behaviour of high strength steel in composite tee beams, *Journal of Constructional Steel Research, Special Issue: 2nd World Conference on Steel Construction*, **46**(1–3), 203–204.
- Vrcelj, Z. and Uy, B. (2002), Strength of slender concrete-filled steel box columns incorporating local buckling, *Journal of Constructional Steel Research*, **58**(2), 275–300.

8.8 Appendix: notation

A	cross-sectional area of section
A_e	effective area of cross-section
A_g	gross cross-sectional area
b	plate width
b_1	region of component plate subjected to residual tension, σ_{rt}
b_2	region of component plate subjected to residual compression, σ_{rc}
b_e	effective width
E	elastic modulus
I	second moment of area of section
k	local buckling coefficient
L	effective length of column
N	axial force
N_c	critical load including nonlinear materials and geometry
N_{c1}	buckling load when elastic local buckling occurs
N_{c2}	buckling load when inelastic local buckling occurs
N_{cr}	critical load (bifurcation)
N_{ol}	local buckling load
N_{pl}	plastic squash load
$N_{pl,Rd}$	plastic axial design resistance
N_{Rd}	axial design resistance

N_s	squash load
R	ratio of residual stress to nominal yield stress
t	plate thickness
α	stress gradient parameter ($=\sigma_{\text{minimum}}/\sigma_{\text{maximum}}$)
α_c	parameter to account for member and cross-section slenderness
α_{lb}	parameter to account for local buckling, $0 \leq \alpha_{lb} \leq 1.0$
β	parameter for residual stresses and geometric imperfections
δ	out of plane displacement
ν	Poisson's ratio
σ	stress
σ_{ol}	local buckling stress
σ_{rc}	residual compressive stress
σ_{rt}	residual tensile stress
σ_y	yield stress

Buckling and postbuckling of stiffened composite structures

B G FALZON, Imperial College London, UK

9.1 Introduction

The evolution of lightweight aeronautical structures to their present form is largely based on early experimental work investigating the behaviour of thin-walled structures under compression loading. Schuman and Back (1930) were among the first to demonstrate that metallic plates with supported unloaded edges were able to carry load beyond initial buckling. Cox (1945) showed that aluminium panels with attached z -stiffeners also exhibited postbuckling strength with the ratio of global buckling to local skin buckling being a function of stiffener spacing. Stein (1959a) investigated the response of an aluminium plate supported by a series of equally spaced knife-edge supports, forming skin bays, under uniaxial compression. The phenomenon of mode-jumping was observed during the testing of this panel where the skin-bays initially buckled into five half-waves, followed by a mode-shape change to six half-waves which occurred ‘in a violent manner’, followed by seven and finally eight half-waves before global collapse. Only the first mode-jump occurred within the elastic range of the material.

Recent years have shown a steady increase in the replacement of traditional metallic alloys, in military and civil aerostructures, with laminated carbon–fibre composite material because of their superior specific strength and stiffness. While the design of certain metallic structural components allows for buckling below the design limit load, the same confidence in the design of composite aerostructures has yet to be widely adopted. There are several inhibiting factors that have limited the use of postbuckling composite designs in aerostructures, particularly in the primary structure where the potential for weight reduction is greatest. Among these is damage tolerance and the sensitivity to through-thickness stresses. Reducing the extent of mechanical fasteners by co-curing, co-bonding or secondary bonding the stiffeners to the skin offers the possibility of significantly lighter structures and lower production costs. Unfortunately, the low through-thickness strength, coupled with the potentially high peel and shear stresses at the skin–stiffener interface, may

lead to delamination and cause premature failure of the structure. Furthermore, mode-jumping is an energy-dissipating phenomenon and may release enough energy, if it occurs at high loading, to cause catastrophic failure by unstable crack propagation initiating at these relatively weak skin–stiffener interface regions. Indirect experimental evidence of this occurrence has been reported by Romeo and Frulla (1994) and Falzon *et al.* (2000). It is therefore imperative that reliable analytical and numerical tools are developed that can accurately predict the behaviour of postbuckling composite stiffened structures.

Large deflection equations for thin isotropic plates were first presented by Von Kármán (1910) and used for investigating the postbuckling behaviour of compressively loaded thin plates (see Von Kármán *et al.*, 1932). Koiter (1943) presented an analysis for infinitely long plates loaded far into the postbuckling region where the mode-shape half-wavelength was a constantly varying function of applied loading. Stein (1959b) converted Von Kármán's equations into an infinite set of linear differential equations by expanding the displacement expressions into a power series in terms of an arbitrary parameter and solved, to a second order approximation, for a simply supported plate. Stein postulated that the interaction of load versus displacement curves indicated the possibility of mode-jumping where the buckling half-wave for a given end-displacement was such that the load was a minimum. Supple (1970) presented a two-mode analysis of a simply supported postbuckling plate based on a Ritz–Galerkin energy approximation to explain mode-jumping qualitatively. Nakamura and Uetani (1979) used higher-order displacement functions to predict mode-jumping quantitatively using an energy minimisation approach. A similar approach was used by Stoll (1994) in his investigation of mode-jumping of high aspect-ratio plates for a range of boundary conditions and loading. Stein (1959a) presented a theoretical basis for mode-jumping using a three-element column connected by linear torsional springs and supported laterally by nonlinear extension springs. The analysis was able to capture many of the features observed in postbuckling plates undergoing mode-jumping. This model is essentially a beam on a nonlinear elastic foundation and a variation of this model has been used more recently by Everall and Hunt (2000) to investigate the effects of boundary conditions on mode-jumping. Falzon and Cerini (2004b) have also used this model to demonstrate the effectiveness of a hybrid (static/dynamic) numerical technique for capturing mode-jumping, and this work will be discussed later in this chapter.

The analysis of the postbuckling behaviour of laminated plates is more complicated because of the possible coupling between in-plane extension and shear, bending and twisting or in-plane deformations and bending. The development of Von Kármán's (1910) large deflection equations for anisotropic plates may be found in the monograph by Lekhnitskii (1968). These equations are difficult to solve analytically and are usually simplified to the specially orthotropic case where all couplings disappear. An early study by Yusuff

(1952) dealt with the postbuckling of simply supported specially orthotropic plates with initial curvature and loaded in uniaxial compression. Harris (1975) investigated the stiffness immediately beyond buckling of antisymmetric laminates. Stein (1983) identified two additional parameters, to those required for buckling, to characterise the postbuckling response of specially orthotropic plates for a complete range of dimensions and material properties. Romeo and Frulla (1994) presented an analysis of symmetric panels under combined biaxial and shear loading and with combinations of paired simply supported and clamped boundary conditions on the loaded and unloaded edges. Good correlation was achieved with their experimental results and with analytical results by Minguet *et al.* (1989) who used a 'line search' energy minimisation technique.

Modelling postbuckling stiffened composite structures presents yet another level of complexity. The analytical and semi-analytical approaches discussed above give valuable insight into the postbuckling behaviour of plates, yet despite their considerable complexity they are restricted to basic geometries and well-defined boundary conditions. Considerable effort has been undertaken by various researchers to both experimentally observe the response of postbuckling stiffened composite structures to compressive loading and to try to predict this behaviour using numerical methods, predominantly the finite element method. Starnes *et al.* (1985), Stevens *et al.* (1995), Kong *et al.* (1998), Falzon and Steven (1997), Falzon *et al.* (2000) and Falzon (2001) presented combined experimental and finite element investigations into the postbuckling response and subsequent failure of flat stiffened composite panels while Knight and Starnes (1988) and Kweon *et al.* (1995) adopted a similar approach in their study of the postbuckling and failure of curved stiffened composite panels. Damage was observed to initiate at a point in the panel corresponding to either a node-line or an anti-node-line of the buckle mode.

In this chapter, experimental observations will be presented to highlight the complex response of postbuckling stiffened composite structures under uniaxial compression loading. Initial failure sites are identified and their occurrence discussed. This will lead to a brief survey of current finite element modelling practices and potential pitfalls. A robust and efficient solution algorithm implemented by the author and co-workers will be described which is capable of handling abrupt nonlinear behaviour associated with limit or bifurcation points. Current finite element modelling approaches to capture damage initiation and progression in stiffened composite structures are also presented.

9.2 Experimental observations

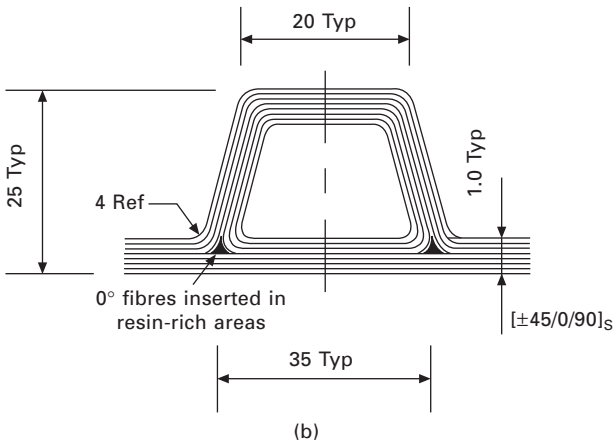
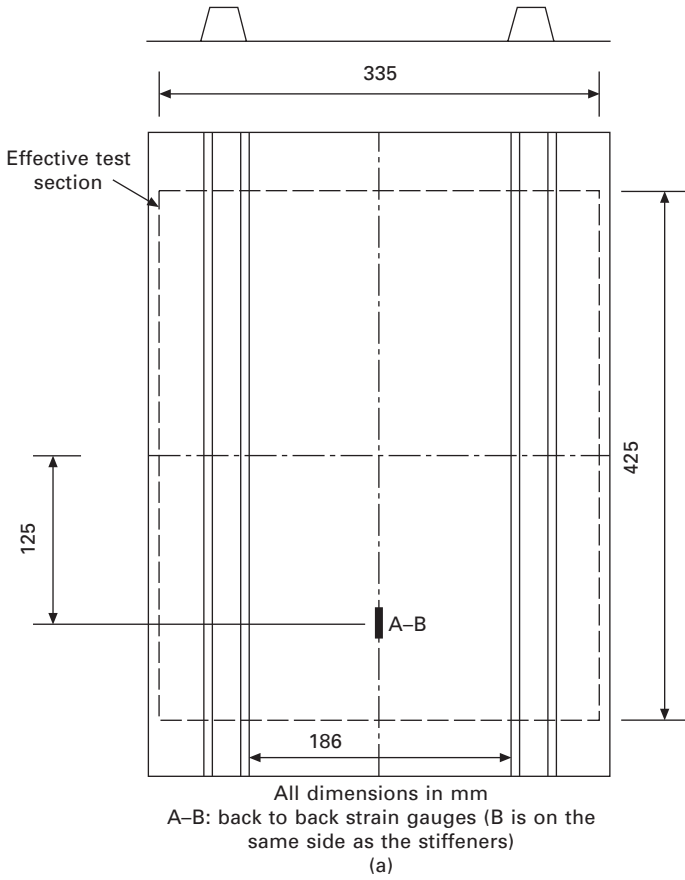
The potential for lightweight postbuckling design of stiffened composite structures has been demonstrated through a number of experimental

programmes undertaken by the author and co-workers, Falzon and Steven (1995, 1996, 1997), Falzon *et al.* (2000), Falzon (2001) and Stevens *et al.* (1995, 1997). A selection of panel configurations, incorporating different lay-up schemes, stiffener cross-sections and stiffener separation, were tested in uniaxial compression until failure. This type of test primarily simulates the behaviour of the upper wing surface in flight, lower fuselage sections and control surfaces. These panels were all made from unidirectional pre-impregnated carbon-fibre composite laminae and designed to fail at a load well beyond that required to cause initial local skin-buckling. The loaded ends were potted in a resin and fibreglass mixture and machined parallel to ensure a uniform loading and imposing a near-clamped boundary condition. The panels were placed in a compression-testing hydraulic machine and loaded quasi-statically under displacement control.

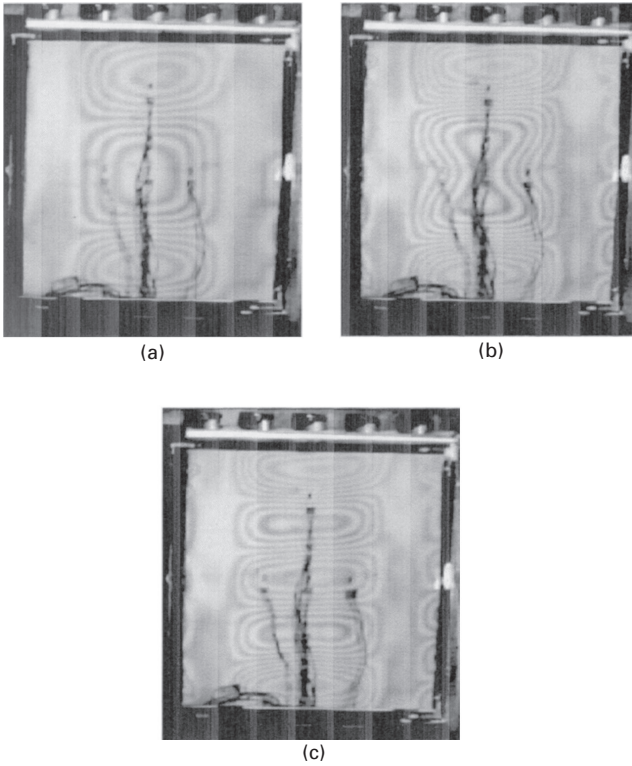
Stiffened postbuckling structures have been shown not to be particularly imperfection-sensitive, that is, slight geometric imperfections do not lead to significant reductions in the local, or indeed, global stability loads. This is in marked contrast to the behaviour of curved or cylindrical shells loaded in uniaxial compression (Yamaki, 1984) or spherical shells under an external pressure load (Yamada and Yamada, 1983), which exhibit large reductions in buckling strength in the presence of comparatively small geometric imperfections. Indeed, the notion that an optimum stiffened structure is one with coincident local and global buckling leads to high imperfection-sensitivity. This may result in a sudden collapse at loads significantly below those predicted theoretically. A detailed discussion of this phenomenon is given in the monographs by Singer *et al.* (1998, 2002).

9.2.1 Hat-stiffened panel

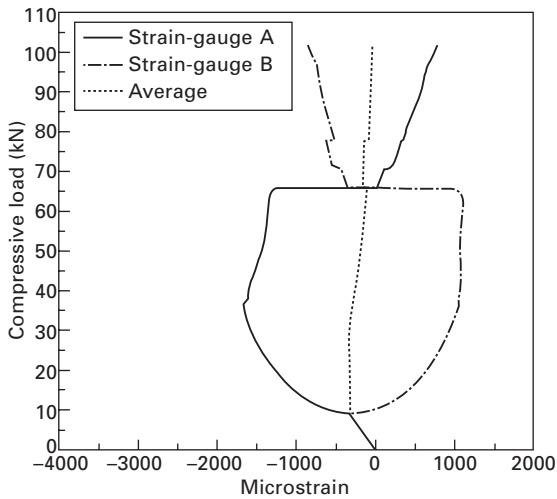
The hat-stiffened panel shown in Fig. 9.1(a) was designed to be highly postbuckling and incorporated two integrated hat-stiffeners as detailed in Fig 9.1(b). This panel was designed to be representative of lightly loaded thin-skinned secondary structure which buckles under operational loads. The shadow Moiré technique (Kobayashi, 1993) was used to qualitatively observe the out-of-plane displacements where the contours represent constant displacement. Figure 9.2 shows the Moiré fringe pattern at different loading stages. The panel had a nominal skin thickness of 1 mm, and initial buckling of the central skin bay occurred at 9.4 kN. This buckling load was deduced from back-to-back strain gauges where the buckling point was determined by noting the change in membrane strain taken as the average of the two strain gauge readings. The mode-shape contained three half-waves and, upon additional loading, the crests of these half-waves were observed to flatten out as evidenced by the strain-gauge results in Fig. 9.3 which show a gradual reduction in the bending strain beyond a loading of approximately 40 kN.



9.1 (a) Hat-stiffened panel; (b) stiffener detail.



9.2 Moiré fringe patterns for hat-stiffened panel at loading; (a) 40 kN, (b) 66 kN ($t = -0.04$ s), (c) 66 kN ($t = 0.04$ s).



9.3 Results of back-to-back strain-gauges mounted on the skin-bay of a hat-stiffened panel.

This phenomenon was described by Koiter (1963) and is due to the increasing membrane stiffness deep in postbuckling. The initial buckling mode shape was observed to grow gradually with increasing load, confirming that initial buckling of plated structures is stable.

The central half-wave was observed to extend vertically and a gradual secondary instability was observed at the skin–stiffener boundaries, leading to a splitting of this central half-wave as shown in Fig. 9.2(b). A similar observation was made by Chai (2002) in his study of unilaterally constrained plates with all edges fully clamped, where this splitting continued until the central half-wave had transformed to two separate half-waves. The hat-stiffened panel did not exhibit this complete formation and at a loading of 66 kN, a dynamic mode-jump to five half-waves was observed. The final mode-shape is shown in Fig. 9.2(c). The initial location of the strain-gauges in Fig. 9.3 indicates a buckle crest, sometimes referred to as an anti-node line. At the mode-jump, the bending strains recorded at this location were dramatically reduced, indicating that this location was close to a newly formed buckling node-line. The panel failed catastrophically at a loading of 103 kN, which was nearly 11 times higher than the initial buckling load of the skin-bay.

Hat stiffened-panels were also tested by Stevens *et al.* (1997) but no mode-jumping was reported. Two configurations were tested, one where the flanges on the stiffeners were untapered and the other where the flanges were tapered by a single four-ply drop-off. The four bottom plies in a flange of eight-ply thickness were cut short to achieve the taper by the enveloping top four plies. By loading the panels at a very slow rate in a hyper-stiff testing machine, some tests were successfully terminated before catastrophic collapse to reveal failure initiating at the skin–stiffener interface of a buckling node-line. These regions correspond to areas of maximum twisting moment and the geometric discontinuity between the skin and the flange gives rise to interlaminar shear stresses at the edge of the skin–stiffener interface.

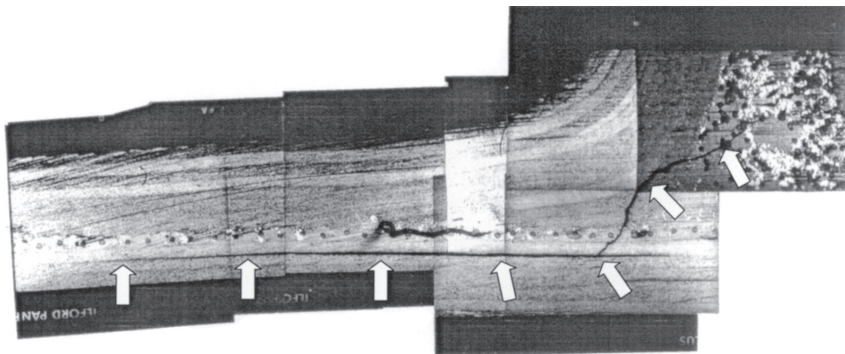
High interlaminar shear stresses initiated delamination failure at the edge of the skin–stiffener interface which then propagated towards the stiffener web. A detailed discussion of edge effects in the failure of composite structures is given by Davies *et al.* (1986). This interlaminar shear stress may be alleviated by flange tapering but, surprisingly, in the tests carried out by Stevens *et al.* (1997), the panels with tapered flanges failed at a lower loading than those without tapering, where failure was still observed to initiate at a node-line. These tests highlighted the local nature of failure initiation and indicated that the design of the taper may play a significant role in determining failure initiation in stiffened composite panels.

9.2.2 I- and J-stiffened panels

Tests on I- and J-stiffened panels by Stevens *et al.* (1995) revealed failure initiation in regions corresponding to buckle crests. At these locations, the twisting moments are a minimum but the direct bending moments are a maximum. There are two mechanisms that may lead to failure initiation.

Bending moments are induced in the skin–stiffener flange region and the stiffness discontinuity at the edge of the flange gives rise to peel stresses. In a buckled configuration, these peel stresses will be tensile on one side of the stiffener web and compressive on the other. Delamination at the skin–stiffener interface may initiate at the free edge of the tensile region and propagate towards the base of the stiffener web. Flange tapering reduces the magnitude of peel stresses and the panels tested in this programme all had tapered flanges.

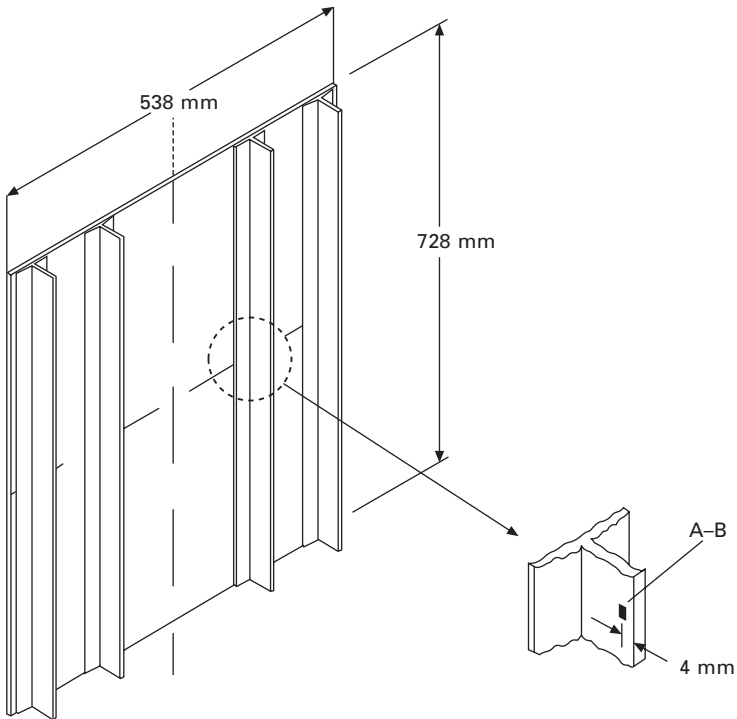
The other possible initial failure mechanism, and the one that was observed, arises from the constraint applied by the torsional stiffness of the stiffener cap. As the skin buckled, a bending moment in the stiffener web was generated, which increased linearly with a maximum occurring at the base of the stiffener web. This resulted in the formation of cracks at the triangular region underneath the web and bounded on each side by the stiffener flanges, which propagated along the tensile skin–stiffener interface as shown in Fig. 9.4. These cracks were observed to propagate along the stiffener for a length of approximately one-half of the buckled half-wave and outwards towards the edge with no further appreciable increases with subsequent loading. The reversal in sign of the peel stress with each quarter-wave has a stabilising effect on crack propagation and, with increased loading, other failure initiation sites were formed before catastrophic failure.



9.4 Micrograph of fractured skin–stiffener interface. Source: (Ricci 1994.)

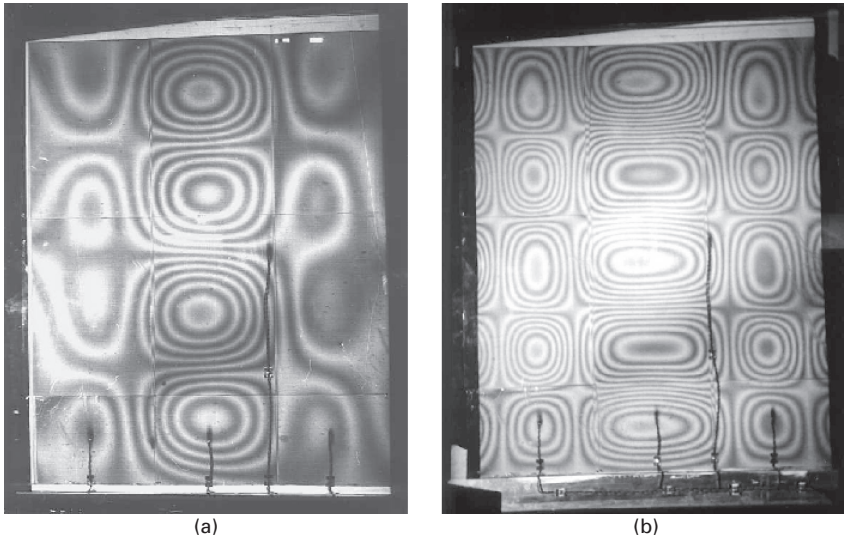
9.2.3 Blade-stiffened panel

Two identical blade-stiffened panels, shown in Fig. 9.5, were tested until failure by Falzon *et al.* (2000). Four stiffeners were secondary bonded to the skin using a film adhesive between tapered flanges of the stiffener and the skin. The stiffeners were not evenly spaced, with the spacing between the central two stiffeners being twice that of the outer adjacent stiffeners. The initial buckling load of the first panel was measured at 105 kN while the second panel buckled at 110 kN. The buckled mode-shape, of four half-waves, for the three skin-bays is shown in Fig. 9.6(a). The first panel failed catastrophically at a loading of 573 kN while the second panel was observed to undergo a sudden mode-jump to five half-waves at a loading of 570 kN as shown in Fig. 9.6(b). The proximity of the failure load of the first panel to the load at which the second panel underwent a mode-jump suggests that a secondary instability in the first panel may have precipitated failure.



9.5 Blade-stiffened panel.

The second panel was unloaded to allow for the placement of extra strain-gauges around a stiffener node-line where damage was observed to initiate from a visual inspection of the failed first panel. Upon reloading, the mode-jump occurred at 548 kN which was slightly lower than the load recorded for

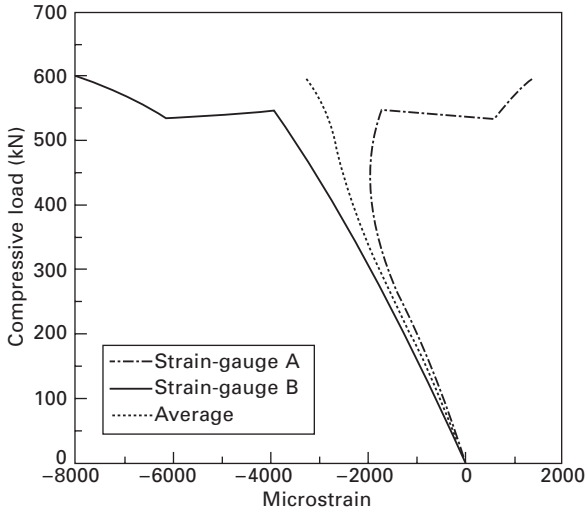


9.6 Moiré fringe patterns for blade-stiffened panel at loading: (a) 300 kN, (b) 570 kN.

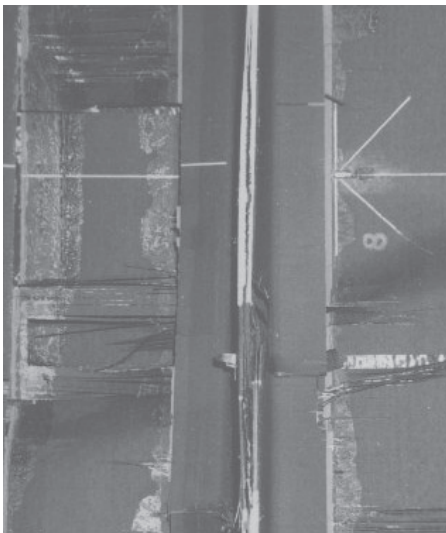
the first load cycle. This may be attributed to inevitable matrix cracking although no significant acoustic emission was detected until final failure. The absence of acoustic emission indicated that no appreciable damage had developed in the panel prior to collapse.

It will be recalled that the strain-gauge results in Fig. 9.3 showed a sudden reduction in bending strain due to the appearance of a buckling node-line. The inevitable obverse effect of this is that regions within a buckled structure will jump from a state of relatively low strain to an appreciably higher one. An example of this is shown in Fig. 9.7 for a pair of strain-gauges mounted on the stiffener web at a nodal line as shown in Fig. 9.5. The relatively low torsional stiffness of the I-stiffeners resulted in stable stiffener rotation under increasing compressive loading. This rotation will be shown to have had a significant bearing in explaining the failure mechanism associated with this type of panel. The second panel failed catastrophically at a loading of 601 kN.

The stiffeners, for the most part, remained attached to the skin but mid-plane delamination at the free-edge of the stiffener web was observed at the failure locations as shown in Fig. 9.8. This is in contrast to the failure observed in the I-, J- and hat-stiffened panels where failure initiated at a skin–stiffener interface. Blade-stiffeners have relatively low torsional stiffness. Therefore the loading action that initiated failure in the previous panels could not develop and a different failure initiation mechanism was found away from the skin–stiffener interface. The stiffener rotation gave rise to high interlaminar shear stresses τ_{xz} on a node-line at the free edge of the stiffener web (Falzon *et al.*, 2000).



9.7 Results of back-to-back strain-gauges mounted on the web of a blade-stiffener.



9.8 Failure locations in a blade-stiffened panel.

9.3 Finite element modelling

9.3.1 Linear eigenvalue analysis

A common starting point in the numerical analysis of the buckling of stiffened composite panels is to perform a linear eigenvalue analysis. The implicit assumption with this type of analysis is that initial imperfections in the

structure are negligible or, at least, the structure is not imperfection-sensitive. The applied loading is also assumed to be conservative and a linear function of displacements. To understand how the buckling load may be obtained from an eigenvalue analysis, consider the tangential stiffness matrix, \mathbf{K}_t , at a point along an equilibrium path, which is made up of the sum of the material stiffness matrix, \mathbf{K} , and the geometric stiffness matrix \mathbf{K}_σ :

$$\mathbf{K}_t = \mathbf{K} + \mathbf{K}_\sigma \quad 9.1$$

\mathbf{K}_σ accounts for the effects that membrane forces have on the bending stiffness of a structure and is formulated independently of \mathbf{K} . Now if a structure is loaded such that compressive membrane forces are generated, it may be argued that for a permissible deformation mode, \mathbf{K}_σ will reduce the overall stiffness to zero for a given load magnitude. Hence at this instance the tangential stiffness matrix, \mathbf{K}_t is singular. The load at which this occurs is the buckling load of the structure.

In a finite element analysis, the applied load is usually based on some design criterion, usually the maximum in-service load that the structure is likely to experience multiplied by a safety factor. If this load is referred to f_{ext} we usually want to know whether this exceeds the buckling load. By the linearity assumption, multiplying the applied loading f_{ext} by a scaling factor λ , will result in a corresponding increase in \mathbf{K}_σ whose terms are linear functions of applied load:

$$f_C = \lambda f_{\text{ext}} \Rightarrow \mathbf{K}_{\sigma C} = \lambda \mathbf{K}_\sigma \quad 9.2$$

where the subscript C refers to the scaled values. Therefore if f_C is the initial buckling load then the stiffness is singular and may be expressed as:

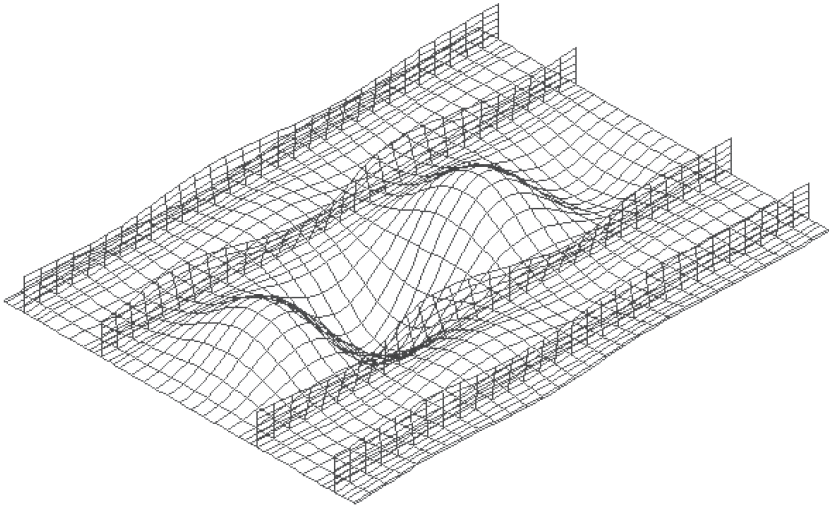
$$(\mathbf{K} + \lambda \mathbf{K}_\sigma) z = 0 \quad 9.3$$

where z corresponds to the deformation, from an initial configuration, when the overall stiffness becomes singular through the scaling of \mathbf{K}_σ by λ . Equation 9.3 is an eigenvalue problem where λ is referred to as the eigenvalue and z the corresponding eigenvector. The lowest value of λ that satisfies this equation yields the buckling load when multiplied by the applied loading f_{ext} . Hence, by Eq. 9.2, f_C becomes the critical buckling load for the structure. Higher buckling modes may be found and therefore the eigenvalue problem may be expressed more generally as:

$$(\mathbf{K} + \lambda_i \mathbf{K}_\sigma) z_i = 0 \quad 9.4$$

In practice, the determination of higher buckling modes is usually less significant, although the user may, nonetheless, be interested in knowing whether there are any other eigenvalues clustered around the critical eigenvalue. This would imply an intertwining of numerous secondary branches whereby the correct determination of a stable post-secondary instability equilibrium path cannot be guaranteed (Riks *et al.*, 1996).

Figure 9.9 shows the buckled mode-shape for the second blade-stiffened panel, discussed in Section 9.2.3, using a linear eigenvalue analysis. The predicted initial buckling load was 3.5% higher than that measured experimentally and the mode shape exhibited the expected four half-waves in the skin bays. The second eigenvalue corresponded to a load that was 5.4% higher than the experimental buckling load with a mode-shape corresponding to five half-waves. Despite the proximity of these two eigenvalues the panel did not undergo a mode-jump from four half-waves to five half-waves until a loading of over five times the initial buckling load was reached.



9.9 Buckling mode shape for a blade-stiffened panel obtained from a linear eigenvalue analysis.

9.3.2 Geometrically nonlinear analysis

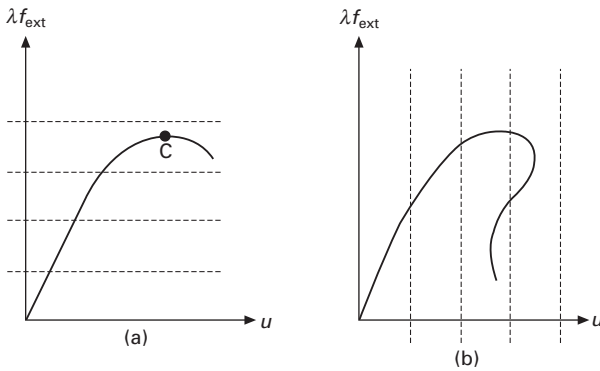
An eigenvalue analysis will not yield accurate information on the critical buckling load if geometric imperfections are substantial or the structure is sensitive to small imperfections. Even though postbuckling flat stiffened panels are not imperfection sensitive, panels with coincident local and global buckling loads may exhibit such behaviour. Also, no quantitative information on the buckled mode-shape can be extracted. A better way forward in the finite element modelling of the buckling and postbuckling response of plated structures is to use nonlinear analysis. The use of quasi-static continuation methods are based on the application of incremental loads or displacements to capture the nonlinear response of a structure across a specified load history. The set of equilibrium equations that must be solved at each increment are given by:

$$\mathbf{r}(\mathbf{u}, \lambda) = \mathbf{f}_{\text{int}} - \lambda \mathbf{f}_{\text{ext}} = 0 \tag{9.5}$$

where $\mathbf{r}(\mathbf{u}, \lambda)$ is the residual or out-of-balance force vector, \mathbf{u} is the vector of displacements, \mathbf{f}_{int} is the internal force vector given by $\mathbf{K}_t \mathbf{u}$, \mathbf{f}_{ext} is the external reference load vector and λ is a load scaling parameter.

Newton–Raphson methods

The Newton–Raphson-based solution algorithms are the most widely used routines for solving standard nonlinear problems and form the backbone of most commercial nonlinear finite element packages. The reader is referred to the monograph by Bathe (1996) for the implementation details of these algorithms. Newton–Raphson schemes are iterative solution schemes and can be used under either displacement or load control. In the presence of highly nonlinear behaviour these methods are known to fail. Figure 9.10(a) shows the potential problems using load control where the load is applied as a series of fixed load increments while Fig. 9.10(b) shows a similar problem for displacement control where a set of displacements are prescribed incrementally. This type of behaviour is sometimes referred to as *snap-through* or *snap-back* behaviour and is analogous to the behaviour observed in postbuckling stiffened panels undergoing mode-jumping. Hence more sophisticated numerical procedures are required to reliably capture the response of these structures.



9.10 Potential problems in tracing a highly nonlinear equilibrium path using (a) load control and (b) displacement control.

It is worth making a distinction between a limit point and a bifurcation point at this stage of the discussion. The nature of such critical points along an equilibrium path requires different numerical approaches for their identification and to advance the solution beyond these points. A point along an equilibrium path where the tangent is normal to the load axis is referred

to as a *limit point*. An example of a limit point is shown in Fig. 9.10(a) and is denoted by C . A simple *bifurcation point* represents the intersection of two equilibrium curves, often referred to as the primary and secondary curves for an initial bifurcation point. At a bifurcation point, the primary curve becomes unstable and hence the structure will assume a different deformation mode commensurate with an equilibrium state along the stable secondary path.

The buckling of a perfect structure corresponds to a bifurcation point. Nonlinear finite element continuation methods cannot traverse such points without the requirement of extra computational effort (Crisfield, 1997). In practice, the presence of imperfections within a structure removes a bifurcation point and only a single equilibrium path exists. This equilibrium path may be highly nonlinear and hence the need for advanced numerical procedures capable of traversing limit points. One such group of procedures is collectively referred to as the arc-length methods.

Arc-length methods

Arc-length methods were first proposed by Riks (1979) and Wempner (1971), with later modifications proposed by Crisfield (1981). These methods use both the scaling parameter λ and the displacement vector, \mathbf{u} , as constraint variables. For a finite element model with n degrees-of-freedom, the arc-length method requires the solution of $n + 1$ variables and the added constraint equation is represented in Eq. 9.6:

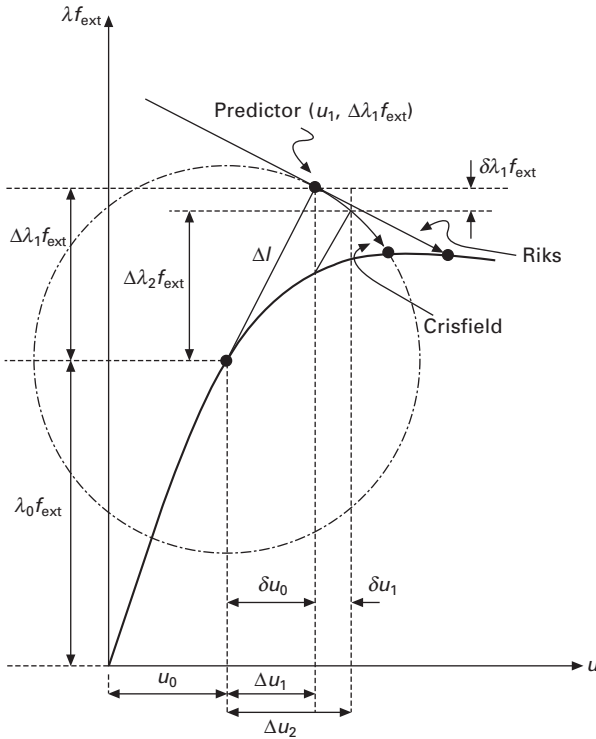
$$\Delta \mathbf{u}^T \Delta \mathbf{u} + \Delta \lambda^2 \psi^2 \mathbf{f}_{\text{ext}}^T \mathbf{f}_{\text{ext}} = \Delta l^2 \quad 9.6$$

where, with reference to Fig. 9.11, $\Delta \mathbf{u}$ and $\Delta \lambda$ are the incremental changes in displacement and load respectively, Δl is the arc-length and ψ is a scaling parameter.

Riks' formulation iterates along a hyperplane orthogonal to the tangent of length Δl from a previously converged point along the equilibrium path. Crisfield's method iterates along a hypersphere, where the arc-length constraint is also employed for corrector iterations, and is less likely to fail in the vicinity of sharp limit points. Crisfield has further shown that the loading terms have little influence on the solution process and advocated setting $\psi = 0$. The iterations within each increment are usually still performed using a modified Newton–Raphson scheme.

Solving Eqs 9.5 and 9.6 simultaneously is not readily amenable to finite element analysis since the augmented stiffness matrix will not be symmetric or banded. Using an approach suggested by Batoz and Dhatt (1979) this system of equations reduces to a quadratic in $\delta \lambda$ which represents an iterative change in the applied load:

$$a_1 \delta \lambda^2 + a_2 \delta \lambda + a_3 = 0 \quad 9.7$$

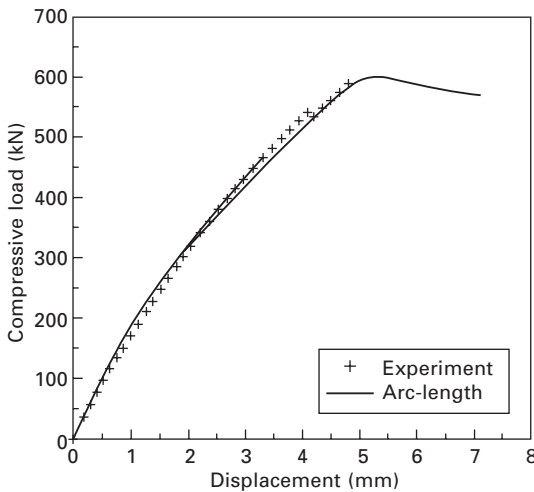


9.11 Constraint schemes proposed by Riks and Crisfield.

The reader is referred to the monograph by Crisfield (1991) for the derivation of the quadratic coefficients. This implies two possible solutions for the load increment and the correct choice of $\delta \lambda$, at the predictor stage, is central to this method's effectiveness. One possibility is to match the sign of $\delta \lambda$ with the determinant of the stiffness matrix. In practice this is achieved by looking at the terms of the diagonal matrix D of the factored stiffness matrix $K_t = LDL^T$ where L is a lower unit triangular matrix. If all terms on the diagonal are positive, this implies the stiffness matrix is positive definite and hence a positive sign for the load increment is chosen. If a negative diagonal is encountered, this is equivalent to detecting a negative eigenvalue and implies that a critical point has been passed. This critical point could be either a limit point or a bifurcation point, but the arc-length method breaks down in the vicinity of bifurcation points. It is common practice within a finite element model to introduce geometric imperfections to remove bifurcation points. Other schemes for the selection of the correct load increment have also been proposed by Hellweg and Crisfield (1998), De Souza Neto and Feng (1999) and Cerini and Falzon (2005), among others.

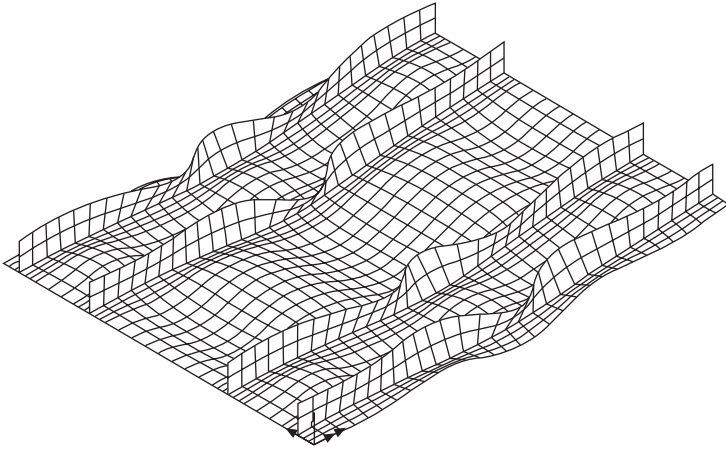
A finite element model of the second blade-stiffened panel presented in

Section 9.2.3 was developed and an imperfection corresponding to the first two eigenmodes, and scaled such that the maximum out-of-plane displacement was 5% of the skin thickness, was added to the pristine geometry. The mode-jump was predicted to occur at a loading that was 14% lower than the experimentally observed value. This discrepancy may be attributed to the introduction of imperfections that bore little resemblance to any imperfections that existed in the actual test panel. The experimental and finite element curves are shown in Fig. 9.12. It is noted that the mode-jump is characterised by a sharp ‘snap-back’. At a loading of 601 kN the solution indicated collapse of the panel, which was, remarkably, the same as the experimental failure load recorded for the panel. Figure 9.13 shows the deformed state just before final failure and the high stiffener-web rotations at the mid-span of the panel were consistent with the observed failure mechanism leading to the panel’s catastrophic collapse.



9.12 Load versus end-displacement curves for the blade-stiffened panel (arc-length method).

Arc-length methods are shown to be able to capture highly non-linear behaviour, including mode-jumping in stiffened composite structures, but they may still run into difficulty in the presence of very sharp snap-backs or if inappropriate imperfections are added that do not remove all the bifurcation points that are likely to be encountered. It should not be surprising that trying to capture transient events using quasi-static continuation techniques may run into difficulty. Riks *et al.* (1996) further pointed out that the stable paths that the structure follows before and after a mode-jump may not be statically connected by unstable equilibrium paths, so that such methods are bound to fail.



9.13 Panel deformation at the point of collapse (601 kN).

Dynamic methods

The presence of transient phenomena in a highly postbuckled panel suggests that a dynamic solution algorithm might be better suited for analysis. In general, the static equilibrium equation, Eq. 9.5, is augmented with inertial and damping forces:

$$\mathbf{M}\ddot{\mathbf{u}} + \mathbf{C}\dot{\mathbf{u}} + \mathbf{r}(\mathbf{u}, \lambda) = 0 \quad 9.8$$

where \mathbf{M} is the mass matrix, \mathbf{C} is the damping matrix and $\ddot{\mathbf{u}}$ and $\dot{\mathbf{u}}$ are the acceleration and velocity vectors respectively. For a given set of initial conditions the solution process is stepped through time at specified load increments. Within each load increment the solution is monitored until the dynamic terms are reduced to within a set tolerance.

Various direct time-integration schemes have been proposed for the solution of dynamical systems (Hitchings, 1992) and these may be subdivided into two main groups. The first group is referred to as *implicit methods* and is based on satisfying Eq. 9.8 exactly for some time $t + \Delta t$. This implies that ${}^{t+\Delta t}\mathbf{u}$ (the displacement at time $t + \Delta t$) requires knowledge of ${}^{t+\Delta t}\ddot{\mathbf{u}}$ and ${}^{t+\Delta t}\dot{\mathbf{u}}$ and the solution is solved iteratively using a predictor-corrector procedure such as a Newton–Raphson scheme. The tangential stiffness matrix \mathbf{K}_t , may be shown to be augmented by additional terms involving the mass and stiffness matrices and hence the system can still be equilibrated when \mathbf{K}_t is singular. While this method is unconditionally stable (i.e. Δt may be large) for well-behaved problems, it is still susceptible to numerical difficulties for highly nonlinear problems and hence a small Δt will usually be required to ensure convergence. Caputo *et al.* (2002) used an implicit Newmark scheme in their study of the postbuckling behaviour of a stiffened panel representative of the non-pressurised rear fuselage of the ATR 42-72 commuter aircraft.

The second group is termed *explicit methods*, where it is assumed that for a sufficiently small time-step Δt , only the acceleration changes significantly and thus ${}^{t+\Delta t}\ddot{\mathbf{u}}$ is determined from ‘historical’ values only:

$${}^{t+\Delta t}\ddot{\mathbf{u}} = \mathbf{M}^{-1} \{ {}^{t+\Delta t}\lambda \mathbf{f}_{\text{ext}} - {}^t\mathbf{C}^t \dot{\mathbf{u}} - {}^t\mathbf{K}_t {}^t\mathbf{u} \} \quad 9.9$$

Standard explicit methods further assume that the mass matrix can be diagonalised, and by using an appropriate time-stepping scheme, the solution may be progressed without the need of matrix factorisation. This method, while being very stable for highly nonlinear problems is conditionally stable and requires a time-step of the order of the inverse of the maximum resonant frequency, ω_{max} , of the structure. Bisagni (2000) undertook a comparative study of implicit and explicit dynamic schemes in her study of postbuckling composite shells that exhibit highly nonlinear behaviour. Despite the small time-step required for stability in an explicit procedure, the computational time required for this analysis was significantly less than that required for the implicit dynamic analysis.

In general, to establish static equilibrium, at least one cycle of the fundamental frequency ω_{min} , must be completed so that the number of steps is of the order of $\omega_{\text{max}}/\omega_{\text{min}}$ during the dynamic phase of the analysis. This results in a very high number of time steps as these two frequencies are usually orders of magnitude apart. The damping matrix is often idealised as proportional (or Rayleigh) damping and is expressed as:

$$\mathbf{C} = \alpha \mathbf{K}_t + \beta \mathbf{M} \quad 9.10$$

where α is a constant that controls damping at high frequencies and β is a constant that controls damping at low frequencies. Because of the large spread in resonant frequencies of a typical structure, choosing adequate damping coefficients becomes difficult. Hence the requirement for a large number of steps is augmented by a very slow rate of convergence.

In the modelling of postbuckling stiffened composite structures undergoing mode-jumping, we are often only interested in locating a stable post-mode-jumping equilibrium path without the need of accurately representing the behaviour during the transient phase. It is therefore not necessary to retain the actual mass and damping matrices since once a static solution is recovered, these matrices multiply null acceleration and velocity vectors. It was also stated earlier that the explicit method assumes a diagonal mass matrix. This is not strictly necessary although it does improve the computational efficiency. However, since the interest lies in recovering a static solution, emphasis is shifted to improving the computational efficiency in achieving this goal, i.e. by reducing the ratio $\omega_{\text{max}}/\omega_{\text{min}}$. If a diagonal \mathbf{M} is retained, then some terms may be selectively scaled, leading to a reduction in ω_{max} , but typically less than an order of magnitude, with ω_{min} remaining largely unaffected. Hence a more efficient scheme was sought for reducing this frequency ratio.

These considerations led to the development of a modified explicit dynamic analysis whereby the diagonal form of \mathbf{M} was abandoned and, along with the damping matrix \mathbf{C} , replaced with the tangent stiffness matrix:

$$\bar{\mathbf{K}}_t^{t+\Delta t} \ddot{\mathbf{u}} + (\alpha {}^t\mathbf{K}_t + \beta \bar{\mathbf{K}}_t)' \dot{\mathbf{u}} + {}^t\mathbf{K}_t {}^t\mathbf{u} - {}^{t+\Delta t}\lambda \mathbf{f}_{\text{ext}} = 0 \quad 9.11$$

where ${}^t\mathbf{K}_t$ is the current stiffness matrix and $\bar{\mathbf{K}}_t$ is a previous estimate of the tangent stiffness matrix. This reduces the difference between ω_{max} and ω_{min} by orders of magnitude. α is usually chosen to critically damp ω_{max} and β chosen to critically damp ω_{min} . Therefore:

$$\begin{aligned} {}^{t+\Delta t} \ddot{\mathbf{u}} &= \bar{\mathbf{K}}_t^{-1} [{}^{t+\Delta t}\lambda \mathbf{f}_{\text{ext}} - {}^t\mathbf{K}_t(\alpha' \dot{\mathbf{u}} + {}^t\mathbf{u})] - \beta' \dot{\mathbf{u}} \\ &= \bar{\mathbf{K}}_t^{-1}(\mathbf{q}_{\text{ext}} - \tilde{\mathbf{q}}_{\text{int}}) - \beta' \dot{\mathbf{u}} \end{aligned} \quad 9.12$$

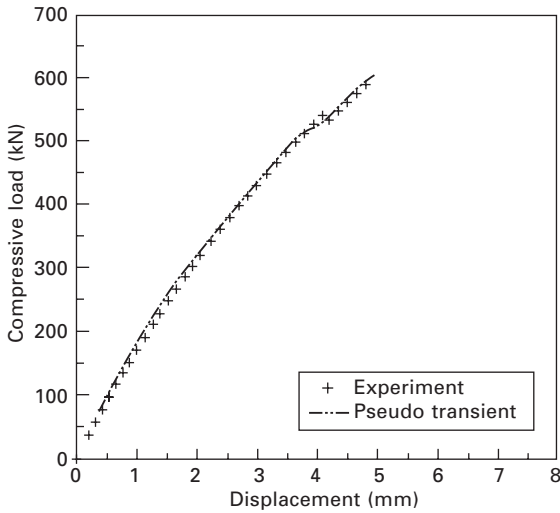
Once the acceleration has been calculated it may be assumed to vary linearly between time t and $t + \Delta t$. Integrating this linear expression yields ${}^{t+\Delta t} \dot{\mathbf{u}}$ and integrating again gives ${}^{t+\Delta t} \mathbf{u}$. The norm of the out-of-balance force ($\mathbf{q}_{\text{ext}} - \tilde{\mathbf{q}}_{\text{int}}$) is then compared with the norm of the load increment. If the ratio exceeds a specified convergence factor then the next step is computed. If this ratio is below the convergence factor, the next load increment is applied. $\bar{\mathbf{K}}_t$ is typically computed at the start of each load increment and is updated only if the out-of-balance norm increases significantly over one or more previous time steps or, as a check against slow convergence, if more than a specified number of steps are taken for a given load increment.

A further improvement in computational efficiency was obtained by reducing the problem to a first-order one and setting the damping matrix equal to the stiffness matrix $\bar{\mathbf{K}}_t$:

$${}^{t+\Delta t} \dot{\mathbf{u}} = \bar{\mathbf{K}}_t^{-1} ({}^{t+\Delta t} \lambda \mathbf{f}_{\text{ext}} - {}^t\mathbf{K}_t {}^t\mathbf{u}) = \bar{\mathbf{K}}_t^{-1} (\mathbf{q}_{\text{ext}} - \tilde{\mathbf{q}}_{\text{int}}) \quad 9.13$$

By assuming that the velocity varies linearly over the time-step, the displacements may be obtained and convergence checks carried out that are identical to those for the full second order system. This method allows for the use of a comparatively large time-step compared to a standard explicit analysis. In fact, Falzon and Cerini (2004a) have shown that if $\bar{\mathbf{K}}_t$ is updated at every time-step, the condition for stability is that Δt should be less than or equal to unity. In practice, Δt was limited to less than or equal to 0.2.

The blade-stiffened panel discussed in Section 9.2.3 was modelled using this first order 'pseudo-transient' scheme (Falzon and Hitchings, 2003). The load versus end-displacement curve is shown in Fig. 9.14. The mode-jump was predicted to occur at a loading of approximately 517 kN which was 5% lower than the experimental value and closer than that predicted using the arc-length method. The solution was also able to accurately capture panel collapse at a loading of 602 kN.



9.14 Load versus end-displacement curves for the blade-stiffened panel (pseudo-transient method).

Combined quasi-static/pseudo-transient method

The pseudo-transient method provides a robust means of modelling the structural response of highly nonlinear behaviour and is not susceptible to the same problems associated with quasi-static continuation methods. In the absence of highly nonlinear behaviour, continuation methods are very efficient and thus a numerical scheme which combines the advantages of quasi-static and transient techniques seems a logical progression in the modelling of postbuckling stiffened panels. Riks *et al.* (1996) and Caputo *et al.* (2002) have demonstrated this combined scheme using quasi-static and implicit dynamics procedures and the switching from one solution procedure to the other was performed interactively using restarting schemes available in most commercial finite element packages. Falzon and Cerini (2004a) have automated this procedure within an in-house finite element code using the arc-length method and the pseudo-transient analysis discussed above.

The arc-length method (or indeed any other non-linear solution method such as a Newton–Raphson scheme) is used while the response of the panel, to a given compressive loading, is quasi-static. This behaviour is characterised by a positive definite tangential stiffness matrix. Using the decomposition of this stiffness matrix, $\mathbf{K}_t = \mathbf{LDL}^T$, a positive definite matrix will have all diagonal terms (pivots) in \mathbf{D} greater than zero. When a critical point is passed, a negative pivot will result. At this stage of the analysis, a ‘bracketing procedure’ is used to determine the location of the critical point more accurately. Once this has been located with sufficient accuracy, a load increment which is just above this point is used to initiate the transient phase of the analysis.

To prevent the solution from tracking back along the same equilibrium path, use is made of eigenmode injection. Close to the critical point, the eigenvalue, λ_C , will be close to zero and the corresponding eigenvector, v_C , is scaled and used as the displacement increment. It is worth noting that eigenvalue extraction for large problems is computationally expensive but Fujii and Noguchi (2002) have shown that λ_C and v_C may be directly extracted from the LDL^T decomposition of K_t :

$$\lambda_C \approx \frac{(d_{ii})_{\min}}{|l_i|^2} \quad v_C \approx \frac{l_i}{|l_i|} \quad 9.14$$

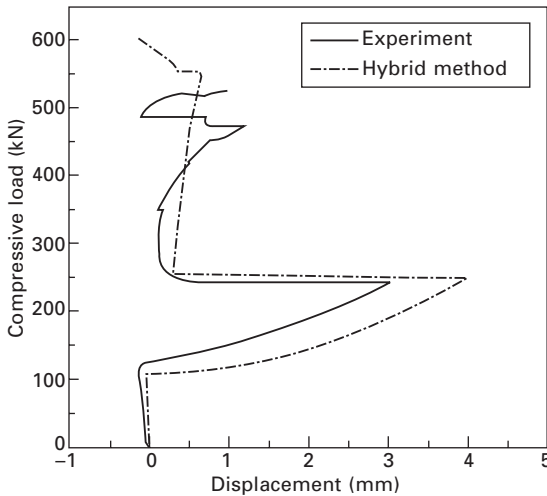
where $(d_{ii})_{\min}$ is the smallest diagonal entry in D and l_i is the corresponding column of $(L^T)^{-1}$.

This transient phase is stepped through pseudo-time until convergence is reached within a set tolerance and then the solution procedure switches back to the quasi-static routine. By identifying the critical points directly and using eigenmode injection, there is no longer the need to introduce initial imperfections into the geometry to remove bifurcation points as would be required if the arc-length method was used exclusively. The type of critical point may also be deduced by noting that for a bifurcation point $v_C^T \mathbf{q}_{\text{ext}} = 0$ and $\partial\lambda/\partial s \neq 0$ which represents the differential change in load with respect to an arc-length parameter, s , where the incremental form of this is given in Eq. 9.6. A limit point is defined by $\partial\lambda/\partial s = 0$ and $v_C^T \mathbf{q}_{\text{ext}} \neq 0$. A nondimensional current stiffness parameter κ , which relates the current stiffness to the initial stiffness, may also be used to indicate a limit point as $\kappa \rightarrow 0$.

Falzon and Cerini (2004b) demonstrated the numerical efficiency and robustness of this automated hybrid procedure by comparing the CPU time, using the different solution techniques discussed in this chapter, in the modelling of a beam on a nonlinear elastic foundation. The beam was modelled using two-node truss elements connected with linear rotational springs and supported at the nodes by extensional springs whose restoring force was proportional to the cube of their extension. The cubic-spring type of support simulated the behaviour of a simply supported plate under uniaxial compression and the model was shown to undergo several mode-jumps with increasing load. A number of different mesh densities were also investigated. Where convergence was achieved using the arc-length method, this proved to be the most computationally efficient (shortest CPU time). This was followed by the hybrid procedure, the pseudo-transient procedure, the implicit and explicit schemes. The CPU time for the full explicit method was shown to be orders of magnitude higher than that for the hybrid procedure.

A finite element model of a uniaxial compression-loaded I-stiffened carbon-fibre composite panel, which was experimentally tested to failure, was developed and solved using the automated hybrid procedure. The panel, of length 790 mm and width 604 mm, was made from T300/914C unidirectional

pregreg with four equally spaced stiffeners, secondary-bonded onto the skin. The skin bays were observed to buckle in five half-waves at a loading of approximately 119 kN and a mode-jump to six half-waves occurred at a loading of 244 kN. A further mode-jump, where the outer skin bays buckled into seven half-waves, was observed at a loading of 485 kN. Audible cracks were heard at loadings above 300 kN, indicating matrix microcracking. The out-of-plane displacement at the centre of the panel was measured and compared with that predicted from the finite element model, as shown in Fig. 9.15. As is evident, the finite element model predicted the initial mode-jump to occur at a loading of 235 kN which was only 2.8% higher than the experimentally observed value. The second mode-jump was predicted to occur at a loading of 552 kN which was 13.8% higher than that observed experimentally. This discrepancy is due to the considerable extent of matrix microcracking under this high loading, which reduces the overall stiffness of the panel and was not accounted for in the finite element modelling.

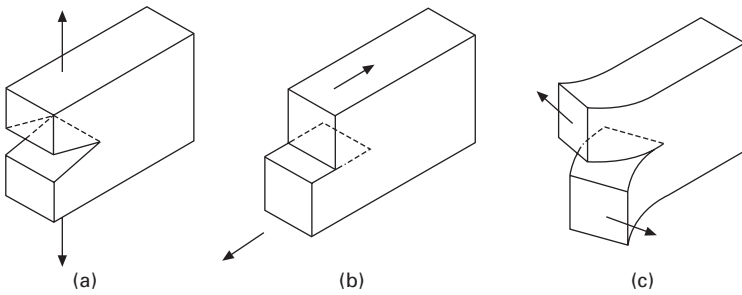


9.15 Out-of-plane displacement at the centre of the I-stiffened panel.

9.4 Modelling failure

The experimental observations discussed in Section 9.2 highlighted the vulnerability of co-cured, co-bonded or secondary-bonded stiffened composite structures to delamination failure at the skin–stiffener interface. Delamination results from the relatively weak interface strength to through-thickness and shear stresses. This problem is exacerbated when the panel is in a postbuckled state. Hyer and Cohen (1988), Cohen and Hyer (1992) and Kassapoglou and DiNicola (1992) have investigated the distribution of stresses at the skin–stiffener interface, and the resulting stress singularities at the edge of this

interface suggest that the use of stress-based criteria for failure prediction is inappropriate. The use of fracture mechanics principles to predict delamination is more suitable and has been the subject of a considerable amount of research in recent years. A total strain energy release rate (G_T), defined as the amount of energy required to create a crack surface is partitioned into three components: G_I which is the energy release rate associated with an opening mode (tension); G_{II} is the energy release rate due to sliding (shear) and sometimes G_{III} is also considered which is associated with a ‘scissoring’ mode. These are shown schematically in Fig. 9.16. The implementation of delamination modelling within a finite element context is primarily achieved through the use of either the Virtual Crack Closure technique (VCCT) which is based on the presence of a pre-existing crack or by incorporating interface elements at potential crack sites which can model both initiation and propagation.



9.16 Crack extension modes: (a) mode I; (b) mode II; (c) mode III.

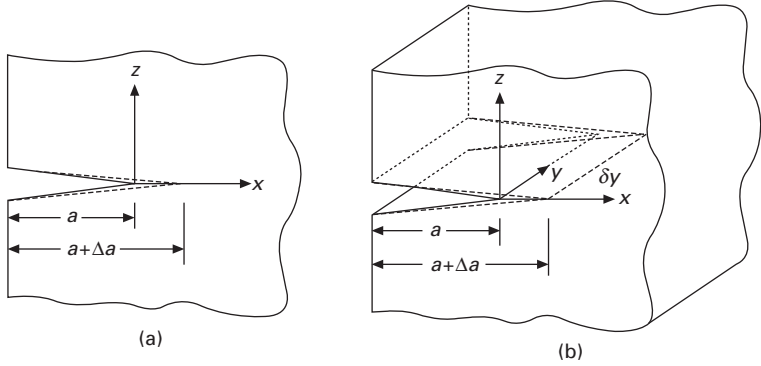
9.4.1 The virtual crack closure technique

The VCCT is an extension of a two-step crack closure technique originally proposed by Irwin (1958). As the name implies, the two-step technique requires two finite element solutions for predicting the energy release rate resulting from the growth of a crack, of initial length a , by a predetermined length Δa , and is based on the assumption that the energy released in opening the crack is identical to the work required to close it. The strain energy release rate, under constant displacement, is given by:

$$G = -\frac{\partial U}{\partial a} \tag{9.15}$$

where U is the total strain energy per unit thickness. For a two-dimensional configuration, shown in Fig. 9.17(a), $G = G_I + G_{II}$ ($G_{III} = 0$) and each component may be expressed as:

$$G_I = \lim_{\Delta a \rightarrow 0} \left\{ -\frac{1}{2\Delta a} \int_0^{\Delta a} \sigma_{zz}(x, 0) w(x - \Delta a, 0) dx \right\}$$



9.17 Crack configurations: (a) 2D; (b) 3D.

$$G_{II} = \lim_{\Delta a \rightarrow 0} \left\{ -\frac{1}{2\Delta a} \int_0^{\Delta a} \tau_{xz}(x, 0)u(x - \Delta a, 0) dx \right\} \quad 9.16$$

where σ_{zz} is the peel stress, τ_{xz} is the interlaminar shear stress, w is the opening displacement and u is the sliding displacement.

This may be extended to three dimensions, Fig. 9.17(b), where $G = G_I + G_{II} + G_{III}$ and each component is given by:

$$G_I = \lim_{\Delta a \rightarrow 0} \left\{ -\frac{1}{2\Delta a\delta y} \int_y^{y+\delta y} \left[\int_0^{\Delta a} \sigma_{zz}(x, y, 0)w(x - \Delta a, y, 0) dx \right] dy \right\}$$

$$G_{II} = \lim_{\Delta a \rightarrow 0} \left\{ -\frac{1}{2\Delta a\delta y} \int_y^{y+\delta y} \left[\int_0^{\Delta a} \tau_{xz}(x, y, 0)u(x - \Delta a, y, 0) dx \right] dy \right\}$$

$$G_{III} = \lim_{\Delta a \rightarrow 0} \left\{ -\frac{1}{2\Delta a\delta y} \int_y^{y+\delta y} \left[\int_0^{\Delta a} \tau_{yz}(x, y, 0)v(x - \Delta a, y, 0) dx \right] dy \right\}$$

9.17

where v is the displacement associated with sliding in the y -direction and τ_{yz} the corresponding interlaminar shear stress. These integral equations are evaluated numerically from the nodal displacements and forces calculated from finite element analysis.

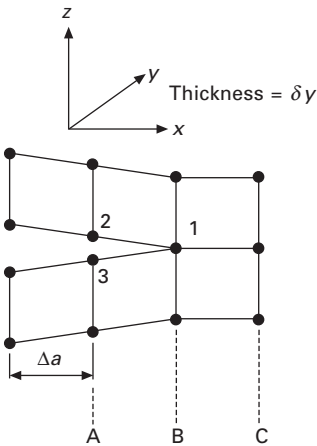
In a two-step analysis the first finite element solution will yield forces ahead of the crack front over a distance Δa , which represents the subsequent length of crack extension. The crack is then extended over Δa and a second finite element analysis will yield the displacements corresponding to the forces in the previous solution. Rybicki and Kanninen (1977) extended this method by obtaining sufficient accuracy using a one-step VCCT procedure.

This method requires a fine mesh around the crack front such that a crack extension of Δa does not significantly alter the stress-state of this crack front. Hence the method requires the crack front to be sufficiently removed from any edge or change in mesh density such that the stress field is self-similar across the crack front. In its basic form the VCCT also assumes that the mesh is symmetric about the crack plane and for three-dimensional problems the mesh should also be orthogonal to the crack front.

Consider the two-dimensional crack shown in Fig. 9.18 where the crack is modelled using four-node quadrilateral finite elements. For a sufficiently small Δa , it may be assumed that the displacements at A for a crack tip at B are a good approximation to the displacements at B for a crack tip at node C. Hence, the energy release rates may be calculated using a single finite element analysis:

$$G_I = -\frac{1}{2\delta y \Delta a} [F_{z1}(w_2 - w_3)]$$

$$G_{II} = -\frac{1}{2\delta y \Delta a} [F_{x1}(u_2 - u_3)] \tag{9.18}$$



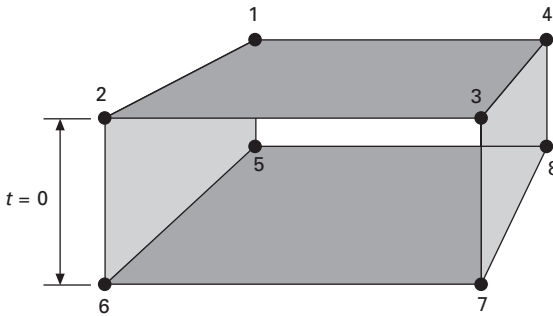
9.18 Node sequence for a crack modelled with four-node 2D elements.

F_{x1} and F_{z1} are the internal forces at node 1, in the x and y directions respectively, extracted from either the elements above or below the crack path. Similar expressions for eight-node quadrilateral and three-dimensional elements may be found in Falzon and Hitchings (2002). Wang *et al.* (1994, 1995), Wang and Raju (1996), Raju *et al.* (1993, 1996), Krueger *et al.* (2000) and Krueger and O'Brien (2001) used the VCCT in their study of skin-stiffener debonding for a range of configurations and loading conditions. These studies have concentrated on characterising the onset of debonding.

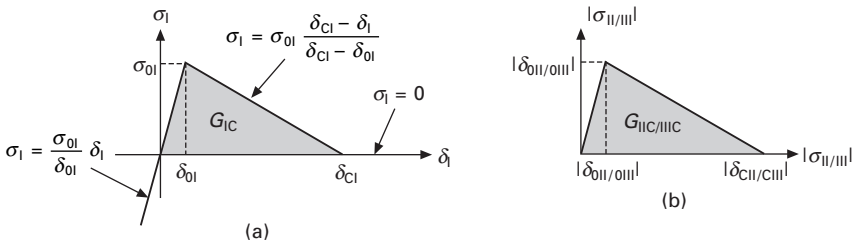
Hitchings *et al.* (1996) have also used the VCCT coupled with a delamination criterion for mixed-mode loading and a mesh-moving algorithm to model crack propagation. A review by Krueger (2004) outlines recent advances in the development of VCCT for dealing with different sized elements at the crack front and arbitrarily shaped crack fronts.

9.4.2 Interface elements

Interface elements are decohesion elements, usually of zero thickness or of a finite thickness representing a resin-rich layer, which are inserted between composite layers or at well-defined interfaces such as the skin–stiffener interfaces of a stiffened panel. Unlike the VCCT, interface elements do not require an initial crack and have the potential of being better suited for studies involving both crack initiation and propagation. Zero-thickness elements are characterised by nodes at the top and bottom of coincident surfaces as shown in Fig. 9.19 for a linear interface element. Delamination is modelled by introducing a traction law between the two surfaces of the interface element. A bilinear traction law for mode I and mode II/III is shown in Fig. 9.20 although other forms, such as a polynomial relationship, as used by Chen *et al.* (1999), may also be used.



9.19 A linear interface element for 3D analysis.



9.20 Traction laws for interface element for mode I and mode II/mode III delamination.

With reference to Fig. 9.20(a), the high initial stiffness, associated with Mode I, holds the interface together until a critical stress, σ_{0I} is reached, corresponding to displacement δ_{0I} . With subsequent loading a negative stiffness represents the accumulation of damage at the interface, representative of microcracking in the resin. This region of damage is termed a process zone and makes the precise determination of a crack front problematic. A critical displacement, δ_{CI} , is reached when the accumulated energy per unit area, represented by the area under the curve, reaches the critical energy release rate G_{IC} :

$$G_{IC} \int_0^{\delta_{CI}} \sigma(\delta) d\delta \quad 9.19$$

For clarity, a crack front, within the context of this formulation, will usually refer to the line at the edge of the process zone where complete decohesion has occurred. A high penalty stiffness is also used when the stresses are compressive to prevent interpenetration of the two surfaces. Figure 9.20(b) shows similar relationships from modes II and III. A delamination is usually propagated using an interaction law of the form:

$$\left(\frac{G_I}{G_{IC}} \right)^{\frac{\alpha}{2}} + \left(\frac{G_{II}}{G_{IIC}} \right)^{\frac{\alpha}{2}} + \left(\frac{G_{III}}{G_{IIIC}} \right)^{\frac{\alpha}{2}} = 1 \quad 2 \leq \alpha \leq 4 \quad 9.20$$

proposed by Mi *et al.* (1997) which encompasses both the widely used linear ($\alpha = 2$) and quadratic ($\alpha = 4$) laws. Numerous other criteria have been proposed but no single criterion has been shown to be equally effective in all circumstances.

The softening behaviour of interface elements makes the analysis highly nonlinear which may lead to convergence difficulties using implicit solution schemes. Hence there still exists some mesh sensitivity associated with the use of interface elements. Indeed, the non-smooth load/deflection response resulting from the use of an insufficiently refined mesh gives rise to sharp ‘snap-throughs’ and ‘snap-backs’ similar to those associated with mode-jumping. In this instance, though, this behaviour is strictly an artefact of the solution scheme and the density of the mesh used. Sophisticated solution schemes have been proposed to avoid the need for very fine meshes around the process zone. Crisfield and Alfano (2002) used an adaptive scheme for increasing the order of the interpolation functions of the elements around the process zone. Another scheme was later proposed, Alfano and Crisfield (2003), whereby the solution was made more robust using local arc-length control and line-search schemes.

An explicit dynamic analysis, as discussed in Section 9.3.2, could be used to recover a quasi-static solution for solving delamination problems using interface elements. This method is conditionally stable and hence the necessary

small time-steps would make this a computationally expensive option. The use of pseudo-transient solution schemes should yield an improved robustness similar to that achieved in modelling mode-jumping. This work is currently under way by the author and co-workers and will lead the way for the development of a robust numerical tool capable of modelling postbuckling panels which may undergo mode-switching and delamination failure at the skin–stiffener interface.

9.5 Concluding remarks

A unified study into the response of postbuckling stiffened composite structures under uniaxial compression has been presented. The experimental investigations showed the abrupt mode-jumps that occur in highly postbuckling structures and that may initiate damage in vulnerable regions such as the skin–stiffener interface. These secondary instabilities may also give rise to convergence difficulties using implicit quasi-static finite element solution schemes. An automated hybrid quasi-static implicit/pseudo-transient solution scheme was shown to be robust and computationally efficient in capturing these mode-jumps.

Experimental observations revealed that failure initiated at the skin–stiffener interface at either a buckling node-line or an anti-node line. This was shown to be the result of high interlaminar and peel stresses at these locations. Local geometric features of the stiffener were shown to have a significant influence on the distribution and magnitude of these stresses. The relatively weak through-thickness strength of composite laminates made from prepregged unidirectional carbon–fibre plies made these locations particularly vulnerable. The use of the virtual crack closure technique and decohesion interface elements for modelling delamination failure in finite element analysis were also presented.

This chapter has concentrated on the analysis of stiffened composite structures made from unidirectional carbon–fibre plies which is the dominant form of carbon–fibre material used on current and proposed composite aerostructures because of their superior in-plane mechanical performance. Woven carbon–fibre fabrics exhibit considerably higher interlaminar fracture toughness but at the cost of lower mechanical performance in compression because of the undulation of the fibres. It is worth noting that major research programmes are currently under way, investigating alternative manufacturing routes and material systems aimed at reducing the vulnerability of skin–stiffener interfaces to through-thickness stresses. One possibility is by the resin infusion of three-dimensional dry carbon–fibre pre-forms of the skin and stiffeners. Another emerging technology is the use of ‘z-pinning’ where carbon–fibre pins of an approximate diameter of 0.3 mm and a density of a few hundred per square centimetre are inserted through the uncured stiffeners

and skin. These pins are held in a foam carrier and inserted using an ultrasonic gun.

9.6 References

- Alfano, G. and Crisfield, M.A. (2003), Solution strategies for the delamination analysis based on a combination of local-control arc-length and line searches, *International Journal for Numerical Methods in Engineering*, **58**(7), 999–1048.
- Bathe, K.-J. (1996), *Finite Element Procedures*, Prentice Hall, New Jersey, USA.
- Batoz, J.L. and Dhatt, G. (1979), Incremental displacement algorithms for non-linear problems, *International Journal for Numerical Methods in Engineering*, **14**, 1262–1266.
- Bisagni, C. (2000), Numerical analysis and experimental correlation of composite shell buckling and post-buckling, *Composites Part B: Engineering*, **33**, 655–667.
- Caputo, F., Esposito, R., Perugini, P. and Santoro, D. (2002), Numerical-experimental investigation on post-buckled stiffened composite panels, *Composite Structures*, **55**, 347–357.
- Cerini, M. and Falzon, B.G. (2005), Use of arc-length method for capturing mode jumping in postbuckling aerostructures, *AIAA Journal*, **43**, 681–689.
- Chai, H. (2002), On the post-buckling of bilaterally constrained plates. *International Journal of Solids and Structures*, **39**, 2911–2926.
- Chen, J., Crisfield, M.A., Kinloch, A.J., Busso, E.P., Matthews, F.L. and Qiu, Y. (1999), Predicting progressive delamination of composite material specimens via interface elements, *Mechanics of Composite Materials and Structures*, **6**, 301–317.
- Cohen, D. and Hyer, M.W. (1992), Influence of geometric nonlinearities on skin–stiffener interface stresses, *AIAA Journal*, **30**(4), 1055–1062.
- Cox, H.L. (1945), *Compression tests on seven panels of monocoque construction*, Aeronautical Research Council R & M No. 2042, London, UK.
- Crisfield, M.A. (1981), A fast incremental/iterative solution procedure that handles ‘snap-through’, *Computers & Structures*, **13**, 55–62.
- Crisfield, M.A. (1991), Non-Linear Finite Element Analysis of Solids and Structures, Volume 1, *John Wiley & Sons*, Chichester, UK.
- Crisfield, M.A. (1997), Non-Linear Finite Element Analysis of Solids and Structures, Volume 2, *John Wiley & Sons*, Chichester, UK.
- Crisfield, M.A. and Alfano, G. (2002), Adaptive hierarchical enrichment for delamination fracture using a decohesive zone model, *International Journal for Numerical Methods in Engineering*, **54**(9), 1369–1390.
- Davies, G.A.O., Buskell, N. and Stevens, K.A. (1986), Edge effects in failure of compression panels, *Euromech 214 Symposium on Composites*, Amsterdam, The Netherlands.
- De Souza Neto, E.A. and Feng, Y.T. (1999), On the determination of the path direction for arc-length methods in the presence of bifurcations and snap-backs, *Computational Methods in Applied Mechanical Engineering*, **179**, 81–89.
- Everall, P.R. and Hunt, G.W. (2000), Mode jumping in the buckling of struts and plates: a comparative study, *International Journal of Non-Linear Mechanics*, **35**, 1067–1079.
- Falzon, B.G. (2001), The behaviour of damage tolerant hat-stiffened composite panels loaded in uniaxial compression, *Composites Part A: Applied Science and Manufacturing*, **32**, 1255–1262.
- Falzon, B.G. and Cerini, M. (2004a), An automated combined quasi-static/pseudo-dynamic

- procedure for capturing mode-switching in postbuckling structures, *11th European Conference on Composite Materials*, Rhodes, Greece, 31 May–3 June.
- Falzon, B.G. and Cerini, M. (2004b), Modelling postbuckling composite structures, *International Conference on Computational and Experimental Engineering and Science*, Madeira, Portugal, 26–29 July.
- Falzon, B.G. and Hitchings, D. (2002), The behaviour of compressively loaded stiffener runout specimens – Part II: Finite element analysis, *Journal of Composite Materials*, **37**(6), 481–501.
- Falzon, B.G. and Hitchings, D. (2003), Capturing mode-switching in postbuckling composite panels using a modified explicit procedure, *Composite Structures*, **60**, 447–453.
- Falzon, B.G. and Steven, G.P. (1995), Behaviour of hat-stiffened thin-skinned carbon–fibre composite panels, *AIAA/ASME/AHS/ASC 36th Structures, Structural Dynamics and Materials Conference*, New Orleans, USA, 10–12 April.
- Falzon, B.G. and Steven, G.P. (1996), A combined experimental and numerical investigation into the postbuckling of hat-stiffened panels containing circular cutouts, *APCOM96*, Seoul, Korea, 16–18 September.
- Falzon, B.G. and Steven, G.P. (1997), Buckling mode transition in hat-stiffened composite panels loaded in uniaxial compression, *Composite Structures*, **37**, 253–267.
- Falzon, B.G., Stevens, K.A. and Davies, G.A.O. (2000), Postbuckling behaviour of a blade-stiffened composite panel loaded in uniaxial compression, *Composites Part A: Applied Science and Manufacturing*, **31**, 459–468.
- Fujii, F. and Noguchi, H. (2002), The buckling mode extracted from the LDL^T – decomposed larger-order stiffness matrix, *Communications in Numerical Methods in Engineering*, **18**(7), 459–467.
- Harris, G.Z. (1975), The buckling and post-buckling behavior of composite plates under biaxial loading, *International Journal of Mechanical Sciences*, **17**, 187–202.
- Hellweg, H.-B. and Crisfield, M.A. (1998), A new arc-length method for handling sharp snap backs, *Computers & Structures*, **66**(5), 704–709.
- Hitchings, D. (1992), *A Finite Element Primer*, NAFEMS, Glasgow, UK.
- Hitchings, D., Robinson, P. and Javidrad, F. (1996), A finite element model for delamination propagation in composites, *Computers & Structures*, **60**(6), 1093–1104.
- Hyer, M.W. and Cohen, D. (1988), Calculations of stresses in stiffened composite panels, *AIAA Journal*, **26**(7), 852–857.
- Irwin, G.R. (1958), Fracture, in *Handbuch der Physik*, vol. V, Springer, New York, USA.
- Kassapoglou, C. and DiNicola, A.J. (1992), Efficient stress solutions at skin-stiffener interfaces of composite stiffened panels, *AIAA Journal*, **30**(7), 1833–1839.
- Knight, Jr, N.F. and Starnes, Jr, J.H. (1988), Postbuckling behaviour of selected curved stiffened graphite–epoxy panels loaded in axial compression, *AIAA Journal*, **26**(3), 344–352.
- Kobayashi, A.S. (ed) (1993), *Handbook on Experimental Mechanics*, John Wiley & Sons, New York, USA.
- Koiter, W.T. (1943), *The effective width of infinitely long, flat rectangular plates under various conditions of edge restraint*, NLL Report S287, Amsterdam, The Netherlands.
- Koiter, W.T. (1963), Introduction to the post-buckling behaviour of flat plates. *Colloquium on the Post-buckling of Plates in Metal Structures*, University of Liege, Belgium.
- Kong, C.W., Lee, I.C., Kim, C.G. and Hong, C.S. (1998), Postbuckling and failure of stiffened composite panels under axial compression, *Composite Structures*, **42**, 13–21.

- Krueger, R. (2004), Virtual crack closure technique: history, approach and applications, *Applied Mechanics Review*, **57**(2), 109–143.
- Krueger, R. and O'Brien, T.K. (2001), A shell/3D modelling technique for the analysis of delaminated composite laminates, *Composites Part A: Applied Science and Manufacturing*, **32**, 25–44.
- Krueger, R., Cvitkovich, M.K., O'Brien, T.K. and Minguet, P.J. (2000), Testing and analysis of composite skin/stringer debonding under multi-axial loading, *Journal of Composite Materials*, **34**(15), 1263–1300.
- Kweon, J.H., Hong, C.S. and Lee, I.C. (1995), Postbuckling strength of graphite/epoxy laminated cylindrical panels loaded in compression, *AIAA Journal*, **35**(2), 217–222.
- Lekhnitskii, S.G. (1968), *Anisotropic Plates*, Gordon and Breach Science Publishers, New York USA.
- Mi, Y., Crisfield, M.A., Hellweg, H.B. and Davies, G.A.O. (1997), Finite element method and progressive failure modelling of composite structures, In *Computational Plasticity: Fundamentals and Applications. Part 1*, Owen, J. et al. (eds), CIMNE Barcelona, 239–254.
- Minguet, P.J., Dugundji, J. and Lagace, P. (1989), Postbuckling behaviour of laminated plates using a direct energy-minimisation technique, *AIAA Journal*, **27**(12), 1785–1792.
- Nakamura, T. and Uetani, K. (1979), The secondary buckling and post-secondary-buckling behaviours of rectangular plates, *International Journal of Mechanical Sciences*, **21**, 265–286.
- Raju, I.S., Sistla, R., Krishnamurthy, T. and Lotts, C.G. (1993), Fracture mechanics analyses for skin–stiffener debonding, *AIAA Conference Paper 93–1502*, 3698–3714.
- Raju, I.S., Sistla, R. and Krishnamurthy, T. (1996), Fracture mechanics analyses for skin–stiffener debonding, *Engineering Fracture Mechanics*, **54**(3), 371–385.
- Ricci, R. (1994), 'Postbuckling induced failure of composite stiffened panels', PhD Thesis, Department of Aeronautics, Imperial College London, UK.
- Riks, E. (1979), An incremental approach to the solution of snapping and buckling problems, *International Journal of Solids and Structures*, **15**, 529–551.
- Riks, E., Rankin, C.C. and Brogan, F.A. (1996), On the solution of mode jumping phenomena in thin-walled shell structures, *Computational Methods in Applied Mechanics and Engineering*, **136**, 59–92.
- Romeo, G. and Frulla, G. (1994), Non-linear analysis of anisotropic plates with initial imperfections and various boundary conditions subjected to combined biaxial compression and shear loads, *International Journal of Solids and Structures*, **31**(6), 763–783.
- Rybicki, E.F. and Kanninen, M.F. (1977), A finite element calculation of stress intensity factors by a modified crack closure integral, *Engineering Fracture Mechanics*, **9**, 931–938.
- Shuman, L. and Back, G. (1930), *Strength of rectangular plates under edge compression*, NACA Technical Report No. 356, Washington DC, USA.
- Singer, J., Arbocz, J. and Weller, T. (1998), *Buckling Experiments*, Vol. 1, John Wiley & Sons, New York, USA.
- Singer, J., Arbocz, J. and Weller, T. (2002), *Buckling Experiments*, Vol. 2, John Wiley & Sons, New York, USA.
- Starnes, Jr, J.H., Knight, Jr, N.F. and Rouse, M. (1985), Postbuckling behaviour of selected flat stiffened graphite–epoxy panels loaded in compression, *AIAA Journal*, **23**(8), 1236–1246.

- Stein, M. (1959a), *The phenomenon of change in buckle pattern in elastic structures*, NACA Technical Report R-39, Langley Aeronautical Laboratory, USA.
- Stein, M. (1959b), *Loads and deformations of buckled rectangular plates*, NACA Technical Report R-40, Langley Aeronautical Laboratory, USA.
- Stein, M. (1983), Postbuckling orthotropic composite plates loaded in compression, *AIAA Journal*, **21**(12), 1729–1735.
- Stevens, K.A., Ricci, R. and Davies, G.A.O. (1995), Buckling and postbuckling of composite structures, *Composites*, **26**(3), 189–199.
- Stevens, K.A., Specht, S. and Davies, G.A.O. (1997), Postbuckling failure of carbon–epoxy compression panels, *Proceedings of ICCM-11*, Gold Coast, Australia, 14–18 July.
- Supple, W.J. (1970), Changes in wave-form of plates in the post-buckling range, *International Journal of Solids and Structures*, **6**, 1243–1258.
- Stoll, F. (1994), Analysis of snap phenomenon in buckled plates, *International Journal of Non-Linear Mechanics*, **29**(2), 123–138.
- Von Kármán, T. (1910), Festigkeitsprobleme im Maschinenbau, *Encyklopädie der Mathematischen Wissenschaften*, **4**(4), 311–385.
- Von Kármán, T., Sechler, E.E. and Donnell, L.H. (1932), The strength of thin plates in compression, *ASME Transactions*, APM-54-5, **54**(2), 53–57.
- Wang, J.T. and Raju, I.S. (1996), Strain energy release rate formulae for skin–stiffener debond modelled with plate elements, *Engineering Fracture Mechanics*, **54**(2), 211–228.
- Wang, J.T., Raju, I.S. and Sleight, D.W. (1994), Fracture mechanics analysis of composite skin–stiffener debond configurations with shell elements, *AIAA Conference Paper*, 94-1389, 676–693.
- Wang, J.T., Raju, I.S. and Sleight, D.W. (1995), Composite skin–stiffener debond analyses using fracture mechanics approach with shell elements, *Composites Engineering*, **5**(3), 277–296.
- Wempner, G.A. (1971), Discrete approximations related to nonlinear theories of solids, *International Journal of Solids and Structures*, **7**, 1581–1599.
- Yamada, M. and Yamada, S. (1983), Agreement between theory and experiment on large-deflection behaviour of clamped shallow spherical shells under external pressure, *Proceedings IUTAM Symposium on Collapse*, London, Cambridge University Press, Cambridge, UK, 431–441.
- Yamaki, N. (1984), *Elastic Stability of Circular Cylindrical Shells*, vol. **27**, Applied Mathematics and Mechanics, Elsevier, Amsterdam, The Netherlands.
- Yusuff, S. (1952), Large Deflection Theory for orthotropic rectangular plates subjected to edge compression, *Journal of Applied Mechanics*, **19**, 445–450.

Analysing the strength and ductility of plated structures

T U S A M I and H B G E, Nagoya University, Japan

10.1 Introduction

Thin-walled steel structures have found wide applications in bridge piers, suspension or cable-stayed bridge towers and others. Such structures are vulnerable to damage caused by local and global buckling. The knowledge of this phenomenon has increased dramatically since the 1960s and has been well documented in the literature (e.g. Fukumoto 1997 and Galambos 1998). However, the attention on them has mainly focused on strength issues. Following the damage in thin-walled structures observed in the 1995 Hyogoken–Nanbu earthquake, the importance of ductility, which plays a similar or more important role in the structural earthquake-resistance ability, has been widely recognized and has attracted the attention of researchers.

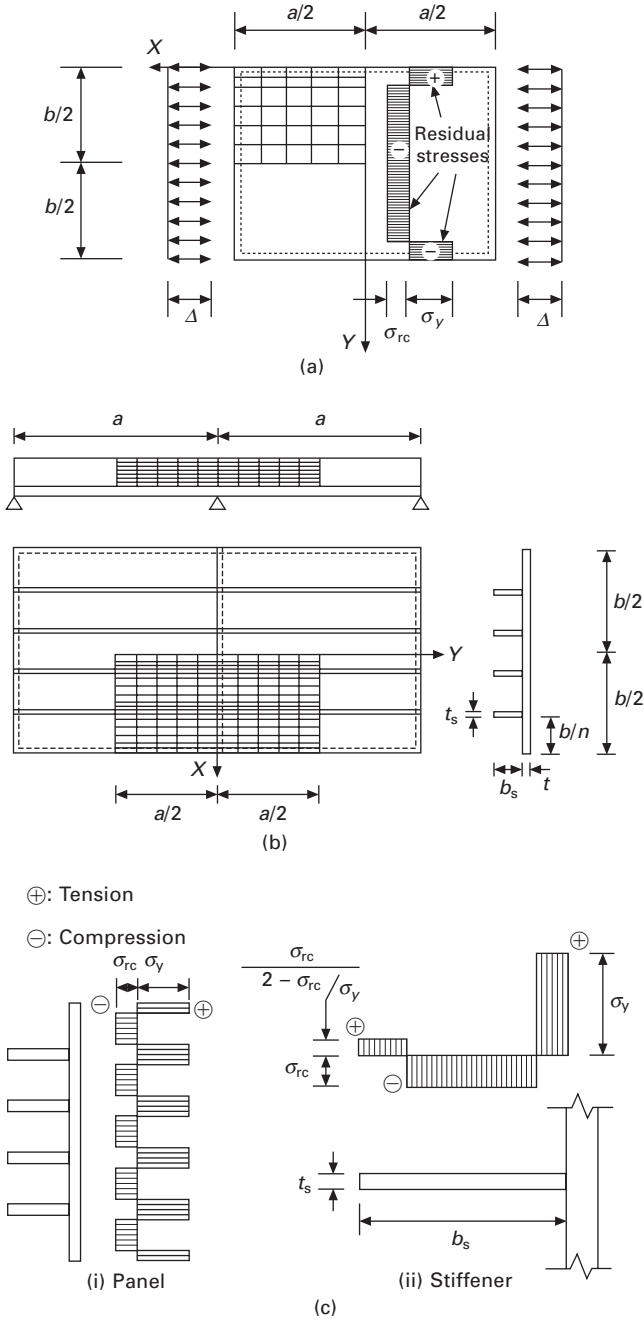
Extensive studies on strength and ductility have been carried out over the past few years. In this chapter, empirical equations obtained either from experiments or from analyses are summarized.

10.2 Component plates

A large number of steel structures are composed of thin-walled plates. A knowledge of strength and ductility of their component plates is very important to provide a reliable design of such structures. Through a large deformation numerical analysis, the authors have extensively surveyed the behavior of both unstiffened and stiffened plates under either compression (Usami *et al.* 1995; Usami and Ge 1998) or shear loading (Usami *et al.* 1999; Kasai *et al.* 2001).

10.2.1 Plates in compression

Figure 10.1 shows simply supported unstiffened and stiffened plates under compression. The distribution of residual stresses considered is an ideal rectangular pattern as shown in Fig. 10.1, which might be induced by the



10.1 Plates in compression: (a) unstiffened plate; (b) stiffened plate; (c) residual stresses assumed in the stiffened plate.

welding along the simply supported unloaded edge. The tensile and compressive residual stresses are assumed to be, respectively, σ_y and $0.3\sigma_y$ where σ_y is the yield stress. In allowing for initial geometrical imperfections, a half-wave sinusoidal form in both the length and width directions is assumed for unstiffened plates:

$$\delta = \delta_p \cos\left(\frac{x}{a}\pi\right) \sin\left(\frac{y}{b}\pi\right) \tag{10.1}$$

where a = plate length, b = plate width, x and y = coordinates, and δ_p is the maximum deflection with a value of $b/150$. For stiffened plates, following initial deflection equations including both the global and local distortions are assumed:

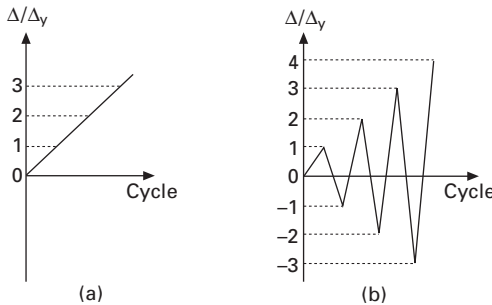
$$\delta = \delta_G + \delta_L \tag{10.2}$$

$$\delta_G = \frac{a}{1000} \sin\left(\frac{\pi}{a}y\right) \cos\left(\frac{\pi}{b}x\right) \tag{10.3}$$

$$\delta_L = \frac{b/n}{150} \sin\left(\frac{\pi}{a/n}y\right) \cos\left(\frac{\pi}{b/n}x\right) \tag{10.4}$$

where n = number of subpanels separated by stiffeners ($n = 1$ for unstiffened plates).

To investigate the effect of the loading history on the behavior of plates, two loading patterns are employed, as shown in Fig. 10.2. The case in Fig. 10.2(a) corresponds to monotonic loading, while Fig. 10.2(b) illustrates the case of cyclic loading. Here, we stipulate that the compressive displacement is positive. A two-sided cyclic loading program indicates that the plate is applied with alternative compression and tension loads. The two-side cyclic loading program is also simply referred to as cyclic loading in the following description.



10.2 Loading patterns: (a) monotonic loading; (b) cyclic loading (Δ is the specified displacement and Δ_y is the yield displacement).

A kind of two-surface model (2SM) developed at Nagoya University (Shen *et al.* 1995) was adopted to model the material nonlinearity that can accurately trace the cyclic behavior of steel. The general-purpose FEM program ABAQUS (1998) and the shell element S4R in its element library are employed in the analysis.

The main parameter controlling the strength and ductility of unstiffened and stiffened plates is the plate width–thickness ratio, defined by:

$$R_f = \frac{b}{nt} \sqrt{\frac{12(1 - \nu^2)}{4\pi^2}} \sqrt{\frac{\sigma_y}{E}} \quad 10.5$$

in which E = Young's modulus, ν = Poisson's ratio, and t = plate thickness.

For stiffened plates, the stiffener's slenderness ratio is another key parameter, defined as:

$$\bar{\lambda}_s = \frac{1}{\sqrt{Q}} \frac{a}{r_s} \frac{1}{\pi} \sqrt{\frac{\sigma_y}{E}} \quad 10.6$$

where r_s = radius of gyration of T-shaped cross-section centered on one longitudinal stiffener with a width of b/n , and Q = local buckling strength of plate panels given by:

$$Q = \frac{1}{2R_f} [\beta - \sqrt{\beta^2 - 4R_f}] \quad 10.7$$

$$\beta = 1.33 R_f + 0.868 \quad 10.8$$

Moreover, there is another commonly used parameter γ_c / γ_c^* , related to the characteristics of stiffened plate and interdependent with $\bar{\lambda}_s$. Here, γ_c is the relative flexural rigidity of the stiffener and γ_c^* is the optimum value of γ_c obtained from linear elastic buckling theory (DIN 4114, 1953). The relative flexural rigidity, γ_c , is defined as:

$$\gamma_c = \frac{EI_s}{bD} \quad 10.9$$

$$D = \frac{t^3 E}{12(1 - \nu^2)} \quad 10.10$$

where EI_s = out-of-plane flexural rigidity of the stiffener, and D = out-of-plane flexural rigidity per unit width of the plate. Equation [10.9] can be further rewritten as:

$$\gamma_c = \frac{t_s b_s^3 / 3}{bt^3 / 11} \quad 10.11$$

where b_s = width of stiffener, t_s = thickness of stiffener. On the other hand,

equations for the optimum value of γ_c obtained from linear elastic buckling theory (DIN 4114, 1953) are

$$\gamma_c^* = \begin{cases} 4\alpha^2 n \left(1 + n \frac{b_s t_s}{bt} \right) - \frac{(\alpha^2 + 1)^2}{n} & (\alpha < \alpha_0) \\ \frac{1}{n} \left\{ \left[2n \left(1 + n \frac{b_s t_s}{bt} \right) - 1 \right]^2 - 1 \right\} & (\alpha_0 \leq \alpha) \end{cases} \quad 10.12$$

where α = aspect ratio (= a/b) and α_0 = limit aspect ratio defined by

$$\alpha_0 = \sqrt[4]{1 + n\gamma_c} \quad 10.13$$

It should be noted that Eq. [10.12] is concerned with compression loading and formulae for the optimum stiffener rigidity that are applicable to shear panels will be given in the next section.

Strength

Empirical strength equations have been developed by Usami (1990, 1993) for unstiffened plates based on tests and numerical analyses. The equations are given by:

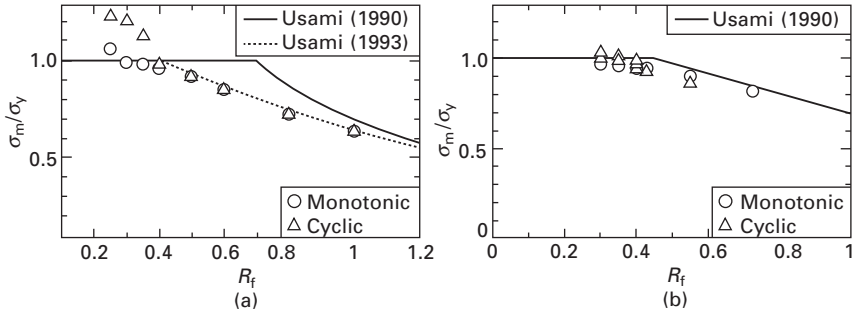
$$\frac{\sigma_m}{\sigma_y} = \frac{0.7}{R_f} \leq 1.0 \quad 10.14$$

$$\frac{\sigma_m}{\sigma_y} = \frac{1}{2R_f} [(1.33R_f + 0.868) - \sqrt{(1.33R_f + 0.868)^2 - 4R_f}] \leq 1.0 \quad 10.15$$

These two equations, plotted in Fig. 10.3(a), are compared with the numerical results through the analytical model presented above. It can be observed that the empirical formula based on numerical results (i.e. Eq. [10.15]) generally gives predictions on the safe side compared with those by the empirical formula based on test results (i.e. Eq. [10.14]). Except for cases with small width–thickness ratio ($R_f < 0.4$), the analytical points of both the monotonic and cyclic cases follow the proposed numerical formula (Eq. [10.15]) very well. This is because in the case of plates with small width–thickness ratios, the strain-hardening and cyclic strain-hardening effects result in an increase in strength, and the ultimate strength is even larger than the squash load.

In Fig. 10.3(b), the computed ultimate strengths of stiffened plates are compared with the corresponding values obtained using the equation (Usami 1990):

$$\frac{\sigma_m}{\sigma_y} = 1.24 - 0.54R_f \leq 1.0 \quad 10.16$$



10.3 Strength of plates in compression: (a) unstiffened plate; (b) stiffened plate.

From this figure, it is observed that the analytical points lie a little below the strength curve. It should be noted that this strength curve was chosen to agree with the mean of results of the tests on stiffened plates (Usami 1990).

Ductility

In a paper by Usami *et al.* (1995), ductility of the plate was defined with the failure strain, ϵ_u , which is at a point corresponding to 95% of the maximum average strength, σ_m , after the peak point. This definition seems to be occasionally inadequate for the results of cyclic analysis because the strength σ_u corresponding to the failure strain ϵ_u defined in such a way will be larger than the squash load for thick-walled plates. For this reason, the strength σ_u corresponding to ϵ_u is adopted as per the following definitions:

$$\frac{\sigma_u}{\sigma_y} = 0.95 \frac{\sigma_m}{\sigma_y} \tag{10.17}$$

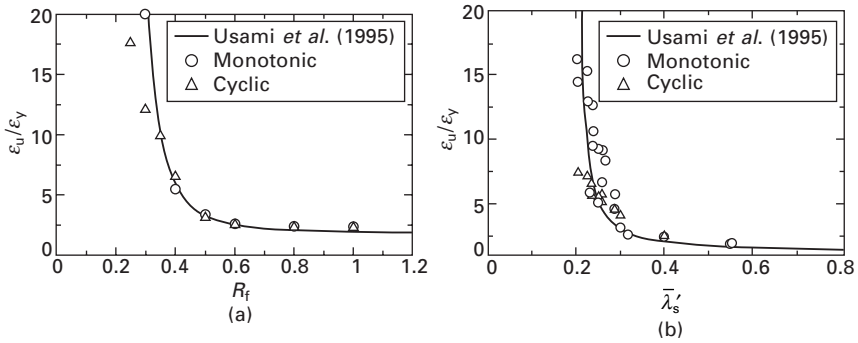
for relatively thin-walled sections without significant cyclic strain-hardening effect; and

$$\frac{\sigma_u}{\sigma_y} = 0.95 \frac{\sigma_p}{\sigma_y} \tag{10.18}$$

for relatively thick-walled sections with significant cyclic strain-hardening effect. Here, σ_p is the first peak strength before the occurrence of cyclic strain-hardening effect.

Failure strains of all the unstiffened and stiffened plates analyzed are plotted against R_f in Fig. 10.4. In the case of unstiffened plates, an empirical equation proposed by Usami *et al.* (1995) is also shown in the figure. The equation is expressed as a function of R_f in the form of:

$$\frac{\epsilon_u}{\epsilon_y} = \frac{0.07}{(R_f - 0.2)^{2.53}} + 1.85 \leq 20.0 \tag{10.19}$$



10.4 Ductility of plates in compression: (a) unstiffened plate; (b) stiffened plate.

In the case of stiffened plates, Usami *et al.* (1995) developed an empirical equation based on the monotonic results, given as

$$\frac{\epsilon_u}{\epsilon_y} = \frac{0.145}{(\bar{\lambda}_s - 0.2)^{1.11}} + 1.19 \leq 20.0 \tag{10.20}$$

This equation is expressed as a function of slenderness ratio parameter $\bar{\lambda}_s$ defined by Eq. [10.6], and effects of other parameters such as R_f , γ_c/γ_c^* and α , which are related to the stiffener’s slenderness ratio parameter, are thought to have been accounted for. But a further study by Usami and Ge (1998) showed that this equation overestimates the ductility of plates with small aspect ratios (e.g. $\alpha = 0.5$). To accurately account for the effect of aspect ratio on the failure strains of stiffened plates, a modified parameter $\bar{\lambda}'_s$ was introduced to replace the $\bar{\lambda}_s$ in Eq. [10.20]. The modified slenderness ratio parameter is defined as:

$$\bar{\lambda}'_s = \frac{1}{\sqrt[3]{\alpha}} \bar{\lambda}_s \tag{10.21}$$

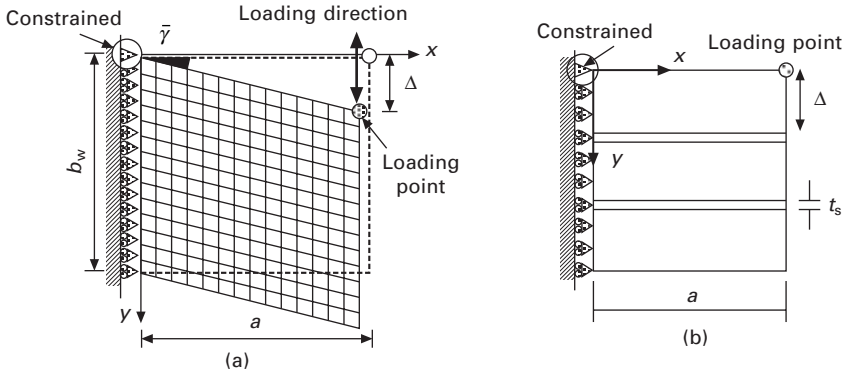
Figure 10.4(b) illustrates the computed failure strains and predictions by Eq. 10.20 with $\bar{\lambda}_s$ replaced by $\bar{\lambda}'_s$.

In the case of very stocky plates, the ductility capacity obtained from either the analysis or Eqs [10.19] and [10.20] is extremely high. The allowable ductility should be limited to 20.0 in order to inhibit excessive localized strains in the web and to avoid structural damage caused by low-cycle fatigue.

10.2.2 Plates in shear

As is well known, shear deformation might be pre-eminent in connection panels of steel frames. Therefore the failure strain of the plates in shear can be considered as one of ductility indices in the analysis of such frame structures.

In the past decades, although a large number of investigations have been conducted on web plates in shear, most of them were limited to shear strengths under monotonic loading (Galambos 1998). For this reason, an effort has been made recently on the ductility capacity of thin-walled plates in shear (Usami *et al.* 1999; Kasai *et al.* 2001). An analytical model, in which all edges are simply supported for out-of-plane displacements but kept straight for in-plane displacements, is developed as shown in Fig. 10.5 for plates subjected to shear loading. Both the residual stresses and initial deflections, which are in the same forms as in the case of compressive loading case, were accounted for.



10.5 Plates in shear: (a) unstiffened plate; (b) stiffened plate.

The key parameter that affects the shear strength and ductility of plated structures is the slenderness ratio that is defined as

$$R_\tau = \sqrt{\frac{\tau_y}{\tau_{cr}}} = \frac{b}{nt} \sqrt{\frac{12(1 - \nu^2)}{k_s \pi^2}} \sqrt{\frac{\tau_y}{E}} \tag{10.22}$$

in which τ_y = yield stress in shear ($= \sigma_y / \sqrt{3}$ based on the von Mises yield condition), τ_{cr} = elastic shear-buckling stress, and k_s = buckling coefficient for shear-buckling stress, which is approximated by the following equation (Galambos 1998):

$$k_s = \begin{cases} 4.00 + 5.34/\alpha_{sub}^2 & \text{for } \alpha_{sub} \leq 1 \\ 5.34 + 4.00/\alpha_{sub}^2 & \text{for } \alpha_{sub} \geq 1 \end{cases} \tag{10.23}$$

where α_{sub} is the aspect ratio of subpanels (i.e. $n\alpha$).

For stiffened plates subjected to shear loading, the optimum rigidity of the stiffener is another important factor. The optimum rigidity of the stiffener can be defined in several ways as discussed by Dubas and Gehri (1986). Most of the definitions intend to achieve the maximum buckling strength of

a stiffened plate with the smallest stiffener dimensions. For example, formulas determined in such a way (DIN 4114, 1953) are given by

$$\gamma_s^* = 5.4\alpha_{\text{sub}}^2(-1 + 2\alpha_{\text{sub}} + 2.5\alpha_{\text{sub}}^2 - \alpha_{\text{sub}}^3) \quad 10.24$$

for plates with $n = 2$ (one longitudinal stiffener) and $0.5 \leq \alpha_{\text{sub}} \leq 2.0$,

$$\gamma_s^* = 12.1\alpha_{\text{sub}}^2(-1 + 4.4\alpha_{\text{sub}}) \quad 10.25$$

for plates with $n = 3$ (two longitudinal stiffeners) and $0.3 \leq \alpha_{\text{sub}} \leq 1.0$.

The optimum can also be defined as the rigidity at which the critical load of the stiffened plate is equal to the critical load of an individual subpanel. Based on this definition, Chusilp and Usami (2002a) proposed simplified formulas for the optimum rigidity of the stiffener, determined numerically by using the theoretical data of the buckling coefficient. A case of the stiffener arrangements is designated as $LpTq$, in which p and q = numbers of longitudinal and transverse stiffeners, respectively. Approximate formulas for the optimum rigidity are proposed for plates L1T1, L2T2 and L3T3 as:

$$\gamma_s^* = \left(\frac{23.1}{n_s^{2.5}} - \frac{1.35}{n_s^{0.5}} \right) \frac{(1 + \alpha_{\text{sub}}^{3/n_s - 0.3})^{2n_s - 1}}{1 + \alpha_{\text{sub}}^{5.3 - 0.6n_s - 3/n_s}} \quad 10.26$$

and for the plates L1T0, L2T0 and L3T0 as:

$$\gamma_s^* = \frac{27.3n_s^{0.6}\alpha_{\text{sub}} - 23.3\alpha_{\text{sub}}}{0.20n_s^{0.7} - 0.60/\alpha_{\text{sub}} + 0.52/\alpha_{\text{sub}}^2} \quad 10.27$$

where n_s = number of the parallel stiffeners ($= n - 1$). The above two equations are applicable for the parameter ranges of $n_s = 1, 2$, or 3 and $0.5 \leq \alpha_{\text{sub}} \leq 2.0$. For the plates L0T1, L0T2, and L0T3, the approximate formula can be derived by replacing α_{sub} in Eq. [10.27] with $1/\alpha_{\text{sub}}$ and multiplying the resulting expression by α_{sub} . For plates with only two longitudinal stiffeners (i.e. L2T0 plates), Eq. [10.27] becomes:

$$\gamma_s^* = \frac{18.1\alpha_{\text{sub}}}{0.325 - 0.60/\alpha_{\text{sub}} + 0.52/\alpha_{\text{sub}}^2} \quad 10.28$$

The optimum rigidity determined by Eq. [10.28] will be larger than that by Eq. [10.25], particularly for plates with large aspect ratios (Chusilp and Usami 2002a).

Strength

There are many ways to predict the ultimate strength of unstiffened plates in shear (Galambos 1998). In this section, computed maximum shear strengths, τ_u/τ_y , of the plates analyzed are compared with empirical formulas. The

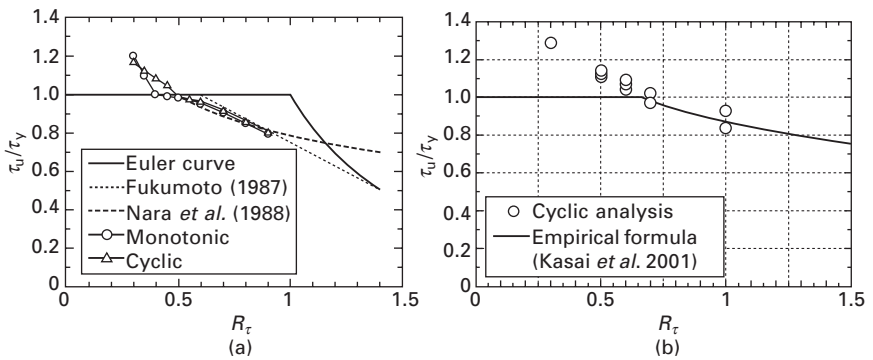
following equation is given in a Japanese buckling guideline (Fukumoto 1987):

$$\frac{\tau_u}{\tau_y} = \begin{cases} 1 & (R_\tau \leq 0.6) \\ 1 - 0.614(R_\tau - 0.6) & (0.6 \leq R_\tau \leq \sqrt{2}) \\ 1/R_\tau^2 & (\sqrt{2} < R_\tau) \end{cases} \quad 10.29$$

Nara *et al.* (1988) proposed an equation based on the elasto-plastic large-displacement analysis as:

$$\frac{\tau_u}{\tau_y} = \left(\frac{0.486}{R_\tau} \right)^{0.333} \leq 1.0 \quad (0.486 \leq R_\tau \leq 2) \quad 10.30$$

Figure 10.6(a) shows a comparison between the analytical results (Usami *et al.* 1999) and the two equations above as well as Euler curve. From this figure, it can be seen that the computed results are in good agreement with the empirical formula by Nara *et al.* (1988). On the other hand, the maximum shear strengths are almost the same even for different loading patterns except for the plates with $R_\tau \leq 0.4$, and therefore it can be concluded that the effect of the loading history on the shear strength is insignificant.



10.6 Strength of plates in shear: (a) unstiffened plate; (b) stiffened plate.

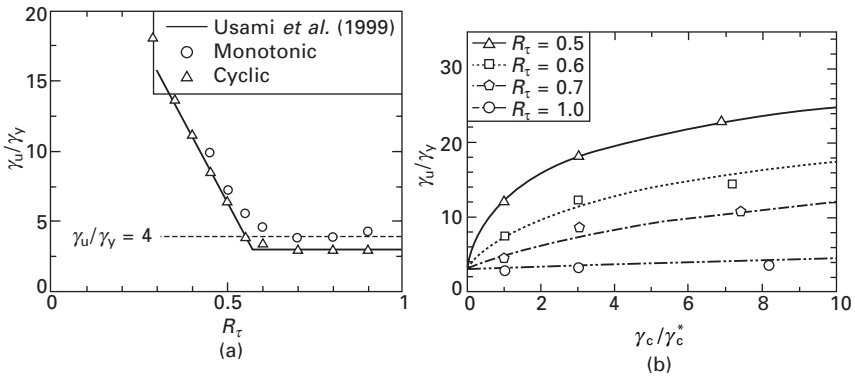
For stiffened plates, Kasai *et al.* (2001) proposed a formula similar to Eq. [10.30]:

$$\frac{\tau_u}{\tau_y} = \left(\frac{0.662}{R_\tau} \right)^{0.333} \leq 1.0 \quad 10.31$$

Comparison between the proposed equation and analyzed results is shown in Fig. 10.6(b).

Ductility

Similarly for the plates under compression, the ductility of plates in shear is defined as the shear strain at a point corresponding to 95% of either the maximum shear strength when $\tau_u/\tau_y \leq 1.0$, or the strength at the first-peak point when $\tau_u/\tau_y > 1.0$. Failure strains, γ_u/γ_y , of all the analyzed unstiffened plates are determined in such a way and plotted against R_τ in Fig. 10.7(a) (Usami *et al.* 1999). It can be observed that in the range of $R_\tau \geq 0.6$, failure strains are almost the same for different plates under an identical loading case. Values of γ_u/γ_y are about 4 for the monotonic loading, and approximately 3 for the two-side cyclic loading. With respect to the distortion capacity of unreinforced web plates in the beam–column joints under monotonic loading, a limit value, $4\gamma_y$, was proposed by Krawinkler and Popov (1982). Obviously, this fact is supported by the present results. However, it seems more appropriate to adopt $3\gamma_y$ as its limit value for the use in seismic design considering the random nature of earthquakes.



10.7 Ductility of plates in shear: (a) unstiffened plate; (b) stiffened plate.

For plates with $R_\tau < 0.6$, the failure shear strain is increased as R_τ is reduced. Also, γ_u/γ_y is somewhat affected by the loading history and the difference is large when R_τ is quite small (e.g. $R_\tau \leq 0.4$). Here, a lower bound curve given below is suggested for practical use (Usami *et al.* 1999):

$$\frac{\tau_u}{\tau_y} = \begin{cases} -47R_\tau + 30 \leq 20.0 & (R_\tau < 0.575) \\ 3 & (R_\tau \geq 0.575) \end{cases} \quad 10.32$$

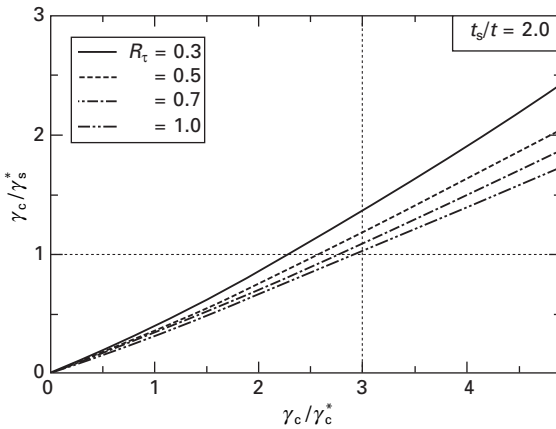
This equation is also plotted in Fig. 10.7(a). Clearly, the predictions will be conservative for the monotonic loading history.

For stiffened plates, Kasai *et al.* (2001) found that the ductility depends on not only the width–thickness ratio parameter but also the relative rigidity

of the stiffener. Figure 10.7(b) shows comparisons of the ductility from the analysis and corresponding approximate equation given by

$$\frac{\gamma_u}{\gamma_y} = 5.9 \log \left(1 + 0.0307 \frac{\gamma_c / \gamma_c^*}{R_\tau^7} \right) + 3.0 \leq 20.0 \tag{10.33}$$

It should be noted that the optimum value of relative rigidity of the stiffener referenced is the optimum relative flexural rigidity, γ_c^* , instead of the one with respect to shear loading, γ_s^* . A relation between γ_c^* (Eq. [10.12]) and γ_s^* (Eq. [10.28]) is illustrated in Fig. 10.8, and we can find that γ_c / γ_c^* is about 3 times γ_c / γ_s^* .



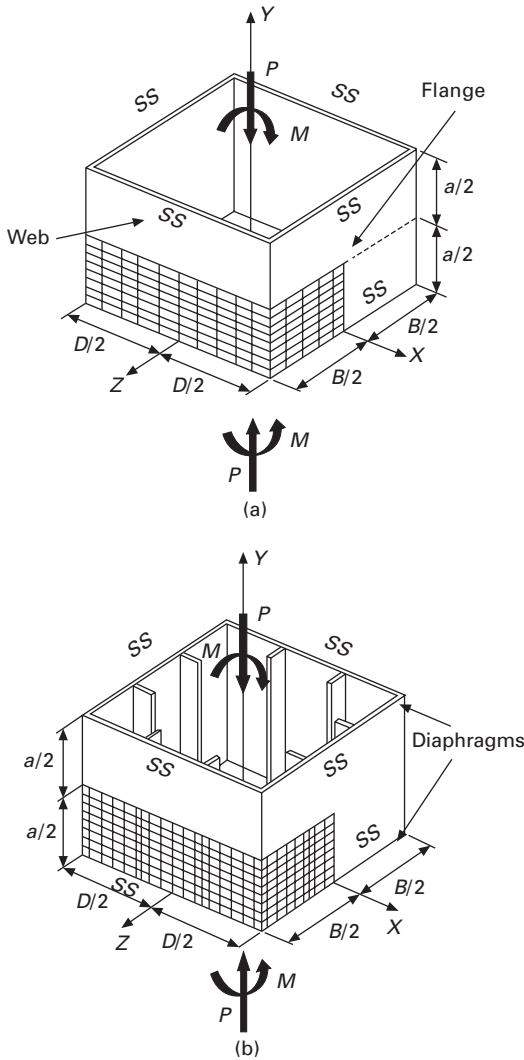
10.8 Relation of optimum flexural and shear rigidities.

10.3 Stub-columns

In the analyses of component plates presented above, there is an inherent assumption that the interactive effects between adjacent component plates of thin-plated structures at their conjuncts are neglected (Usami *et al.* 1991). This negligence has induced the inaccuracy for some structures as mentioned above. Thus, the attention of researchers has been directed to stub-columns subjected to either combined action of compression and bending or shear loading.

10.3.1 Box-shaped stub-columns subjected to combined compression and bending

Stub-columns of box sections with and without longitudinal stiffeners have been studied by Zheng *et al.* (2000a) and Ge *et al.* (2004). The analytical models of such stub-columns are shown in Fig. 10.9, which represent a part



10.9 Box-shaped stub-columns under combined compression and bending: (a) unstiffened stub-column; (b) stiffened stub-column (SS = simply supported edge).

of a long column between the diaphragms. All edges are assumed to be simply supported. The same residual stress distributions as those of unstiffened or stiffened plates (Fig. 10.1) are used for the unstiffened and stiffened stub-columns, respectively. The assumed initial deflection patterns are also similar to those of the component plates except that for stiffened stub-columns, the number of local initial deflections along the longitudinal direction should be determined by checking whether giving the lowest ductility (Zheng *et al.*

2000a). This is due to the component plate of a box stub-column having a different buckling mode from that of isolated plate due to the interaction effects of adjacent plates at their junctions. The direction of the initial deflections is assumed inward (or inward at the place with the maximum value of deflection) for the flange plates, while outward for web plates. Owing to symmetry of loading and geometry, only a quarter or half of the stub-column is analyzed. The model of the stub-column is analyzed under a monotonically increasing bending moment and a constant axial force.

Besides the flange width–thickness ratio R_f and the stiffener slenderness ratio $\bar{\lambda}_s$, the magnitude of axial load P is another main parameter for the behavior of box stub-columns.

Strength

For unstiffened stub-columns, an interaction strength equation has been proposed through numerical analyses by Ge *et al.* (1995), as:

$$\left(\frac{M_m}{M_u}\right)^{C_1} + \left(\frac{P}{P_u}\right)^{C_2} = 1.0 \quad 10.34$$

with

$$C_1 = 0.271R_f + 0.719 \quad 10.35$$

and

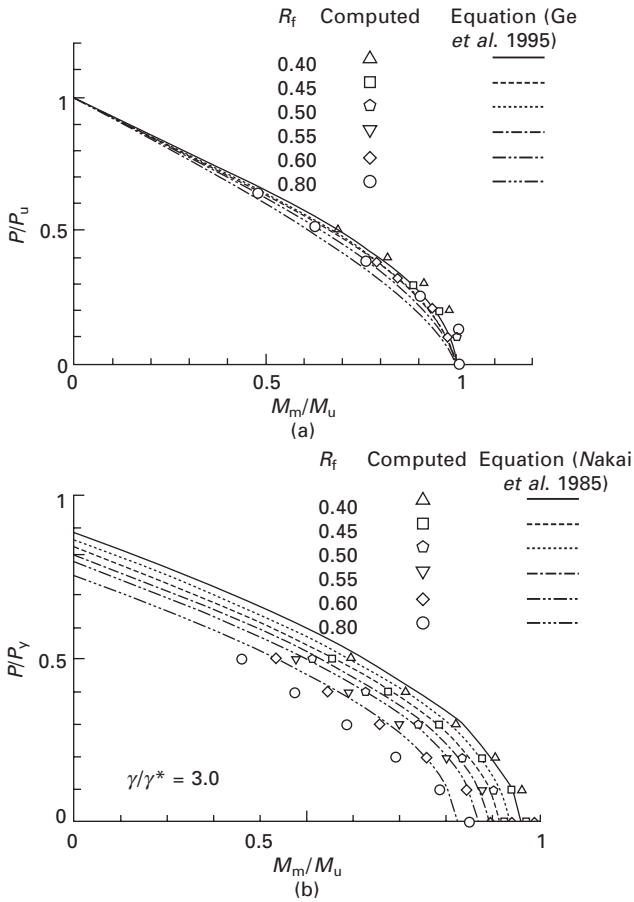
$$C_2 = 1.33/R_f^{0.401} \quad 10.36$$

In Eq. [10.34], P_u and M_u are the ultimate strengths under pure compression and pure bending respectively. Figure 10.10(a) illustrates this equation compared with the computed maximum strength (M_m), and a general agreement can be observed from the figure.

In the case of stiffened stub-columns, Nakai *et al.* (1985) proposed a method to predict the maximum strength of stub-columns under compression and bending based on experimental results. The method was developed by modifying the fully plastic interaction curve by a factor related to the ultimate strength of box stub-columns in pure compression. The computed maximum strengths are compared in Fig. 10.10(b) with the predictions based on the method of Nakai *et al.* (1985). It is observed that two groups of results are basically consistent.

Ductility

Similar to the aforementioned plates, the ductility of the stub-column is evaluated by using the failure strain $\varepsilon_u/\varepsilon_y$ defined as a point corresponding to



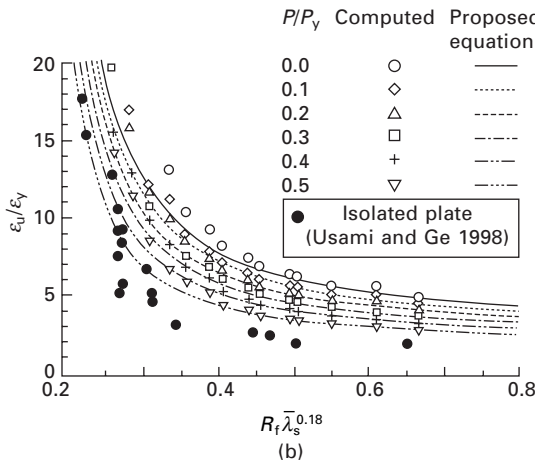
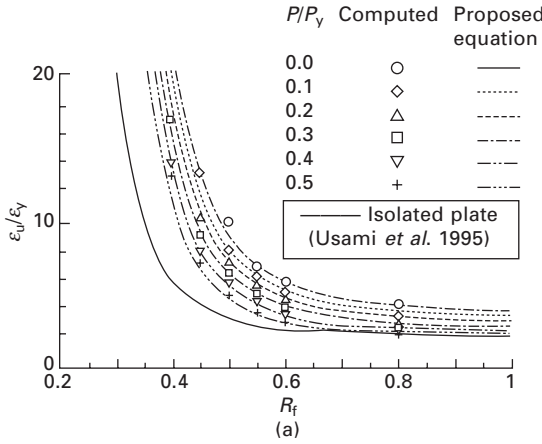
10.10 Strength of box-shaped stub-columns under combined compression and bending: (a) unstiffened stub-column; (b) stiffened stub-column.

95% of the maximum strength after the peak at the bending moment versus average compressive strain curve (Zheng *et al.* 2000a).

For unstiffened stub-columns, the computed ϵ_u/ϵ_y versus R_f and P/P_y relations are presented in Fig. 10.11(a), from which it is observed that the failure strain decreases with the increase of either R_f or P/P_y . Considering the effect of axial load, an equation of failure strain, ϵ_u/ϵ_y , versus flange width-thickness ratio parameter, R_f , is fitted as follows:

$$\frac{\epsilon_u}{\epsilon_y} = \frac{0.108(1 - P/P_y)^{1.09}}{(R_f - 0.2)^{3.26}} + 3.58(1 - P/P_y)^{0.839} \leq 20.0 \quad 10.37$$

The applicable range of this equation is $R_f = 0.2 \sim 0.8$ and $P/P_y = 0.0 \sim 0.5$.



10.11 Ductility of box-shaped stub-columns under combined compression and bending: (a) unstiffened stub-column; (b) stiffened stub-column.

As for stiffened stub-columns, the computed failure strains, ϵ_u/ϵ_y , are presented in Fig. 10.11(b). An equation of ϵ_u/ϵ_y versus $R_f \bar{\lambda}_s^{0.18}$, considering the effect of axial load, is fitted as follows:

$$\frac{\epsilon_u}{\epsilon_y} = \frac{0.8(1 - P/P_y)^{1.94}}{(R_f \bar{\lambda}_s^{0.18} - 0.168)^{1.25}} + 2.78(1 - P/P_y)^{0.68} \leq 20.0 \quad 10.38$$

For the above equation R_f ranges from 0.2 to 0.7 (this parameter is limited to 0.5 in Japan Road Association 2002), $\bar{\lambda}_s$ is in a scope from 0.18 to 0.75, and P/P_y is between 0.0 to 0.5. It should be noted that this equation is fitted to give slightly smaller prediction of failure strains for the cases with small

values of $R_f \bar{\lambda}_s^{0.18}$. This is for the reason that the numerical results are based on monotonically loading conditions and when applied to long columns with small values of $R_f \bar{\lambda}_s^{0.18}$, they are found to yield larger ductility predictions compared with the cyclic experimental and numerical results (Zheng *et al.* 2000b).

Some computed results of isolated plates (monotonic) presented above are also plotted in Fig. 10.11, in the form of ϵ_u/ϵ_y versus R_f or $R_f \bar{\lambda}_s^{0.18}$. It is observed that the failure strains of stub-columns subjected to compression and bending are larger than those of isolated plates under pure compression. When the axial load approximates the pure compression state, two procedures will give close predictions. This observation is consistent with the conclusion drawn by Usami *et al.* (1991).

It should be noted that for both Eqs. [10.37] and [10.38] the applicable range of the axial force is up to $0.5P_y$. However, the axial force variation may be very large and even close to the squash load of the section in bridge structures such as steel arch bridges (Usami *et al.* 2004). For this reason, Ge *et al.* (2004) carried out more FEM studies to account for wider range of axial compression with an upper limit of P_y , and proposed the revised ultimate strain formulas, as shown below:

For unstiffened box sections:

$$\frac{\epsilon_u}{\epsilon_y} = \frac{0.24}{(R_f - 0.2)^{2.8} (1 + P/P_y)^{2.4}} + \frac{2.8}{(1 + P/P_y)^{0.6}} \leq 20.0, (0.0 \leq P/P_y \leq 1.0) \tag{10.39}$$

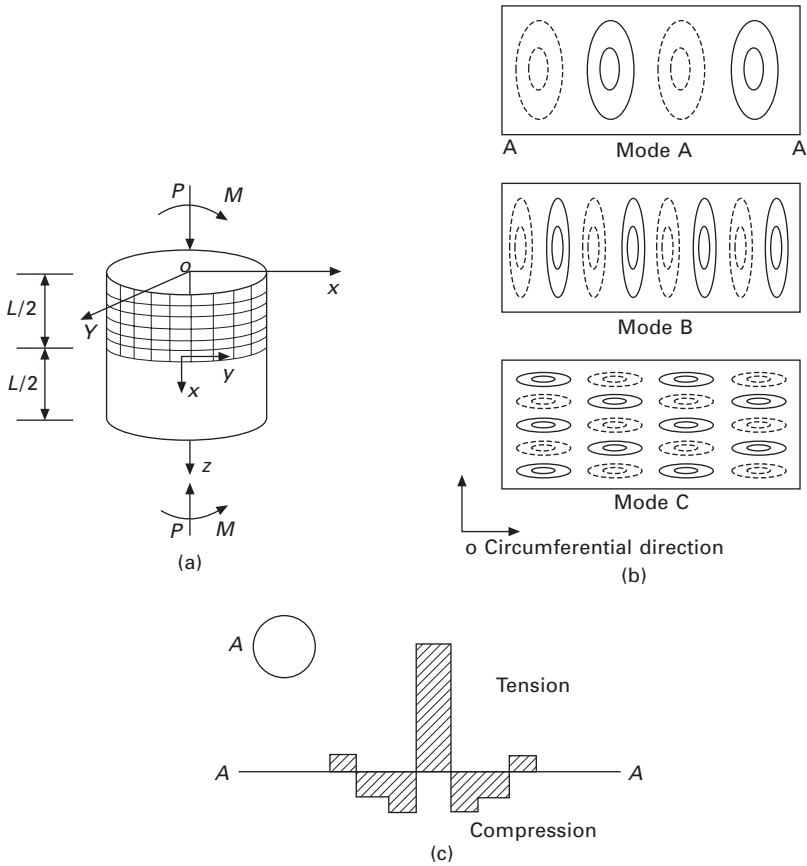
For stiffened box sections:

$$\frac{\epsilon_u}{\epsilon_y} = \frac{0.7}{(R_f \bar{\lambda}_s^{18} - 0.18)^{1.3} (1 + P/P_y)^{2.2}} + \frac{3.2}{(1 + P/P_y)} \leq 20.0, (0.0 \leq P/P_y \leq 1.0) \tag{10.40}$$

10.3.2 Pipe-shaped stub-columns subjected to either pure compression or combined compression and bending

Strength and ductility of pipe-sectioned stub-columns under compression and bending shown in Fig. 10.12 have been analyzed (Gao *et al.* 1998a) using a similar method to that for box stub-columns. Sinusoidal initial geometrical deflection curve is considered both in the longitudinal and circumferential directions. The following initial deflection equation is assumed:

$$w = w_{\max} \sin\left(\frac{m\pi x}{L}\right) \sin\left(\frac{ny}{R}\right) \tag{10.41}$$



10.12 Pipe-shaped stub-columns under combined compression and bending: (a) pipe-shaped stub-column; (b) initial modes; (c) distribution of residual stresses.

where w = outward displacement, w_{\max} = maximum initial deflection, L = cylinder length, R = radius of the cylinder, x and y = longitudinal and circumferential coordinates in the local coordinate system, as shown in Fig. 10.12(a). Two constants, m and n , are the numbers of half sine-waves along the longitudinal and circumferential directions, respectively (see Fig. 10.12b). The cylinder has been opened out and pulled straight in the figure, where the two points (namely, A) are coincident at the true circumference. Experimental measurements conducted by the researchers (Chen and Ross 1977; Ostapenko 1977) gave some basic information on the residual stress distribution. In this analysis, an idealized form of residual stress distribution due to welding is assumed, as shown in Fig. 10.12(c).

Stub-columns of pipe-shaped section subjected to pure compression

It has been found that a single half-wave initial deflection along a cylinder with different values of L/D would produce a significantly different strength (Harding 1978). Here, L and D are the length and diameter of the pipe-sectional stub-column, respectively. In addition, it is well known that the occurrence of local buckling will be liable for the cylinders with large values of the radius–thickness ratio parameter R_t , defined by:

$$R_t = \frac{\sigma_y}{\sigma_{cr}} = \sqrt{3(1 - \nu^2)} \frac{\sigma_y}{E} \frac{D}{2t} \quad 10.42$$

where t denotes the wall thickness of the column. It is found from the analysis that for the same value of R_t , there is always a critical value of L/D which gives the minimum ultimate strength. Based on the computed results, a critical length that gives the minimum ultimate strength of a pipe-sectioned stub-column under pure compression is fitted in the form of:

$$\frac{L}{D} = \frac{0.585}{R_t^{0.08}} - 0.580 \quad (R_t \leq 0.50) \quad 10.43$$

From elastic shell theory (Timoshenko and Gere 1961), the elastic critical wavelength of half sine-waves into which the shell buckles, for $\nu = 0.3$, is

$$L_{cr} = \pi \sqrt[4]{\frac{D^2 K}{4 E t}} = \pi \sqrt[4]{\frac{D^2 t^2}{48(1 - \nu^2)}} = 1.22 \sqrt{D t} \quad 10.44$$

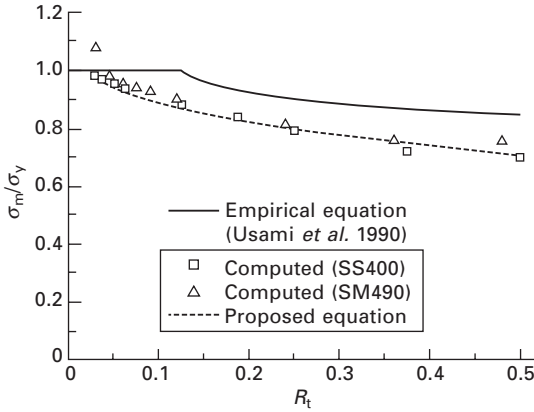
where $K = Et^3/[12(1 - \nu^2)]$ is the bending stiffness of the shells. It can be found that the computed length in each case is almost the same as its elastic critical wavelength, L_{cr} , which means that Eq. [10.44] (Timoshenko and Gere 1961) is also valid in elastoplastic range.

Strength

To obtain the ultimate strength and ductility of the cylinders, cylinders with R_t varying from 0.03 to 0.5 are analyzed. The cylinder lengths are determined from Eq. [10.43]. Computed ultimate strength, σ_m/σ_y , is plotted against R_t , as shown in Fig. 10.13. The solid line denotes an empirical equation proposed by Usami *et al.* (1990), which represents an average strength curve of test results, given by:

$$\frac{\sigma_m}{\sigma_y} = 0.80 + \frac{0.025}{R_t} \leq 1.0 \quad (0.125 \leq R_t \leq 0.50) \quad 10.45$$

All computed results are a little lower than those obtained by the empirical equation. The following proposed equation is found to give a satisfactory accordance to the computed ultimate strengths:



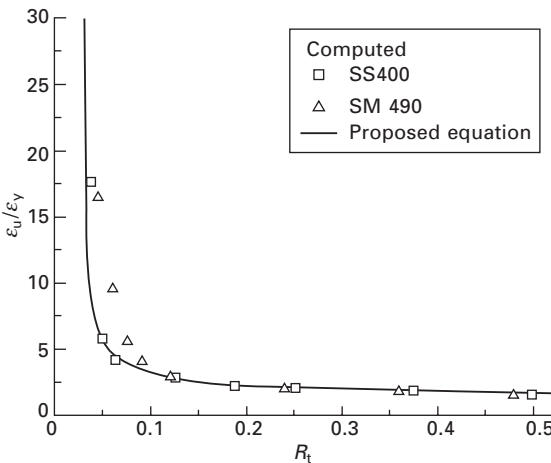
10.13 Strength of pipe-shaped stub-columns in compression.

$$\frac{\sigma_m}{\sigma_y} = 1 - 0.43\sqrt{R_t - 0.03} \quad (0.03 \leq R_t \leq 0.50) \quad 10.46$$

When $R_t = 0.03$, we have $\sigma_m/\sigma_y = 1.0$ and this implies that no local buckling occurs at this value of R_t .

Ductility

The curve of failure strain versus R_t is plotted in Fig. 10.14. As indicated in this plot, the ductility behavior of the cylinder is significantly sensitive to R_t when it is less than 0.1. An equation of the normalized average failure strain ϵ_u/ϵ_y versus R_t is fitted as:



10.14 Ductility of pipe-shaped stub-columns in compression.

$$\frac{\epsilon_u}{\epsilon_y} = \frac{0.445}{(R_t - 0.03)^{0.6}} + 1.0 \leq 20.0 \quad (0.03 \leq R_t \leq 0.50) \quad 10.47$$

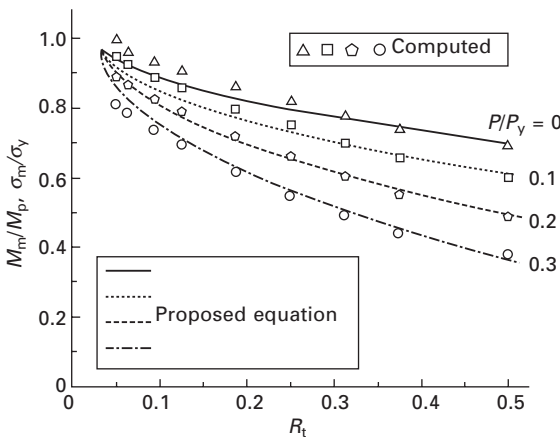
To investigate the validity of the proposed equation for different materials, cylinders made of two different materials (i.e. SS400 and SM490) are analyzed. For the same small R_t ratios, the cylinder of SM490 steel yields close strength (Fig. 10.13) but a little large failure strain (Fig. 10.14), compared with that of SS400 steel. The reason for safe-side predictions of ductility is due to a difference in the yield plateau and strain hardening assumed for the two kinds of steel.

Stub-columns of pipe-shaped section subjected to combined compression and bending

Using the analytical model and method similar to those for box stub-columns, the pipe-shaped stub-columns under combined compression and bending were analyzed to probe the relation of strength and ductility to the main parameters such as R_t and P/P_y .

Strength

The ultimate strengths of all the analyzed cylinders are shown in Fig. 10.15. The ultimate bending moment, M_u , normalized by the fully plastic moment, M_p , is taken as the ordinate and the radius–thickness ratio, R_t , is adopted as the abscissa. A general equation accounting for both the effect of the parameter, R_t , and the axial load, P/P_y , on the ultimate strength is found to fit the analyzed results well:



10.15 Strength of pipe-shaped stub-columns under combined compression and bending.

$$\frac{M_u}{M_p} = 1 - 0.43\sqrt{R_t - 0.03} \left(1 + \frac{P}{P_y}\right)^{2.90},$$

(0.03 ≤ R_t ≤ 0.50, 0.0 ≤ P/P_y ≤ 0.3)

10.48

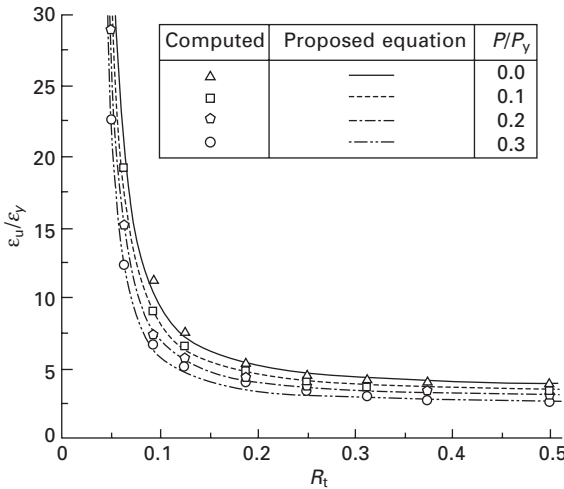
Ductility

Figure 10.16 shows the curves of R_t versus the computed normalized failure strains, ε_u/ε_y. It is found that when the values of R_t exceed 0.1, the failure strain decreases rather slowly with the increase in R_t, and otherwise the cylinders show high sensitivity to R_t. The relative position of the curves for the four load cases indicates that the failure strain increases as the axial load decreases. An equation of failure strains was fitted as follows:

$$\frac{\epsilon_u}{\epsilon_y} = \frac{0.12(1 + 4P/P_y)}{(R_t - 0.03)^{1.45}(1 + P/P_y)^5} + 3.6(1 - P/P_y)$$

≤ 20.0 (0.03 ≤ R_t ≤ 0.50, 0.0 ≤ P/P_y ≤ 0.3)

10.49



10.16 Ductility of pipe-shaped stub-columns under combined compression and bending.

As the same consideration for stub-columns with box sections, Ge *et al.* (2004) also carried out more FEM studies to account for wider range of axial compression with an upper limit of P_y, and proposed the revised ultimate strain formula, as:

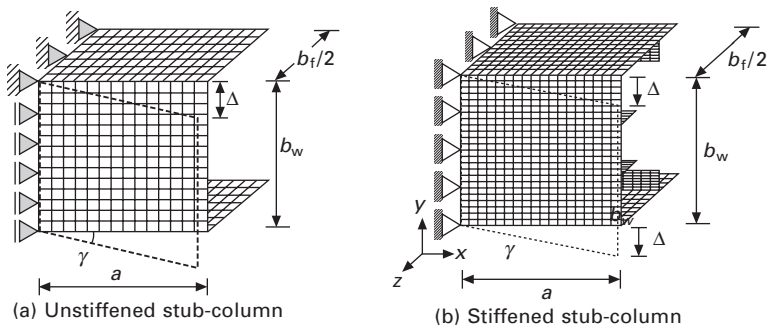
$$\frac{\epsilon_u}{\epsilon_y} = \frac{0.14(1.1 - P/P_y)^{1.8}}{(R_f - 0.03)^{1.4}} + \frac{3}{(1 + P/P_y)^{0.7}}$$

$$\leq 20.0 \quad (0.03 \leq R_f \leq 0.50, 0.0 \leq P/P_y \leq 1.0) \quad 10.50$$

10.3.2 Box-shaped stub-columns subjected to shear loading

In section 10.2.2, shear strength and ductility of plates were presented and all concepts underlining those shear models mentioned above were originally developed for isolated plates. To investigate inelastic behavior of box members, the emphasis should be placed on the contributions of the flanges to the shear resistance of the member. Because flanges are generally slender, the web tension field may not be able to anchor against the flanges effectively. In this section, the flange contributions to the shear behavior are accounted for and newly developed approximation formulas are presented for prediction of strength and ductility of unstiffened and stiffened box sections subjected to shear loading.

In practice, intermediate diaphragms are usually provided with adequate strength and stiffness so that the web shear failure is limited within a web panel divided by the diaphragms. It is, therefore, assumed that the diaphragms are rigid in the flexural and axial senses. This assumption greatly simplifies an investigation of the whole member to a portion between the diaphragms, as shown in Fig. 10.17 (Kasai *et al.* 2002; Chusilp and Usami 2002b). In the case of stiffened box sections, both webs and flanges are equally spaced by two longitudinal stiffeners. The modeled portion has the web width, b_w , and flange width, b_f , while the length between the diaphragms, a , is varied by means of the web aspect ratio, $\alpha = a/b_w$. The use of this simple flange configuration would yield lower-bound results for other cases of flange



10.17 Box-shaped stub-columns subjected to shear loading: (a) unstiffened stub-column; (b) stiffened stub-column.

geometry which varies broadly in practice. Only half of the box section is considered because of the symmetry. Residual stresses and initial deflections as for stub-columns in compression and bending are considered. To distinguish from the isolated web plate model, the present box section model is referred to as the web-flange model while the former is referred to as the web model in the following context.

Strength

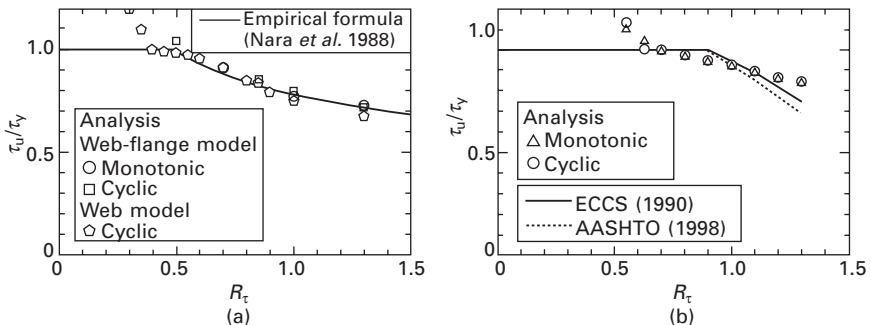
All the computed strengths from both the monotonic and cyclic analyses are plotted with the width–thickness ratio parameter of the web in Fig. 10.18. In the case of unstiffened plates, the results of isolated web plates using the web model, empirical formula by Nara *et al.* (1988) for isolated web plates are also shown in the figure and it can be seen that this equation can also be used for box sections (Kasai *et al.* 2002).

For the stiffened box sections, the obtained maximum transverse loads are compared with the results computed in accordance with ECCS (1990) and AASHTO (1998). The methods suggested by ECCS and AASHTO are simple but reflect the shear-resisting mechanism well. According to ECCS, the shear strength model by Porter *et al.* (1975) is modified for box girders by neglecting all flange contributions and simplifying the inclination of the tension field stresses to one-half of the inclination of the web diagonal. The maximum shear strength is then calculated from:

$$\tau_u = \tau_{cr} + \sigma_{ty} \sin^2 \frac{\theta_d}{2} \left(\cot \frac{\theta_d}{2} - \cot \theta_d \right) \leq \tau_y \tag{10.51}$$

$$\sigma_{ty} = -\frac{3}{2} \tau_{cr} \sin 2\theta_d + \sqrt{\sigma_y^2 + \tau_{cr}^2 \left(\frac{9}{4} \sin^2 2\theta_d - 3 \right)} \tag{10.52}$$

where σ_{ty} = web membrane stress in the tension field that fulfills the yield



10.18 Strength of box-shaped stub-columns subjected to shear loading: (a) unstiffened stub-column; (b) stiffened stub-column.

condition in addition to the critical shear stress; and $\theta_d = \tan^{-1} \frac{1}{\alpha} =$ inclination of the web diagonal. Based on the theories of Basler (1961) and Cooper (1967), it is suggested in AASHTO that the maximum shear strength be determined by

$$\tau_u = \tau_{cr} + \frac{\sqrt{3} (\tau_y - \tau_{cr})}{2\sqrt{1 + \alpha_s^2}} \leq \tau_y \quad 10.53$$

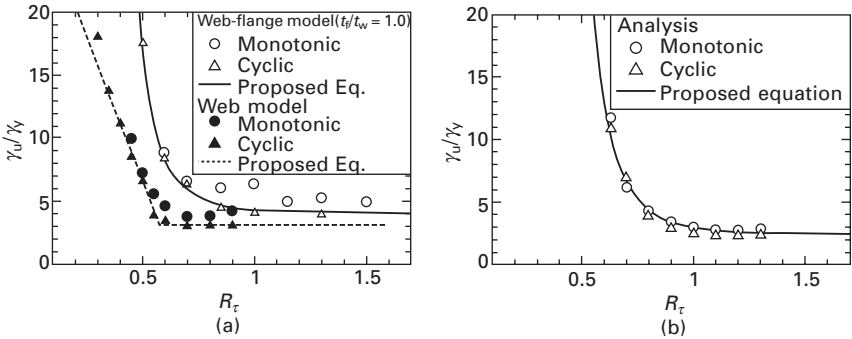
The shear strengths computed from Eqs. [10.51] and [10.53] are limited to the shear yield strength so as to ignore the effect of the strain hardening. These shear strength models are valid only if the web's longitudinal stiffeners possess sufficient out-of-plane flexural stiffness so that they remain straight until the maximum load (Cooper 1967; Porter *et al.* 1975). Comparisons of the obtained maximum transverse loads and the results predicted by ECCS and AASHTO indicate that there exists a good agreement between the analysis and prediction. Considering box girders with slender webs ($R_\tau \geq 1.1$), ECCS gives conservative results (12% for $R_\tau = 1.3$) owing to the neglect of the flange contributions. The AASHTO method results in a greater underestimation (18% for $R_\tau = 1.3$), despite the fact that Basler's formula overestimates the tension field action by representing the case where the tension field fully develops throughout a web panel instead of a limited band (Gaylord 1963). The primary reason for this underestimation is that the assumption regarding the tension field development adopted in AASHTO does not agree with the actual shear behavior (Cooper 1967). It is observed in the analyses that a single tension field develops in the web independently of longitudinal stiffeners, rather than in each individual web subpanel as assumed by Cooper. For stocky-web box sections having $\tau_u \leq \tau_y$ (strain hardening being not prominent), both ECCS and AASHTO produce some overestimations but less than 6%. From these investigations, the ECCS method seems more appropriate for practical design because it gives sufficiently accurate predictions and relies on assumptions that reasonably agree with the actual shear-resisting mechanism (Chusilp and Usami 2002b).

Ductility

To determine the ductility capacity of steel box sections with unstiffened webs, one can use the formula derived by Kasai *et al.* (2002):

$$\frac{\gamma_u}{\gamma_y} = \frac{0.142}{(R_\tau - 0.18)^4} + 4.0 \leq 20.0 \quad 10.54$$

The predicted results are plotted in Fig. 10.19(a) together with results from both the monotonic and cyclic analyses. In the figure, the results of the web



10.19 Ductility of box-shaped stub-columns subjected to shear loading: (a) unstiffened stub-column; (b) stiffened stub-column.

model and the corresponding empirical formula (Eq. [10.32]) are also shown for comparison. It can be seen that there is greater ductility in the web-flange model than predicted by the web model. This indicates that although the contribution of flange on the strength can be ignored, the post-peak strength is increased owing to the so-called frame function of the flange. On the other hand, attention should be paid when this equation is applied to sections with $t_f/t_w < 1.0$. In such cases, no increase in ductility due to the effect of flange can be expected and it is better to use the formula for isolated webs as shown in Eq. [10.32] that gives lower bound estimates of the ductility capacity.

In the case of stiffened box sections, the parametric study has revealed that the contributions by stiffened flanges are practically ignored and the effects of the web stiffener’s rigidity and web aspect ratio are negligible. Only the web slenderness is necessarily considered in the ductility assessment. Based on the analysis results, a simple formula is proposed for estimating the ductility capacity of box sections reinforced with two longitudinal web stiffeners (Chusilp and Usami 2002b):

$$\frac{\gamma_u}{\gamma_y} = \frac{0.5}{R_\tau^{6.0}} + 2.5 \leq 20.0 \tag{10.55}$$

The ductility capacity obtained from Eq. [10.55] is plotted with the analysis results in Fig. 10.19(b). For very stocky webs, the ductility capacity obtained from the analysis is extremely high. The allowable ductility is also limited to the value of 20.0 in order to inhibit excessive localized strains in the web and avoid structural damage caused by low-cycle fatigue.

10.4 Cantilever columns

Cantilever-type steel columns are widely used as bridge piers in the urban area of Japan. Seismic design of such steel bridge piers is very important for

the urban transportation network, which became much clearer after the 1995 Hyogoken–Nanbu earthquake. The piers are characterized by a relatively large plate width–thickness ratio, which makes them susceptible to coupled local and overall instability. As stated by Galambos (1998), the failure of steel bridge piers in the 1995 Hyogoken–Nanbu earthquake is mainly attributed to the loss of strength and ductility due to severe local and overall buckling.

A large number of cyclic tests and analyses have been conducted to study the cyclic behavior of steel box columns. Precise numerical analytical methods are inevitably of great importance for investigating the inelastic behavior of such columns in detail. Compared with experiments, an advanced analytical method is much more economical. To predict accurately the cyclic behavior of steel structures, a modified two-surface plasticity model (2SM) has been developed at Nagoya University (Shen *et al.* 1995) on the basis of a material model proposed by Dafalias and Popov (1975). The accuracy of the 2SM has been verified by extensive experimental data, and its validity in predicting the cyclic behavior of various steel structures has already been established (e.g. Usami and Ge 1998; Gao *et al.* 1998b; Ge *et al.* 2000; Usami *et al.* 2000). It has been shown that compared to the bilinear isotropic hardening model (B-IH) and bilinear kinematic hardening model (B-KH), the 2SM can predict the experimental hysteretic curve with good accuracy.

Cyclic behavior, strength, and ductility of steel columns with pipe or box sections, as shown in Fig. 10.20, were investigated by Gao *et al.* (1998b), Ge *et al.* (2000), and Usami *et al.* (2000). Definitions of strength and ductility of cantilever-type columns are shown in Fig. 10.21. In the figure, H_y is the yield lateral load and δ_y is the yield lateral displacement. Here H_y is taken the smaller of the following two equations (e.g. Ge *et al.* 2000):

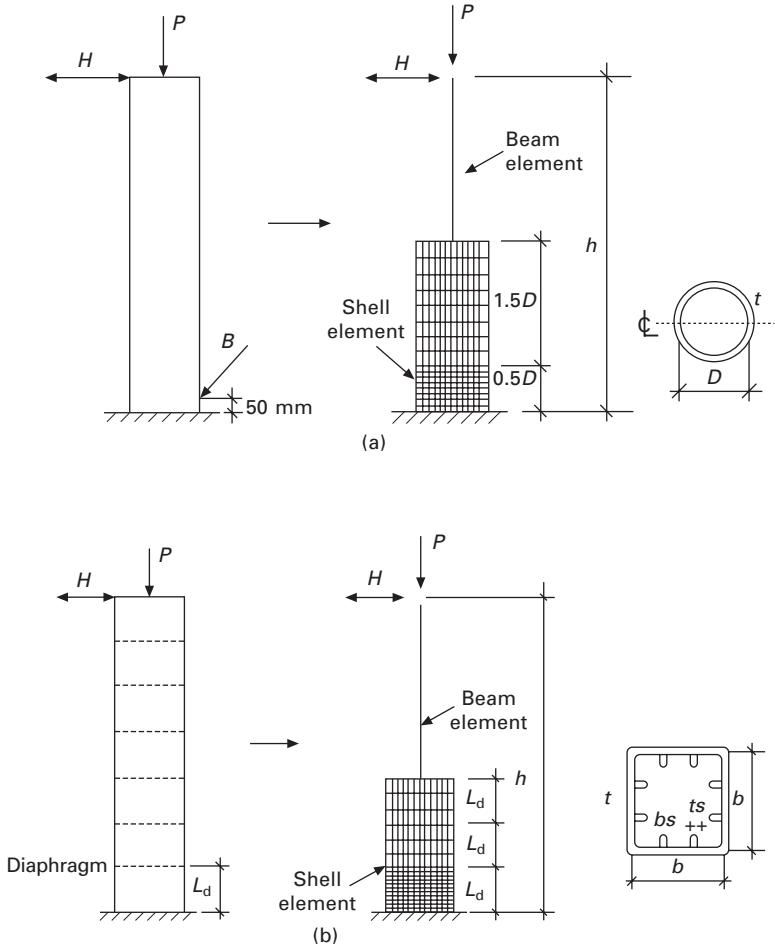
$$H_y = \frac{M_y}{0.85h} \left(1 - \frac{P}{P_E} \right) \left(1 - \frac{P}{P_u} \right) \quad 10.56$$

$$H_y = \frac{M_y}{h} \left(1 - \frac{P}{P_y} \right) \quad 10.57$$

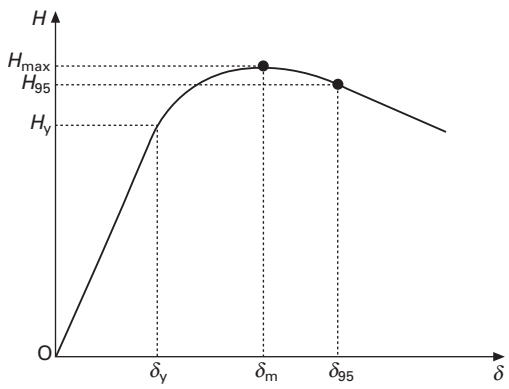
where M_y is the yield moment of the cross-section, P_E the Euler's buckling load of a cantilever column, and P_u the ultimate strength of a centrally loaded column, which is determined from the following equation adopted in the Japanese specification for highway bridges (Japan Road Association 2002).

$$\frac{P_u}{P_y} = \begin{cases} 1.0 & (\bar{\lambda} \leq 0.2) \\ 1.109 - 0.545 \bar{\lambda} & (0.2 \leq \bar{\lambda} \leq 1.0) \\ 1/(0.773 + \bar{\lambda}^2) & (\bar{\lambda} \geq 1.0) \end{cases} \quad 10.58$$

The yield displacement, δ_y , is then calculated from the following equation neglecting transverse shear deformation:



10.20 Cantilever-type steel columns with (a) pipe or (b) box sections.



10.21 Definitions of strength and ductility factors.

$$\delta_y = \frac{H_y h^3}{3EI} \quad 10.59$$

Although the ductility factor, δ_m/δ_y , is physically clear, it does not fully reflect the cyclic loading characteristics and the plate does not experience obvious plastic deformation. On the other hand, δ_{y5}/δ_y seems to be a better choice in that it can accurately account for the effect of cyclic characteristics and make full use of the strength of steel at the stage of plastic deformation.

10.4.1 Box columns without longitudinal stiffeners

A detailed summary of recent experiments on the strength and ductility of steel cantilever box columns under cyclic lateral loading with a constant axial load has been presented by Usami (1996). The local buckling of a specimen without longitudinal stiffeners occurs first in the flange plates near the column base immediately after the peak lateral load, and then extends to the web plates. The buckling mode is found as a half sine-wave shape along both the column height direction and flange width or web depth direction, although inwards in flanges and outwards in webs. For most cases, such buckling is observed in the range of about $0.7b$ (b is the width of the flange) or between the transverse diaphragms.

Strength

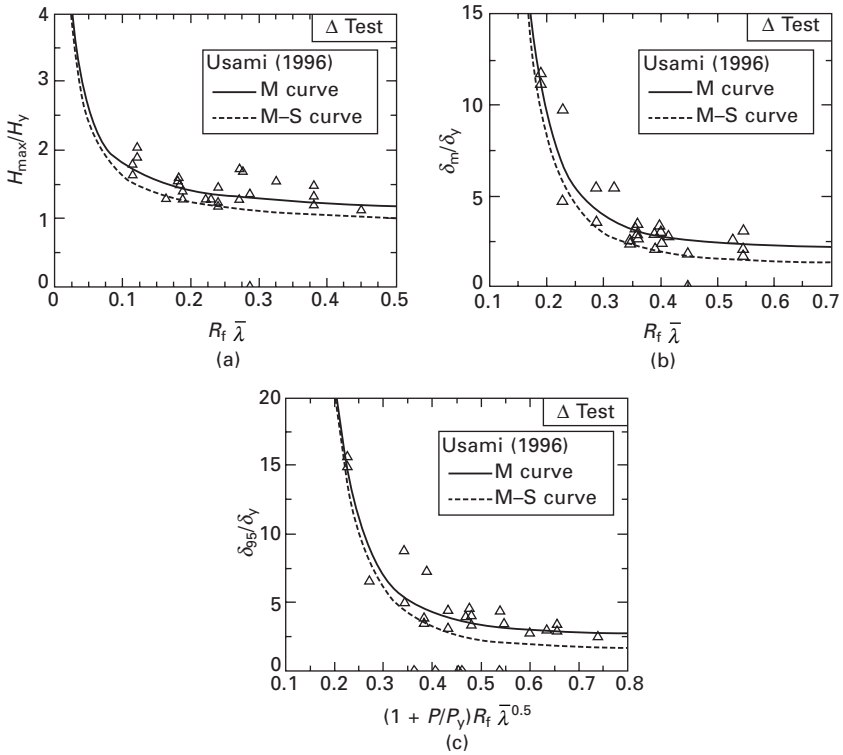
From the tests, the main parameters controlling the strength of the cantilever-type columns without stiffeners are found to be the flange width–thickness ratio parameter, R_f , and column slenderness ratio parameter $\bar{\lambda}$. The empirical equation proposed by Suzuki and Usami (1995) and Usami (1996) is:

$$\frac{H_{\max}}{H_y} = \frac{0.0782}{R_f \bar{\lambda}} + 1.03 \quad (S = 0.175) \quad 10.60$$

This equation is plotted in Fig. 10.22(a) together with experimental data. In the above equation, S is the standard deviation and $\bar{\lambda}$ is given by:

$$\bar{\lambda} = \frac{2h}{r} \frac{1}{\pi} \sqrt{\frac{\sigma_y}{E}} \quad 10.61$$

Here h is the column height and r is the radius of gyration of cross section. Eq. [10.60] was fitted corresponding to the average curve of the test data (i.e. the M curve plotted in Fig. 10.22 by the solid line) and the lower bound curve was also proposed as Eq. [10.60] minus the standard deviation S , as the $M-S$ curve shown in Fig. 10.22 by the dashed line.



10.22 Experimental data-based predictions of strength and ductility of unstiffened box-sectional steel columns.

Ductility

To predict the ductility of cantilever-type columns, the following two empirical formulas have been proposed (Suzuki and Usami 1995; Usami 1996):

$$\frac{\delta_m}{\delta_y} = \frac{0.0262}{\{R_f \sqrt{\lambda}\}^{3.5}} + 2.14 \quad (S = 0.850) \tag{10.62}$$

$$\frac{\delta_{95}}{\delta_y} = \frac{0.0670}{\{(1 + P/P_y)R_f \sqrt{\lambda}\}^{3.5}} + 2.60 \quad (S = 1.09) \tag{10.63}$$

Because the effect of axial load on the ductility parameter δ_m/δ_y is very small when the curve is normalized by H_y and δ_y , and is not taken into consideration in fitting the equation of δ_m/δ_y . On the other hand, the axial load has a great influence on the postbuckling behavior. Therefore, the effect of axial load is considered in deriving the equation of the ductility parameter δ_{95}/δ_y . Comparisons of the proposed prediction curves and experimental data are plotted in Figs 10.22(b) and (c).

10.4.2 Box columns with longitudinal stiffeners

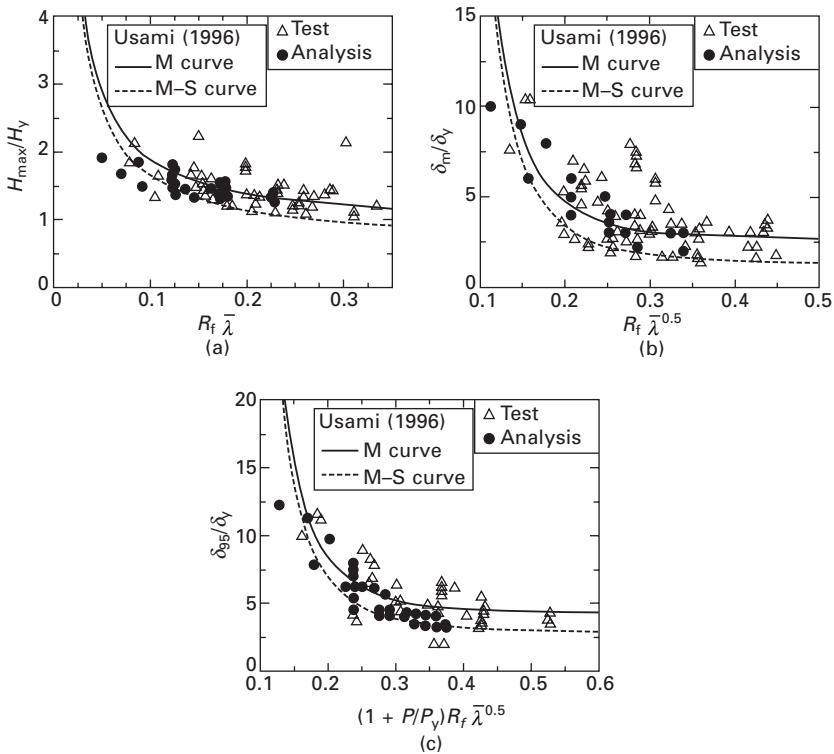
Strength and ductility

Comparison of the analytical results with test results is shown in Fig. 10.23. The solid circle mark stands for the analysis, and the empty triangular mark represents the test recently conducted in Japan. Based on the test results, three empirical formulae of strength and ductility were proposed as follows (Suzuki and Usami 1995; Usami 1996):

$$\frac{H_{\max}}{H_y} = \frac{0.101}{R_f \bar{\lambda}} + 0.88 \quad (S = 0.242) \tag{10.64}$$

$$\frac{\delta_m}{\delta_y} = \frac{0.00759}{(R_f \sqrt{\bar{\lambda}})^{3.5}} + 2.59 \quad (S = 1.32) \tag{10.65}$$

$$\frac{\delta_{95}}{\delta_y} = \frac{0.0147}{[(1 + P/P_y) R_f \bar{\lambda}^{0.5}]^{3.5}} + 4.20 \quad (S = 1.40) \tag{10.66}$$



10.23 Experimental data-based predictions of strength and ductility of stiffened box-sectional steel columns.

The applicable restrictions of these curves are

$$0.3 \leq R_f \leq 0.7, 0.25 \leq \bar{\lambda} \leq 0.5, P/P_y \leq 0.2, \gamma_c/\gamma_c^* \geq 3.0 \quad 10.67$$

The above equations are plotted in Fig. 10.23. The solid line in each plot denotes the fitted equations with average values of test results, while the dashed line represents the $M-S$ curve. It is observed that for the most part, the computed results are close to the fitted curves. However, when the value of $R_f \bar{\lambda}$ becomes very small, the curves will predict higher results, especially for the ultimate strength (see Fig. 10.23a). Moreover, the influence of the modified stiffener's equivalent slenderness ratio parameter $\bar{\lambda}'_s$ is not reflected in the above equations. Therefore, a set of new formulae for both the ultimate strength and the ductility based on the analytical results was proposed later by Usami *et al.* (2000). Incorporating the effect of $\bar{\lambda}'_s$ on the ultimate strength and ductility of the columns, the equations that provide satisfactory predictions to the computed results are fitted as follows:

$$\frac{H_{\max}}{H_y} = \frac{0.10}{(R_f \bar{\lambda} \bar{\lambda}'_s)^{0.5}} + 1.06 \quad (S = 0.07) \quad 10.68$$

$$\frac{\delta_m}{\delta_y} = \frac{0.22}{R_f \sqrt{\bar{\lambda} \bar{\lambda}'_s}} + 1.20 \quad (S = 0.59) \quad 10.69$$

$$\frac{\delta_{95}}{\delta_y} = \frac{0.25}{(1 + P/P_y) R_f \sqrt{\bar{\lambda} \bar{\lambda}'_s}} + 2.31 \quad (S = 0.64) \quad 10.70$$

The applicable ranges of the parameters are

$$0.25 \leq R_f \leq 0.56, 0.20 \leq \bar{\lambda} \leq 0.5, P/P_y \leq 0.3, \gamma_c/\gamma_c^* \geq 1.0 \quad 10.71$$

The above fitted equations are plotted in Fig. 10.24. It can be seen that the curves represent the tendency with the variation of all the main parameters.

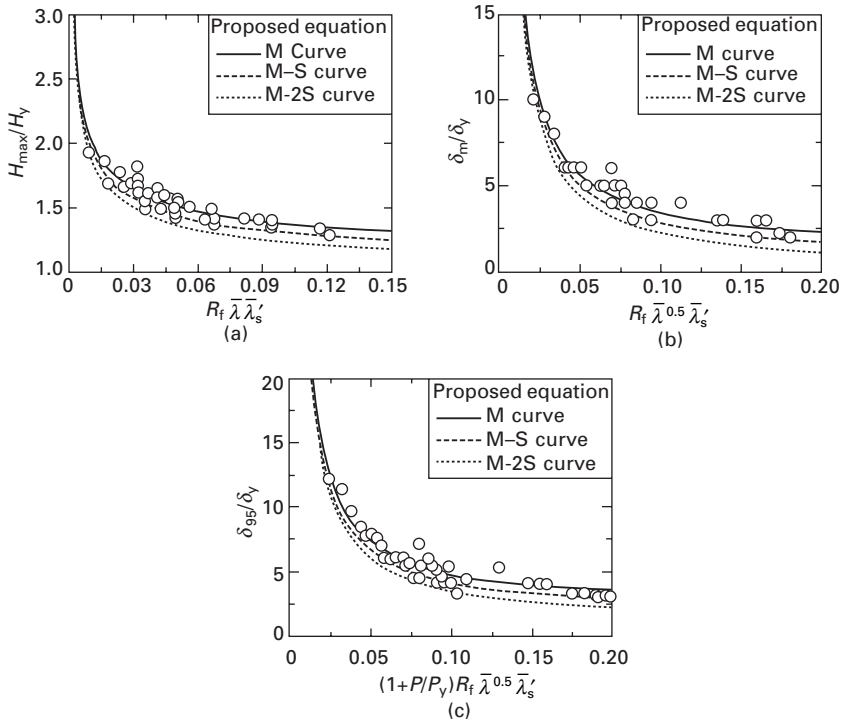
10.4.3 Cantilever box columns made of pipe sections

Strength

The computed ultimate strengths of the steel pipe columns, H_{\max}/H_y are plotted against a multiplication of the parameters R_t and $\bar{\lambda}$ in Fig. 10.25(a). The equation that provides a satisfactory fit to the computed ultimate strength is as follows (Gao *et al.* 1998b):

$$\frac{H_{\max}}{H_y} = \frac{0.02}{(R_t \bar{\lambda})^{0.8}} + 1.10 \quad 10.72$$

As is seen from Fig. 10.25(a), for a constant R_t , the ultimate strength increases



10.24 Analytical results-based predictions of strength and ductility of stiffened box-sectional steel columns.

with the decrease in $\bar{\lambda}$. Likewise, for a constant $\bar{\lambda}$, the strength is improved as R_t decreases.

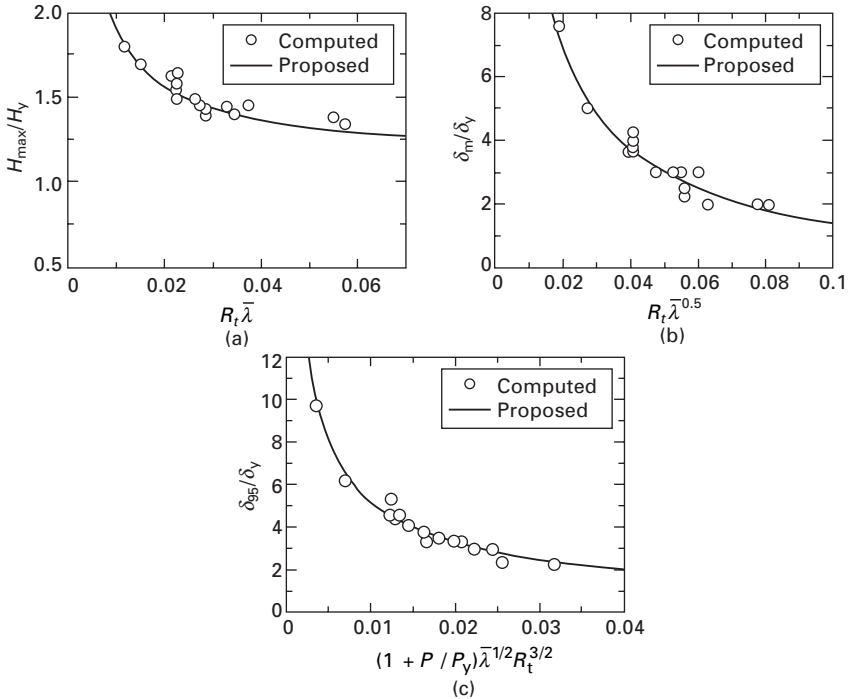
Ductility

The computed values of δ_m/δ_y and δ_{95}/δ_y are plotted against integrated factors of R_t , $\bar{\lambda}$, and/or P/P_y in Figs 10.25(a) and (b). The following two equations are found to fit the discrete data quite well:

$$\frac{\delta_m}{\delta_y} = \frac{1}{3(R_t \sqrt{\bar{\lambda}})^{0.8}} - \frac{2}{3} \tag{10.73}$$

$$\frac{\delta_{95}}{\delta_y} = \frac{0.24}{(1 + P/P_y)^{2/3} \bar{\lambda}^{1/3} R_t} \tag{10.74}$$

Eqs. [10.73] and [10.74] indicate that for a given ductility demand, the critical value of R_t and $\bar{\lambda}$ can be obtained when either of them is determined.



10.25 Analytical results-based predictions of strength and ductility of pipe-sectional steel columns.

10.5 Concluding remarks

With the object of providing more information to the seismic design use, some recent progress in the strength and ductility of thin-walled steel structures have been reviewed in this chapter. The studies on the isolated plates under monotonic and cyclic compression or shear, box-shaped stub-columns subjected to compression and bending, pipe-shaped stub-columns in pure compression or combined action of compression and bending have been summarized. Some pertinent empirical equations of strength and ductility are also presented.

10.6 References

AASHTO, (1998), ‘AASHTO LRFD bridge design specifications’, 2nd Ed., American Association of State Highway and Transportation Officials, Washington, DC.

ABAQUS/Standard User’s Manual, Version 5.7. (1998). Hibbit, Karlsson & Sorensen, Inc., Pawtucket, R.I.

Basler, K. (1961), Strength of plate girders in shear, *J. Struct. Div., ASCE*, **87**(7), 151–180.

Chen, W.F. and Ross, D.A. (1977), Test of fabricated tubular columns. *J. Struct. Div., ASCE*, **103**(ST3), 619–634.

- Chusilp, P. and Usami, T. (2002a), New elastic stability formulas for multiple-stiffened shear panels. *J. Struct. Eng., ASCE*, **128**(6), 833–836.
- Chusilp, P. and Usami, T. (2002b), Strength and ductility of steel box girders under cyclic shear. *J. Struct. Eng., ASCE*, **128**(9), 1130–1138.
- Cooper, P.B. (1967), Strength of longitudinally stiffened plated girders. *J. Struct. Div., ASCE*, **93**(2), 419–451.
- Dafalias, Y.F. and Popov, E.P. (1975), A model of nonlinear hardening materials for complex loading. *Acta Mech.*, **21**, 173–192.
- DIN 4114, Blatt2 (1953), Stahbau, Stabilitätsfalle (Knickung, Kippung, Beulung), Berechnungsgrundlagen, Richtlinien, Berlin, Germany (in German).
- Dubas, P. and Gehri, E., eds. (1986), Behavior and design of steel plated structures. ECCS Technical Committee 8.3, Publ. No. 44, European Convention for Constructional Steelwork, Brussels, Belgium.
- ECCS (1990), European recommendations for the design of longitudinally stiffened webs and of stiffened compression flanges. Publ. No. 60, Tech. Working Group 8.3, European Convention for Constructional Steelwork, Brussels.
- Fukumoto, Y. ed. (1987), Guidelines for stability design of steel structures. Subcommittee on Stability Design, Committee on Steel Structures, JSCE (in Japanese).
- Fukumoto, Y. ed. (1997), *Structural Stability Design – Steel and Composite Structures*. Elsevier Science Ltd, Oxford.
- Galambos, T.V. ed. (1998), *Guide to Stability Design Criteria for Metal Structures*, 5th ed. John Wiley & Sons, Inc., New York.
- Gao, S.B., Usami, T. and Ge, H.B. (1998a), Ductility of steel short cylinders in compression and bending. *J. Eng. Mech., ASCE*, **124**(2), 176–183.
- Gao, S.B., Usami, T. and Ge, H.B. (1998b), Ductility evaluation of steel bridge piers with pipe sections. *J. Eng. Mech., ASCE*, **124**(3), 260–267.
- Gaylord, E.H. (1963), Discussion of ‘strength of plate girders in shear,’ by K. Basler, *Trans., ASCE*, **128**(2), 712–719.
- Ge, H.B., Usami, T. and Oda, H. (1995), A formulation of the moment–thrust–curvature relation for locally buckled unstiffened steel box stub-columns. *Struct. Mech./Earthquake Eng., JSCE*, **519/I-32**, 79–87.
- Ge, H.B., Gao, S.B. and Usami, T. (2000), Stiffened steel box columns. Part 1: cyclic behavior. *Earthquake Eng. Struct. Dyn.*, **29**(11), 1691–1706.
- Ge, H.B., Kono, T. and Usami, T. (2004), Failure strain of steel segments subjected to combined compression and bending and application to dynamic verification of steel arch bridges. *J. Struct. Eng., JSCE*, **50A**, 1479–1488.
- Harding, J.E. (1978), The elasto-plastic analysis of imperfect cylinder, *Proc. Instn. Civ. Engrs.*, Part 2, **65**, 875–892.
- Japan Road Association (2002), *Specifications for Highway Bridges, Part V, Seismic Design*, JRA, Tokyo, Japan.
- Kasai, A., Watanabe, T., Amano, M. and Usami, A. (2001), Strength and ductility evaluation of stiffened steel plates subjected to cyclic shear loading. *J. Struct. Eng., JSCE*, **47A**, 761–770.
- Kasai, A., Watanabe, T., Amano, M. and Usami, A. (2002), Strength and ductility of unstiffened box section members subjected to cyclic shear loading. *Struct. Eng./Earthquake Eng., JSCE*, **703/I-59**, 129–140.
- Krawinkler, H. and Popov, E.P. (1982), Seismic behavior of moment connections and joints. *J. Struct. Div., ASCE*, **108**(2), 373–391.
- Nakai, H., Kitada, T. and Miki, T. (1985), An experimental study on ultimate strength of

- thin-walled box stub-columns with stiffeners subjected to compression and bending. *Struct. Eng./Earthquake Eng., JSCE*, **2**(2), 87–97.
- Nara, S., Deguchi, Y. and Fukumoto, Y. (1988), Ultimate strength of steel plate panels with initial imperfections under uniform shearing stress. *Struct. Eng./Earthquake Eng., JSCE*, **392/I-9**, 265–271.
- Ostapenko, A. (1977), Local buckling of welded tubular columns. Fritz Engrg. Lab., Lehigh Univ., Report 406, 11.
- Porter, D.M., Rockey, K.C. and Evans, H.R. (1975), The collapse behavior of plate girders loaded in shear. *Struct. Engrg.*, **53**(8), 313–325.
- Shen, C., Mamaghani, I.H.P., Mizyno, E. and Usami, T. (1995), Cyclic behavior of structural steels. II: theory. *J. Eng., Mech., ASCE*, **121**, 1165–1172.
- Suzuki, M. and Usami, T. (1995), Estimating formulas of strength and deformation capacity of steel bridge pier model under cyclic loading. *Struct. Eng./Earthquake Eng., JSCE*, **519/I-32**, 115–125.
- Timoshenko, S.P. and Gere, J.M. (1961), *Theory of Elastic Stability*, McGraw-Hill, New York.
- Usami, T. (1990), Experimental verification of ultimate strengths for plane rigid frames. *J. Struct. Eng., JSCE*, **36A**, 79–88.
- Usami, T. (1993), Effective width of locally buckled plates in compression and bending. *J. Struct. Eng., ASCE*, **119**, 1358–73.
- Usami, T. ed. (1996), Interim guidelines and new technologies for seismic design of steel structures. Committee on New Technology for Steel Structures (CNTSS), JSCE (in Japanese).
- Usami, T. and Ge, H.B. (1998), Cyclic behavior of thin-walled steel structures – numerical analysis. *Thin-Walled Structures*, **32**, 41–80.
- Usami, T., Aoki, T., Kato, M. and Wada, M. (1990), Failure test on tubular steel stub-column in compression and bending. *Proc. of Struct. Eng./Earthquake Eng., JSCE*, **416(I-13)**, 255–65.
- Usami, T., Wada, M., Kato, M. and Ge, H.B. (1991), Ultimate compression strength of plate assemblies. *Proc. Int. Conf. Steel & Aluminium Structures*, Singapore, 471–480.
- Usami, T., Suzuki, M., Mamaghani, I.H.P. and Ge, H.B. (1995), A proposal for check of ultimate earthquake resistance of partially concrete-filled steel bridge piers. *Struct. Mech./Earthquake Eng., JSCE*, **508/I-31**, 69–82.
- Usami, T., Ge, H.B. and Amano, M. (1999), Strength and ductility of plates in shear. *Proc. 2nd Int. Conf. Advances in Steel Structures*, Hong Kong, 563–570.
- Usami, T., Gao, S.B. and Ge, H.B. (2000), Stiffened steel box columns. Part 2: ductility evaluation. *Earthquake Eng. Struct. Dyn.*, **29**(11), 1691–1706.
- Usami, T., Lu, Z.H., Ge, H.B. and Kono, T. (2004), Seismic design of steel arch bridges against major earthquakes. Part 1: dynamic analysis approach. *Earthquake Eng. Struct. Dyn.*, **33**(11), 1337–1354.
- Zheng, Y., Usami, T. and Ge, H.B. (2000a), Ductility of thin-walled steel box stub-columns. *J. Struct. Eng., ASCE*, **126**(11), 1304–1311.
- Zheng, Y., Usami, T. and Ge, H.B. (2000b), Ductility evaluation procedure for thin-walled steel structures, *J. Struct. Eng., ASCE*, **126**(11), 1312–1319.

N E S H A N M U G A M , National University of
Singapore, Singapore

11.1 Introduction

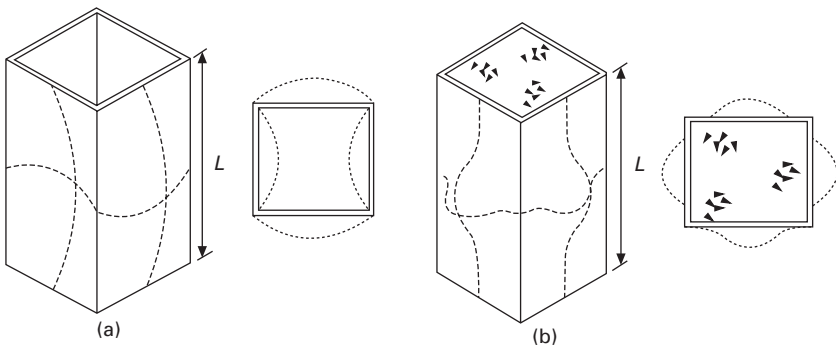
Steel–concrete composite columns are examples of an efficient use of systems that involve interactive behaviour of structural steel components with concrete. Recent developments in composite columns make use of both the strength and fire resistance of concrete, thus providing an economical structural element. Since 1995, composite columns for high-rise buildings have gained acceptance as a viable alternative to structural steel or reinforced concrete columns. Composite columns also offer considerable flexibility for variations in construction shapes without significant loss of structural efficiency.

Researchers have suggested analytical methods and design procedures for composite columns, and design codes have been formulated (Shanmugam and Lakshmi, 2001). Large discrepancies among various design codes exist in terms of geometric and strength parameters, even when the same design philosophy is adopted. The disagreement among the results indicates that more accurate design guidelines are required. Further, with the development of high-strength concrete and structural steel, there is a need to develop a good understanding of the fundamental behaviour of slender composite columns under uniaxial and biaxial bending. A number of theoretical and experimental studies have been reported in the past. Neogi *et al.* (1969) conducted a short-term test on 18 eccentrically loaded circular concrete-filled steel tubular columns bent into a single curvature with lengths varying from 1.4 m to 3.3 m. A simple design procedure suitable for manual calculation has been proposed recently (Wang and Moore, 1997). In this method the properties of the bare steel section are replaced with those of the composite section in accordance with the recommendations given in BS 5950 for bare steel columns. Design formulae for composite columns, based on standards given by ISO for steel structures, with appropriate modifications have been proposed by Kato (1996). Experiments in which full-scale infilled columns were tested to failure in the late 1980s and early 1990s (Prion and Boehme, 1989; Rangan and Joyce, 1992; Shakir-Khalil and Mouli, 1990; Shakir-Khalil and Zeghiche,

1989), provide extensive data that strengthen our knowledge of the behaviour of real columns. These experimental results are useful to understand the elastic and ultimate load behaviour and for developing an appropriate analytical model.

Local buckling in steel plates influences the flexural and buckling strength capacities of composite columns. For tubes with concrete infill, the contained concrete effectively prevents the inward buckling of the steel tube while the compressive strength of the concrete is in turn increased by the steel tube that produces a triaxial state of stress. This pattern of local buckling leads to a higher load-carrying capacity compared with that of a bare steel tube. Grimault and Janss (1994) proposed an effective area approach to account for the local buckling effects. Empirical relationships for local buckling strength of steel tubes filled with concrete by assuming the plate elements to have all edges clamped were given by Sakai *et al.* (1985) and Wright (1993). Ge and Usami (1992) tested short columns with different concrete compressive strengths. When the columns were filled with high-strength concrete, the buckling strengths of the columns were lower than those columns filled with normal strength concrete.

Ge and Usami (1992) also studied local buckling modes of stiffened and unstiffened infilled columns. The stiffeners contributed largely to the overall buckling of columns even when stiffener rigidities were small since local buckling of longitudinal stiffeners is prevented by the presence of concrete. The buckling mode of a bare steel tube without any restraint as shown in Fig. 11.1(a) is considered to be simply supported on all four edges. Thus, the plates are able to buckle either inward or outward. Buckling mode of steel tubes filled with concrete is shown in Fig. 11.1(b). The plate can only buckle outward since the inward buckling is prevented by the concrete restraint.



11.1 Buckling modes of steel and composite sections: (a) steel sections; (b) composite sections.

The behaviour of thin-walled circular steel tubes filled with high-strength concrete for use in tall buildings formed the basis of an experimental

investigation by Uy and Das (1997). An empirical reduction factor that accounts for the effect of infilled concrete prism size and the concrete strength class was introduced to evaluate the compressive strength of concrete (Bradford, 1996). Research has been directed to investigate the use of high-strength concrete (Kilpatrick, 1996; Uy and Patil, 1996). Finite element modelling using the software ABAQUS was developed to examine the ultimate load-carrying capacity and load-deflection relationship up to and beyond failure (Shakir-Khalil and Al-Rawdan, 1996). Mirza and Skrabek (1992) examined the effects of concrete and steel strengths, the cross-sectional dimensions, the presence of reinforcing bars on the strength of encased composite columns. Effects of stiffeners in preventing or minimizing local buckling in stiffened and unstiffened infilled columns were investigated (Ge and Usami, 1992, 1994). Kitada (1998) has shown that the ductility of the composite beam-columns under large axial compression is small for rectangular cross-section compared to circular cross-section.

Uy and Bradford (1994, 1996) used the semi-analytical finite strip method to determine the minimum buckling stress for various boundary conditions. The method uses the sine-squared function for the longitudinal displacement and a cubic polynomial for the transverse displacement. The value of the buckling coefficient k for steel plates restrained by a rigid medium (infilled concrete) was found to be 10.30, higher than the corresponding value for a simply supported plate that is equal to 4.0. This result showed that the strength of steel is greatly enhanced by the presence of concrete. The energy method was used to determine the plate slenderness of steel plates with different boundary conditions including steel plates in contact with a rigid medium (Wright, 1993). Columns designed to resist axial force by concrete alone can be economized by the use of thin-walled fabricated steel columns (Bridge and Webb, 1992). Watson and O'Brien (1990) noted that the local buckling capacity of steel tubes is increased when in contact with concrete. This was based on the empirical evaluation by Matsui (1993) who tested composite steel-concrete frames and observed an increase in local buckling load. Research on thin walled concrete-filled steel box columns has been undertaken by Bridge *et al.* (1995), Uy and Bradford (1994, 1996), Uy (1998) and Uy and Patil (1996). Uy (1998) used the finite strip method to determine the plate slenderness for simply supported steel plates with and without residual stresses. It was shown that the plates without residual stresses have a much larger plate slenderness than those with residual stresses. This shows that residual stresses reduce significantly the strength of steel plates.

Uy (2000) has also proposed a simple model to predict the strength of composite columns under axial and combined bending and axial loading. This model accounts for local buckling in terms of effective width as per the Australian Standard AS4100. The cross-section analysis is carried out by the finite strip method. The effect of width to thickness ratio on the strength

capacity of in-filled composite columns has been highlighted by Bridge and O'Shea (1995), Uy (1998) and Liang and Uy (1999). In a concrete-filled steel box column, the compressive strength of the encased concrete may be increased since concrete is completely encased by the steel tube. This depends on column wall slenderness, b/t , ratio. In addition to this, steel plates are also restrained by concrete so that their resistance to local buckling is much higher than those unrestrained by concrete. For steel–concrete composite columns, design codes such as Eurocode 4, BS 5950, BS-5400 and ACI-318-83 do not consider local buckling of slender steel plates. In order to determine the ultimate strength of a short concrete-filled slender box column, the local buckling strength of slender steel plates has to be predicted by employing a theoretical analysis.

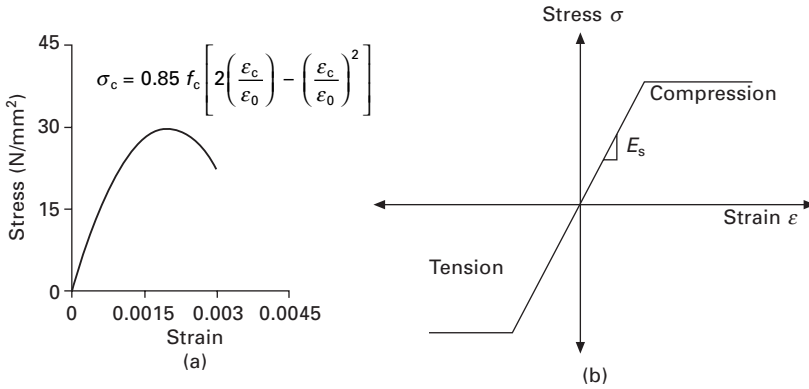
This chapter is concerned with a semi-analytical method to predict the elastic and ultimate load behaviour of square and rectangular steel–concrete composite columns accounting for local buckling in the case of thin-walled columns. The nonlinear analysis technique by Yang and Kuo (1994) is used and the incremental equilibrium equation of slender composite column is formed based on the updated Lagrangian formulation. The Generalised Displacement Control (GDC) method is then applied to solve the incremental equation. The strength analysis is carried out for concentric and eccentric loads with initial imperfections and the effects of local buckling accounted for in terms of the effective width (Shanmugam *et al.*, 1989). The proposed method can model nonuniform compression and can thus consider biaxial bending and axial compression. The effective width formulae used in the analysis allows for any magnitude of residual stresses. The column is pinned and subjected to a combined action of axial compression and biaxial bending. The accuracy of the proposed method is assessed by comparing the analytical values with the corresponding experimental results. The effects of key parameters on the ultimate load behaviour of steel–concrete composite columns are also considered in this chapter.

11.2 Theoretical analysis

11.2.1 Assumptions

The following assumptions have been made in the analysis:

- Constitutive relationships for concrete and steel are known; stress–strain curves for concrete and steel as shown in Fig. 11.2 are assumed where effects of strain hardening of steel, shear strain and tensile strength of concrete, the influence of creep and shrinkage are neglected.
- An adequate bond exists between steel and concrete elements.
- Cross-sections remain plane during various stages of loading resulting in linear distribution of strain.



11.2 Stress–strain relation for (a) concrete (b) steel.

- Maximum amplitude for initial lack of straightness is 0.001 times the column length.
- Failure occurs when the extreme fibre compressive strain in concrete reaches a limiting value of 0.003.

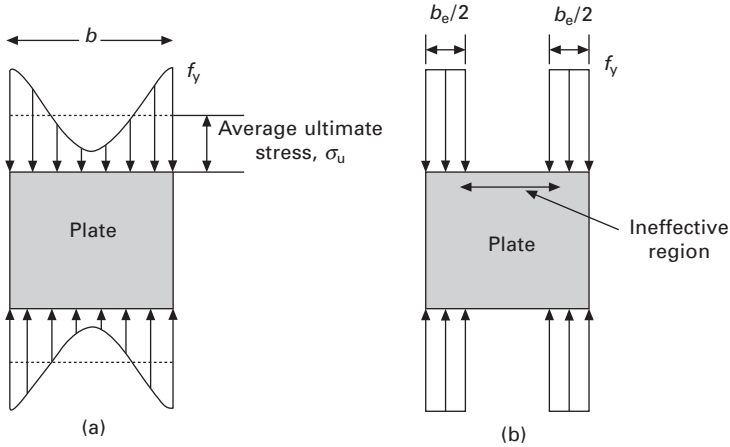
11.2.2 Local buckling

In the case of concrete-filled composite columns, slender steel tubes are subjected to local buckling. It can be assumed that the edges along the corners are constrained because of the presence of concrete. Therefore, the component plates in the tube buckle in a similar manner to plates clamped along the longitudinal edges. Effects of such buckling are accounted for in terms of an effective width model. The effective width concept has been established to provide an approximation of the ultimate strength of a thin, flat plate simply supported on two unloaded edges when it is subjected to compression. It may also be applicable for plates clamped on all four sides. This concept is based on the stress redistribution of a steel plate with an average ultimate stress, σ_u , as shown in Fig. 11.3(a). The only portion across the width to resist the loading is the effective width, b_e , but the centre portion of the plate does not carry any loading (Fig. 10.3b). A single effective width equation to account for local buckling and welding residual stresses was derived by Shanmugam *et al.* (1989) using Faulkner’s effective width formulae and the procedures given by Mulligan and Pekoz (1984).

The effective width b_e for a plate under uniform compression is given by:

$$\frac{b_e}{b} = \frac{C_1}{\beta^2} + \frac{C_2}{\beta} + C_3 + C_4\beta \quad \text{for } \beta \geq 0.526 \tag{11.1}$$

$$\frac{b_e}{b} = R_r \quad 0 < \beta < 0.526 \tag{11.2}$$



11.3 (a) Ultimate stress distribution; (b) effective width concept in a plate under compression.

where

$$C_1 = 0.277(R_r - 1.901C_2 - C_3 - 0.526C_4) \quad 11.3$$

$$C_2 = -3C_4\beta_y^2 - 2C_3\beta_y \quad 11.4$$

$$C_3 = \frac{0.526R_r}{(0.526 - \beta_y)} - 1.5C_4(0.526 + \beta_y) \quad 11.5$$

$$C_4 = \frac{2R_r(0.526\beta_y - 0.277)}{(0.526 - \beta_y)^3} \quad 11.6$$

$$\beta = \frac{b}{t} \sqrt{\frac{12(1 - \nu^2)}{\pi^2 k}} \varepsilon \quad 11.7$$

in which ε = uniform compressive strain and $k = 10.30$. The strength reduction ratio, R_r , caused by residual stresses is defined as:

$$R_r = 1 - \sigma'_{rc} \frac{E_t}{E} \frac{\beta_y^2}{1.052\beta_y - 0.277}, \quad \beta_y \geq 0.526 \quad 11.8$$

$$R_r = 1 - \sigma'_{rc} \frac{E_t}{E} \quad 0 \leq \beta_y \leq 1.413 \quad 11.9$$

in which σ'_{rc} is the compressive residual stress divided by the material yield stress σ_y .

The ratio of the tangent modulus to Young's modulus is given by:

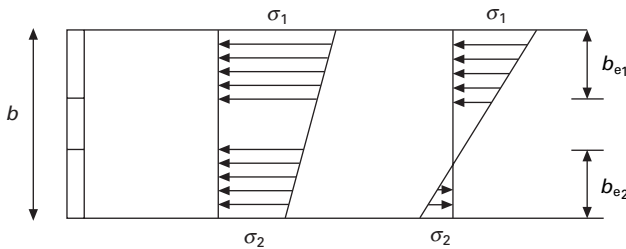
$$\frac{E_t}{E} \left(\frac{13.087\beta_y^2}{13.1 + 3.268\beta_y^4} \right)^2 \quad 0 \leq \beta_y \leq 1.413 \quad 11.10$$

$$\frac{E_t}{E} = 1.0, \quad \beta_y > 1.413 \quad 11.11$$

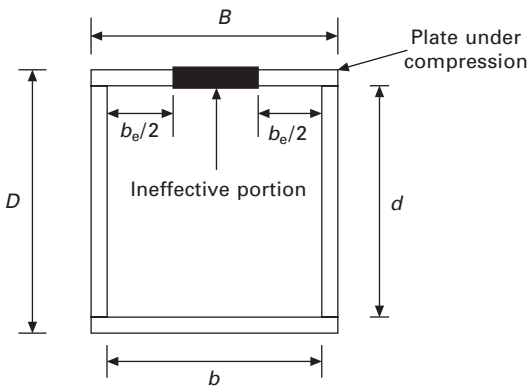
When a column cross-section is subjected to biaxial bending in addition to axial compression, the stresses along the loaded edges of a plate element become nonuniform as shown in Fig. 11.4. It is known that the compression flange buckles locally as the columns bend about the major axis. Then, the ineffective region is excluded from the cross-section as shown in Fig. 11.5. The effective width in this case is modified as:

$$\frac{b_{e1}}{b} = 0.5 \left(\frac{C_1}{\beta^2} + \frac{C_2}{\beta} + C_3 + C_4 \beta \right) \quad \text{for } \beta \geq 0.526 \quad 11.12$$

$$\frac{b_{e1}}{b} = 0.5R_r \quad 0 < \beta < 0.526 \quad 11.13$$



11.4 Effective width of plate under compression and bending.



11.5 Effective cross-section subjected to combined bending.

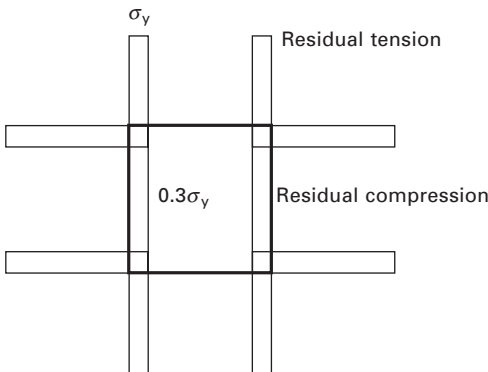
$$\frac{b_{e2}}{b} = (1 + 0.44\alpha) \frac{b_{e1}}{b} \quad \text{for } \alpha \leq 1.0 \quad 11.14$$

$$\frac{b_{e2}}{e} = 1.44 \frac{b_{e1}}{b} + \frac{(\alpha - 1)}{\alpha} \quad \text{for } \alpha > 1.0 \quad 11.15$$

in which $\alpha = 1 - \sigma_2/\sigma_1$, where σ_1 and σ_2 are the maximum and minimum edge stresses. Local buckling of the component plates is thus accounted for by using the above effective width formulae.

11.2.3 Residual stresses

Residual stresses in welded steel tubes, produced during cooling of the welded sections, can have a significant influence on the material stress–strain behaviour of the tubes. The effect of residual stress on the ultimate strength of steel plates has been shown by Shanmugam *et al.* (1989) for a hollow steel box column. Residual stress level of 30% of the yield stress in the compression zone was found to be a maximum based on the available data. Uy (1998) showed that residual stresses cause a slight increase in stiffness in the elastic range, but the ultimate strength is not affected. If a slender steel plate with residual stress is loaded in compression, then the ultimate stress of the steel plate will decrease because of additional residual compressive stress. In other words, the effective width of steel plate should be reduced. An idealised residual stress pattern as shown in Fig. 11.6 is incorporated in the analysis through the effective width formula.



11.6 Residual stress distribution.

11.2.4 Axial strength capacity

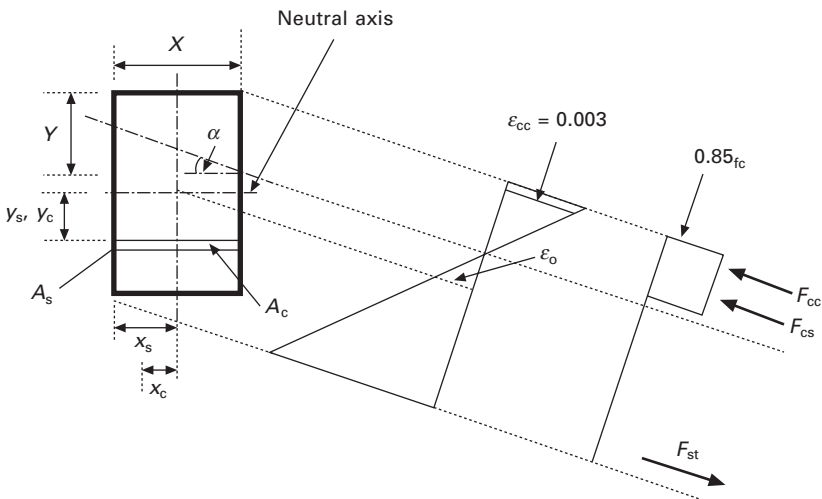
The ultimate compressive strength of a composite cross-section is related to the design strength of concrete and steel by the relation:

$$N_u = A_e f_{yd} + 0.85 A_c f_{cd} \quad 11.16$$

in which A_e represents the effective steel area determined by the effective width formula, A_c the cross-sectional area of concrete in the axial direction and f_{yd} and f_{cd} the corresponding design strengths. The reduction in strength of steel plates caused by residual stresses and local buckling is accounted for by adopting the total effective steel area calculated from the proposed effective width formula. The reduction factor for the cylinder compressive strength of concrete is taken as 0.85.

11.2.5 Cross-section analysis

Moment–curvature–thrust (M- ϕ -P) relationships are important in the analysis of long column behaviour. A finite slice approach is used herein to compute the M- ϕ -P relationship numerically in which the concrete and steel areas in the cross-section are discretised into small areas. In doing so, the effective steel section is considered in the analysis based on the effective width formulae. Axial forces are determined by summing up elemental forces and internal moments by adding the moment due to elemental forces. Effects such as strain hardening of steel and finite nonzero stresses in concrete below the neutral axis position are usually considered secondary and are neglected. The distributions of strain and stress in a typical section of the composite column are shown in Fig. 11.7. The coordinate system is chosen to pass through the centroid of the section. The displacements in the column are assumed to be small, so that the total curvature in the two major bending



11.7 Typical strain and stress distribution.

planes denoted as K_x and K_y can be represented in the form of second derivatives of the displacements as:

$$K_x = \frac{\partial^2 u}{\partial x^2} \quad 11.17$$

$$K_y = \frac{\partial^2 v}{\partial y^2} \quad 11.18$$

The resultant strain distribution corresponding to the curvatures K_x , K_y and the axial compressive strain ϵ_0 are assumed to be uniformly distributed over each element of the cross-section when subjected to axial force and moment; the strain at any position can be expressed as:

$$\epsilon = \epsilon_0 + K_x y + K_y x \quad 11.19$$

The resultant stress distribution in each element is obtained by using the material properties of the corresponding element. Given the axial load and corner strain ϵ_{cc} , $M-\phi$ values in each principal direction can be found by iteration of the neutral axis position to satisfy the force equilibrium equation. By repeating the procedure for successive increments of extreme fibre strain ϵ_{cc} until it reaches the crushing strain of the concrete ϵ_u , a set of $M-\phi$ relations are obtained. ϵ_{cc} is assumed to vary from zero to 0.003 until the moment value reaches a maximum. The neutral axis angle for each increment of strain should be kept constant. The $M-\phi$ relations are computed if agreement with the applied load is within a tolerance limit. If not, the extreme strain is altered and the procedure from the previous step is repeated. Thus, the complete moment–curvature relationship is constructed.

For a column subjected to biaxial loading, moments and curvatures about principal axes are calculated as follows:

Moment about X axis:

$$M_x = \sum (A_c \sigma_c y_c + A_s \sigma_s y_s) \quad 11.20$$

where A_c and A_s are elemental areas of concrete and steel strips respectively, σ_c and σ_s corresponding stresses, y_c and y_s , the distances between the centroid of elemental areas and plastic centroid of the whole cross-section along the y -direction.

Moment about Y axis:

$$M_y = \sum (A_c \sigma_c x_c + A_s \sigma_s x_s) \quad 11.21$$

in which x_c and x_s represent the distance between the centroid of the elemental area and the plastic centroid of the whole cross-section along the x direction.

The curvature about the X and Y axes are, respectively:

$$K_x = \epsilon_{cc}/Y \quad \text{and} \quad K_y = \epsilon_{cc}/X \quad 11.22$$

where X and Y are the intercepts of neutral axis on the directions parallel to breadth and depth, respectively of the cross-section and ϵ_{cc} refers to the extreme concrete fibre strain (Fig. 11.3). The two moments M_x and M_y are related to the resultant moment M as:

$$M^2 = M_x^2 + M_y^2 \tag{11.23}$$

Similarly for curvature along both axes, the resultant curvature is given by

$$K^2 = K_x^2 + K_y^2 \tag{11.24}$$

where

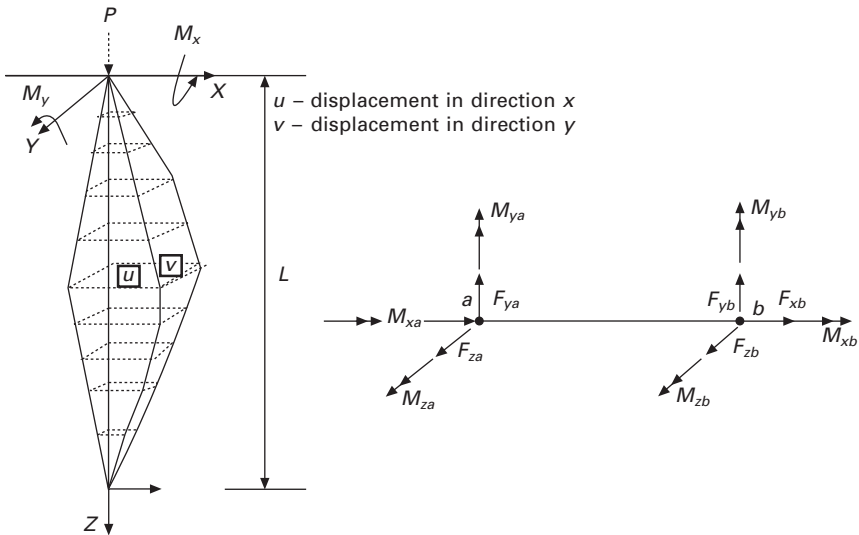
$$K_x = K \sin \alpha \quad \text{and} \quad K_y = K \cos \alpha \tag{11.25}$$

where α is the angle of inclination of neutral axis with respect to the X -axis.

11.2.6 Column strength analysis

The behaviour of composite columns is highly nonlinear since the M - ϕ - P relationships vary from section to section along the length of the member. It is, therefore, essential to adopt a numerical technique in order to simplify the analysis. The procedure used for the analysis can be summarised as follows:

- The entire column is broken down at the nodal points or nodes along the length into a number of line elements as shown in Fig. 11.8. Each cross-section is discretised into a finite element and analysed with the stress distribution as shown in Fig. 11.7.



11.8 Column subjected to biaxial loading.

- Stiffness equations are derived for each element in terms of the nodal degrees of freedom. This step ensures the equilibrium of individual elements to be satisfied. The standard stiffness matrix for the space frame element having nodal forces and moments was used in the analysis. Flexural and axial rigidities (referred to as EI and EA) in the stiffness matrices are derived using the slope of the moment–curvature and axial load-shortening curves, respectively. The slope for each element is obtained by the method of bisections from the actual curves generated by the cross-sectional analysis.
- By transforming the element stiffness equations from local coordinates to a common global coordinate system for each element, all the element equations are assembled to yield the global stiffness equations. This ensures satisfaction of compatibility and equilibrium conditions for the entire column at each nodal point.
- By imposing appropriate geometric boundary conditions, the structure will achieve its kinematic stability, as indicated by the positive definiteness of the stiffness matrix.
- For a given set of applied loading, the nodal displacements can then be solved from the structure stiffness equations.

For a typical load-deflection response, the phenomena such as softening, stiffening, loading and unloading are typified by the occurrence of critical points such as limit points and snap-back points. Incremental stiffness equations for each element in the structure can be expressed in a general form as:

$$[K]\{U\} = \{^2P\} - \{^1P\} \quad 11.26$$

where

$[K]$ structure stiffness matrix, $\{U\}$ structure displacement increment vector, $\{^2P\}$ total loads to be applied on the structure and $\{^1P\}$ external loads applied to the structure at the beginning of the incremental step.

The GDC method, proposed by Yang and Shieh (1990), is used to solve the incremental equilibrium equation (Eqn. 11.26) considering its numerical stability near all types of limit points. With the superscript ‘ i ’ denoting the current load increment step and the subscript ‘ j ’ denoting the current iteration number, Eq. 26 can be rewritten as:

$$[K_{j-1}^i]\{\delta U_j^i\} = \{P_j^i\} - \{F_{j-1}^i\} \quad 11.27$$

where $[K_{j-1}^i]$ is the tangent stiffness matrix formed at the beginning of the j th iteration based on the known element details at $(j-1)$ th iteration, $\{\delta U_j^i\}$ the iterative displacement vector obtained for the j th iteration, $\{P_j^i\}$ the total external nodal loads applied on the structure at j th iteration, and $\{F_{j-1}^i\}$ the internal element forces summed at each node of the structure up to the $(j-1)$ th iteration during the i th load increment.

A generalised stiffness parameter (GSP) is introduced to compute the iterative parameter until the convergence of incremental equilibrium equation

is achieved. In GSP^i for any load increment, 'i' is defined as the ratio of the norm of the first iterative displacement vector of the first load increment step to those at the current load increment step:

$$GSP^i = \frac{\{\delta\hat{U}_1^1\}^T \{\delta\hat{U}_1^1\}}{\{\delta\hat{U}_1^{i-1}\}^T \{\delta\hat{U}_1^i\}} \quad 11.28$$

where $\{\delta\bar{U}_j^i\}$ represents the iterative residual displacement vector at the j th iteration of the i th load increment and $\{\delta\hat{U}_j^i\}$ the iterative tangential displacement vector at the j th iteration of the i th load increment. For the first load increment, GSP^1 value is equal to one. The first iterative load parameter of the first load increment, $\delta\lambda_1^1$ is equal to the input value, and for the subsequent load increments, it can be computed using the known GSP^i value of that particular load increment as:

$$\delta\lambda_1^i = \pm \delta\lambda_1^1 |GSP^i|^{1/2} \quad 11.29$$

The iterative load parameter, $\delta\lambda_j^i$ for all the subsequent iterations ($j > 1$) is computed using the following expression:

$$\delta\lambda_j^i = - \frac{\{\delta\hat{U}_1^{i-1}\}^T \{\delta\bar{U}_j^i\}}{\{\delta\hat{U}_1^{i-1}\}^T \{\delta\hat{U}_j^i\}} \quad 11.30$$

As the GDC method is based on the bounded characteristics of load parameter and displacement increments, it is able to bypass the limit points without causing any numerical instability.

11.2.7 Convergence criteria

For each load increment, the equilibrium equation is solved by iterations until the unbalanced force vector $\{R_{j-1}^i\}$ becomes negligible. This is indirectly achieved by the following energy criteria:

$$\frac{|\{\delta U_j^i\}^T \{R_{j-1}^i\}|}{|\{\delta U_1^i\}^T \{\delta\lambda_1^i \{\hat{P}\}\}|} < \rho_E \quad 11.31$$

in which ρ_E is a user-specified tolerance, usually chosen between 1×10^{-6} and 1×10^{-10} . Alternatively, to terminate the iteration for nonconverging and slow-converging systems, a maximum number of iterations per load step is also imposed.

The M - ϕ - P and load-axial strain relationship plots are the final outcome of the cross-section analysis. For every load increment, the M - ϕ - P and load-axial strain relationship plots are thus used to update the structure stiffness matrix to ensure the equilibrium. After the stiffness has been modified, the

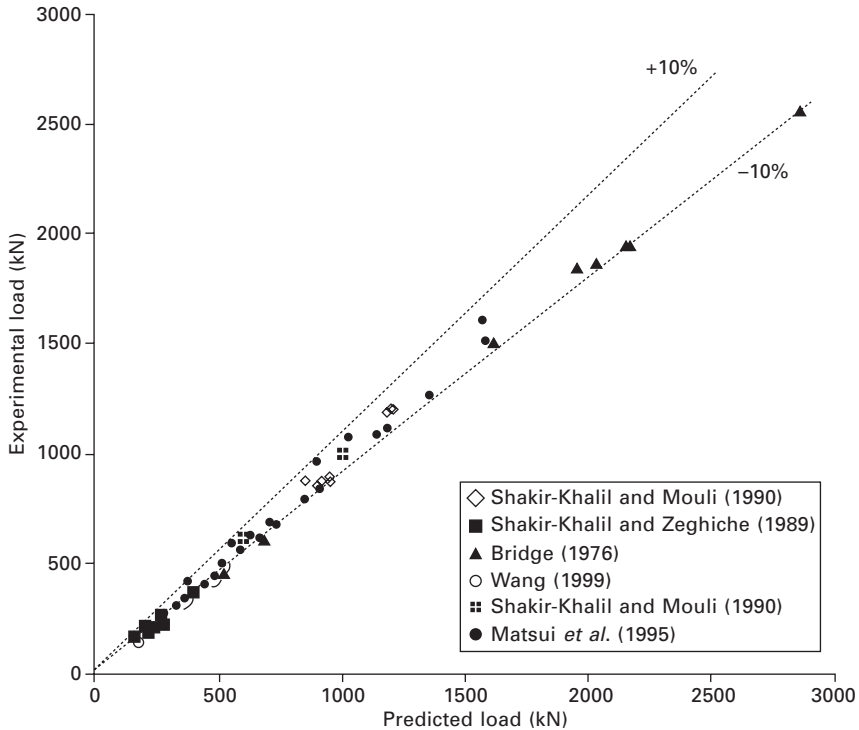
solution of Eq. 11.27 (by GDC method) gives the final results for forces and lateral deformations of the column along its length. The complete solution of the column analysis results in column strength and deformation which can be obtained in graphical or numerical forms. The corresponding results for axial strength, axial shortening and load deformation relationships are presented and discussed for a number of columns tested by other researchers in the following sections.

11.3 Numerical results

This section provides some numerical studies using the proposed method. A number of researchers have carried out tests to failure on tubular columns, compact or slender, filled with concrete. A few of those columns, results for which have been reported in the literature, are analysed by using the proposed method (Lakshmi and Shanmugam, 2000a, b, 2002) and the results presented in the form of interaction diagrams and load-deflection plots. Parameters such as concrete and steel strengths, the cross-sectional dimensions of section, and eccentricity of applied loading are considered.

11.3.1 Columns of compact steel sections

Tests on pin-ended composite columns having steel tubes of compact sections were carried out by Bridge (1976). Columns were loaded eccentrically about any axis; parameters such as thickness of the steel tube t , eccentricity e , length L , and angle at which the line of load is inclined to the horizontal axis were considered in the study. Shakir-Khalil and Zeghiche (1989) tested 2.76 m long rectangular columns of section $120 \times 80 \times 5$ RHS under biaxial load applied at eccentricities about major (e_x) and minor (e_y) axes. Further tests on rectangular columns ($120 \times 80 \times 5$ RHS and $150 \times 100 \times 5$ RHS) of 3 m length were carried out by Shakir-Khalil and Mouli (1990). Columns tested by Matsui *et al.* (1995) were also considered. The columns were of square cross-sections of 149.8 mm width and 4.27 mm thickness. The steel tube of yield strength 412 N/mm^2 was filled with concrete of compressive strength 31.9 N/mm^2 . The length of the columns varied from 600 mm to 4.5 m covering a wide range of column slenderness and, the eccentricities about both axes varied from zero to a maximum of 125 mm. Simply supported slender composite columns of 4 m long were tested by Wang (1999). The rectangular section $120 \times 80 \times 6.3$ of grade S275 tube infilled with concrete of grade C25/30 was subjected to a load applied at eccentricities about both axes. All the columns referred above are analysed by the present method and the predicted results for ultimate load along with the reported experimental values are summarised in Fig. 11.9.



11.9 Experimental and analytical strengths for columns of compact steel sections.

11.3.2 Columns of thin-walled steel sections

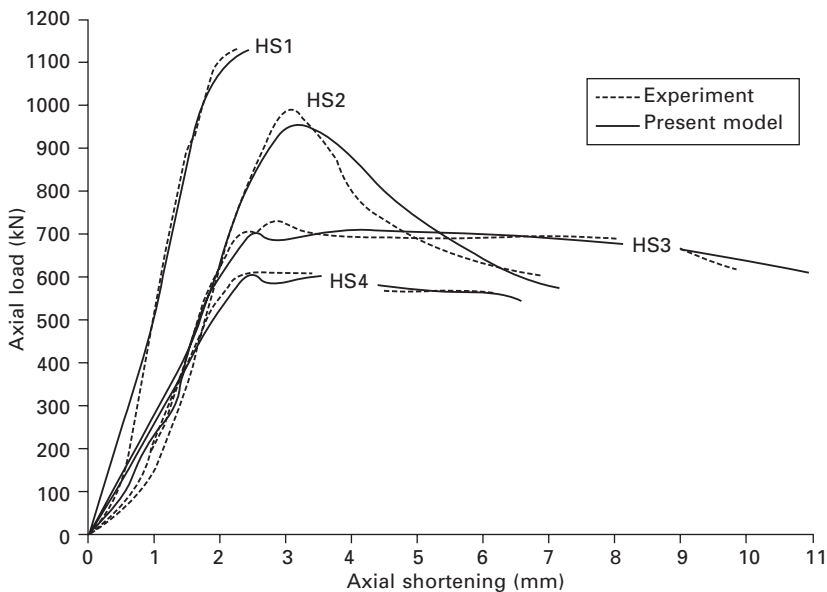
Five series of short columns (HS1 to HS4, HS7 to HS10, NS1 to NS4, NS7 to NS10 and NS13 to NS16) with a value of b/t ratio ranging from 40 to 100 were tested to failure by Uy (2000). The upper limit for compact plate slenderness values is less than 40 according to most of the international codes and, therefore, the results provide valuable data for slender sections. Dimensions of the test specimens in each of the series were kept the same, and specimens in a particular series tested under loads applied with different eccentricities. Details of the test specimens are listed along with the experimental failure load in Table 11.1 and, the corresponding predicted values summarised in the table. Comparison between the two values ($N_{\text{expt}}/N_{\text{pred}}$) is also given in the table. N_{pred} represents the predicted ultimate strength based on the proposed method and N_{expt} the ultimate strength obtained from the experiment. It can be seen from the table that, in most cases, the proposed design model produces conservative predictions of the ultimate strength of short steel box columns filled with concrete.

Table 11.1 Comparison of ultimate strength with test results by Uy (2000)

Series	Specimen	B (mm)	L (mm)	e (mm)	b/t	f_c (N/mm ²)	N_{expt} (kN)	N_{pred} (kN)	$N_{\text{expt}}/$ N_{pred}
1	HS1	126	360	0	40	50	1114	1114.0	1.00
	HS2	126	360	20	40	50	996	948.6	1.05
	HS3	126	360	40	40	50	739	684.3	1.08
	HS4	126	360	50	40	50	619	584.0	1.06
2	HS7	156	450	0	50	50	1708	1856.5	0.97
	HS8	156	450	25	50	50	1426	1398	1.02
	HS9	156	450	50	50	50	1203	1227.6	0.98
	HS10	156	450	60	50	50	959	922.4	1.04
3	NS1	186	540	0	60	32	1555	1439.8	1.08
	NS2	186	540	37	60	32	1069	1037.9	1.03
	NS3	186	540	56	60	32	1133	1180.2	0.96
	NS4	186	540	84	60	32	895	836.4	1.07
4	NS7	246	720	0	80	38	3095	3034.0	1.02
	NS8	246	720	48	80	38	2255	2068.8	1.09
	NS9	246	720	74	80	38	1900	1938.8	0.98
	NS10	246	720	100	80	38	1279	1229.8	1.04
5	NS13	306	900	0	100	38	4000	3809.5	1.05
	NS14	306	900	0	100	38	4253	3901.8	1.09
	NS15	306	900	0	100	38	4495	4162.0	1.08
	NS16	306	900	0	100	38	4581	4979.0	0.92

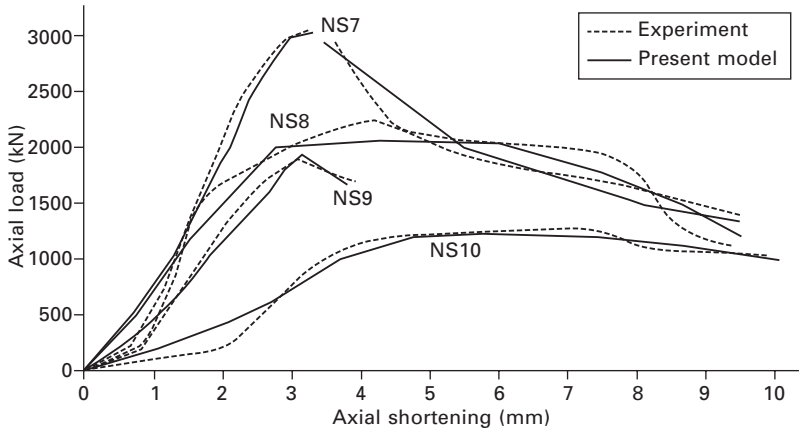
11.3.3 Axial load-shortening curves

Axial load-shortening curves provide useful information on axial stiffness, yielding and failure mechanism of columns. They are also capable of monitoring local buckling behaviour of the steel tube. Load-shortening curves for typical columns obtained experimentally are presented along with the corresponding theoretical curves in Figs 11.10 and 11.11. Curves for columns with wall plate slenderness of 40, somewhat thicker walls, are given in Fig. 11.10 and those for column wall plate slenderness 80, susceptible to local buckling, in Fig. 11.11. For columns tested under axial load, the peak load reduced fairly rapidly, whereas for those columns under bending, the reduction was less dramatic.



11.10 Load-axial shortening curves for specimens in series 1 (HS1 to HS4).

It is observed that the stresses developed on the tensile flange in each column do not reach the yield strain before failure of columns. This means that tensile stress failure is not critical in these columns. At the beginning, all steel plates develop compressive strain due to axial compression force. Before the peak load is reached, the tension flange develops tensile strain. It is due to local buckling that reverse tensile stresses only develop near the ultimate load. This is sometimes known as elastic unloading. It is mainly due to bending moment caused by eccentricity of load. However, it is found that tensile strain on the plate does not exceed the steel yield strain.

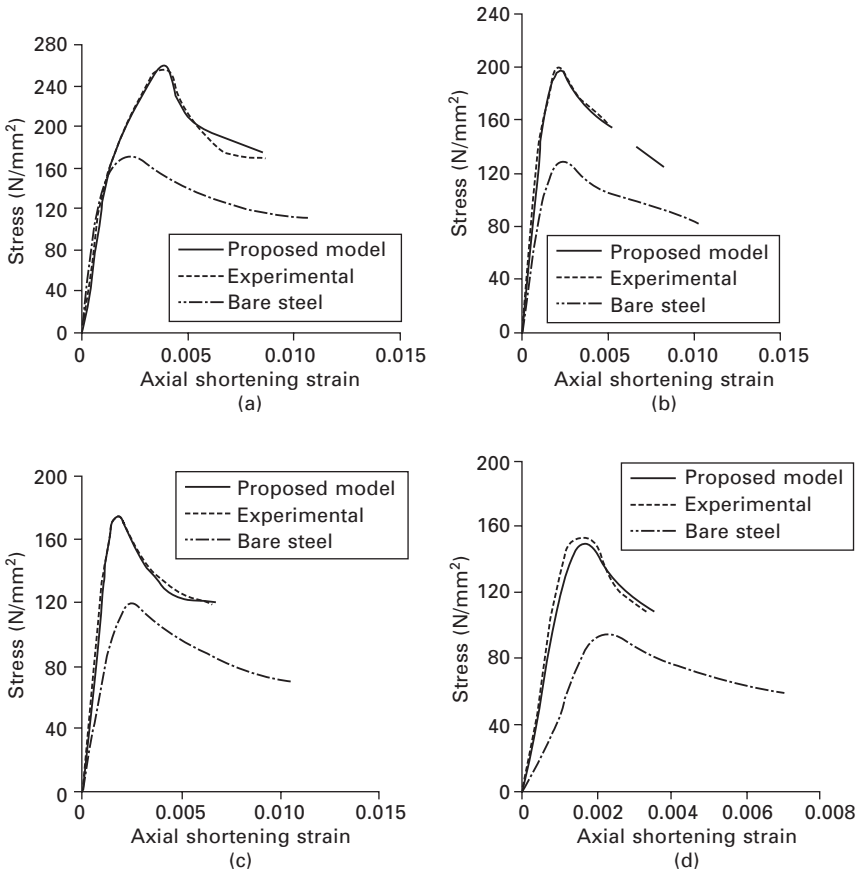


11.11 Load-axial shortening curves for specimens in series 4 (NS7 to NS10).

Load-axial shortening curves are generated for the thin-walled box columns infilled with concrete and tested by Bridge *et al.* (1995). In these tests column wall plate slenderness, b/t values were varied from 56 to 130. All tubes were manufactured from mild steel sheet with a measured thickness of 2.142 mm. The steel tubes having yield stress equal to 282 N/mm^2 and Young's modulus of $199\,400 \text{ N/mm}^2$ were filled with concrete of nominal strength 20 N/mm^2 . The average residual compressive stress was measured as 50 N/mm^2 . The axial stress-strain relationships are shown in Fig. 11.12(a)–(d) for b/t ratios of 56, 74.7, 93.4 and 130.7, respectively. All steel plates develop compressive strain due to axial compression. The reverse tensile stresses develop near the ultimate load due to bending moment caused by eccentricity of load. It implies that steel can develop full plastic stress before columns fail. In addition, the load drops suddenly after concrete reaches the crushing strain. When concrete crushes at ultimate load, it causes stress redistribution in steel. The results also show that the effect of local buckling is significant as the slenderness ratio of the steel plate is increased. It is also found that the in-filled columns have a greater axial capacity and higher stiffness than the hollow steel box columns.

11.3.4 Eurocode 4

Interaction diagrams for columns tested by Uy (2000) were generated using the proposed method. For each cross-section, an interaction diagram was obtained as per Eurocode 4. This approach in Eurocode 4 allows the full mean compressive strength of the cylinder to be utilised, but local buckling is ignored by limiting the plate slenderness to within compact plate limits. The interaction diagrams obtained by using the proposed method are presented

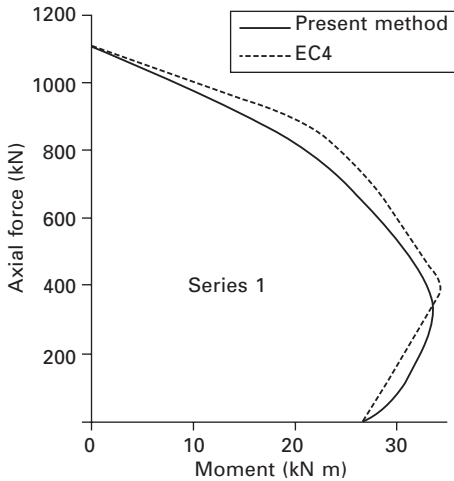


11.12 Comparison of axial shortening curves with bare steel sections for specimens tested by Bridge *et al.* (1995): (a) $b/t = 56.0$; (b) $b/t = 74.7$; (c) $b/t = 93.4$; (d) $b/t = 130.7$.

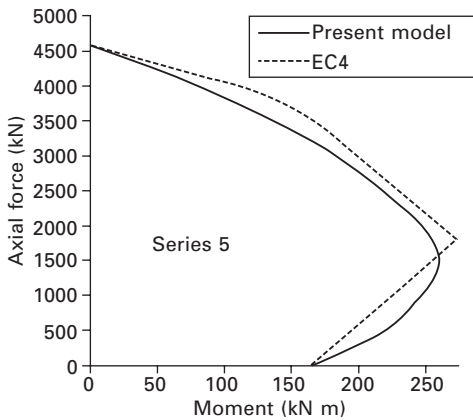
along with those obtained by EC4 in Figs 11.13 and 11.14 for typical columns shown in Table 11.1. It is obvious from the figures that Eurocode 4 gives a higher strength for all points. The Eurocode model is found to overestimate the results since it is based on a rigid plastic analysis that assumes fully crushed concrete and fully yielded steel. This is particularly true for pure compression and bending and not on other points of the interaction curve. But in the present analysis, steel is partially elastic and has not fully yielded when the concrete has crushed.

11.4 Parametric studies

The proposed method is used to study the influence of key parameters on the behaviour and ultimate load of steel–concrete composite columns. Each of



11.13 Comparison of model and Eurocode 4 for series 1.



11.14 Comparison of model and Eurocode 4 for series 5.

the parameters is studied independently by keeping the rest of the parameters constant for a particular column. Details of the study are given in this section. A 3.0 m long composite column made of a steel box section $150 \times 100 \times 5$ mm with concrete infill was considered. Both the column ends were assumed to be pinned. Typical values of material and geometrical properties of the cross-section used in the studies are:

- Young’s modulus $E = 2 \times 10^5 \text{ N/mm}^2$
- Yield stress $f_y = 300 \text{ N/mm}^2$
- Concrete strength $f_{cu} = 40 \text{ N/mm}^2$
- Steel tube wall thickness $t = 5 \text{ mm}$

- Poisson's ratio $\mu = 0.3$
- Box cross-section $d \times b \times t = 150 \times 100 \times 5 \text{ mm}^3$
- Cross-section aspect ratio $d/b = 1.5$
- Plate slenderness of the steel tube $b/t = 30$
- Residual stress $\sigma_r = 0.0 \sigma_y$
- Initial column deflection $\delta_0 = L/1000$, L being the column length.

For each case study, the above values can be varied and, the range of variation and the values of various parameters for each case are listed in Table 11.2. Each of the parameters and its effect on the behaviour of in-filled columns is studied in detail and the results are presented herein.

11.4.1 Axial load

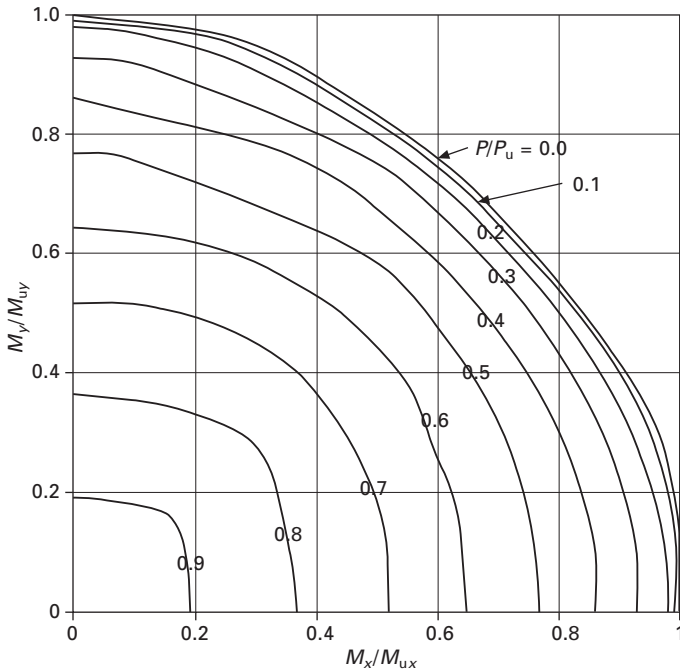
A tensile axial load tends to straighten the column and hence increases its stiffness. However, when a compressive axial load acts through an initial curvature, the effect of load is adverse and such a load acting at an eccentricity causes secondary moments. This in turn increases lateral deflection and consequently reduces the column stiffness and its stability. Figure 11.15 shows the nondimensionalised biaxial interaction envelope for different axial load ratios. M_{ux} and M_{uy} in the figure represent the ultimate moment capacity of the section about major and minor axes, respectively. It can be seen from the figure that the moment capacity decreases significantly as the axial force increases. The drop in moment capacity becomes larger as the axial load increases. The effect of M_x and M_y are similar as they were nondimensionalised with respect to ultimate moment capacity about the corresponding principal axes.

11.4.2 Load eccentricity

Eccentricity can be of any form arising from initial imperfections in the tube wall, eccentricity of load, initial deflection or curvature, or from residual stresses that are nonsymmetrical. In all cases, eccentricity would result in reduction of the ultimate strength. Eccentrically loaded columns deflect laterally soon after the load application and the stress redistribution begins at an early stage of loading. The criterion for the analysis is equilibrium of the internal and external forces and moments. A series of analyses are performed on rectangular composite columns made of steel tube with a yield strength of 300 N/mm^2 and infill concrete having a compressive strength of 40 N/mm^2 . All other parameters are kept the same as those for the column considered under axial load in Section 11.4.1, except for values of the end eccentricity of the axial load about major axis, which was assigned values equal to 0, 5,

Table 11.2 Parameters and their range of variation

Notations	Case 1 Axial load	Case 2 Eccentricity ratio	Case 3 Initial out-of- straightness	Case 4 Residual stress	Case 5 Column slenderness	Case 6 Plate slenderness	Case 7 Concrete strength	Case 8 Yield strength of steel tube
E (N/mm ²)	2×10^5	2×10^5	2×10^5	2×10^5	2×10^5	2×10^5	2×10^5	2×10^5
f_y (N/mm ²)	300	300	300	300	300	300	300	250–355
f_{cu} (N/mm ²)	40	40	40	40	40	40	40–60	40
T (mm)	5	5	5	5	5	5	5	5
μ	0.3	0.3	0.3	0.3	0.3	0.3	0.3	0.3
$d \times b \times t$ (mm)	150×100 $\times 5$	150×100 $\times 5$	150×100 $\times 5$	150×100 $\times 5$	150×100 $\times 5$	150×100 $\times 5$	150×100 $\times 5$	150×100 $\times 5$
d/b	1.5	1.5	1.5	1.5	1.5	1.5	1.5	1.5
b/t	30	30	30	30	30	30	30	30
σ_r (N/mm ²)	0	0	0	0.0 to 0.3 σ_y	0	0	0	0
δ_0 (mm)	$L/1000$	$L/1000$	1/5000 to 1/250	$L/1000$	$L/1000$	$L/1000$	$L/1000$	$L/1000$
Additional parameters	Uni- axial and biaxial	$e/D = 0$ to 0.4	$e = 15$ mm	$\Delta_0 = 1/5000$ to 1/250	$e = 15$ mm	$f_c = 40$ to 60 N/mm ²	$b/t = 40$ to 60	$e = 15$ mm



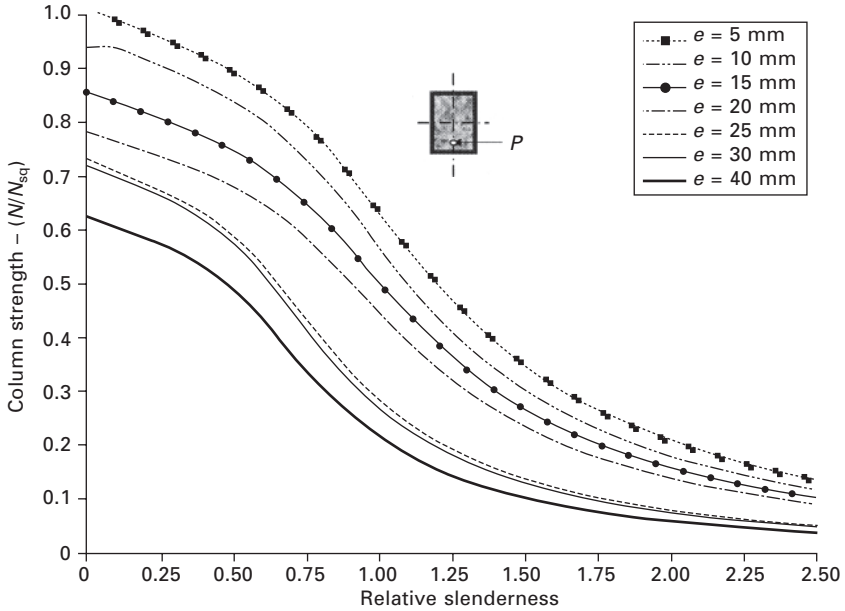
11.15 Interaction diagrams to show the effects of axial load.

10, 15, 20, 25, 30 and 40 mm. End eccentricity is expressed as a nondimensional parameter known as the eccentricity ratio, e/d , varying from 0 to 0.4 (d being the depth of the column cross-section in the plane of bending). These values of eccentricity cover a wide range that could occur in practice. The columns are assumed to have an initial out-of-straightness with a maximum central value of $L/1000$ where L is the column length.

Typical column curves are given in Fig. 11.16. The results show that an increase in load-eccentricity reduces the load carrying capacity of the column and the reduction is larger when the eccentricity increases. This is due to the presence of an end moment as a result of larger eccentricity. The results also show that larger eccentricity reduces significantly the column stability, with the instability criterion of failure occurring at lower column slenderness values as the eccentricity increases.

11.4.3 Initial out-of-straightness

An axially loaded perfectly straight slender column can reach the Euler load. However, real columns are not perfectly straight because of the initial curvature. Initial curvature causes the column to bend even at lower level of applied load and consequently this produces an increase in member stresses. The greater the initial curvature, the greater will be the bending effect.

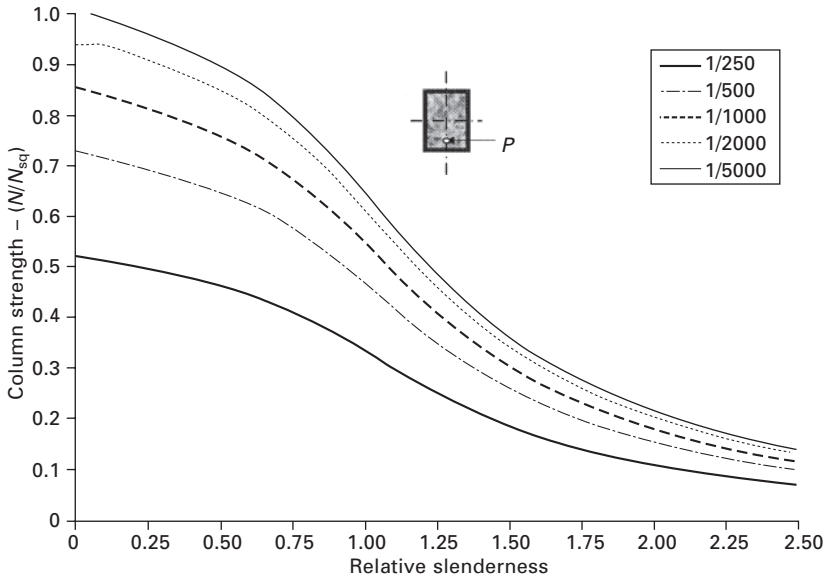


11.16 Column curves for varying load eccentricities.

To study the effect of initial imperfections on ultimate strength, in addition to the basic value of initial central deflection ($L/1000$), four other values of $L/5000$, $L/2000$, $L/500$ and $L/250$ are considered. Values of other parameters are listed in Table 11.2. The range of initial values chosen gives an even spread of initial out-of-straightness from almost straight ($L/5000$) to a relatively large imperfection ($L/250$). A series of analyses are performed using different values of initial central deflection at zero residual stress under uniaxial bending with a nominal eccentricity of 15 mm. The assumed initial imperfection of $L/1000$ in the current analysis is close to the fabrication tolerances in most design specifications. The results are presented in the form of column curves in Fig. 11.17, in which the nondimensional column strength (N/N_{sq}) is plotted against the relative column slenderness λ^* . Column strength is non-dimensionalised against squash load, $N_{sq} (A_s f_y + A_c f_c)$, and the relative column slenderness λ^* is given by:

$$\lambda^* = \sqrt{\frac{N_{sq}}{N_{crit}}} = \frac{\lambda}{\pi} \sqrt{\frac{A_s f_y + A_c f_c}{E_s A_s + E_c A_c}} \tag{11.32}$$

As would be expected, the increase in magnitude of initial out-of-straightness results in the reduction of column strength. It is obvious that the strength of composite column decreases as the initial out-of-straightness increases. However, it is worth noting that increasing the initial out-of-straightness of the column from $L/5000$ to $L/2000$ does not alter the column strength



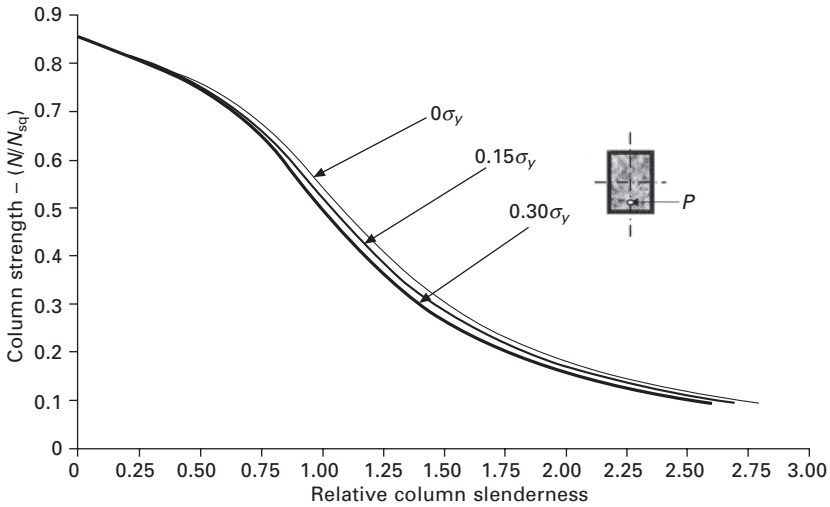
11.17 Column curves for varying initial out-of-straightness.

significantly. But increasing the initial out-of-straightness from $L/2000$ to $L/500$ and further below tends to reduce the strength of column by large value. The effect of initial out-of-straightness of the column on the strength is not severe for stocky columns. As for the slender columns, the strength reduces as the initial out-of-straightness increases. The strength reduction effect caused by initial out-of-straightness on slender columns is not unexpected since the imperfection is a function of column length.

11.4.4 Residual stresses

Bending rigidity of a column cross-section is reduced by the presence of residual stresses and, instability occurs at a lower load than that obtained without residual stresses accounted for. To investigate the effects of residual stresses, two distinct values of residual stresses ($0.15\sigma_y$ to $0.30\sigma_y$) were chosen. Two sets of analyses are performed on rectangular composite column of cross-section $150 \times 100 \times 5$ mm with all other parameters identical as in the earlier case. The columns are assumed to have initial out-of-straightness of $L/5000$, $L/2000$, $L/500$ and $L/250$.

Figure 11.18 shows a typical comparison for column curves for a nominal initial out-of-straightness of $L/1000$. The column curves for residual stress of intensities $0.0\sigma_y$, $0.15\sigma_y$ and $0.3\sigma_y$ are compared and found that the reduction in column strength is encountered in the range of relative column slenderness of 0.75 to 2. It is clear from the figure that residual stresses affect the

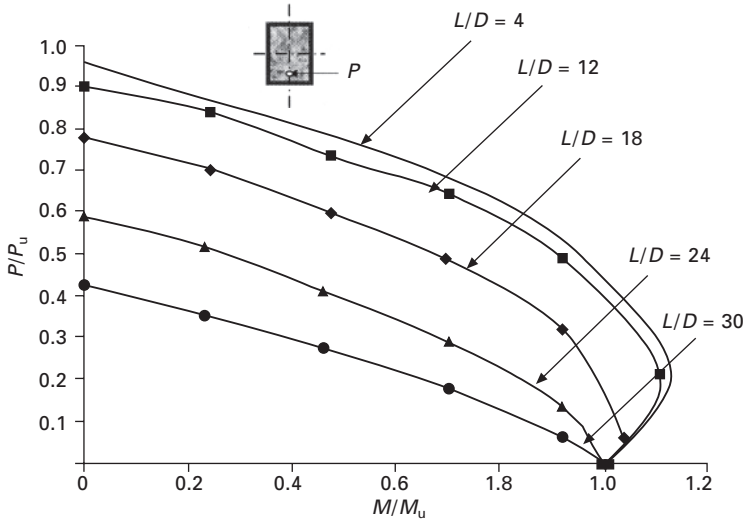


11.18 Effect of residual stresses on column curves.

strength of columns marginally in the range of relative column slenderness from 0.5 to 1.75, where the column strength is reduced by at least 5% of squash load. The rate of reduction in load-carrying capacity decreases as the relative column slenderness increases. The reduction in column strength is notable in the range of relative slenderness between 0.6 to 1.5. Beyond this range, the residual stress pattern has little or negligible effect on the column strength. The effect of residual stress becomes small when the column slenderness ratio is large.

11.4.5 Column slenderness

An eccentrically loaded column deflects laterally because of moments acting along its height. For short columns, these deflections are small and do not affect the strength. Large lateral deflections in slender columns result in significant secondary moments due to axial load acting through an additional eccentricity. Hence at a given axial load level, the moment resistance of a slender column can be much lower than that of a short column. Columns considered in Section 11.4.1 are analysed to investigate the effect of column slenderness. All other parameters are kept identical except for the value of the column slenderness expressed as a ratio between length of the column and depth of cross-section. Figure 11.19 shows the interaction curves for different values of column slenderness ratio L/D , 4 to 30, where L is the unsupported length of the column and D its larger cross-section dimension. Tests on columns in the past have been restricted to L/D ratio of 30 and hence this limit was imposed in this study. It is unlikely that columns of



11.19 Variation of column strength with column slenderness.

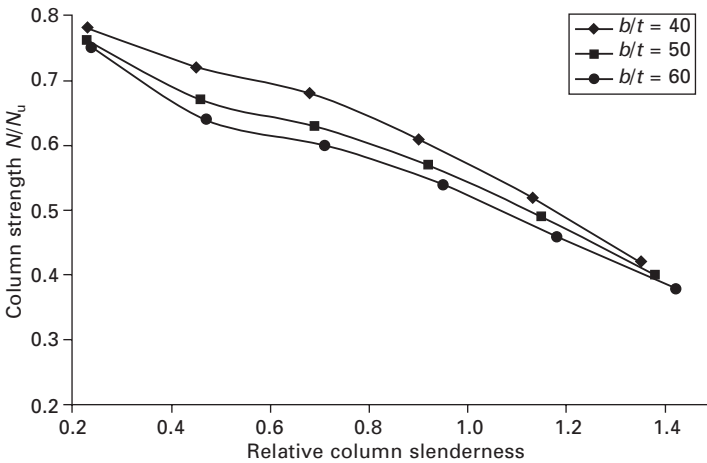
slenderness greater than 30 would be required for the type of multi-storey structures envisaged for composite columns. It can be observed from the figure that the load reduction increases substantially with the increase of column slenderness. The effect of column slenderness on the maximum load is evident from these curves. The results indicate that for slender columns, the failure load is reached before the full load-moment capacity of the section can be utilised. If the maximum load is defined as the point of instability, then this behaviour could be considered as overall column instability, as opposed to the instability for the stocky columns where the full load-moment capacity of the section can be attained.

11.4.6 Column tube wall slenderness

Plates with larger b/t ratios exhibit local buckling and lower ultimate strength. In order to determine the effect of local buckling in concrete-filled box columns, it is essential to analyse columns with different width–thickness (plate slenderness) ratios. Analysis is carried out on a rectangular composite column, 3 m long made of steel tube (yield strength of 300 N/mm^2) with concrete infill (compressive strength of 40 N/mm^2). A composite column of cross-section $150 \times 100 \times 5 \text{ mm}$ was subjected to uniaxial eccentricity about the major axis at a nominal value of 15 mm. Three different values of plate slenderness ratio, b/t , ranging from 40 to 60 are considered with all other parameters identical to those given in Section 11.4.1. These values of plate slenderness cover the range that is commonly encountered in practice. For those columns with plate slenderness ratios equal to 50 to 70, effect of local

buckling is taken into consideration. For plate with a b/t ratio of 40, local buckling does not govern as it falls under the category of compact section. The columns are assumed to have an initial out-of-straightness with a maximum central value of $L/1000$, L being the column length.

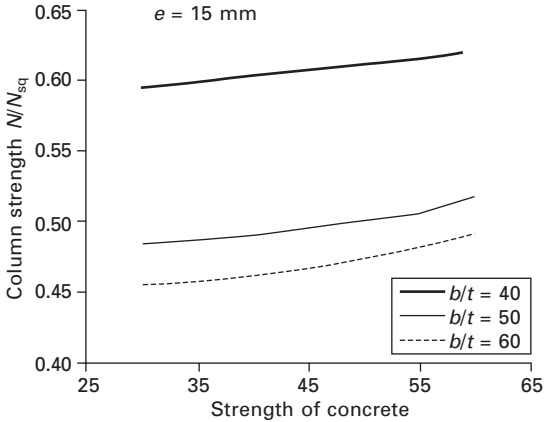
The variations of column strength with relative column slenderness are shown in Fig. 11.20 for composite columns filled with concrete having compressive strength equal to 40 N/mm^2 . It can be seen from the figure that the nondimensional column strength decreases with the relative column slenderness. The effect of plate slenderness on column strength is obvious. The difference in column strength is more pronounced when the relative column slenderness is in the range of 0.5 and 0.8. It is also observed that the curves for different values of b/t are close to each other at higher column slenderness. It indicates that the effect of plate slenderness on ultimate strength of slender columns is not significant.



11.20 Variation of column strength with relative slenderness for $f_c = 40 \text{ N/mm}^2$.

11.4.7 Compressive strength of concrete

Figure 11.21 shows the variation of nondimensional column strength, with compressive strength of concrete infill at different plate slenderness ratios, b/t . Concrete strengths of 30 to 60 N/mm^2 are chosen to investigate its influence on the ultimate strength and column behaviour. Values of other parameters involved are listed in Table 11.2. These curves are plotted for a nominal uniaxial eccentricity of 15 mm about the major axis. It can be observed that the nondimensional column strength increases gradually with the compressive strength of concrete. The increase, although not evident, is almost at a constant rate of about 2% before strength of concrete reaches 55 MPa . The effect of

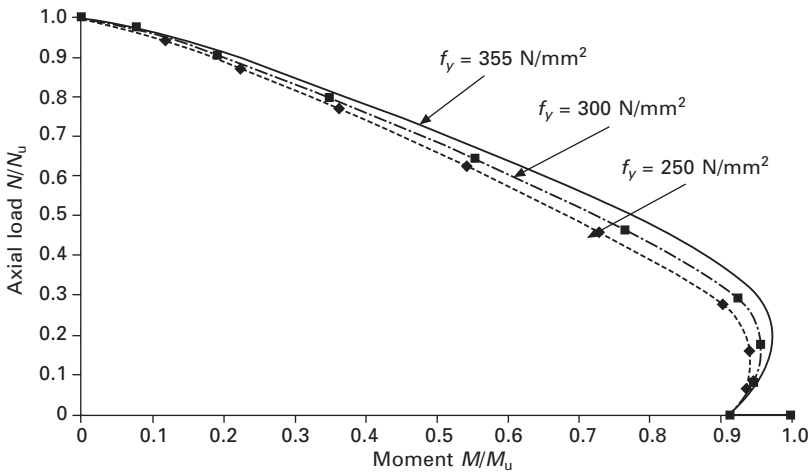


11.21 Variation of column strength with concrete compressive strength.

plate slenderness on column strength is obvious in the figure as the curves corresponding to b/t equal to 50 and 60 lie well below the one corresponding to $b/t = 40$. When the compressive strength f'_c exceeds 55 MPa, the nondimensional column strength increases at a slightly higher rate of 3.5%.

11.4.8 Yield strength of steel tube

Effect of variation in nominal yield strength can be studied from interaction envelopes as shown in Fig. 11.22. Three different values of yield stress of steel tube, viz. 250, 300 and 355 N/mm², are considered in the study. The



11.22 Interaction diagram for various yield strengths.

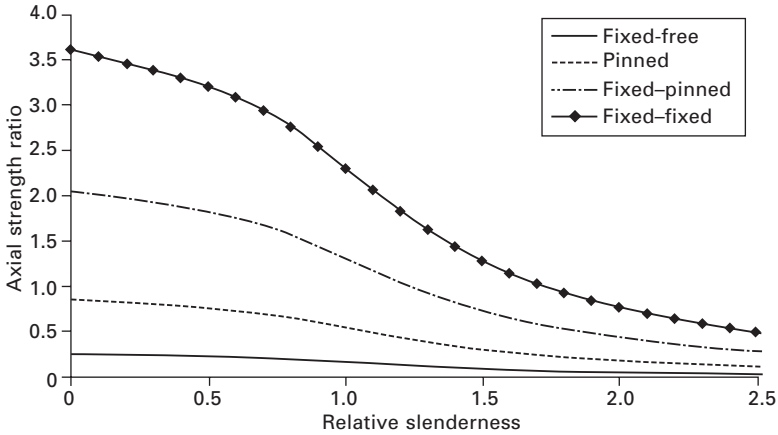
curves are generated for 3 m long composite columns of cross-section $150 \times 100 \times 5$ mm subjected to uniaxial bending at a nominal eccentricity of 15 mm about the major axis. The compressive strength of concrete infill is taken as 40 N/mm^2 in all three cases. The figure shows that the cross-section initially sustains increasing magnitude of moment as the axial force increases from zero, similar to the behaviour seen in reinforced concrete sections. In this range of applied loading, an infilled composite section will generally exhibit a ductile failure owing to yielding of the steel tube in tension prior to crushing of concrete and local buckling of those portions of steel tube in compression. As the axial force is increased further beyond the point of maximum moment, an infilled composite section exhibits rapid deterioration of moment capacity and hence results in brittle failure. From the interaction curves, it can be noted that there is a minimal variation in the load-moment interaction behaviour due to the variation in the yield strength of steel. Also the ultimate load and moment capacities remain unchanged for a minimum increase in the yield strength of steel tube.

11.4.9 Column end restraints

Joint flexibility is one of the key factors in any frame design since connections behave nonlinearly to the applied bending moment. There are no perfectly pinned or fully rigid connections in practical or real framed structures. The joint conditions are essential in the second-order inelastic analysis which considers all non-linearities in a frame design. Thus the effect of end restraint is an important factor that could affect the behaviour and column strength.

The boundary conditions commonly encountered in practice are fixed–pinned, fixed–fixed and fixed–free. The effect of restraints can be considered in the analysis by appropriate modifications in the stiffness matrix. An identification matrix to distinguish the active (unrestrained) from the non-active (restrained) degrees of freedom for each element is used herein. The calculation of deflections in the elastic–plastic range of materials is complex, and hence computer based numerical procedures are used to obtain the solution.

A rectangular composite column of 3 m long made of steel tube ($150 \times 100 \times 5$ mm) with yield strength of 300 N/mm^2 and in-fill concrete with compressive strength equal to 40 N/mm^2 was analysed. The column was subjected to uniaxial eccentricity about the major axis at a nominal value of 15 mm. The steel tube is compact ($b/t = 30$) and, therefore, local buckling does not govern the failure. The columns are assumed to have a nominal value of $L/1000$ for initial out-of-straightness. Results were obtained for columns with four different end conditions, viz. pinned–pinned, fixed–fixed, fixed–pinned and fixed–free. The results are summarised in the form of column curves in Fig. 11.23. It is clear from the figure that the columns with fixed–fixed condition displays significantly higher strength compared to other boundary conditions.



11.23 Column curves for different end conditions.

11.5 Concluding remarks

An analytical method to predict the inelastic and ultimate load behaviour and to compute the ultimate strength of steel–concrete composite columns of square and rectangular cross-sections has been proposed. This approach eliminates the limitation of the conventional analysis in which a deflection shape or pattern is usually assumed. Effects of local buckling in column walls are accounted for in terms of effective width and, in the formula to compute the effective widths, residual stress effects are also built in. Based on the results, the moment capacity of columns is found to decrease with the increase in applied axial load. For the eccentrically loaded columns, load-carrying capacity is found to drop significantly with increase of eccentricity. The effect of local buckling has been found to be significant in thin walled composite columns and should therefore be included in the existing codes of practice.

11.6 References

- Bradford, M.A. (1996), 'Design strength of slender concrete-filled rectangular steel tubes.' *ACI Struct. J.*, **93**(2), 229–235.
- Bridge, R.Q. (1976), 'Concrete-filled steel tubular columns.' *Civil Engrg. Trans., Institution of Engineers. Australia*, **18**, 127–133.
- Bridge, R.Q. and Webb, J. (1992), 'Thin walled circular concrete filled steel tubular columns.' *Proc. 2nd International Engrg. Found. Conf. of Composite Constr*, Potosi, USA; 634–649.
- Bridge, R.Q., O'Shea, M.D., Gardner, P., Grigson, R. and Tyrell, J. (1995), 'Local buckling of square thin-walled steel tubes with concrete in-fill.' *Proc. International Conference on Structural Stability and Design*, Sydney; 307–314.

- Bridge, R.Q. and O'Shea, M.D. (1995), 'Circular thin walled concrete filled steel tubes.' *PSSC'95 4th Pacific Structural Steel Conference, Steel-Concrete Composite Structures*, **3**, 53–60.
- Ge, H. and Usami, T. (1992), 'Strength of concrete-filled thin walled steel box columns: experiment.' *J. Struct. Engrg., ASCE*, **118**(11), 3036–3054.
- Ge, H. and Usami, T. (1994), 'Strength of concrete-filled thin walled steel box columns: experiment.' *J. Constr. Steel Res.*, **37**, 607–612.
- Grimault, T. and Janss, R. (1994), Experimental study on compression strength of concrete filled square tubular steel columns. *ASCE J Struct Div.*, **40**, 411–417.
- Kato, B. (1996), 'Column curves of steel-concrete composite members.' *J. Constr. Steel Res.*, **39**(2), 121–135.
- Kilpatrick, A.E. (1996), 'The behaviour of high-strength composite concrete columns.' PhD thesis, Curtin University of Technology, Australia.
- Kitada, T. (1998), 'Ultimate strength and ductility of state of art concrete-filled steel bridges piers in Japan.' *Engrg. Struct.*, **20**(4–6), 347–354.
- Lakshmi, B. and Shanmugam, N.E. (2000a), 'Behaviour of steel-concrete composite columns.' *Proc. of 6th ASCCS Intl. Conf. on Steel and Concrete Composite Structures*, California, USA, 449–456.
- Lakshmi, B. and Shanmugam, N.E. (2000b), 'RHS/SHS columns with concrete in-fill.' *Proc. of Structures Congress 2000*, ASCE, Pennsylvania, USA.
- Lakshmi, B. and Shanmugam, N.E. (2002), 'Non-linear analysis of in-filled steel-concrete composite column.' *J Struct Engrg, ASCE*, **128**(7), 922–933.
- Liang, Q.Q. and Uy, B. (1999), 'Parametric study on the structural behaviour of steel plates in concrete-filled fabricated thin-walled box columns.' *Adv. Struct. Engrg*, **2**(1), 57–71.
- Matsui, C. (1993), 'Local buckling of concrete filled steel square tubular columns.' Symposium papers, *IABSE Conference*, Luxembourg; 269–276.
- Matsui, C., Tsuda, K. and Ishibashi, Y. (1995), 'Slender concrete filled steel tubular columns under combined compression and bending.' *Proc. of 4th Pacific Struct. St. Conf.*, Singapore, **3**(10), 29–36.
- Mirza, S.A. and Skrabek, B.W. (1992), 'Statistical analysis of slender composite beam-column strength.' *J. Struct. Engrg., ASCE*, **118**(5), 1312–1331.
- Mulligan, G.P. and Peko, T. (1984), 'Analysis of locally buckled thin-walled columns.' *Proc., 7th Int. Specialty Conf. on Cold-Formed Steel Structure*, St. Lois, MO; 93–126.
- Neogi, P.K., Sen, H.K. and Chapman, J.C. (1969), 'Concrete-filled tubular steel columns under eccentric loading.' *Struct. Engrg.*, **47**(5), 187–195.
- Prion, H.G.L. and Boehme, J. (1989), 'Beam-column behaviour of steel tubes filled with high-strength concrete.' *Fourth International Colloquium*, SSRC, New York, 439–450.
- Rangan, B.V. and Joyce, M. (1992), 'Strength of eccentrically loaded slender steel tubular columns filled with high strength concrete.' *ACI Struct. J.*, **89**(6), 676–681.
- Sakai, T. Sakino, K. and Ishibashi, H. (1985), 'Experimental studies on concrete filled square steel tubular short columns subjected to cyclic shearing force and constant axial force.' *Trans Architectural Inst. Japan (Tokyo)*, **353**, 81–89.
- Shakir-Khalil, H. and Al-Rawdan, A. (1996), 'Composite construction in steel and concrete III.' *Proc. of Engrg, Foundation Conference*, Swabian Conference Center, Germany, June, edited by Buckner, D. and Shahrooz, B.M., 222–235.
- Shakir-Khalil, H. and Mouli, M. (1990), 'Further tests on concrete-filled rectangular hollow section columns.' *Struct. Engrg.*, **68**(20), 405–413.

- Shakir-Khalil, H. and Zeghiche, J. (1989), 'Experimental behaviour of concrete-filled rectangular hollow-section columns.' *Struct. Engr.*, **67**(19), 346–353.
- Shanmugam, N.E. and Lakshmi, B. (2001), 'State of the art report on steel–concrete composite columns.' *J. Construct. Steel Res.*, **57**(10), 1041–1080.
- Shanmugam, N.E., Richard Liew, J.Y. and Lee, S.L. (1989), 'Thin walled steel box columns under biaxial loading.' *J. Struct. Engng. ASCE*, **115**, 2706–2726.
- Uy, B. (1998), 'Local and post-local buckling of concrete-filled steel welded box columns.' *J. Const. St. Res.*, **47**, 47–72.
- Uy, B. (2000), 'Strength of concrete filled steel box columns incorporating local buckling.' *ASCE J. Struct. Engng.*, **126**, 341–352.
- Uy, B. and Bradford, M.A. (1994), 'Local buckling of concrete-filled high strength steel box columns for tall buildings: behaviour and design.' *Struct. Design Tall Buildings*, **3**, 75–93.
- Uy, B. and Bradford, M.A. (1996), 'Elastic local buckling of steel plate in composite steel–concrete.' *Engng Struct.* **18**(3), 193–200.
- Uy, B. and Das, S. (1997), 'Behaviour and design of concrete filled fabricated steel box columns.' *Proc. 15th Austr. Conf. on the Mechanics of Struct. and Materials*, Balkema, Rotterdam, December, ed. by R.H. Grzebieta, R. Al-Mahaidi and J.L. Wilson, 129–134.
- Uy, B. and Patil, S.B. (1996), 'Concrete-filled high strength steel box columns for tall buildings: behaviour and design.' *Struct. Design Tall Buildings*, **5**, 75–94.
- Wang, Y.C. (1999), 'Tests on slender composite columns.' *J. Constr. St. Res.*, **49**, 25–41.
- Wang, Y.C. and Moore, D.B. (1997), 'A design method for concrete-filled hollow section composite columns.' *Struct. Engr.*, **75**(21), 368–372.
- Watson, K.B. and O'Brien, L.J. (1990), 'Tubular composite columns and their development in Australia.' *Structural Engineering Conference*, Adelaide; 186–190.
- Wright, H.D. (1993), 'Buckling of plates in contact with a rigid medium.' *Struct. Engr.*, **71**(12), 209–215.
- Yang, Y.B. and Kuo, S.R. (1994), 'Theory and analysis of nonlinear framed structures.' Prentice Hall, Singapore.
- Yang, Y.B. and Shieh, M.S. (1990), 'Solution method for nonlinear problems with multiple critical points.' *AIAA J.*, **28**(12), 2110–2116.

11.7 Appendix: notation

The following symbols are used in this paper:

- A_s, A_c = elemental area of steel and concrete strips respectively
- b/t = breadth to thickness ratio
- D = depth/diameter of cross-section
- e_x = eccentricity about major axis
- e_y = eccentricity about minor axis
- E_s = elastic modulus of steel
- EI = flexural stiffness of cross-section
- EA = axial stiffness of cross-section
- f_y = yield strength of steel tube
- f_{cu} = compressive strength of concrete
- f_{yd}, f_{cd} = design strengths of structural steel and concrete respectively

- f_{sd} = design strength of steel tube
 F_{cs} = total compressive force in steel tube
 F_{st} = total tensile force in steel tube
 F_{cc} = total compressive force in concrete
 $\{F_{j-1}^i\}$ = vector of total internal elemental forces up to $(j - 1)$ th iteration of i th load increment
 GSP^i = generalised stiffness parameter at i th load increment
 k = buckling coefficient
 K = resultant curvature
 K_x, K_y = curvature about x - and y -axes respectively
 $[K]$ = structure stiffness matrix
 $[K_{j-1}^i]$ = tangent stiffness matrix formed at the beginning of the j th iteration of i th load increment
 L = length of column
 M = bending moment
 M_u = ultimate moment of resistance
 M_x, M_y = moment about x - and y -axes respectively
 $N_{pl,rd}$ = ultimate load of composite cross-section
 N_u = squash load of composite cross-section
 P = applied axial load
 P_{expt}, P_{test} = experimental strength of column
 P_{cal} = calculated strength of column by using the proposed analytical method
 $\{^2P\}$ = total load to be applied
 $\{^1P\}$ = external load at the beginning of the incremental step
 $\{P_j^i\}$ = vector of total external nodal loads at j th iteration of i th load increment
 $\{R_{j-1}^i\}$ = vector of unbalanced forces during $(j - 1)$ th iteration of i th load increment
 t = thickness of steel tube
 u, v = lateral deflection along x and y directions respectively
 $\{U\}$ = structure displacement vector
 x_c, x_s = distance from centroid of elemental area of concrete and steel respectively, to plastic centroid of the cross-section along x direction
 X, Y = intercepts of neutral axis with x - and y -axes
 y_c, y_s = distance from centroid of elemental area of concrete and steel respectively, to plastic centroid of the cross-section along y direction
 α = inclination of neutral axis with x -axis
 $\{\delta U_j^i\}$ = iterative displacement vector at j th iteration of i th load increment
 $\{\delta \bar{U}_j^i\}$ = iterative residual displacement vector at j th iteration of i th load increment

$\{\delta\hat{U}_j^i\}$ = iterative tangential displacement vector at j th iteration of i th load increment;

$\delta\lambda_1^1$ = initial load parameter

$\delta\lambda_1^i$ = iterative load parameter for the j th iteration of i th load increment

ε = strain at any fibre of cross-section

ε_{cc} = extreme concrete fibre strain

ε_o = strain at plastic centroid of cross-section

ε_u = crushing strain of concrete

φ = curvature

ρ_E = specified tolerance

σ_c, σ_s = stress in concrete and steel respectively

Analysis of corrugated web plates in bridge structures

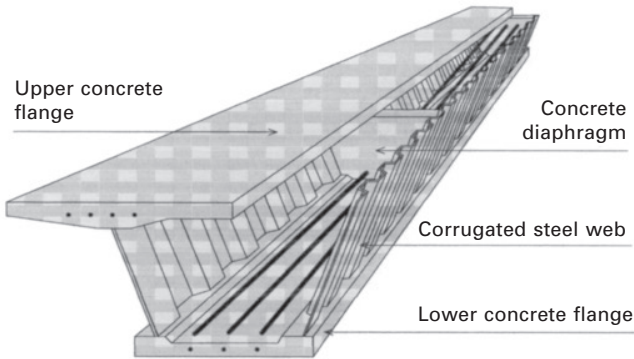
E WATANABE, C MACHIMDAMRONG and
T UTSUNOMIYA, Kyoto University, Japan,
M KANO, JIP Techno Science Corporation, Japan
and T KADOTANI, Japan Highway Public
Corporation, Japan

12.1 Introduction

This chapter describes in two parts the methods for predicting the buckling strength of corrugated webs. The first part introduces a simple but general plate model with edges elastically restrained against rotation to represent generally supported corrugated webs for accurate prediction of their elastic shear buckling capacities. The corrugated plates are modeled as orthotropic Mindlin plates. Elastic rotational springs are provided along the boundary edges of the plate to account for the torsional restraint from adjacent boundary members. The buckling loads of corrugated plates are predicted using the Ritz method. The proposed analysis covers the entire range of elastically and rotationally restrained plates, from simply supported to clamped edges, and transition curves of plate buckling capacities are presented. In the second part, material and geometrically nonlinear formulation is presented for evaluating the elasto-plastic buckling loads in practical problems. In this formulation, a finite element method is used to represent the folded plate structure, taking into consideration the elasto-plastic state and finite deformations. It will be shown that such analysis can predict the buckling results accurately as evidenced from experimental verifications that test the specimens into the highly nonlinear regions.

12.2 Elastic buckling of corrugated plates

Prestressed concrete girders with corrugated steel webs (*PCGCSW* for short), as shown in Fig. 12.1, is a new concrete–steel composite structural system that has been recently utilized in superstructures of highway bridges in France and Japan. The replacement of conventional flat steel webs by corrugated steel webs provides PCGCSW with a higher shear buckling capacity in the webs even without providing additional vertical stiffeners (Combault, 1992; Johnson and Cafolla, 1997; Research Group, 1998). The replacement of concrete webs by corrugated steel webs reduces the weight of the superstructure



12.1 Prestressed concrete girder with corrugated steel webs, PCGCSW.

significantly. In addition, the corrugated webs contribute little to the longitudinal stiffness of PCGCSW so that the prestressing forces can be easily and precisely introduced in the concrete flanges. Despite its many advantages over conventional girders, uncertainties and problems concerning analysis and design of PCGCSW still persist and require further studies.

In view of the fact that corrugated plates extend three-dimensionally, the rigorous analysis similarly requires a three-dimensional treatment, demanding large computer memory and fast computation methods. In this respect, replacing such a three-dimensional structure by an ideal orthotropic plate may considerably reduce the computational difficulty. This simplified approach by approximating the corrugated plate with an orthotropic plate is used in the subsequent formulation to overcome the three-dimensional problems. To treat the supporting conditions of the corrugated plates, the Mindlin plate theory is applied since the boundary conditions can be specified in a more exact manner when compared with Kirchhoff's thin plate theory.

In predicting the elastic shear buckling capacity of the plate, a formula has been derived by Easley (1975) on the basis of Kirchhoff's thin plate theory and simply supported conditions. This formula is adopted in the design manual of prestressed concrete box girders with corrugated steel webs and was proposed by the Research Group of Composite Structures with Corrugated Steel Webs of Japan (Research Group, 1998).

Buckling analysis of corrugated plates is, in general, based on the assumption that the plate is an orthotropic flat plate with an equivalent stiffness (Easley, 1975; Timoshenko and Gere, 1963). To verify the validity of such an assumption, experiments and numerical analyses seem to be the only solutions (Easley and McFarland, 1969; Luo and Edlund, 1996; Elgaaly *et al*, 1996). By regarding the corrugated plate as an orthotropic plate, a number of analytical approaches have been proposed that involves considering vibration problems (Stein and Housner, 1978; Dickinson and Blasio, 1986). Nonclassical edge

conditions were studied by Laura and Luisoni (1978), Laura and Grossi (1978), Mizusawa and Kajita (1987) and Chang and Chang (1997).

In contrast to the Kirchhoff thin plate theory, the Mindlin plate theory takes into account the effect of transverse shear deformation which becomes very important in thick plates (Mindlin, 1951). Dawe and Roufaeil (1980) studied the vibration of the Mindlin plate by the Ritz method. Marinetti and Oliveto (1995) derived general solution and stiffness matrices for the vibration and buckling Mindlin plate problems by making use of sinusoidal functions. The vibration analysis on Mindlin plates with nonclassical boundary conditions can be found in the works of Chung *et al.* (1993), and Saha and Kar (1996).

The aim of this chapter is to make a more precise prediction of the elastic shear buckling capacity of corrugated plates, especially when their edges are restrained against rotation. The Mindlin plate theory is adopted to model the plates. The Ritz method is employed with trigonometric series selected as the trial functions, as these functions satisfy the geometric boundary conditions. The elastic shear buckling capacity of the plate is then calculated by a standard eigenvalue extraction procedure.

12.2.1 Orthotropic rectangular Mindlin plate

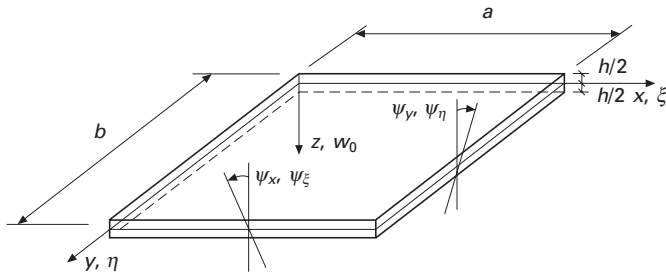
The theoretical analysis is based on the assumption that a corrugated web can be analyzed as a rectangular, orthotropic, and flat plate with uniform thickness. This assumption was proposed by Easley and McFarland (1969) with the following conditions:

- The number of repeating corrugations between diaphragms is sufficiently large and the dimension of the corrugations is small enough;
- The overall buckling behavior is focused rather than the localized buckling phenomena;
- The buckled patterns do not depend on the local corrugation shapes.

By adopting the Mindlin plate theory, the displacement fields can be expressed in the following form:

$$\begin{aligned} u(x, y, z) &= z\psi_x(x, y) \\ v(x, y, z) &= z\psi_y(x, y) \\ w(x, y, z) &= w_0(x, y) \end{aligned} \tag{12.1}$$

where $u(x, y, z)$, $v(x, y, z)$, $w(x, y, z)$, $w_0(x, y)$, ψ_x and ψ_y refer to the displacements along the x -, y -, z -axes and in the middle surface, the rotations in the x - and y -directions, respectively as shown in Fig. 12.2. By adopting infinitesimal displacement theory, the cross-sectional rotations of the plate, ψ_x and ψ_y , shearing strains, γ_{xz} and γ_{yz} , and the displacement of the plate, w_0 , are related as follows:



12.2 Mindlin plate geometry.

$$\psi_x(x, y) = \gamma_{xz} - \frac{\partial w_0}{\partial x}$$

$$\psi_y(x, y) = \gamma_{yz} - \frac{\partial w_0}{\partial y} \tag{12.2}$$

The relationship between the stress and strain for orthotropic material in the plane stress condition is given by:

$$\sigma = D\varepsilon \tag{12.3}$$

where σ and ε represent the stress and the strain in vector forms and are given respectively by:

$$\sigma^T = [\sigma_x \ \sigma_y \ \tau_{xy} \ \tau_{xz} \ \tau_{yz}] \tag{12.4}$$

$$\varepsilon^T = [\varepsilon_x \ \varepsilon_y \ \gamma_{xy} \ \gamma_{xz} \ \gamma_{yz}] \tag{12.5}$$

and D is the elastic constitutive matrix given by:

$$D = \begin{bmatrix} \frac{E_x}{1 - \nu_x \nu_y} & \frac{\nu_x E_x}{1 - \nu_x \nu_y} & 0 & 0 & 0 \\ \frac{\nu_y E_x}{1 - \nu_x \nu_y} & \frac{E_y}{1 - \nu_x \nu_y} & 0 & 0 & 0 \\ 0 & 0 & G_{xy} & 0 & 0 \\ 0 & 0 & 0 & K_x G_{xz} & 0 \\ 0 & 0 & 0 & 0 & K_y G_{yz} \end{bmatrix} \tag{12.6}$$

where E_x and E_y refer to the modulus of elasticity in the x - and y -directions, respectively; ν_x refers to Poisson's ratio, designating the transverse strain in the y -direction when a unit stress is applied in the x -direction and ν_y Poisson's ratio designating the transverse strain in the x -direction when a unit stress is applied in the y -direction; K_x and K_y refer to the transverse shear correction coefficients in the $x - z$ and $y - z$ planes; G_{xy} , G_{xz} and G_{yz} denote the shear modulus of elasticity in $x - y$, $x - z$ and $y - z$ planes, respectively.

The strain energy U_1 stored in the plate can be obtained from the aforementioned stress-strain relationship and Hooke's law as:

$$\begin{aligned}
 U_1 = \int_V \boldsymbol{\varepsilon}^T D \boldsymbol{\varepsilon} dV = \frac{1}{2} \int_0^b \int_0^a \{ & (v_y D_x + v_x D_y) \frac{\partial \psi_x}{\partial x} \frac{\partial \psi_y}{\partial y} \\
 & + D_x \left(\frac{\partial \psi_x}{\partial x} \right)^2 + D_y \left(\frac{\partial \psi_y}{\partial y} \right)^2 + D_{xy} \left(\frac{\partial \psi_x}{\partial y} + \frac{\partial \psi_y}{\partial x} \right)^2 \\
 & + K_x h G_{xz} \left(\psi_x + \frac{\partial w_0}{\partial x} \right)^2 + K_y h G_{yz} \left(\psi_y + \frac{\partial w_0}{\partial y} \right)^2 \} dx dy
 \end{aligned}$$

12.7

where

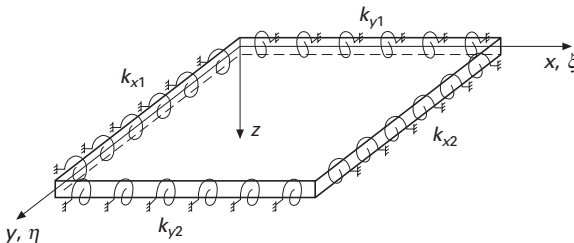
$$D_x = \frac{E_x h^3}{12(1 - \nu_x \nu_y)}, D_y = \frac{E_y h^3}{12(1 - \nu_x \nu_y)}, D_{xy} = \frac{G_{xy} h^3}{12}$$

and h denotes the plate thickness.

Figure 12.3 shows a general plate elastically restrained against rotations along the edges. This elastic restraint covers the two extreme cases of edge conditions, viz. simply supported edge and clamped edge (Chung *et al.*, 1993). Let k_{x1} , k_{x2} , k_{y1} and k_{y2} represent the rotational spring constants in the x -direction along the edges $x = 0$ and $x = a$; in the y -direction along the edges $y = 0$ and $y = b$, respectively. The strain energy stored in the rotational springs, U_2 , can be expressed as:

$$\begin{aligned}
 U_2 = \frac{1}{2} \int_0^a (k_{y1} \psi_y^2|_{y=0} + k_{y2} \psi_y^2|_{y=b}) dx \\
 + \frac{1}{2} \int_0^b (k_{x1} \psi_x^2|_{x=0} + k_{x2} \psi_x^2|_{x=a}) dy
 \end{aligned}$$

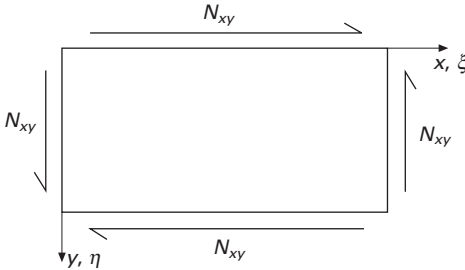
12.8



12.3 A plate with rotational springs.

The potential energy V_1 of the plate due to the in-plane shear load, N_{xy} , as shown in Fig. 12.4, is given by:

$$V_1 = - \int_0^b \int_0^a N_{xy} \frac{\partial w_0}{\partial x} \frac{\partial w_0}{\partial y} dx dy \tag{12.9}$$

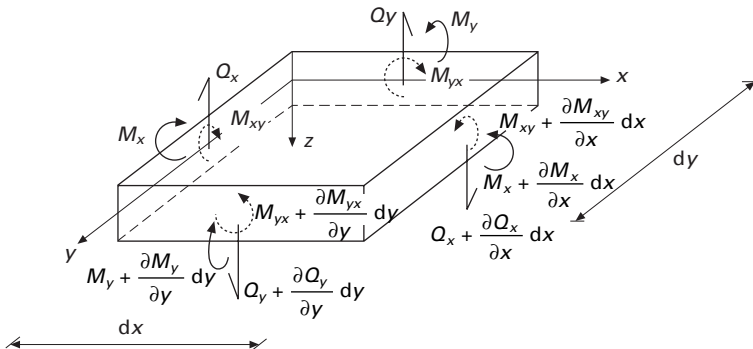


12.4 A plate under in-plane shear.

The potential energy of the external loads V_2 as shown in Fig. 12.5 is given by:

$$\begin{aligned} V_2 = & \int_0^a [(M_y \psi_y + M_{yx} \psi_x + Q_y w_0)|_{y=b} \\ & - (M_y \psi_y + M_{yx} \psi_x + Q_y w_0)|_{y=0}] dx \\ & - \int_0^b [(M_x \psi_x - M_{xy} \psi_y + Q_x w_0)|_{x=a} \\ & - (M_x \psi_x - M_{xy} \psi_y + Q_x w_0)|_{x=0}] dy \end{aligned} \tag{12.10}$$

where M_x refers to the bending moment in the x -direction, and M_{xy} the



12.5 Notations for stress resultants.

twisting moment in the x -direction around the x -axis along the y -direction, respectively.

The total potential energy functional Π of a rectangular orthotropic Mindlin plate can be written as follows:

$$\Pi = U_1 + U_2 + V_1 + V_2 \tag{12.11}$$

12.2.2 Ritz method

For determining the buckling load, the Ritz method is used. Crucial to this method is the selection of an admissible trial function. Here we adopt the trigonometric series that satisfy the following hard-type simply supported edge conditions (Liew *et al.*, 1998):

$$\begin{aligned} w_0(\xi, \eta) &= \sum_{i=1}^m \sum_{j=1}^n A_{ij} \sin(i\pi\xi) \sin(j\pi\eta) \\ \psi_\xi(\xi, \eta) &= \sum_{i=1}^m \sum_{j=1}^q B_{ij} \cos(i\pi\xi) \sin(j\pi\eta) \\ \psi_\eta(\xi, \eta) &= \sum_{i=1}^r \sum_{j=1}^s C_{ij} \sin(i\pi\xi) \cos(j\pi\eta) \end{aligned} \tag{12.12}$$

where $\xi = x/a$ and $\eta = y/b$, respectively. These series always result in $w_0 = 0$ along all edges and $\psi_\xi = 0$ on $y = 0$ and $y = b$. However $\psi_\eta \neq 0$ on $x = 0$ and $x = a$. The total potential energy functional Π can be obtained by substituting Eqs (12.7) to (12.10) into Eq. (12.11):

$$\begin{aligned} \Pi &= \frac{1}{2\alpha} \int_0^1 \int_0^1 \{ \alpha(v_y D_x + v_x D_y) \frac{\partial \psi_\xi}{\partial \xi} \frac{\partial \psi_\eta}{\partial \eta} \\ &+ D_x \left(\frac{\partial \psi_\xi}{\partial \xi} \right)^2 + \alpha^2 D_y \left(\frac{\partial \psi_\eta}{\partial \eta} \right)^2 \\ &+ D_{xy} \left(\alpha \frac{\partial \psi_\xi}{\partial \eta} + \frac{\partial \psi_\eta}{\partial \xi} \right)^2 + K_x h G_{xz} \left(\alpha \psi_\xi + \frac{\partial w_0}{\partial \xi} \right)^2 \\ &+ \alpha^2 K_y h G_{yz} \left(b \psi_y + \frac{\partial w_0}{\partial \eta} \right)^2 - 2\alpha N_{xy} \left(\frac{\partial w_0}{\partial \xi} \frac{\partial w_0}{\partial \eta} \right) \} d\xi d\eta \\ &+ \frac{\alpha D_y}{2} \int_0^1 (K_{y1} \psi_\eta^2|_{\eta=0} + K_{y2} \psi_\eta^2|_{\eta=1}) d\xi \\ &+ \frac{D_x}{2\alpha} \int_0^1 (K_{x1} \psi_\xi^2|_{\xi=0} + K_{x2} \psi_\xi^2|_{\xi=1}) d\eta \end{aligned} \tag{12.13}$$

where $\alpha = a/b$.

For convenience, the following dimensionless parameters of elastically rotational springs will be defined in the x - and y -directions, respectively:

$$\begin{aligned} K_{x1} &= \frac{ak_{x1}}{D_x} \quad \text{and} \quad K_{x2} = \frac{ak_{x2}}{D_x} \\ K_{y1} &= \frac{bk_{y1}}{D_y} \quad \text{and} \quad K_{y2} = \frac{bk_{y2}}{D_y} \end{aligned} \quad 12.14$$

The potential energy of the load expressed by Eq. (12.10) vanishes naturally for the case of hard-type, simply supported edges. By substituting the trigonometric series given in Eq. (12.12) into the total potential energy, and after differentiation with respect to the Ritz coefficients A_{ij} , B_{ij} and C_{ij} , the following equations are obtained:

$$\begin{aligned} \frac{\partial \Pi}{\partial A_{ij}} &= \frac{h}{4\alpha} \{K_x G_{xz} (i\pi)^2 + \alpha^2 K_y G_{yz} (j\pi)^2\} A_{ij} \\ &+ \frac{\alpha K_x h G_{xz}}{4\alpha} (i\pi) B_{ij} + \frac{\alpha b K_y h G_{yz}}{4} (j\pi) C_{ij} \\ &- N_{xy} \sum_{\substack{k=1 \\ i \pm k = \text{odd}}}^m \sum_{\substack{l=1 \\ j \pm l = \text{odd}}}^n \frac{8ijkl}{(k^2 - i^2)(j^2 - l^2)} A_{kl} = 0 \end{aligned} \quad 12.15$$

$$\begin{aligned} \frac{\partial \Pi}{\partial B_{ij}} &= \frac{aK_x h G_{xz}}{4\alpha} (i\pi) A_{ij} \\ &+ \frac{1}{4\alpha} \{D_x (i\pi)^2 + \alpha^2 D_{xy} (j\pi)^2 + K_x h G_{xz} a^2\} B_{ij} \\ &+ \frac{D_x}{2} \sum_{k=1}^p \{k_{x1} + k_{x2} (-1)^{i+k}\} B_{kj} \\ &+ \frac{1}{8} \{v_x D_y + v_y D_x\} + 2D_{xy} \{i\pi\} (j\pi) C_{ij} = 0 \end{aligned} \quad 12.16$$

$$\begin{aligned} \frac{\partial \Pi}{\partial C_{ij}} &= \frac{abK_y h G_{yz}}{4} (j\pi) A_{ij} \\ &+ \frac{1}{8} \{v_x D_y + v_y D_x\} + 2D_{xy} \{i\pi\} (j\pi) B_{ij} \\ &+ \frac{1}{4\alpha} \{\alpha^2 D_y (j\pi)^2 + D_{xy} (i\pi)^2 + \alpha^2 K_y h G_{yz} b^2\} C_{ij} \\ &+ \frac{\alpha^2 D_y}{2} \sum_{l=1}^s \{k_{y1} + k_{y2} (-1)^{j+k}\} C_{il} = 0 \end{aligned} \quad 12.17$$

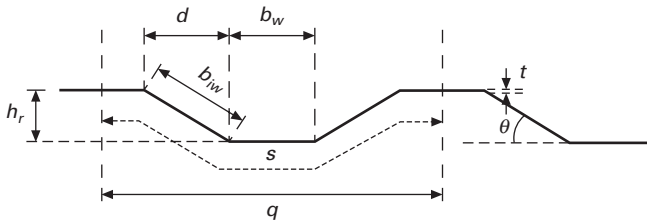
The foregoing equations can be rearranged and written in the following matrix form:

$$\begin{bmatrix} K'_{11} & K'_{12} & K'_{12} \\ \cdot & K'_{22} & K'_{23} \\ \text{Sym} & \cdot & K'_{33} \end{bmatrix} \begin{pmatrix} A_{ij} \\ B_{ij} \\ C_{ij} \end{pmatrix} - N_{xy} \begin{pmatrix} A_{ij} \\ 0 \\ 0 \end{pmatrix} = \begin{pmatrix} 0 \\ 0 \\ 0 \end{pmatrix} \quad 12.18$$

If m, n, p, q, r and s in Eq. (12.12) are all taken to be equal to n , the size of the stiffness matrix will be $3n^2 \times 3n^2$. The overall elastic shear buckling load of a plate is then calculated by finding the solution of the eigenvalue problem given by Eq. (12.18). This can be done through a conventional eigenvalue extraction procedure.

12.2.3 Equivalent elastic constants for orthotropic plate

In order to carry out an analysis based on the foregoing formulation, a corrugated plate will be conveniently transformed into an equivalent orthotropic, shear deformable plate with appropriate structural moduli. Elastic constants required for this purpose are flexural stiffnesses in two principal directions D_x and D_y , torsional stiffness D_{xy} , plate stiffness $\nu_x D_y + \nu_y D_x$ and transverse shear stiffnesses in two principal directions, $K_x h G_{xz}$ and $K_y h G_{yz}$, respectively. The evaluation of the elastic constants may be made in reference to Fig. 12.6 which shows the cross-section of a corrugated plate. For convenience, the directions of the lowest flexural plate stiffness and the highest are designated by x - and y -directions, respectively as shown in Fig. 12.7.

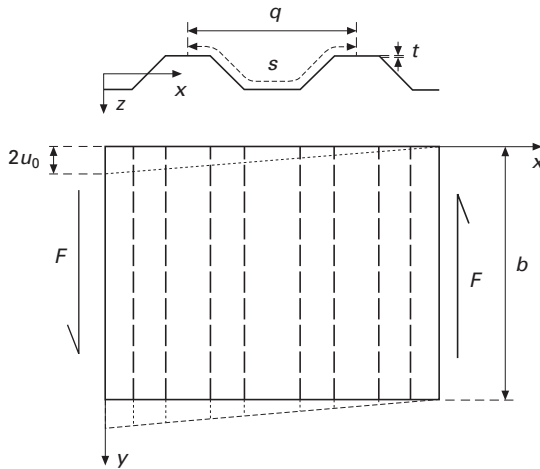


12.6 Cross-sectional geometry of a corrugated plate.

Flexural stiffness

The equivalent flexural stiffness in the x -direction D_x , and the y -direction D_y , can be approximated by (Easley and McFarland, 1969; Peterson and Cord, 1960):

$$D_x = \frac{q}{s} \frac{Et^3}{12} \quad 12.19$$



12.7 A corrugated plate under simple in-plane shear.

$$D_x = \frac{EI_y}{q} \tag{12.20}$$

The moment of inertia in the y-direction, in Eq. (12.20), can be calculated by the following equation:

$$I_y = 2 \left(b_w t \frac{h_r^2}{4} + \frac{b_w t^3}{12} + \frac{b_{iw}^3 t}{12} \sin^2 \theta \right) \tag{12.21}$$

Although the plate stiffness $(v_x D_y + v_y D_x + 2D_{xy})/2$ is usually neglected (Peterson and Card, 1960), the term involving D_{xy} was retained as suggested by Easley and McFarland (1969). The terms $v_x D_y + v_y D_x$ can also be neglected when $D_y \gg D_x$, which is usually the case for corrugated plates (Easley and McFarland, 1969).

In design manuals, the equivalent flexural stiffnesses are defined by (Research Group, 1998):

$$D_x = \frac{Et^3}{12(1 - \nu^2)} \tag{12.22}$$

$$D_y = \frac{s}{q} \frac{E(t^3 + th_r^2)}{6} \tag{12.23}$$

Equation (12.19) is used to represent the flexural stiffness of the plate in the same way as a curved beam, while Eq. (12.22) assumes that the plate is flat without any corrugation. The flexural stiffness in the y-direction is given exactly by Eq. (12.20) but may be approximated by Eq. (12.23).

Torsional stiffness

The effective shear modulus of elasticity, G_{xy}^{eff} in the equation must be considered with respect to the corrugated configuration and the method of attachment. For a corrugated plate that attaches continuously to the supports, the shear strain due to uniform in-plane shear load is also uniform throughout the material (Hussain and Libove, 1976; Rothwell, 1968). In short, the shear modulus G of material is equal to the ratio of the uniform shear stress, $F/(bt)$, and the shear strain in the corrugated plate is u_0/s as shown in Fig. 12.7, where $s (= 2b_w + 2b_{iw})$ refers to the developed width of a single corrugation and u_0 refers to the vertical displacement. However, for an equivalent orthotropic plate, the shear strain in the plate is u_0/q . Thus, the effective shear modulus G_{xy}^{eff} can be defined as $G_{xy}^{eff} = Gq/s$. The equivalent torsional stiffness D_{xy} of the corrugated plate, after substituting the relationship $G = E/[2(1 + \nu)]$ of an isotropic material, can be expressed as:

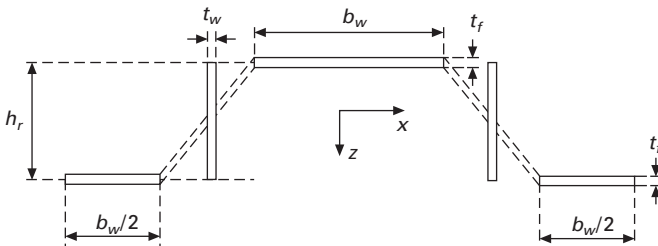
$$D_{xy} = \frac{s}{q} \frac{Et^3}{6(1 + \nu)} \tag{12.24}$$

which is exactly the same as that used by Easley and McFarland (1969).

In the case of a discrete attachment, the effective shear modulus is lower than that given in Eq. (12.24), depending on the method of attachment (Hussain and Libove, 1976; Rothwell, 1968).

Transverse shear stiffness

In order to estimate the transverse shear stiffness in the y -direction, $K_y h G_{yz}$, one wavelength of the corrugated web is simply considered as a simple beam. Inclined strips of cross-section of a corrugated web were made presumably at right-angles to the remaining parts with the equivalent cross-sectional area as shown in Fig. 12.8. The formula for estimating the transverse shear correction factor for a thin-walled rectangular tube, which is mathematically equivalent to the transformed section, is (Omidvar, 1998):



12.8 Transformed cross-section of corrugated web to approximate transverse shear stiffness.

$$K_y = \frac{H_1}{H_2 + rv(H_3 + H_4 + H_5 + H_6)} \quad 12.25$$

where

$$H_1 = 10(1 + 3m)^2;$$

$$H_2 = 12 + 72m + 150m^2 + 90m^3 + 30n^2m(1 + m);$$

$$H_3 = -2 + 3m + 15m^2; H_4 = -n^2(25m + 15m^2);$$

$$H_5 = -n^2(15m + 45m^2); H_6 = -15m - 45m^2$$

$$m = \frac{b_w t_f}{h_r t_w}, n = \frac{b_w}{h_r}, r = \frac{G}{E}, t_f = t, t_w = \frac{b_{iw} t}{h_r}$$

The thickness h in K_y for the transverse shear stiffness is replaced with the average thickness t_{av} of the corrugated section, i.e.

$$t_{av} = \frac{st}{q} \quad 12.26$$

The shear modulus, G_{yz} , is simply given by the plate shear modulus G . For the transverse shear stiffness factor in the x -direction, $K_x h G_{xz}$ the average thickness of the corrugated section is used and the shear correction factor, K_x , is taken as $5/(6 - \nu)$ (Stephen, 1997).

12.2.4 Elastically supported orthotropic Mindlin plates

Folding of flat metal sheets into corrugated sheets is well known to provide higher shear buckling capacity than the unfolded (flat) ones. This can be anticipated by considering the formula for global shear buckling capacity of flat plates that directly relates to the flexural stiffnesses that considerably increase when the plates are corrugated. The formula for global elastic shear buckling capacity of the corrugated plates has been derived by Easley (1975), and is adopted in the design manual for PCGCSW. However, the formula was based on Kirchhoff's thin plate theory with simply supported edges. This raises the question on the feasibility of the application of the formula for general edge conditions. Therefore, to make a more precise prediction on the global elastic shear buckling strength of corrugated web plates, we propose that they be modeled as orthotropic rectangular thick plates (Mindlin plates). Elastically rotational restraints on their boundary edges are considered and taken into account in the form of rotational springs. The prediction of the buckling capacity of such plates is carried out by using the Ritz method. The general elastic rotationally restraint condition covers the limiting boundary conditions of the simply supported and clamped edges and, therefore, we could show the transition curves of plate buckling capacities from the case of

simply supported to the case of clamped support by viewing the entire range of rotational restrained condition.

12.2.5 Elastic buckling analysis

Three different simple geometric shapes of corrugated plates are studied. The wavelength of each corrugated shape, q , is fixed at 125 mm. Equal panel width is considered, i.e. $b_w = b_{iw}$. Only the angle of horizontal inclination θ is varied at 30, 37 and 45 degrees. The constant thickness t of the plates is taken to be 2 mm. The relevant dimension parameters, as shown in Fig. 12.6, are then derived consequently. The material is assumed to be elastic with Young's modulus $E = 2.06 \times 10^{11}$ N/m² and Poisson's ratio $\nu = 0.3$.

The calculations are made for six different plates with various combinations of three angles of horizontal inclination θ , with plate dimensions $a \times b = 1 \text{ m} \times 1 \text{ m}$ and $a \times b = 2 \text{ m} \times 1 \text{ m}$. In each case, only simple or fixed edges in the x -direction are considered whereas the supported edges in the y -direction are considered to be restrained by elastically rotational springs and their stiffnesses vary uniformly from 1.0 to 10^{10} Nm/m so as to cover the stiffness range of simply supported to fixed supported cases.

The flexural stiffnesses, D_x and D_y approximated by Eqs (12.19) and (12.20) will be referred to as Approximate Formula 1, and those by Eqs (12.22) and (12.23) as Approximate Formula 2. The dimension parameters and calculated elastic constants of the plates are summarized in Table 12.1.

Table 12.1 Parameters of corrugated plates

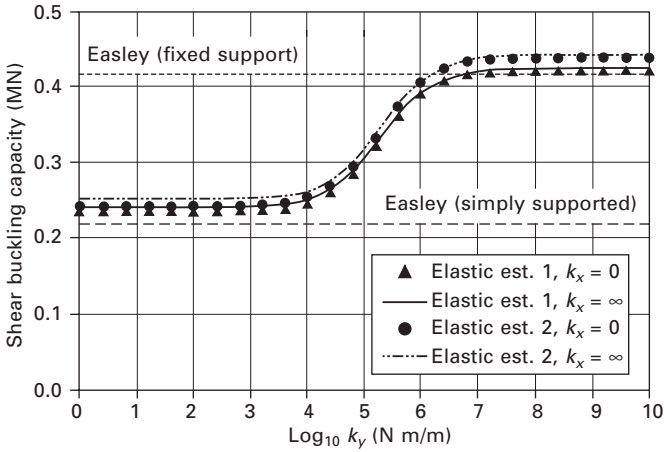
Plate parameters		Angle of inclination (°)		
		30	37	45
q	[mm]		125	
s	[mm]	133.97	138.99	146.45
h_r	[mm]	16.75	20.91	25.89
^a D_x	[10 ² N m ² /m]	1.2814	1.2351	1.1723
^a D_y	[10 ⁴ N m ² /m]	2.0715	3.3469	5.4000
^b D_x	[10 ² N m ² /m]	1.5092	1.5092	1.5092
^b D_y	[10 ⁴ N m ² /m]	2.0936	3.3698	5.4241
D_{xy}	[10 ³ N m ² /m]	2.2646	3.0543	3.2181
K_x		0.8772	0.8772	0.8772
K_y		0.2644	0.3098	0.3463

^a Approximate formula 1 [Eqs (12.19) and (12.20)]

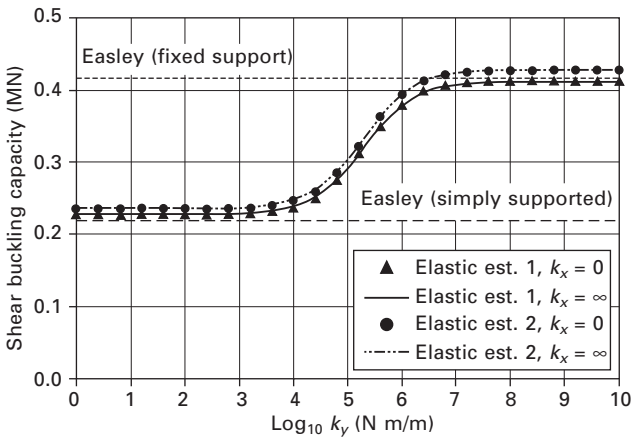
^b Approximate formula 2 [Eqs (12.22) and (12.23)]

12.2.6 Numerical results and discussion

The computed shear buckling capacities are shown in Figs 12.9 to 12.14. Note that $k_x = 0$ and $k_x = \infty$ in the figures are associated with simply supported



12.9 Shear buckling capacity for 1 m x 1 m plate with $\theta = 30^\circ$.

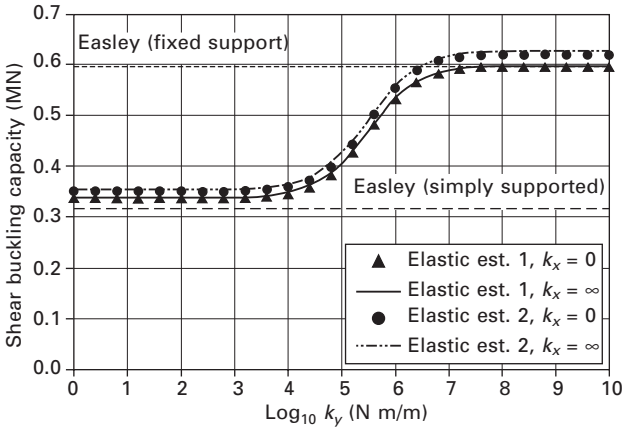


12.10 Shear buckling capacity for 2 m x 1 m plate with $\theta = 30^\circ$.

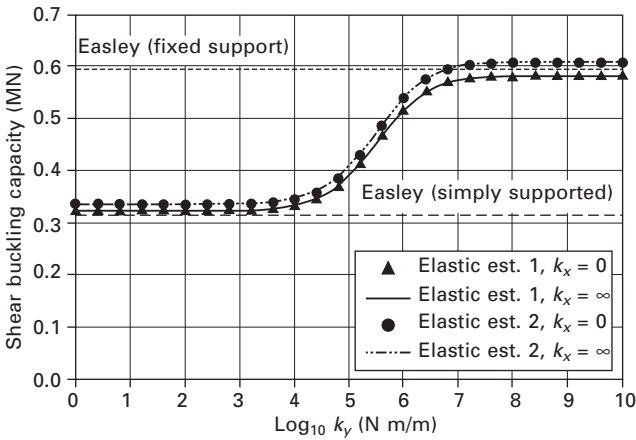
and fixed edges in the x -direction, respectively. Two horizontal lines in the figures show the estimated buckling capacities that are calculated using Easley's formula or the design formula adopted by the Research Group (1998). The upper and lower lines represent predicted buckling capacities of the plates with fixed and simply supported edges in the y -direction. Easley's formula is given by:

$$P_{cr,G}^e = 36\beta \frac{\sqrt[4]{D_x D_y^3}}{b} \tag{12.27}$$

where β is set to be either 1.0 or 1.9 for plates with simply supported or fixed



12.11 Shear buckling capacity for 1 m × 1 m plate with $\theta = 37^\circ$.

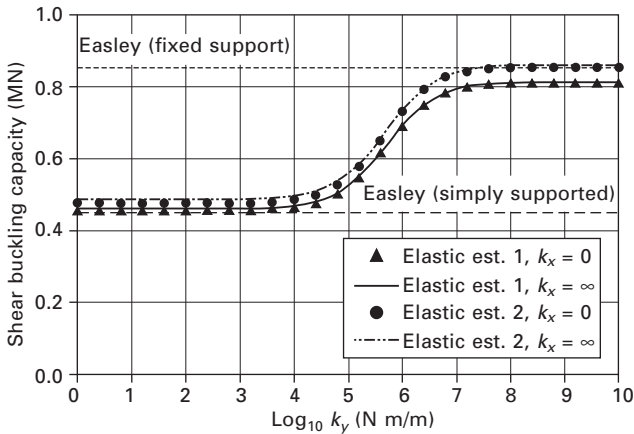


12.12 Shear buckling capacity for 2 m × 1 m plate with $\theta = 37^\circ$.

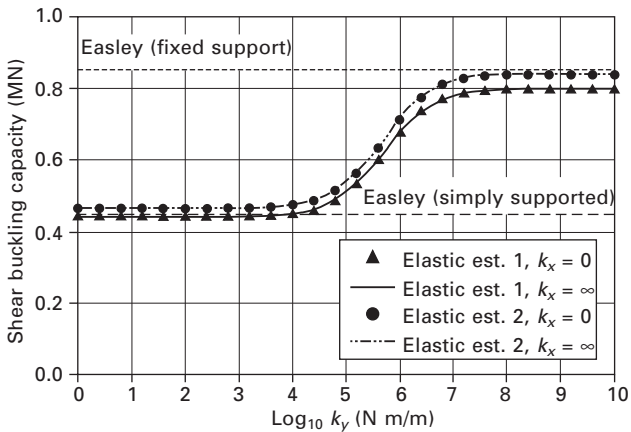
edges in y-direction, respectively and the flexural stiffnesses, D_x and D_y , are calculated from Approximate Formula 2.

From the figures, it is found that the Ritz analyses yield buckling capacities in agreement with those calculated by Eq. (12.27) for both simply supported and fixed edges. For plates with high aspect ratios (i.e. 2 m × 1 m), the Ritz analyses yield buckling capacities that are lower than those associated with plates having low aspect ratios (i.e. 1 m × 1 m). This result is expected from the elementary shear buckling analysis of plates.

The difference in buckling capacities calculated on the basis of Approximate Formulas 1 and 2 may be considered to be small.



12.13 Shear buckling capacity for 1 m × 1 m plate with $\theta = 45^\circ$.



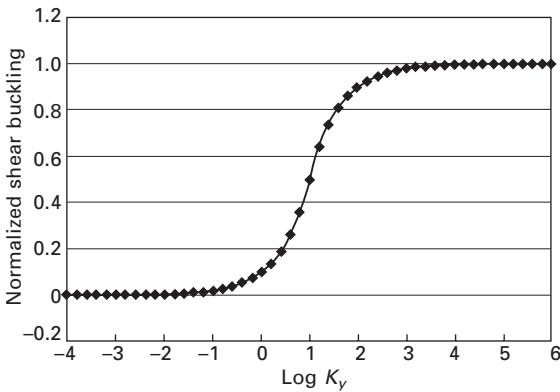
12.14 Shear buckling capacity for 2 m × 1 m plate with $\theta = 45^\circ$.

12.2.7 Effect of rotational restraint

As can be seen in all Figs 12.9 to 12.14, by increasing the stiffness of rotational restraint k_y , the buckling capacity of the plate increases from the value associated with a simply supported edge to that of a fixed edge. The shift in buckling capacity is evident over a specific range of stiffness. On the other hand, for a given rotational restraint stiffness in the y -direction, no significant difference is observed in the buckling capacities of plates with simply supported and with fixed edges in the x -direction. It is clear that the supported edges in the direction of plate's lower flexural stiffness (x -direction) can be neglected when estimating the buckling capacities of corrugated plates.

When the rotational spring constant in the y -direction is made dimensionless by Eq. (12.14), it is found that there is a specific transition zone of buckling

capacity from that of a simple supported edge to a fixed edge. The transition zone spans over a specific range of rotational stiffness, regardless of the corrugated shapes and dimensions. The dimensionless rotational spring constant of approximately 10^{-2} is found to be the lower bound or equivalent to the simply supported case. For the upper bound or the fixed support case, the dimensionless value may be taken as 10^4 as can be seen from Fig. 12.15. Therefore, one can fully realize the maximum resistance of corrugated plates to shear buckling if the dimensionless rotational restraint parameter can be made to take the value of 10^4 .



12.15 Non-dimensionalized shear buckling strength vs non-dimensionalized rotational restraint parameter, K_y .

12.3 Elasto-plastic and finite displacement analysis of plates

The theory of elasto-plastic and finite displacement analysis of steel plated structures is formulated under the following assumptions and idealizations (Komatsu *et al.*, 1975, Kano *et al.*, 1997):

- Material constituting the steel plates is homogeneous and isotropic, and the elasto-plastic body is isotropic, kinematic, and combined strain hardening that obeys von Mises' yield criterion as well as the associated flow rule.
- Kirchhoff's hypothesis is valid for plate panels.
- Each finite plate element is divided into several layered sub-elements. Stress and stiffness in each layer changes linearly in the direction perpendicular to the layer.

12.3.1 Deformation of plate

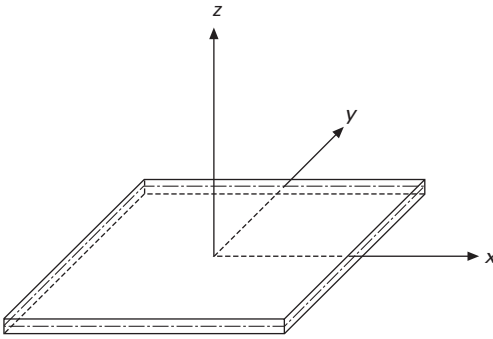
Displacement function

Figure 12.16 shows the coordinate axes used for the considered plate. Let $\Delta u(x, y)$, $\Delta v(x, y)$ and $\Delta e(x, y)$ be the displacement increment for the x -, y - and z -direction of a point (x, y) on the neutral surface of the plate, respectively. Following Kirchhoff's hypothesis, the displacement increments of an arbitrary point in the plate can be expressed as:

$$\Delta U(x, y, z) = \Delta u(x, y) - z \frac{\partial \Delta w(x, y)}{\partial x} \quad 12.28$$

$$\Delta V(x, y, z) = \Delta v(x, y) - z \frac{\partial \Delta w(x, y)}{\partial y} \quad 12.29$$

$$\Delta W(x, y, z) = \Delta w(x, y) \quad 12.30$$



12.16 Coordinate axes used for plate model.

Relationship between strains and displacements

The strain increments of an arbitrary point in the plate can be represented as follows:

$$\Delta \varepsilon_x = \frac{\partial \Delta U}{\partial x} + \frac{1}{2} \left(\frac{\partial \Delta W}{\partial x} \right)^2 = \frac{\partial \Delta u}{\partial x} - z \frac{\partial^2 \Delta w}{\partial x^2} + \frac{1}{2} \left(\frac{\partial \Delta w}{\partial x} \right)^2 \quad 12.31$$

$$\Delta \varepsilon_y = \frac{\partial \Delta V}{\partial y} + \frac{1}{2} \left(\frac{\partial \Delta W}{\partial y} \right)^2 = \frac{\partial \Delta v}{\partial y} - z \frac{\partial^2 \Delta w}{\partial y^2} + \frac{1}{2} \left(\frac{\partial \Delta w}{\partial y} \right)^2 \quad 12.32$$

$$\begin{aligned} \Delta \gamma_{xy} &= \frac{\partial \Delta V}{\partial x} + \frac{\partial \Delta U}{\partial y} + \frac{\partial \Delta W}{\partial x} \frac{\partial \Delta W}{\partial y} \\ &= \frac{\partial \Delta v}{\partial x} + \frac{\partial \Delta u}{\partial y} - z \left(2 \frac{\partial^2 \Delta w}{\partial x \partial y} \right) + \frac{\partial \Delta w}{\partial x} \frac{\partial \Delta w}{\partial y} \end{aligned} \quad 12.33$$

Let $\Delta\boldsymbol{\epsilon} = (\Delta\epsilon_x \quad \Delta\epsilon_y \quad \Delta\gamma_{xy})^T$ be the incremental strain vector. From Eqs (12.31)–(12.33), the following equation can be obtained:

$$\Delta\boldsymbol{\epsilon} = \begin{Bmatrix} \Delta\epsilon_x \\ \Delta\epsilon_y \\ \Delta\gamma_{xy} \end{Bmatrix} = \begin{Bmatrix} \frac{\partial\Delta u}{\partial x} \\ \frac{\partial\Delta v}{\partial y} \\ \frac{\partial\Delta v}{\partial x} + \frac{\partial\Delta u}{\partial y} \end{Bmatrix} - z \begin{Bmatrix} \frac{\partial^2\Delta w}{\partial x^2} \\ \frac{\partial^2\Delta w}{\partial y^2} \\ 2\frac{\partial^2\Delta w}{\partial x\partial y} \end{Bmatrix} + \begin{Bmatrix} \frac{1}{2}\left(\frac{\partial\Delta w}{\partial x}\right)^2 \\ \frac{1}{2}\left(\frac{\partial\Delta w}{\partial y}\right)^2 \\ \frac{\partial\Delta w}{\partial x} \frac{\partial\Delta w}{\partial y} \end{Bmatrix} \quad 12.34$$

This incremental strain vector can be divided into a linear term and a non-linear term, namely,

$$\Delta\boldsymbol{\epsilon} = \Delta\boldsymbol{\epsilon}_L + \Delta\boldsymbol{\epsilon}_{NL} \quad 12.35$$

The linear and the non-linear terms are expressed as follows:

$$\Delta\boldsymbol{\epsilon}_L = \begin{Bmatrix} \frac{\partial\Delta u}{\partial x} \\ \frac{\partial\Delta v}{\partial y} \\ \frac{\partial\Delta v}{\partial x} + \frac{\partial\Delta u}{\partial y} \end{Bmatrix} - z \begin{Bmatrix} \frac{\partial^2\Delta w}{\partial x^2} \\ \frac{\partial^2\Delta w}{\partial y^2} \\ 2\frac{\partial^2\Delta w}{\partial x\partial y} \end{Bmatrix} \quad 12.36$$

$$\Delta\boldsymbol{\epsilon}_{NL} = \begin{Bmatrix} \frac{1}{2}\left(\frac{\partial\Delta w}{\partial x}\right)^2 \\ \frac{1}{2}\left(\frac{\partial\Delta w}{\partial y}\right)^2 \\ \frac{\partial\Delta w}{\partial x} \frac{\partial\Delta w}{\partial y} \end{Bmatrix} \quad 12.37$$

12.3.2 Element stiffness matrix

Suppose the structural system satisfies the equilibrium condition under the state $(n + 1)$, the following equation can be obtained from the principle of virtual work:

$$\iiint \delta\Delta\boldsymbol{\epsilon}^T(\boldsymbol{\sigma}^{(n)} + \Delta\boldsymbol{\epsilon}) \, dV = \delta\Delta\mathbf{u}^T \mathbf{P}^{(n+1)} \quad 12.38$$

where $\boldsymbol{\sigma}^{(n)}$ is the stress at the state n , $\Delta\boldsymbol{\sigma}$ the stress increment from the state n to the state $(n + 1)$, $\mathbf{P}^{(n+1)}$ the applied load at the state $(n + 1)$, $\delta\Delta\mathbf{u}$ the virtual displacement increment, and $\delta\Delta\boldsymbol{\epsilon}$ the strain increment corresponding to the virtual displacement increment.

As described in the previous section, the strain increment $\Delta\boldsymbol{\epsilon}$ can be divided into the linear term $\Delta\boldsymbol{\epsilon}_L$ and the non-linear term $\Delta\boldsymbol{\epsilon}_{NL}$:

$$\Delta\boldsymbol{\epsilon} = \Delta\boldsymbol{\epsilon}_L + \Delta\boldsymbol{\epsilon}_{NL} \quad 12.39$$

The relationship between the stress increment and the strain increment can be expressed via the material property matrix \mathbf{D} as follows:

$$\Delta\boldsymbol{\sigma} = \mathbf{D} \Delta\boldsymbol{\epsilon} = \mathbf{D}(\Delta\boldsymbol{\epsilon}_L + \Delta\boldsymbol{\epsilon}_{NL}) \quad 12.40$$

By substituting Eq. (12.40) into Eq. (12.38) and neglecting the terms higher than third order, the following equation can be obtained:

$$\begin{aligned} & \iiint \delta\Delta\boldsymbol{\epsilon}_L^T \mathbf{D} \Delta\boldsymbol{\epsilon}_L dV + \iiint \delta\Delta\boldsymbol{\epsilon}_{NL}^T \boldsymbol{\sigma}^{(n)} dV \\ & + \iiint \delta\Delta\boldsymbol{\epsilon}_L^T \boldsymbol{\sigma}^{(n)} dV = \delta\Delta\mathbf{u}^T \mathbf{P}^{(n+1)} \end{aligned} \quad 12.41$$

The third term on the left side of Eq. (12.41) can be represented with the inner force $\mathbf{F}^{(n)}$ at the state n as follows:

$$\delta\Delta\mathbf{u}^T \mathbf{F}^{(n)} = \iiint \delta\boldsymbol{\epsilon}_L^T \boldsymbol{\sigma}^{(n)} dV \quad 12.42$$

The substitution of Eq. (12.42) into Eq. (12.41) yields:

$$\begin{aligned} & \iiint \delta\Delta\boldsymbol{\epsilon}_L^T \mathbf{D} \Delta\boldsymbol{\epsilon}_L dV + \iiint \delta\Delta\boldsymbol{\epsilon}_{NL}^T \boldsymbol{\sigma}^{(n)} dV \\ & = \delta\Delta\mathbf{u}^T (\mathbf{P}^{(n+1)} - \mathbf{F}^{(n)}) \end{aligned} \quad 12.43$$

The linear and the nonlinear strain increments are defined with the nodal displacement increment $\Delta\mathbf{u}$ as follows:

$$\Delta\boldsymbol{\epsilon}_L = \mathbf{B}_L \Delta\mathbf{u} \quad 12.44$$

$$\Delta\boldsymbol{\epsilon}_{NL} = \mathbf{B}_{NL} \Delta\mathbf{u} \quad 12.45$$

The substitution of Eqs (12.44) and (12.45) into Eq. (12.43) furnishes

$$\begin{aligned} & \delta\Delta\mathbf{u}^T \left(\iiint \mathbf{B}_L^T \mathbf{D} \mathbf{B}_L dV \right) \Delta\mathbf{u} \\ & + \delta\Delta\mathbf{u}^T \iiint \mathbf{B}_{NL}^T \boldsymbol{\sigma}^{(n)} dV = \delta\Delta\mathbf{u}^T (\mathbf{p}^{(n+1)} - \mathbf{F}^{(n)}) \end{aligned} \quad 12.46$$

By defining the first and the second term of Eq. (12.46) as

$$\left(\iiint B_L^T D B_L dV \right) \Delta u = K \Delta u \quad 12.47$$

$$\iiint B_{NL}^T \sigma^{(n)} dV = K_G \Delta u \quad 12.48$$

the equilibrium equation of the structural system is given by

$$(K + K_G) \Delta u = P^{(n+1)} - F^{(n)} \quad 12.49$$

where K is the stiffness matrix associated with infinitesimal displacement and K_G is the geometric stiffness matrix.

12.3.3 Constitutive law

Elastic

The relationship between stress and strain in the elastic state is given by:

$$\begin{Bmatrix} \sigma_x \\ \sigma_y \\ \tau_{xy} \end{Bmatrix} = \frac{E}{1 - \nu^2} \begin{bmatrix} 1 & \nu & 0 \\ \nu & 1 & 0 \\ 0 & 0 & \frac{1 - \nu}{2} \end{bmatrix} \begin{Bmatrix} \varepsilon_x \\ \varepsilon_y \\ \gamma_{xy} \end{Bmatrix} \quad 12.50$$

Yield criterion

It is known that the yielding of steel does not depend on the isotropic components of the stress tensor. The von Mises yield criterion is a hypothesis that defines the occurrence of yielding when the yield function f vanishes, i.e.

$$f = J_2 - \frac{1}{3} \sigma_y^2 = 0 \quad 12.51$$

where σ_y refers to the yield stress in one-dimensional problem and J_2 is the second invariant of stress deviator s_{ij} , in which

$$J_2 = \frac{1}{2} s_{ij} s_{ij} = \frac{1}{2} \sum_{i=1}^3 \sum_{j=1}^3 s_{ij} s_{ij};$$

$$s_{ij} = \sigma_{ij} - \frac{\delta_{ij}}{3} \sigma_{kk} = \sigma_{ij} - \frac{\delta_{ij}}{3} \sum_{k=1}^3 \sigma_{kk} \quad 12.52$$

The repeated indices such as ij and kk represent the implied sum. Indices 1, 2, and 3 designate the coordinates x , y and z in the case of three-dimensional

Cartesian coordinate system as shown in Fig. 12.16. This implied sum will be adopted hereafter unless otherwise stated. It is easy to show that:

$$\frac{\partial J_2}{\partial \sigma_{ij}} = s_{ij} \quad 12.53$$

The yield condition given by Eq. (12.51) can also be expressed as:

$$\sqrt{3J_2} = \sigma_y \quad 12.54$$

The yield function in a multidimensional problem can also be evaluated by $f_0(\sigma_{ij}) = \sqrt{3J_2}$, just like the case of a one-dimensional problem. Then the equivalent stress $\bar{\sigma}$ can be defined by

$$\bar{\sigma} = f_0(s_{ij}) = \left(\frac{3}{2} s_{ij} s_{ij} \right)^{\frac{1}{2}} \quad 12.55$$

Plastic flow theory

There are two major ways of describing the stress–strain relationship in the plastic problem, namely the incremental strain theory (flow theory) and the total strain theory (deformation theory). In the flow theory, which is path-dependent, the total strain can be obtained by integrating the infinitesimal strain increment along the loading path. On the other hand, the latter theory assumes that there should be a relationship between the plastic strain and the stress deviator that is independent of the loading path. The method presented in this section is based on the flow theory.

In the incremental strain theory, by assuming plastic potential $g(\sigma_{ij}, \xi_k)$, which is a function of the stress σ_{ij} and a loading path parameter ξ_k , the plastic strain increment $d\varepsilon_{ij}^p$ is given by

$$d\varepsilon_{ij}^p = d\lambda \frac{\partial g}{\partial \sigma_{ij}} \quad 12.56$$

where $d\lambda$ is a non-negative scalar parameter. Equation (12.56) means that the plastic strain increment $d\varepsilon_{ij}^p$ is given as an outward normal vector on the equipotential surface $g = 0$. If the loading surface $f = 0$, is adopted as the equipotential surface $g = 0$, Eq. (12.56) can be rewritten as:

$$d\varepsilon_{ij}^p = d\lambda \frac{\partial f}{\partial \sigma_{ij}} \quad 12.57$$

Equation (12.57) is called the associated flow theory. In the case where the function f agrees with von Mises' yield function, it is called the Prandtl–Reuss theory. We shall treat the steel as a Prandtl–Reuss material.

The incremental plastic work dW^P can be defined by the stress components σ_{ij} and the incremental plastic strain components $d\varepsilon_{ij}^P$ or by the equivalent stress $\overline{\sigma}$ given by Eq. (12.55) and the incremental equivalent plastic strain $d\varepsilon^P$:

$$dW^P = \sigma_{ij}d\varepsilon_{ij}^P = \overline{\sigma}d\varepsilon^P \tag{12.58}$$

where $\overline{d\varepsilon^P}$ is given by

$$\overline{d\varepsilon^P} = \left(\frac{2}{3} d\varepsilon_{ij}^P d\varepsilon_{ij}^P \right)^{\frac{1}{2}} \tag{12.59}$$

Using Eqs (12.51), (12.53) and (12.57), the plastic work increment dW^P is represented as follows:

$$\begin{aligned} dW^P &= \sigma_{ij}d\varepsilon_{ij}^P = s_{ij}d\varepsilon_{ij}^P \\ &= s_{ij}d\lambda \frac{\partial f}{\partial \sigma_{ij}} = s_{ij}d\lambda \frac{\partial J_2}{\partial \sigma_{ij}} = s_{ij}d\lambda s_{ij} = 2d\lambda J_2 \end{aligned} \tag{12.60}$$

Since $J_2 > 0$ in view of Eq. (12.52), the sign of dW^P coincides with that of $d\lambda$. The loading and unloading states can, therefore, be judged by the sign of $d\lambda$:

- $d\lambda > 0$ loading (plastic behavior)
- $d\lambda = 0$ neutral (plastic behavior)
- $d\lambda < 0$ unloading (elastic behavior)

Hardening rules

In this section, isotropic, kinematic and combined hardening rules will be described on the basis of the von Mises yield condition. The loading surface is represented by the translation of the center of the yield surface α_{ij} in the kinematic hardening rule and by the increase in the radius of the yield surface in the isotropic hardening rule.

Then the loading surface is now given by

$$f = f_0(\sigma_{ij} - \alpha_{ij}) - H \left(\int \overline{d\varepsilon^P} \right) = 0 \tag{12.61}$$

where f_0 is a function composed of stress σ_{ij} and the motion of the center of the loading surface α_{ij} and H is called the hardening function that is dependent on the equivalent plastic strain $\int \overline{d\varepsilon^P}$. In this equation $f_0(\sigma_{ij} - \alpha_{ij})$ represents the equivalent stress as follows:

$$\bar{\sigma} = f_0 (\sigma_{ij} - \alpha_{ij}) \quad 12.62$$

By multiplying both sides of Eq. (12.53) by S_{ij} and upon the substitution of Eq. (12.55) and in consideration of the identity of $s_{ij} = \sigma_{ij} - \alpha_{ij}$, the following equation can be obtained:

$$(\sigma_{ij} - \alpha_{ij}) \frac{\partial f_0}{\partial \sigma_{ij}} = \bar{\sigma} \quad 12.63$$

In view of Eq. (12.63), the following strain hardening ratios may be conveniently defined:

- isotropic hardening ($H' =$ strain hardening ratio)

$$\frac{\partial f_0}{\partial \sigma_{ij}} (d\sigma_{ij} - d\alpha_{ij}) = H' \overline{d\varepsilon^P} \quad 12.64$$

- kinematic hardening ($H'_k =$ kinematic hardening ratio)

$$\frac{\partial f_0}{\partial \sigma_{ij}} d\alpha_{ij} = H'_k \overline{d\varepsilon^P} \quad 12.65$$

- combined hardening ($H' + H'_k =$ total strain hardening ratio)

$$\frac{\partial f_0}{\partial \sigma_{ij}} d\sigma_{ij} = (H' + H'_k) \overline{d\varepsilon^P} \quad 12.66$$

The incremental plastic work is expressed as

$$dW^P = (\sigma_{ij} - \alpha_{ij}) d\varepsilon_{ij}^P = \overline{\sigma d\varepsilon^P} \quad 12.67$$

From the associated flow theory given by Eq. (12.59),

$$d\varepsilon_{ij}^P = d\lambda \frac{\partial f_0}{\partial \sigma_{ij}} \quad 12.68$$

By substituting Eq. (12.68) into Eq. (12.67) and using the relationship given in Eq. (12.63), the following equation can be obtained:

$$d\lambda = \overline{d\varepsilon^P} \quad 12.69$$

Elasto-plastic material matrix

The total strain increment is thought to be the sum of the elastic and the plastic components in the plastic state:

$$d\varepsilon_{ij} = d\varepsilon_{ij}^e + d\varepsilon_{ij}^P \quad 12.70$$

The constitutive law of the elastic body is represented as:

$$d\sigma_{ij} = D_{ijkl}^e d\varepsilon_{kl} \quad 12.71$$

The substitution of Eqs (12.68) and (12.70) into Eq. (12.71) furnishes:

$$d\sigma_{ij} = D_{ijkl}^e d\varepsilon_{kl} - D_{ijkl}^e d\lambda \frac{\partial f_0}{\partial \sigma_{kl}} \quad 12.72$$

By substituting Eq. (12.72) into Eq. (12.64) and using the relationship of Eq. (12.69), one obtains:

$$d\lambda = \frac{\frac{\partial f_0}{\partial \sigma_{ij}} D_{ijkl}^e d\varepsilon_{kl} - \frac{\partial f_0}{\partial \sigma_{ij}} d\alpha_{ij}}{H' + \frac{\partial f_0}{\partial \sigma_{ij}} D_{ijkl}^e \frac{\partial f_0}{\partial \sigma_{kl}}} \quad 12.73$$

By substituting Eq. (12.65) into Eq. (12.73) and using the relationship of Eq. (12.69), one gets:

$$d\lambda = \frac{\frac{\partial f_0}{\partial \sigma_{ij}} D_{ijkl}^e d\varepsilon_{kl}}{(H' + H'_k) + \frac{\partial f_0}{\partial \sigma_{ij}} D_{ijkl}^e \frac{\partial f_0}{\partial \sigma_{kl}}} \quad 12.74$$

Finally, by substituting Eq. (12.74) into Eq. (12.72), one obtains:

$$d\sigma_{ij} = \left(D_{ijkl}^e - \frac{D_{ijmn}^e \frac{\partial f_0}{\partial \sigma_{mn}} \frac{\partial f_0}{\partial \sigma_{op}} D_{opkl}^e}{(H' + H'_k) + \frac{\partial f_0}{\partial \sigma_{mn}} D_{mnop}^e \frac{\partial f_0}{\partial \sigma_{op}}} \right) d\varepsilon_{kl} \quad 12.75$$

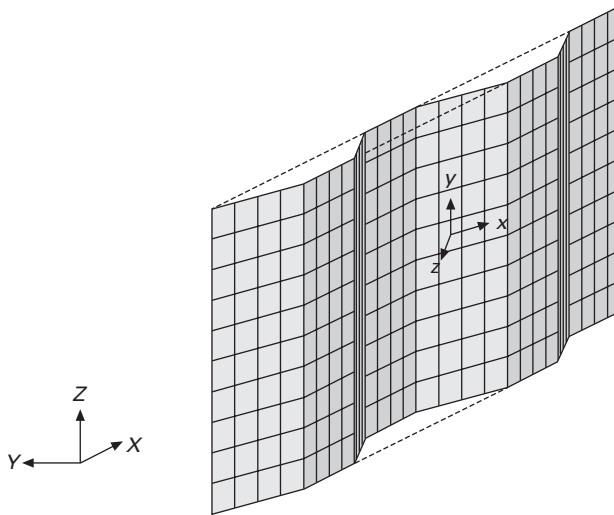
Therefore, the elasto-plastic material property matrix D_{ijkl}^{ep} can be expressed as:

$$D_{ijkl}^{ep} = D_{ijkl}^e - \frac{D_{ijmn}^e \frac{\partial f_0}{\partial \sigma_{mn}} \frac{\partial f_0}{\partial \sigma_{op}} D_{opkl}^e}{(H' + H'_k) + \frac{\partial f_0}{\partial \sigma_{mn}} D_{mnop}^e \frac{\partial f_0}{\partial \sigma_{op}}} \quad 12.76$$

12.3.4 Transformation matrix

Transformation matrix

Figure 12.17 shows the global and local coordinates for corrugated plates. Let e_x , e_y , and e_z be the unit vectors of the x -, y - and z -axes of the local



12.17 Global and local coordinates.

coordinates on a plate element expressed in relation to the global coordinates:

$$\mathbf{e}_x = \begin{Bmatrix} e_{xX} \\ e_{xY} \\ e_{xZ} \end{Bmatrix} \quad 12.77a$$

$$\mathbf{e}_y = \begin{Bmatrix} e_{yX} \\ e_{yY} \\ e_{yZ} \end{Bmatrix} \quad 12.77b$$

$$\mathbf{e}_z = \begin{Bmatrix} e_{zX} \\ e_{zY} \\ e_{zZ} \end{Bmatrix} \quad 12.77c$$

The global coordinates can be related to the local coordinates as follows.

$$\begin{Bmatrix} X \\ Y \\ Z \end{Bmatrix} = \begin{bmatrix} e_{xX} & e_{yX} & e_{zX} \\ e_{xY} & e_{yY} & e_{zY} \\ e_{xZ} & e_{yZ} & e_{zZ} \end{bmatrix} \begin{Bmatrix} x \\ y \\ z \end{Bmatrix} = [\mathbf{T}] \begin{Bmatrix} x \\ y \\ z \end{Bmatrix} \quad 12.78$$

where \mathbf{T} is the transformation matrix given by:

$$\mathbf{T} = [\mathbf{e}_x \quad \mathbf{e}_y \quad \mathbf{e}_z] = \begin{bmatrix} e_{xX} & e_{yX} & e_{zX} \\ e_{xY} & e_{yY} & e_{zY} \\ e_{xZ} & e_{yZ} & e_{zZ} \end{bmatrix} \quad 12.79$$

For example, the nodal displacement vector (six degrees of freedom) based on the global coordinates \mathbf{U}_n can be expressed using the one based on the local coordinates \mathbf{u}_n as:

$$\mathbf{U}_n = \begin{bmatrix} \mathbf{T} & 0 \\ 0 & \mathbf{T} \end{bmatrix} \mathbf{u}_n \quad 12.80$$

The stresses of a plate element based on the global coordinates can be represented using the ones based on the local coordinates and the transformation matrix as follows:

$$\begin{bmatrix} \sigma_X & \tau_{XY} & \tau_{ZX} \\ \tau_{XY} & \sigma_Y & \tau_{YZ} \\ \tau_{ZX} & \tau_{YZ} & \sigma_Z \end{bmatrix} = [\mathbf{T}] \begin{bmatrix} \sigma_x & \tau_{xy} & \tau_{zx} \\ \tau_{xy} & \sigma_y & \tau_{yz} \\ \tau_{zx} & \tau_{yz} & \sigma_z \end{bmatrix} [\mathbf{T}^T] \quad 12.81$$

Element stiffness matrix

For a four-node plate element, the relationship between the incremental nodal force vector $\Delta \mathbf{f}$ and the incremental nodal displacement vector $\Delta \mathbf{u}$ can be expressed using the element stiffness matrix \mathbf{K}_e in the local coordinates as:

$$\Delta \mathbf{f} = \mathbf{K}_e \Delta \mathbf{u} \quad 12.82$$

Using the expanded transformation matrix \mathbf{L} :

$$\mathbf{L} = \begin{bmatrix} \mathbf{T} & \mathbf{T} & & & & \mathbf{0} \\ & & \mathbf{T} & \mathbf{T} & & \\ & & & & \mathbf{T} & \mathbf{T} \\ \mathbf{0} & & & & & \mathbf{T} \end{bmatrix} \quad 12.83$$

the relationship between the incremental nodal displacement vector based on the global coordinates $\Delta \mathbf{U}$ and the one based on the local coordinates $\Delta \mathbf{u}$ of the four-node plate element can be represented as:

$$\Delta \mathbf{U} = \mathbf{L} \Delta \mathbf{u} \quad 12.84$$

In a similar manner, the incremental nodal force vector based on the global

coordinates ΔF can be represented using the one based on the local coordinates Δf as:

$$\Delta F = L \Delta f \tag{12.85}$$

By substituting Eqs. (12.82) and (12.84) into Eq. (12.85), the following equation can be obtained:

$$\Delta F = (L K_e L^T) \Delta U \tag{12.86}$$

Therefore, the element stiffness matrix K in the global coordinates can be expressed as:

$$K = L K_e L^T \tag{12.87}$$

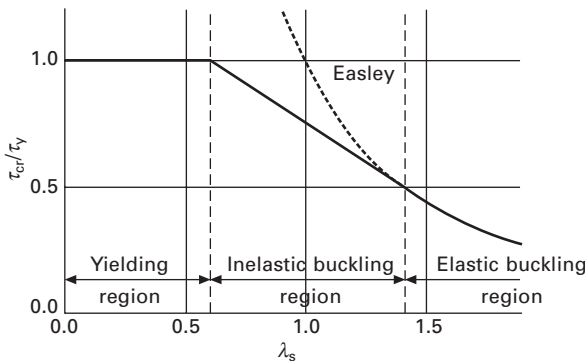
12.3.5 Parametric study of elasto-plastic and finite displacement analysis

Shear buckling strength of corrugated steel webs

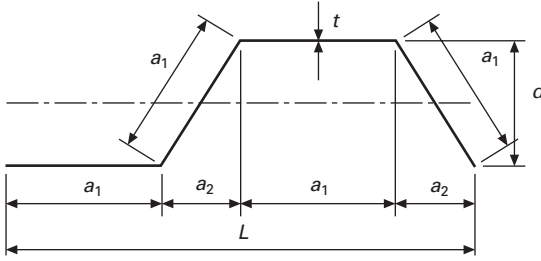
Figure 12.18 shows the shear buckling strength curve proposed by Research Group of Composite Structure with Corrugated Steel Web (Research Group, 1998). The inelastic global buckling strength of corrugated steel web is evaluated as explained below. The elastic global shear buckling strength of corrugated steel web (Easley, 1975) is expressed in a slightly different form from that given in Eq. (12.27). This modified form is given by

$$\tau_{cr,G}^e = \frac{36 \beta E I_y^{1/4} I_x^{3/4}}{h^2 t} \tag{12.88}$$

where β is a parameter of end restraint, E Young’s modulus, h the depth of web, t the thickness of web, and I_x, I_y the moments of inertia per unit length as follows (see Fig. 12.19):



12.18 Shear buckling strength curve.



12.19 Shape of corrugation.

$$I_x = \frac{\frac{1}{12}a_1t^3 + \frac{1}{3}a_1td^2}{a_1 + \sqrt{a_1^2 - d^2}} \quad I_y = \frac{t^3}{12(1 - \nu^2)} \quad 12.89$$

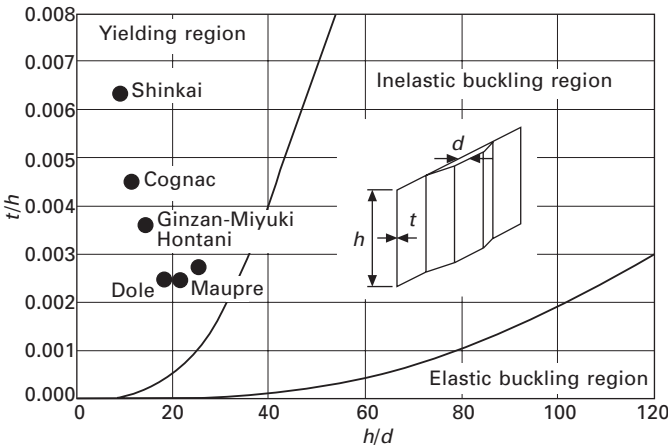
The shear buckling parameter λ_s is defined by:

$$\lambda_s = \sqrt{\tau_y / \tau_{cr,G}^e} \quad 12.90a$$

Then the global shear buckling strength is evaluated in terms of λ_s :

$$\frac{\tau_{cr,G}}{\tau_y} = \begin{cases} 1.0 & \dots \lambda_s \leq 0.6 \\ 1.0 - 0.614(\lambda_s - 0.6) & \dots 0.6 < \lambda_s \leq \sqrt{2} \\ 1/\lambda_s^2 & \dots \sqrt{2} < \lambda_s \end{cases} \quad 12.90b$$

Figure 12.20 shows the relationship between the ratios t/h and h/d of existing bridges (marked by circles in the figure). The yielding, inelastic buckling, and elastic buckling regions are shown.

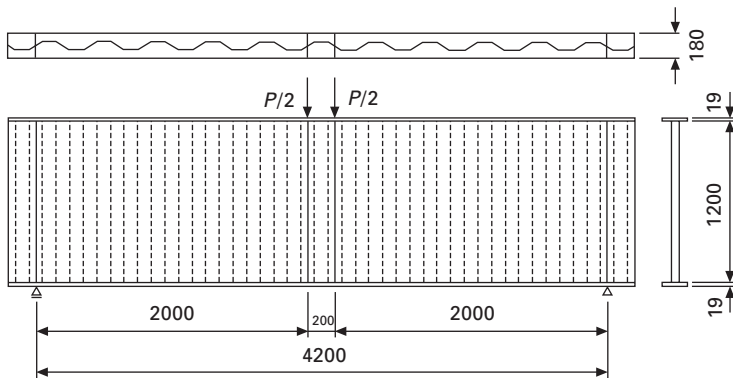


12.20 Yielding, inelastic buckling and elastic buckling regions.

and elastic buckling regions (SM490, for example) shown in Fig. 12.18 can be transformed likewise into three regions. It is found that most of the existing bridges have been designed in the yielding region (where yielding precedes buckling). But if corrugated steel webs are to be adopted for longer span prestressed concrete box girders such as those used in cable-stayed bridges in the near future, the depth of web h may become larger and thus the corrugated webs may be designed in the inelastic buckling region. Parametric studies, therefore, are carried out to investigate the validity of the shear buckling strength curve of Fig. 12.18.

Analytical models

An analytical model is shown in Fig. 12.21, which is a simply supported beam composed of a corrugated steel web with steel flanges (Watanabe *et al.*, 2001). The analytical cases are chosen in relation with Table 12.2 so that not only the yielding zone but also the inelastic buckling zone in Fig. 12.20 can be covered. The wavelength of corrugation of the web is 400 mm. Thickness of web plate, t , and depth of corrugation, d , are taken as variables. The flange plates are 180 mm wide and are thick enough against the yielding and local buckling. The material is assumed to be fully elasto-plastic and the initial deflections and residual stresses are not considered in the analyses.



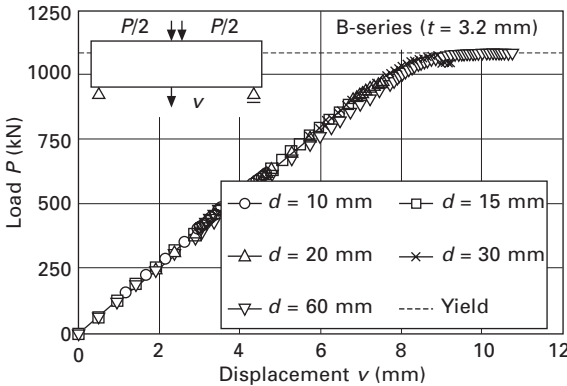
12.21 Analytical model (unit: mm).

Results of parametric analyses

The relationship between the load P and the vertical deflection v , and the load P and the out-of-plane deflection w for B-series are shown in Figs 12.22 and 12.23, respectively. It is found that the shear strength is considerably reduced and the nonlinearity can be seen in the early loading level when the depth of corrugation d becomes smaller.

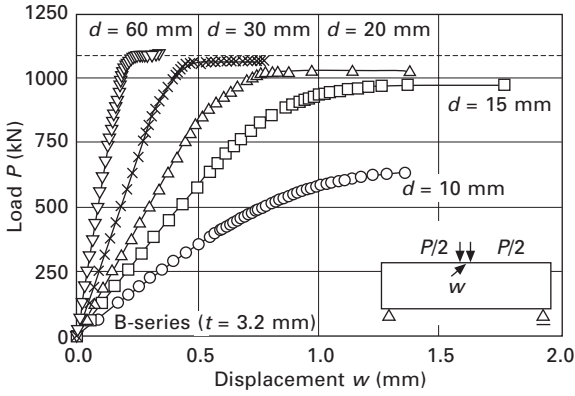
Table 12.2 Analytical cases

Case	h (mm)	t (mm)	σ_y (MPa)	d (mm)	h/d	t/h
A-1				10	120	
A-2				15	80	
A-3	1200	2.3	245	20	60	0.0019
A-4				30	40	
A-5				60	20	
B-1				10	120	
B-2				15	80	
B-3	1200	3.2	245	20	60	0.0027
B-4				30	40	
B-5				60	20	
C-1				10	120	
C-2				15	80	
C-3	1200	4.5	245	20	60	0.0038
C-4				30	40	
C-5				60	20	
D-1				10	120	
D-2				15	80	
D-3	1200	6.0	245	20	60	0.0060
D-4				30	40	
D-5				60	20	
E-1				10	120	
E-2				15	80	
E-3	1200	9.0	245	20	60	0.0075
E-4				30	40	
E-5				60	20	

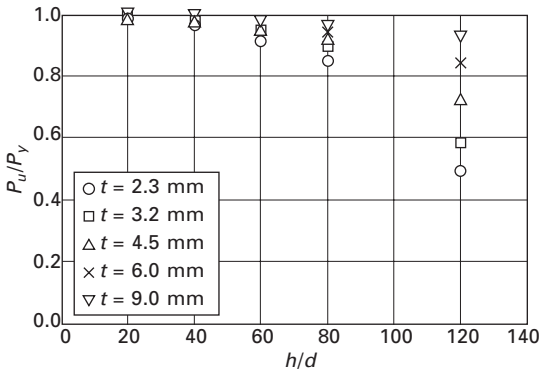


12.22 Relationship between P and v .

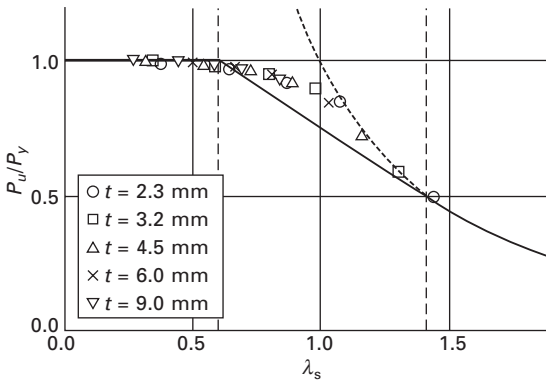
Figure 12.24 shows the shear strengths for all analytical cases considered. The remarkable reduction of shear strength can be seen in a larger region of h/d . In Fig. 12.25, the results are plotted with the shear strength curve as



12.23 Relationship between P and w .



12.24 Shear strength related to h/d .



12.25 Shear strength related to λ_s .

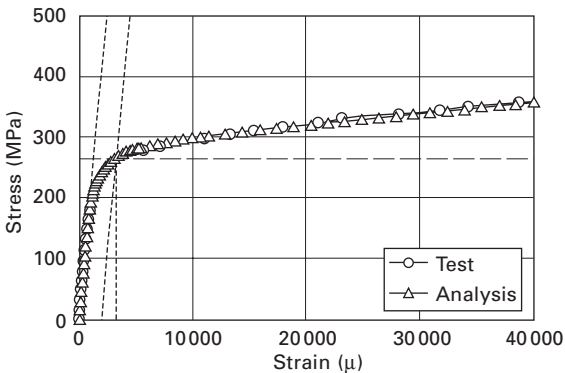
given by Eq. (12.88) and this curve is similar to the elastic portion of the curves shown in Fig. 12.18 that are obtained from Eq. 12.90b). From this observation, the shear strength curve of Fig. 12.18 may be thought to be appropriate in the inelastic buckling region since neither the residual stresses nor the geometrical imperfections have been considered. If these complicating effects are taken into account, the strengths may further decrease as predicted by the proposed shear strength curve.

12.3.6 Experimental study

Experimental tests of corrugated steel web without concrete flanges

Test program

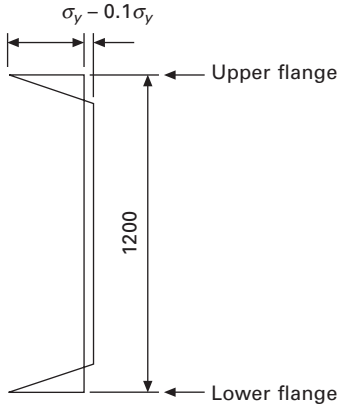
In order to investigate the validity of the modeling and the accuracy of the nonlinear analysis code used for the elasto-plastic and finite displacement analyses, experimental verifications were carried out (Watanabe *et al.*, 2001). Three types of specimens, namely B-3 ($d = 20$ mm), B-4 ($d = 30$ mm), and B-5 ($d = 60$ mm) as shown in Table 12.2 were tested. Although the shape of the specimens remains the same but their material properties are slightly different from the analytical models of the parametric studies. The results of the material tensile tests are shown in Fig. 12.26 and the material properties of the specimens in Table 12.3. Because the constitutive law is different from the one used for the analytical models, the elasto-plastic and finite displacement analyses are carried out again. In the analyses, the stress–strain curve is fitted to this result as shown in Fig. 12.26. The residual stress distribution due to welding of the flange plates to the web is considered in the analyses but for simplicity the typical distribution is adopted for plate girders as shown in Fig. 12.27.



12.26 Stress–strain curve.

Table 12.3 Material properties of specimens without concrete slabs

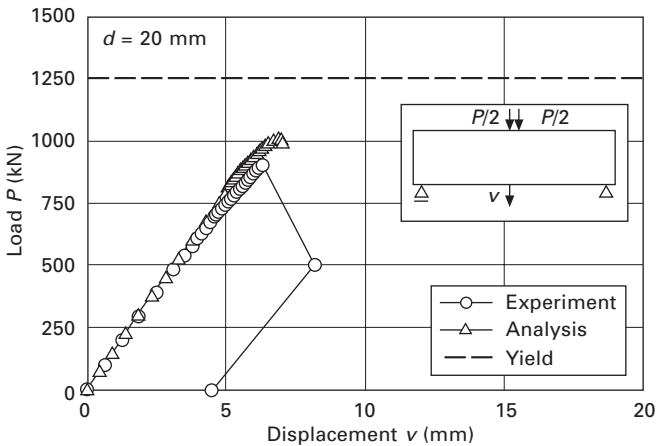
Specimen	Depth of corrugation d (mm)	Young's modulus E (MPa)	Poisson's ratio ν	Yield stress σ_y (MPa)
B-3	20	211,603	0.272	283.37
B-4	30	211,603	0.272	283.37
B-5	60	203,002	0.261	266.26



12.27 Residual stress distribution.

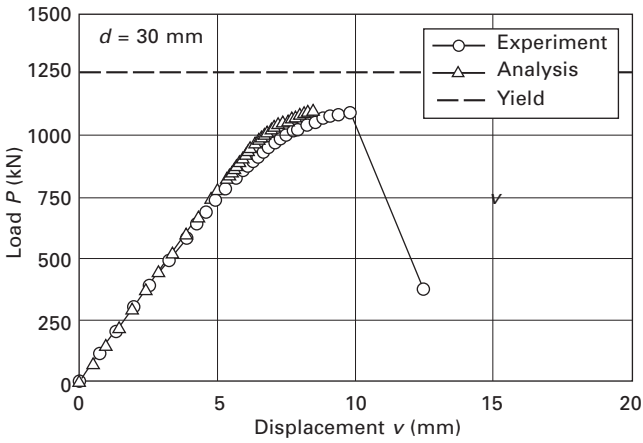
Results of tests

The relationship between the load P and the vertical deflection v for B-3 ($d = 20$ mm), B-4 ($d = 30$ mm), and B-5 ($d = 60$ mm) are shown in Fig. 12.28, Fig. 12.29 and Fig. 12.30, respectively. The relationship between

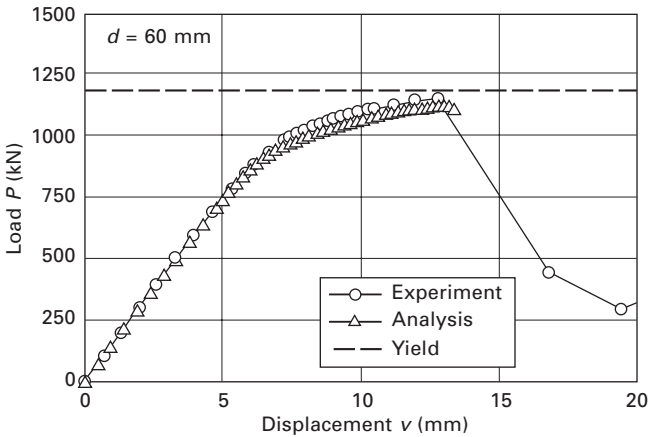


12.28 Relationship between P and v (B-3).

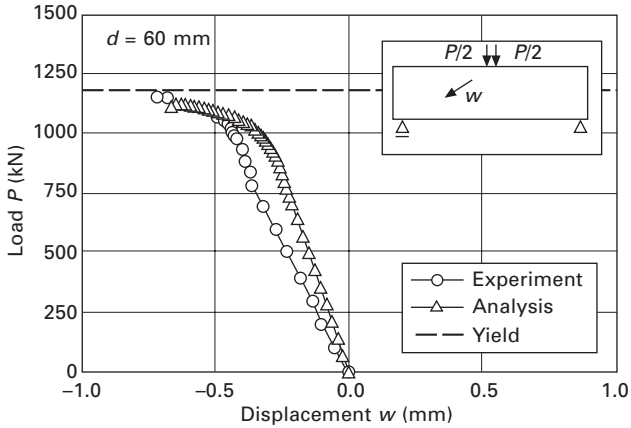
the load P and the out-of-plane deflection w for B-5 is shown in Fig. 12.31. These figures show that the experimental results agree well with the analytical results. Figure 12.32 shows the experimental and the analytical results of the shear strength of B-3, B-4, and B-5 as compared with the shear strength curve of Fig. 12.18. In the case of small depth of corrugation d (B-3: $d = 20$ mm), there is a difference between the results obtained from the experiment and from the analysis. This difference in results is due to the severe geometrical nonlinearity. The shear strength of the test specimens is smaller than the one obtained from the shear strength curve of Fig. 12.18. The strength curve of Fig. 12.18 is based on pure shear buckling and it may not be compared precisely with the results of this study where the test specimens are subjected



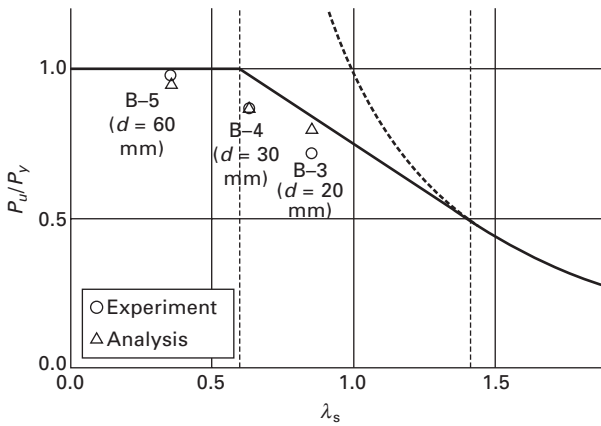
12.29 Relationship between P and v (B-4).



12.30 Relationship between P and v (B-5).



12.31 Relationship between P and w (B-5).



12.32 Relationship between shear strength and λ_s .

to the combination of shearing force and bending moment. However, it is found that the effect of the residual stress on the shear strength should not be ignored.

Experimental verification on corrugated steel web with concrete flanges

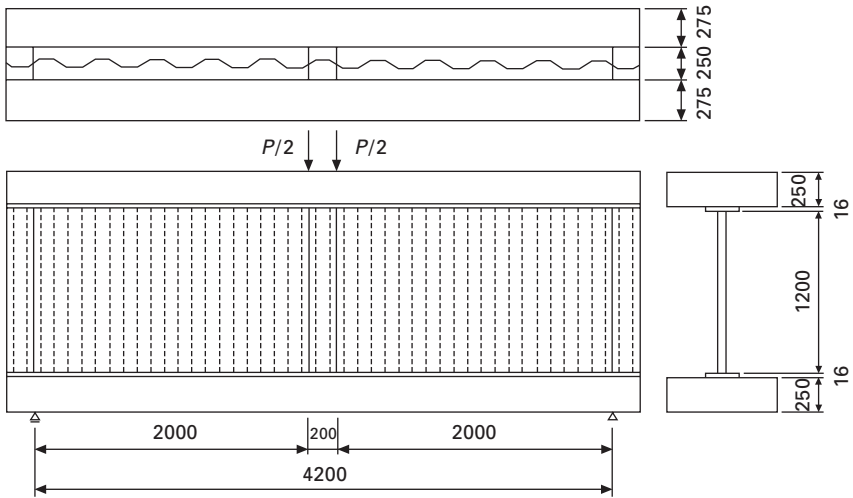
Test program

The experimental tests of a simply supported beam composed of a corrugated steel web with concrete slabs are carried out to investigate the effect of shear buckling of a corrugated steel web on the ultimate strength of the whole girder (Watanabe *et al.*, 2002; Kadotani *et al.*, 2002). Three types of specimens,

namely BC-3 ($d = 20$ mm), BC-4 ($d = 30$ mm), and BC-5 ($d = 60$ mm) as described in Table 12.4 are provided for the tests. As shown in Fig. 12.33, the width and the depth of the concrete slabs are 800 and 250 mm, respectively.

Table 12.4 Material properties of specimens with concrete slabs

Specimen	Corrugated steel web			Concrete slab		
	Depth of corrugation d (mm)	Young's modulus E (MPa)	Poisson's ratio ν	Yield stress σ_y (MPa)	Young's modulus E (MPa)	Poisson's ratio ν
BC-3	20	200,000	0.3	297.0	31,000	0.16
BC-4	30	200,000	0.3	297.0	31,000	0.16
BC-5	60	200,000	0.3	297.0	31,000	0.16

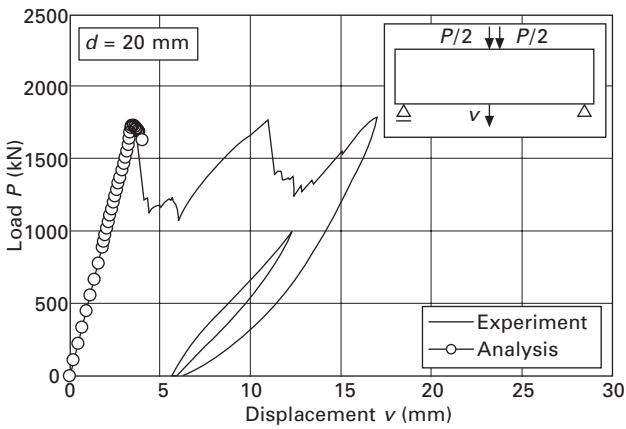


12.33 Analytical model (unit: mm).

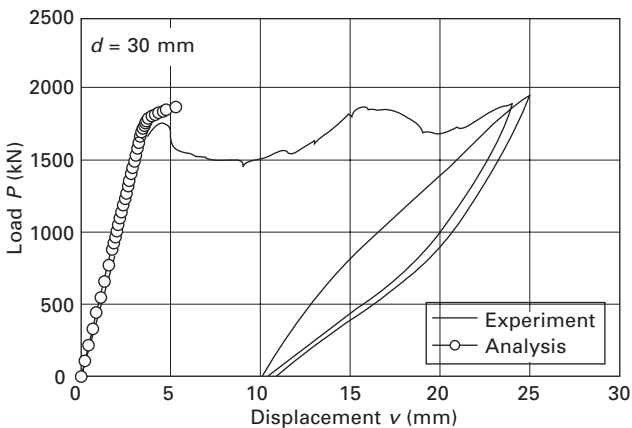
There are various kinds of nonlinearity to be considered, such as geometrical and material nonlinearity of the corrugated steel web, material nonlinearity of the concrete slabs, nonlinearity due to slippage between steel flanges and concrete slabs, and so forth. At this stage of study, however, only the geometrical and material nonlinearities of the corrugated steel web are considered and the corrugated steel web and the concrete slabs are assumed to be rigidly connected. In the elasto-plastic and finite displacement analyses, the concrete slabs are modeled as elastic bodies.

Results of tests

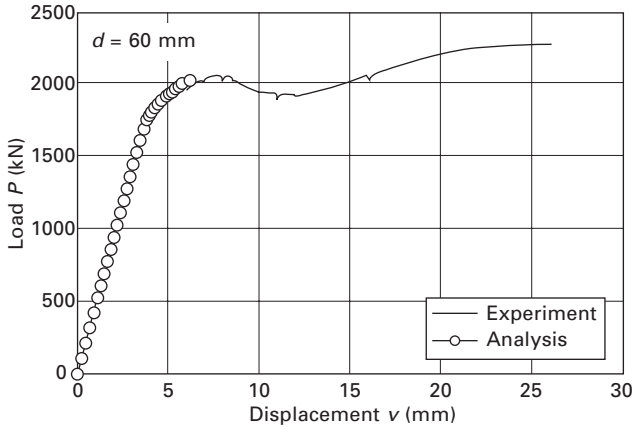
The relationship between the load P and the vertical deflection v about BC-3 ($d = 20$ mm), BC-4 ($d = 30$ mm), and BC-5 ($d = 60$ mm) is shown in Figs 12.34 to 12.36, respectively. These figures show that the load P increases even after the occurrence of shear buckling of the corrugated steel web. The specimens are observed to have sufficient load-carrying capacity and ductility. The results of the experiments agree well with those obtained by the numerical analyses. However, the postbuckling behavior cannot be fully followed owing to the problem of ill-convergence in the numerical computations. Figure 12.37 shows the experimental and the analytical shear strength results of BC-3, BC-4, and BC-5 as compared with those of B-3, B-4, and B-5 and



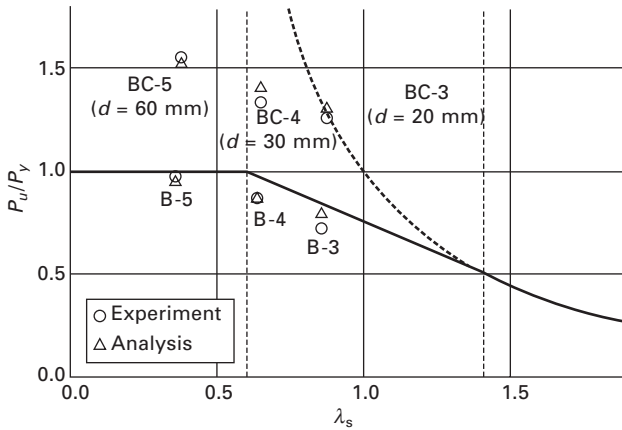
12.34 Relationship between P and v (BC-3).



12.35 Relationship between P and v (BC-4).



12.36 Relationship between P and v (BC-5).



12.37 Relationship between shear strength and λ_s .

with the shear strength curve of Fig. 12.18. From this figure, it is found that the shear strength of the corrugated steel web with concrete slabs is about one and a half as high as the one of the corrugated steel web without concrete slabs.

12.4 Concluding remarks

The overall elastic buckling capacities of corrugated plates was determined by modeling the corrugated plates as orthotropic Mindlin plates and minimizing the energy function using the Ritz method. It is established that the formula for predicting the global elastic shear buckling capacity that is adopted in the design manual (Research Group, 1998) yields values comparable with the

Ritz buckling results. However, this study extends the formula to cover the more realistic elastically rotational restrained edges.

The influence of elastically rotational restraint on the buckling capacities of corrugated plates was investigated and it was found that the type of supporting edges in the direction of plate's lower flexural stiffness, either that of a simple or fixed support has little effect on its buckling capacity. On the other hand, its buckling capacity is greatly affected by the magnitude of rotational restraint imposed on its supporting edges in the direction of plate's higher flexural stiffness. It was also shown that there is a specific range of dimensionless rotational spring constant in the direction of plate's higher flexural stiffness that causes the buckling capacity to vary from that of a simply supported case to the clamped support case. The rotational spring constant ranges from approximately 10^{-2} to 10^4 .

In the past, all of the existing corrugated webs in bridges were designed only in the plastic zone. Thus, a material and geometrically nonlinear analysis is formulated to evaluate practical problems of the elasto-plastic buckling loads. Based on the results of the parametric studies of the elasto-plastic and finite displacement analyses and experiment test results of simply supported beams with corrugated steel web, the following conclusions may be drawn:

- Considerably good agreement can be seen between the results of the experiments and the elasto-plastic and finite displacement analyses.
- The results of the parametric studies show the validity of the shear strength curve of the corrugated steel web.
- The shear strength of the test specimens may be reduced to some extent due to residual stresses and geometrical imperfections.

12.5 References

- Chang, T.P. and Chang, H.C. (1997), 'Vibration and buckling analysis of rectangular plates with nonlinear elastic end restraints against rotation', *International Journal of Solids and Structures*, **34**(18), 2291–2301.
- Chung, J.H., Chung, T.Y. and Kim, K.C. (1993), 'Vibration analysis of orthotropic Mindlin plates with edges elastically restrained against rotation', *Journal of Sound and Vibration*, **163**(1), 151–163.
- Combault, J. (1992), 'The Maupre viaduct near Charolles, France', *Journal of Prestressed Concrete, Japan*, **34**(1), 63–71 (in Japanese, Translator: Ohura, T.).
- Dawe, D.J. and Roufaeil, O.L. (1980), 'Rayleigh–Ritz vibration analysis of Mindlin plates', *Journal of Sound and Vibration*, **69**(3), 345–359.
- Dickinson, S.M. and Blasio, A.D. (1986), 'On the use of orthogonal polynomials in the Rayleigh–Ritz method for the study of the exural vibration and buckling of isotropic and orthotropic rectangular plates', *Journal of Sound and Vibration*, **108**(1), 51–62.
- Easley, J.T. (1975), 'Buckling formulas for corrugated metal shear diaphragms', *Journal of the Structural Division, ASCE*, **101**(ST7), 1403–1417.
- Easley, J.T. and McFarland, D.E. (1969), 'Buckling of light-gage corrugated metal shear diaphragms', *Journal of the Structural Division, ASCE*, **95**(ST7), 1497–1516.

- Elgaaly, M., Hamilton, R.W. and Seshadri, A. (1996), 'Shear strength of beams with corrugated webs', *Journal of Structural Engineering, ASCE*, **122**(4), 390–398.
- Hussain, M.I. and Libove, C. (1976), 'Trapezoidally corrugated plates in shear', *Journal of the Structural Division, ASCE*, **102**(ST5), 1109–1131.
- Johnson, R.P. and Cafolla, J. (1997), 'Corrugated webs in plate girders for bridges', *Proceedings of the Institution of Civil Engineers, Structures and Buildings*, **123**(May), 157–164.
- Kadotani, T., Aoki, K., Ashizuka, K., Mori, T., Tomimoto, M. and Kano, M. (2002), 'Shear buckling behavior of prestressed concrete girders with corrugated steel webs', *Proceedings of the First Fib Congress 2002*, Osaka, October, 269–276.
- Kano, M., Yamano, T., Nibu, M. and Kitada, T. (1997), 'A computer program, USSP, for analyzing ultimate strength of steel plated structures', *Proceedings of the 5th International Colloquium on Stability and Ductility of Steel Structures*, Nagoya, Japan, July, 763–770.
- Komatsu, S., Kitada, T. and Miyazaki, S. (1975), 'Elastic-plastic analysis of compressed plate with residual stress and initial deflection', *Proceedings of JSCE*, No. 244, 1–14 (in Japanese).
- Laura, P.A.A. and Grossi, R. (1978), 'Transverse vibration of a rectangular plate elastically restrained against rotation along three edges and free on the fourth edge', *Journal of Sound and Vibration*, **59**(3), 355–368.
- Laura, P.A.A. and Luisoni, L.E. (1978), 'Vibrations of orthotropic rectangular plates with edges possessing different rotational flexibility and subjected to in-plane forces', *Computers and Structures*, **9**(6), 527–532.
- Liew, K.M., Wang, C.M., Xiang, Y. and Kitipornchai, S. (1998), *Vibration of Mindlin Plates: Programming the p-Ritz Method*, Elsevier, Oxford, UK.
- Luo, R. and Edlund, B. (1996), 'Shear capacity of plate girders with trapezoidally corrugated webs', *Thin-Walled Structures*, **26**(1), 19–44.
- Marinetti, A. and Oliveto, G. (1995), 'A sinusoidal stiffness matrix for buckling and vibration analyses of rectangular Mindlin plates', *Journal of Sound and Vibration*, **187**(3), 435–449.
- Mindlin, R.D. (1951), 'Influence of rotatory inertia and shear on flexural motions of isotropic, elastic plates', *Journal of Applied Mechanics, ASME*, **18**, 31–38.
- Mizusawa, T. and Kajita, T. (1987), 'Vibration and buckling of rectangular plates with nonuniform elastic constraints in rotation', *International Journal of Solids and Structures*, **23**(1), 45–55.
- Omidvar, B. (1998), 'Shear coefficient in orthotropic thin-walled composite beams', *Journal of Composites for Construction, ASCE*, **2**(1), 46–56.
- Peterson, J.P. and Card, M.F. (1960), 'Investigation of the buckling strength of corrugated webs in shear', *Technical Report NASA, TN D-424*, National Aeronautics and Space Administration, Washington.
- Research Group of composite structures with corrugated steel webs (1998), *Design Manual of PC Box Girders with Corrugated Steel Webs* (Draft), Tokyo, Japan, (in Japanese).
- Rothwell, A. (1968), 'The shear stiffness of at-sided corrugated webs', *The Aeronautical Quarterly*, **19**, 224–234.
- Saha, K.N. and Kar, R.C. (1996), 'Free vibration analysis of rectangular Mindlin plates with elastic restraints uniformly distributed along the edges', *Journal of Sound and Vibration*, **192**(4), 885–904.
- Stein, M. and Housner, J.M. (1978), 'Application of a trigonometric finite difference procedure of numerical analysis of compressive and shear buckling of orthotropic panels', *Computers and Structures*, **9**(1), 17–25.

- Stephen, N.G. (1997), 'Mindlin plate theory: best shear coefficient and higher spectra validity', *Journal of Sound and Vibration*, **202**(4), 539–553.
- Timoshenko, S.P. and Gere, J.M. (1963), *Theory of Elastic Stability*, McGraw Hill., New York
- Watanabe, E., Kadotani, T., Miyauchi, M., Tomimoto, M. and Kano, M. (2001), 'On reliability of corrugated steel web in prestressed concrete box girder bridges', *Proceedings of the 8th International Conference on Structural Safety and Reliability*, Newport Beach, California, 17–21 June (CD-ROM).
- Watanabe, E., Kano, M. and Kadotani, T. (2002), 'Safety and durability of prestressed concrete box girder bridges with corrugated steel webs', *Proceedings of the Structural Engineers World Congress (SEWC2002)*, Yokohama, 9–12 October (CD-ROM).

Interaction of curvature on the stability and design of curved plate girders

J S DAVIDSON, The University of Alabama at Birmingham, USA

13.1 Introduction

The use of horizontally curved girders in the design of highway bridges and interchanges in large urban areas has increased dramatically in recent years. The need for the smooth dissemination of congested traffic and the limitation of right-of-way, along with economic and environmental considerations, has encouraged this trend. Emphasis on aesthetic considerations has also motivated increased use of curved configurations.

When curved bridge superstructures were first introduced, they were generally composed of a series of straight girders used as chords. Although the cost of superstructures using curved girders may be high, the total cost of the curved girder bridge system has been found to be less than that of the system employing a series of straight girders for the same bridge since a substantial portion of the substructure can be eliminated. Also, using continuous curved girders permits the use of shallower sections as well as a reduction in the slab overhang of outside girders.

In the early years of modern bridge design, engineers were reluctant to use curved girders because of the mathematical complexities associated with design. Curved girders are subjected not only to flexural stresses, but also to very significant torsional stresses, even under pure gravitational loading. In addition, deflection, cross-section distortion, and deflection amplification (large displacement) effects are much more pronounced in curved girder systems. The inherent rotation characteristics of horizontally curved girders require that the diaphragms and bracing that are used in straight girder systems simply to prevent premature lateral buckling become very important (primary) load-carrying components in curved systems. Over the past two decades, the availability of digital computers to carry out complex analyses, along with advancements in fabrication and erection technology, have made horizontally curved girder superstructures a viable and cost efficient option for designers.

13.1.1 Origins of curved beam theory

Research prior to the mid-1960s on the behavior of curved girders was generally limited to theoretical work on the linear elastic static behavior of isolated curved members. The earliest theoretical work on curved beam theory is attributed to St. Venant (1843) over 150 years ago. Since then, a number of other European and Japanese researchers have contributed to the analysis of curved beams (McManus *et al.* 1969). These researchers include Timoshenko (1905), Gottfield (1932), Umanskii (1948), Dabrowski (1964, 1965, 1968), Vlasov (1961), Shimada and Kuranashi (1966), and others. Comprehensive presentations of the basic theory of thin walled beams including flexure, torsion, distortion, and stress distribution is provided in several texts (Vlasov 1961, Dabrowski 1968, Kollbrunner and Basler 1969, Heins 1975, Nakai and Yoo 1988). Since the mid-1960s an emphasis in curved girder research in the United States and Japan has been placed on the practical use of curved beam theory towards the design of horizontally curved bridges.

13.1.2 Design perspective and historical review

Generally speaking, there are two geometric configurations of girders used in steel superstructure bridges: I-shaped cross-sections and box girders. The I-girder is an 'open' section and is characterized by a low torsional resistance. The twisting of the I-girder results in significant normal stresses in the flanges that are in addition to major axis flexural stresses. The strength and spacing of diaphragms and cross-frames must be carefully designed to manage these stresses to acceptable levels. Transverse and longitudinal stiffeners play a significant role in restraining web distortion. The single curved I-girder is inherently unstable and, at typical bridge girder lengths, is very flexible and susceptible to large deformation. Extreme care must be taken in handling and erecting. The box girder behaves as a 'closed' section with generally improved torsional resistance over the I-section, but with its share of complications in fabrication and erection stages. Internal and external cross-frames and diaphragms must be carefully designed to reduce cross-section distortion, but external bracing is often removed after the concrete deck has cured.

In 1965, US Steel (*Highway Structures Design Handbook* 1965) published an approximate procedure called 'V-load Analysis' for determining moments and shears in horizontally curved open-framed highway bridges. It is theoretically pure with regard to torsion due only to curvature and load distribution for static equilibrium. The method does not account for lateral bracing between girders in the plane of the flanges. The accuracy of the method with regard to live load depends upon the ability of the user to assign appropriate loads to the girders prior to the V-load analysis. It has been noted

that the live load distribution factors used in straight bridge design do not appropriately represent the distribution in curved bridges and researchers have proposed equations for curved bridge design (US Steel Corp. 1984, Heins and Jin 1984, Brockenbrough 1986).

In 1969 a comprehensive pooled funds research project, referred to as CURT (Consortium of University Research Teams), sponsored by 25 participating US state highway departments was initiated under the direction of the Federal Highway Administration (FHWA) to study the behavior of curved bridges and to develop design requirements. This work was performed throughout the 1970s and resulted in the Guide Specifications for Horizontally Curved Highway Bridges (subsequently referred to as the Guide Specifications), which was officially adopted in 1980 and has been used in its same basic form ever since. The Guide Specifications include Working Stress Design (WSD) provisions and Load Factor Design (LFD) provisions, and deal with both 'I' and 'box' shape girder bridge superstructures. Strength formulations for the web, flanges, and stiffeners are emphasized. Experience indicates that the strength formulations have been at least adequate in that there have been no reported failures of these bridges in the US by overload. However, the Guide Specifications in its original form is disjointed and difficult to use, and due to a lack of continuity with straight bridge standards, it has never been adopted as an integral part of the AASHTO Standard Specifications for Highway Bridges.

There have been changes to the Guide Specifications in the form of Interim Specifications, resulting from several nationally coordinated research projects. In 1992, a comprehensive research project administered by the FHWA, the 'Curved Steel Bridge Research Project' (subsequently referred to as the FHWA-CSBRP), was initiated to conduct fundamental research into the behavior of curved steel flexural members and bridges that would lead to the development of LRFD specifications for curved bridge design.

The only other bridge design document that specifically addresses curved bridge design is the Japanese 'Guidelines for the Design of Horizontally Curved Girder Bridges' by the Hanshin Expressway Public Corporation (Hanshin 1988). Several researchers have demonstrated disparity in the strength formulations between the Japanese and American curved bridge design guides, which further emphasizes the need for additional research.

13.2 Stability during construction

Curved girders are susceptible to problems from the beginning. Residual stresses formed during curved plate girder fabrication can be significantly greater than those induced to straight plate girders and affect the strength of the girder. Ensuring proper camber is difficult. Transporting and shipping girders with significant curvature becomes problematic. Girders must be

carefully restrained to prevent instability during shipping and overhangs must be carefully checked. Once at the job site, placing the girders becomes cumbersome.

13.2.1 Fabricating

Generally there are three methods of fabricating curved steel I-girders: (1) cut curving, (2) heat curving, and (3) cold curving.

Cut curving

Cut curving involves flame cutting the flanges to the desired curvature from a standard steel plate. The advantage of this method is that there is no limit on the radius of curvature that can be obtained. This method of fabrication involves careful planning for economical cutting of the flange plates to minimize the amount of scrap generated. In addition, adhering to consistency in plate thickness and steel grades allows the fabricator to economize by combining and nesting plates (Grubb *et al.* 1996). After the individual flange sections are cut, the required sections that make up the shipping piece are usually spliced together by full penetration butt welds. The web plates are held to the required curvature by special fixtures that are tack welded to the flange plates. After tack welding, automatic welding is used to weld the full length of the web to the flange. Adjustments to curvature are often made by controlled application of heat.

Heat curving

Heat curving is an economical and popular method of fabricating curved steel I-girders and is generally used for longer radii. Heat curving is accomplished by simultaneously heating one side of the top and bottom flanges of a fabricated straight I-girder to introduce residual curvature after cooling. The application of heat can be continuous, strip, or V-type. In continuous heating, the flange edges are heated along their length. In strip heating, the flanges are heated in rectangular strips at regular intervals until the required curvature is attained. In V-type heating, the top and bottom flanges are heated in truncated triangular or wedge-shaped areas having their bases along the flange edge and spaced at regular intervals along each flange.

The heat curving operation can be carried out with the web in the vertical or horizontal position. When the web is in the vertical position, braces or supports are used such that the tendency of the girder to deflect laterally during the heat curving process will not cause the girder to overturn. When the web is in the horizontal position, the girder is supported at the ends and at the intermediate supports to obtain uniform curvature. Intermediate transverse

stiffeners can be attached either before or after heat curving. However, the stiffeners are attached only to the web; welding to the flanges is carried out after the required curvature has been obtained. Bearing stiffeners are usually attached after heat curving unless provisions are made for shrinkage of girder components. Longitudinal stiffeners can be either flame cut or heat curved and then welded to the girder. Cambering the girders is also required before heat curving. The girder webs are cut to the required camber, taking into account the allowance for shrinkage due to cutting, welding, and heat curving. Once the heat curving operation is completed and the girders have cooled to a uniform temperature, horizontal curvature and vertical camber are checked.

Cold bending

The third method of imparting curvature to I-girders is to cold-bend a fabricated straight I-girder into the required curvature. In the cold-curving process, the straight I-girder is bent plastically to obtain an over-bent curvature and released. The relaxed configuration results in the required curvature. While heat curving is currently the most economic method of fabrication, it is a labor-intensive process that is not exact. Similarly, cut curving is labor intensive in that handling of curved shapes in the shop is more expensive than handling a straight girder and usually involves material wastage. In comparison, cold curving is fast, efficient, and precise, and could be one of the most economical methods of fabricating a curved I-girder. However, the possibility of fracture due to localized load effects has raised concerns and has delayed its acceptance for bridge structures.

Residual stresses

Plate girder fabrication introduces residual stresses and camber loss. This is particularly true for heat-curved girders. Residual stresses are created whenever a member is permanently deformed or distorted in a nonuniform manner and persist in a material or a component under uniform temperature in the absence of externally applied loads. Very little information is available on the residual stresses developed in flame cut and welded I-section curved girders (Bradford *et al.* 2001). Based on research by Kishima *et al.* (1969), Culver and Nasir (1969) suggested a residual stress pattern for welded I-sections. Brockenbrough (1970) reported that the magnitude and distribution of heat-curved girders are functions of dimensions and material properties of the straight girder and the curving procedure.

13.2.2 Transporting

Stability challenges that are exacerbated by curvature can occur while transporting girders from the fabrication plant to the construction site. Steel

bridge girders can be transported by highways, railways, waterways, or a combination of the three, depending on where the bridge is to be constructed. The weight, height, and width of the girder sections may be limited by the transporting method chosen. The transporting mode must ensure that the girders can be delivered to the site without deforming the cross-section and inducing additional stresses.

The location of splices and the overall geometry of the section can be designed so that the girder will be easier to maneuver. Proper restraint against vertical, longitudinal, and transverse movement must be considered. For straight girders, lateral restraint is provided only at vertical supports, while curved girders may overhang and additional support may be required to prevent instability.

13.2.3 Erecting

There is a tendency for bridge engineers to focus on the integrity of the traffic load-bearing configuration of the bridge and not on the partially completed structure or the 'erection stages' of the job (Weinhold 1997). This perception is rapidly changing with new specifications that require the design engineer to investigate the stability of the partially completed structure.

Lifting

Overall stability of single long slender girders during lifting is a major concern during the construction of highway bridges. Stability is achieved by adequate lateral bracing of compression flanges. For straight girders, an approximate determination of the stability of a girder may be made by taking the ratio of the overall length of the girder to the compression flange width. A rule of thumb based on experience (Weinhold 1997) indicates that girders with $l/b < 60$ will be stable during erection. For $60 < l/b < 80$ stability is questionable, but can be achieved. For $l/b > 80$, the girder will be unstable and will require temporary support. Such guidance is not available for curved girders. Bridge girders are often erected by one crane using one or two pick-up points, or by using two cranes with one pick-up point each. Lifting of girders in straight bridge construction presents little difficulty as the center of gravity coincides with the centroidal axis of beam cross-section. However, a horizontally curved girder introduces rotation during lifting as the center of gravity does not coincide with the centroidal axis of beam cross-section. Depending on the length of the beam, lateral-torsional buckling or significant nonlinear deflection behavior may occur, thus shifting the center of gravity and causing rigid body instability.

The calculation of optimum pick points for two lifting points can be approximated by treating the curved girder as a circular arc in plan and

assuming that the section is prismatic (Grubb *et al.* 1996). However, bridge girders are often nonprismatic, which creates additional problems for locating the balance points. In practice erectors often 'weigh' a piece; the girder may be lifted a few inches and put down repeatedly until the balance points are located. For curved girders, this may take several trials. Wire rope slings or girder clamps are usually used for attaching the free edges of the top flange at the pick-up points. Owing to the inherent tendency of a curved girder to twist, high stresses may occur at the attachment locations. These intense stresses may occur on the inside (concave) or outside (convex) edge of the girder flange, depending on the direction in which the girder rotates.

The lifting and support mechanism used depends on the length of the beam. While longer girders necessitate the use of spreader beams, shorter girders can be lifted with single or double cable slings. In addition, when inclined cables are used, a component of the cable force in the horizontal plane that causes minor axis bending must be taken into account. Two parallel girders can be bolted together by the diaphragms or cross-frames and lifted as one piece. Lifting of girders in pairs helps resist wind loads and may save time. Horizontal stiffening trusses can be added to the compression flanges before lifting. However, the ability to lift two girders at once depends on crane capacity available at the jobsite.

Erecting and sequencing (site assembly)

Proper erecting and sequencing of curved girders is essential during construction. The placement sequence of the girders and diaphragms or cross-frames should be carefully planned so that fit-up problems are minimized. Diaphragms or cross-frames are bolted between each girder to provide stability and to control deflection of the girders. The fabricator normally assembles the bridge components prior to delivery to the jobsite to ensure that fit-up problems will not occur. Once the girders have been loaded for transporting and unloaded for placement, camber changes may cause further fit-up problems. In addition, the configuration of the partially completed structure must be stable. Unlike straight girders, curved girders depend on adjacent girders for stability.

Several approaches can be adopted for erecting and stabilizing curved girders. Grubb *et al.* (1996) describe three methods for proper erection and stabilization. In the first method, if the crane capacity is available, paired erection is desirable. After erecting the first pair of girders, individual girders can be erected successively and connected to adjacent girders by cross-frames. This increases the torsional stiffness, thereby adding stability to the system. A second method of erecting each girder is to use one crane to pick up the girder and place it, while another crane supports the girder to which it is connected. While both cranes hold their girders, the diaphragms or

cross-frames are bolted into place. The addition of the second girder and cross-bracing between them changes the governing instability mode from flexural torsional buckling of single girder to flexural buckling of two girders acting together as a unit. This method requires adequate area for mobilization of two cranes. A third method is to use temporary false-work towers or bents to shore the girders, which requires ground space that is often not available.

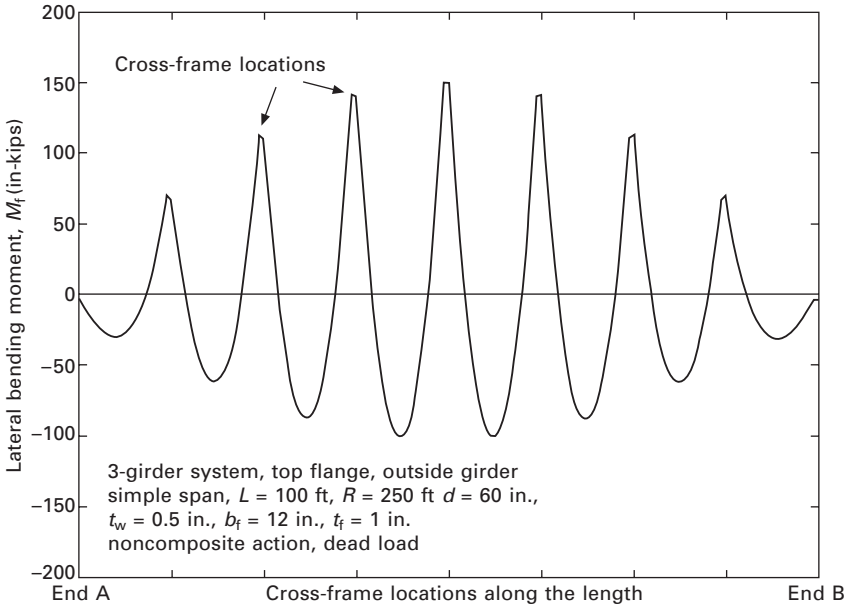
There are no widely adopted guidelines for erecting curved I-girders and few researchers have studied the large-scale erection behavior of curved I-girders. Important recent studies include Linzell (1999), Galambos *et al.* (1996), Simpson (2000) and Chavel and Earls (2001). Although several CURT era researchers studied the behavior of curved girders through experimental methods, a weakness was that the tests involved only small-scale model bridges and medium-scale models of individual components under idealized loading and boundary conditions.

13.3 Cross-frame interval design

In straight girder bridges, the primary function of the cross-frames and diaphragms is to prevent premature lateral buckling of the girder; therefore the cross-frame members are designed as secondary members. However, in curved bridge systems, the cross-frames and diaphragms have the added responsibility of restraining the rotation of the girder, thereby reducing the warping stresses in the flanges and reducing the vertical deflection of the system. The spacing interval between cross-frames, therefore, becomes a critical design parameter for limiting warping stress and deflection to acceptable levels. Furthermore, there is growing sentiment in the bridge engineering community to minimize the number of cross-frames because of cost and fatigue.

In the curved I-girder bridge system, non-uniform torsion results in warping normal stresses in the flanges. The combination of vertical major-axis moment and 'bimoment' produces linearly varying normal stresses across the flange. Lateral flange bending results in peak moments at either the cross-frame location or at approximately the mid-point between cross-frames, in a manner similar to a continuous beam subjected to a uniformly distributed load. An illustration of the variation in lateral flange bending moments along a simply supported span is shown in Fig. 13.1.

Davidson *et al.* (1996) investigated the cross-frame spacing requirements of horizontally curved I-girder bridges. The finite element method was used to determine dominant parameters and to develop equations for the preliminary design of the cross-frame spacing needed to achieve a required warping-to-bending stress ratio (f_w/f_b). The equation was determined to be of the following form based on a preliminary design target f_w/f_b of 0.25:



13.1 Effect of cross-frames on lateral bending moments in the flanges.

$$S_{\max} = L \left[-\ln \left(\frac{Rb_f}{2000 L^2} \right) \right]^{-1.52} \tag{13.1}$$

where S_{\max} (m) is the design spacing between cross-frames, L (m) is the span length of the exterior girder, R (m) is the radius of curvature of the exterior girder, and b_f (mm) is the compression flange width, or

$$S_{\max} = L \left[-\ln \left(\frac{Rb_f}{24 L^2} \right) \right]^{-1.52} \tag{13.2}$$

where units are L (ft), R (ft), and b_f (in). Using existing bridge designs, results obtained from Eqs 13.1 and 13.2 were compared to that of a similar equation developed by Yoo and Littrell (1986) and to that obtained from using a simple distributed lateral load approximation. The comparisons revealed a good correlation obtained from Eqs 13.1 and 13.2 and the lateral load approximation, but the Yoo–Littrell equation resulted in less accurate results.

13.4 Influence of curvature on lateral-torsional stability

There have been numerous theoretical developments on the buckling and large displacement of curved beams that involve simplifying assumptions

required to derive and solve governing equations. A comprehensive review and comparison of these theories was presented by Kang (1992) and Kang and Yoo (1994a,b). There are disparities and disagreements among researchers and their theories. In addition, most of the analytical results presented thus far involve the in-plane behavior, such as the buckling of arches, and very little information of practical use on the lateral-torsional behavior of horizontally curved beams loaded normal to the plane of curvature has been presented. Analytical data on the behavior of singly symmetric and nonprismatic sections and on the effects of the lateral restraints provided by cross-frames and diaphragms is practically nonexistent. In reality, the influence of cross-frame spacing and rigidity cannot be excluded from a lateral-torsional buckling curvature effect definition and the system-wide behavior must be considered.

Nishida *et al.* (1978) presented work which used the large deflection theory of curved members to derive the critical elastic moment for a horizontally curved beam subjected to equal end moments. Note from Eq. 13.3 that the critical moment approaches that of the straight girder as the radius of curvature approaches infinity:

$$M_{cr} = \sqrt{\left(1 - \frac{L^2}{\pi^2 R^2}\right) \left(\frac{\pi^2 E I_y}{L^2}\right) \left(GJ + \frac{\pi^2 E C_w}{L^2}\right)} \quad 13.3$$

where L = unbraced length, R = radius of curvature, I_y = weak axis moment of inertia, E = Young's modulus, G = shear modulus, J = torsional rigidity of the section, C_w = warping constant, b = flange width, t_w = web thickness, and h = depth between flange centroids.

Kang (1992) demonstrated that a large variation in torsional rigidity ratio has little effect on the critical load ratio of the lateral buckling of horizontally curved girders loaded normal to the plane of curvature and that the subtended angle is the dominating parameter. The results from finite element analyses were used to form a regression equation for the reduction in lateral-torsional buckling of the curved girder over that of the straight (Yoo *et al.* 1996):

$$y = (1 - \gamma x^\beta)^\alpha \quad 13.4$$

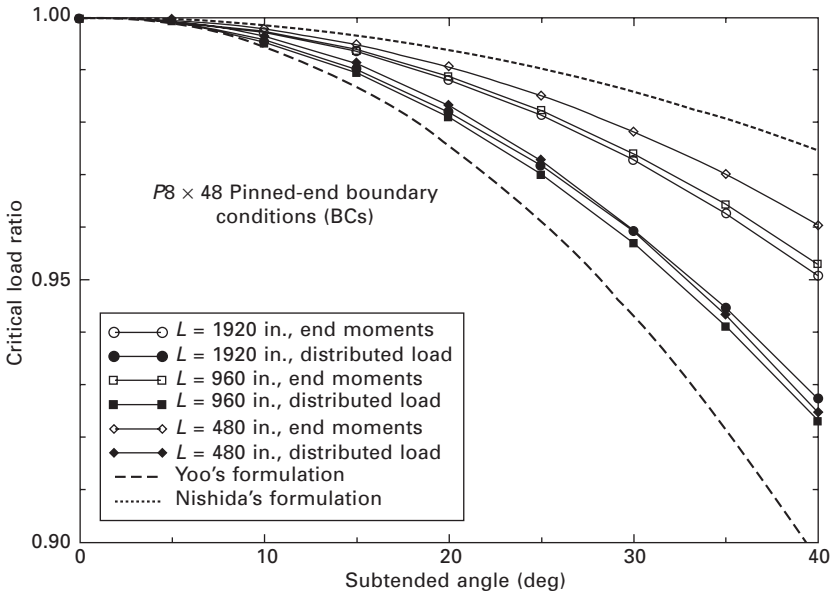
where y = critical moment ratio (curved/straight), x = subtended angle in radian, $\alpha = 2.152$, $\beta = 2.129$, and $\gamma = 0.1058$.

13.4.1 Effect of curvature on L-T stability of single girders with end-support conditions

The finite element method was used to model a set of numerical 'test' girders of widely varying dimensions and end-support conditions, including symmetric, unsymmetric, and nonprismatic girders loaded normal to the plane of curvature. The subtended angle was varied from 0 to 40 degrees and the critical loads

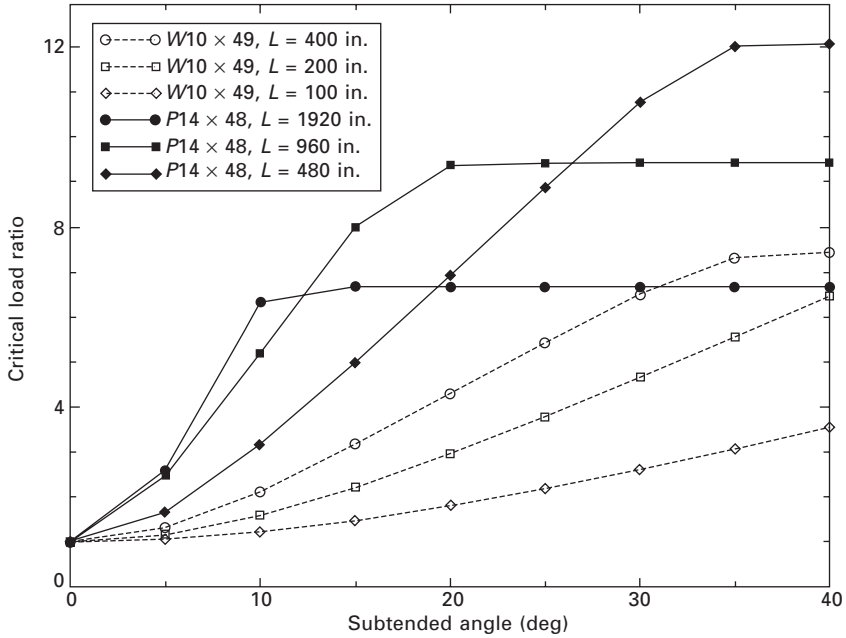
were normalized to the critical loads of the straight girder with the same cross-section dimensions and lengths, thus giving a clear view of the effect of increasing curvature on the elastic buckling behavior. Figure 13.2 illustrates the effect of curvature on the elastic lateral-torsional buckling behavior of single curved girders with end-support conditions only (Davidson 1996). The dotted lines represent Eqs (13.3) and (13.4). The following trends were noted:

- The distributed load condition results in a smaller critical load ratio than end moments.
- Increasing length resulted in little effect on the critical load ratio.
- The critical load ratio trend was not significantly different for the unsymmetrical cases and the nonprismatic cases.
- There is less than a 10% decrease in critical load for all pinned end cases with subtended angle up to 40 degrees and less than 1% up to 10 degrees.
- The Nishida (Eq. 13.3) and Yoo (Eq. 13.4) equations bounded all results.

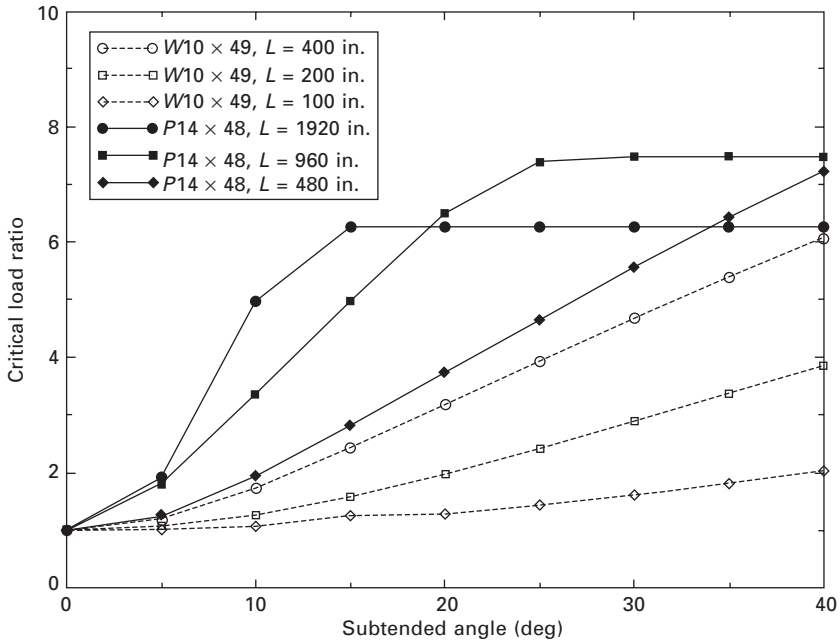


13.2 Illustration of curvature effects on the lateral-torsional buckling of simply supported curved beams.

Other boundary conditions including fixed-end conditions, fixed-end conditions with free warping, and pinned-end conditions where warping was restrained were analyzed using a curved beam finite element program, CVSTB1, developed by Kang (1992). Figures 13.3 and 13.4 illustrate that the critical ratio increases for fixed-end conditions. In research conducted by Pfeiffer



13.3 Critical load ratio for fixed-end conditions with warping unrestrained.

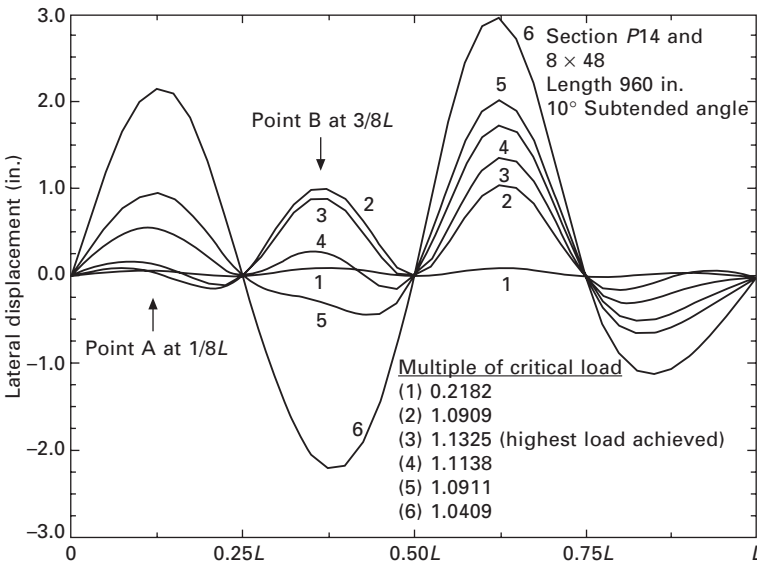


13.4 Critical load ratio for fixed-end conditions.

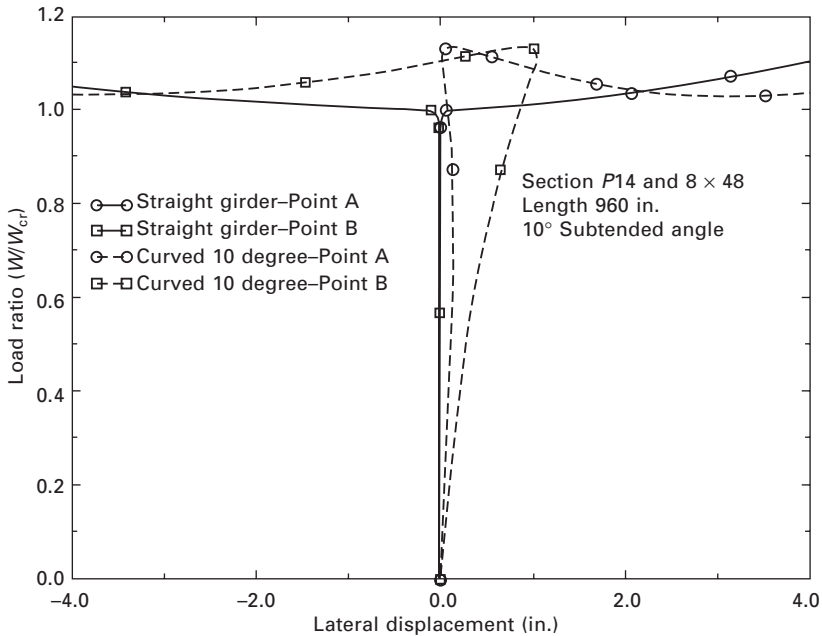
(1981), the same trends of increasing critical loads were noted for fixed–fixed boundary conditions and fixed–pinned boundary conditions. This was attributed to: (1) coupling of the axial deformation and the radial displacement that exists in curved beams and (2) an effective increase in torsional stiffness due to curvature, i.e. there is less rotation of the cross-section present in the curved beam buckling mode shapes than in that of the straight beam.

13.4.2 Effect of curvature on L-T buckling of girders with intermediate lateral supports

Boundary conditions that simulate the effect of the lateral restraints provided by the cross-frames in the curved girder system were also considered. As curvature is increased, the buckling modeshape changes from that of an ‘S’ shape as in the straight girder to that of an ‘M’ shape where the lateral displacement of the entire compression flange is in the outward radial direction. For buckling in the ‘S’ shape to occur in horizontally curved girders, the compression flange must initially displace away from the center of curvature until sufficient lateral flange moment is reached at the restraints to cause the compression flange to ‘snap’ through towards the center of curvature. This ‘snap through’ behavior is illustrated in Figs 13.5 and 13.6 using an incremental geometric nonlinear analysis. This behavior becomes less likely as curvature is increased and will always occur at loads greater than the critical load of



13.5 Illustration of incremental displacement of the top flanges with lateral restraints at 1/4 L.



13.6 Illustration of incremental lateral displacements with lateral restraints at $1/4 L$.

the respective straight girder of the same length, boundary conditions, and cross-section dimensions.

13.5 Effect of curvature on flange plate stability

Plate components of the girder in compression must be proportioned to prevent premature local instability. Design specifications stipulate width-thickness ratios for design of the section as 'compact' or 'non-compact,' where 'compact' refers to the ability of the section to reach substantial plastic strains prior to local instability. The effects of curvature and warping stresses on elastic flange buckling were investigated analytically by Culver and Frampton (1970) and on inelastic flange buckling by Culver and Nasir (1971), Komatsu *et al.* (1975), and Komatsu and Kitada (1981). Kang and Yoo (1990) conducted an analytical study that examined the allowable flexural stresses permitted by the Guide Specifications using finite element modeling of the whole cross-section. His results indicated that there may be a significant curvature effect on local buckling. Davidson and Yoo (1996) demonstrated that there is a reduction in the elastic buckling strength of curved compression flanges owing to the presence of warping stress gradient across the flange. The primary factors contributing to the reduction were determined to be the

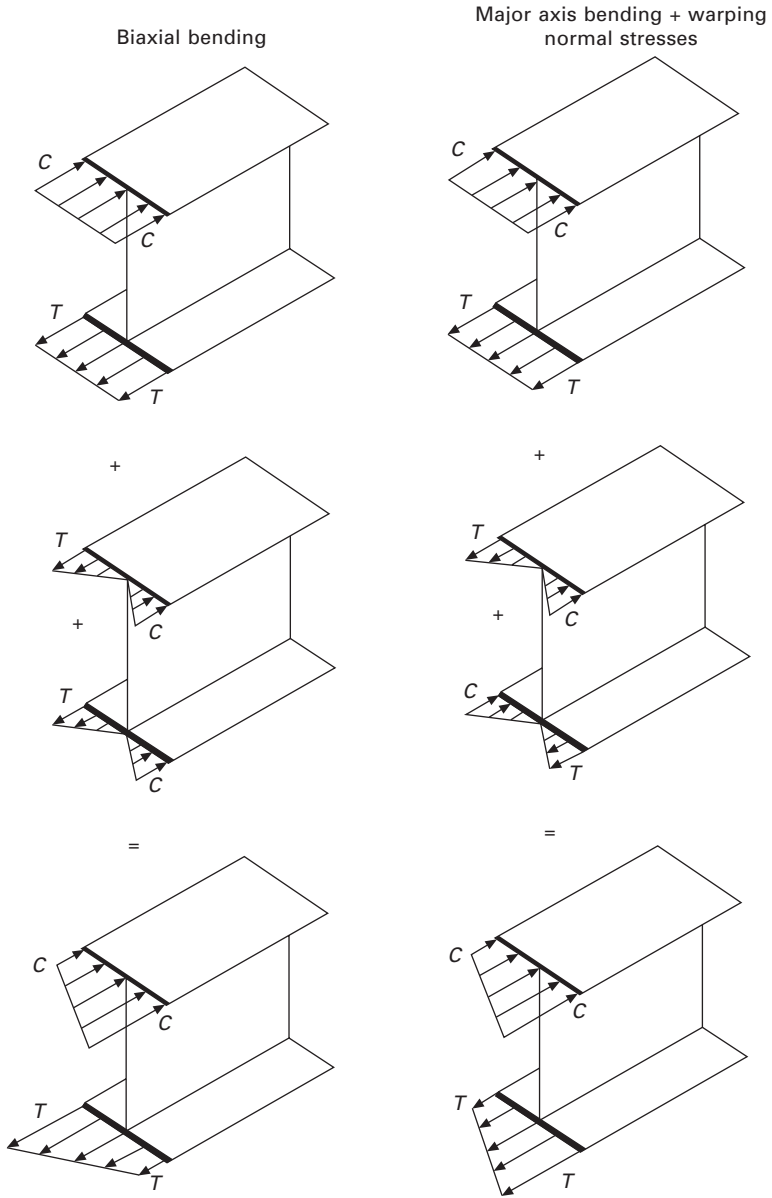
warping stress gradient and the rotational resistance provided by the web. An equation representing the curvature effect was developed.

The Japanese have also conducted analytical research on the local buckling behavior of curved compression flanges and concluded that the influence of the stress gradient due to warping cannot be omitted in evaluating the buckling strength of I-girders with substantial curvature (Komatsu *et al.* 1975, Komatsu and Kitada 1981, Nakai *et al.* 1981, Fujii and Ohmura 1987, Nakai and Yoo 1988). The Japanese suggest approximately 30% increase in the required curved compression flange thicknesses to eliminate potential local buckling where warping stress is 'predominant' (Komatsu and Kitada 1981, Hanshin 1988, Nakai and Yoo 1988, Japan Road Association 1990).

13.5.1 Elastic stability of centerline stiffened plates with stress gradient

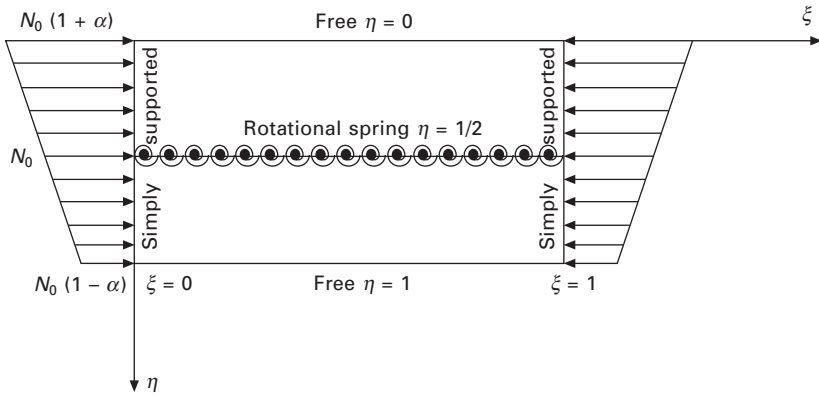
Many researchers have analyzed the elastic buckling behavior of isolated plates subjected to a stress gradient, with a recent review provided by Madhavan and Davidson (2003, 2004). However, practically all of the research was carried out on plates with boundary conditions only at the edges. When a stress gradient is present, the solutions that have only edge boundary conditions are not applicable to the flange plates of I-beams unless the interaction between the two sides of the plate coupled with the centerline rotational resistance provided by the web is appropriately considered. The vectorial addition of major axis bending normal stress with minor axis bending normal stresses or torsional warping normal stress results in linearly varying compressive stresses across the width of I-beam flanges as illustrated in Fig. 13.7. The effect of warping normal stress gradient on elastic buckling can be described by considering the I-beam flange as an isolated plate system with the web interaction idealized as a boundary condition. Figure 13.8 illustrates the analytical model of the plate subjected to uniaxial eccentric compression with the loaded edges simply supported, non-loaded edges free, and rotationally stiffened along the centerline. The eccentricity of compression is described in terms of the load eccentricity parameter α . For $\alpha > 1$, a portion of the flange is subjected to tension (Fig. 13.9). The rotational stiffness provided by the web is symbolically represented as the stiffness of a rotational spring and the symbol ' I '. A relationship between the rotational resistance provided by the web plate and the idealized rotational spring will be established.

The effect of stress gradient on buckling capacity is expressed in terms of critical load ratio (ψ), which is defined as the ratio of elastic critical buckling capacity of a plate subjected to a stress gradient ($\alpha > 0$) normalized to that of uniform compression ($\alpha = 0$). In terms of application to I-shaped flexural members, the critical load ratio can be interpreted as the ratio of elastic critical buckling capacity of the flange plate subjected to combined bending



13.7 Longitudinal flange stresses due to biaxial bending and major axis bending plus warping normal stresses.

and warping or minor axis bending stresses to the flange buckling capacity due to the major axis bending component of stress at the web-flange intersection.



13.8 Analytical model: plate with rotational stiffness at the center subjected to stress gradient.

Figure 13.10 shows a plot of critical load ratio versus stress gradient with increase in rotational stiffness from rotation free ($\Gamma = 0$) to rotation fixed ($\Gamma = \infty$) resulting from a Galerkin series solution (Madhavan and Davidson 2004). For the rotation fixed condition, the solution converges to the result obtained from the classical solution of the clamped/free half plate system. The behavior of the flange plate with varying rotational stiffness along the web flange intersection demonstrated a decrease in buckling capacity with increase in α . While the decrease in buckling capacity is only 2% for the rotation free condition (simple boundary, $\Gamma = 0$), following a convex path, there is a 45% decrease for rotation restrained condition (clamped boundary, $\Gamma = \infty$) with a concave path. The differences exhibited between the rotation free condition and the rotation restrained condition demonstrates that, unlike the flange plates of I-girders subjected to uniform compression, a stress gradient results in an interaction between the half flange plates on either sides of the web–flange intersection that is coupled with the rotational resistance provided by the web.

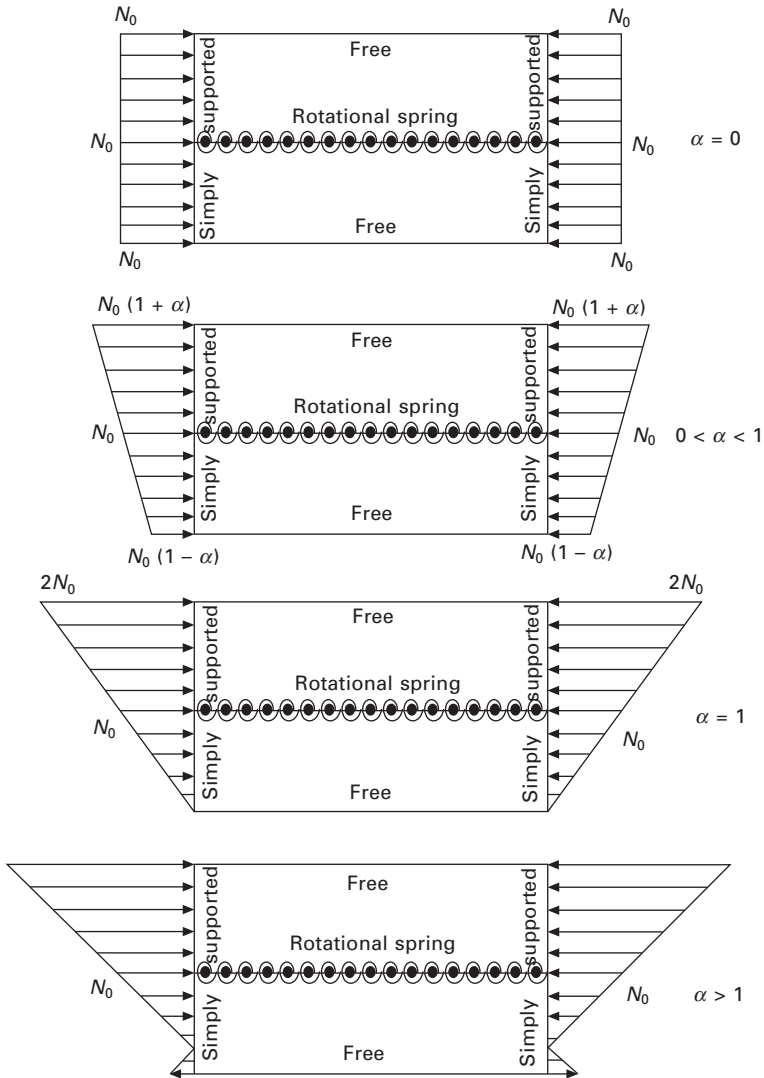
The relationship between the critical load ratio (ψ), the rotational resistance at web–flange intersection (Γ), and the variable eccentric loading (α) can be written in the following form (Madhavan and Davidson 2005):

$$\psi = \frac{1}{1 + f(\alpha, \Gamma)} \tag{13.5}$$

where $f(\alpha, \Gamma)$ is given by:

$$f(\alpha, \Gamma)_{0 < \alpha < 1} = (-0.0077\Gamma^2 + 0.1467\Gamma + 0.0205)\alpha \tag{13.6}$$

Equation 13.6 is based on the Galerkin solution and is applicable for $0 \leq \alpha \leq 1$ and $\Gamma \leq 10$.

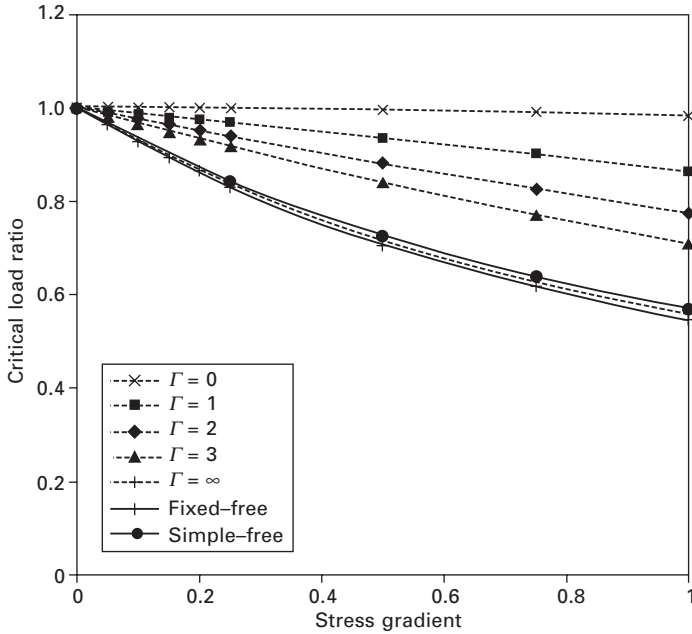


13.9 Definition of load eccentricity parameter α .

13.5.2 Definition of compactness for flanges with stress gradient

Cross-section classification

In general, structural members are classified as compact, non-compact or slender. When the slenderness of the cross-section (λ) is less than the compact section slenderness limit (λ_p), the sections are referred to as compact sections. Compact sections are assumed to reach full plastic moment capacity without

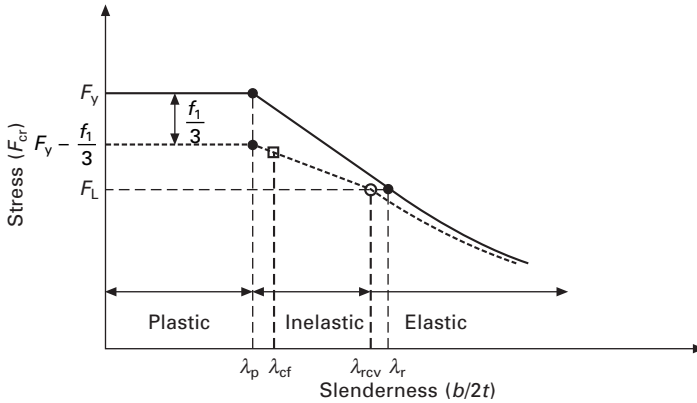


13.10 Reduction in critical load with load eccentricity.

local buckling. When the slenderness of the cross-section is between compact section limit, and non-compact section limit (λ_r), the sections are referred to as non-compact sections. Non-compact sections assume that local buckling occurs after yielding has initiated, and failure of flanges is due to a combination of yielding and buckling. Most practical bridge girders are designed in the inelastic range.

When the slenderness of the cross-section is greater than the noncompact section limit, the sections are referred as slender cross-sections. In slender cross-sections, local buckling occurs prior to yielding. Although practical girders are not designed to fail due to elastic buckling, a theory-based approach for estimating the capacity of slender flange plates is essential. A linear transition is typically adopted by connecting the compact section limit and noncompact section limit. The transition zone takes into account the effect of residual stresses and moment gradient.

For horizontally curved steel I-girders, it is logical to define an additional type of section: a compact-flange section. Compact flange sections consist of a compact flange and a non-compact web, thereby permitting a larger lateral moment due to curvature to be sustained in combination with a given vertical moment. That is, a compact flange section considers yielding of the higher-stressed half of the flange plate while the other side remains elastic. The slenderness limits are generically illustrated in Fig. 13.11.



13.11 Slenderness limit definitions for local buckling of curved I-girder flange plate.

Non-compact section limit (λ_r)

The AASHTO LRFD (2001) standard specifications limit the flange slenderness of straight girders ($b_f/2t_f$) to 12, which is based on a practical upper limit ‘to ensure the flange will not distort excessively when welded to web’ and to prevent susceptibility of damage to the flange during construction (AASHTO 2001). White *et al.* (2001) proposed a non-compact limit for flanges of bridge I-girders based on AISC (1999):

$$\lambda_r = \frac{b_f}{2t_f} \leq \left(1.9 \sqrt{\frac{E}{F_L \sqrt{\frac{2D_c}{t_w}}}} \right) \tag{13.7}$$

where b_f is the total flange width (in), t_f is the flange thickness (in), D_c is the depth of the web in compression (in) and F_L is the flexural stress corresponding to the onset of significant inelasticity taken as the smaller of $(F_{yc} - F_{rs})$ or F_{yw} , and F_{rs} approximates the effect of residual stresses within the compression flange.

The Guide Specifications define non-compact flanges as flanges that are permitted to reach the peak yield stress in the flange tip without local buckling. The limiting width-to-thickness ratio of the flange is given by:

$$\frac{b_f}{2t_f} \leq 0.51 \sqrt{\frac{E}{|(f_b + f_1)|}} \leq 11.5 \tag{13.8}$$

where f_1 is the total factored lateral flange bending stress at the section under consideration (ksi) and f_b is the factored average flange stress at the section under consideration (ksi). Equation 13.8 takes a conservative approach of

considering the peak stress ($f_b + f_l$) as uniformly applied stress across the flange width. The upper limit of 11.5 is based on experimental observations by Mozer and Culver (1975) and analytical observations by Culver and Nasir (1969). Experiments carried out by Mozer and Culver (1975) on two heat-curved and two cut curved I-girders with $b_f/2t_f = 11.5$ concluded that this limit was adequate if both vertical bending and lateral flange bending stresses are considered and the capacity is limited to initial yielding at the flange tips. Investigations by Culver and Nasir (1969) also revealed that flange local buckling begins to have a significant detrimental effect on the strength in the vicinity of this limit. This ratio was the approximate limit within the AASHTO straight girder specifications for yield strength of 36 ksi in effect at the time of Mozer's research (AASHTO 2003).

For flange plates of a curved I-girder, or a straight I-girder subjected to lateral and vertical bending, α can be taken as the ratio of lateral bending to vertical bending stresses. The elastic buckling stress acting in a curved I-girder flange plate is expressed in terms of the straight girder flange given by:

$$(F_{cr})_{cv} = (F_{cr})_{st} \psi \quad 13.9$$

ψ can be considered as a reduction in buckling stress due to stress gradient. The suffix st refers to straight girder and cv refers to curved girder. For flange plates of straight I-girders, the Euler elastic buckling expression can be represented as:

$$(F_{cr})_{st} = k_c \frac{\pi^2 E}{12(1 - \nu^2)(b_f/2t_f)^2} \quad 13.10$$

The buckling coefficient k_c depends on loading conditions, aspect ratio of the plate, and rotational resistance provided by the web. For flange plates of curved I-girders, the critical buckling stress can be expressed as:

$$(F_{cr})_{cv} = \left[k_c \frac{\pi^2 E}{12(1 - \nu^2)(b_f/2t_f)^2} \right] \psi \quad 13.11$$

Here $k_c = 4/(2D_c/t_w)^{0.5}$ (AASHTO 2001), D_c is the depth of web in compression, t_w is the thickness of web plate.

Following the procedure typically used to establish slenderness ($b_f/2t_f$) limits of a compression plate necessary to prevent local buckling before the onset of inelasticity (F_L):

$$\frac{(F_{cr})_{cv}}{F_L} = \frac{1}{\lambda_{cv}^2} \leq 1.0 \quad 13.12$$

where

$$\lambda_{cv} = \sqrt{\frac{F_L}{(F_{cr})_{cv}}} = \frac{b_f}{2t_f} \sqrt{\frac{F_L 12(1 - \nu^2)}{\pi^2 E k_c \psi}} \quad 13.13$$

For design in the elastic range $1/\lambda^2 \leq 1.0$. Hence,

$$\left(\frac{b_f}{2t_f}\right)_{cv} \leq \left[1.9 \sqrt{\frac{E}{F_L \sqrt{\frac{2D_c}{t_w}}}} \right] \sqrt{\psi} \quad 13.14$$

$$\left(\frac{b_f}{2t_f}\right)_{cv} \leq \left(\frac{b_f}{2t_f}\right)_{st} \sqrt{\psi} \quad 13.15$$

where ψ is based on Eqs 13.5 and 13.6 above,

$$\psi = \frac{1}{1 + (-0.0077\Gamma^2 + 0.1467\Gamma + 0.0205)(f_1/f_b)} \quad 13.16$$

The rotational stiffness parameter Γ represents a rigidity ratio that reflects the relative rotation resistance provided by the web and the flange given by:

$$\Gamma = r \frac{b_f}{D} \quad 13.17$$

where b_f is the flange width, D is the flexural rigidity defined as:

$$D = \frac{Et_f^3}{12(1 - \nu^2)} \quad 13.18$$

and r is the rotational stiffness provided by the web given by (Culver and Nasir 1969):

$$r = \frac{E}{3(1 - \nu^2)} \frac{t_w^3}{d_w} \quad 13.19$$

where t_w and d_w are the thickness and depth of the web. Γ is less than 0.5 for thin-web plate girders commonly used in bridges and other situations requiring deep flexural members. Therefore, taking $\Gamma = 0.5$, Eq. 13.16 can be reduced to a simpler form:

$$\psi = \frac{10}{10 + (f_1/f_b)} \quad 13.20$$

This represents a theoretical basis for defining the non-compact section slenderness limit with consideration to a stress gradient across the compression flange due to torsion or minor axis bending. However, its appropriateness for bridge specifications has not yet been considered.

Compact section limit (λ_p)

A number of researchers have developed equations intended to predict the reduction in ultimate strength of curved I-girders over that of straight girders due to the effects of curvature. Thorough summaries have been provided by Davidson (1996), Simpson (2000), and White *et al.* (2001). The allowable normal flange stress in the Guide Specifications for 'Allowable Stress Design' are based on the research that Culver (1972) and co-researchers conducted as part of the CURT project. The 'Load Factor Design' portion of the Guide Specifications is based on research by Galambos (1978) as an extension of work performed in the CURT project at Carnegie-Mellon University. The parts of the design equations that represent strength reduction due to curvature are quite complex and cumbersome. Nakai and co-researchers (Nakai and Kotoguchi 1983, Nakai *et al.* 1983) proposed an interaction equation for limiting the stresses in horizontally curved I-girders based on theoretical and experimental research in the elastic range. The equations represent interaction for allowable stress in the compression flange including the presence of warping and the reduced lateral buckling strength of the girder due to curvature.

In a series of research investigations (Yoo and Pfeiffer 1983, Kang 1992, Yoo *et al.* 1996), it was demonstrated that a large variation in the torsional rigidity has little effect on the critical load ratio (curved/straight) for the lateral buckling of horizontally curved girders loaded normal to the plane of curvature and that the subtended angle is the dominating parameter. A curvature reduction equation was derived from a regression of data resulting from an elastic finite element investigation using curved beam elements which include warping (Kang 1992). Although this strength reduction equation was developed based upon an elastic theory, it was proposed (Yoo *et al.* 1996) that the reduction in critical moment of curved girders results from the presence of the rotational component of the girder behavior and likewise there would be a similar reduction in ultimate moment capacity. Previous ultimate strength tests by others on curved I-girders appear to verify this conjecture (Yadlosky 1993, Yoo *et al.* 1996).

Yoo and Davidson (1997) presented yield interaction equations that were based on the static equilibrium of the I-shape girder under vertical moment and lateral flange moments resulting from nonuniform torsion. Equations were presented for singly symmetric composite and noncomposite I-shapes for both positive and negative moment. Complete plastification for compact sections, partial yield penetration for the compact-flange sections, and initial yield at the flange tip for non-compact sections were considered for a total of 18 interaction cases. A computer program was created and the reduction due to curvature was demonstrated for a number of geometry and load conditions.

Davidson (Davidson 1996, Davidson and Yoo 2000) developed models of the curved I-girder test frame used in the FHWA-CSBRP to study the

propagation of yielding in a curved I-girder frame and to relate yield behavior to ultimate strength predictors developed by others. The test frame consisted of three full-scale bridge girders spaced at 2.67 m (8.75 ft) with the center girder of length 27.5 m (90 ft) and radius of curvature of 61 m (200 ft), connected by cross-frames. A section of the outside girder was designed for 'test specimens' of various dimensions. The initial yield and ultimate strength moments resulting from the finite element investigation were compared to the yield interaction equations presented by Yoo and Davidson (1997). It was noted that an excellent correlation results for the ultimate strength of the doubly symmetric sections, but that the interaction equations result in less accurate comparisons for singly symmetric sections. Yielding was noted to propagate simultaneously in the tension and compression flanges for doubly symmetric sections but propagated only through the compression flange in the singly symmetric sections (Davidson 1996, Davidson and Yoo 2000). A good correlation was also noted between the interaction equation for non-compact sections and M_y from the finite element results. In general it was noted that failure is characterized by a gradual distortion of the web and inelastic buckling of the compression flange. The absence of transverse stiffeners in one of the specimens was shown to significantly affect behavior. Since the ultimate strength predictor equations assume that full plastification of the cross-section occurs, the inaccuracy with respect to singly symmetric curved sections was attributed to the discrepancy between the assumed and observed plastic condition at ultimate strength.

The AASHTO LRFD standard specifications define compact flange section as:

$$\frac{b_f}{2t_f} \leq 0.382 \sqrt{\frac{E}{F_y}} \quad 13.21$$

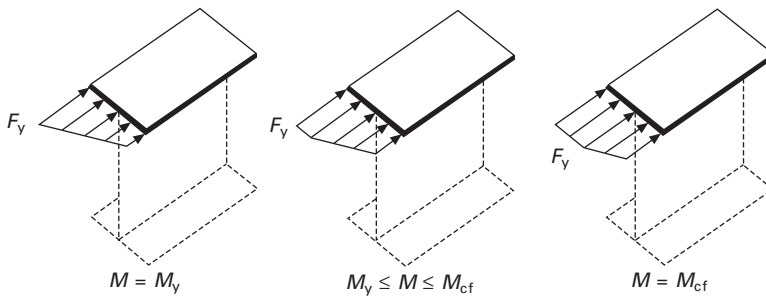
The Guide Specifications stipulate a compactness limit of 9.0 for $F_y = 50$ ksi, which is essentially the same as the straight girder requirement of 9.2 (for $E = 29000$ ksi and $F_y = 50$ ksi, Eq. 13.21 reduces to 9.2). Since the assumed stress distribution is the same for curved plastic cross-sections as for straight plastic cross-sections, there is a tendency to consider the straight girder compactness limit given by Eq. 13.21 as applicable to curved girders. However, owing to the lateral displacement characteristic of behavior that actually increases as yielding progresses across the flange(s), the strains may be much greater in the flange(s) and the web to reach the assumed plastic configuration. The ability of a compact girder that is subjected to significant warping or lateral bending to reach the plastic strain distribution assumed for a 'plastic moment' condition has not been demonstrated.

In the plastic range ($\lambda < \lambda_p$), yielding of the flanges due to lateral bending in a curved girder will reduce the capacity available for vertical bending. In the approach by Hall *et al.* (1999), the lateral bending stress evaluated by the

one-third rule is employed to estimate the reduced vertical bending capacity of flanges in the plastic range. The one-third rule was originally developed as a restriction on the flange capacity predicted by McManus's (1971) strength equations, based on the assumption that the flange section is compact. The term 'one-third rule' reflects a reduction of one-third of the lateral bending stress from the yield stress to account for the available flexural resistance. Therefore, the limit on flexural strength implied in Fig. 13.11 reflects this reduction in strength due to lateral bending of the flange.

Compact-flange section limit (λ_{pf})

The compact flange section limit refers to compact flange and a non-compact web. Since one edge of the curved girder flange is subjected to relatively higher stress than the other edge, yielding will initiate at the flange tip and progress towards the web. When compactness is defined based on yielding of one half of the flange plate as illustrated in Fig. 13.12, the flange is classified as compact-flange.



13.12 Conceptual representation of compact-flange stress distribution.

Recently, an approach based on the work by Lay (1965) for determining the compactness requirement of flanges of I-girder subjected to uniform compression was extended for defining the compact flange requirements of a horizontally curved girder (Davidson and Madhavan 2005). Lay's model is based on buckling of yielded flanges. The compact-flange limit was expressed as:

$$\lambda_{cf} = \left(\frac{b}{2t} \right) = \left[\frac{2}{\sqrt{4 - \alpha}} \right] \lambda_p \tag{13.22}$$

in which the subscript cf refers to compact flange. The terms in the square brackets of Eq. 13.22 can be considered as an amplification factor that increases the $b/(2t)$ ratio with increase in α . When α becomes zero, the compact-flange

requirements reduces to straight girder equations. However the implication is minimal; the increase in slenderness from compact section to compact flange section for a value of $\alpha = 0.5$ is only approximately 7%. Furthermore, the accuracy and applicability of this approach is still being investigated.

13.6 Effect of curvature on web plate stability and distortion

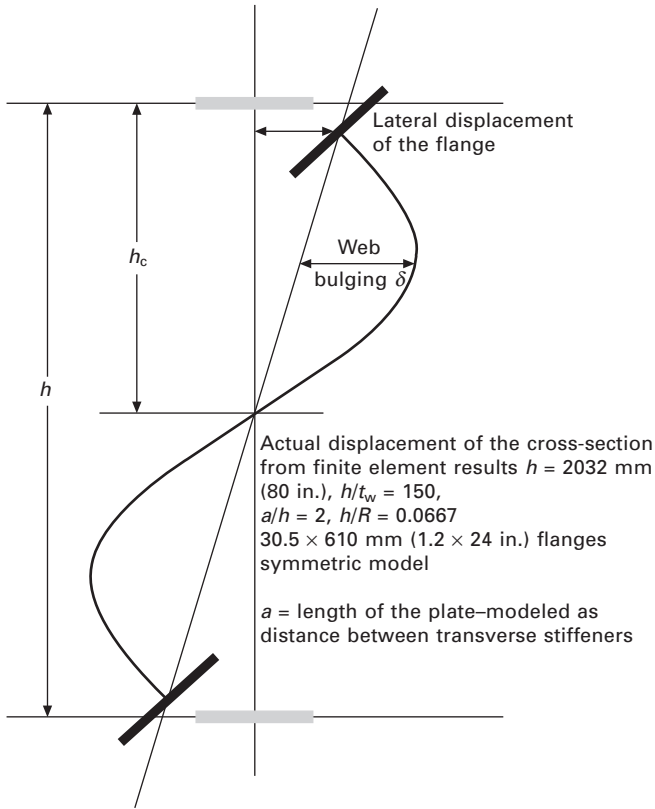
13.6.1 Pure bending

The primary role of the webs of I-shaped plate girders in the region of high moment is to maintain the relative distance between flange plates. Efficient design of plate girders therefore requires that the flange plates carry most of the primary moment and that the web be designed as 'slender' as structurally possible. Because of this, web depth thickness limitations, transverse stiffener spacing and rigidity, and longitudinal stiffener location and rigidity for straight girders are largely based on buckling considerations.

For straight girders, the buckling behavior of the web plate is easily and accurately analyzed using simplified boundary and loading conditions. However, for curved plate girders, the presence of curvature greatly complicates behavior and design considerations. Curvature induces both warping of the cross-section and, more importantly for web considerations, transverse displacement of the web (distortion), and also causes the longitudinal membrane stresses in the web to become a nonlinear distribution through the web depth. The web slenderness requirements in the Guide Specifications are based upon work done as part of the CURT project during the early- and mid-1970s (Culver *et al.* 1972a,b,c, 1973). Japanese researchers performed both analytical and experimental research on the behavior of the curved web panel, resulting in a formulation for the reduction in strength of the curved plate girder. The reduction represented in US design guides and that suggested by Japanese researchers is based solely on the curvature of the panel and represents a regression of analytical data. Also, the research in which design equations were based involved aspect ratios of 1.5 or less and was limited to symmetric sections. Therefore, the applicability of the resulting reduction equations is limited. A rigorous analysis of behavior and review of relative curved web behavior research and comparison between US and Japanese design equations is presented by Davidson *et al.* (1999a,b, 2000a,b) and Davidson and Yoo (2002, 2004).

Curved web behavior

An example of the displacement of the doubly symmetric cross-section is shown in Fig. 13.13. The distortional displacement results in plate bending



13.13 Displacement of the curved plate girder cross-section.

stresses that would not occur in the flat panel under pure vertical bending moment. Furthermore, as curvature and panel slenderness are increased, the membrane stress distribution becomes increasingly nonlinear through the depth of the section (Davidson *et al.* 1999a).

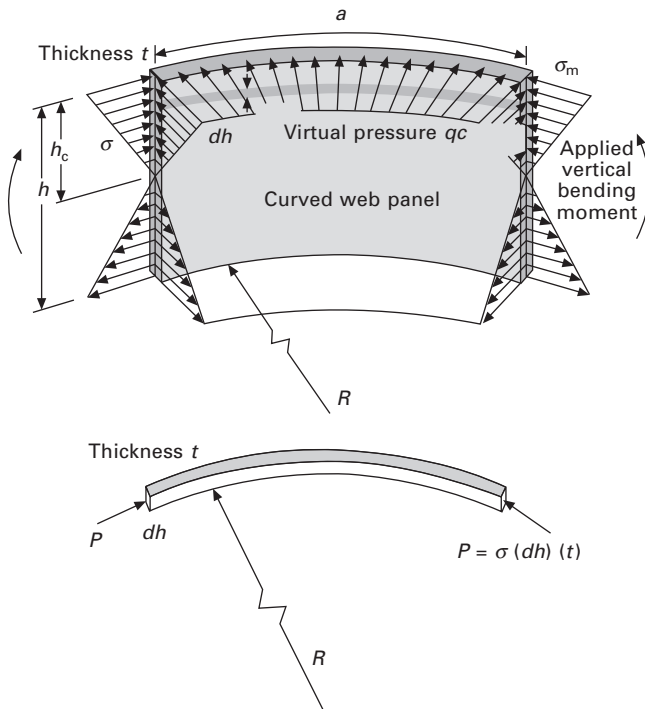
Elastic buckling

Investigations on the bifurcation buckling load for curved web panels under pure bending and shear and combined bending and shear were done as early as 1973 by Abdel-Sayed, but without flange rigidity included in the mathematical models. Abdel Sayed and others demonstrated that curvature does not reduce the buckling load of curved web panels. Davidson *et al.* (1999a) verified that the critical loads of curved web panels are indeed higher than flat panels and that the buckled mode shapes for flat and curved panels were practically identical for curvature within the range of curved steel bridge girders.

Analytical model: lateral pressure analogy

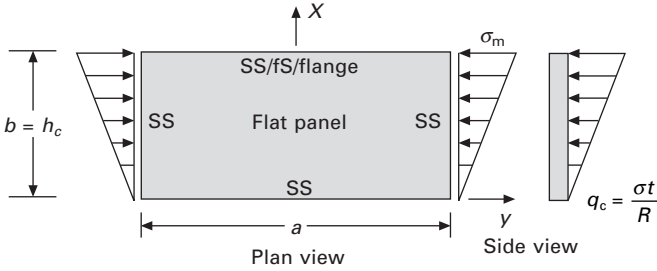
The amount of transverse or ‘bulging’ displacement can be approximated by using a ‘lateral pressure’ analogy (Davidson *et al.* 1999a). Consider a virtual width strip, dh , of the curved web panel of thickness t and radius R under vertical bending stress as shown in Fig. 13.14. Because of the non-collinearity of the resultant force, P , due to vertical bending moment on the virtual strip, a lateral ‘virtual’ distributed load results along the unit strip, which, after considering that the radius is very large with respect to the panel length, can be viewed as a virtual pressure through the depth of the girder:

$$q_c = \frac{P}{R} = \frac{\sigma t}{R} \tag{13.23}$$



13.14 Lateral pressure analogy.

Since the distortion of the cross-section results from vertical bending moment and the transverse displacement of the deformed cross-section will cross the undeformed vertical axis at the neutral axis, the displacement behavior is analogous to that of a flat plate of length a , thickness t , and width h_c , simply supported on the bottom edge, with a linearly increasing transverse load as illustrated in Fig. 13.15. Using this analogy, the displacements and plate



13.15 Theoretical development for flat panel.

bending moments can be approximated (Davidson *et al.* 1999a). For the maximum ‘bulging’ transverse displacement, the value of α is derived by considering the fourth (flange) edge of the model as simple support. In reality, the flange will provide a rotational rigidity between fixed and simple. For the maximum plate bending stress occurring at the top of the web (flange/web juncture) the case where the fourth edge is fixed will provide a conservative value of β . Following this approach, the maximum displacement and bending stress of the panel, respectively, can then be approximated by:

$$\delta_{\max} = \frac{\alpha h_c^4 \sigma_m 12(1 - \nu^2)}{E t^2 R} \tag{13.24}$$

$$M_{b\theta} = \frac{\beta h_c^2 t \sigma_m}{R} \tag{13.25}$$

where α and β are constants that depend on the location of the displacement or moment, respectively, and aspect ratio only, h_c is the height of the web in compression, and σ_m is the stress at the web/flange line resulting from vertical bending moment.

Geometric nonlinear effects

Significant geometric nonlinearity occurs in the displacement behavior of curved web panels, which may increase the displacements and stresses significantly. Geometric nonlinear analyses were conducted to quantify the amount of amplification in such a way that the amplification may be applied to the results from the lateral pressure analogy to get a conservative approximation for the maximum transverse deflection and maximum stresses (Davidson *et al.* 1999b). Including deflection amplification effects, using values of $\nu = 0.3$, and a conservative value for β of 0.0667, the web slenderness for curved girders can be derived based on maximum stress as:

$$\left[\frac{D}{t_w} \right]_{cv} \leq \left[\frac{D}{t_w} \right]_{st} R_s \tag{13.26}$$

where R_s is the developed curvature reduction factor on D/t_w based on stress considerations:

$$R_s = \sqrt{\frac{1}{\psi_w}} \quad 13.27$$

$$\psi_w = \sqrt{1 + 0.161\left(\frac{D_c}{t_w}\right)\left(\frac{D_c}{R}\right) + 0.128\left(\frac{D_c}{t_w}\right)^2\left(\frac{D_c}{R}\right)^2} \\ \times \left[1 + 1.5\left(\frac{D_c}{R}\right)^{0.5}\right] \quad 13.28$$

where D_c is the depth of the web in compression and t_w is the thickness of the web plate.

13.6.2 Influence of longitudinal stiffeners

The same approach was used for web panels with longitudinal stiffeners (Davidson *et al.* 2000b). Web panels with longitudinal stiffeners placed in the compression region only and in both the compression and tension regions were considered. The stiffeners were placed on the inside-of-curvature side only and at the optimum location with respect to the buckling behavior ($0.4D_c$). Again, a lateral pressure analogy was used to derive closed-form solutions for the maximum ‘bulging’ displacement and plate bending stresses, and nonlinear effects were investigated and quantified. It was noted that the geometric amplification behavior for one and two longitudinal stiffeners is considerably less than that demonstrated for no longitudinal stiffeners.

The reduction in vertical moment carrying capacity for the panel with one or two longitudinal stiffeners was derived by considering the increase in stress at the flange/web juncture, either top or bottom, where the maximum stress due to combined membrane and plate bending action will occur. The curved girder required slenderness, D/t_w , can be represented as a reduction factor on the allowable web slenderness for straight girder design as:

$$\psi_{w-t} = \sqrt{1 + 0.161\left(\frac{D-D_c}{t_w}\right)\left(\frac{D-D_c}{R}\right) + 0.128\left(\frac{D-D_c}{t_w}\right)^2\left(\frac{D-D_c}{R}\right)^2} \quad 13.29$$

and

$$\psi_{w-c} = \sqrt{1 + 0.0384\left(\frac{D_c}{t_w}\right)\left(\frac{D_c}{R}\right) + 0.00728\left(\frac{D_c}{t_w}\right)^2\left(\frac{D_c}{R}\right)^2} \quad 13.30$$

where the subscripts *c* and *t* refer to compression and tension regions. For the case where one longitudinal stiffener is placed in the compression area, the larger of Eq. (13.29) and Eq. (13.30) should be used. For the case where a longitudinal stiffener is placed in the compression and tension regions, Eq. (13.29) should be used.

13.6.3 Pure shear

The web of a plate girder stiffened by flanges and transverse stiffeners has considerable post buckling strength due to ‘truss’ or ‘tension field’ action from the interaction of the buckled web, flanges, and stiffeners. This ability has been well established and has been used in ASD, LFD, and LRFD format design codes for straight girders. However, the lack of research on curved girders has kept tension field action out of curved bridge design approach.

Early analytical work on the elastic stability of stiffened cylindrical shells subjected to pure shear was conducted by Batdorf (Batdorf 1947, Batdorf *et al.* 1947) and then by Stein and co-researchers (Stein and Fralich 1949, Stein and Yeager 1949). In these works, equilibrium equations were derived assuming all four edges of the web panel to be simply supported. Equilibrium equations were solved using the finite difference method. Mariani *et al.* (1973) later extended the work of Stein and Yeager to include the case of the curved plate with multiple stiffeners under pure shear and developed an optimal stiffener spacing criterion to establish stiffener requirements for curved girder webs. From the work of these researchers it is generally agreed that the buckling load of the curved web panel is greater than that of the straight girder with the same aspect ratio, slenderness ratio, and boundary conditions.

Experimental research on the ultimate and postbuckling reserve strength of curved girders has been conducted by Mozer *et al.* (1971) as part of the CURT project. It was observed from these tests that there is a decrease in the postbuckling strength with increase in curvature, although the measured shear strengths are within 10% of the ultimate shear strength by straight girder theory, which could be considered to be within the range of acceptable experimental error. Also, the experimental investigation by Mozer *et al.* indicated that, in areas of negative bimoment (tending to bend the compression flange inward), the web behaves more like that of a straight girder and can carry the ultimate shear strength predicted for a straight girder with similar proportions.

The Japanese have also conducted a series of experimental tests on the ultimate strength of web panels under pure shear, pure bending, and their combinations (Nakai *et al.* 1984a,b,c, 1985a,b). Their results agree that curvature has little effect on the elastic critical shear load but that there is some decrease in ultimate strength. Like the Guide Specifications, the Japanese design specifications do not recognize postbuckling reserve strength for curved plate girders due to lack of research in this area (Hanshin 1988).

Lee and Yoo (1999) studied the bifurcation buckling and ultimate strength analysis of curved web panels subjected to pure shear using the finite element method. The analysis revealed that the curved web panels are capable of developing considerable postbuckling strength after the bifurcation point. The results also suggested that straight girder equations developed by Lee *et al.* (1994) and Lee and Yoo (1999) can be used to effectively predict the shear strength of curved web panels subjected to pure shear.

Davidson *et al.* (1996) presented results on the buckling and ultimate strength of curved web panels in pure shear. The finite element method was used with combined geometric and material nonlinear solution sequences to analyze typical plate girder web panels of various curvatures. The aspect ratios of the panels were also varied to compare the effects of transverse stiffener spacing for curved panels to that of straight. The results from the buckling analyses agreed with that of previous research whereas the elastic critical load of the curved panel was determined to be greater than that of the comparable flat panel. Furthermore, the finite element analyses revealed no substantial decrease in ultimate strength of the curved panel with respect to that of the straight (flat). It was observed that, although distinctive bifurcation buckling phenomena did not occur, curved web panels are able to sustain shear loadings beyond the elastic buckling points. It was also observed that the ultimate strength and behaviors of curved web panels with curvature in the practical range exhibited no significant differences as compared with those of straight girder webs.

These conclusions were also demonstrated through recent work by Shanmugam and co-researchers (Mahendrakumar *et al.* 2000, Shanmugam *et al.* 2003). Furthermore, the work by Shanmugam was extended into a unique experimental and analytical program that addressed curved web panels with openings (Shanmugam *et al.* 2002, Lian and Shanmugam 2003, 2004).

13.6.4 Combined bending and shear

In reality, there will generally be transverse shear present along with the vertical bending of the bridge girder. However, in the majority of straight bridge girder situations, the nominal strength in bending is not influenced by shear, nor is the nominal shear strength influenced by bending. Particularly in slender webs where ‘bend-buckling’ may occur, the bending stress is redistributed so that the flanges carry an increased share. The shear strength, however, is not reduced as a result of ‘bend-buckling’ because most of the shear strength is from tension field action with only a small contribution from the portion of the web adjacent to the flange.

Mikami and Furunishi (1981) presented work involving shear along with bending in Japanese journals and later in the *ASCE Journal of Engineering Mechanics* (1984), but this work was limited to cases where the applied

shear stress equals the applied vertical bending stress at the top of the panels. From these investigations it was concluded that the presence of shear along with bending did adversely affect the moment carrying capacity of the beam but no formulations for design use were presented.

Abdel-Sayed (1973) studied the prebuckling and elastic buckling behavior of curved web panels under pure bending, pure shear, and combined bending and shear and showed that, in all cases, the elastic critical load of the curved panel was greater than that of the comparable flat panel. In this investigation the lateral and torsional rigidities of the flanges were not considered.

Nakai and co-researchers (Nakai *et al.* 1984a,b, 1985a) conducted experimental studies on the buckling and ultimate strength behavior of the curved I-girder web panels under combined bending and shear. A circular interaction curve was fitted to the buckling values from the tests and interaction curves also resulted for the ultimate strength of the curved girders involving the theoretical nominal strengths for pure shear and pure bending.

Under combined bending and shear, Davidson *et al.* (2000a) verified that the elastic buckling load under any combination of shear with vertical bending stresses resulted in higher critical loads for the curved panel over that of the straight. It was concluded that the use of design equations presented for pure bending would result in conservative designs up to $V/V_n = 0.6$, where V is the calculated shear force over the web and V_n is the nominal shear resistance defined for pure shear. Linear-elastic static, buckling, and geometric nonlinear static solutions were used. The finite element method was used to understand the overall behavior of the system and to evaluate the applicability of predictor equations for curved webs subjected to pure bending towards panels subjected to a combination of bending and shear.

13.7 Concluding remarks

This chapter presented an overview of the influence of curvature on global stability, flange plate stability, web plate distortion, and ultimate strength based upon recent analytical research conducted in the US. A brief historical review of research leading to the AASHTO Guide Specifications for Horizontally Curved Girders is presented. Challenges associated with fabricating, transporting, lifting, and erecting were described since curved plate girders are most vulnerable to local and global instabilities in construction and transporting configurations. However, the work presented herein focuses on behavioral challenges and does not necessarily represent formulations appropriate for future bridge specifications.

Although curvature results in a gradual reduction in elastic lateral-torsional buckling resistance of simply supported beams, it was demonstrated that the addition of curvature actually increases the buckling load for beams with more rigid end conditions and curved girders with intermediate lateral restraints.

Since cross-frame intervals must be carefully designed to prevent excessive warping normal stresses in the compression flange and deflection during construction, there does not appear to be a concern for curvature-related decrease in lateral-torsional buckling stability once intermediate bracing is in place. There is, however, concern for torsional instability of unbraced sections during erection, particularly with the tendency for highly-optimized designs using increasingly slender girder sections.

The influence of the warping stress gradient on elastic stability of the compression flange plate was discussed and an approach for integrating curvature-related reduction into the flange plate slenderness requirement was presented. Likewise, an overview of strength definitions based on the ability of plastic strain to progress across the flange plate reflects a problem that has not been solved. Current dialogue in the US is focused on accepting the compact flange definition used for straight girder design as applicable for curved girders, and basing the allowable flexural stress in compact flanges on subtracting one-third of the stress resulting from lateral flange moments from the stress allowed for an ultimate strength definition of the flange.

Curvature has a profound effect on the behavior of slender webs of plate girders. Distortional displacements and stresses induced in the web can be significant. Furthermore, the behavior is very nonlinear, both in terms of the relationship between load and distortional displacement, and in terms of the distribution of normal stresses over the depth of the web. Transverse and longitudinal stiffeners play an integral role in restraining curvature-induced distortion. Equations developed to guide an increase in web thickness were presented. Finally, recent analytical investigation on the effects on curvature on regions of high shear indicate that there is not enough adverse effect to warrant curvature-specific criteria, and that post-buckling reserve strength can be considered.

13.8 Acknowledgement

The assistance of Mahendra Madhavan and Ramy Abdalla, graduate research assistants in the Department of Civil and Environmental Engineering, University of Alabama at Birmingham is gratefully acknowledged. The synthesis of bridge stability research was partially sponsored through the University Transportation Center for Alabama, US DOT Contract DTR598-G-0028.

13.9 References

- AASHTO (2001), AASHTO LRFD Bridge Design Specifications, American Association of State Highway and Transportation Officials, Washington, DC.
- AASHTO (2003), Guide Specifications for Horizontally Curved Highway Bridges, American Association of State Highway and Transportation Officials, Washington, DC.

- Abdel Sayed, G. (1973), 'Curved webs under combined shear and normal stresses.' *Journal of Structural Division, ASCE*, **99**(ST3), pp. 511–525.
- AISC (1999), 'Load and Resistance Factor Design Specification for Structural Steel Buildings.' American Institute of Steel Construction, Chicago, IL.
- Batdorf, S.B. (1947), 'A simplified method of elastic stability analysis for thin cylindrical shells. II modified equilibrium equation.' NACA TN No. 1342, National Advisory Committee for Aeronautics, Washington, DC.
- Batdorf, S.B., Stein, M. and Schildcrout, M. (1947), 'Critical shear stress of curved rectangular plates.' NACA TN No. 1342, National Advisory Committee for Aeronautics, Washington, DC.
- Bradford, M.A., Uy, B. and Pi, Y.L. (2001), 'Behavior of unpropped composite girders curved in plan under construction loading.' *Engineering Structures*, **23**, pp. 779–789.
- Brockenbrough, R.L. (1970), 'Criteria for heat curving steel beams and girders.' *Journal of the Structural Division, ASCE*, **96**(ST10), pp. 2209–2226.
- Brockenbrough, R.L. (1986), 'Distribution factors for curved I-girder bridges.' *Journal of Structural Engineering, ASCE*, **112**(10), pp. 2200–2215.
- Chavel, B.W. and Earls, C.J. (2001), 'Evaluation of erection procedures of the horizontally curved steel I-girder Ford City bridge.' Report No. CE/ST 18, Department of Civil and Environmental Engineering, University of Pittsburgh.
- Culver, C.G. (1972), 'Design Recommendations for Curved Highway Bridges,' Project 68-32, Commonwealth of Pennsylvania Department of Transportation, June.
- Culver, C.G. and Frampton, R.E. (1970), 'Local instability of horizontally curved members.' *Journal of the Structural Division, ASCE*, **96**(ST2), pp. 7079–7099.
- Culver, C.G. and Nasir, N. (1969), 'Instability of horizontally curved members, flange buckling studies.' Report 68-32, Report submitted to the Pennsylvania Department of Highways by the Department of Civil Engineering, Carnegie-Mellon University.
- Culver, C.G. and Nasir, N. (1971), 'Inelastic flange buckling of curved plate girders.' *Journal of the Structural Division, ASCE*, **97**(ST4), pp. 1239–1257.
- Culver, C.G., Dym, C. and Brogan, D. (1972a), 'Bending behaviors of cylindrical web panels.' *Journal of the Structural Division, ASCE*, **98**(ST10), pp. 2201–2308.
- Culver, C.G., Dym, C. and Brogan, D. (1972b), 'Instability of horizontally curved members, bending behaviors of cylindrical web panels.' Submitted to the Pennsylvania Department of Highways by the Department of Civil Engineering, Carnegie-Mellon University, January.
- Culver, C.G., Dym, C. and Brogan, D. (1972c), 'Instability of horizontally curved members, shear buckling of cylindrical web panels.' Submitted to the Pennsylvania Department of Highways by the Department of Civil Engineering, Carnegie-Mellon University, June.
- Culver, C.G., Dym, C.L. and Uddin, T. (1973), 'Web slenderness requirements for curved girders.' *Journal of the Structural Division, ASCE*, **99**(ST3), pp. 417–430.
- Dabrowski, R. (1964), 'The analysis of curved thin walled girders of open sections.' *Der Stahlbau*, **33**(12), pp. 364–372, December.
- Dabrowski, R. (1965), 'Warping torsion of curved box girders of non-deformable cross section.' *Der Stahlbau*, **34**(5), pp. 135–141, May.
- Dabrowski, R. (1968), 'Curved Thin Walled Girders, Theory and Analysis.' Translated from German by Amerongen, C.V. Cement and Concrete Association, Number 144, Springer Verlag, Berlin, Germany.
- Davidson, J.S. (1996), 'Nominal bending and shear strength of curved steel I-girder bridges,' PhD. Dissertation, Auburn University, Auburn Alabama, August.

- Davidson, J.S. and Madhavan, M. (2005), 'Flange Compactness Definition for Horizontally Curved Bridge Girders.' North American Steel Construction/Structural Stability Research Council (SSRC), *Proceedings of the 2005 Annual Stability Conference*, Montreal, Quebec, Canada, 6–9 April.
- Davidson, J.S. and Yoo, C.H. (1996), 'Local buckling of curved I-girder flanges.' *Journal of Structural Engineering, ASCE*, **122**(8), 936–947.
- Davidson, J.S. and Yoo, C.H. (2000), 'Evaluation of strength formulations for horizontally curved flexural members.' *Journal of Bridge Engineering, ASCE*, **5**(3), 200–207.
- Davidson, J.S. and Yoo, C.H. (2002), 'Stability of horizontally curved I-girder web panels.' *Proceedings of the 2002 Structural Stability Research Council*, Seattle Washington, 24–27, April, pp. 95–118.
- Davidson, J.S. and Yoo, C.H. (2004), 'Analytical model to evaluate the distortion of curved thin-walled web panels.' *Proceedings of the Fourth International Conference on Thin-Walled Structures*, 22–24, June Loughborough, UK, pp. 215–223.
- Davidson, J.S., Keller, M.A. and Yoo, C.H. (1996), 'Cross-frame spacing and parametric effects in horizontally curved I-girder bridges.' *Journal of Structural Engineering, American Society of Civil Engineers*, **122**(9), pp. 1086–1096.
- Davidson, J.S., Ballance, S.R. and Yoo, C.H. (1999), 'Analytical model of curved I-girder web panels subjected to bending.' *Journal of Bridge Engineering, ASCE*, **4**(3), pp. 204–212.
- Davidson, J.S., Ballance, S.R. and Yoo, C.H. (1999b), 'Finite displacement behavior of curved I-girder web subjected to bending.' *Journal of Bridge Engineering, ASCE*, **4**(3), pp. 213–220.
- Davidson, J.S., Ballance, S.R. and Yoo, C.H. (2000a), 'Behavior of curved I-girder webs subjected to combined bending and shear.' *Journal of Bridge Engineering, ASCE*, **5**(2), pp. 165–170.
- Davidson, J.S., Ballance, S.R. and Yoo, C.H. (2000b), 'Effects of longitudinal stiffeners on curved I-girder webs.' *Journal of Bridge Engineering, ASCE*, **5**(2), pp. 171–178.
- Fujii, K. and Ohmura, H. (1987), 'Local buckling and width thickness ratio in flanges of curved I-girders.' *Proceedings of the Japanese Society of Civil Engineers, Structural Eng./Earthquake Eng.*, Japan.
- Galambos, T.V. (1978), 'Tentative load factor design criteria for curved steel bridges,' Research Report No. 50, Department of Civil Engineering, Washington University, St. Louis, MO, May, pp. 1–1~C-20.
- Galambos, T.V., Hajar, J.F., Huang, W.H., Pulver, B.E. and Rudie, B.J. (1996), 'Stresses in a steel curved girder bridge.' Report No. MN/RC-96/28, Minnesota Department of Transportation, St. Paul, Minnesota.
- Gottfield, H. (1932), 'The analysis of spatially curved steel bridges' (in German), *Die Bautechnik*, p. 715.
- Grubb, M.A., Yadosky, J.M. and Duwadi, S.R. (1996), 'Construction issues in steel curved bridges.' Transportation Research Record 1544, TRB, National Research Council, Washington, DC, pp. 64–70.
- Hall, D.H., Grubb, M.A. and Yoo, C.H. (1999), 'Improved design specifications for horizontally curved steel girder highway bridges.' NCHRP Report 424, National Cooperative Highway Research Program, Washington, DC.
- Hanshin (The Hanshin Expressway Public Corporation and Steel Structure Study Committee) (1988). 'Guidelines for the Design of Horizontally Curved Girder Bridges (Draft),' The Hanshin Expressway Public Corporation, October.
- Heins, C.P. (1975), *Bending and Torsion Design in Structural Members*, Lexington Books, Lexington, MA.

- Heins, C.P. and Jin, J.O. (1984), 'Live load distribution on braced curved I-girders.' *Journal of Structural Engineering, ASCE*, **110**(3), pp. 523–530.
- Highway Structures Design Handbook* (1965), Vol. 1, United States Steel, ADUSS, 88–1895-01.
- Japan Road Association (1990), 'Specifications for Highway Bridges, Part I: Common Specifications.' 'Part II: Steel Bridge Specifications.' Maruzen, Tokyo, February.
- Kang, Y.J. (1992), 'Nonlinear theory of thin walled curved beams and finite element formulation.' PhD dissertation, Auburn University, Auburn, Alabama.
- Kang, Y.J. and Yoo, C.H. (1990), 'Flexural stress of curved bridge girders.' Structural Stability Research Council, *1990 Annual Technical Session, Stability of Bridges*, St. Louis Missouri, 10–11 April.
- Kang, Y.J. and Yoo, C.H. (1994a), 'Thin walled curved beams. I: Formulation of nonlinear equations.' *Journal of Engineering Mechanics, ASCE*, **120**(10), pp. 2072–2101.
- Kang, Y.J. and Yoo, C.H. (1994b), 'Thin walled curved beams. II: analytical solutions for buckling of arches.' *Journal of Engineering Mechanics, ASCE*, **120**(10), pp. 2072–2101.
- Kishima, Y., Alpsten, G.A. and Tall, L. (1969), 'Residual stresses in welded shapes of flame-cut plates in ASTM A572 (50) steel.' Fritz Engineering Laboratory Report No. 321.2, Lehigh University.
- Kollbrunner, C.F. and Basler, K. (1969), *Torsion in Structures – An Engineering Approach*. Translated from German by E.C. Glauser with annotations and an appendix by B.G. Johnston. Springer-Verlag, Berlin, New York.
- Komatsu, S. and Kitada, T. (1981), 'Ultimate strength characteristics of outstanding steel plate with initial imperfection under compression.' *Proceedings of the Japanese Society of Civil Engineers*, No. 314, pp. 15–27, October (in Japanese).
- Komatsu, S., Kitada, T. and Miyazaki, S. (1975), 'Elastic plastic analysis of compressed plate with residual stress and initial deflection.' *Proceedings of the Japanese Society of Civil Engineers*, No. 244, pp. 1–14, December (in Japanese).
- Lay, M.G. (1965), 'Flange local buckling in wide flange shapes.' *Journal of the Structural Division, ASCE*, **91**(ST6), pp. 95–116.
- Lee, S.C. and Yoo, C.H. (1999), 'Strength of curved I-girder web panels under pure shear.' *Journal of Structural Engineering, ASCE*, **125**(8), 847–853.
- Lee, S.C., Davidson, J.S. and Yoo, C.H. (1994), 'Shear buckling coefficients of plate girder web panels.' *Computers & Structures*, **59**(5), pp. 789–795.
- Lian, V.T. and Shanmugam N.E. (2003), 'Plate girder curved in plan with circular web openings.' *Thin-Walled Structures*, **41**, pp. 245–269.
- Lian, V.T. and Shanmugam, N.E. (2004), 'Design of horizontally curved plate girder webs containing circular openings.' *Thin-Walled Structures*, **42**, pp. 719–739.
- Linzell, D.G. (1999), 'Studies of full-scale horizontally curved steel I-girder bridge systems under self weight.' PhD Dissertation, School of Civil and Environmental Engineering, Georgia Institute of Technology.
- Madhavan, M. and Davidson, J.S. (2003), 'Elastic local buckling of curved I-girder flanges.' North American Steel Construction/Structural Stability Research Council (SSRC), *Proceedings of the 2003 Annual Stability Conference*, Baltimore, Maryland, pp. 599–617.
- Madhavan, M. and Davidson, J.S. (2004), 'Elastic buckling of plates subjected to uniaxial eccentric compression.' *Proceedings of the Fourth International Conference on Thin-Walled Structures*, 22–24, June Loughborough, UK, pp. 533–540.
- Madhavan, M. and Davidson, J.S. (2005), 'Elastic buckling of centerline-stiffened plates

- subjected to a linearly varying stress distribution.' North American Steel Construction/Structural Stability Research Council (SSRC), *Proceedings of the 2005 Annual Stability Conference*, Montreal, Quebec, Canada, 6–9 April.
- Mahendrakumar, M., Shanmugam, N.E. and Thevendran, V. (2000), 'Behaviour of web panels curved in plan.' American Society of Civil Engineers, *Proceedings, Structures Congress 2000*, Philadelphia, Pennsylvania.
- Mariani, N., Moger, J.D., Dym, C.L. and Culver, C.G. (1973), 'Transverse stiffener requirements for curved webs.' *Journal of the Structural Division, ASCE*, **99**(ST4), pp. 757–771.
- McManus, P.F. (1971), 'Lateral buckling of curved plate girders.' PhD dissertation, Carnegie Mellon University, Pittsburgh, Pennsylvania.
- McManus, P.F., Nasir, G.A. and Culver, C.G. (1969), 'Horizontally curved girders state-of-the-art.' *Journal of Structural Engineering, ASCE*, **95**(ST5), pp. 853–870.
- Mikami, I. and Furunishi, K. (1981), 'Nonlinear behavior of cylindrical web panels under bending and shear.' *Theoretical and Applied Mechanics*, Vol. 29, University of Tokyo Press, Tokyo, Japan, pp. 65–72.
- Mikami, I. and Furunishi, K. (1984), 'Nonlinear behavior of cylindrical web panels.' *Journal of Engineering Mechanics, ASCE*, **110**(2), pp. 230–251.
- Mozer, J. and Culver, C.G. (1975), 'Horizontally curved highway bridges, stability of curved plate girders-P1.' FHWA, Contract No. FH-11-7389, Washington, DC.
- Mozer, J., Ohlson, R. and Culver, C.G. (1971), 'Horizontally curved highway bridges stability of curved plate girders.' Carnegie Mellon University, Report No. P2, Research Project HPR 2(111), September.
- Nakai, H. and Kotoguchi, H. (1983), 'A study on lateral buckling strength and design aid for horizontally curved I-girder bridges,' *Proceedings of the Japanese Society of Civil Engineers*, No. 339, December, pp. 195–204.
- Nakai, H. and Yoo, C.H. (1988), *Analysis and Design of Curved Steel Bridges*, McGraw-Hill Book Co., New York.
- Nakai, H., Muramatsu, S., Yoshikawa, N., Kitada, T. and Ohminami, R. (1981), 'A survey for web plates of the horizontally curved girder bridges.' *Bridge and Foundation Engineering*, 15, pp. 38–45, May (in Japanese).
- Nakai, H., Kitada, T. and Ohminami, R. (1983), 'Experimental study on bending strength of horizontally curved girder bridges,' *Proceedings of the Japanese Society of Civil Engineers*, No. 340/I-2, December, pp. 19–28 (in Japanese).
- Nakai, H., Kitada, T. and Ohminami, R. (1984a), 'Experimental study on ultimate strength of web panels in horizontally curved girder bridges subjected to bending, shear, and their combinations.' *Proceedings of SSRC 1984, Annual Technical Session and Meeting*, SSRC, San Francisco, pp. 91–102, April.
- Nakai, H., Kitada, T., Ohminami, R. and Fukumoto, K. (1984b), 'Experimental study on shear strength of horizontally curved plate girders.' *Proceedings of the Japanese Society of Civil Engineers*, No. 350/I 2, October, pp. 281–290 (in Japanese).
- Nakai, H., Kitada, T., Ohminami, R. and Fukumoto, K. (1984c), 'A proposition for designing transverse stiffeners of horizontally curved girders in ultimate state.' *Memoirs of the Faculty of Engineering*, Osaka City University, Japan, Vol. 25, December, pp. 111–131.
- Nakai, H., Kitada, T. and Ohminami, R. (1985a), 'Experimental study on buckling and ultimate strength of curved girders subjected to combined loads of bending and shear.' *Proceedings of the Japanese Society of Civil Engineers*, No. 356/I3, pp. 445–454, April (in Japanese).

- Nakai, H., Kitada, T. and Ohminami, R. (1985b), 'Proposition for designing intermediate transverse stiffeners in web plate of horizontally curved girders.' *Proceedings of the Japanese Society of Civil Engineers*, No. 362/I4, October, pp. 249–257 (in Japanese).
- Nishida, S., Yoshida, H. and Fukumoto, Y. (1978), 'Large deflection analysis of curved members with thin walled open cross section.' *24th Symposium of Structural Engineering*, February, pp. 77–84 (in Japanese).
- Pfeiffer, P.A. (1981), 'Elastic stability of curved beams.' Master thesis, Marquette University, Milwaukee, Wisconsin.
- Shanmugam, N.E., Lian, V.T. and Thevendran, V. (2002), 'Finite element modeling of plate girders with web openings.' *Thin-Walled Structure* **40**, pp. 443–464.
- Shanmugam, N.E., Mahendrakumar, M. and Thevendran, V. (2003), 'Ultimate load behaviour of horizontally curved plate girders.' *Journal of Constructional Steel Research*, **59**(4), pp. 509–529.
- Shimada, S. and Kuranishi, S. (1966), '*Formulas for Calculation of Curved Beam*,' (in Japanese), Gihodo, Tokyo.
- Simpson, M.D. (2000), 'Analytical investigation of curved steel girder behavior.' PhD Thesis, Department of Civil Engineering, University of Toronto, Canada.
- St. Venant, B. (1843), 'Mémoire sur le calcul de la resistance et la flexion des pièces solides a simple ou a double courbure, en prenant simultanément en consideration les divers efforts auxquels eiles peuvent entre soumises dans tous les sens.' *Comptes Rendus, l'Academie des Sciences de Paris*, **17**, pp. 1020–1031 (in French).
- Stein, M. and Fralich, R.W. (1949), 'Critical shear stress of infinitely long, simply supported plates with transverse stiffeners.' NACA TN No. 1851, National Advisory Committee for Aeronautics, Washington, DC.
- Stein, M. and Yeager, D.J. (1949), 'Critical shear stress of a curved rectangular panel with a central stiffener.' NACA TN No. 1972, National Advisory Committee for Aeronautics, Washington, DC.
- Timoshenko, S.P. (1905), *On the Stability of In Plane Bending of an I-beam*. Izvestiya St. Petersburg Politekhnikheskoqo Instituta, IV–V.
- Umanskii, A.A. (1948), *Spatial Structures*, Moscow (in Russian).
- United States Steel Corp. (1984), 'V-load analysis, an approximate procedure, simplified and extended for determining moments and shears in designing horizontally curved open framed highway bridges.' *USS Highway Structures Design Handbook*, Volume 1, Chapter 12, Pittsburgh, PA.
- Vlasov, V.Z. (1961), *Thin Walled Elastic Beams*, 2nd Edition, National Science Foundation, Washington, DC.
- Weinhold, S.A. (1997), 'Erection engineering for steel bridge superstructures.' *Modern Steel Construction*, Vol. 11 (Web reprint), October.
- White, D.W., Zureick, A.H., Phoawanich, N. and Jung, S.K. (2001), 'Development of Unified Equations for Design of Curved and Straight Steel Bridge I-Girder,' Final Report, prepared for American Iron and Steel Institute Transportation and Infrastructure Committee, Professional Service Industries, Inc. and Federal Highway Administration, School of Civil and Environmental Engineering, Georgia Institute of Technology, Atlanta, Ga.
- Yadlosky, J.M. (1993), 'Curved steel bridge research project, Summary Work Plan (1.0),' HDR Interim Report (DTFH61-92-C-00136) submitted to the Federal Highway Administration, HDR Engineering, Inc., Pittsburgh, PA, December.
- Yoo, C.H. and Davidson, J.S. (1997), 'Yield interaction equations for nominal bending strength of curved I-girders.' *Journal of Bridge Engineering, ASCE*, **2**(2), pp. 37–44.

- Yoo, C.H. and Littrell, P.C. (1986), 'Cross bracing effects in curved stringer bridges.' *Journal of Structural Engineering, ASCE*, **112**(9), pp. 2127–2140.
- Yoo, C.H. and Pfeiffer, P.A. (1983), 'Elastic stability of curved members,' *Journal of Structural Engineering, ASCE*, **109**(12), pp. 2922–2940.
- Yoo, C.H., Kang, Y.J. and Davidson, J.S. (1996), 'Buckling analysis of curved beams by finite element discretization.' *Journal of Engineering Mechanics, ASCE*, **122**(8), pp. 762–770.

Buckling failure of structures consisting of curved plates

P A N S O U R I A N , The University of Sydney, Australia

14.1 Introduction

Early work on the stability of singly curved plates under lateral pressure was based on the Donnell stability equations, modified by Batdorf (1947). While it is more accurate to apply Flügge's (1973) equations in coupled form to the buckling problem for either uniform or variable pressure, the former solutions remain useful especially in the 'medium' range of plates. Almroth (1962) gave solutions based on the minimum potential energy principle for a centrally located and variable band of pressure. As the skew in the pressure rises from zero (uniform pressure) to maximum (cosine variation), the buckling pressure rises monotonically from that calculated for a uniform pressure distribution. The rise is most pronounced in long cylinders (40%), reaching 60% in thicker cylinders. In shorter cylinders, the gain is less pronounced.

Weingarten (1962) solved the Donnell equation modified by Batdorf for the buckling of cylinders subjected to a lateral pressure varying linearly in the meridional direction, but uniform circumferentially. Using a harmonic series formulation and the Galerkin method, he established the homogeneous system of equations, the determinant of which, when set equal to zero, yielded the critical pressure. For cylindrical plates that are not very short, and the linear pressure is replaced by a *uniform* pressure equal to the mean, then the maximum error is less than 5%, thus replacing the complex nonuniform problem by the simpler case of uniform pressure buckling.

While many theoretical analyses in the literature have been performed within the framework of the Donnell linear stability theory with simple supports, it is more accurate to apply Flügge's equations (1973) in coupled form to the buckling problem for uniform or variable pressure, with classical or diverse boundary conditions. The differences in the two solutions are exacerbated as the length of the cylinder increases.

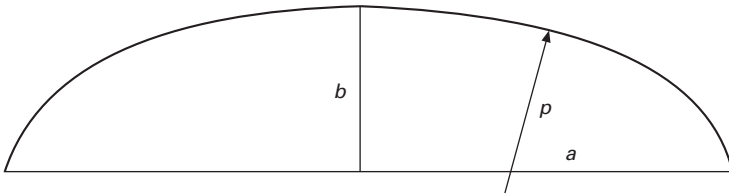
In this chapter, an abridged version is given of theoretical developments that are given fuller scope in the author's and others' publications. Closures of pressure and other vessels are examined for buckling under internal pressure;

buckling under uniform and nonuniform external pressure is considered for classical boundary conditions and for end warping restraint; the susceptibility of collapse of corrugated curved plates is investigated. Theories are compared with experimental data, and prototype failures illustrated. Finally, the effect of differential settlement of the foundation of tank structures is examined for distortion and buckling.

14.2 Cylindrical structures

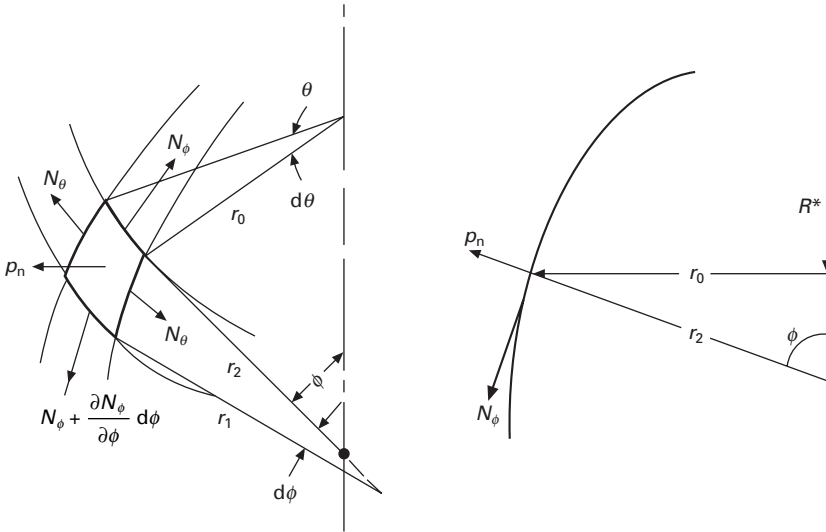
14.2.1 Internal pressure

In general, internal pressure does not cause buckling failures in containment structures, except in the case of junctions between different components which may incorporate a doubly curved section; a typical example is that of a cylindrical vessel closed with a spherical cap via a torispherical junction, or with an ellipsoid of revolution (Fig. 14.1). Membrane theory applied to the ellipsoid (Fig. 14.2) subjected to internal pressure p shows that the meridional stress is everywhere tensile, and equals $\sigma_\phi = pa/t$ at the equator, where a is the major axis and t the wall thickness; on the other hand the circumferential stress becomes $\sigma_\theta = \frac{pa}{t} \left(1 - \frac{a^2}{2b^2}\right)$ where b is the minor axis, and clearly this stress becomes compressive if $a^2 > 2b^2$, indicating a sharply curved closure or knuckle. The compression is also predicted by the full bending theory or by finite element theory.



14.1 Section of ellipsoid of revolution.

The above compressive stress can lead to buckling failure as has indeed been observed by Blackler and Ansourian (1988) during the pressurisation of two stainless steel full-scale tanks with torispherical closures. The measured meridional displacements are shown in Fig. 14.3. The knuckle suffered considerable distortion as it moved inwards, while the spherical end translated almost as a rigid body, the cylinder remaining almost undeformed. Buckle formation was sudden and accompanied by a low-pitched rumbling sound. Buckles generally occurred at zones of maximum imperfections, at or adjacent to meridional weld lines. The sensitivity to geometric imperfections was



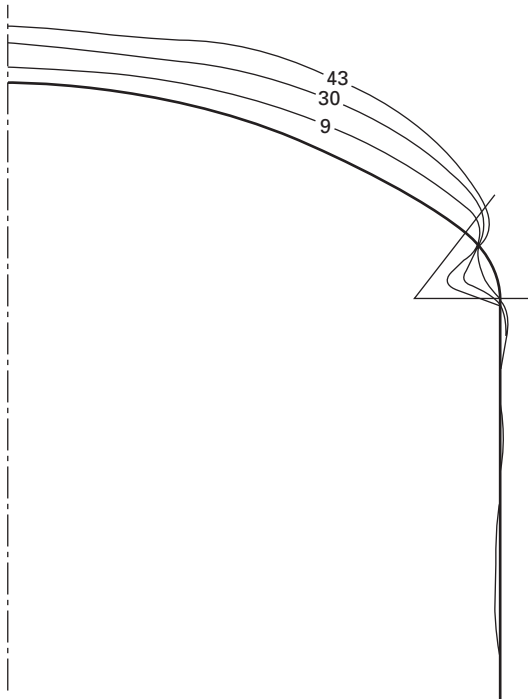
14.2 Axisymmetric curved plate with membrane stress-resultants:
 R^* = sum of all vertical force components from top of shell to location ϕ ; r_1 = meridional radius of curvature at a point of a shell (infinite for cylinder and cone); r_2 = radius of curvature in plane perpendicular to meridian plane (the distance between the point on the shell to the point on the axis of rotation intersected by the perpendicular to the shell); r_0 = radius of parallel circle; $r_2 = r_0 / \sin \phi$. The surface area of the small element is $dA = r_1 r_2 \sin \phi d\phi d\theta$.

low. Failure was by elastic-plastic buckling, well predicted by the expression derived by Galletly (1986):

$$\frac{p_D}{\gamma F} = \frac{80(r/D)^{0.825}}{(D/t)^{1.5} (R_s/D)^{1.15}} \quad 14.1$$

where p_D is the allowable internal design pressure for safety factor > 1.5 , $\gamma = 1.0$ for crown and segment steel heads and 1.6 for cold spun steel heads, F is the yield stress, r is the knuckle radius, R_s is the sphere radius and D is the cylinder diameter.

Teng (2004) also conducted numerous investigations of buckling failures under internal pressure at junctions between cylinders and cones without stiffening ring beams, and between cylinders and flat ends. He concluded that the plastic limit load provides a conservative estimate of failure load because of the strength reserve of geometric non linearity. While he found that the buckling of thin shell junctions shows stable postbuckling, he warns of possible weld fracture at large deformations.



14.3 Measured meridional shape at internal pressure buckling.

14.2.2 Uniform external pressure

This section deals with buckling under uniform external pressure, examples of which abound in civil/mechanical engineering, marine, ballistic and aerospace structures. Earlier work on the stability of cylinders under external pressure was based on the Donnell stability equations, modified by Batdorf (1947). While it is more accurate to apply Flügge’s (1973) equations in coupled form to the buckling problem for either uniform or variable pressure, the former solutions remain useful especially in the ‘medium’ range of thin cylinders. The Donnell stability equation for a cylinder of radius R and thickness t is given in Brush and Almroth (1975):

$$D\nabla^8 w + \frac{(1 - \nu^2)}{R^2} C \frac{\partial^4 w}{\partial x^4} + \frac{p}{R} \nabla^4 \frac{\partial^2 w}{\partial \theta^2} = 0 \tag{14.2}$$

$$D = \frac{Et^3}{12(1 - \nu^2)}$$

$$C = \frac{Et}{(1 - \nu^2)}$$

$$\nabla^8 = \nabla^4 \nabla^4$$

$$\nabla^4 = \frac{\partial^4}{\partial x^4} + 2 \frac{\partial^4}{\partial x^2 \partial \theta^2} + \frac{\partial^4}{\partial \theta^4}$$

where w is the radial deflection, x is the meridional direction, θ the circumferential angle and p is the uniform external pressure. This linear differential equation with constant coefficients is satisfied by the solution:

$$w = A_{nm} \sin \frac{n\pi x}{L} \sin m\theta \quad n = 1, 2, 3, \dots, m = 1, 2, 3, \dots, 14.3$$

which also satisfies the end boundary conditions of zero radial deflection, and zero curvature at $x = 0$ and $x = L$, where L is the length of the cylinder. When minimised with respect to m and n , the critical pressure p for buckling becomes:

$$p_{cr} = \left\{ \left[\left(\frac{n\pi R}{L} \right)^2 + m^2 \right]^2 \frac{D}{m^2 R^3} + \frac{\left(\frac{n\pi R}{L} \right)^4}{R m^2 \left[\left(\frac{n\pi R}{L} \right)^2 + m^2 \right]^2} (1 - \nu^2) C \right\}_{\min} \quad 14.4$$

The minimum value of p always requires $n = 1$, so that the buckling mode has the shape of a single half sine wave encompassing the length of the cylinder, and m full waves in the circumferential direction. It should be noted that m is the number of *full* waves around the circumference. For cylinders with $L^2/Rt > 100$, i.e. not too 'short', Eq. 14.4 is closely approximated by:

$$p_{cr} = \frac{0.92 E}{\frac{L}{R} \left(\frac{R}{t} \right)^{2.5}} \quad 14.5$$

and the number of full waves is given by:

$$m = 2.74 \sqrt{\frac{R}{L} \sqrt{\frac{R}{t}}} \quad 14.6$$

Blackler and Ansourian (1986a,b) showed that the buckling pressure rises above the value given by equ. 14.4 if meridional (warping) elastic restraints exist at either or both ends. The factor c_b by which the buckling pressure rises is given by:

$$c_b = 1.0 + \sum_{n=1}^2 \beta_n \quad 14.7$$

$$\beta_n = 0.067 \left(\frac{k_n L}{Et} \right)^{0.32} \leq 0.23 \quad 14.8$$

where k is the stiffness of the elastic restraint at either end. For infinite meridional restraint at one end, the buckling pressure rises by a factor of 1.23; this would be the typical situation at the base of a cylindrical silo attached to a stiff foundation.

The buckling collapse of thin-walled cylinders does not show the high imperfection sensitivity shown by cylinders under axial compression, but the effect of imperfections is nevertheless significant. *API Bulletin 2U* (1987) specifies an imperfection factor $\alpha = 0.8$ for fabricated cylinders that meet the tolerance requirement of 1% of the nominal diameter. ECCS (1988) specifies $\alpha = 0.5$ for cylinders that are circular to within 0.5% of the radius measured from the true centre, a requirement more severe than API. From a number of tests published in the literature, Blackler and Ansourian (1988) concluded that in relatively squat cylinders, the imperfection factor remains approximately constant at 0.7, reducing at low values of the buckling wavenumber m ; the relationship was expressed as:

$$\alpha = 0.21 + 0.05m \leq 0.70 \quad 14.9$$

In summary, the collapse pressure of an imperfect cylinder with elastic end restraints is given by:

$$p_u = c_b c_s p_{cr} \quad 14.10$$

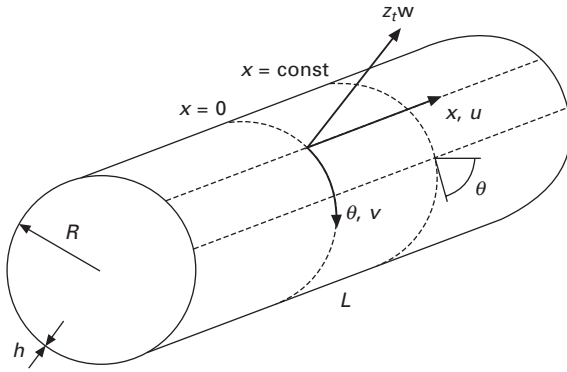
where c_b is given by Eqs 14.7 and 14.8, $c_s (= \alpha)$ by Eq. 14.9, and p_{cr} by Eq. 14.5.

14.2.3 Nonuniform external pressure

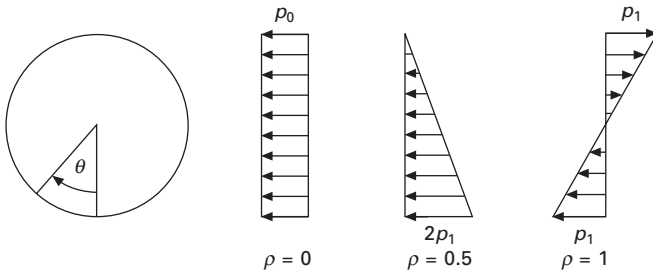
It is found generally that it is more accurate to apply Flügge's (1973) equations in coupled form to the buckling problem under uniform or variable pressure. In this more refined theory, the in-plane displacements are not neglected when compared with transverse deflections of the surface. The differences in the two solutions are exacerbated as the length of the cylinder increases. A further advantage of the method is that solutions can be obtained for non-classical edge conditions. The usual assumption of a homogeneous and isotropic material holds, while the Fourier series representation of the displacement functions includes a sufficient number of harmonics for results of high accuracy.

Consider a thin, elastic circular cylindrical shell of length L , radius R and thickness h (Fig. 14.4), compressed by a nonuniform lateral pressure $p(\theta)$ (Figs 14.5 and 14.6). The external load and the stress resultants on a shell element are given in Fig. 14.7 with their positive directions.

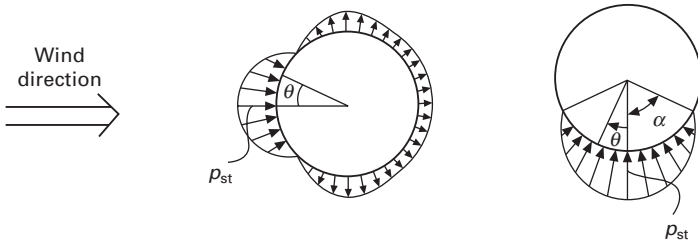
As a membrane prebuckling state is assumed, the stability problem is



14.4 Cylinder coordinate system.



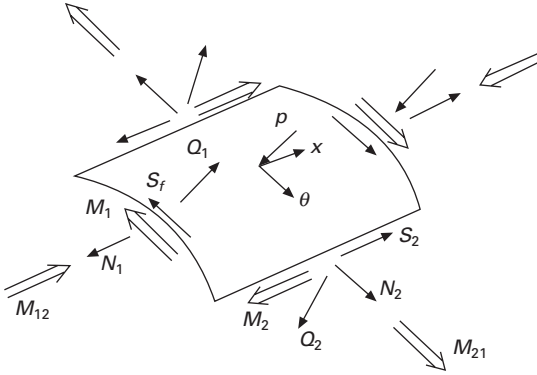
14.5 Fluid pressure distribution and skew factor ρ .



14.6 Wind and partial (patch) pressure distribution.

reduced to solving Flügge's partial differential equations which relate the small incremental nondimensional displacements \bar{u} , \bar{v} , \bar{w} to \bar{x} ($\bar{u} = u/R$, $\bar{v} = v/R$, $\bar{w} = w/R$ and $\bar{x} = x/R$) and θ :

$$\begin{aligned}
 L_{11}(\bar{u}) + L_{12}(\bar{v}) + L_{13}(\bar{w}) &= 0 \\
 L_{21}(\bar{u}) + L_{22}(\bar{v}) + L_{23}(\bar{w}) &= 0 \\
 L_{31}(\bar{u}) + L_{32}(\bar{v}) + L_{33}(\bar{w}) &= 0
 \end{aligned}
 \tag{14.11}$$



14.7 Stress resultants.

where the linear partial differential operator L_{11} is:

$$L_{11}(u) = \frac{\partial^2 u}{\partial x^2} + \left[\frac{1-\mu}{2R^2} \left(1 + \frac{h^2}{12R^2} \right) - \frac{p}{DR} \frac{h^2}{12} \right] \frac{\partial^2 u}{\partial \theta^2} \tag{14.12}$$

Full details are given in Vodenitcharova and Ansourian (1996, 1998). The longitudinal coordinate is nondimensionalised as $\bar{x} = x/R$; the incremental displacements are \bar{u} , \bar{v} and \bar{w} . In a complete cylinder, the incremental displacements must satisfy circumferential periodicity, and are assumed as series:

$$\begin{aligned} \bar{u}(\bar{x}, \theta) &= \sum_{n=0}^{\infty} \bar{U}_n \cos(\lambda \bar{x}) \cos(n\theta) \\ \bar{v}(\bar{x}, \theta) &= \sum_{n=0}^{\infty} \bar{V}_n \sin(\lambda \bar{x}) \sin(n\theta) \\ \bar{w}(\bar{x}, \theta) &= \sum_{n=0}^{\infty} \bar{W}_n \sin(\lambda \bar{x}) \cos(n\theta) \end{aligned} \tag{14.13}$$

where n is the circumferential wavenumber and $\lambda = m\pi/l$, $l = L/R$. Only one half-sine function is taken meridionally ($m = 1$). Thus, Eqs 14.11 produce a system of linear homogeneous algebraic equations in \bar{U}_n , \bar{V}_n and \bar{W}_n with variable coefficients, the first of which is:

$$\sum_{n=0}^{n=\infty} \cos(n\theta) \left\{ \begin{aligned} &\bar{U}_n \left[-\lambda^2 - n^2 \left[\frac{1-\mu}{2} \left(1 + \frac{h^2}{12R^2} \right) - \frac{p(\theta)R}{D} \frac{h^2}{12} \right] \right] \\ &+ \frac{1+\mu}{2} n \lambda \bar{V}_n + \lambda \bar{W}_n \left(\mu - \frac{h^2}{12R^2} \frac{1-\mu}{2} n^2 \right. \\ &\quad \left. + \frac{p(\theta)R}{D} \frac{h^2}{12} + \frac{h^2}{12R^2} \lambda^2 \right) \end{aligned} \right\} = 0 \tag{14.14}$$

Two cases of circumferential variation are considered: hydrostatic (Tables 14.1–14.4), defined in a horizontal cylinder as a linear variation from crown to invert; and partial (patch), where a sinusoidal pressure acts over a limited part of the circumference. In all these cases, since there is circumferential variation in pressure, all harmonics are coupled, and the algebraic equations have variable coefficients, whereas in the case of uniform pressure, the harmonics are uncoupled and the coefficients constant. Thus, the stability problem is reduced to the determination of the minimum value of pressure at $\theta = 0$ that results in a nontrivial solution of the homogeneous system 14.4.

Table 14.1 Uniform (p_{cr}) and hydrostatic buckling pressure (p_{st})
 $L/R = \pi/4$

R/h	Uniform		Hydrostatic					
	$p_{cr}/E \times 10^{-9}$	n_{cr}	ρ	$p_{st}/E \times 10^{-9}$	ρ	$p_{st}/E \times 10^{-9}$	ρ	$p_{st}/E \times 10^{-9}$
100	13 960	9	0.1	14 540	0.3	15 070	0.5	15 440
200	2333	11		2425		2502		2557
300	832.0	13		857.4		882.5		900.3
400	399.7	13		411.2		422.6		430.5
500	225.7	14		232.9		239.0		243.3
600	141.8	15		146.5		150.2		152.8
700	96.29	16		99.01		101.4		103.1
800	68.47	16		70.56		72.23		73.39
900	50.93	17		52.34		53.54		54.39
1000	38.94	17		40.09		40.97		41.60

Table 14.2 Uniform (p_{cr}) and hydrostatic buckling pressure (p_{st})
 $L/R = \pi$

R/h	Uniform		Hydrostatic					
	$p_{cr}/E \times 10^{-9}$	n_{cr}	ρ	$p_{st}/E \times 10^{-9}$	ρ	$p_{st}/E \times 10^{-9}$	ρ	$p_{st}/E \times 10^{-9}$
100	3001	4	0.1	3258	0.3	3565	0.5	3772
200	528.2	4		568.4		610.1		639.6
300	195.2	5		205.0		217.7		227.3
400	92.4	5		98.84		105.0		109.2
500	53.31	5		56.4		59.61		61.91
600	33.97	5		35.69		37.57		38.96
700	22.73	6		24.16		25.43		26.33
800	16.33	6		17.26		18.14		18.76
900	12.34	6		12.84		13.47		13.91
1000	9.37	6		9.86		10.31		10.66

In the *hydrostatic* case, the cylinder is horizontal and the fluid pressure linearly distributed with height (Fig. 14.5); the skew is $\rho = [p_1/(p_0 + p_1)]$ and the pressure is:

Table 14.3 Uniform (p_{cr}) and hydrostatic buckling pressure (p_{st})
 $L/R = 2\pi$

R/h	Uniform		Hydrostatic					
	$p_{cr}/E \times 10^{-9}$	n_{cr}	ρ	$p_{st}/E \times 10^{-9}$	ρ	$p_{st}/E \times 10^{-9}$	ρ	$p_{st}/E \times 10^{-9}$
100	1577.0	4	0.1	1695	0.3	1854	0.5	1995
200	256.4	4		279.6		312.4		336.5
300	96.71	5		103.9		112.6		119.5
400	45.27	5		49.21		54.07		57.36
500	26.11	5		28.20		30.67		32.44
600	17.20	5		18.06		19.34		20.39
700	11.43	6		12.23		13.10		13.77
800	8.04	6		8.67		9.34		9.80
900	5.99	6		6.43		6.93		7.26
1000	4.61	6		4.94		5.30		5.56

Table 14.4 Uniform (p_{cr}) and hydrostatic buckling pressure (p_{st})
 $L/R = 4\pi$

R/h	Uniform		Hydrostatic					
	$p_{cr}/E \times 10^{-9}$	n_{cr}	ρ	$p_{st}/E \times 10^{-9}$	ρ	$p_{st}/E \times 10^{-9}$	ρ	$p_{st}/E \times 10^{-9}$
100	803.4	4	0.1	881.5	0.3	1011	0.5	1114
200	122.7	4		135.3		159.7		180.5
300	47.39	5		51.69		58.20		63.71
400	24.17	5		26.07		28.60		30.79
500	13.10	5		14.33		16.14		17.43
600	8.10	5		8.87		10.07		10.90
700	5.49	6		6.00		6.77		7.33
800	3.97	6		4.33		4.83		5.21
900	3.03	6		3.27		3.60		3.86
1000	2.40	6		2.54		2.76		2.94

$$p = p_0 + \frac{\rho}{1 - \rho} p_0 \cos \theta \tag{14.15}$$

where p_0 is the pressure at mid-height of the cylinder. $\rho = 0$ corresponds to uniform pressure; $\rho = 0.5$ to zero pressure at the top, and $\rho = 1$ to $p = -p_1$ at the top and $+p_1$ at the bottom. The hydrostatic pressure can also be expressed as:

$$p = \sum_{r=0}^{r=1} a_r \cos (r\theta) \text{ where } a_0 = p_0, a_1 = \frac{\rho}{1 - \rho} p_0 \tag{14.16}$$

The *partial* pressure, normal to the surface and linearly distributed with

height above the invert of the cylinder (Fig. 14.6), is expressed in terms of the maximum pressure p_{st} as:

$$p(\theta) = \frac{\cos \theta - \cos \alpha}{1 - \cos \alpha} p_{st}, \theta \in (0, \pm \alpha) \tag{14.17}$$

Since $p(\theta)$ must be a continuous symmetric function of θ , it is expanded as an even series:

$$p(\theta) = \frac{a_0}{2} + \sum_{k=1}^{\infty} a_k \cos(k\theta) \tag{14.18}$$

Solving for the Fourier coefficients, the patch pressure for half-angle α is (Ansourian, 2004):

$$\begin{aligned} p(\theta) = & \frac{p_{st}}{\pi(1 - \cos \alpha)} (\sin \alpha - \alpha \cos \alpha) \\ & + \frac{p_{st}}{\pi(1 - \cos \alpha)} (-0.5 \sin 2\alpha + \alpha) \cos \theta \\ & + 2 \frac{p_{st}}{\pi(1 - \cos \alpha)} \\ & \sum_{k=2}^{k=\infty} \left\{ -\frac{1}{k} \cos \alpha \sin k\alpha + 0.5 \left[\frac{1}{k+1} \sin(k+1)\alpha + \frac{1}{k-1} \sin(k-1)\alpha \right] \cos k\theta \right\} \end{aligned} \tag{14.19}$$

Following the development in Vodenitcharova and Ansourian (1998), highly accurate results are obtained for the buckling pressure under patch loading ($\alpha = 18.5 - 90^\circ$); these are summarised in Tables 14.5–8 and in Fig. 14.8. The distribution of wind pressure around the circumference is idealised as:

Table 14.5 Wind and patch loading buckling pressure (p_{st})
 $L/R = \pi/4$

R/h	Wind pressure $p_{st}/E \times 10^{-9}$	Patch loading $p_{st}/E \times 10^{-9}$			
		$\alpha = 90^\circ$	$\alpha = 60^\circ$	$\alpha = 36.7^\circ$	$\alpha = 18.5^\circ$
100	19 110	16 150	17 220	19 510	26 170
200	3081				
300	1069				
400	505.7				
500	283.6	251.4	263.3	288.9	357.7
600	176.9				
700	118.8				
900	84.2				
800	62.2				
1000	47.4	42.8	44.5	48.2	58.6

Table 14.6 Wind and patch loading buckling pressure (p_{st})
 $L/R = \pi$

R/h	Wind pressure $p_{st}/E \times 10^{-9}$	Partial (patch) loading $p_{st}/E \times 10^{-9}$			
		$\alpha = 90^\circ$	$\alpha = 60^\circ$	$\alpha = 36.7^\circ$	$\alpha = 18.5^\circ$
100	6098	4167	4743	6036	8098
200	962.7	697.0			
300	329.5	245.8			
400	154.4	117.5			
500	85.93	66.34	72.9	86.33	126.9
600	53.28	41.61			
700	35.60	28.07			
800	25.11	19.96			
900	18.47	14.77			
1000	14.04	11.30	12.27	14.31	20.23

Table 14.7 Wind and patch loading buckling pressure (p_{st})
 $L/R = 2\pi$

R/h	Wind pressure $p_{st}/E \times 10^{-9}$	Partial (patch) loading $p_{st}/E \times 10^{-9}$			
		$\alpha = 90^\circ$	$\alpha = 60^\circ$	$\alpha = 36.7^\circ$	$\alpha = 18.5^\circ$
100	3953	2288	2706	3628	4288
200	601.7				
300	202.4				
400	93.79				
500	51.73	35.77	40.64	51.09	70.90
600	31.86				
700	21.17				
800	14.86				
900	10.86				
1000	8.24	6.04	6.80	8.19	11.99

$$p(\theta) = q_z[-0.5 + 0.4 \cos(\theta) + 0.8 \cos(2\theta) + 0.3 \cos(3\theta) - 0.1 \cos(4\theta) - 0.05 \cos(5\theta)] \quad 14.20$$

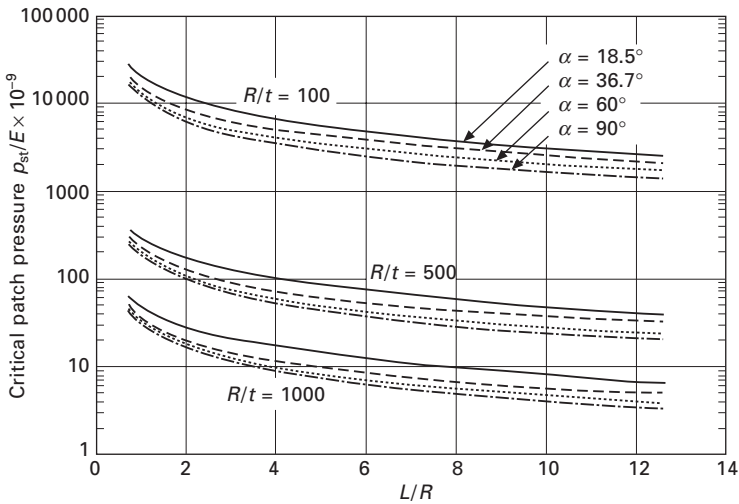
where q_z is the free stream gust dynamic wind pressure at wind speed V ; this distribution is also adopted in Australian Standard AS1170.2 'Wind forces' (AS 1989) Results are also summarised in Tables 14.5–8.

14.2.4 Axial compression

Thin-walled cylinders in uniform axial compression fail suddenly by the formation of diamond-shaped buckles. The failure stress is strongly affected

Table 14.8 Wind and patch loading buckling pressure (p_{st})
 $L/R = 4\pi$

R/h	Wind pressure $p_{st}/E \times 10^{-9}$	Partial (patch) loading $p_{st}/E \times 10^{-9}$			
		$\alpha = 90^\circ$	$\alpha = 60^\circ$	$\alpha = 36.7^\circ$	$\alpha = 18.5^\circ$
100	2826	1314	1660	1989	2393
200	410.7				
300	134.9				
400	61.34				
500	33.37	19.91	23.33	31.37	37.66
600	20.34				
700	13.41				
800	9.36				
900	6.81				
1000	5.13	3.31	3.83	5.06	6.44



14.8 Buckling under partial (patch) pressure distribution.

by small imperfections and this phenomenon has attracted extensive research since before 1945 until today, summarised by Rotter (2004). This form of buckling is delayed by internal pressure, by localisation of the compressive stress, and by stiffening. In the present context of curved plates, the specific problem of collapse of corrugated plates as used in silo structures under the action of drag caused by bulk solid friction is examined (Ansourian and Glaesle, 2002). For the storage of products from the primary and mining industries, large-scale silos are often constructed of steel, where the wall may be either of plain sheet or corrugated. A significant problem is local failure of the corrugations. This does not necessarily cause catastrophic collapse,

but may cause lean of the structure and out-of-roundness, effectively requiring major repair. The vertical load arises primarily through frictional drag of the bulk solids partly against the wall and partly against itself, exacerbated by flow overpressures. Failure occurs by yielding at the critical section defined by a trough of the corrugations under a biaxial stress system including axial, bending and circumferential stresses; amplification of the vertical moment arises from additional deflection of the curved shell. The critical axial force P to cause failure has been derived as:

$$P = \frac{1}{2} (\sqrt{4e^2 + t^2} - 2e) \left(\sqrt{4F_y^2 - \frac{3c^2 p_h^2 R^2}{t^2}} - \frac{cp_h R}{t} \right) \quad 14.21$$

where e is the eccentricity of the resultant vertical force relative to the centroid of the critical section, typically about 30% greater than the half corrugation depth, p_h is the lateral pressure of the bulk material (Ansourian and Glaesle, 2002).

More refined analysis would include the second order effects of the eccentric axial force, which amplify the first order moment. A lower bound to this amplification may be evaluated on the assumption that the corrugation remains elastic for most of the loading history. On this assumption, the new eccentricity becomes

$$\frac{e}{1 - \frac{12P(0.7L)^2}{\pi^2 Et^3}}$$

In a typical situation, the amplification is in the order of 10%.

14.3 Experimental behaviour

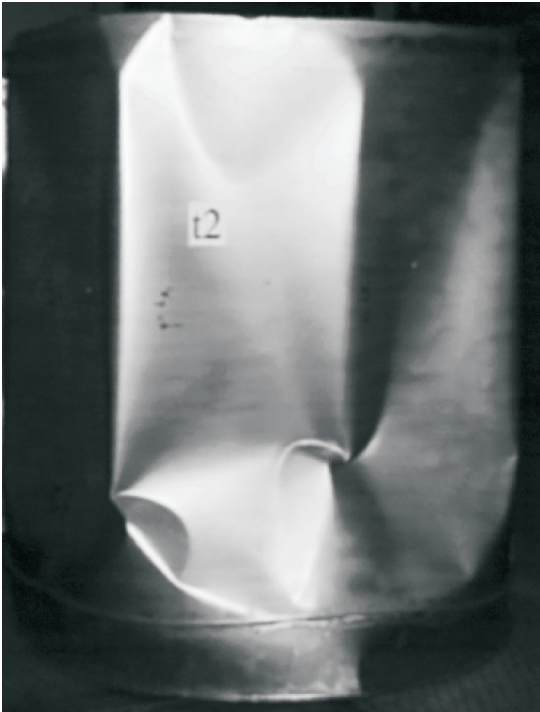
Considerable experimental effort has been exerted around the world to gain a clear understanding of the response of cylinders under external pressure. In this section, thin-walled cylinders are considered in the slenderness regime close to $R/h = 1000$, common in silos and tanks. It is clear that the response of these cylinders depends strongly on the restraint conditions at the two ends of the cylinder. These restraints are radial, tangential, axial and rotational. A detailed study of this effect is given in Vodenitcharova and Ansourian (1996) in the context of the Flügge formulation, and includes numerical data for many combinations of restraint. The buckling strength of thin cylinders under uniform or nonuniform pressure is very low when the two ends are free (wavenumber $n = 2$), and reaches a maximum when fully clamped at both ends; while a wide range of strengths is encompassed within the two extremes, the most significant rise occurs in a 'free' cylinder with the addition of radial restraint at each end; the addition of tangential restraint has an

almost negligible effect. Of particular significance is the case of nonsymmetric boundary conditions in which one end of the cylinder has radial and axial restraint, while the other end is entirely free. This is typically the case of a tank bolted to the foundations but totally free at the top. Here, the buckling strength does not reach the 'full' restraint value, but is nevertheless high with a 48-fold increase over the 'free' condition. At least one major silo failure is attributed to such a loss of stiffness by failure of the anchorage of the vertical stiffeners into the foundation.

Early experiments on cylinders and curved plates led to the erroneous conclusion that small imperfections had a negligible effect on buckling strength. It is, however, likely that the strength gain due to additional restraint (e.g. meridional) over and above the 'classical' restraints assumed in calculations, may have masked the significant imperfection sensitivity that is now generally accepted. It is now clear that the effect of initial imperfections is significant, whether the pressure is uniform or not, causing a reduction in initial buckling pressure of up to 50%.

In the case of slender shells, the experimentally observed response to incremental external pressure may be described as prebuckling, initial buckling, general buckling, postbuckling and collapse. The latter stage may be observed in Fig. 14.9. In the prebuckling phase, displacements remain small although some nonlinearity may exist due to amplification of initial deformations; there are no plastic deformations and recovery upon pressure release is complete. At initial buckling, one or more buckles form in the area of greatest imperfection, accompanied by large deflections and some plasticity; a deep rumble caused by vibration of the wall may be heard in the larger specimens. Buckling is of the snap-through type and gives no warning; upon release and reload, the same buckles will reappear at slightly reduced pressure. As pressure rises, the global buckling pattern develops, normally with a lesser number of lobes than predicted by perfect cylinder bifurcation theory, for example 12 lobes versus 15; this effect is caused by imperfections which govern the formation of the initial and final buckling pattern, ensuring that several buckles have longer wavelength than the 'perfect' prediction. With maximum imperfections in the range $5t - 10t$, initial buckling is observed in the range $0.4p_{cr} - 0.7p_{cr}$, where p_{cr} is the bifurcation pressure of the perfect shell, computed taking account of the actual edge conditions, while the general buckling pattern occurs later in the range $0.6p_{cr} - 0.9p_{cr}$. The observed wavenumber is invariably smaller than perfect shell predictions.

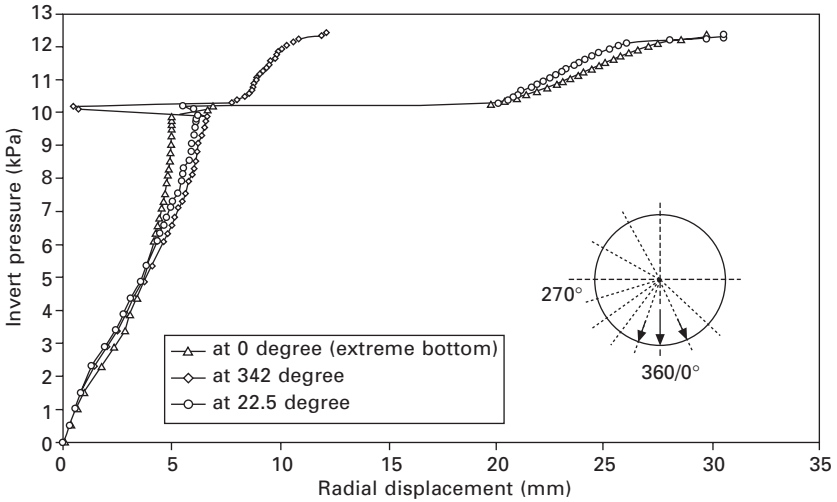
Formation of the general buckling pattern does not normally announce imminent collapse. The post-buckling regime in which the buckling pattern is strongly amplified and pronounced plasticity develops, ends by a local plastic torsional failure of the ridge or V-shaped 'curved beam' bent in the meridional direction, at the nodal line of the circumferential buckles (Fig. 14.9, $D = 1$ m, $R/t = 910$, $L/R = 2$). In the absence of fractures of welds or



14.9 Cylinder buckling under external pressure. Note torsional failure of 'ridge'.

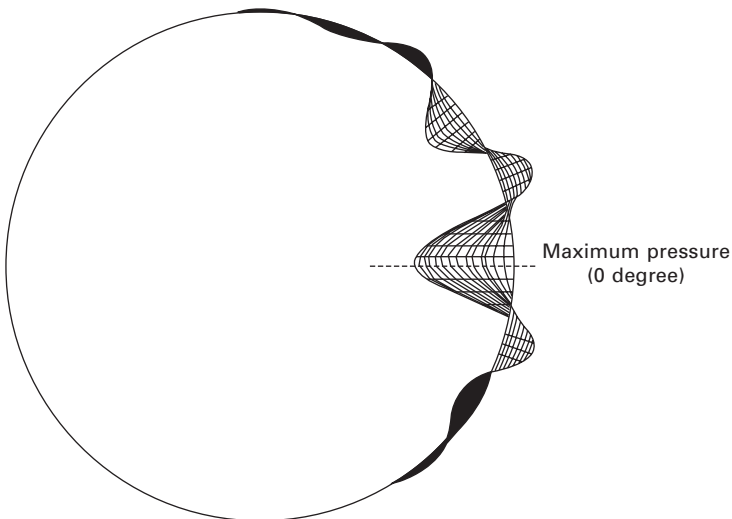
other connections in the neighbourhood of the ridge under the high distortions caused by buckling, the postbuckling range can become significant, and can raise the collapse load of the shell to a maximum of $1.4p_{cr}$ (a minimum of 10% is normally available). However, use of this reserve in design is inadvisable because of the danger of buckles appearing on the shell surface at working loads.

Tests on horizontal cylinders (Ansourian *et al.*, 1995, Sengupta, 1997) subjected to hydrostatic external pressure by submersion in a water tank and additional internal vacuum have shown that the response of the shell is not unlike that under uniform external pressure in terms of buckling behaviour and ultimate strength. In contrast to uniform pressure testing, a resultant force now acts on the cylinder, which therefore must be restrained; the restraint is normally applied at the end supports where the 'classical' boundary restraints are also applied. Further, the force resultant applies global bending to the cylinder and the resulting meridional compressive stresses may reduce the buckling pressure. Tests were carried out on 1 m diameter cylinders in the slenderness range $R/h = 500-900$ with $L/R = 1.55-2.38$. A typical response is shown in Fig. 14.10. The level of imperfection in the zone of peak buckling

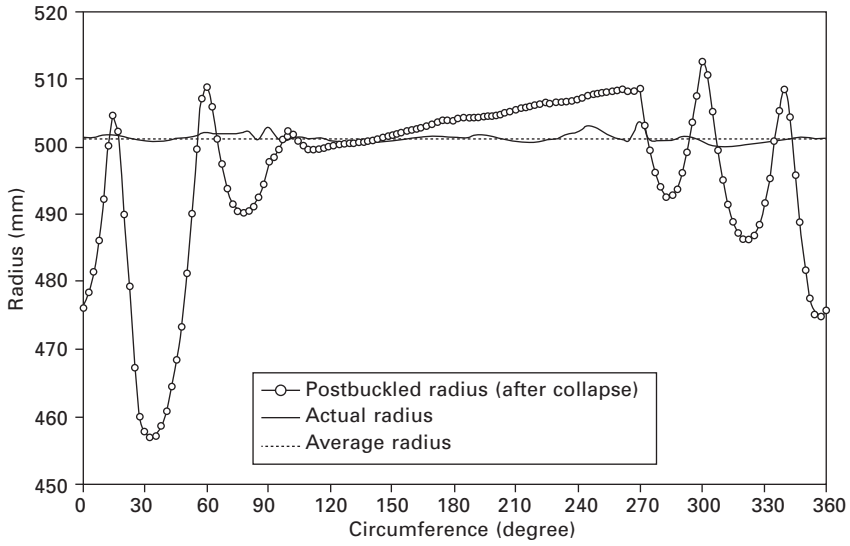


14.10 Horizontal tank immersion ($R/h = 670$, $L/R = 1.55$).

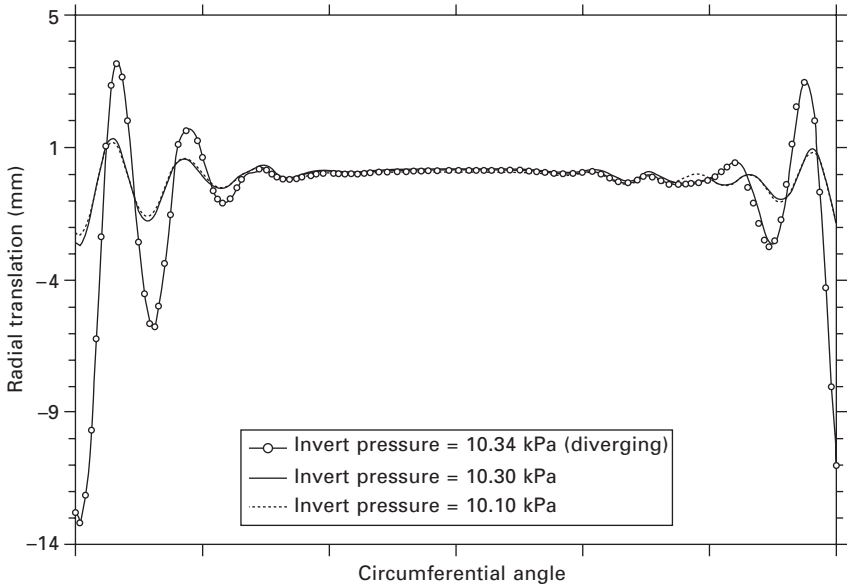
deformations is of the order of t . The full buckling pattern is of decaying sinusoidal form (Fig. 14.11) and is developed at 90% of the linear buckling prediction, but the collapse pressure is slightly higher. The wavenumber is reduced by 1 from the predicted value of 10. The geometry at the mid-span section near collapse is shown in Fig. 14.12, while nonlinear analysis predictions based on the measured initial imperfections is shown in Fig. 14.13. The experimental global buckling pressure was found to be slightly less than the



14.11 Horizontal tank immersion – decaying buckling mode.



14.12 Horizontal tank immersion – initial and final midspan geometry.

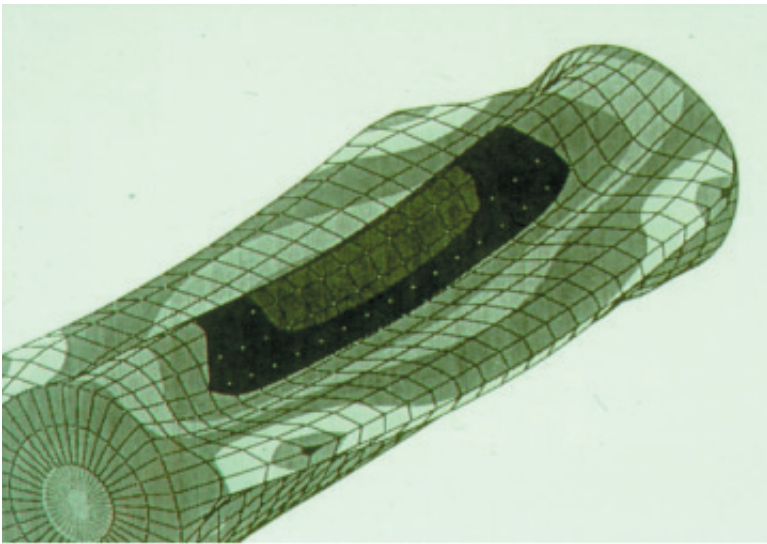


14.13 Horizontal tank immersion – non-linear analysis prediction.

linear ‘perfect’ shell predictions, but a postbuckling reserve existed before final collapse.

14.4 Prototype failures

Buckling failure of silos and tanks under the action of vacuum or external pressure typically due to wind is not uncommon. A steel header tank of diameter 3 m, length 12 m and $R/t = 250$ imploded through inadequate venting that allowed a small vacuum to form. Nonlinear finite element analysis for the combined effects of self-weight, initial imperfections, partial hydrostatic pressure and uniform external pressure due to vacuum, revealed that failure could be expected at a vacuum of 22 kPa (2.2 m vacuum head; Fig. 14.14).



14.14 Header tank – finite element prediction.

A steel silo discharging bran failed by buckling under external pressure when a plug of bulk material slid down with no pressure relief at the top. The silo was of 4.5 m diameter, 23 m height and 6 m wall thickness. The observed circumferential buckling wavelength of 2 m is in full agreement with the predicted number of buckling waves $m = 7$ in a fully developed buckling pattern; the level of vacuum required for the observed failure is estimated as 15 kPa. Another silo suffered total implosion when failure of the discharge hopper created high vacuum as a plug of bulk material slid under gravity. The failure of these silos and of the header tank above emphasises the importance of effective venting of these slender structures having limited buckling capacity.

External pressure is also created by wind, causing a risk of buckling failure. In a bulk solid container, the structure is at especial risk when empty. A 16.5 m diameter tank 27 m high buckled under wind load during construction. The failure, characteristic of cylinders under external pressure with no radial restraint at one end, extended down to a step in wall thickness from 8 to 10 mm. Failure occurred while the top strake was only tack-welded to the strake below, but attracted full wind pressure. Minimal temporary bracing would have prevented failure. A group of six 15 m diameter and 15 m high empty wheat silos failed under wind loading. They were constructed of vertically corrugated sheeting stiffened vertically by 48 Z-section stringers. The wind speed at failure was estimated to have been very close to a design wind speed. The potential buckling strength of the walls was reduced by the flexibility of the joints in the vertical stringers and by yielding of the holding-down fittings, leading to partial loss of restraint against radial and vertical movement. This failure emphasises the importance of the holding down detail and of the continuity of the vertical stiffeners.

Because of economy, stiffening of corrugated silos has in the past not always continued to the top of the structure. This fact has had a negative influence on stability, as several examples of failures have shown (Figs 14.15, 14.16). Owing to compression and exterior eccentricity of the stiffener, the corrugated sheet immediately above the first bolt translates inwards (Fig. 14.17). It is concluded that the abrupt introduction of stiffening causes very high local stress in the corrugated sheet. The area around the first bolt therefore yields and precipitates failure of the sheeting.

14.5 Buckling through differential settlement

Foundations of large steel cylindrical tanks for bulk and fluid storage tend to be shallow and may consequently suffer differential settlement under load. These tanks are ductile and are able to tolerate limited settlement without distress. The measured settlement values when plotted relative to the tilt plane have an irregular shape that can be expressed as a Fourier series in n harmonics (Jonaidi and Ansourian, 1998). Several theories have been developed, ranging from inextensional to membrane and semi-bending theory, but the finite element method remains paramount for the analysis of shells of variable thickness, for stiffened shells and for the effects of buckling, large displacements and plasticity.

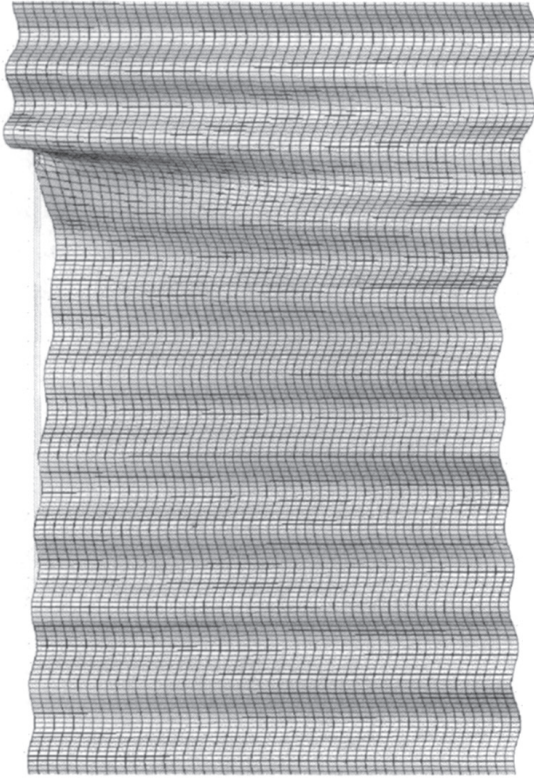
Inextensional theory is valid only for open-top tanks subjected to settlements of low n , and excludes the effects of (1) rigidity of any primary wind girder, and (2) variation of shell thickness. An analogy is used in this regard where a part of the shell is considered as a deep beam over the shell height. The measured settlement values when plotted relative to the tilt plane have an irregular shape that can be expressed as a Fourier series: by considering the



14.15 Failure by corrugation collapse.



14.16 Corrugation collapse at end of stiffeners.

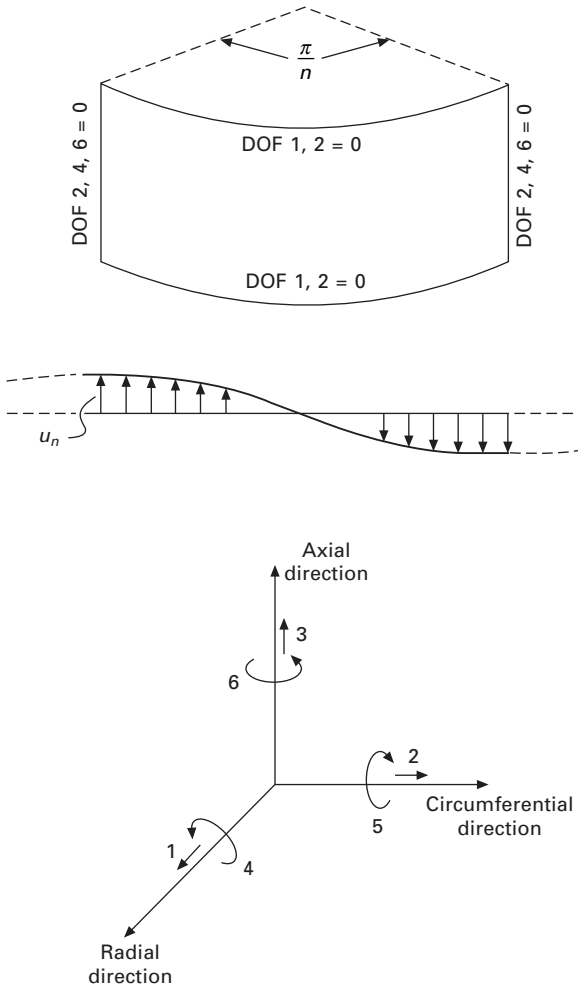


14.17 Finite element analysis (FEA) of corrugation at end of stiffener.

n th component of that series, the differential settlement u at the shell base ($x = 0$) is:

$$u = u_n \cos (n\phi) \quad \text{or} \quad u = u_n \cos \left(\frac{ny}{r} \right) \tag{14.22}$$

The same pattern is repeated at the top of the shell, but now in the horizontal plane; where the shell base moves *down*, the shell top deflects radially *out* (Fig. 14.18 and 14.19). Lines AA_1 and BB_1 rotate due to deep beam action, and points A_1 and B_1 approach each other; were A_1B_1 a straight line, the movement would be difficult and accompanied with high horizontal membrane forces; but A_1B_1 is a circular arc, and the displacement can occur by a decrease in the radius of curvature of A_1B_1 . To make this movement possible the adjoining panels must move *in*, involving inextensional lengthening and increase in radius of curvature. It follows that primary circumferential bending occurs in the top layer of the shell rather than membrane compression or tension. In this theory, mid-section in-plane strains are assumed to be zero, or $\epsilon_x = \epsilon_{x\phi} = \epsilon_\phi = 0$. For the n th Fourier component, the displacements are:



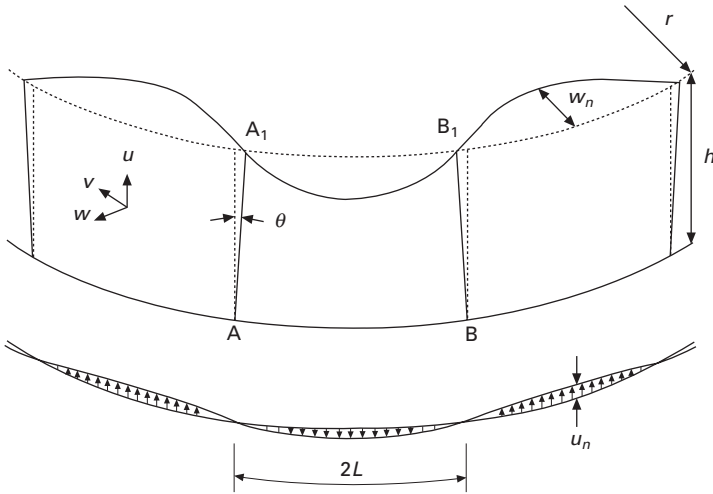
14.18 Settlement: loading, geometry and boundary conditions.

$$\begin{aligned}
 u &= u_n \cos(n\varphi) \\
 v &= v_n \sin(n\varphi) \\
 w &= w_n \cos(n\varphi)
 \end{aligned}
 \tag{14.23}$$

Neglect of the circumferential strains results in the relation between radial deflection and base settlement:

$$w_n = \frac{h}{r} n^2 u_n
 \tag{14.24}$$

Therefore, the distortion is proportional to the aspect ratio and the square of the harmonic number. A shortcoming of this theory is that the solution is



14.19 Shell deformation due to settlement.

independent of the wall thickness, but is satisfactory at $n < 4$, in the absence of a primary wind girder. Kamyab and Palmer (1989) gave a better solution for radial deflection w and vertical membrane force N_x in the presence of the girder:

$$w_n = \frac{h}{r} n^2 u_n \frac{1}{1 + AI_{\text{ratio}}} \quad 14.25$$

$$A = n^2 (n^2 - 1)^2 \frac{2 + \nu}{12(1 - \nu^2)} \left(\frac{h}{r}\right)^2 \left(\frac{t}{r}\right)^2 + n^4 (n^2 - 1)^2 \frac{1}{36(1 - \nu^2)} \left(\frac{h}{r}\right)^4 \left(\frac{t}{r}\right)^2 \quad 14.26$$

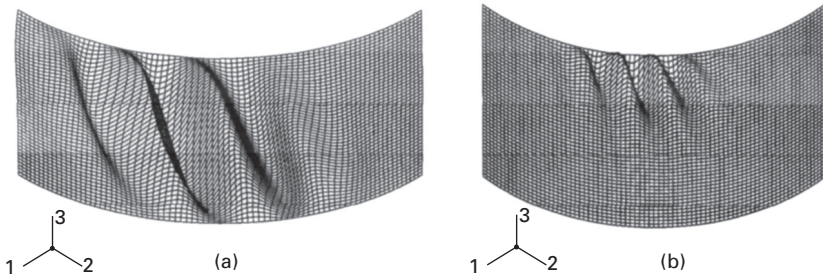
$$N_{nx} = \frac{h}{r} n^2 u_n \frac{BEI_{\text{ratio}}}{1 + AI_{\text{ratio}}} \quad 14.27$$

$$B = n^2 \frac{(n^2 - 1)^2}{12(1 - \nu^2)} \left(\frac{h}{r}\right)^2 \left(\frac{t}{r}\right)^3 \quad 14.28$$

In the above expressions, I_{ratio} is the ratio of circumferential bending rigidity of the primary wind girder to shell rigidity, or $\frac{12I_g(1 - \nu^2)}{ht_{\text{max}}^3}$. The solution is applicable over a much wider range of n , but not beyond a critical value. Inaccuracies also arise from the neglect of bending, as may be determined by comparison with finite element solutions; the typical maximum error for the range of n considered, is approximately 10–20%.

Finite element analysis provides the most accurate and general solution, and is extended to linear buckling and nonlinear response (Jonaidi and Ansourian 2000). The model consists of one half-wave ($n = 2$) of a cylindrical shell, supported along two generators and along two circular edges normal to the axis (Fig. 14.18), with boundary conditions as shown. In this ‘local’ model, a highly refined mesh was possible, yielding high accuracy.

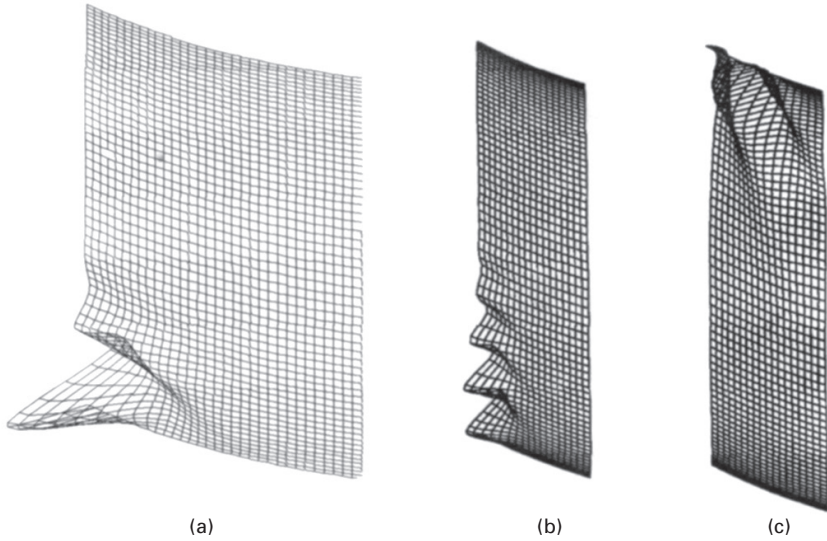
Linear buckling analyses using highly refined meshes were made for tank structures of wall slenderness in the range $r/t = 300$ – 2000 , and geometry $h/r = 0.3$ – 3 . Radial and circumferential displacements were restrained at the base and top, modelling closed-top tanks. Differential settlements at harmonic n from 2 to 24 were imposed at the base and the first eigenvalue extracted. For t uniform and low n (< 5), the critical stresses depend on both r/t and h/r , and the buckling mode is mainly one of shear (Fig. 14.20a). With increasing height however, local meridional buckling occurs near the base at moderate n (Fig. 14.21a, $n = 6$). At higher n , local buckling near the base occurs and the effect of height disappears, i.e. behaviour is dominated by axial compression. In the case of *tapered* shells, buckling occurs at the top of the shell even for moderate and higher n . The shear buckling mode can be seen even at $n = 12$ (Fig. 14.21c, $T_{\text{ratio}} = 5$). The thinner area at the top, subjected to shear stresses caused by circumferential restraint, is more likely to buckle than the thicker shell at the base under axial compression.



14.20 Shear buckling for uniform and tapered shells ($h/r = 0.7$, $r/t = 1000$).

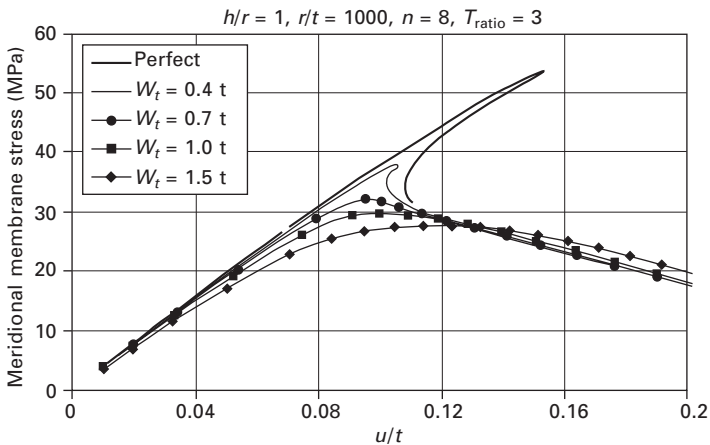
Following an analysis of the results and examination of the buckling modes, it was found that the maximum meridional stresses (σ_x) at the base depends on both r/t and h/r ; and the buckling mode is one of shear. This mode is shown in Fig. 14.20(a) for uniform thickness and 14.20(b) for tapered wall. For $n = 2$, the best fit is given by:

$$\sigma_x = \frac{1.267 E}{\sqrt{(1 - \nu^2)}} \left(\frac{h}{r}\right)^{0.438} \left(\frac{t}{r}\right)^{1.198} \quad 14.29$$



14.21 Buckling mode for cylinders ($h/r = 1$, $r/t = 1000$): (a) $n = 6$, uniform thickness, (b) $n = 12$, tapered thickness, $T_{ratio} = 3$, (c) $n = 12$, $T_{ratio} = 5$.

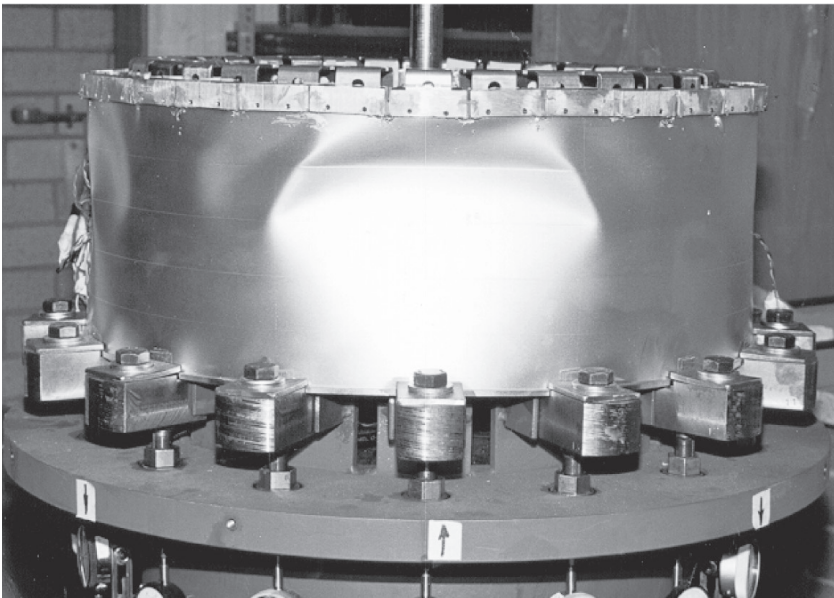
While the linear study provided an insight into the dominant modes, a nonlinear analysis is required for the ultimate response. Geometry parameters of $r/t = 1000$ and $h/r = 1$ are chosen, representative of medium/large tanks. The wall is assumed to have uniform or tapered thickness ($T_{ratio} = 3$). Under highly localised displacement (e.g. $n = 8$), the linear buckling mode is one of shear in the thinner upper plates, but the nonlinear response is shown in Fig. 14.22



14.22 Stresses at base for stepped shell, imperfection amplitude W_t , $n = 8$, imperfection affine to buckling mode.

at several imperfection amplitudes in the range $W_i = 0 - 1.5t$. The sensitivity to imperfection is high: the maximum meridional membrane stress at $W_i = 1.5t$ is half the value for the perfect cylinder. This is due to the high meridional stresses which create a condition closer to cylinders in uniform axial compression.

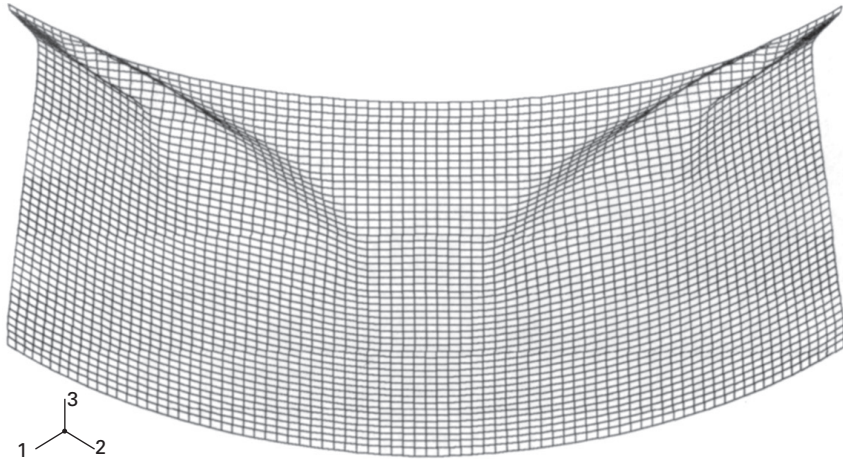
Experiments were performed by Jonaidi (1998) to study the effects of harmonic settlements on open-top and closed-top specimens of uniform and stepped wall thickness. The specimens were generally of 600 mm diameter and 200 mm height with four courses of thickness 1.25 mm, 1 mm, 0.75 mm and 0.5 mm (Fig. 14.23). In a study of the effect of moderately localised settlement, the harmonic pattern $n = 4$ was chosen and settlements were imposed in 0.025 mm increments until large buckling displacements were observed. The settlement caused large buckling deformations in the upper parts of the shell. The general deformation was that of a large inward dimple above the crown of the cosine settlement curve, together with inclined dimples typical of shear buckling above the nodes of the cosine curve. The lower parts of the shell were always free of buckles. The ultimate configuration was well predicted in a nonlinear analysis (Fig. 14.24).



14.23 Upward settlement in Test 6, $n = 4$, stepped wall thickness, note large inward deformation at the top

14.6 Concluding remarks

In this chapter, overstressing and buckling failure of slender curved plates were examined, and abridged developments provided of theories given fuller



14.24 Deformed shape from nonlinear FEA, $n = 4$, stepped wall thickness.

scope in the author's and others' publications. Closures of pressure and other vessels were examined for buckling under internal pressure. Buckling under uniform and nonuniform external pressure was considered for classical boundary conditions and for end warping restraint. The susceptibility to collapse of corrugated curved plates was investigated. Theories were compared with experimental data, and prototype failures critically examined. Finally, the effects of differential settlement of the foundation of tank structures on distortional and plate buckling was studied.

14.7 References

- Almroth, B.O. (1962), Buckling of a cylindrical shell subjected to non-uniform pressure, *J. Applied Mechanics, Trans. ASME*, **84**, 675–682.
- Ansourian, P. (2004), Cylinders under non-uniform external pressure. *Buckling of Thin Metal Shells*, Edited by J.G. Teng and J.M. Rotter, Spon Press, London, UK, 175–197.
- Ansourian, P. and Glaesle, M. (2002), Aspects of corrugated silos. *Proc. ICASS'02, Intl. Conf. on Advances in Steel Structures, Hong Kong*, Edited by S.L. Chan, J.G. Teng and K.F. Chung, Elsevier, Oxford Vol. **2**, 713–720.
- Ansourian, P., Showkati, H., Sengupta, M. and Vodenitcharova, T. (1995), The behaviour of cylindrical shells under uniform and non-uniform external pressure. *Fourteenth Australasian Conference on the Mechanics of Structures and Materials, Hobart*, 630–636.
- API Bulletin 2U (1987), Bulletin on stability design of cylindrical shells, American Petroleum Institute, Washington DC.
- AS 1170.2 (1989), *Australian Standard SAA Loading Code Part 2: Wind loads*. Standards Australia.
- Batdorf, S.B. (1947), A simplified method of elastic-stability analysis for thin cylindrical shells; *NACA Report*, **874**, 1–26.

- Blackler, M.J. and Ansourian, P. (1986a), Buckling behaviour of a full-scale tank under internal and external pressure. *Civ. Eng. Trans., IEAust.*, **CE28**(3), 216–221.
- Blackler, M.J. and Ansourian, P. (1986b), The influence of elastic end restraints on cylinder stability under wind loading. *10th Australasian Conf. on Mechs. of Structs. and Mats.*, 241–246.
- Blackler, M.J. and Ansourian, P. (1988), The failure of two torispherical shells under internal pressure. *Proc. Instn. Mech. Engrs., London*, **202**(A3), 183–191. (Kenneth Harris James Prize of the Instn. of Mech. Engrs., London, 1988.)
- Brush, D.O. and Almroth, B.O. (1975), *Buckling of Bars, Plates and Shells*, McGraw-Hill, New York.
- ECCS (European Convention for Constructional Steelwork) (1988). Buckling of Steel Shells, European Recommendations No. 56, Brussels.
- Flügge, W. (1973). *Stresses in Shells*. Springer Verlag, Berlin.
- Galletly, G.D. (1986), A simple design equation for preventing buckling in fabricated torispherical shells under internal pressure. *Trans. ASME, J. Press. Vess. Technol.*, **108**, 521–526.
- Jonaidi, M. (1998). *PhD Thesis, University of Sydney*. Effects of differential settlement on storage tank shells.
- Jonaidi, M. and Ansourian, P. (1998), Harmonic settlement effects on uniform and tapered tank shells. *Thin-walled Structures*, **31** (1–3), 237–255.
- Jonaidi, M. and Ansourian, P. (2000), Buckling behaviour of closed and open top cylindrical shells subjected to meridional edge deformation. *Proc. 3rd Intl. Conf. on Coupled Instabilities in Metal Structures*, Eds. D. Camotim, D. Dubina and J. Rondal, Imperial College Press, Lisbon, 411–418.
- Kamyab, H. and Palmer, S.C. (1989), Analysis of displacements and stresses in oil storage tanks caused by differential settlement. *Proc. Instn. Mech. Engrs., Part C*, **203**, C1, 60–70.
- Rotter, J.M. (2004), Cylindrical shells under axial compression. *Buckling of Thin Metal Shells*, edited by J.G. Teng and J.M. Rotter, Spon Press, Londn, UK 369–408.
- Sengupta, M. (1997), *PhD Thesis, University of Sydney*. The behaviour of cylindrical shells under external pressure.
- Teng, G.J. (2004), Shell junctions. *Buckling of Thin Metal Shells*, edited by J.G. Teng, and J.M. Rotter, Spon Press, London, UK, 369–408.
- Vodenitcharova, T. and Ansourian, P. (1996), Buckling of circular cylindrical shells subject to uniform lateral pressure. *Engineering Structures*, **18**(8), 604–614.
- Vodenitcharova, T. and Ansourian, P. (1998), Hydrostatic, wind and non-uniform lateral pressure solutions for containment vessels. *Thin-walled Structures*, **31**(1,3), 221–236.
- Weingarten, V.I. (1962), The buckling of cylindrical shells under longitudinally varying loads. *Journal of Applied Mechanics, ASME*, **29**, 81–85.

Local buckling and postbuckling analysis of light gauge steel members

J R H O D E S , University of Strathclyde UK

15.1 Introduction

Light gauge steel structural members, generally manufactured by cold-rolling from steel sheet or strip material, are extremely common throughout the world. These members can have substantial advantages over alternative types of construction due to the limitless variation in cross-sectional shapes that can be produced and the high strength to weight ratios available from the use of thin material.

The variation in cross-sectional shapes possible with light gauge steel members, coupled to the high width to thickness ratios used in the walls of such members, leads to complexities in the design of these members. The possibilities of local buckling of the component walls and a variety of other buckling potentialities arise, and must be taken into account in the design analysis of such members. Over a number of years the various types of buckling observed in light gauge members have been examined by a substantial number of investigators and a large number of design specifications have been developed throughout the world that take into account the different types of buckling and the interaction that occurs between the different modes.

Light gauge cold-formed steel members have been used in building construction for over 150 years (Yu 2000), but the growth in structural use and understanding of the behaviour of structures made this way started during the second world war and the first design specification for this type of construction was produced in the USA in 1946 (American Iron and Steel Institute 1946). The first UK specification was produced in 1961 (BSI 1961), although a proposed specification due to Shearer-Smith (1951) had been published some 10 years earlier. The 1970s saw an upsurge in interest in this field in Europe and in the 1980s new UK codes (1987) and European Recommendations (ECCS 1987) for design in cold-formed steel were produced as well as a new American code (1986). This interest has continued since then, and the first Eurocode dealing with cold-formed steel was published in 1996 (CEN 1996a). Particular types of cold-formed steel structures have

their own inherent design complexities, and new design specifications have been produced in the past decade dealing specifically with stainless steel (CEN 1996b) and storage racking (Federation Européenne de la Manutention 2000).

Since about 1980 there has also been a progressive increase in the strength of steel used in the manufacture of cold-formed sections. Prior to this period the type of steel most widely used in the construction industry was of about 200 MN/m^2 yield strength whereas at the present time many companies are producing members with about 400 MN/m^2 yield strength, and indeed there has recently been substantial use in Australia of cold-formed tubes of yield strength 1350 MN/m^2 .

The major structural advantages of cold-formed steel members lie with the thinness of the material that can be used, leading to extremely lightweight construction, and this, combined with the trend towards using higher-strength steel, promotes the occurrence of failure modes that do not arise, or are rare in occurrence, in conventional steel structures. Thus the advantages that can be gained by the use of cold-forming are bought at the expense of the requirement to use increased sophistication in the design analysis.

Perhaps the major factor that arises in the design of cold-formed steel members is the susceptibility of these members to a wide variety of buckling modes. The thin walls of such members are often liable to suffer local buckling in compression, and this must be taken into account in the design of almost any cold-formed steel structural member. Local buckling is stable in the elastic range, and locally buckled members may have substantial postbuckling strength. However, local buckling does modify the behaviour of a member, and the effects of local buckling on member behaviour, and its interaction with other buckling modes, must be considered in design.

Another factor that causes complexity in cold-formed steel design arises from the fact that cold-formed members, in addition to being thin-walled, are in most cases open sections, and are extremely flexible and weak in resistance to torsion. This brings the requirement to ensure that the loading is introduced to such structures in such a way that torsional behaviour is minimised, and also introduces the possibility of torsional buckling, torsional-flexural buckling and lateral torsional buckling in cold-formed members.

Another source of complexity is found in the methods used to connect cold-formed steel members. In comparison with hot-rolled structures, welding is used to a much smaller degree, and a plethora of connection types and methods exists, including the use of bolts, rivets, screws and adhesives, together with a number of connection types in which the connection is made by deforming the materials of adjoining members to form the joints. Connections in cold-formed steel members in the main lack complete rigidity, and the semi-rigid nature of the connections can have a substantial effect on the structural behaviour.

In this chapter, a number of the various modes of buckling observed in light gauge members will be described and analysed.

15.2 Local buckling in plates and systems of plates

15.2.1 Brief introduction

The first theoretical examination of plate buckling was by Bryan (1891) who solved the problem of a simply supported plate under uniform compression. Since then numerous researchers have investigated local instability in plates under a wide variety of loading and boundary conditions using many different methods of analysis. There are a number of excellent textbooks which have described the main results of these investigations, for example those by Timoshenko and Gere (1961) and Bulson (1970), and the reader is referred to these for a general study of plate instability.

With regard to plate postbuckling analytical approaches, only the two methods most often used by the author, namely the 'semi-energy method' and the so-called 'lower bound method' will be briefly described here, since these are equally applicable to single plates and systems of plates.

15.2.2 Energy equations

The strain energy stored in a locally buckled elastic plate is given by the summation of that due to out-of plane bending, V_1 , and that due to in-plane deformations, V_2 . These can be written:

$$V_1 = \frac{D}{2} \iint \left\{ \left(\frac{\partial^2 w}{\partial x^2} + \frac{\partial^2 w}{\partial y^2} \right)^2 - 2(1 - \nu) \left[\frac{\partial^2 w}{\partial x^2} \frac{\partial^2 w}{\partial y^2} - \left(\frac{\partial^2 w}{\partial x \partial y} \right)^2 \right] \right\} dx dy \quad 15.1$$

$$V_2 = \frac{t}{2} \iint [\sigma_x \epsilon_x + \sigma_y \epsilon_y + 2\tau_{xy} \gamma_{xy}] dx dy \quad 15.2$$

In the above equations w is the out-of plane deflection of the plate, σ_x , σ_y and τ_{xy} are the membrane stresses in the plate, ϵ_x , ϵ_y and γ_{xy} are the membrane strains in the plate, ν is Poisson's ratio and D is the plate flexural rigidity. The equations are specifically applicable to initially perfect plates but if it is assumed that the local imperfections have the same form as the deflections, the imperfect case can be derived rather simply from the results obtained for the perfect plate. If a number of plates act together to form a structural member, then the total strain energy is obtained by summing that in the

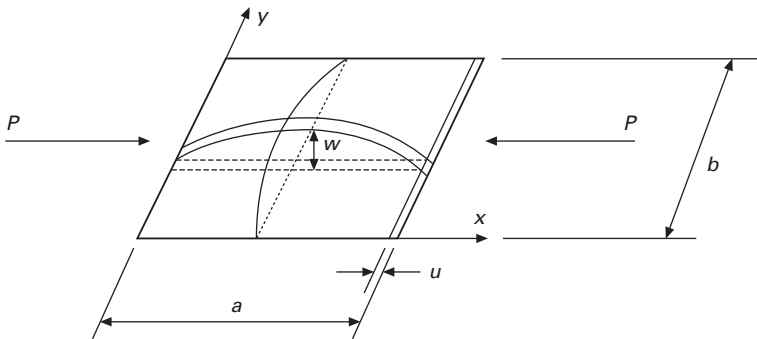
individual plates, while of course, ensuring that compatibility conditions are satisfied where the plates are connected.

In applying either of the analysis methods mentioned, the approach begins by assuming, for a given end displacement on a plate or member, a form for the out-of-plane displacements w (and the in-plane displacements v if required). The in-plane stresses and strains are then determined in terms of the applied end displacement and the magnitude coefficients of the assumed out-of-plane displacements from compatibility conditions. The strain energy is then written in terms of the end displacement and the magnitude coefficients of the assumed displacements and the Principle of Minimum Potential Energy is applied to obtain the relationship between the applied end displacement and the assumed plate displacements.

15.2.3 The lower bound method

As a simple example, consider a flat plate, simply supported on all edges and subjected to a uniform displacement u in the x direction as shown in Fig. 15.1. Using the ‘lower bound’ approach, the average strain in the x direction at any position across the plate is determined by computing the change in length of a compressed and curved element, as detailed in the figure. This strain is given by

$$\epsilon_x = \frac{u}{a} - \frac{1}{2a} \int \left(\frac{\partial w}{\partial x} \right)^2 dx \tag{15.3}$$



15.1 Simply supported flat plate under uniform compression.

In the lower bound method, it is assumed that stresses in the y direction and shear stresses do not exist, so that the membrane stress in the x direction is given simply by $\sigma_x = E\epsilon_x$, where E is the modulus of elasticity. The strain energy due to the in-plane effects is then simplified as the only contribution

is from stresses and strains in the x -direction. By substituting this in Eq. (15.2), V_2 may be expressed as:

$$V_2 = \frac{Eta}{2} \int \left[\frac{u}{a} - \frac{1}{2a} \int \left(\frac{\partial w}{\partial x} \right)^2 dx \right] dy \quad 15.4$$

The strain energy due to out-of-plane effects, V_1 , is as given by Eq. (15.1).

If we now assume a form for the deflections, i.e. $w = A \sin \frac{\pi x}{a} \sin \frac{\pi y}{b}$, where A is the magnitude coefficient, and by substituting this into the energy equations and performing the integrations, we have:

$$V = V_1 + V_2 = \frac{Etab}{2} \left\{ \varepsilon^2 + \frac{3}{128} \left(\frac{\pi}{a} \right)^4 A^4 - \frac{1}{4} \varepsilon \left(\frac{\pi}{a} \right)^2 A^2 \right\} \\ + \frac{Dab}{8} \left\{ \left(\frac{\pi}{a} \right)^2 + \left(\frac{\pi}{b} \right)^2 \right\}^2 A^2 \quad 15.5$$

where ε is the nominal strain in the x direction, equal to u/a .

The Principle of Minimum Potential Energy is now employed by differentiating the strain energy with respect to A and equating this to zero. (Note that since ε is a specified value then only minimisation of the strain energy is required.) By carrying this out and performing some rearrangements, we obtain:

$$A^2 = \frac{16}{3} \left(\frac{a}{\pi} \right)^2 \left\{ \varepsilon - \frac{\pi^2 D}{b^2 t E} \left[\frac{b}{a} + \frac{a}{b} \right]^2 \right\} \quad 15.6$$

Thus the deflection magnitude A is given as ε varies. Knowing this, we can obtain the average strain and stress at any position across the plate by substitution into Eq. (15.3), and the total load by integrating the stresses across the plate. It should perhaps first be mentioned that Eq. (15.6) suggests

that A^2 is negative, i.e. A is imaginary, if $\varepsilon < \frac{\pi^2 D}{b^2 t E} \left[\frac{b}{a} + \frac{a}{b} \right]^2$. This indicates the point at which A begins to have a non-imaginary value, i.e. the buckling point. At this point $A = 0$ and

$$\sigma_{CR} = E \varepsilon_{CR} = \frac{\pi^2 D}{b^2 t} \left[\frac{b}{a} + \frac{a}{b} \right]^2 \quad 15.7$$

This is the well-known expression for the local buckling stress of an elastic plate simply supported on all edges. As the exact deflected form for this case was used, the exact (according to elastic thin plate theory) value of the buckling stress arises. Note that the buckling stress is often written as:

$$\sigma_{CR} = K \frac{\pi^2 D}{b^2 t} \quad 15.8$$

where in this particular case $K = \left[\frac{b}{a} + \frac{a}{b} \right]^2$ with a minimum value of 4 for the case $a = b$, i.e. a square plate.

By substituting Eq. (15.6) into Eq. (15.3), we can evaluate the strain, and hence the stress at any point across the plate, i.e.:

$$\sigma_x = E \left[\varepsilon - \frac{4}{3} (\varepsilon - \varepsilon_{CR}) \sin^2 \frac{\pi y}{b} \right] \quad 15.9$$

The average stress is therefore equal to the nominal strain times E at the plate edges and reduces towards the centre. At end displacements substantially greater than critical, the stress according to Eq. (15.9) becomes tensile. This occurrence has been observed in testing, but it should be noted that the solution becomes increasingly inaccurate as the loading progresses beyond buckling because (a) there are inherent inaccuracies in the lower bound approach and (b) the buckled shape changes as buckling progresses.

15.2.4 Reduced modulus of elasticity, E^*

To complete the example under examination, if we integrate the stresses across the plate and multiply by the plate thickness, we find that the variation of load with nominal end displacement is:

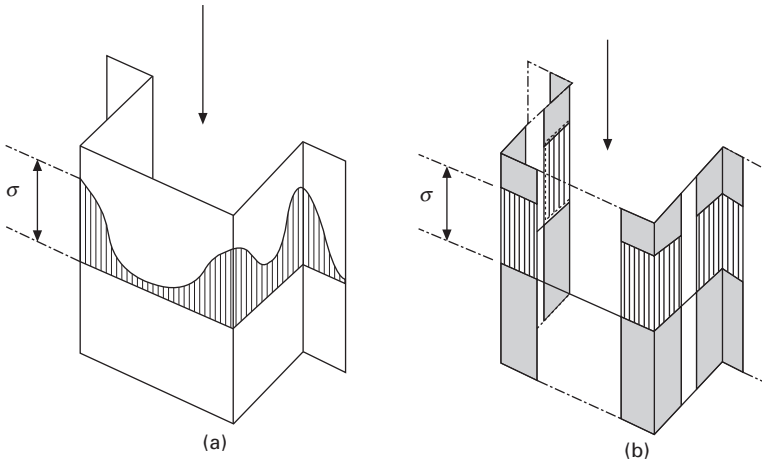
$$P = Etb \left[\varepsilon - \frac{2}{3} (\varepsilon - \varepsilon_{CR}) \right] = \frac{Etb}{3} (\varepsilon + 2\varepsilon_{CR}) \quad 15.10$$

Thus the increase in load per unit end displacement occurs at only one-third of the prebuckling rate, i.e. the axial stiffness is reduced to one-third of its prebuckling value. This reduction in stiffness is often described in terms of a reduced modulus of elasticity, E^* . In this case, the reduced stiffness $dP/d\varepsilon$ is equal to $Etb/3$, whereas the prebuckling stiffness is Etb . Thus we have $E^*/E = 1/3$.

15.2.5 Effective width concept

A method of describing the effects of local buckling that is extremely widely used in design is the effective width approach. This approach has been known for a long time in shipbuilding as a rule of thumb design tool but it was first quantified analytically by von Kármán *et al.* (1932) and subsequently used, researched and modified by many researchers, most notably Winter (1947). This approach recognises that on supported edges of a plate, or at the unbuckled corners of a section, the stress is not greatly affected by local buckling, while

at areas far from supported edges the stresses are substantially reduced. The effective width approach simplifies the stress distribution by considering that locations near supported edges are completely effective in resisting axial displacement, and behaves as if no buckling effects were present, while areas far from the supported edges are completely ineffective and carry no stress. This is illustrated in Fig. 15.2 in the case of a compressed member. Using this approach the effective width of a plate, b_e , is such that the load-end displacement relationship is as specified by analysis or experimentation.



15.2 Stress system in a compressed strut and effective width idealisation (a) Stress variation across section; (b) effective width simplification.

For the example used we have, from Eq. (15.10) for the simple example case:

$$\begin{aligned}
 P &= Etb \left[\varepsilon - \frac{2}{3}(\varepsilon - \varepsilon_{CR}) \right] = \frac{Etb}{3} [\varepsilon + 2\varepsilon_{CR}] \\
 &= \frac{tb}{3} [\sigma + 2\sigma_{CR}] = \sigma t b_e \\
 \therefore \quad \frac{b_e}{b} &= \frac{1}{3} \left[1 + 2 \frac{\sigma_{CR}}{\sigma} \right] \tag{15.11}
 \end{aligned}$$

Thus, the effective width is equal to the full width at the point of buckling, and reduces thereafter.

15.2.6 Effects of imperfections

So far it has been considered that the plate under examination is perfectly flat. No plate, however, is perfectly flat and the imperfections occurring in

plates can have a substantial effect on their behaviour. It is generally considered that the most serious imperfections have the same form as the local buckles. If this is assumed to be the case then the governing equations can be modified with little effort to take the imperfections into account. For a plate with total deflection magnitude coefficient A and initial imperfection magnitude A_0 then, if the imperfect plate is initially stress free, the bending stresses are proportional to $(A - A_0)$ while the changes in membrane stress due to out-of-plane effects are proportional to $(A^2 - A_0^2)$. Thus the terms containing A^2 in V_1 can be replaced by $(A - A_0)^2$ and those containing A^2 in V_2 can be replaced by $(A^2 - A_0^2)$. Equation (15.5) can be rewritten:

$$V = \frac{Etab}{2} \left\{ \varepsilon^2 + \frac{3}{128} \left(\frac{\pi}{a} \right)^4 (A^2 - A_0^2)^2 - \frac{1}{4} \varepsilon \left(\frac{\pi}{a} \right)^2 (A^2 - A_0^2) \right\} + \frac{Dab}{8} \left\{ \left(\frac{\pi}{a} \right)^2 + \left(\frac{\pi}{b} \right)^2 \right\}^2 (A - A_0)^2 \quad 15.12$$

For the imperfect case, the simple relationship between A and ε becomes more complicated and it is simpler to write ε in terms of A rather than A in terms of ε . Thus:

$$\varepsilon = \frac{3}{16} \left(\frac{\pi}{a} \right)^2 (A^2 - A_0^2) + \frac{\pi^2 D}{b^2 t E} \left[\frac{b}{a} + \frac{a}{b} \right]^2 \left(1 - \frac{A_0}{A} \right) \quad 15.13$$

In this case the simplest method of displaying the results is to specify the deflection magnitude A and evaluate ε and the corresponding stresses and loads. This hampers the simplicity of the approach but does not lead to any undue complexity.

15.2.7 The semi-energy method

The semi-energy method was first proposed by Marguerre (1937). This approach avoids the inaccuracies inherent in the lower bound method by taking into account the true membrane stress field induced by the out-of-plane deflections. To do this, the compatibility equation introduced by von Karman (1910) is used to evaluate the in-plane strain and stress situations induced by the out-of-plane deflections rather than the simplistic approximation of the lower bound method. The compatibility equation, for a perfect plate, is:

$$\frac{\partial^4 F}{\partial x^4} + 2 \frac{\partial^4 F}{\partial x^2 \partial y^2} + \frac{\partial^4 F}{\partial y^4} = E \left[\left(\frac{\partial^2 w}{\partial x \partial y} \right)^2 - \frac{\partial^2 w}{\partial x^2} \frac{\partial^2 w}{\partial y^2} \right] \quad 15.14$$

where F is a stress function such that $\sigma_x = \partial^2 F / \partial y^2$, $\sigma_y = \partial^2 F / \partial x^2$, $\tau_{xy} = \partial^2 F / \partial x \partial y$. This can be solved for a wide variety of plate buckling problems and does not lead to undue complexity, but does take substantially more effort to explain. For the purposes of this chapter, it is sufficient to say that if the plate is simply supported on the loaded edges the stress distributions obtained for a given end displacement are the same as those given by the lower bound method plus a periodically varying correction function that ensures the satisfaction of compatibility condition between out-of-plane and in-plane displacements. If the exact deflected form is specified for this method, then the exact solution corresponding to elastic plate theory is obtained. As in the case of the lower bound method, the presence of imperfections of the same shape as the local buckles can be easily taken into account by the modification of the deflection magnitude coefficients in an identical manner.

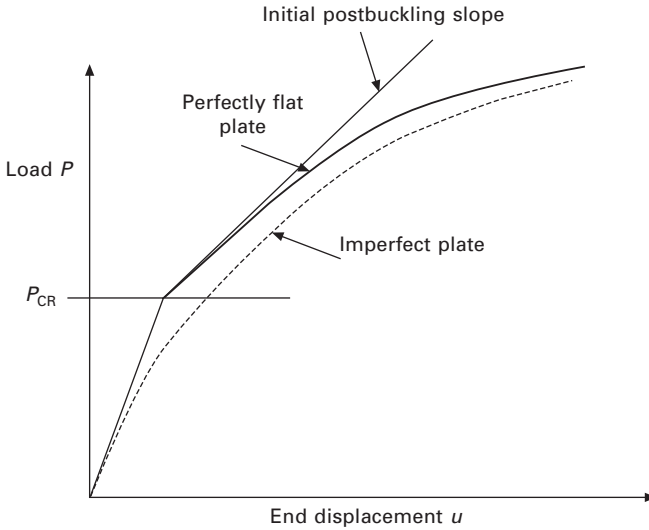
15.2.8 Behaviour in the advanced elastic postbuckling range

As buckling progresses, the shape of the local buckles changes and the stiffness of the plate reduces further. This can be taken into account analytically in a number of ways, using either the lower bound method or the semi-energy method, by providing the means for the assumed displaced form to change as loading progresses. Classically this is carried out by providing a number of different displacement functions, each with a different magnitude coefficient, and evaluating the strain energy in terms of all magnitude coefficients. The application of the Principle of Minimum Potential Energy with respect to each magnitude coefficient in turn results in a series of nonlinear equations which are then solved for specified increments of end displacement to provide the complete solution. For the particular example considered, the load-end displacement behaviour obtained on this basis is shown in Fig. 15.3.

15.2.9 Failure of thin steel plates and members

Failure of thin steel plates and members in the presence of local buckling is usually, although not always, associated with the onset of plasticity. If local buckling has occurred, then compressed elements of a plate or plate system generally fail very shortly after yielding occurs. Thus it is generally assumed in design specifications that plasticity in compression is synonymous with failure. In members such as beams where tension elements may reach yield while compression elements are still elastic, then the member may have substantial post-yield strength and continue to carry increasing load until the compressed locally buckled elements attain yield.

Even in the case of members that have attained their peak loading, it is



15.3 Load-end displacement path for compressed plate.

often desirable to have knowledge of the post-failure behaviour. This is important, for example, in the case of multiple redundant structures when the residual capacity of a failed member can postpone the onset of complete structure failure, or in vehicle energy absorption systems where the absorption of energy by 'failed' members is used to bring the vehicle to a halt. Research in these fields has resulted in large strides in the knowledge of post-failure behaviour of a wide variety of structural members and components. However, these considerations are outside the scope of this chapter, which will be concerned with behaviour up to failure only.

15.3 Finite strip type analysis

15.3.1 Background

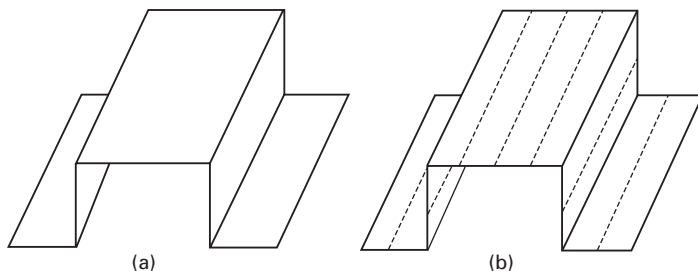
The finite strip method has been used for the analysis of buckling of thin-walled members for quite a long time now. The formulation of this approach is generally credited to Cheung (1968), although Wittrick (1968) used a similar type of approach to deal with buckling and vibration problems. Over the years, many researchers have used and extended the applicability of this approach. In considering the finite strip method, it is often stated that this approach requires substantially less computing power than the parent finite element method, and this is true, but becoming less important every year as computing capability increases. Another advantage which could be claimed, however, is that the processing of the output from the finite strip analysis is generally much simpler than from the finite element output, and it may well

be easier in many cases to examine the findings of the finite strip analysis for comparison with alternative approaches.

In this chapter, a particular finite strip type approach is briefly outlined, with some attention being focused on several alternative strip formulations. The two different postbuckling analysis methods outlined in the previous section are used in this approach to determine the postbuckling behaviour. The approach is not new, having been first developed for teaching Masters students in the mid-1970s, but there have been several extensions carried out over the years, and much of the postbuckling analysis material incorporated has not been widely distributed.

15.3.2 Finite strip layout

The thin-walled member under examination may be considered as a series of thin plates joined along their edges as shown in Fig. 15.4. Figure 15.4(b) shows a typical finite strip layout in which several strips, denoted by the dotted lines, are used in each plate element. Figure 15.4(a) shows a somewhat more ambitious finite strip layout in which one strip is used for each plate element. In such a case, either lower accuracy of solution results, or greater complexity of strip is required. When the member is acted upon by some external loads, the walls will deform. The deformations of the wall consist of in-plane and out-of-plane deformations. If we consider that the member undergoes buckling with no change in the applied load during buckling then the variation of strain energy due to in-plane and out-of-plane deformations can be evaluated, as can the potential lost by the applied loading, in terms of the deformation magnitudes. Precisely what deformation magnitudes are considered depends upon the particular strip formulation. By applying the Principle of Minimum Potential Energy, the relative magnitudes of the different deformations can be evaluated together with the minimum buckling condition.



15.4 Finite strip layouts.

In the approach described here, the in-plane displacements are analysed on the basis of the simple beam theory which specifies a single value for

each element, while the out-of-plane displacements are based on plate theory, with a larger array of variables. For the examination of buckling of members with simply supported ends, a sine wave describes exactly the buckling shape for in-plane and out-of-plane effects along a prismatic member with unvarying axial load and moment. In this chapter, for simplicity, the sine wave variation along the member will be considered exclusively, although it should be mentioned that relatively simple trigonometric functions (e.g. $\frac{\pi x}{L}$

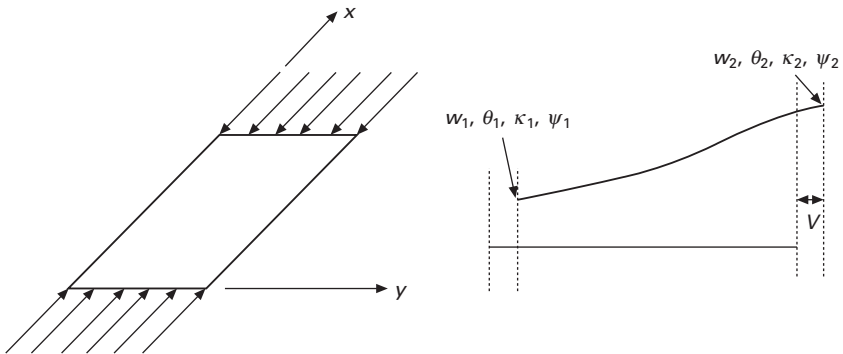
$\sin \frac{m\pi x}{L}$ for fixed ends and $\sin \frac{\pi x}{2L} \sin \frac{m\pi x}{2L}$ for simply supported–fixed ends) can also be used to give high accuracy for other standard boundary conditions (Rhodes and Khong 1988).

The member under examination is considered to be under some combination of axial force and bending. In some cases, the variation of stresses around the section prior to buckling is known, e.g. uniformly compressed members, or can easily be determined, e.g. beams under simple beam theory, while for other cases the dependency of the stress variation around the cross-section requires that a separate first order analysis be carried out to establish the loading situation.

At the point of buckling, for any strip as shown in Fig. 15.5 the analysis assumes that the in-plane deformations due to buckling can be written as:

$$v(x, y) = v \sin \frac{\pi x}{a} \tag{15.15}$$

where a is the strip length or the buckle half-wavelength.



15.5 Displacements in a finite strip.

The out-of-plane displacements of a strip are written in different forms for different strips. The four different types of strip used are given below.

15.3.3 Linear strips

With this type of strip, the displacements vary linearly in the y -direction, i.e.

$$w(x, y) = (w_1 + b\theta_1\eta) \sin \frac{\pi x}{a} \quad 15.16$$

where w_1 and θ_1 are the displacement and slope at $y = 0$, b is the strip width and $\eta = y/b$. The boundary conditions for in-plane and out-of-plane displacements at the junction of adjacent strips are that the slopes of each strip in the y direction are equal and the displacements of each adjacent edge in the x and y directions are equal. These last two are generally written in terms of the in-plane and out-of-plane displacements, v and w .

Examination of Eq. (15.16) suggests that since the slope does not vary across the strip, and from compatibility thus also sets the slope for the next and subsequent strips, then the two variables, together with a single in-plane variable v_1 , completely describe the deformation system within the member. This seems, at first thought, rather strange and, at best, unhelpful. Regardless of how many strips, or indeed how many plate elements, that are in the member, a total of three unknowns, or three degrees of freedom, results. This is in essence the classical situation regarding bending and torsion of thin-walled beams in the absence of any cross-sectional distortion. The approach here gives an alternative method of deriving the relevant flexural and torsional-flexural buckling loads, or, if desired, any of the classical cross-sectional properties. Apart from this, these strips can be used in conjunction with any of the other strip types to cut down solution time, although this is not a great problem nowadays.

15.3.4 Cubic strips

With this type of strip, the displacements follow a cubic law around the cross-section:

$$w(x, y) = \{w_1[1 - 3\eta^2 + 2\eta^3] + b\theta_1[\eta - 2\eta^2 + \eta^3] + w_2[3\eta^2 - 2\eta^3] + b\theta_2[\eta^3 - \eta^2]\} \sin \frac{\pi x}{a} \quad 15.17$$

where w_2 and θ_2 are the displacement and slope at $y = b$.

In this case the number of unknowns or degrees of freedom given by n strips is $(2n + 3)$. This is probably by far the most widely used strip at the present time. It is not particularly accurate for examination of local buckling when used as a single strip per plate element, but requires only two or three strips per plate to give reasonable accuracy under the worst conditions. Perhaps the main drawback to this formulation is that it does not lend itself easily to the rigorous postbuckling analysis procedure preferred by the writer, which

requires satisfaction of stress function boundary conditions which are substantially different for adjacent strips aligned at the same angle than for adjacent strips which have substantial variation of angle of orientation.

15.3.5 Quintic strips

The quintic strip utilises polynomial functions of the fifth degree to specify the cross-strip out-of-plane deflections. As the slopes and displacement on the strip edges are sufficient to satisfy all the necessary boundary conditions, the two additional quantities whose magnitudes are specified by the strip displacement functions are arbitrary. In the functions shown below, the cross-strip curvatures at edges 1 and 2 are selected, but these do not need to satisfy continuity or any other consideration when comparing adjacent strips. The displacements can be written as follows:

$$\begin{aligned}
 w(x, y) = & \{w_1[1 - 10\eta^3 + 15\eta^4 - 6\eta^5] + b\theta_1[\eta - 6\eta^3 + 8\eta^4 - 3\eta^5] \\
 & + 0.5b^2\kappa_1[\eta^2 - 3\eta^3 + 3\eta^4 - \eta^5] + w_2[10\eta^3 - 15\eta^4 + 6\eta^5] \\
 & + b\theta_2[-4\eta^3 + 7\eta^4 - 3\eta^5] \\
 & + 0.5b^2\kappa_2[\eta^3 - 2\eta^4 + \eta^5]\} \sin \frac{\pi x}{a}
 \end{aligned} \tag{15.18}$$

where κ_1 and κ_2 are the curvatures across the strip at $y = 0$ and $y = b$, respectively.

These strips are perfectly suitable for use in evaluating buckling loads employing a single strip per plate. They also permit accurate assessments of postbuckling behaviour at loads close to buckling. The one area in which there is something left to be desired is the postbuckling behaviour predicted far beyond buckling. This again may well be dependent upon the analysis method used, but the use of these strips with the perturbation method of plate analysis introduced initially by Stein (1959) produced less than perfect predictions for the far-postbuckling range. To improve upon this, septic strips were developed.

15.3.6 Septic strips

Here two further arbitrary quantities are required and the third derivatives of w with respect to y at both edges were taken as the arbitrary coefficients, simply to extend the approach already used for quintic strips. The septic strip displacements are

$$\begin{aligned}
 w(x, y) = & \{w_1[1 - 35\eta^4 + 84\eta^5 - 70\eta^6 + 20\eta^7] \\
 & + b\theta_1[\eta - 20\eta^4 + 45\eta^5 - 36\eta^6 + 10\eta^7] \\
 & + 0.5b^2\kappa_1[\eta^2 - 10\eta^4 + 20\eta^5 - 15\eta^6 + 4\eta^7] \\
 & + \frac{b^3\chi_1}{6}[\eta^3 - 4\eta^4 + 6\eta^5 - 4\eta^6 + \eta^7] \\
 & + w_2[35\eta^4 - 84\eta^5 + 70\eta^6 - 20\eta^7] \\
 & + b\theta_2[-15\eta^4 + 39\eta^5 - 34\eta^6 + 10\eta^7] \\
 & + 0.5b^2\kappa_2[5\eta^4 - 14\eta^5 + 13\eta^6 - 4\eta^7] \\
 & + \frac{b^3\chi_2}{6}[-\eta^4 + 3\eta^5 - 3\eta^6 + \eta^7]\} \sin \frac{\pi x}{a}
 \end{aligned} \tag{15.19}$$

where χ_1 and χ_2 are the third derivatives of w with respect to y at $y = 0$ and $y = b$, respectively.

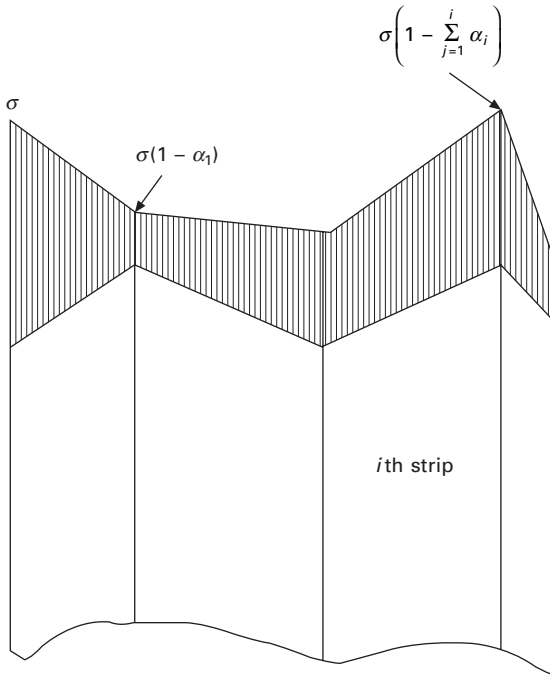
15.3.7 Generalisation of plate buckling and postbuckling analysis

In any strip in-plane and out-of-plane deformations may be present and the simultaneous occurrence of both types of deformations must be taken into account. In addition, when dealing with loading other than uniform compression the capability to examine systems of plates subjected to varying axial stress is required. The finite strip-type method used here is set up to analyse members in which each strip can be subjected to any combination of uniform and linearly varying stress across the strip, as indicated in Fig. 15.6.

The analysis procedure is described by Rhodes (1987) and in greater detail by Khong (1988). The buckling stress is evaluated neglecting the higher-order effects using standard procedures, and the eigenvector corresponding to the minimum buckling stress is then used as a single displacement function in the postbuckling analysis to obtain values for the reduced axial stiffness and reduced bending stiffnesses. For example, the reduced axial stiffness immediately after buckling obtained on the basis of the lower bound method is given by:

$$\frac{E^*}{E} = 1 - \frac{\sum_{i=1}^N \left[t_i \int_0^{b_i} (Y_i^2 + v_i^2) dy_i \right]^2}{\sum_{i=1}^N b_i t_i \sum_{i=1}^N t_i \int_0^{b_i} (Y_i^2 + v_i^2)^2 dy_i} \tag{15.20}$$

where N is the number of strips, b_i and t_i are the width and thickness of the



15.6 Variation of applied stresses around a cross-section.

i th strip and Y_i and v_i are the in-plane and out-of-plane deformations in the i th strip obtained from the eigenvector. Similar types of expressions are obtained in the case of the semi-energy method, with additional terms in the denominator due to the periodically varying stresses.

It should be mentioned that in the presence of in-plane displacements v the above equation is obtained from a consideration of two consecutive half wavelengths, as there can be directionality in the postbuckling behaviour which cancels out over two half-wavelengths. Thus, strictly speaking, this equation does not tell the complete story for postbuckling behaviour if the buckling is not local buckling. However, local buckling is the primary concern with regard to subsequent interaction with other buckling modes. As will be discussed at a later stage, buckling modes that involve substantial in-plane displacement generally promote failure rapidly and the postbuckling strength is small.

15.4 Comparison of different strip formulations

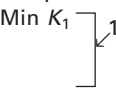
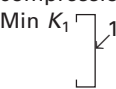
15.4.1 Local buckling

Some limited buckling analysis results are now shown for illustration of the prediction capacity of the different strip formulations. In terms of buckling

analysis, the linear strip by itself is incapable of predicting local buckling, and can be used only for evaluating overall buckling behaviour.

Table 15.1 shows some typical buckling results for simple plate and section cases. In all cases the nondimensional buckling coefficient, K is quoted. In the case of sections the buckling coefficient is related in terms of the plate element labelled '1'

Table 15.1 Buckling coefficients for plates and sections for different strip formulations

Member description	Cubic strips	Quintic strip	Septic strip
Square plate simply supported on all edges subjected to uniform compression	1 strip $K = 4.2583$ 2 strips $K = 4.0086$ 3 strips $K = 4.0017$ 4 strips $K = 4.0005$ 8 strips $K = 4.0000$	$K = 4.0007$	$K = 4.0000$
Plate fixed on unloaded edges and uniformly compressed, with buckle half wavelength varied to find minimum buckling coefficient	1 strip $K = \infty$ 2 strips $K = 7.226$ 4 strips $K = 6.991$ 8 strips $K = 6.972$ 16 strips $K = 6.971$	$K = 6.981$	$K = 6.971$
Plate with unloaded edges simply supported subject to in-plane bending with buckle half wavelength varied to find minimum buckling coefficients	1 strip $K = 27.386$ 2 strips $K = 25.444$ 4 strips $K = 23.964$ 8 strips $K = 23.886$ 16 strips $K = 23.881$	$K = 24.083$	$K = 23.891$
Plain channel $50 \times 100 \times 1$, uniformly compressed— Min K_1 	1 strip/element $K_1 = 2.93$ 2 strips/element $K_1 = 2.91$ 4 strips/element $K_1 = 2.91$	$K_1 = 2.91$	$K_1 = 2.91$
Lipped channel $20 \times 50 \times 100 \times 1$, uniform compression — Min K_1 	1 strip/element $K_1 = 7.08$ 2 strips/element $K_1 = 5.51$ 4 strips/element $K_1 = 5.44$ 8 strips/element $K_1 = 5.44$	$K_1 = 5.44$	$K_1 = 5.44$

For cubic strips, results for different numbers of strips per element are shown, while for quintic and septic strips a single strip per plate element is used in all cases. As it can be seen, both quintic and septic strips give extremely similar results, and these are in turn very similar to the results obtained for the largest number of cubic strips shown in each case. These results are, in fact, more or less exact for the problems examined, and the use of quintic or septic strips is likely to produce results within 1% of the exact answer for any problem of the type examined. For cubic strips, the accuracy of a single strip varies from case to case, but in general two strips per element are required to ensure accuracy better than 5%, and four strips per element to ensure accuracy better than 1%.

15.4.2 Postbuckling stiffness

Table 15.2 shows the initial reduction in postbuckling stiffness for simply supported plate elements of various buckle half wavelength to plate width ratios. The ratios examined cover the practical variation completely. The results of Cox (1945) are the same as those of a number of other investigators, and can be looked on as 'exact' values of the initial postbuckling stiffness.



Table 15.2 Initial postbuckling stiffnesses of simply supported plates

Buckle length a/b	Cubic E^*/E	Quintic E^*/E	Septic E^*/E	Cox (1945) E^*/E
0.8	0.333	0.375	0.376	0.376
0.9	0.333	0.390	0.392	0.392
1.0	0.333	0.407	0.409	0.408
1.1	0.333	0.425	0.427	0.426
1.2	0.333	0.442	0.444	0.443

From the table, it may be seen that the cubic strip employing the lower bound method, gives a reduction in axial stiffness to one-third of the prebuckling stiffness, independently of the buckle length. This is the result of using averaged values, and is actually the same as the result given by the other methods if the half wavelength is made very small. Both quintic and septic strips give very similar answers, very close to the exact values. The same high degree of accuracy results for any plate problems examined by the quintic or septic strips. In the case of the cubic strips using the lower bound method, of all the common plate problems, the simply supported plate gives probably the poorest correlation between the lower bound method and more rigorous methods.

For other boundary conditions, the disparity between lower bound and rigorous analysis is generally less than is found for the simply supported plate. To illustrate this, Table 15.3 shows the buckling coefficients and initial

Table 15.3 Comparison of buckling coefficients and initial postbuckling stiffnesses from cubic (lower bound) and quintic (lower bound (lb) and semi-energy) strips

Member description	One cubic strip	Two cubic strips	Four cubic strips	One quintic strip
Plate fixed–simply supported on unloaded edges	$K_{\min} = 6.990$ at $l/b = 0.69$ $E^*/E = 0.413$	$K_{\min} = 5.482$ at $l/b = 0.80$ $E^*/E = 0.413$	$K_{\min} = 5.415$ at $l/b = 0.80$ $E^*/E = 0.396$	$K_{\min} = 5.410$ at $l/b = 0.80$ $E^*/E = 0.450$ $E^*/E(lb) = 0.396$
Plate fixed–fixed on unloaded edges	$K_{\min} = \infty$	$K_{\min} = 7.226$ at $l/b = 0.69$ $E^*/E = 0.484$	$K_{\min} = 6.991$ at $l/b = 0.67$ $E^*/E = 0.443$	$K = 6.981$ at $l/b = 0.66$ $E^*/E = 0.489$ $E^*/E(lb) = 0.449$
Plate fixed–free on unloaded edges	$K_{\min} = 1.344$ at $l/b = 1.67$ $E^*/E = 0.575$	$K_{\min} = 1.285$ at $l/b = 1.63$ $E^*/E = 0.544$	$K_{\min} = 1.281$ at $l/b = 1.63$ $E^*/E = 0.543$	$K_{\min} = 1.281$ at $l/b = 1.65$ $E^*/E = 0.548$ $E^*/E(lb) = 0.543$
Plain channel 50 × 100 × 1, uniformly compressed – Min K_1 	$K_{1\min} = 2.934$ at $l/b_1 = 1.33$ $E^*/E = 0.571$	$K_{\min} = 2.911$ at $l/b_1 = 1.33$ $E^*/E = 0.556$	$K_{\min} = 2.910$ at $l/b_1 = 1.33$ $E^*/E = 0.556$	$K_1 = 2.910$ at $l/b_1 = 1.33$ $E^*/E = 0.564$ $E^*/E(lb) = 0.556$
Lipped channel 20 × 50 × 100 × 1, uniform compression – Min K_1 	$K_{1\min} = 7.079$ at $l/b_1 = 0.69$ $E^*/E = 0.632$	$K_{1\min} = 5.506$ at $l/b_1 = 0.79$ $E^*/E = 0.734$	$K_{1\min} = 5.444$ at $l/b_1 = 0.80$ $E^*/E = 0.728$	$K_1 = 5.44$ at $l/b_1 = 0.80$ $E^*/E = 0.751$ $E^*/E(lb) = 0.728$

postbuckling stiffness values for plates with different boundary conditions on the unloaded edges, and also for the plain and lipped channel sections of Table 15.1. In these cases quintic strips, one per plate, were used for both lower bound and semi-energy method analyses and the buckle half-wavelength to cause minimum buckling stresses was considered in each case. As may be seen, the difference between the initial postbuckling stiffnesses computed by the lower bound approach is in general within a few per cent of those computed using the more rigorous approach.

To illustrate the difference between cubic and quintic strips, and the lower bound and semi-energy method results graphically, Fig. 15.7 shows the variations in buckling stresses, axial tangent stiffnesses and flexural tangent stiffnesses for a hat section strut under compression. There are three distinct different buckling modes shown in this figure, and these three modes will be discussed at a later stage. The cubic strip results, using the lower bound method to evaluate the postbuckling stiffnesses, are shown as solid lines and the quintic strip results, using the semi-energy method, are shown as lines with circular markers. Four cubic strips per plate element were used, while one quintic strip was employed per plate element. As may be observed, only for very short half-wavelengths, dominated by local buckling, is there any significant difference in the postbuckling axial stiffness between the lower bound and the semi-energy methods. The septic strip approach results are not shown as they are indistinguishable from the quintic strip results.

In the examination of further cases only the cubic strip, with lower bound analysis, will be used.

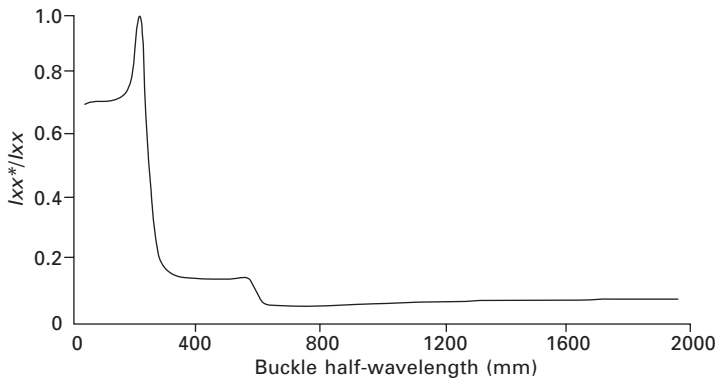
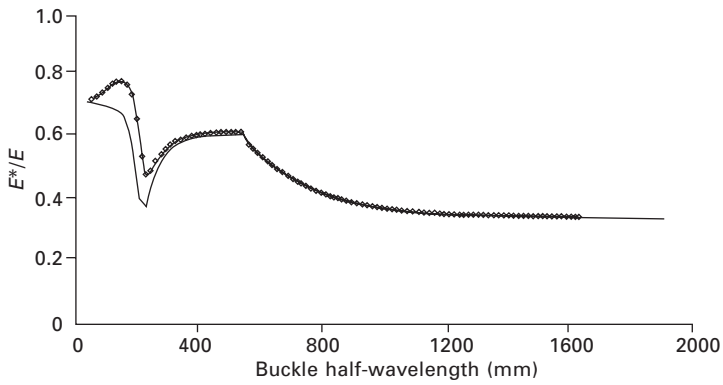
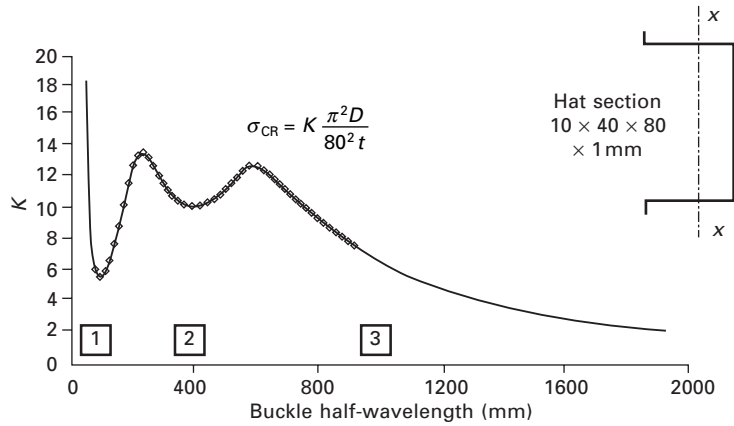
15.5 Compression members

15.5.1 Buckling stresses for lipped channel

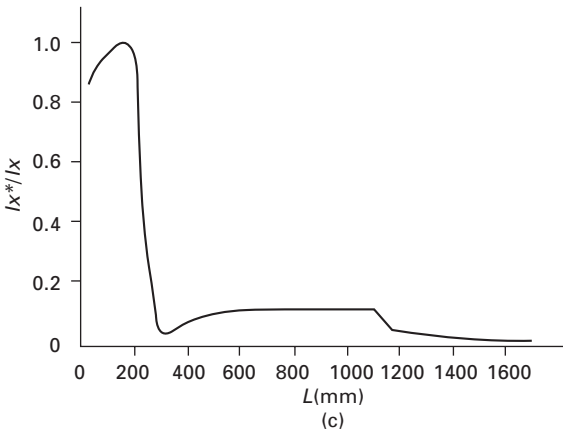
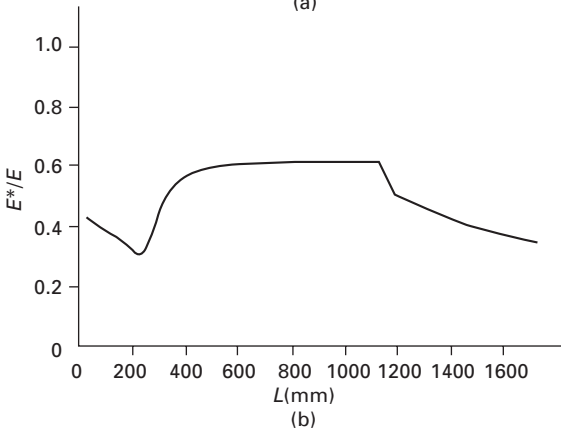
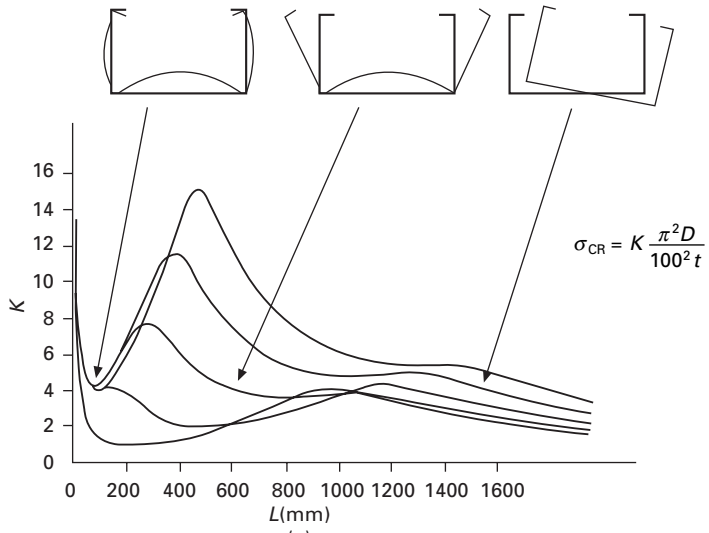
Figure 15.8 shows the variation of buckling coefficients with buckled half wavelength for lipped channel struts under pure compression. The channels are of dimensions 100 mm web, 100 mm flange and 2 mm thick. Five different lip widths are considered, 10 mm, 20 mm, 30 mm, 40 mm and a very small lip of 1 mm. The curves show substantial differences for each case, although they all have common features. With the exception of the curve for the section with the smallest lips all curves have three areas of importance, indicating three different buckling modes in each case.

For short buckled half wavelengths, the curves are similar with a minimum buckling coefficient of approximately 4 at a buckle half-wavelength of around 100 mm. The type of buckling that arises here is purely *local buckling* of the plate elements, with no movement of any of the corners.

As the half-wavelength increases, the different lip widths produce widely varying buckling behaviour with a minimum buckling coefficient approximately



15.7 Buckling stresses and post buckling behaviour of a hat section strut.



15.8 Buckling stresses and postbuckling stiffness of lipped channels.

2 for the smallest lip width and greater than 5 for the largest. This type of behaviour is now universally termed *distortional buckling* (see Hancock 1985) and has the buckled form shown in the figure. The width of the lips has very substantial effects on distortional buckling, as these must bend in-plane during this type of buckling.

For even longer half-wavelengths the buckling coefficients again reduce with increasing half-wavelength, but there is not such a great difference between the coefficients for different lip widths as for the distortional buckling case. For the longer wavelengths, the buckling mode combines lateral displacement with twisting, and is termed *torsional-flexural buckling*.

In the case of the section with 1mm lips, these lips are virtually negligible and the member behaves as a plain (unlipped) channel. In this case local buckling and distortional buckling are synonymous. This illustrates the reason why edge stiffeners such as lips are so important in light gauge members, as the lack of a lip of any consequence reduces the initial buckling coefficient from around 4 to less than 0.9 for the case considered,

It may be observed that flexural buckling about the horizontal neutral axis was not indicated on any of the curves. For this particular shape of section, flexural buckling would only occur if the member was extremely long. For open cross-sections, the low torsional rigidity often induces torsional-flexural buckling with regard to the symmetry axis before purely flexural buckling about the orthogonal axis, except in the cases of cross-sections in which the second moment of area about the symmetry axis is substantially greater than that about the orthogonal axis.

15.5.2 Postbuckling stiffness

The initial postbuckling axial stiffness variation with buckle half-wavelength is shown in Fig. 15.8b for the cross-section with 10 mm lips. This indicates that in the range where local buckling occurs, $L < 200$, the axial tangent stiffness is reduced by about 60% for this case, in the distortional buckling range the tangent stiffness is reduced by only 40%, while in the torsional-flexural buckling the axial stiffness reduces further as the half wavelength increases.

This suggests that there can be significant postbuckling reserves of strength for other modes of buckling than local buckling. However this is not the complete story. Figure 15.8(c) shows the variation in flexural stiffness about the $x-x$ (horizontal) axis immediately after buckling and, while in this case the immediate reduction due to local buckling is not very great, the reduction due to distortional and torsional-flexural buckling is extremely severe, with the flexural rigidity reducing by 90% or so in this case under distortional buckling and by even more under torsional-flexural buckling. In addition these longer half-wavelengths of buckling incur substantial in-plane bending

effects with consequent large increases in membrane stresses, and to all intents and purposes significant postbuckling capacity is unlikely to be found for these modes.

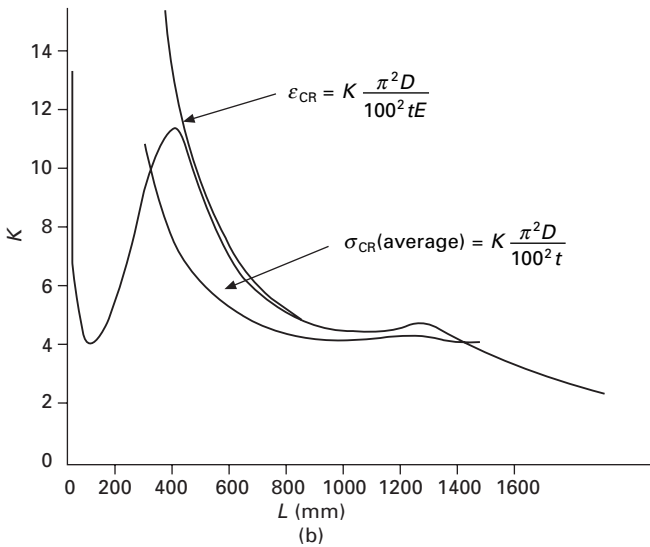
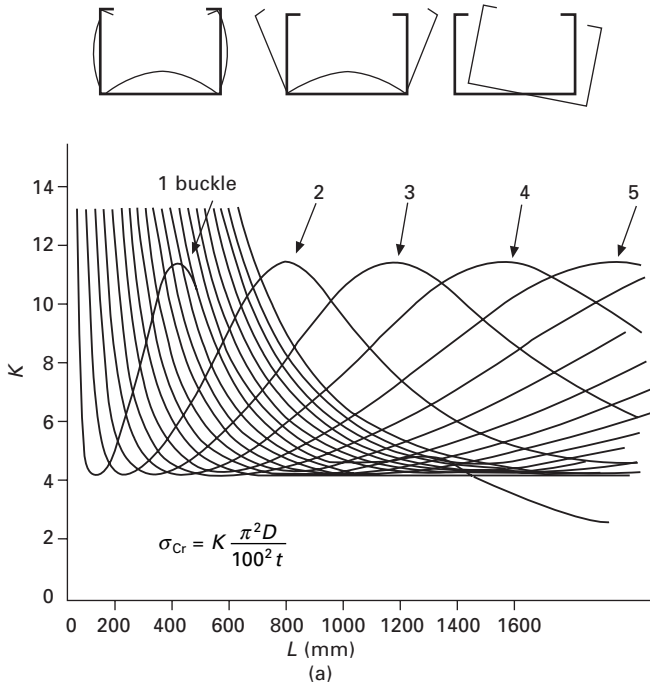
It should also be mentioned that the end conditions, assumed simply supported by the finite strip formulation used here, are extremely important in the cases of distortional and torsional-flexural buckling. It has been observed, e.g. Seah *et al.* (1991), that in the case of asymmetric stiffeners such as lips, the postbuckling behaviour is directional for distortional buckling. Although the buckling stress is unaffected by this, the postbuckling stiffnesses shown for this mode are not the minimum stiffnesses, but the average of the stiffnesses that would be obtained if two consecutive half-wavelengths were considered, as mentioned earlier. This further suggests that potential postbuckling capacity under nonlocal buckling may be disregarded.

15.5.3 Interaction of modes

For the members with 10 mm and 20 mm wide lips, the minimum distortional buckling stress is less than the minimum local buckling stress. In such a case if the member is of sufficient length, distortional buckling will occur at the stress indicated by the relevant curve. For members with larger lips, however, the same cannot be said. Local buckling is periodic, and for a long member under uniform load a number of buckle half-wavelengths occur along the length as shown in Fig. 15.9(a) for the member with 30 mm lips. Thus local buckling has occurred prior to distortional buckling. The buckling stresses were evaluated without taking the presence of local buckling, and its associated effects on the stress distribution and stiffness of the member, into account; and any buckling coefficient greater than the minimum local buckling coefficient is therefore invalid. The interaction of local buckling with the mode under investigation must be taken into account.

There are existing methods available for dealing with interaction of local buckling with other specific modes, such as Euler buckling (e.g. Rhodes and Harvey 1977). However, if the specific mode with which interaction will occur has not been established (local buckling may even have the effect of changing the next mode), then this mode must be approached with knowledge of how local buckling is progressing in the lead up to that mode.

The finite strip type approach used here has the capability of taking account of the interaction of the first buckling mode with any other mode corresponding to a higher half-wavelength. To do this, the first minimum is detected and the postbuckling characteristics are recorded. In the examination of higher wavelength buckling the stress system is incremented based on the postbuckling analysis of the first mode and the effects of displacements in the first mode on the axial and bending stiffnesses of each strip are taken into account when incrementing the stresses until buckling occurs in the higher mode.

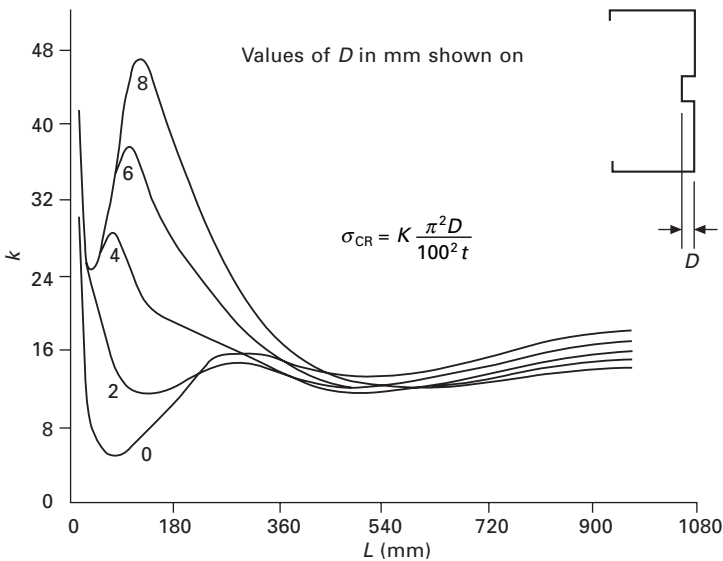


15.9 (a) Multiple buckle half-wavelengths; (b) interaction curves.

The buckling coefficients for the member with 30 mm wide lips obtained by this method are shown in Fig. 15.9(b). The two additional lines indicate the higher-mode buckling coefficients obtained using the postlocal buckling analysis, the upper line representing the strains and the lower line representing the average stresses. In this case the curve representing the strain coefficients is quite close to the original curve, which did not incorporate local buckling effects, while the curve representing the average stresses lies significantly below the original curve, indicating the degree to which the higher mode buckling is reduced by the local buckling effects.

15.5.4 Intermediately stiffened members

To prevent, or postpone, local buckling, intermediate stiffeners are often used in light gauge steel members. As in the case of lips or edge stiffeners these delay local buckling but suffer, albeit at higher loads, from distortional buckling. This is illustrated in the case of a 1 mm thick lipped channel section with a web 100 mm wide, flanges 50 mm wide and lips 15 mm wide incorporating a 10 mm wide stiffener at mid-flange. Figure 15.10 shows the variation in buckling stresses for this member with variation in half wavelength for five different stiffener depths: 0, 2 mm, 4 mm, 6 mm and 8 mm.



15.10 Buckling stresses for lipped channel with intermediately stiffened web.

As it can be observed, the minimum local buckling coefficient for the member with no stiffener is just over 5.5. The introduction of a small stiffener,

2 mm deep more than doubles the local buckling stress, while intermediate stiffeners of depth 4 mm and greater raise the local buckling coefficient to about 25, at which point the flat element between stiffener and the web edge buckles. However, regardless of the stiffener depth there is not a great deal of difference between the distortional buckling resistance and for any member of about 500 mm length or greater distortional buckling occurs at a similar stress, buckling coefficient just over 12, as the distortional buckling is driven by the flange. Indeed the nonstiffened member shows slightly greater distortional buckling resistance than the intermediately stiffened members, according to the figure, although this would be decreased because of the early local buckling and subsequent interaction.

15.6 Buckling in beams

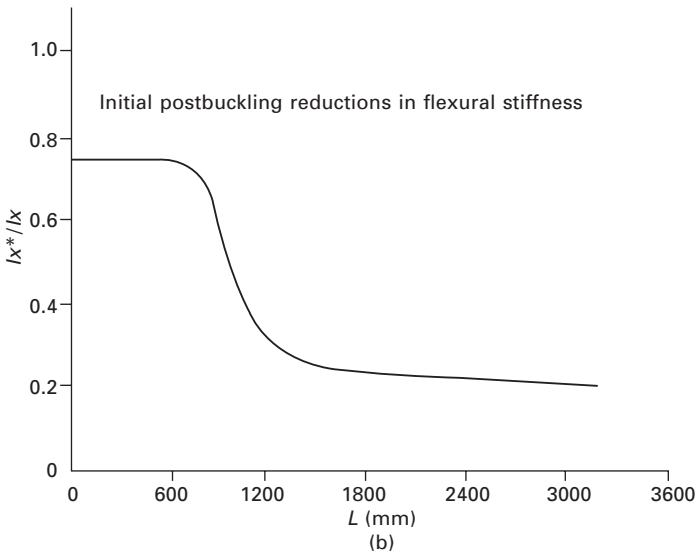
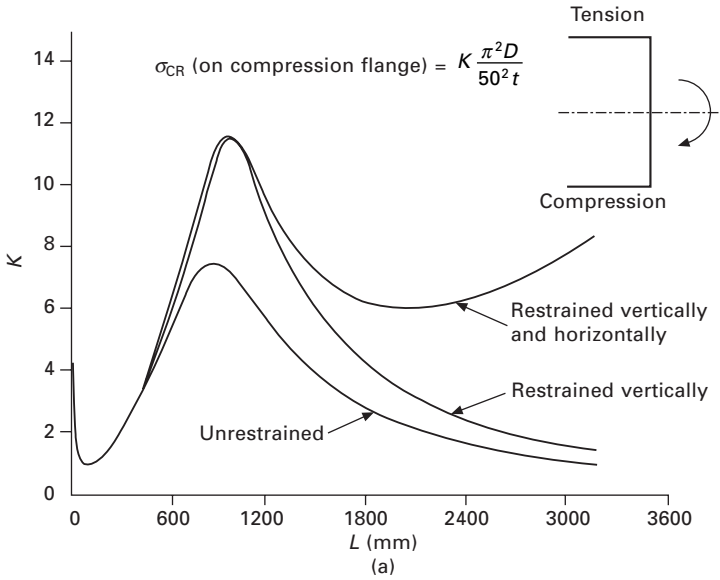
15.6.1 Plane channel beam

Beams probably make up the bulk of light gauge steel members. In most cases, such as roof purlins and floor beams, light gauge steel beams are constrained at their loading points by cladding, flooring, etc. and the effects of the constraining media should be taken into account in design.

Figure 15.11 shows the behaviour of a 1 mm thick plane channel beam with 50 mm wide flanges and 100 mm deep web under bending about its symmetry axis. Three buckling curves are shown here: (1) in which the beam is unrestrained, (2) in which the tension flange is restrained rotationally and vertically at its central point and (3) in which the tension flange is restrained rotationally, vertically and horizontally at its central point.

The first mode of buckling is local buckling. It occurs at the same maximum bending stress for all three cases, which would be expected. The onset of the second mode for the beams with restrained flanges occurs at a significantly higher stress than for the unrestrained beam. As the wavelength increases, the curve for the beam with restraint only on vertical movement and rotation of the tension flange centre point during buckling decreases much more than that for the beam whose tension flange is also restrained horizontally and that reaches a minimum and increases further as the half-wavelength increases.

This second mode is *lateral-torsional* buckling, which is akin to torsional-flexural buckling in columns. This type of buckling was often termed lateral buckling in the past, see for example Allen and Bulson (1980), when the lateral movement was the more significant of the buckling displacements for beams such as hot-rolled I-sections in which the main cause of this phenomenon was the large difference in bending rigidity of such a beam about its major and minor axes. In the case of light gauge beams, the torsional aspect is often the dominant factor in this behaviour and indeed, as we shall see, beams bent about their minor principal axis can also be subject to lateral-torsional buckling.

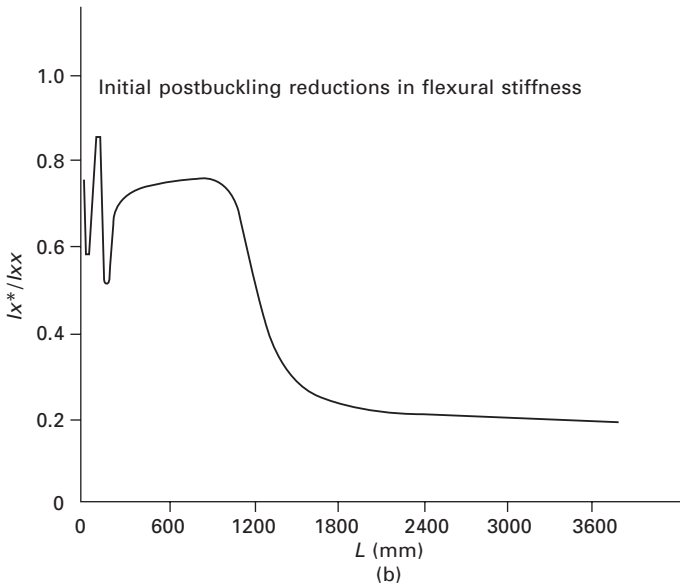
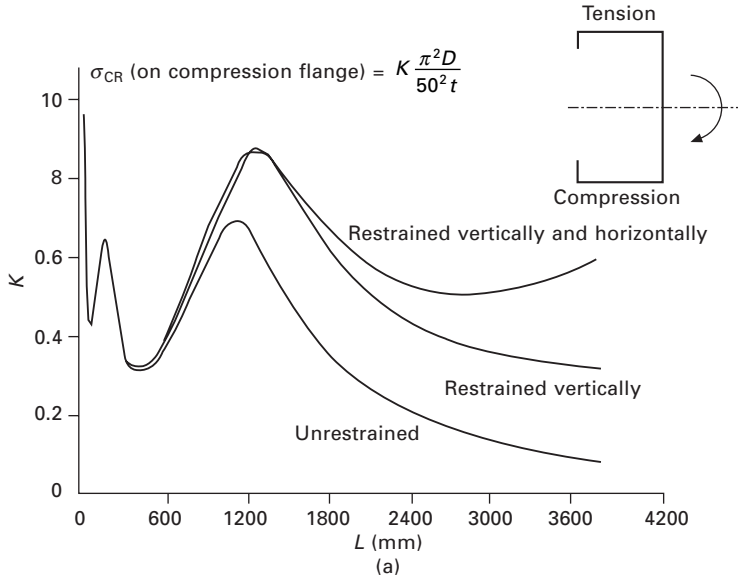


15.11 Buckling stresses for plain channel beam.

Figure 15.11(b) shows the variation of the postbuckling flexural stiffness with variation in half-wavelength for the unrestrained beam. This figure indicates that under local buckling there is only about 25% reduction in flexural rigidity, but lateral torsional buckling induces a substantially greater loss in flexural stiffness.

15.6.2 Lipped channel beam

Figure 15.12(a) shows the variation in maximum stress at buckling with variation in half-wavelength for a 1 mm thick lipped channel beam with a web 120 mm deep, flanges 50 mm wide and 10 mm wide lips. Here there are

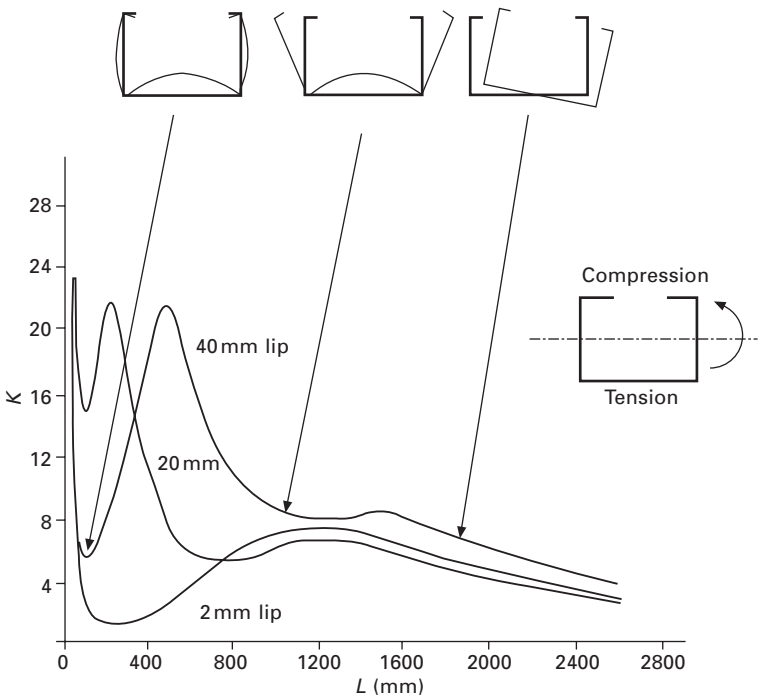


15.12 Buckling stresses for lipped channel beam.

three buckling modes, local buckling, distortional buckling involving the compression flange and compression lip, and lateral-torsional buckling. For the lip geometry examined here the minimum stress for distortional buckling is substantially less than for local buckling. As in the case of the plane channel section beam, the same three different degrees of restraint are afforded to the tension flange, and similar results are attained for the effects of these restraints. Figure 15.12(b) shows the postbuckling reduction in flexural stiffness for the most highly restrained case, with similar results to the plain channel case.

15.6.3 Lipped channel beam bent about an axis perpendicular to the symmetry axis

Here the lipped channel member examined as a strut in the first example is considered in bending about a horizontal axis. If the bending direction was such that the web was in compression, then the only buckling mode that would be observed is local buckling. However, if bending is such that the lips are in compression, more interesting features are observed, as may be seen in Fig. 15.13.



15.13 Lipped channel bent about minor axis to cause lip compression.

In this case three different lip widths are illustrated: 2 mm, 20 mm and 40 mm. From the figure, it may be observed that for the wider lips three modes are seen, with only two for the very small lips. It may also be observed that the local buckling stress for the member with 20 mm lips is substantially greater than that for the member with 40 mm lips. This is because local buckling occurs mainly in the lips, and narrower lips resist buckling much more strongly than wide lips. The narrow lips offer, however, much lower resistance to in-plane bending than the wide lips, so that the second mode, distortional buckling, for the member with narrow lips occurs at a substantially lower stress than for the member with wide lips. Local buckling and distortional buckling are synonymous for the member with very small lips.

As the half-wavelength increases, the torsional-flexural buckling load occurs in all three cases. It is worth noting that the second moment of area of the cross-section about the x axis is less than that about the y axis for all three cases, and is indeed not much more than half of that about the y axis for the member with the smallest lips.

15.7 Future trends in analysis and design

15.7.1 Current design specifications

Design specifications at the present time deal with local buckling and its effects on beams and compression members using the effective width approach, with most specifications using a slightly modified version of the effective width equation originally produced by Winter (1947), i.e.

$$\frac{b_e}{b} = \sqrt{\frac{\sigma_{CR}}{\sigma}} \left(1 - 0.2 \sqrt{\frac{\sigma_{CR}}{\sigma}} \right) \quad 15.21$$

where the effective width of each individual element is determined to obtain an effective cross-section. The critical stress that causes local buckling in a plate element depends on the member geometry and varies from section to section. The British Standard, BS 5950: Part 5 gives graphs and formulae covering elements in a number of common structural members. For elements in other cross-sections, either rigorous analysis can be used to determine the critical stress or, as in the majority of design codes, specific values of the buckling coefficient are given for elements with different boundary or loading conditions.

In determining the compressive strength of a member in the absence of any other type of buckling the general approach is to obtain the effective widths for each element in turn, with σ set equal to the material yield stress. In recent design codes, e.g. Eurocode 3: Part 1.3, the use of the effective width expression and related buckling coefficients has been extended to deal with a variety of other situations, for example members with elements subjected to stress gradients.

Many specifications also require determination of the effective widths and effective width locations for elements subjected to varying stresses, and this, compounded by the use of multiple stiffeners and complex cross-sections, has led to the situation that a great deal of labour can be expended in evaluation of the effective cross-section.

In the design of columns and beams some specifications, e.g. Eurocode 3, provide buckling formulae for modes such as Euler buckling, lateral-torsional buckling, torsional-flexural buckling, distortional buckling based on the full cross-section. The designer then uses these together with the effective cross-section approach to evaluate the member capacity. For some situations, for example in determination of the distortional buckling capacity, iterative approaches are suggested. This adds to the labour involved and although the effective width approach models the actual situation well, it is often thought to be cumbersome.

15.7.2 Direct strength method

This has led to alternative approaches being suggested, such as the direct strength method, originally proposed by Schafer and Pekoz (1998). This approach is based on the concept that the evaluation of the initial buckling load for any cross-section, however complex, can be accomplished easily by numerical means such as the finite strip method. Having obtained this, the section capacity can then be directly related to the buckling load by simple formulae, and the time and labour involved in carrying out subsequent effective width calculations for multiple plate elements can be avoided. This approach, which requires substantial testing for validation, has been growing in popularity in the USA and, more recently, in Australia. This type of approach was applied in the early years of thin-walled structural analysis in which simple cross sections, such as angles, cruciforms, H and C sections were tested and the ultimate load empirically related to the critical load using simple power laws based on the test results. However, the fact that different laws are required for different cross-sections does produce simple estimates of the load capacity of such members, but, as could be expected, the power laws were different for each particular section. The method does not really take adequate account of the differences caused by cross-sectional geometry on postbuckling behaviour, and at best will produce results with a nonspecific degree of approximation which can only be determined on the basis of tests. In any case, just as it is relatively easy nowadays to determine buckling loads using numerical methods, there are a number of programs available to extend the analysis into the postbuckling range, i.e. to go the whole way by computer rather than stop after the first hurdle.

This would seem to be the best approach, and finite strip analysis such as that shown here is ideally suited for such a purpose. In addition to the finite

strip approach, there are other numerical or seminumerical methods that can be used to perform complete analysis of light gauge members through the postbuckling range.

15.7.3 Finite element method

The finite element method, in which a structure is discretised into a large number of small elements, has grown dramatically in popularity and in simplicity of use over the last 40 years largely because of the production of user-friendly computer packages. This trend does not show any sign of abating. All large manufacturing companies, and many smaller companies, now own and operate finite element packages. It is likely that in the not too distant future finite element packages will take over the design analysis of structures just as today computer packages are widely used for structural layout.

At the present time, for day-to-day design analysis, general finite element packages may be viewed to some extent as sledgehammers, too big to crack nuts with, and there are more specifically orientated numerical approaches used by researchers in this field, such as the finite strip method, that are particularly suited to the analysis of light gauge steel structural members.

15.7.4 Generalised beam theory

Generalised beam theory provides an alternative to finite strip analysis, and so it should be mentioned here. This approach was introduced in Germany by Schardt and the early publications were in German, with the first paper in English, to the writer's knowledge, being produced in 1983. Space requirements prevent any detailed discussion of this approach, and it perhaps suffices to say that it is similar in applicability, although different in background, to the finite strip method. A recent review of this method is given by Camotim *et al.* (2004).

15.8 Concluding remarks

In this chapter, the analysis of light gauge steel beams and columns using a finite strip type approach has been presented. The different buckling modes have been described and the postbuckling behaviour has been examined. It has been observed that three essentially similar modes of buckling occur in beams and columns, i.e. local buckling, distortional buckling and torsional-flexural or lateral-torsional buckling.

The general methods used in design codes have been very briefly described and the trends in design analysis have been briefly discussed. The complexity of design with regard to cold-formed steel members and structures has continually increased as their use has grown. With trends towards more

slender members, of higher-yield strengths, the complexity will continue to grow. Modern design specifications have taken substantial steps in providing analysis methods. The 'simplified' design rules are becoming increasingly complex, and can nowadays involve greater labour than rigorous analysis using numerical methods.

There are situations in which design codes permit numerical analysis. Indeed the FEM code for storage racking requires a first level second order analysis for racking design. The time has perhaps come when design specifications should incorporate numerical analysis software, or give an approved list of software for use in design to the code.

15.9 References

- Allen, H.G. and Bulson, P.S. (1980), *Background to Buckling*. McGraw-Hill, New York.
- American Iron and Steel Institute (1946), *Specification for the design of light gage steel structural members* (latest Edition 1996), AISI, Washington, DC.
- British Standards Institution (1961), *Addendum No. 1 to BS 449. Specification for the Use of Cold Formed Steel Sections in Buildings*, BSI, London.
- British Standards Institution (1987), BS 5950: Part 5. *Code of Practice for the Design of Cold Formed Sections, 1987*. (Latest Edition 1998), BSI, London.
- Bryan, G.H. (1891), On the stability of a plane plate under thrusts in its own plane with applications to the 'Buckling' of the sides of a ship. *Proc. London. Math. Soc.* **22**, 54.
- Bulson, P.S. (1970), *The Stability of Flat Plates*, Chatto and Windus, London.
- Camotim, D., Silvestre, N., Goncalves, R. and Borges Dinis, P. (2004), GBT analysis of thin-walled members: new formulations and applications, in Loughlan, J. (ed.) *Thin-walled Structures: Recent Advances and Future Trends in Thin-walled Structures Technology*. Canopus Publishing, Bath.
- CEN ENV 1993-1.3 (1996a), *Eurocode3: Design of Steel Structures – Part 1.3: General Rules – supplementary rules for cold-formed thin gauge members and sheeting*.
- CEN ENV 1993-1.4 (1996a), *Eurocode3: Design of Steel Structures – Part 1.4: General Rules – supplementary rules for stainless steel*.
- Cheung, Y.K. (1968), The finite strip method in the analysis of elastic plates with two opposite simply supported ends, *Proc. Inst. C. Eng.*, **40**, 1–7.
- Cox, H.L. (1945), *The Buckling of Plates and Shells*. Pergamon, London.
- ECCS (1987), *European Recommendations for the Design of Light Gauge Steel Members*, European Convention for Constructional Steelwork, Brussels.
- Federation Européenne de la Manutention (2000), *Section X, Recommendations for the design of pallet racking and shelving*.
- Hancock, G.J (1985), Distortional buckling of steel storage rack columns. *ASCE J Struct. Eng.* **111**,1, 2770–2783.
- Khong, P.W (1988), Development of a microcomputer finite strip analysis for thin-walled structures. Ph.D. thesis, University of Strathclyde.
- Marguerre, K. (1937), The apparent width of the plate in compression, *NACA TA No. 833*, Washington.
- Rhodes, J. (1987), A simple microcomputer finite strip analysis. *Dynamics of Structures*, ed. J.M. Roesset, American Society of Civil Engineers, Reston, VA.
- Rhodes, J. and Harvey, J.M. (1977), Interaction behaviour of plain channel columns

under concentric or eccentric loading. *2nd Int. Colloquium on the Stability of Steel Structures*, Liege.

- Rhodes J. and Khong, P.W. (1988), Linear and non-linear analysis on the micro using finite strips, *Proc. Stress Analysis and the Micro*, Brunel University, London.
- Schafer, B.W. and Pekoz, T. (1998), Direct strength prediction of cold-formed steel members using numerical elastic buckling solutions. *Proc. 14th Int. Spec. Conf. on Cold-formed Steel Structures*. St. Louis.
- Seah, L.K., Rhodes, J. and Lim, B.S. (1991), Collapse behaviour of edge stiffened thin-walled sections. *Proc ICSAS91*, Singapore, Elsevier Science Publishers,
- Shearer Smith, W. (1951), Cold formed sections in structural practice with a proposed design specification. *The Structural Engineer*, **XXIX**, 165–178.
- Stein, M. (1959), The phenomenon of change in buckle pattern in elastic structures. NASA Tech. Rep. No. R-39.
- Timoshenko, S.P. and Gere, J.M. (1961), *Theory of Elastic Stability*. McGraw-Hill, New York.
- Von Karman, T. (1910), *Encyklopadie der mathematischen wissenschaften*, Vol. 4 , 349.
- Von Karman, T., Sechler, E.E. and Donnel, L.H. (1932), Strength of thin plates in compression, *Trans. ASME, Journal of Applied Mechanics*, **54**, 53–57.
- Winter, G. (1947), *Strength of Thin Steel Compression Flanges*, Cornell Univ. Eng. Exp. Stn, Reprint No. 32.
- Wittrick, W.H. (1968), ‘A unified approach to the initial buckling of stiffened panels in compression’, *Aero. Quarterly*, **19** (1968), 256–83.
- Yu, W.W. (2000), *Cold-formed Steel Design*. 3rd Edition. Wiley, New York.

-
- AASHTO specifications for girders 401, 402, 405
- adaptive materials 173
- aeronautical structures 170, 236–37
- aluminium-alumina 162, 163–5, 166, 167
- aluminium-zirconia 162, 163, 164
- angle-ply laminated plates 184–8
- annular plates 133–8
- anti-node lines (buckle crests) 242, 243
- antisymmetric angle-ply laminated plates 184–8
- arc-length methods 250–3, 256
- AS4100 307
- tapered beams 21–2, 23, 24
- aspect ratios 123–124, 126, 160–1
- associated flow theory 361
- asymptotic solutions 178–84
- automated hybrid quasi-static/pseudo-transient method 256–8
- axial compression
- concrete-filled steel box columns 325, 326, 327
- cylindrical structures 433–5
- work done by axial forces 10–12, 13–14
- axial load-shortening curves 321–22, 323
- axial restraints 435–6
- axial stiffness reduction for light gauge steel members 465–6, 468–70, 471
- under compression 472, 473–4
- axial strength capacity 312–3
- axisymmetric buckling 129–33
- balance points 387–8
- beam parameter K 14–15, 18, 22
- beams
- composite steel-concrete 217, 218
- interaction buckling 228–31
- local buckling 222–24
- light gauge steel members 477–81
- lipped channel beam 479–80
- lipped channel beam bent about an axis perpendicular to symmetry axis 480–81
- plane channel beam 477–8
- bend-buckling 413
- bending
- combined compression and bending in stub-columns
- box-shaped 280–5
- pipe-shaped 289–91
- curved web plate stability and distortion combined with shear 413–4
- longitudinal stiffeners 411–2
- pure bending 407–411
- lipped channel beam bent about an axis perpendicular to the symmetry axis 480–1
- bents 389
- Bessel functions 131
- β parameter 226, 227
- biaxial compression 154, 158
- bifurcation 216
- bifurcation criterion 131, 132
- bifurcation points 249–50, 251, 257
- bilinear thick plate element 57, 67–9
- elastic and geometric stiffness matrices 63–7
- geometry and displacement field 63–5
- implementation 66–7
- plate assumptions 63
- stress-strain relationship 65
- performance compared with other plate elements 68–9
- blade-stiffened panels 244–6
- arc-length method 251–2, 253
- pseudo-transient method 255–6
- Bleich's theory of plasticity 118

- box columns *see* cantilever columns;
 - concrete-filled steel box columns;
 - stub-columns
- box girders 383
- bridge piers 294–5
- bridges
 - corrugated web plates in bridge structures *see* corrugated web plates
 - curved girders 382–4
 - see also* curved plate girders
 - shear buckling strength of corrugated steel webs 368–69
- BS5950 18–21, 23, 24
- buckle crests (anti-node lines) 242, 243
- buckling coefficients 307
 - light gauge steel members 470–3, 475, 476
 - finite strip method 467–70
 - mesh-free methods for stiffened and corrugated plates 101–8
 - for shear-buckling stress 276
- buckling displacements vector 8–10
- buckling eigenproblem 14
- buckling load factor 11, 14, 63
 - rectangular plates 36–44, 45, 46, 47, 48, 50, 51, 52, 53
- buckling point 455
- buckling shapes 40–3, 46–7, 49, 50, 51, 52, 53
- buckling stability matrix 14
- buckling stress 97, 108–109
 - exact relationship between plastic buckling stress and elastic buckling stress 138–41
 - flange plates of curved I-girders 402
 - light gauge steel members 455–6
- buckling stress factors
 - annular plates 136–8
 - circular plates 132–3, 134
 - polygonal plates 138, 141, 142, 143
 - rectangular plates 123–5, 126, 128–9, 130, 131
- camber loss 386
- cantilever columns 294–302
 - made of pipe sections 300–2
 - with longitudinal stiffeners 299–300
 - without longitudinal stiffeners 297–8
- carbon-fibre composites, stiffened *see* stiffened composite structures
- centreline stiffened plates 396–9, 400
- ceramic-metal plates 147–69
 - additional parametric studies 161–5
 - mechanical buckling 161–3
 - thermal buckling 163–5, 166, 167
- comparisons with other formulations 157–61
- displacement finite element model 148–57
- thermal postbuckling of FGM hybrid laminated plates 193–99
- numerical results 157–65
- circular plates 129–33
 - basic equations 129–30
 - buckling solutions 130–3, 134
 - clamped 131
 - simply supported 132–3
- classical thin plate theory (CPT) *see* Kirchhoff plate theory
- codified rules *see* design codes
- cold bending 386
- cold-formed steel members 451–2
 - see also* light gauge steel members
- collapse 436–7
- column curves 231–2
 - concrete-filled steel box columns 327, 328, 329–30, 331, 332, 334–5
- column slenderness 326, 330–1
- column strength analysis 315–17
- column wall slenderness (plate slenderness)
 - see* width-to-thickness ratio
- columns, composite steel-concrete 217–18
 - interaction buckling 231–2
 - local buckling 225–8, 229, 230
- combined hardening 362–3
- compact-flange sections 400
 - section limit 406–7
- compact sections 318–19, 395, 399–400
 - section limit 399, 401, 404–6
- compactness of flanges with stress gradient 399–407
- compatibility equation 458–9
- completeness order basis function 99–100, 101, 102
- composite modulus 151
- composite steel-concrete members 214–35
 - background to buckling 219–22
 - global buckling 214–16, 221, 231
 - interaction buckling 214–16, 221–22
 - local buckling 214–16, 219–20
- box columns *see* concrete-filled steel box columns
- forms of 217–18
 - beams 217, 218
 - columns 217–18
- interaction buckling 228–32
 - beams 228–31

- columns 231–2
- local buckling 222–8
 - beams 222–4
 - columns 225–8, 229, 230
- compression
 - axial *see* axial compression
 - biaxial 154, 158
 - combined compression and bending in
 - box-shaped stub-columns 280–5
 - laminated plates 172–3
 - light gauge steel members under 470–7
 - mesh-free methods 100–12
 - pipe-shaped stub-columns 285–91
 - combined compression and bending 289–91
 - pure compression 287–9
 - plates in 269–75
 - uniaxial 154, 158–60, 162–3, 164
- compressive strength
 - of concrete 326, 332–3
 - concrete-filled steel box columns 312–13
- concrete
 - compressive strength of 326, 332–3
 - stress-strain relationship 308, 309
- concrete-filled steel box columns 218, 230, 305–39
 - local buckling 225, 226, 227, 229, 306–7, 309–312
 - numerical results 318–23
 - axial load-shortening curves 321–2, 323
 - compact steel sections 318–19
 - Eurocode 4 322–3, 324
 - thin-walled steel sections 319–20
 - parametric studies 323–35
 - axial load 325, 326, 327
 - column end restraints 334–5
 - column slenderness 326, 330–1
 - column tube wall slenderness 326, 331–2
 - compressive strength of concrete 326, 332–3
 - initial out-of-straightness 326, 327–9
 - load eccentricity 325–7, 328
 - residual stresses 326, 329–30
 - yield strength of steel tube 326, 333–4
- theoretical analysis 308–18
 - assumptions 308–9
 - axial strength capacity 312–13
 - column strength analysis 315–17
 - convergence criteria 317–18
 - cross-section analysis 313–15
 - local buckling 309–12
 - residual stresses 310, 312
 - conforming plate element 57
 - connections/joints 452
 - construction, stability during 384–9
 - continuous heating 385
 - control voltage 192–3, 194, 198–9
 - convergence criteria 317–18
 - corrugated plates 81–3, 112–13
 - estimation of equivalent properties 85–9
 - mesh-free model formulation 89–98
 - see also* sinusoidally corrugated plates; trapezoidally corrugated plates
 - corrugated silos 441, 442, 443
 - corrugated web plates 340–81
 - elastic buckling 340–56
 - effect of rotational restraint 355–6
 - elastic buckling analysis 352
 - elastically supported orthotropic Mindlin plates 351–2
 - equivalent elastic constants for orthotropic plate 348–51
 - numerical results 352–5
 - orthotropic rectangular Mindlin plate 342–6
 - Ritz method 346–8
 - elasto-plastic and finite displacement analysis *see* elasto-plastic and finite displacement analysis
 - shear buckling strength 367–9
 - CPU time 257
 - cracks 237, 243, 259–64
 - extension modes 259
 - interface elements 262–4
 - virtual crack closure technique 259–62
 - critical buckling stress *see* buckling stress
 - critical cross-section 21–2, 22–3
 - critical energy release rate 263
 - critical load (buckling load)
 - ceramic-metal plates 153, 154, 158–60, 162–3, 164
 - composite columns 221
 - influence of curvature
 - flange plate stability 396–8, 400
 - lateral-torsional stability 391–4
 - mesh-free methods for stiffened and corrugated plates 97, 99–100, 101, 102, 109–12, 113
 - Ritz method 346–8
 - stiffened composite structures 247
 - tapered beam 15–18, 19, 20, 21
 - critical load factor *see* buckling load factor
 - critical moment
 - curved girder 391
 - tapered beam 15, 16–17, 23

- critical pressure 426
- critical stress *see* buckling stress
- critical temperature
 - ceramic-metal plates 155, 160–1, 163–5, 166, 167
 - laminated plates
 - FGM hybrid laminated plates 196–8
 - with piezoelectric actuators 192, 193
- cross-frames 388–9
- cross-frame interval design 389–90
- cross-ply laminated plates 158–60
 - thermal postbuckling of symmetric plates 188–90
 - plates with piezoelectric layers 191–3
- cross-section analysis 313–15
- cross-section classification 399–407
- cubic strips 463–4, 467–70
 - see also* finite strip method
- CURT project 384
- curvature 13
 - see also* curved plate girders
- curvature terms 26–7, 36–40, 41–2, 46, 47, 48
- curved plate girders 382–421
 - cross-frame interval design 389–90
 - design perspective and historical review 383–4
 - effect of curvature on flange plate stability 395–407
 - centreline stiffened plates with stress gradient 396–9, 400
 - definition of compactness for flanges with stress gradient 399–407
 - effect of curvature on web plate stability and distortion 407–14
 - influence of curvature on lateral-torsional stability 390–5
 - buckling of girders with intermediate lateral supports 394–5
 - single girders with end-support conditions 391–4
 - origins of curved beam theory 383
 - stability during construction 384–9
 - erecting 387–9
 - fabricating 385–6
 - transporting 386–7
- curved plates *see* cylindrical structures
- cut curving 385, 386
- cyclic loading 271
- cylindrical structures 422–50
 - axial compression 433–5
 - differential settlement 441–8, 449
 - experimental behaviour 435–40
 - internal pressure 423–5
 - nonuniform external pressure 427–33, 434
 - prototype failures 440–1, 442, 443
 - uniform external pressure 425–7
- damping 253, 254, 255
- deformation theory of plasticity 117–18, 361
 - annular plates 136, 137, 138
 - circular plates 132–3, 134
 - polygonal plates 139–41, 142, 143
 - rectangular plates 120–2, 123–4, 125, 126, 129, 130, 131
- degrees of freedom
 - displacement finite element model 156–7
 - nonlinear finite element 4
- delamination modelling 258–64
 - interface elements 262–4
 - virtual crack closure technique 259–62
- 'design by buckling analysis' method 22–3
- design codes
 - composite steel-concrete columns 231–2
 - concrete-filled steel box columns 305, 308
 - curved plate girders 383–4, 395, 401–2, 404, 405, 407, 412
 - light gauge steel members 451–2, 481–2, 484
 - tapered steel members 18–22, 23, 24
- design strengths 18–23
- diamond-shaped buckles 433–5
- differential settlement 441–8, 449
- dimensionless critical load
 - ceramic-metal plates 158–60
 - elastic critical load for tapered steel members 15–18, 19, 20, 21, 22
- dimensionless critical moment 15, 16–17
- dimples 448
- direct strength method 482–3
- 'discrete Kirchhoff hypothesis' 56
- displacement control 249
- displacement finite element model 148–57
 - additional parametric studies 161–5, 166, 167
 - comparisons with other formulations 157–61
 - finite element interpretation 156–7
 - functionally-graded plates 151–3
 - mechanical and thermal buckling 154–6
 - stability analysis 153–4
- displacement vector 64–5
- displacements
 - approximation for stiffened and corrugated plates 89–90

- relationship between strains and 357–8
- distortional buckling 470–6
 - interaction with other modes 474–6
 - lipped channel beams 479–81
 - postbuckling stiffness 472, 473–4
- Donnell stability equations 422, 425–6
- ductility 269–304
 - cantilever columns
 - made of pipe sections 301–2
 - with longitudinal stiffeners 299–300
 - without longitudinal stiffeners 298
 - plates
 - in compression 274–5
 - in shear 279–80
 - stub-columns
 - box-shaped subjected to combined compression and bending 282–5
 - box-shaped subjected to shear 293–4
 - pipe-shaped subjected to combined compression and bending 290–1
 - pipe-shaped subjected to pure compression 288–9
- dynamic methods for stiffened composite structures 253–6
 - combined quasi-static/pseudo-transient method 256–8
- earthquakes 269, 295
- Easley's formula 353–4
- eccentricity
 - cylindrical structures 435
 - load eccentricity *see* load eccentricity
- eccentricity ratio 326, 327
- effective shear modulus 350
- effective width
 - composite columns 226, 229, 230
 - concrete-filled steel box columns 309–12
 - light gauge steel members 456–7
 - design specifications 481–2
- eigenmode injection 256–7
- eigenvalue analysis, linear 246–8
- elastic buckling curves 14–18, 19, 20, 21, 22
 - 'design by buckling analysis' 22–3
- elastic buckling moment 23
- elastic buckling stress, relationship to plastic buckling stress 138–41
- elastic constitutive matrix 343
- elastic critical moment 21, 23
- elastic critical wavelength 287
- elastic local buckling 215–16, 221–2
- elastic modulus
 - rectangular plates 121–2
 - reduced *see* reduced elastic modulus
 - thermal postbuckling of FGM hybrid laminated plates 193–5, 196
- elastic region 367–9, 399–401
- elastic stiffness 62–3
 - derivation of elastic stiffness matrix for bilinear plate element 63–7
- elastic unloading 321
- elasticity tensor 62, 65
- elasto-plastic and finite displacement analysis 356–78
 - constitutive law 360–4
 - deformation of plate 357–8
 - element stiffness matrix 358–60, 366–7
 - experimental study 372–8
 - webs with concrete flanges 375–8
 - webs without concrete flanges 372–5
 - parametric study 367–72
 - transformation matrix 364–7
- elasto-plastic material matrix 363–4
- electric loads 191–9
 - thermal postbuckling of FGM hybrid laminated plates 193–9
 - thermal postbuckling of symmetric cross-ply laminated plates with piezoelectric layers 191–3
- element stiffness matrix 358–60, 366–7
- ellipsoid of revolution 423
- equivalent elastic properties
 - corrugated plates 82–3, 85–9
 - sinusoidally corrugated plates 88–9
 - trapezoidally corrugated plates 86–8
 - orthotropic Mindlin plate 348–51
- equivalent single layer theory 148
- equivalent slenderness 18–21
- erection of curved girders 387–9
- Euler elastic buckling expression 402
- Eurocode 4 (EC 4) 322–3, 324
- explicit dynamic analysis 254, 263
- external pressure
 - experimental behaviour of cylindrical structures 436–40
 - nonuniform 427–33, 434
 - prototype failures 440–1
 - uniform 425–7
- fabrication of curved girders 385–6
- failure
 - modelling 258–64
 - interface elements 262–4
 - virtual crack closure technique 259–62

- thin steel plates and members 459–60
- failure strain 274–5
 - see also* ductility
- Federal Highway Administration ‘Curved Steel Bridge Research Project’ (FHWA-CSBRP) 384
- fibre curvature diagram 13
- finite element method 81, 83
 - cylindrical structures 440
 - differential settlement 441, 446–8, 449
 - displacement finite element model *see* displacement finite element model
 - light gauge steel members 483
 - plate stability analysis 56–70
 - derivation of elastic and geometric stiffness matrices 63–7
 - formulation 58–63
 - linearisation of internal force vector 61–3
 - numerical examples 67–9
 - total Lagrangian formulation of geometrically nonlinear continuum 58–60
 - stiffened composite structures 246–58
 - arc-length methods 250–3, 256
 - combined quasi-static/pseudo-transient method 256–8
 - dynamic methods 253–6
 - geometrically nonlinear analysis 248–58
 - linear eigenvalue analysis 246–8
 - Newton–Raphson methods 249–50
 - tapered steel members
 - linear 7–14
 - nonlinear 4–7
- finite slice approach 313–15
- finite strip method 81, 307
 - light gauge steel members 460–81
 - background 460–1
 - buckling in beams 477–81
 - comparison of different strip formulations 466–70, 471
 - compression members 470–7
 - cubic strips 463–4, 467–70
 - finite strip layout 461–2
 - generalisation of plate buckling and postbuckling analysis 465–6
 - linear strips 463, 466–7
 - quintic strips 464, 467–70
 - septic strips 464–5, 467–8
- first order shear deformation plate theory *see* Mindlin plate theory
- fixed-end conditions 392–4
- flanges
 - box-shaped stub-columns subjected to shear loading 291–4
 - composite steel-concrete members 218, 225, 226, 228, 230
 - effect of curvature on flange plate stability 395–407
 - centreline stiffened plates with stress gradient 396–9, 400
 - definition of compactness for flanges with stress gradient 399–407
 - flexural stiffness 87–8, 348–9
 - flow theory of plasticity *see* incremental/flow theory of plasticity
 - Flügge’s equations 422, 427–9
 - Fourier series 441–4
 - fracture mechanics 259
 - full transformation method 97–8
 - functionally-graded materials (FGMs) 147–8, 173
 - thermal postbuckling of FGM hybrid laminated plates 193–9*see also* ceramic-metal plates
- Galerkin function 59–60
- GDC method 316–17
- general buckling 436
- generalised beam theory 483
- generalised stiffness parameter (GSP) 316–17
- geometric stiffness matrix 247
 - bilinear plate element 62–3
 - derivation 63–7
- geometrically nonlinear continuum 58–60
- global buckling
 - composite steel-concrete members 214–16, 221, 231
 - curved plates 436
- graphite/epoxy composite 192–3, 194
- grillage model 81
- Guide Specifications for Horizontally Curved Highway Bridges 384, 401, 404, 405, 407
- Hanshin ‘Guidelines for the Design of Horizontally Curved Girder Bridges’ 384
- hardening rules 362–3
- hat section strut 470, 471
- hat-stiffened panels 239–42
- headed shear studs 228–31
- header tank 440
- heat curving 385–6

- higher-order shear deformation plate theory 174
- horizontal tank immersion tests 437–40
- hot-rolled composite steel-concrete beams 223, 224
- hybrid laminated plates 193–9
- hydrostatic external pressure 430–1, 437–40
- Hyogoken–Nanbu earthquake 269, 295
- I-shaped cross-sections (I-girders) 383
 - see also* curved plate girders
- I-stiffened panels 243, 257–8
- immovability condition 177–8
- imperfection factor (cylinders) 427
- imperfection parameter 181
- imperfections
 - cylindrical structures 427, 433–4, 436
 - light gauge steel members 457–8
- implicit dynamic methods 253–4
- incremental/flow theory of plasticity 117–18, 361–2
 - annular plates 136, 137, 138
 - circular plates 132–3, 134
 - polygonal plates 139–41, 142, 143
 - rectangular plates 120, 123–4, 125, 126, 129, 130, 131
- incremental strain vector 358
- inelastic local buckling 215–16, 221–2
- inelastic region 367–9, 399–401
- inextensional theory 441–5
- initial buckling 436
- initial out-of-straightness 326, 327–9
- interaction buckling
 - composite steel-concrete members 214–16, 221–2, 228–32
 - beams 228–31
 - columns 231–2
 - light gauge steel members 474–6
- interaction diagrams 322–3, 324
- interface elements 262–4
- interlaminar shear stresses 242, 245
- intermediate lateral supports 394–5
- intermediate stiffeners 476–7
- internal force vector 60, 66
 - linearisation of 61–3
- internal pressure 423–5
- isolated plates 269–80
 - in compression 269–75
 - in shear 275–80
- isotropic hardening 362–3
- J-stiffened panels 243
- joints/connections 452
- Kantorovich method 27–8, 29–36
 - derivation of buckling equations 30–2
 - solution procedure 32–6
- kinematic hardening 362–3
- Kirchhoff–Love hypothesis 171
- Kirchhoff plate theory (classical thin plate theory) 26, 56
 - exact relationship between plastic buckling stress and elastic buckling stress 138–41
 - plastic buckling 118
- knuckle 423–4
- Lagrange polynomials 156
- laminated plates 170–213
 - analytical method and asymptotic solutions 178–84
 - governing equations 174–8
 - thermal postbuckling of antisymmetric angle-ply laminated plates 184–8
 - thermal postbuckling of FGM hybrid laminated plates 193–9
 - thermal postbuckling of symmetric cross-ply laminated plates 188–90
 - with piezoelectric layers 191–3
- lateral flange bending moments 389, 390
- lateral pressure analogy 409–10
- lateral restraints 394–5
- lateral-torsional buckling (lateral buckling)
 - lipped channel beams 479–80
 - plane channel beams 477–8
 - tapered steel members *see* tapered steel members
- lateral-torsional stability of curved plate girders 390–5
- lifting curved girders 387–8
- light gauge steel members 451–85
 - buckling in beams 477–81
 - compression members 470–7
 - buckling stresses for lipped channel 470–3
 - interaction of modes 474–6
 - intermediately stiffened members 476–7
 - postbuckling stiffness 472, 473–4
 - finite strip type analysis *see* finite strip method
- future trends in analysis and design 481–3
 - current design specifications 481–2
 - direct strength method 482–3
 - finite element method 483
 - generalised beam theory 483

- local buckling in plates and systems of plates 453–60
 - behaviour in advanced elastic postbuckling range 459
 - effective width 456–7
 - effects of imperfections 457–8
 - energy equations 453–4
 - failure 459–60
 - lower bound method 454–6
 - reduced modulus of elasticity 456
 - semi-energy method 458–9
- limit points 249–50, 251, 257
- linear eigenvalue analysis 246–8
- linear finite element analysis
 - buckling of cylindrical structures 446–7
 - tapered steel members 7–14
- linear momentum 59
- linear operators 175, 203–8
- linear strips 463, 466–7
- linear temperature change 155, 166
- linearisation of internal force vector 61–3
- lipped channel beams 479–80
 - bent about an axis perpendicular to the symmetry axis 480–1
- lipped channel struts 470–7
- load-axial shortening curves 321–2, 323
- load-axial strain relationship 317–18
- load control 249
- load eccentricity
 - concrete-filled steel box columns 325–7, 328
 - curved plate girders 396–9, 400
- load-end displacement path 459, 460
- load-out-of-plane deflection relationship 369, 371, 373–4, 375
- load-vertical deflection relationship 369, 370, 373, 374, 377, 378
- local buckling
 - composite steel-concrete forms 214–16, 219–20, 222–8
 - beams 222–4
 - columns 225–8, 229, 230
 - modes 215
 - concrete-filled steel box columns 225, 226, 227, 229, 306–7, 309–12
 - curved girders 395–6
 - cylindrical structures 446
 - light gauge steel members 452
 - beams 477–81
 - under compression 470–7
 - finite strip method 466–8
 - plates and systems of plates 453–60
- local buckling coefficient 219–20
- local buckling stress 219–20
- longitudinal stiffeners
 - box columns with 299–300
 - curved web panels 411–12
- lower bound method 454–6, 470, 471
 - effective width concept 456–7
 - effects of imperfections 457–8
- material coordinate system 58
- matrix microcracking 258
- mechanical loading
 - ceramic-metal plates 154, 161–3, 164
 - laminated plates 172
- membrane-bending effect 66–7
- meridional stresses 423, 425, 446–8
- mesh-free methods 80–116
 - estimation of equivalent properties 85–89
 - formulation for stiffened and corrugated plates 89–98
 - displacements approximation 89–90
 - enforcement of essential boundary conditions 97–8
 - stability analysis of stiffened plates 93–7
 - transformation equations 90–3
- mesh-free Galerkin method 84–5
- numerical examples 100–12
 - clamped stiffened square isotropic plate with one stiffener under in-plane compression 108
 - simply supported stiffened plate under in-plane compression 100–5
 - simply supported rectangular stiffened plate with two stiffeners under in-plane compressions 108–109
 - simply supported stiffened plate with two stiffeners under in-plane compression 105–7
 - sinusoidally corrugated plate under uniaxial in-plane compression 111–12
 - stiffened sinusoidally corrugated plate under uniaxial in-plane compression 112, 113
 - stiffened trapezoidally corrugated plate under uniaxial in-plane compression 111
 - trapezoidally corrugated plate under uniaxial in-plane compression 109–11
 - validation studies 99–100
- Mindlin plate theory 26, 28–9, 117, 119–20, 138

- ceramic-metal plates 156, 157–61, 162, 163, 164
- elastic buckling of corrugated webs 341–56
 - elastically supported orthotropic plates 351–2
 - equivalent elastic constants 348–51
 - orthotropic rectangular Mindlin plate 342–6
- exact relationship between plastic buckling stress and elastic buckling stress 138–41
- minimum potential energy, principle of 27, 31, 454, 455, 459, 461
- mode-jumping 236, 237, 242, 244–5, 252, 258
- Moiré fringe patterns 239, 241, 244, 245
- moment-curvature-thrust relationships 313–15, 317–18
- moments, work done by 12–14
- monotonic loading 271
- motion of a continuum 58–60

- Newton–Raphson methods 249–50
- nodes, number of 90, 91, 97–8, 99–100, 101, 102
- non-compact sections 400
 - section limit 400, 401–3
- nonconforming plate element 56–7
- nondimensional linear operators 179, 208–11
- nonlinear finite element analysis
 - cylindrical structures 447–8, 449
 - stiffened composite structures 248–58
 - tapered steel members 4–7
- nonlinear force resultant 151
- nonlinear temperature change 155, 160–1, 165, 167
- nonuniform external pressure 427–33, 434
- nonuniform temperature change *see*
 - parabolic temperature loading;
 - tent-like temperature loading
- numerical analysis, design codes and 484

- one-third rule 405–6
- optimum rigidity of stiffener 276–7, 279–80
- orthotropic model 81
- orthotropic plates
 - analysing corrugated plates as 82–3
 - Mindlin plate theory and elastic buckling of corrugated webs 342–56
 - elastically supported 351–2
 - equivalent elastic constants 348–51
 - rectangular Mindlin plate 342–6
- parabolic temperature loading 175, 212–13
 - thermal postbuckling of symmetric cross-ply laminated plates 188–90
 - with piezoelectric layers 191–3, 194
- parametric studies
 - ceramic-metal plates 161–5
 - mechanical buckling 161–3
 - thermal buckling 163–5, 166, 167
- elasto-plastic and finite displacement analysis 367–72
- analytical models 369
- results 369–72
- shear buckling strength of corrugated steel webs 367–9
- partial (patch) buckling pressure 430, 431–3, 434
- peel stresses 243
- perturbation technique 178–84
- piezoelectric actuators 173
 - thermal postbuckling of symmetric cross-ply laminated plates with 191–3, 194
- pinned-end conditions 392
- pipe-shaped stub-columns 285–91
 - combined compression and bending 289–91
 - pure compression 287–9
- pipe sections, cantilever columns made of 296, 300–2
- plane channel beams 477–8
- plastic buckling 117–46
 - annular plates 133–8
 - circular plates 129–33
 - exact relationship between plastic buckling stress and elastic buckling stress 138–41
 - polygonal plates 138–41
 - rectangular plates 119–29, 130, 131
- plastic flow theory *see* incremental/flow theory of plasticity
- plastic region 367–9, 399–401
- plasticity
 - failure and 459
 - theories 117–18, 119–22, 361
 - see also* deformation theory of plasticity; incremental/flow theory of plasticity
- plate slenderness *see* width-to-thickness ratio
- plate stiffness 348, 349
- Poisson's ratio 85, 87–9
- polygonal plates 138–41
 - basic equations 138

- exact relationship between plastic buckling stress and elastic buckling stress 138–41
- plastic buckling stress factors for polygonal shapes 141, 142, 143
- postbuckling
 - cylindrical structures 436–40
 - light gauge steel members
 - under compression 472, 473–4
 - finite strip method 465–6, 468–70, 471
 - stiffened composite structures *see* stiffened composite structures
- potential energy
 - rectangular orthotropic Mindlin plate 344–6
 - stability analysis 153
 - stiffened plates 93–6
- Prandtl–Reuss theory 361
- prebuckling 436
- pressure
 - internal 423–5
 - nonuniform external 427–33, 434
 - uniform external 425–7
- prestressed concrete girders with corrugated steel webs (PCGCSW) 340–1, 351
- process zone 263
- proportional (Rayleigh) damping 254
- prototype failures 440–1, 442, 443
- pseudo-transient method 255–6, 263–4
 - combined quasi-static/pseudo-transient method 256–8
- PZT-5A 192–3, 194
- quasi-static continuation methods 248–53
 - arc-length methods 250–3, 256
 - combined quasi-static/pseudo-transient method 256–8
 - Newton–Raphson methods 249–50
- quintic strips 464, 467–70
- radial deflection 443, 444–5
- radial restraints 435–6
- radius ratio 136–8
- radius-thickness ratio parameter 287–91
- Ramberg–Osgood elastoplastic characteristic 121–2
- Rayleigh (proportional) damping 254
- rectangular plates 26–55
 - buckling 28–36
 - basic equations 28–9
 - derivation of buckling equations 30–2
 - Kantorovich procedure 29–30
 - solution procedure 32–6
 - numerical examples 36–44, 45, 46, 47, 48, 49, 50, 51, 52, 53
 - plastic buckling 119–29, 130, 131
 - basic equations 119–22
 - solutions for plates with two opposite sides simply supported 125–9, 130, 131
 - solutions for simply supported plates 122–5, 126
- reduced elastic modulus 456
 - postbuckling stiffness of light gauge steel members 465–6, 468–70, 471
 - under compression 472, 473–4
- reduced integration technique 57, 66
- reduced stiffness matrices 178
- Reissner–Mindlin theory of thick plates 57
 - see also* Mindlin plate theory
- relative column slenderness 328, 329, 332
- relative flexural rigidity 272–3
- residual stresses
 - composite steel-concrete beams 223, 224
 - composite steel-concrete columns 226, 227
 - concrete-filled steel box columns 307, 310, 312
 - parametric studies 326, 329–30
 - corrugated steel webs 372, 373, 375
 - curved girder fabrication 386
 - plates in compression 269–71
- resonant frequency 254
- Ritz method 342, 346–8, 354
- rotational restraints
 - corrugated web plates 344, 347, 351–2
 - effect of 355–6
 - cylindrical structures 435–6
- rotational stiffness 396–8
- scaling factors 99–100, 101, 102
- ‘scissoring’ crack extension mode 259–64
- secant modulus 121–2
- secant stiffness matrix 4–5
- semi-energy method 458–9, 470, 471
- septic strips 464–5, 467–8
- sequencing 388–9
- settlement, differential 441–8, 449
- shadow Moiré technique 239, 241, 244, 245
- shape functions 85, 156
- shear
 - box-shaped stub-columns subjected to shear loading 291–4
 - component plates in 275–80

- crack extension mode 259–64
- curved web panels 412–13
 - combined bending and shear 413–14
- loading of ceramic-metal plates 154, 158
- work done by shear forces 12–14
- shear buckling
 - corrugated webs 375–6, 377–8
 - shear buckling capacities 352–5
 - shear buckling strength 367–72, 374
 - cylindrical structures 446
- shear correction factor k 29, 36
- shear deformation 57, 160
- shear deformation plate theory 171
 - first order *see* Mindlin plate theory
 - higher-order 174
 - third order 156, 157–61, 162, 163, 164
- shear locking phenomenon 57
- shear modulus 350, 351
- silicon nitride 195–9
- silos 434–5, 440, 441, 442
- sinusoidally corrugated plates 81–2, 85
 - equivalent elastic properties 88–9
 - under uniaxial in-plane compression 111–12
 - stiffened plates 112, 113
- site assembly 388–9
- skin bays 236
- slender column buckling load 232
- slender cross-sections 400
- slenderness limits 319
 - composite steel-concrete beams 223, 224
 - composite steel-concrete columns 227, 230
 - flanges with stress gradient 399–407
- slenderness ratio 272, 275, 276
- slip theory of plasticity 117
- smart structures 173
- snap-through (snap-back) behaviour 249, 252, 263, 394–5, 436
- spacecraft 170
- spatial coordinate system 58
- square plates
 - finite element analysis 67–9
 - plastic buckling stress factors 141, 143
- stainless steel 195–9
- steel
 - stress-strain relationship 308, 309
 - yield strength 452
- steel-concrete composite members *see* composite steel-concrete members; concrete-filled steel box columns
- steel tube, yield strength of 326, 333–4
- stiffened composite structures 236–68
 - experimental observations 238–46
 - blade-stiffened panels 244–6
 - hat-stiffened panels 239–42
 - I- and J-stiffened panels 243
 - finite element modelling 246–58
 - geometrically nonlinear analysis 248–58
 - linear eigenvalue analysis 246–8
 - modelling failure 258–64
 - interface elements 262–4
 - virtual crack closure technique 259–62
- stiffened plates 80–1, 83, 112–13
 - centreline stiffened plates with stress gradient 396–9, 400
 - clamped square plate with one stiffener
 - under in-plane compression 108
 - under compression 269–71, 273–4, 275
 - mesh-free model formulation 89–98
 - stability analysis 93–7
 - under shear 276–7, 278, 279–80
 - simply supported under in-plane compressions 100–5
 - with two stiffeners 105–7, 108–9
- stiffeners
 - box-shaped stub-columns with combined compression and bending 280–1, 282–3, 284–5
 - under shear 291, 292–3, 294
 - cantilever box columns with longitudinal stiffeners 299–300
 - corrugated silos 441, 442, 443
 - fabricating curved girders 385–6
 - and local buckling of composite steel-concrete columns 306–7
- storage tanks 441–8, 449
- strain
 - lower bound method and 454–6
 - relationship between strains and displacements 357–8
- strain energy 344, 453–4
- strain energy release rate 259–64
- strain-gauges 239–42, 244–5, 246
- strength 269–304
 - box-shaped columns subjected to shear loading 292–3
 - cantilever columns
 - made of pipe sections 300–1
 - with longitudinal stiffeners 299–300
 - without longitudinal stiffeners 297–8
 - concrete-filled steel box columns
 - axial strength capacity 312–13
 - column strength analysis 315–17

- numerical results 318–20
- plates
 - in compression 273–4
 - in shear 277–8
- stub-columns
 - box-shaped subjected to combined compression and bending 282, 283
 - pipe-shaped subjected to combined compression and bending 289–90
 - pipe-shaped subjected to pure compression 287–8
- stress gradient
 - centreline stiffened plates with 396–9, 400
 - definition of compactness for flanges with 399–407
- stress-strain relationships
 - bilinear thick plate element 65
 - for concrete and steel 308, 309
 - corrugated steel web without concrete flanges 372
 - orthotropic rectangular Mindlin plate 343
 - plastic buckling 121–2
 - plastic flow theory 361–2
- strip heating 385
- stub-columns 280–94
 - box-shaped
 - combined compression and bending 280–5
 - shear loading 291–4
 - pipe-shaped 285–91
 - combined compression and bending 289–91
 - pure compression 287–9
- symmetric cross-ply laminated plates 188–90
 - with piezoelectric layers 191–3, 194
- tangent modulus 121–2
- tangent stiffness matrix 4–5, 61–3
 - stiffened composite panels 247, 253, 255
- tangential restraints 435–6
- tank structures 441–8, 449
- tapered shells 446–7
- tapered steel members 1–25
 - design strengths 18–23
 - codified rules 18–22, 23, 24
 - design recommendation 22–3
 - elastic buckling curves 14–18, 19, 20, 21, 22
 - linear finite element formulation 7–14
 - nonlinear finite element formulation 4–7
- tapering of flanges 242
- temperature change
 - linear 155, 165, 166
 - nonlinear 155, 160–1, 165, 167
 - parabolic temperature loading *see* parabolic temperature loading
 - tent-like temperature loading *see* tent-like temperature loading
 - uniform *see* uniform temperature rise
- see also* thermal buckling; thermal postbuckling
- temporary false-work towers 389
- tension crack extension mode 259–64
- tent-like temperature loading 175, 212
 - thermal postbuckling of antisymmetric angle-ply laminated plates 184–8
- thermal buckling 148
 - ceramic-metal plates 154–6, 163–5, 166, 167
 - laminated plates *see* laminated plates
- thermal expansion coefficient 151, 193–5, 196
- thermal postbuckling 170–213
 - antisymmetric angle-ply laminated plates 184–8
 - FGM hybrid laminated plates 193–9
 - symmetric cross-ply laminated plates 188–90
 - with piezoelectric layers 191–3, 194
- thermal postbuckling equilibrium path 184
- thermal stress resultants 152–3
- thick plates 117
 - Mindlin plate theory *see* Mindlin plate theory
 - plastic buckling *see* plastic buckling
- thickness ratio 117
 - buckling of rectangular plates 36, 37–40, 46, 47, 48
 - plastic buckling
 - annular plates 137–8, 141, 142, 143
 - circular plates 132–3, 134
 - rectangular plates 123, 124, 129, 130, 131
- thin plate theory *see* Kirchhoff plate theory
- third order shear deformation theory (TSDT) 156, 157–61, 162, 163, 164
- titanium alloy 196–8
- torsion 452
- torsional-flexural buckling 473–6, 480–1
- torsional stiffness 348, 350
- total Lagrangian formulation 58–60
- total strain theory *see* deformation theory of plasticity

- traction laws 262
 - transformation equations 90–3
 - transformation matrix 364–7
 - transition zone 355–6
 - transportation of curved girders 386–7
 - transverse shear stiffness 66–7, 348, 350–1
 - transverse stiffness 82
 - trapezoidally corrugated plates 81–2
 - equivalent elastic properties 85, 86–8
 - under uniaxial in-plane compression 109–11
 - stiffened plate 111
 - Treffitz criterion 153
 - triangular plates 141, 142
 - two-step crack closure technique 259

 - uniaxial compression 154, 158–60, 162–3, 164
 - uniform external pressure 425–7
 - uniform temperature rise
 - ceramic-metal plates 155, 160, 163–5
 - laminated plates 175, 212
 - thermal postbuckling of
 - antisymmetric angle-ply plates 185–7
 - thermal postbuckling of FGM hybrid plates 193–9
 - thermal postbuckling of symmetric cross-ply plates 188, 189
 - with piezoelectric layers 191–3
- V-load analysis 383–4
- V-type heating 385
- vacuum 440
- validation studies 99–100, 101, 102
- variable in-plane forces 26–55
 - buckling of rectangular plates 28–36
 - basic equations 28–9
 - derivation of buckling equations 30–2
 - Kantorovich procedure 29–30
 - solution procedure 32–6
 - numerical examples 36–44, 45, 46, 47, 48, 49, 50, 51, 52, 53
- venting 440
- virtual crack closure technique (VCCT) 259–62
-
- volume fraction
 - ceramic-metal plates 151, 160–1, 162, 163, 164–5, 166, 167
 - FGM hybrid laminated plates 194–5, 196–9
- Von Kármán equations 174–5, 237
 - ceramic-metal plates 148, 149, 154
- von Mises yield criterion 360–1
-
- web-flange model 291–4
- web plate stability and distortion 407–14
 - combined bending and shear 413–14
 - curved web behaviour 407–8
 - elastic buckling 408
 - geometric nonlinear effects 410–11
 - influence of longitudinal stiffeners 411–12
 - lateral pressure analogy 409–10
 - pure shear 412–13
- web slenderness for curved girders 410–12
- welded composite steel-concrete beams 223, 224
- wide flange sections 218, 225, 226, 228, 230
- width-to-thickness ratio (plate slenderness) 272, 307–8
 - ceramic-metal plates 162, 163, 164–5, 166, 167
 - compact-flange section limit 406–7
 - compact section limit 405
 - concrete-filled steel box columns 319–20, 326, 331–3
 - effect of curvature on flange plate stability 395, 401–3, 405, 406–7
 - non-compact section limit 401–3
- wind 441
- work done 10–14
- woven carbon-fibre fabrics 264
-
- yield criterion 360–1
- yield strength
 - steel 452
 - steel tube 326, 333–4
- yielding region 367–69, 399–401
- Young's modulus *see* elastic modulus
-
- z*-pinning 264
- zirconium oxide 196–98